A comprehensive journey on dutch organic clays

From element testing through constitutive modelling towards a novel cyclic multidirectional shear device

Chao, C.

DOI
10.4233/uuid:895bc87e-6cae-46c7-8a58-d173cced3b01

Publication date
2024

Document Version
Final published version

Citation (APA)
Chao, C. (2024). *A comprehensive journey on dutch organic clays: From element testing through constitutive modelling towards a novel cyclic multidirectional shear device*. [Dissertation (TU Delft), Delft University of Technology]. https://doi.org/10.4233/uuid:895bc87e-6cae-46c7-8a58-d173cced3b01

A Comprehensive Journey on Dutch Organic Clays

From Element Testing through Constitutive Modelling towards a Novel Cyclic Multidirectional Shear Device

A Comprehensive Journey on Dutch Organic Clays

From Element Testing through Constitutive Modelling towards a Novel Cyclic Multidirectional Shear Device

Dissertation

for the purpose of obtaining the degree of doctor
at Delft University of Technology
by the authority of the Rector Magnificus Prof. dr ir. T. H. J. J. van der Hagen
chair of the Board for Doctorates
to be defended publicly on
Thursday 31 October 2024 at 15:00 o'clock

by

Ching-Yu Chao

Master of Science in Civil Engineering,
National Cheng Kung University, Tainan, Taiwan,
born in Kaohsiung, Taiwan

This dissertation has been approved by the promotors.

Composition of the doctoral committee:

Rector Magnificus,	chairperson
Prof. dr. ir. C. Jommi,	Delft University of Technology, promotor
Dr. ir. W. Broere,	Delft University of Technology, copromotor

Independent members:

Prof. dr. A. Metrikine,	Delft University of Technology
Prof. dr. ir. L.J. Sluijs,	Delft University of Technology
Prof. dr. E. Romero Morales,	UPC Barcelona, Spain
Prof. dr. R. Felicetti,	Politecnico di Milano, Italy
Ir. J. van der Schrier,	Royal Haskoning DHV, Netherlands

Keywords: Dutch organic soils, element testing, constitutive modelling, bounding surface, elastoplastic-viscoplastic, cyclic-dynamic shearing apparatus.

Printed by: Ipskamp Printing

Front & Back: The cover features a motif that blends an ESEM photomicrograph of Dutch organic clay as the background, overlaid with design drawings of the apparatus developed in this thesis.

ISBN 978-94-6384-652-3

An electronic version of this dissertation is available at
http://repository.tudelft.nl/.

Dedicated to those who have supported me throughout this journey

CONTENTS

SUMMARY

In the Netherlands, natural gas extraction from the Groningen field has induced seismic activities, notably recording the highest magnitude of M_L 3.6 at Huizinge. Despite the lower magnitudes of these induced earthquakes compared to their natural counterparts, their impact is significantly magnified due to the shallow depths at which they occur and the high site amplification over areas with soft soils. In response, the Dutch Research Council (NWO) launched the DeepNL research programme to conduct thorough scientific research into these phenomena. The SOFTTOP project, part of this initiative, aims to fill the knowledge gaps regarding the effects of soft soil deposits on earthquake dynamics and subsequent soil responses. This thesis, nested within the SOFTTOP project, focuses on the cyclic and dynamic behaviours of soft organic clays, which are prevalent in the Netherlands' deltaic subsurface. It starts with a detailed investigation into the monotonic behaviours of these clays, laying the groundwork for further exploration into their cyclic and rate-dependent responses.

Through an extensive experimental programme, a characteristic organic diatomaceous clay from the Netherlands was tested under various stress paths, uncovering limitations in existing models. To address these, an advanced elastoplastic model, JMC-clay, was developed. Starting from a previous formulation for peats, modifications were made to the yield surface shape and the rotational hardening rule, enhancing the models' ability to predict pre-failure behaviours accurately. This foundational work paves the way for studying cyclic behaviour under 'slow' testing conditions, deliberately chosen to minimise the effects of non-uniform pore pressure distribution. The study's exploration into the slow cyclic response of Dutch organic clay has unearthed critical insights into the effects of loading frequency, soil composition, initial stress state, and cyclic stress amplitude on the soil's mechanical properties. Among the findings, the soil's cyclic response significantly depends on the cyclic strain amplitude.

A pivotal aspect of this thesis is extending the JMC-clay model to include cyclic behaviour, incorporating bounding surface plasticity for a more accurate and predictive modelling framework of soil behaviour under cyclic loading conditions. This development, however, brought to light challenges in model validation. Simulations indicated that a larger bounding surface, indicative of a higher apparent over-consolidation ratio (OCR), aligns more closely with experimental observations than anticipated. This suggests that contrary to the expected purely elastoplastic response, creep behaviour plays a significant role during consolidation, necessitating adjustments to the model to capture these observations accurately. The JMC-clay model is extended to include an elastoplastic-viscoplastic bounding surface formulation to capture time-dependent soil response. The strain-rate saturation feature of the coupled elastoplastic-viscoplastic framework requires further investigation with experimental data at a higher loading rate.

However, the existing equipment falls short when conducting 'fast' testing, designing and constructing a cyclic-dynamic multi-directional shear apparatus for organic soft

soils (CYC-DoSS) in-house aimed to fully cover the earthquake frequency spectrum. The development and application of the device, a state-of-the-art earthquake simulator, marks a significant leap in element testing. Designed to overcome the limitations of traditional testing apparatuses, the CYC-DoSS features digitally controlled servo-hydraulic actuators and in-house developed local response sensors, offering a comprehensive suite of measurement capabilities. The inclusion of advanced measurement techniques, such as P-wave and S-wave bender element measurements, accelerometers, and fibre optic pore pressure transducers, alongside custom-developed sensors for capturing detailed deformation patterns, pore pressure responses, and acceleration data, significantly enhances the ability to measure cyclic responses. This is crucial for accurate seismic risk assessment and mitigation strategies and enables a deeper insight into the dynamic behaviours of soft soils under seismic load.

By weaving together experimental research, advanced constitutive modelling, and the deployment of an innovative testing apparatus, this thesis presents a comprehensive approach to unravelling the behaviour of Dutch soft organic clays under seismic conditions. The contributions of this research extend beyond theoretical advancements, offering practical insights and methodologies to enhance the resilience of infrastructure in seismic-prone areas.

SAMENVATTING

Gaswinning uit de Groninger gasvelden heeft in Nederland geleid tot geïnduceerde aardbevingen, met de magnitude M_L 3.6 beving bij Huizinge als zwaarste geregistreerde beving. Ondanks dat de magnitude van deze geïnduceerde bevingen lager is vergeleken met natuurlijke bevingen, zijn de gevolgen aanzienlijk door de relatief geringe diepte waarop zij plaats vinden en de sterke opslingering die optreedt in de bovenste slappe lagen. Naar aanleiding van de Groninger aardbevingsproblematiek heeft de Nederlandse Organisatie voor Wetenschappelijk Onderzoek (NWO) het DeepNL onderzoeks programma gelanceerd, teneinde diepgaand wetenschappelijk onderzoek naar deze verschijnselen uit te doen voeren. Het SOFTTOP project, als onderdeel van dit initiatief, probeert de kennisleemten rondom het gedrag van slappe grondlagen onder aarbevingsbelasting te dichten. Dit proefschrift focust zich, binnen het SOFTTOP project, op het cyclisch en dynamisch gedrag van slappe organische kleisoorten, zoals die veelvuldig voorkomen in de bodem van de Nederlandse delta. Dit proefschrift vangt aan met een uitgebreide studie naar het gedrag van deze kleien onder monotone belasting, hetgeen de basis legt voor nadere studie naar het gedrag onder cyclische en belastingsnelheidsafhankelijke respons.

Door middel van een uitgebreid experimenteel programma is een typisch Nederlandse organische klei, met een aanzienlijk gehalte diatomeeën, getest onder verschillende belastingpaden. Dit heeft de beperkingen van bestaande materiaalmodellen blootgelegd. Om deze tekortkomingen op te lossen is JMC-Clay, een geavanceerd elastoplastisch materiaalmodel, ontwikkeld. Uitgaande van een bestaande modelbeschrijving voor veengronden, zijn aanpassingen gedaan aan de vorm van de bezwijkomhullende en aan de rotational hardening beschrijving, welke de geschiktheid van het model verbeteren om accuraat het materiaalgedrag tot het moment van bewijken te beschrijven. Dit vormt de basis om vervolgens het cyclisch gedrag te bestuderen onder 'traag' veranderende belastingcondities, zo gekozen dat de invloed van niet-uniforme waterspanningsverdeling minimaal is. Deze speurtocht door het traag cyclisch gedrag van Nederlandse organische kleien heeft belangrijke nieuwe inzichten opgeleverd met betrekking tot de invloed van wisselende belastingsnelheden, grondsamenstelling, initieële spannings-condities en de cyclische belastingamplitude op materiaaleigenschappen van de grond. Onder andere is duidelijk geworden dat de geotechnische respons onder cyclische belasting sterk afhangt van de cyclische rekamplitude.

Een kernpunt in dit proefschrift is de uitbreiding van JMC-Clay om ook cyclisch gedrag te kunnen beschrijven, door de invoering van een plastische bezwijkomhullende welke een meer accurate voorspelling van het grondgedrag onder cyclische belasting mogelijk maakt. Deze modelontwikkeling ging hand in hand met uitdagingenom het model ook te kunnen valideren. Modelsimulaties laten zien dat een grotere bezwijkomhullende, behorend bij een hogere dan verwachte overconsolidatie ratio (OCR), meer in lijn ligt met de uitkomsten van laboratoriumproeven. Dit suggereert dat, in tegen-

stelling tot het verwachte zuiver elastoplastiche gedrag, kruip een aanzienlijke invloed heeft op het grondgedrag tijdens consolidatie, en dat aanpassingen aan het materiaalmodel noodzakelijk zijn om dit gedrag accuraat te beschrijven. Het JMC-Clay model is vervolgens uitgebreid met een elastoplastich-viscoplastische bezwijkomhullende om het tijdsafhankelijke grondgedrag te kunnen beschrijven. De reksnelheidsafhankelijke verzadiging die in dit elastoplastisch-viscoplastisch model is besloten vraagt nog verder exeprimentele validatie met laboratoriumproeven bij hogere belastingsnelheden. Bestaande laboratoriumopstellingen schieten echter tekort waar het gaat om het uitvoeren van'snelle' proeven.

Door het eigenhandig ontwerpen en realiseren van een meerassig cyclisch-dynamisch schuifapparaat voor slappe orgaische gronden (CYC-DoSS) tracht dit project het volledige belastingfrequentiespectrum van (geïnduceerde) aardbevingen te bestrijken. De ontwikkeling en eerste toepassing van deze opstelling, een state-of-the-art aardbevingssimulator, betekent een grote sprong voorwaarts in laboratoriumproeven. Specifiek ontwikkeld om de beperkingen van traditionele opstellingen te overkomen, bevat CYC-DoSS digitaal aangestuurde servo-hydraulische aandrijvingen en speciaal ontwikkelde sensoren om de locale grondrespons te meten, waarmee een uitgebreide en veelomvattende set aan meetapparatuur gerealiseerd is. Het gebruik van geavanceerde meettechnieken, zoals P-golf en S-golf bender elements, versnellingsopnemers, waterspanningsmeters op basis van glasvezel, alsook speciaal binnen dit project ontwikkelde sensoren voor het meten van de locale deformatie van de grondmonsters, de waterspanningsfluctuaties en de versnellingen, vergroot de mogelijkheden om het cyclisch gedrag van de grond te meten aanzienlijk. Dit is cruciaal voor een nauwkeurige inschatting van aardbevingsrisico's en het vaststellen vaan beheersmaatregelen, en leidt tot verdiept inzicht in het dynamsich gedrag van slappe gronden onder invloed van aardbevingen.

Door het samensmelten van experimenteel onderzoek, geavanceerd constitutief modelleren van grondgedrag en de ingebruikname van een innovatieve laboratoriumopstelling, levert dit proefschrift een veelomvattende bijdrage aan het begrijpen van het gedrag slappe Nederlandse organische kleien onder aardbevingsbelastingen. Deze bijdrage reikt verder dan enkel theoretisch inzicht, en levert tevens practische kennis en toepassingsmogelijkheden om de betrouwbaarheid van infrastructuur in aardbevingsgevoelige gebieden te verbeteren.

PREFACE

Ralph Waldo Emerson once wrote, "Do not go where the path may lead, go instead where there is no path and leave a trail." As I reflect on the challenging journey that led to this PhD thesis, Emerson's words resonate profoundly with my experience. When I embarked on the study of Dutch organic clays cyclic behaviour, I realised that the available apparatus were inadequate to capture the intricacies and complexities of the response. While established paths existed, they were marked by gaps, revealing uncharted territories of knowledge.

Inspired by Emerson's call, I took the challenge not only of navigating these paths but of creating a new one. The result is the development of an apparatus that I hope will stand as my contribution to forging new directions in this field. The journey was far from easy. From conception to execution, I faced numerous obstacles. Yet, with each challenge, Emerson's words reminded me of the vital role of innovation and perseverance.

This thesis is more than just a scientific investigation into soil mechanics; it embodies my belief that researchers, like explorers, must be unafraid to venture into the unknown, challenge established norms, and create new tools and knowledge to deepening our understanding of the world.

Ching-Yu Chao
Delft, October 2024

1

INTRODUCTION

1

1.1. PROBLEM STATEMENT

In the Netherlands, induced seismic activity is recorded from the Groningen gas field, with the highest magnitude ever registered of M_L 3.6 at Huizinge. Although the magnitude of these induced earthquakes is relatively low compared to the one of natural earthquakes, they still cause damage to buildings and infrastructures due to their shallow depths and high site amplification in areas covered by soft soils (van Thienen-Visser and Breunese, 2015). In 2015, the Dutch Safety Board released a report entitled 'Earthquake Risks in Groningen' highlighting the insufficient attention given to the development of knowledge concerning gas extraction in the Groningen region in the past. In response to this concern, the Dutch Research Council (NWO) initiated the DeepNL research programme. This programme is designed to conduct comprehensive and independent scientific and applied research into the issue.

To elucidate the underlying geotechnical considerations driving this research, it is essential to discuss the specific attributes of shallow soil layers in seismic activity. The top 20-30m of shallow layers below the ground surface are responsible for approximately 80% of site amplification and almost all permanent displacements. Currently, questions concerning the impact of soft deposits on earthquake progression and subsequent soil response remain unanswered. Additionally, existing models do not take into account the short duration and repetitive nature of induced earthquakes, which significantly affect soil layers. There is an urgent need for research to enhance our understanding of how these soft top layers behave during cyclic and dynamic loadings. The SOFTTOP project aimed to address these gaps. It intended to augment the current analysis toolkit with appropriate constitutive models for sand and organic soils, the predominant soil types in the deltaic shallow subsurface. This research is one of the work packages under SOFTTOP, which specifically focused on researching the cyclic and dynamic behaviour of soft organic clays.

Given the broad objectives of the SOFTTOP project, the focus was directed towards a primary constituent of the deltaic shallow subsurface — soft organic clays, which were considered the 'weakest link' of the subsoil in the engineering response. Soft organic clays are predominant natural geomaterials found at the depths commonly explored for geotechnical engineering works in many deltaic areas worldwide. These clays have been characterised in previous studies by their high compressibility and relatively high friction angle, features that significantly influence their geotechnical behaviour. The fabric of these soft soils, often including amorphous organic matter, fibres, stems, wood fragments, and microorganisms like algae and plankton, along with silicate and calcium microfossils (Cheng et al., 2007), profoundly affects their response to stress and other environmental factors. Soft clays are susceptible to stress-induced anisotropy, and can lose their structure under relatively low stresses (Parry and Nadarajah, 1974; Burland, 1990; Hight et al., 1992; Callisto and Calabresi, 1998; Cotecchia and Chandler, 2000; Burland, 1990; Zdravković et al., 2002; McGinty, 2006; Pineda et al., 2016). Additionally, they exhibit time-dependent, or 'creep,' strains (Bjerrum, 1967; Graham et al., 1983; Sheahan et al., 1996).

Investigation into the cyclic behaviour of clay has been conducted by numerous researchers over the past decades. Sangrey et al. (1969) executed cyclic undrained tests on Newfield clay, identifying both excess pore pressure and irrecoverable strains under

cyclic shear stresses. This discovery parallels findings from other researchers who have studied a range of cohesive soils (Takahashi et al., 1980; Sheu, 1985; Zergoun, 1991; Zergoun and Vaid, 1994). Broad consensus across these studies highlights three main factors which govern the cyclic behaviour of clay: the stress or strain amplitude, consolidation history, and loading rate. Evidence suggests that cyclic loading can lead to a decrease in shear strength and stiffness of clay samples from their initial values. It has been experimentally demonstrated that this reduction in strength and stiffness is influenced by the applied stress or strain amplitude, soil structure, sensitivity, and the accumulation of excess pore pressure (Andersen et al., 1980; Azzouz et al., 1989; Yasuhara et al., 1992; Andersen, 2009; Andersen, 2015).

The rapid nature of seismic excitation does not allow enough time for dissipation of excess pore pressure in the in-situ state of clays. Consequently, laboratory experiments are usually performed under undrained conditions to emulate field drainage conditions. 'Slow' cyclic undrained tests, as defined by Boulanger and Idriss (2004), are conducted at a pace which allows pore pressure equalisation within the soil specimen. Conversely, 'fast' cyclic undrained tests do not permit equilibrium of pore pressure within the specimen. To ensure reliable measurement of pore water pressure, the tests are typically performed slowly enough, depending on the hydraulic conductivity and the size of the sample being tested.

To the aim of comprehensive understanding of the soil response under seismic events, it is essential to consider the effect of multidirectional loading, as studies have demonstrated that the response is influenced by multiple loading directions (Rutherford, 2012; Matsuda et al., 2013; Matsuda et al., 2016; Nhan and Matsuda, 2016; Yang et al., 2016). A few multidirectional direct simple shear systems have been developed to explore the soil behaviour under seismic loads (Jaime, 1975; Ishihara and Yamazaki, 1980; Boulanger et al., 1993; Duku et al., 2007; Rutherford and Biscontin, 2013; Rutherford, 2012). Since then, several commercial multidirectional simple shear equipment have been made available (Rudolph et al., 2014; Li et al., 2017), however, typically limited to a range of frequencies with a maximum of 5 Hz. Shafiee et al. (2017) improved the apparatus built by Duku et al. (2007) so that the device can apply realistic earthquake loadings under stress control. Recently, Bhaumik et al. (2023) presented a new multidirectional simple shear device based on the design of Rutherford and Biscontin (2013).

To model the experimental results collected so far, various constitutive approaches have been developed in the past decades. Elastic-plastic models suitable for soft clays are documented in the literature, with notable contributions by Hashiguchi (1977), Sekiguchi and Ohta (1977), Dafalias (1986), Yu (1998), Pestana and Whittle (1999), Wheeler et al. (2003), Dafalias et al. (2006), Jiang and Ling (2010), Sivasithamparam and Castro (2016), among others. Within the class of elastoplastic models featuring rotational hardening, two models are particularly significant for the context of this work: S-CLAY1 (Wheeler et al., 2003) and SANICLAY (Dafalias et al., 2006). They have been developed based on experimental results from central-northern European soft clays, and they have been subsequently refined and validated using data sets for a broad range of clays (e.g., Karstunen et al., 2005; Yildiz et al., 2009; Taiebat et al., 2010; Dafalias and Taiebat, 2014; Seidalinov and Taiebat, 2014; Sivasithamparam et al., 2015; Sivasithamparam and Castro, 2016; Dafalias et al., 2020; Rezania and Dejaloud, 2021). Rotational hardening is a pivotal component,

proving to be fundamental for accurately modelling and predicting the monotonic response of soft clays (Wheeler et al., 2003; Karstunen et al., 2005; Dafalias et al., 2006; Yildiz et al., 2009; Huang et al., 2011; Dafalias and Taiebat, 2013; Rezania et al., 2016; Rezania et al., 2018; Müthing et al., 2018; Shirmohammadi et al., 2021).

Interestingly, the presence of a robust elastoplastic formulation makes the extension to cyclic response relatively straightforward. Owing to its mathematical simplicity, bounding surface plasticity has been adopted by several researchers, such as Rezania et al. (2014) and Seidalinov and Taiebat (2014), to predict the cyclic behaviour of clay. Although quite effective, early bounding surface proposals proved not accurate in predicting pore pressure build up as a consequence of undrained cyclic loading. Amendments to the original formulation include the proposal by Shi et al. (2018), who introduced a hybrid plastic flow rule. The approach aims to more accurately predict the evolution of pore pressure during cyclic loading by eliminating the premature stabilisation observed when using image stress flow rules. In addition to bounding surface plasticity models, researchers have developed a variety of other formulations to capture the cyclic behaviour of clays. For example, Stallebrass and Taylor (1997) introduced a Three Surface Kinematic Hardening model (A3-SKH), which builds upon the established principles of transverse isotropic elasticity put forth by Graham and Houlsby (1983). Meanwhile, Fuentes et al. (2021) extended the existing anisotropic hypoplastic model for clays (Mašín, 2014) to create a new anisotropic hypoplastic model incorporating the Intergranular Strain Anisotropy (Fuentes and Triantafyllidis, 2015). Tafili (2020) bridged hypoplasticity and elastoplasticity in the Anamnesis model, which also accounts for rate effects such as creep and stress relaxation.

Exploring the literature, it was observed that validation and calibration of the previous models was limited in general to compression paths in the meridian plane. However, it is important to note that stress states and paths in real-world scenarios are rarely purely compressive. One crucial feature of these soils is stress-induced plastic anisotropy. While many current models incorporate this feature via a rotational hardening rule, there remains a paucity of information on how this stress-induced plastic anisotropy evolves when subjected to extensional stresses on the meridian plane. Although some attempts have been made to address this gap, most notably on Otaniemi clay and Shanghai soft clay (Wheeler et al., 2003; Huang et al., 2011), further research is still needed. Additionally, although there has been extensive international research on soft organic clays, including efforts to characterise these soils in the Netherlands (Tigchelaar et al., 2001; Den Haan, 2003; Cheng et al., 2004; Cheng et al., 2007; Wegman, 2020), advanced material modelling specifically for Dutch soft organic clays remains underdeveloped.

Current frameworks for modelling the cyclic behaviour of clay each have their own strengths and weaknesses. A study by Duque et al. (2022) assessed the predictive capabilities of four advanced constitutive models—CAM, AHP-ISA, SANICLAY-B, and A3-SKH—in relation to anisotropic fine-grained soils. Various conditions were used to validate these models' accuracy and reliability. Interestingly, only the CAM model could partially replicate the eight-shaped effective stress paths observed in undrained cyclic triaxial tests. SANICLAY-B stood out for its unique ability to realistically reproduce an increasing double strain amplitude following cyclic mobility. Predicting cycles to failure under varying cyclic load amplitudes remains a formidable challenge. While the CAM

and AHP-ISA models showed superior performance in reproducing these curves, they did so at the expense of requiring additional parameters. Notably, none of the models performed as proficiently under conditions of varying initial stress ratios as they did under isotropic conditions.

In light of the rate-dependent nature of soft soil behaviour, a couple of viscoplastic-elastoplastic bounding surface models have been formulated to account for variables such as creep strain, stress relaxation, and rate effects during monotonic loading. A limited number of researchers have attempted to validate or extend these models under cyclic loading conditions (Kaliakin, 1991; Shi et al., 2019; Huang et al., 2022). Nonetheless, most of these studies are restricted to a loading frequency of 2Hz, likely a consequence of the conventional 'slow' test protocols used to ensure uniform pore pressure distribution. As a result, the existing body of work may not fully represent the complex behaviour of soils under the high-frequency, dynamic loading conditions commonly experienced during seismic events.

While the dynamic properties, stress-strain behaviour, and post-cyclic responses of clays have been extensively researched, the specific cyclic behaviour of soft organic clays remains largely unexplored. Some studies have examined the cyclic behaviour of soft marine clays (Vucetic, 1988; Hyodo et al., 1999; Wichtmann et al., 2013; Pan et al., 2022). However, the impact of organic matter on these characteristics is often neglected. This gap is particularly surprising given that previous work by Hight et al. (1992) and Paul and Barras (1999) had shown the substantial influence of organic matter on the monotonic behaviour of soils. For instance, the presence of organic material in the soil matrix of Bothkennar clay was found to significantly affect soil plasticity and compressibility, with organic cement playing a crucial role in maintaining large soil aggregates or pellets. While the significance of the initial stress state preceding cyclic loadings on soils has been underscored by multiple researchers (Wichtmann et al., 2013; Wichtmann and Triantafyllidis, 2018; Tafili et al., 2021; Ushev and Jardine, 2020), efforts to model and characterise the cyclic behaviour under varying initial stress states have been limited. This gap in our understanding is particularly relevant given that soils in real-world conditions are seldom exposed to isotropic stress states.

Filling the previous gap in understanding sof organic clays response under earthquake and dynamic loading conditions necessitates the use of advanced testing equipment capable of assessing the influence of hydro-mechanical coupling on soil behaviour. Traditional simple shear devices—and by extension, their more modern, multidirectional counterparts—have a few limitations (Lucks et al., 1972; Shen et al., 1978; Vucetic and Lacasse, 1982; Saada et al., 1983; Budhu, 1984; Budhu, 1985; Budhu and Britto, 1987; DeGroot et al., 1994; Reyno et al., 2005). One key issue is that these devices cannot control shear stress on the specimen's lateral sides. This makes it impossible to achieve a uniform stress state, which has to be assumed as a hypothesis in processing the results of the tests. Additionally, these conventional setups lack the ability to measure lateral stresses, creating a knowledge gap about the stress state and stress paths within the soil samples.

Accurate pore water pressure measurement is indispensable for the cyclic testing of soils, particularly to evaluate the role of hydro-mechanical coupling on the soils response. In standard configurations, pore water pressure in simple shear devices is de-

rived either from changes in vertical stress in constant-height tests or via pressure transducers situated at the sample's base. Reliable pore water pressure measurements require tests to be conducted at speeds adjusted for uniform pore pressure distribution within the sample. However, recent studies indicate that achieving uniform pore water pressure in soft soils may be a significant challenge, even under controlled, monotonic loading conditions. This is a concern of particular relevance when considering the high loading frequencies typical of earthquakes, where rate effects are pivotal in determining the behaviour of soft soils.

This research aims to start addressing current experimental and theoretical limitations to advance the knowledge on the behaviour of Dutch soft organic clays, starting from monotonic behaviour as a key foundation towards cyclic response, by means of a comprehensive research approach that includes both experimental testing and constitutive modelling. A typical organic diatomaceous clay from the Netherlands was tested in an extensive experimental programme, including monotonic and non-monotonic stress paths on both compression and extension sides. The data confirm a few limitations of currently available models, which are amended by changing the shape of the yield surface and improving the rotational hardening rule. The comparison between experimental data over a variety of stress paths and numerical simulations demonstrates the advantages of the new model over previous ones in accurately describing the pre-failure behaviour.

After thoroughly investigating and accurately capturing the monotonic behaviour of Dutch soft organic clays, the scope of the research is extended to the cyclic behaviour. Specifically, it focuses on the impact of organic matter and initial stress states during 'slow' test conditions, deliberately excluding the influence of non-uniform pore pressure distribution. Data gathered from these 'slow' cyclic tests are employed to further validate and extend the monotonic model, developing a bounding surface formulation.

The limitations of existing multidirectional shear systems, coupled with the critical need to understand the behaviour of soft soils under cyclic and dynamic conditions, have spurred the design and manufacturing of the cyclic-dynamic multidirectional shear apparatus for organic soft soils (CYC-DoSS). This apparatus aims to investigate the multidirectional hydro-mechanical coupled response of soft organic soils commonly found in the deltaic regions of the Netherlands. Notably, the new system addresses several pressing issues: it ensures limited mechanical compliance, permits higher loading frequencies, and provides accurate measurements of stress, strain, and pore water pressure under a wide range of loading rates—both slow and fast. Utilising the newly constructed CYC-DoSS, 'fast' tests can now be performed and their results validated against the proposed bounding surface model.

1.2. RESEARCH OBJECTIVES

The research aims to address significant gaps in the understanding of the behaviour of Dutch soft organic clays under both monotonic and cyclic loading conditions. It focuses on stress-induced plastic anisotropy, the role of organic matter, and the impact of initial stress states in of Dutch soft organic clays. It aims to contribute to the field by:

- Conducting experimental tests: Undertaking a comprehensive experimental testing programme on organic clay samples from the Netherlands. The experiments begin with the static paths to build a foundation for interpreting the cyclic behaviour of the organic clay under 'slow' cyclic tests. The tests aim to understand the limitations of existing constitutive models and improve them, especially concerning the role of organic matter and the plastic anisotropy induced by varied loading conditions.

- Refining existing models: Extending current constitutive models for predicting the behaviour of soft organic clays by incorporating specific factors like organic matter, anisotropy, and time-dependent behaviour. The proposed models undergo rigorous validation through experimental data. After calibration against laboratory data, they can be implemented in numerical platforms to provide a more accurate representation of real-world conditions.

- Developing advanced testing apparatus: Setting up an innovative cyclic shear apparatus called CYC-DoSS. This apparatus aims to provide high-frequency, multidirectional, and complex cyclic loading patterns. Equipped with state-of-the-art measurement systems like bender elements, accelerometers, and pore pressure transducers, it will yield a unique and reliable dataset for model development, calibration, and validation. This addresses existing limitations in current equipment, which cannot control or measure lateral stresses or offer nuanced insights into hydro-mechanical coupling.

This research aims to push the boundaries of current knowledge and technology, providing more reliable models and datasets for the understanding and application of Dutch soft organic clays in the engineering practice.

1

1.3. THESIS ORGANISATION

This thesis begins by studying the behaviour of organic clay under static conditions, which serves as a reliable basis for understanding its cyclic behaviour. The constitutive model is then developed based on experimental observations. Lastly, the thesis presents the development of a new experimental setup. The chapters of the thesis can potentially be converted into independent research papers or are currently under review:

- Chapter 2 delves into a thorough experimental programme on typical organic soft clay from the Netherlands. This chapter explores static stress paths in triaxial compression and extension. The findings point out certain limitations in existing models, which were addressed by modifying the yield surface shape and enhancing the rotational hardening rule.
- Chapter 3 presents results from 'slow' cyclic tests on typical organic soft clay from the Netherlands. The chapter investigates the cyclic response under various initial stress states, organic content, and loading amplitudes. Data from these tests are used to extend and validate the proposed model, adopting a bounding surface formulation.
- Chapter 4 discusses the role of rate-dependency when modelling the cyclic behaviour of organic soft clay. The proposed model is extended to an elastoplastic-viscoplastic bounding surface formulation. The model is validated with a relevant set of experimental data from slow cyclic tests.
- Chapter 5 introduces a cutting-edge multidirectional shear device developed as part of this work and now available at the Geo-Engineering Section at TU Delft. This device surpasses previous equipment by enabling higher loading frequencies and a broader array of multidirectional cyclic loading patterns. Preliminary test results are provided to showcase the complex loading conditions that can be achieved. Thorough validation tests with commercial apparatus are performed on organic soil samples.
- Chapter 6 provides a comprehensive summary of the results, conclusions, and recommendations derived from this research.

The thesis is supplemented by three appendices:

- Appendix A describes the calibration of testing equipment utilised in the thesis.
- Appendix B presents the sensitivity analysis on the model parameters of the JMC-Clay bounding surface model.
- Appendix C provides the sensitivity analysis on the model parameters of the JMC-Clay elastoplastic-viscoplastic bounding surface model.

An illustrative map of the thesis is displayed in Figure 1.1.

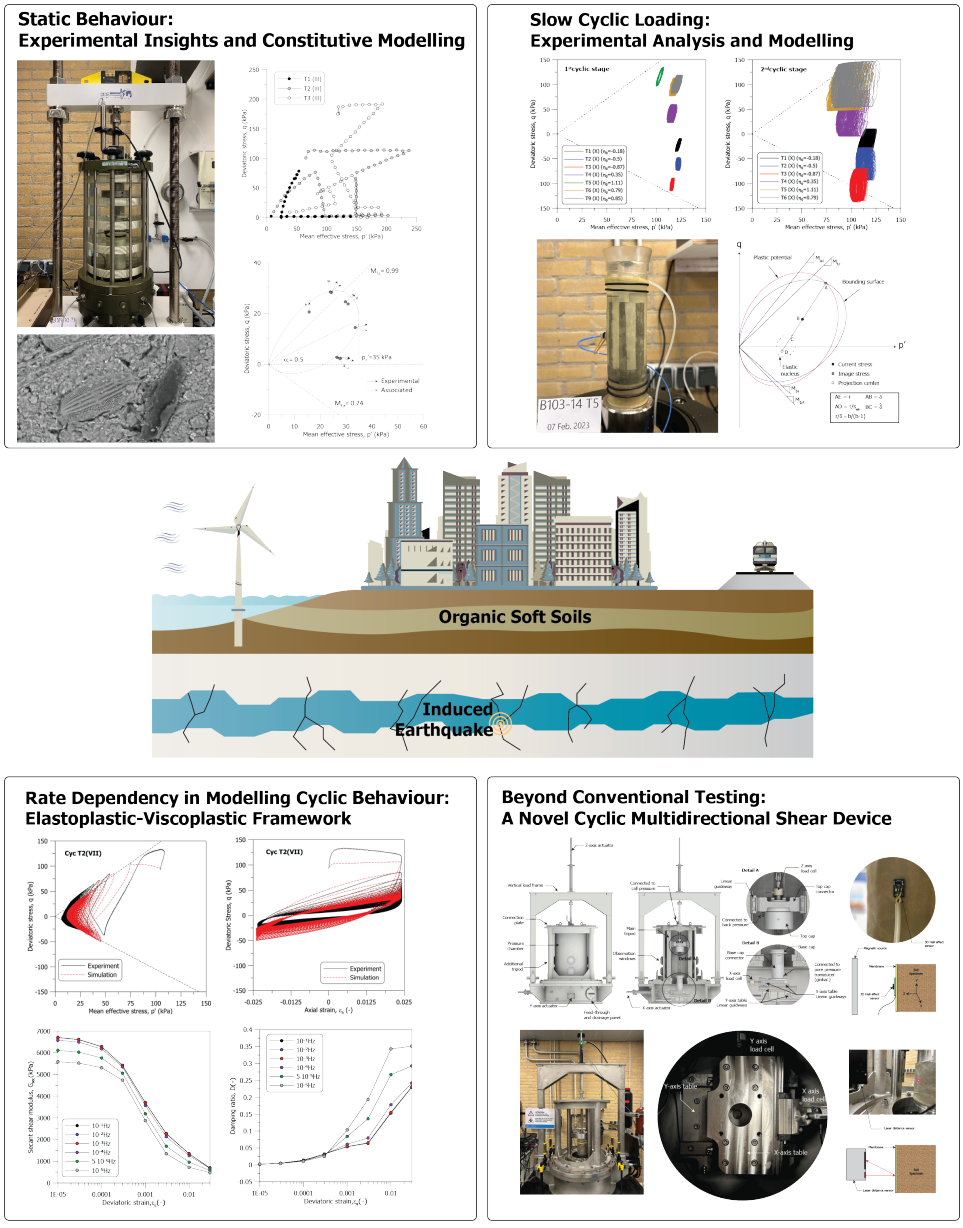

Figure 1.1: Illustrative map of the thesis

BIBLIOGRAPHY

Andersen, K. H. (2009). Bearing capacity under cyclic loading—offshore, along the coast, and on land. the 21st bjerrum lecture presented in oslo, 23 november 2007. *Canadian Geotechnical Journal*, *46*(5), 513–535.

Andersen, K. H. (2015). Cyclic soil parameters for offshore foundation design. *Frontiers in offshore geotechnics III*, *5*.

Andersen, K. H., Rosenbrand, W. F., Brown, S. F., & Pool, J. H. (1980). Cyclic and static laboratory tests on drammen clay. *Journal of the Geotechnical Engineering Division*, *106*(5), 499–529.

Azzouz, A. S., Malek, A. M., & Baligh, M. M. (1989). Cyclic behavior of clays in undrained simple shear. *Journal of Geotechnical Engineering*, *115*(5), 637–657.

Bhaumik, L., Rutherford, C. J., Olson, S. M., Hashash, Y. M., Numanoglu, O. A., Cerna-Diaz, A. A., & Weaver, T. (2023). A multidirectional cyclic direct simple shear device for characterizing dynamic soil behavior. *Geotechnical Testing Journal*, *46*(2).

Bjerrum, L. (1967). Engineering geology of norwegian normally-consolidated marine clays as related to settlements of buildings. *Geotechnique*, *17*(2), 83–118.

Boulanger, R. W., Chan, C. K., Seed, H. B., Seed, R. B., & Sousa, J. B. (1993). A low-compliance bi-directional cyclic simple shear apparatus. *Geotechnical Testing Journal*, *16*(1), 36–45.

Boulanger, R. W., & Idriss, I. M. (2004). *Evaluating the potential for liquefaction or cyclic failure of silts and clays*. Citeseer.

Budhu, M. (1984). Nonuniformities imposed by simple shear apparatus. *Canadian Geotechnical Journal*, *21*(1), 125–137.

Budhu, M. (1985). Lateral stresses observed in two simple shear apparatus. *Journal of Geotechnical Engineering*, *111*(6), 698–711.

Budhu, M., & Britto, A. (1987). Numerical analysis of soils in simple shear devices. *Soils and Foundations*, *27*(2), 31–41.

Burland, J. (1990). On the compressibility and shear strength of natural clays. *Géotechnique*, *40*(3), 329–378.

Callisto, L., & Calabresi, G. (1998). Mechanical behaviour of a natural soft clay. *Géotechnique*, *48*(4), 495–513.

Cheng, X., Ngan-Tillard, D., & Den Haan, E. (2007). The causes of the high friction angle of dutch organic soils. *Engineering geology*, *93*(1-2), 31–44.

Cheng, X., Janssen, H., & Barends, F. B. (2004). A combination of esem, edx and xrd studies on the fabric of dutch organic clay from oostvaardersplassen (netherlands) and its geotechnical implications. *Applied Clay Science*, *25*(3-4), 179–185.

Cotecchia, F., & Chandler, R. (2000). A general framework for the mechanical behaviour of clays. *Géotechnique*, *50*(4), 431–447.

Dafalias, Y. (1986). An anisotropic critical state soil plasticity model. *Mechanics research communications*, *13*(6), 341–347.

Dafalias, Y., Manzari, M. T., & Papadimitriou, A. G. (2006). Saniclay: Simple anisotropic clay plasticity model. *International Journal for Numerical and Analytical Methods in Geomechanics*, *30*(12), 1231–1257.

Dafalias, Y., & Taiebat, M. (2013). Anatomy of rotational hardening in clay plasticity. *Géotechnique*, *63*(16), 1406–1418.

Dafalias, Y., & Taiebat, M. (2014). Rotational hardening with and without anisotropic fabric at critical state. *Géotechnique*, *64*(6), 507–511.

Dafalias, Y., Taiebat, M., Rollo, F., & Amorosi, A. (2020). Convergence of rotational hardening with bounds in clay plasticity. *Géotechnique Letters*, *10*(1), 16–19.

DeGroot, D. J., Germaine, J. T., & Ladd, C. C. (1994). Effect of nonuniform stresses on measured dss stress-strain behavior. *Journal of geotechnical engineering*, *120*(5), 892–912.

Den Haan, E. (2003). Sample disturbance of soft organic oostvaardersplassen clay. *Deformation Characterstics of Geomaterials, Di Benedetto et al.(eds)-2003*, 49–55.

Duku, P. M., Stewart, J. P., Whang, D. H., & Venugopal, R. (2007). Digitally controlled simple shear apparatus for dynamic soil testing. *Geotechnical Testing Journal*, *30*(5), 368–377.

Duque, J., Tafili, M., Seidalinov, G., Mašín, D., & Fuentes, W. (2022). Inspection of four advanced constitutive models for fine-grained soils under monotonic and cyclic loading. *Acta Geotechnica*, *17*(10), 4395–4418.

Fuentes, W., & Triantafyllidis, T. (2015). Isa model: A constitutive model for soils with yield surface in the intergranular strain space. *International Journal for Numerical and Analytical Methods in Geomechanics*, *39*(11), 1235–1254.

Fuentes, W., Mašín, D., & Duque, J. (2021). Constitutive model for monotonic and cyclic loading on anisotropic clays. *Géotechnique*, *71*(8), 657–673.

Graham, J., Crooks, J., & Bell, A. L. (1983). Time effects on the stress-strain behaviour of natural soft clays. *Géotechnique*, *33*(3), 327–340.

Graham, J., & Houlsby, G. (1983). Anisotropic elasticity of a natural clay. *Géotechnique*, *33*(2), 165–180.

Hashiguchi, K. (1977). An expression of anisotropy in a plastic constitutive equation of soils. *Constitutive Equations of Soils*, 302–305.

Hight, D., Bond, A., & Legge, J. (1992). Characterization of the bothkennaar clay: An overview. *Géotechnique*, *42*(2), 303–347.

Huang, M., Liu, Y., & Sheng, D. (2011). Simulation of yielding and stress–stain behavior of shanghai soft clay. *Computers and Geotechnics*, *38*(3), 341–353.

Huang, Z., Shi, L., Sun, H., & Cai, Y. (2022). A simple bounding surface elasto-viscoplasticity model for marine clays under monotonic and cyclic loading. *Ocean Engineering*, *266*, 113129.

Hyodo, M., Hyde, A. F., Yamamoto, Y., & Fujii, T. (1999). Cyclic shear strength of undisturbed and remoulded marine clays. *Soils and Foundations*, *39*(2), 45–58.

Ishihara, K., & Yamazaki, F. (1980). Cyclic simple shear tests on saturated sand in multidirectional loading. *Soils and Foundations*, *20*(1), 45–59.

Jaime, A. (1975). A two-direction cyclic shear apparatus. *5th Pan American Conference on Soil Mechanics and Foundation Engineering, Buenos Aires, Argentina*, *2*, 395–402.

Jiang, J., & Ling, H. I. (2010). A framework of an anisotropic elastoplastic model for clays. *Mechanics Research Communications*, *37*(4), 394–398.

Kaliakin, V. N. (1991). Application of the elastoplastic-viscoplastic bounding surface model to cyclic loading.

Karstunen, M., Krenn, H., Wheeler, S. J., Koskinen, M., & Zentar, R. (2005). Effect of anisotropy and destructuration on the behavior of murro test embankment. *International Journal of Geomechanics*, *5*(2), 87–97.

Li, Y., Yang, Y., Yu, H.-S., & Roberts, G. (2017). Monotonic direct simple shear tests on sand under multidirectional loading. *International Journal of Geomechanics*, *17*(1), 04016038.

Lucks, A. S., Christian, J. T., Brandow, G. E., & Höeg, K. (1972). Stress conditions in ngi simple shear test. *Journal of the Soil Mechanics and Foundations Division*, *98*(1), 155–160.

Mašín, D. (2014). Clay hypoplasticity model including stiffness anisotropy. *Géotechnique*, *64*(3), 232–238.

Matsuda, H., Nhan, T. T., & Ishikura, R. (2013). Prediction of excess pore water pressure and post-cyclic settlement on soft clay induced by uni-directional and multi-directional cyclic shears as a function of strain path parameters. *Soil Dynamics and Earthquake Engineering*, *49*, 75–88.

Matsuda, H., Nhan, T. T., & Sato, H. (2016). Estimation of multi-directional cyclic shear-induced pore water pressure on clays with a wide range of plasticity indices. *Proceedings of the second international conference on civil, structrual and transportation engineering*, 1–8.

McGinty, K. (2006). *The stress-strain behaviour of bothkennar clay* [Thesis].

Müthing, N., Zhao, C., Hölter, R., & Schanz, T. (2018). Settlement prediction for an embankment on soft clay. *Computers and Geotechnics*, *93*, 87–103.

Nhan, T., & Matsuda, H. (2016). A development of pore water pressure model for multi-directional cyclic shearing on normally consolidated clays. *Proceedings of the sixty nineth Canadian geotechnical conference, Vancouver, BC, Canada*, 8.

Pan, K., Yuan, Z., Zhao, C., Tong, J., & Yang, Z. (2022). Undrained shear and stiffness degradation of intact marine clay under monotonic and cyclic loading. *Engineering Geology*, *297*, 106502.

Parry, R., & Nadarajah, V. (1974). Anisotropy in a natural soft clayey silt. *Engineering Geology*, *8*(3), 287–309.

Paul, M., & Barras, B. (1999). Role of organic material in the plasticity of bothkennar clay. *Géotechnique*, *49*(4), 529–535.

Pestana, J. M., & Whittle, A. J. (1999). Formulation of a unified constitutive model for clays and sands. *International Journal for Numerical and Analytical Methods in Geomechanics*, *23*(12), 1215–1243.

Pineda, J., Suwal, L., Kelly, R., Bates, L., & Sloan, S. (2016). Characterisation of ballina clay. *Géotechnique*, *66*(7), 556–577.

Reyno, A., Airey, D., & Taiebat, H. (2005). Influence of height and boundary conditions in simple shear tests. *International Symposium on Frontiers in Offshore Geotechnics*.

Rezania, M., & Dejaloud, H. (2021). Bs-clay1: Anisotropic bounding surface constitutive model for natural clays. *Computers and Geotechnics*, *135*, 104099.

Rezania, M., Dejaloud, H., & Nezhad, M. M. (2014). Sclay1s-bs: An anisotropic model for simulation of cyclic behaviour of clays. In *Geomechanics from micro to macro* (pp. 670–675). CRC Press.

Rezania, M., Nguyen, H., Zanganeh, H., & Taiebat, M. (2018). Numerical analysis of ballina test embankment on a soft structured clay foundation. *Computers and Geotechnics*, *93*, 61–74.

Rezania, M., Taiebat, M., & Poletti, E. (2016). A viscoplastic saniclay model for natural soft soils. *Computers and Geotechnics*, *73*, 128–141.

Rudolph, C., Grabe, J., & Albrecht, I. (2014). Simple shear tests with a varying shearing direction during cyclic shearing. *Géotechnique Letters*, *4*(2), 102–107.

Rutherford, C. J., & Biscontin, G. (2013). Development of a multidirectional simple shear testing device. *Geotechnical Testing Journal*, *36*(6), 858–866.

Rutherford, C. J. (2012). *Development of a multi-directional direct simple shear testing device for characterization of the cyclic shear response of marine clays*. Texas A&M University.

Saada, A. S., Fries, G., & Ker, C.-C. (1983). Stress induced in short cylinders subjected to axial deformation and lateral pressures. *Soils and Foundations*, *23*(1), 114–118.

Sangrey, D., Henkel, D., & Esrig, M. I. (1969). The effective stress response of a saturated clay soil to repeated loading. *Canadian Geotechnical Journal*, *6*(3), 241–252.

Seidalinov, G., & Taiebat, M. (2014). Bounding surface saniclay plasticity model for cyclic clay behavior. *International Journal for Numerical and Analytical Methods in Geomechanics*, *38*(7), 702–724.

Sekiguchi, H., & Ohta, H. (1977). Induced anisotropy and time dependancy in clays. *9th ICSMFE. Tokyo*, p163–175.

Shafiee, A., Stewart, J., Venugopal, R., & Brandenberg, S. (2017). Adaptation of broadband simple shear device for constant volume and stress-controlled testing. *Geotechnical Testing Journal*, *40*(1), 15–28.

Sheahan, T. C., Ladd, C. C., & Germaine, J. T. (1996). Rate-dependent undrained shear behavior of saturated clay. *Journal of Geotechnical Engineering*, *122*(2), 99–108.

Shen, C., Sadigh, K., & Herrmann, L. (1978). An analysis of ngi simple shear apparatus for cyclic soil testing. In *Dynamic geotechnical testing*. ASTM International.

Sheu, W.-Y. (1985). Modeling of stress-strain-strength behavior of a clay under cyclic loading. *Dissertation Abstracts International Part B: Science and Engineering[DISS. ABST. INT. PT. B- SCI. & ENG.]*, *45*(9).

Shi, Z., Finno, R. J., & Buscarnera, G. (2018). A hybrid plastic flow rule for cyclically loaded clay. *Computers and Geotechnics*, *101*, 65–79.

Shi, Z., Hambleton, J. P., & Buscarnera, G. (2019). Bounding surface elasto-viscoplasticity: A general constitutive framework for rate-dependent geomaterials. *Journal of Engineering Mechanics*, *145*(3), 04019002.

Shirmohammadi, A., Hajialilue-Bonab, M., & Dadras-Ajirloo, D. (2021). Application of a simplified anisotropic constitutive model for soft structured clay on embankment failure. *International Journal of Geomechanics*, *21*(8), 04021125.

Sivasithamparam, N., & Castro, J. (2016). An anisotropic elastoplastic model for soft clays based on logarithmic contractancy. *International Journal for Numerical and Analytical Methods in Geomechanics*, *40*(4), 596–621.

Sivasithamparam, N., Karstunen, M., & Bonnier, P. (2015). Modelling creep behaviour of anisotropic soft soils. *Computers and Geotechnics*, *69*, 46–57.

Stallebrass, S., & Taylor, R. (1997). The development and evaluation of a constitutive model for the prediction of ground movements in overconsolidated clay. *Géotechnique*, *47*(2), 235–253.

Tafili, M. (2020). *On the behaviour of cohesive soils: Constitutive description and experimental observations* [Thesis].

Tafili, M., Wichtmann, T., & Triantafyllidis, T. (2021). Experimental investigation and constitutive modeling of the behaviour of highly plastic lower rhine clay under monotonic and cyclic loading. *Canadian Geotechnical Journal*, *58*(9), 1396–1410.

Taiebat, M., Dafalias, Y., & Peek, R. (2010). A destructuration theory and its application to saniclay model. *International Journal for Numerical and Analytical Methods in Geomechanics*, *34*(10), 1009–1040.

Takahashi, M., Hight, D., & Vaughan, P. (1980). Effective stress changes observed during undrained cyclic triaxial tests on clay. *International Symposium on Soils under Cyclic and Transient Loading*, *1*, 201–209.

Tigchelaar, J., Feijter, J. W. d., & Haan, E. J. d. (2001). Shear tests on reconstituted oostvaardersplassen clay. In *Soft ground technology* (pp. 67–81).

Ushev, E., & Jardine, R. (2020). The behaviour of bolders bank glacial till under undrained cyclic loading. *Géotechnique*, 1–19.

van Thienen-Visser, K., & Breunese, J. (2015). Induced seismicity of the groningen gas field: History and recent developments. *The Leading Edge*, *34*(6), 664–671.

Vucetic, M., & Lacasse, S. (1982). Specimen size effect in simple shear test. *Journal of the Geotechnical Engineering Division*, *108*(12), 1567–1585.

Vucetic, M. (1988). Normalized behavior of offshore clay under uniform cyclic loading. *Canadian Geotechnical Journal*, *25*(1), 33–41.

Wegman, T. (2020). Analysis of undrained soil behaviour of dutch organic clay in k0-consolidated triaxial tests.

Wheeler, S. J., Näätänen, A., Karstunen, M., & Lojander, M. (2003). An anisotropic elastoplastic model for soft clays. *Canadian Geotechnical Journal*, *40*(2), 403–418.

Wichtmann, T., Andersen, K., Sjursen, M., & Berre, T. (2013). Cyclic tests on high-quality undisturbed block samples of soft marine norwegian clay. *Canadian Geotechnical Journal*, *50*(4), 400–412.

Wichtmann, T., & Triantafyllidis, T. (2018). Monotonic and cyclic tests on kaolin: A database for the development, calibration and verification of constitutive models for cohesive soils with focus to cyclic loading. *Acta Geotechnica*, *13*(5), 1103–1128.

Yang, M., Taiebat, M., & Vaid, Y. (2016). Bidirectional monotonic and cyclic shear testing of soils: State of knowledge. *Proceedings of the sixty nineth Canadian geotechnical conference, Vancouver, BC, Canada*.

Yasuhara, K., Hirao, K., & Hyde, A. F. (1992). Effects of cyclic loading on undrained strength and compressibility of clay. *Soils and Foundations*, *32*(1), 100–116.

Yildiz, A., Karstunen, M., & Krenn, H. (2009). Effect of anisotropy and destructuration on behavior of haarajoki test embankment. *International Journal of Geomechanics*, *9*(4), 153–168.

Yu, H.-S. (1998). Casm: A unified state parameter model for clay and sand. *International journal for numerical and analytical methods in geomechanics*, *22*(8), 621–653.

Zdravković, L., Potts, D., & Hight, D. (2002). The effect of strength anisotropy on the behaviour of embankments on soft ground. *Géotechnique*, *52*(6), 447–457.

Zergoun, M., & Vaid, Y. (1994). Effective stress response of clay to undrained cyclic loading. *Canadian Geotechnical Journal*, *31*(5), 714–727.

Zergoun, M. (1991). *Effective stress response of clay to undrained cyclic loading* [Thesis].

2

Monotonic Behaviour: Experimental Insights and Modelling

In building science, as in building life, a solid foundation is everything. Without it, nothing holds.

Carl Sagan

The content of this chapter has been submitted as a research article to the International Journal for Numerical and Analytical Methods in Geomechanics.

2.1. ABSTRACT

The engineering behaviour of soft organic clays is influenced by anisotropy, stress history, and the characteristics of organic matter. While their response under compression has been extensively studied, and existing models can effectively replicate these behaviours, questions remain about their behaviour under stress paths other than compression. This study offers a comprehensive analysis of axisymmetric stress paths, including extension, and introduces a new dataset to support the calibration and development of constitutive models. An organic diatomaceous clay from the Netherlands was subjected to an extensive experimental program that included both monotonic and non-monotonic stress paths in both compression and extension. The data reveal a few limitations in current elastic-plastic models, which were addressed by introducing greater flexibility in the yield function shape and enhancing the rotational hardening rule. The newly developed JMC-clay model is evaluated and validated across various stress paths. Comparisons between experimental data and numerical simulations demonstrate the model ability to accurately describe pre-failure behaviour. The findings emphasize that the model performance is particularly sensitive to elastic-plastic compressibility, more so than any other parameter. Moreover, the true challenge in applying this class of anisotropic models lies in accurate initialisation rather than calibration.

2.2. INTRODUCTION

Soft organic soils are commonly found as predominant natural geomaterials at the depths of interest for geotechnical engineering works in many deltaic areas around the world. With the increase in global population, structures and infrastructures construction on soft soils is becoming more and more extensive. Advancing the understanding of the mechanics of these soils is essential to optimise construction techniques, minimise risks, and ensure the long-term integrity of infrastructure. Reliable information is crucial for designing and assessing structures in compliance with both ultimate limit states and serviceability limit states, necessitating accurate predictions of soil behaviour under both pre-failure and failure conditions.

Previous investigations have predominantly focused on compression stress paths in the meridian plane. These studies have revealed that organic clays are characterised by high compressibility, relatively high friction angles, stress-induced anisotropy, possible loss of structure at relatively low stresses, and strain-rate dependency (Parry and Nadarajah, 1974; Burland, 1990; Hight et al., 1992; Callisto and Calabresi, 1998; Zdravković et al., 2002; Pineda et al., 2016; Bjerrum, 1967; Graham et al., 1983; Sheahan et al., 1996). These findings have underpinned the development of various constitutive models within frameworks such as elasto-plasticity, hypo-plasticity, and bounding surface plasticity for simulation and practical applications (Karstunen et al., 2005; Mašín, 2005; Rezania et al., 2018; Seidalinov and Taiebat, 2014). It is worthwhile noting that, once a comprehensive and robust rate-independent model is established, extending it to account for time/rate-dependent responses and/or cyclic behaviour becomes relatively straightforward within frameworks like elastic-viscous-plasticity (Coelho et al., 2021; Leoni et al., 2008; Rezania et al., 2016; Sivasithamparam et al., 2015) or bounding surface (visco)plasticity (Jiang et al., 2012; Rezania and Dejaloud, 2021; Seidalinov and Taiebat, 2014). However, the success of this approach hinges on the parent rate-independent formulation ability to accurately reproduce soil behaviour across a variety of stress paths. Addressing this challenge forms the core focus of this research, representing the first step toward developing a comprehensive modelling approach suitable for organic soft clays.

Focusing on elastic-plastic approaches, numerous models for soft clays have been proposed, particularly following the seminal work of Sekiguchi and Ohta (1977) and Hashiguchi (1977). Most of these models address stress-induced plastic anisotropy through a rotational hardening rule applied to the yield function and plastic potential. Within this category, two models, S-CLAY1 (Wheeler et al., 2003) and SANICLAY (Dafalias et al., 2006), are particularly noteworthy. Both models expand upon the Modified Cam Clay (MCC) formulation (Roscoe and Burland, 1968) by incorporating a rotational hardening rule dependent on plastic strains. The primary difference between these two models lies in their use of associated (S-CLAY1) versus non-associated (SANICLAY) yield and plastic potential functions. The associated formulation simplifies the model, making it easier to calibrate and sufficiently accurate for many applications. However, subtle features of the soil behaviour such as the observed decrease in deviatoric stress before reaching the critical state on the wet side (Pineda et al., 2016), cannot be captured by an associated formulation without additional model complexities. Some researchers attribute this behaviour to loss of structure, which has been modelled as a reduction of the elastic domain, or softening, at increasing stress ratios (Huang et al., 2011; Karstunen et al., 2005).

However, this behaviour can also be modelled by adopting different shapes for the yield surface and plastic potential, thereby leading to the development of a non-associated formulation (Dafalias et al., 2006; Yamada et al., 2001).

Despite extensive global research on soft clays and significant experimental characterisation efforts within the Netherlands (Cheng et al., 2007; Cheng et al., 2004; Den Haan, 2003; Tigchelaar et al., 2001), advanced material modelling of Dutch soft clays lags behind, even as the demand for numerical modelling in engineering practice increases. This research aims to address this gap by achieving two primary objectives: (i) expanding the database of experimental results for soft clays across various triaxial stress paths, including extension paths, which are critical yet seldom thoroughly investigated; and (ii) refining existing elastic-plastic models to better capture pre-failure behaviour and responses under extension stress paths, which are crucial for engineering applications. Recognising that a non-associated formulation is better suited to most Dutch clays, SANICLAY was selected as the starting point. Building on this foundation, a new model, JMC-clay, is proposed, which enhances the yield surface shape and rotational hardening rule to better fit new experimental evidence, including extension stress paths.

2.3. EXPERIMENTAL INVESTIGATION

2.3.1. MATERIAL DESCRIPTION

The material used in the experimental investigation was collected at the Leendert de Boerspolder in the Netherlands, where a full-scale test on a historical regional dyke was performed (Jommi et al., 2019). Samples were retrieved from the soft clay foundation layer using a 106 mm piston sampler at two locations: between 6.1 and 7.3 m below the ground surface underneath the crest of the dyke, and between 3.9 and 4.4 m below the polder. To reduce bio-degradation, the material was stored in a climate-controlled room at 10±1°C and 90% relative humidity. To avoid loss of organic matter, oven-drying for soil classification was performed at 60°C (Head, 1992). The specific gravity of the soil, G_s, was measured with a helium pycnometer (D5550-14, 2014) and the organic content, OC, was assessed by ignition at 440°C (D2974-14, 2014). The material retrieved below the crest of the dyke is a clayey sandy silt with variable organic content ranging from 2.7 to 7.3%. The material from the polder side is a silt with a higher clay fraction (38%) and an organic content of about 4%. The tested samples are divided into groups depending on their organic content and sampling location (groups (III) to (IX) below the crest of the dyke, group (X) from the polder side). Figure 2.1 reports the particle size distribution from wet-sieving and hydrometer analysis for the tested groups. Relevant index properties are summarised in Table 2.1.

An impression of the fabric of the tested material is displayed in Figure 2.2 from ESEM photomicrographs. The fabric is organised in aggregates with a characteristic size of the order of 100μm (Figure 2.2(a)), where silt particles and diatoms microfossils are visible (Figure 2.2(b)).

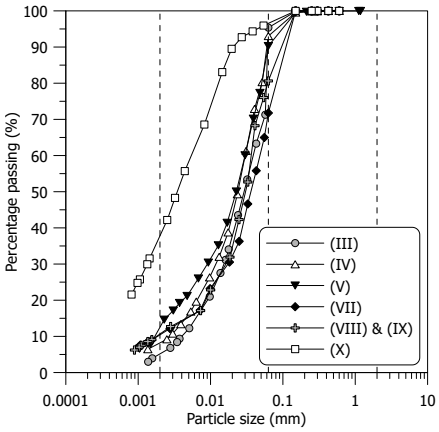

Figure 2.1: Particle size distribution of the tested material

Table 2.1: Index properties of the tested material

Index property	Value
Water content, w (%)	46 - 101
Plastic limit, w_p (%)	30 - 41
Liquid limit, w_l (%)	50 - 102
Plasticity index, I_p	20 - 61
% of particles <0.002 mm	3 - 38
Organic content, OC (%)	2.7 - 7.3
Specific gravity, G_s	2.60 - 2.67

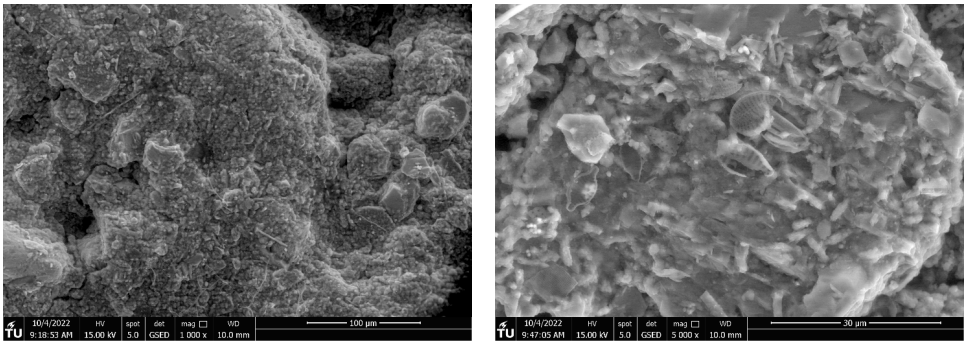

(a) **(b)**

Figure 2.2: ESEM photomicrographs of the tested material (group VIII) at different magnification levels: (a) 1000x and (b) 5000x

2.3.2. TESTING PROGRAMME

Undisturbed samples having a nominal 38 mm diameter and 90 mm height were tested in the triaxial apparatus. Table 2.2 collects an indication of the stress path followed on each sample, the initial void ratio, e_0, the maximum mean effective stress, $p'_{c,max}$, reached during the test and the mean effective stress at the start of the shear, p'_s. The triaxial system includes a submersible 1 kN load cell, back pressure and cell pressure volume controllers with an accuracy of ±1 kPa on pressure and ±200 mm^3 on volume (0.1% full-scale range). A suction cap was used to ensure perfect contact between the load cell and the top cap. All the drained tests were performed under stress control, assuring a maximum excess pore pressure lower than 3 kPa.

Samples from groups (VI) and (IV) were brought to failure with standard TxCD tests or nearly constant p' tests (Figure 2.3(a) and Figure 2.3(b)). Different loading histories (i.e. isotropic and K_0 compression, radial - $\eta = q/p'$ constant - compression and extension paths) and shearing constraints (i.e. TxCU, p' constant, q constant) were imposed on samples from groups (VII), (VIII) and (IX) as displayed in Figure 2.3(c)-2.3(d). K_0 stress-controlled compression tests were performed in the triaxial apparatus with volume change and axial displacement back measurement, allowing for automatic adjustment to guarantee negligible radial strains. Multistage, loading-unloading, radial compression, constant p' and constant q stress paths were followed on the samples from group (III) to better evaluate the non-monotonic pre-failure response (Figure 2.3(e)). Samples from the group (X) were compressed along different radial paths to specifically assess the evolution of anisotropy (Figure 2.3(f)).

Table 2.2: Initial state and type of stress path followed in the triaxial tests

Tube	Sample ID	Test	OC (%)	Group	e_0 (-)	$p'_{c,max}$ (kPa)	p'_s (kPa)
B103-13	T1	Isotropic	6.4	III	1.97	149	26
	T2	K_0*	6.4		1.97	-	11
	T3	Mixed**	6.4		1.91	69	36
B103-13	T1	Mixed	6.0	IV	1.81	67	36
	T2	Mixed	6.0		1.71	68	36
B103-14	T1	p' constant	4.0	VI	1.26	14	14
	T2	TxCD	4.0		1.33	14	14
B103-14	T1	Isotropic	2.9	VIII	1.51	-	7
	T2	K_0	2.9		1.40	-	7
	T3	Mixed	2.9		1.45	70	38
	T4	Mixed	2.9		1.47	70	38
B106-13	T1	Mixed	3.5	VII	1.60	-	5
B106-13	T1	Mixed	2.7	IX	1.22	70	38
	T2	Mixed	2.7		1.24	69	39
	T3	K_0	2.7		1.21	-	6
B101-10	T4	K_0	2.2		1.17	-	7
B101-8	T1	Mixed	4.2	X	2.77	-	6
	T2	Mixed	4.5		2.74	-	6
	T3	Mixed	3.8		2.58	-	5
	T4	Mixed	3.5		2.61	-	7
	T5	Mixed	4.6		2.76	-	5
	T6	Mixed	3.7		2.60	-	6
	T7	Mixed	3.4		2.28	-	6
	T8	Mixed	3.2		2.24	-	5
	T9	Mixed	3.2		2.39	-	5

* K_0 triaxial compression at null lateral strain

** Mixed: various combinations of stress paths at constant stress ratio, p' constant loading-unloading and q constant paths (see Figure 2.3 for the specific soil samples)

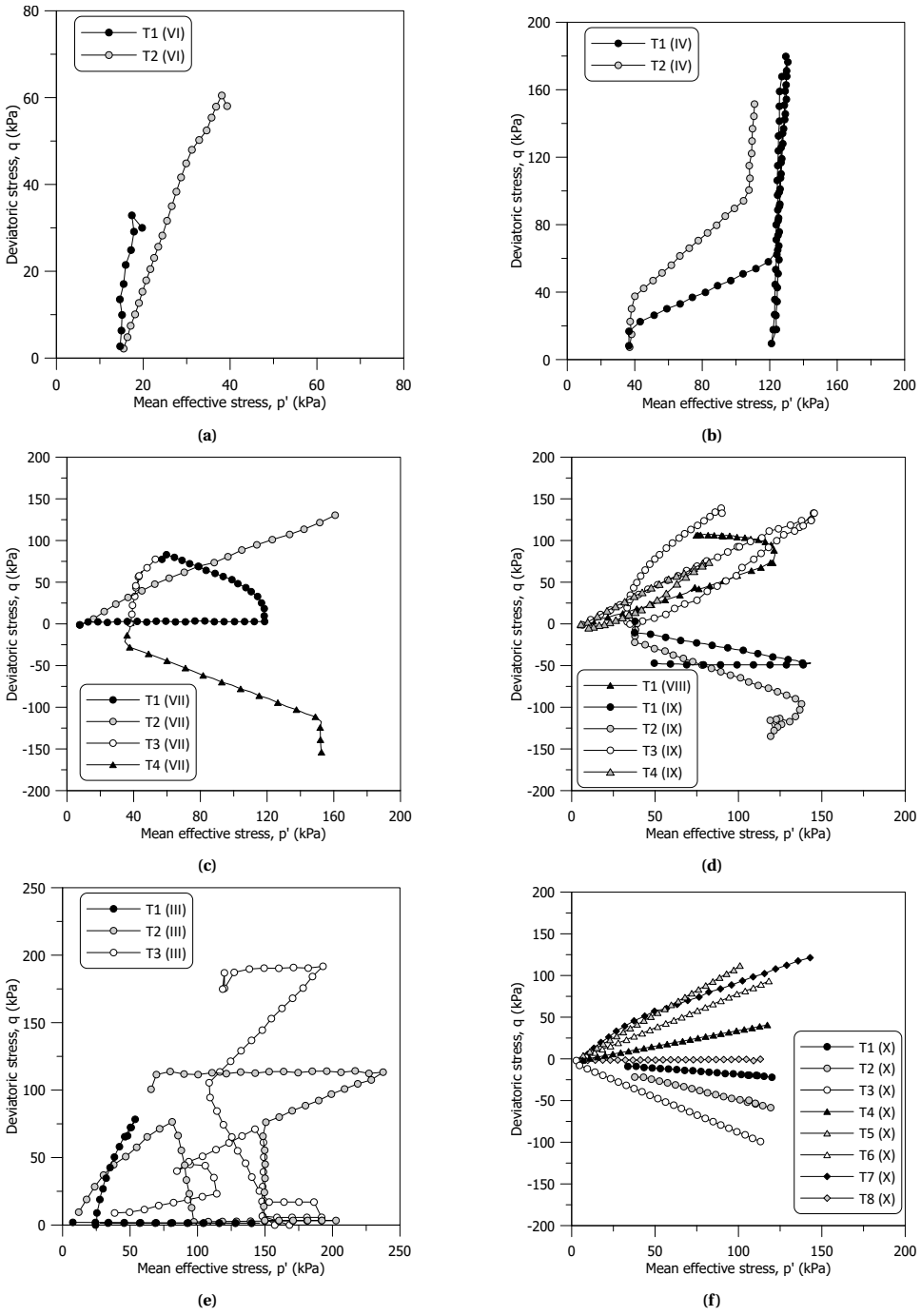

Figure 2.3: Experimental stress paths followed in the triaxial tests for groups of samples: (a) (VI), (b) (IV), (c) (VII), (d) (VIII) - (IX), (e) (III) and (f) (X)

2.4. RESULTS AND INTERPRETATION

The triaxial data are elaborated adopting the common triaxial stress-strain variables: mean effective stress p', deviatoric stress q, volumetric strain, ε_p, and deviatoric strain, ε_q. Compressive stresses and strains are assumed positive. Natural strains (Ludwik, 1909) are adopted to avoid bias in the data interpretation caused by the large displacements attained by the samples (Jommi et al., 2021).

2.4.1. COMPRESSION BEHAVIOUR

The volumetric response upon isotropic and K_0 compression is displayed in Figure 2.4. A unique set of 1D and isotropic compression lines can be identified for each group whose position depends on the initial void ratio as typically observed for silty soils (*e.g.* Nocilla et al., 2006; Ponzoni et al., 2014). The slope of the 1D virgin compression line, λ_{1D-VCL}, is slightly higher than the isotropic compression line, $\lambda_{ISO-NCL}$, as shown in Figure 2.4. An average ratio $\lambda_{1D-VCL}/\lambda_{ISO-NCL} = 1.14$ is found.

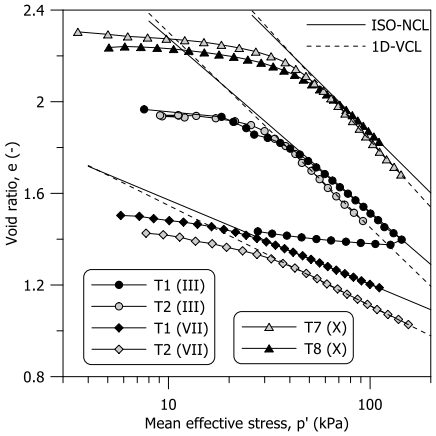

Figure 2.4: Isotropic and K_0 compression paths for samples from groups (III), (VII) and (X)

Dependence of the compression response on the organic content is also expected (Caicedo et al., 2018; Ponzoni, 2017; Reina Leal, 2019). Figure 2.5(a) shows the influence of the organic content on the slope of the compression line for the tested soil, over the stress paths in Figure 2.3. The ratio between the slope of the compression line and the slope of the reloading line with the organic content is presented in Figure 2.5(b), a ratio $\lambda/\kappa \approx 9$ can be found.

The experimental data show a consistent increase in λ from 0.1 to 0.35 with the organic content ranging from 2 to 7%, with the exception of samples from the group (X). The higher compressibility of these samples compared to other groups, despite the similar organic content *e.g.* (VII) and (VIII), might be attributed to their higher clay content (Figure 2.1). However, inspection of ESEM photomicrographs reveals an abundance of large intact diatoms microfossils in the matrix of samples from the group (X) (Figure 2.6) compared to few and small broken diatoms inclusions in group (VIII) (Figure 2.2(b)). The presence of large diatoms justifies an increase in compressibility due to their hollow

skeleton and trapped water in their intraskeletal pore space (Caicedo et al., 2018; Diaz-Rodriguez et al., 1992; Lo, 1962; Mesri et al., 1975; Shiwakoti et al., 2002; Tanaka and Locat, 1999; Zhang et al., 2023).

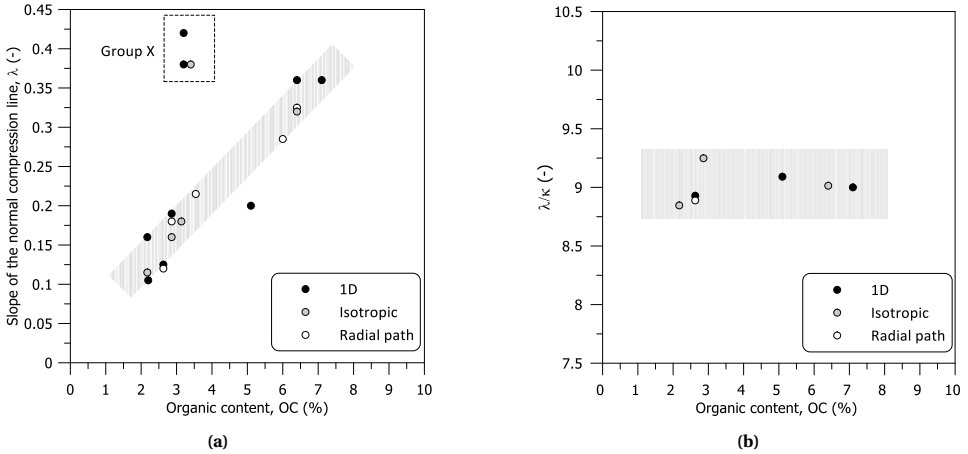

Figure 2.5: Variation of (a) the slope of the compression line with the organic content (b) the ratio between the slope of the compression line and the slope of the reloading line with the organic content

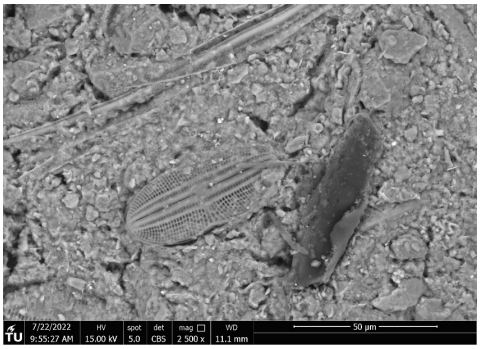

Figure 2.6: ESEM photomicrograph of the tested material from the group (X)

2.4.2. SHEAR BEHAVIOUR

The response upon shearing is summarised in terms of stress ratio, $\eta = q/p'$, versus deviatoric strain for different groups of samples. For the sake of clarity, only the last portion of each stress path up to failure is plotted. The results in Figure 2.7 show an ultimate stress ratio $M_{g,c} = 1.42$ in triaxial compression and $M_{g,e} = 1.05$ in triaxial extension, corresponding to different friction angles $\phi'_c = 35°$ and $\phi'_e = 39.5°$. Samples from group (VI) tested at very low confining stresses, $p' < 25$kPa, attain a peak stress ratio equal to 1.8 before tending asymptotically towards the ultimate stress ratio. Samples T2 and T3 from group (III) showed a slightly higher ultimate stress ratio at large strains due to poor

controllability when the samples approach failure under q – constant stress path (Figure 2.3(e)).

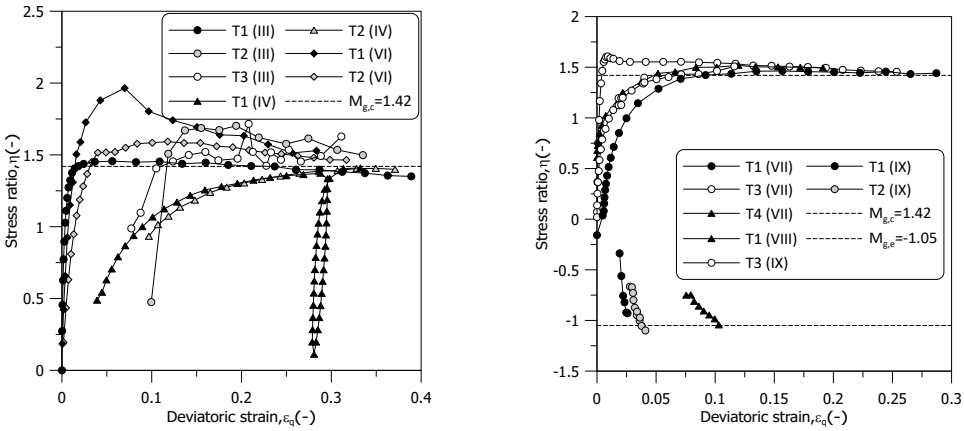

Figure 2.7: Stress ratio versus deviatoric strain during the final shearing stage up to failure for samples from groups: (a) (III), (IV), (VI) and (b) (VII), (VIII), (IX)

The ultimate friction angle in triaxial compression, $\phi'_c = 35°$, gives a reasonably consistent estimate of the at-rest lateral earth pressure coefficient in normally consolidated conditions using Jaky's simplified relationship ($K_0 \cong 1 - \sin\phi'_c = 0.43$) compared to the experimental value, K_0^{NC}(0.43 - 0.48), determined from sample T2 (III), T2 (VII), T3 (IX) and T7 (X). Figure 2.8(a) displays the evolution of the lateral stress ratio, $K_l = \sigma'_r/\sigma'_a$, during the K_0 compression tests. For samples T3 (IX) and T4 (IX), the test included a K_0 loading and unloading path. Figure 2.8(b) reports the development of the lateral stress ratio versus the over-consolidation ratio, OCR, compared with the relationship (Schmidt, 1966).

$$\frac{K_0^{OC}}{K_0^{NC}} = OCR^m \tag{2.1}$$

where K_0^{OC} is the at-rest lateral earth pressure coefficient in over-consolidated conditions and OCR is the over-consolidation ratio in terms of axial effective stress. Figure 2.8(b) proposes a comparison between the experimental data and the commonly adopted values of $m = 0.5$ and $m = \sin\phi'_c$ (Mayne and Kulhawy, 1982). The experimental data seem to suggest $m = 0.42$ for the tested material.

Different responses upon K_0 compression among the tested samples can be observed in Figure 2.8(a). Samples T2 (III), T7 (X) and T9 (X) show a significant decrease in the lateral stress ratio at around $\sigma'_a \approx 50$ kPa, followed by a gradual increase towards the asymptotic value of 0.46. This 'shoulder' shape of the lateral stress ratio has already been noticed by numerous authors (e.g. Leroueil and Vaughan, 1990; Watabe et al., 2003). Cotecchia and Chandler (1997) suggested structure changes associated with the transition between pre- and post-yielding domains as an explanation of this behaviour. Additional

insight on K_0 compression response is provided in Figure 2.9, where the results are plotted in terms of the void index (Burland, 1990), I_v, for both undisturbed and reconstituted samples of each group. The results seem to suggest a more pronounced initial decrease in the lateral stress ratio followed by an increase, for those samples whose state lies well above the ICL (T2 (III), T7 (X), T9 (X)). In contrast, samples T2 (VII), T3 (IX) and T4 (IX), which lie close to the ICL, show a monotonic gradual decrease in the lateral stress ratio.

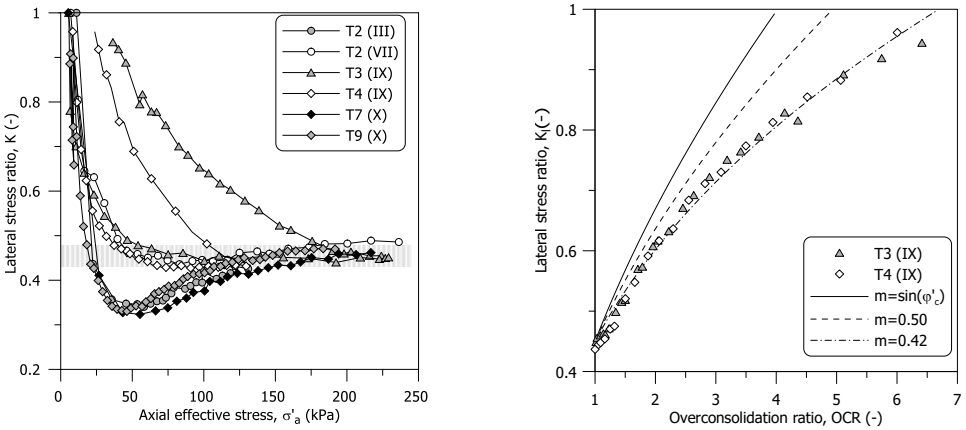

Figure 2.8: Results from K_0 compression tests: (a) evolution of the lateral stress ratio and (b) change in K_0 with the over-consolidation ratio

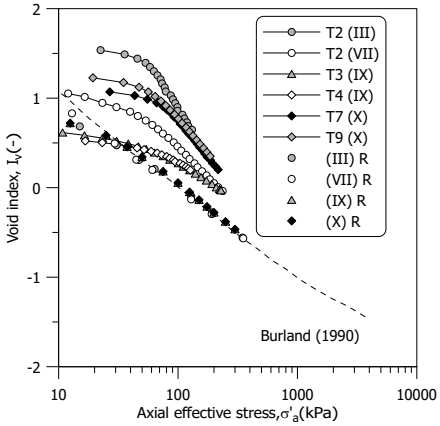

Figure 2.9: Results from the K_0 compression tests in terms of void index

2.4.3. YIELD LOCUS

The initial position and shape of the yield locus for the tested material were derived by exploiting the multiple stress paths in Figure 2.3. Various criteria were adopted for this aim (Becker et al., 1987; Muir Wood, 1990), and the points best matching all of them were eventually chosen (see Muraro and Jommi (2021) for a detailed discussion). The experimental yielding points in Figure 2.10 clearly suggest an anisotropic yield locus, rotated on the p' axis.

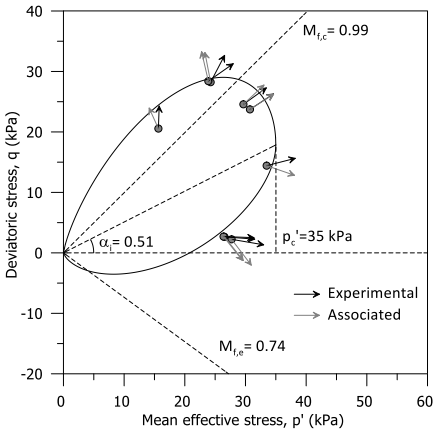

Figure 2.10: Trace of the yield locus on the $p' - q$ space from the estimated yield points and plastic strain increment vectors

To fit the experimental yielding points, the expression proposed by McDowell and Hau (2004) is extended to account for anisotropy:

$$f = 0 = \left(q - p'\alpha_f\right)^2 + \frac{\left(M_f^2 - \alpha_f^2\right)}{k_f - 1} p'^2 - \frac{\left(M_f^2 - \alpha_f^2\right)}{k_f - 1} p_c^2 \left(\frac{p'}{p'_c}\right)^{\frac{2}{k_f}} \tag{2.2}$$

where α_f defines the inclination of yield locus in the $p' - q$ space and p'_c is the preconsolidation mean effective stress. The chosen surface allows enough flexibility in the shape through the two coefficients k_f and M_f. Standard shapes can be recovered, including the anisotropic version of the Modified Cam clay model proposed by Dafalias (1986) for $k_f = 2$. As displayed in Figure 2.10, the experimental yield points are nicely fitted by equation (2.2) with $M_{f,c} = 0.99$, $M_{f,e} = 0.74$, $k_f = 1.25$, and $\alpha_f = 0.51$. The initial inclination of the yield locus was calculated based on the K_0 tests as described by Dafalias et al. (2006). The initial inclination of the yield locus was determined as described by Dafalias et al. (2006), assuming $\kappa/\lambda = 1/9$ and $\nu = 0.2$.

Figure 2.10 also shows a comparison between the experimental plastic strain increment vectors computed along the different stress paths at the onset of yielding and the theoretical ones assuming normality condition with the yield locus in equation (2.2). The volumetric and the deviatoric plastic strain increments, $\delta\varepsilon_p^p$ and $\delta\varepsilon_q^p$, have been derived from the total ones by computing the elastic strains increment, $\delta\varepsilon_p^e$ and $\delta\varepsilon_q^e$, with a hypo-elastic isotropic law with a constant Poisson's ratio, $\nu = 0.2$:

$$\delta\varepsilon_p^e = \frac{\delta p'}{K}; K = \frac{\upsilon p'}{\kappa} \tag{2.3}$$

$$\delta\varepsilon_q^e = \frac{\delta q}{3G}; G = \frac{3(1-2\nu)}{2(1+\nu)}K \tag{2.4}$$

where υ is the specific volume, K is the bulk stiffness, κ is the slope of the unloading-reloading compression line, G is the shear modulus, $\delta p'$ and δq are the increment in mean effective stress and deviatoric stress, respectively. For each radial path, the value of κ has been determined from the experimental data. The comparison in Figure 2.10 suggests that the normality assumption does not hold for the tested material, as already highlighted by other authors on similar soils (Newson and Davies, 1996; Wong and Mitchell, 1975).

2.4.4. ANISOTROPIC PLASTIC DEFORMATION MECHANISM

Nnatural soft clays are expected to exhibit anisotropic response due to both the previous stress history (i.e. depositional conditions) and the subsequent loading (Wheeler et al., 2003). The post-yielding plastic deformation response was analysed in terms of inclination β of the plastic strain increment vectors, where

$$\tan\beta = \frac{\delta\varepsilon_q^p}{\delta\varepsilon_p^p} \tag{2.5}$$

along stress paths at constant stress ratio.

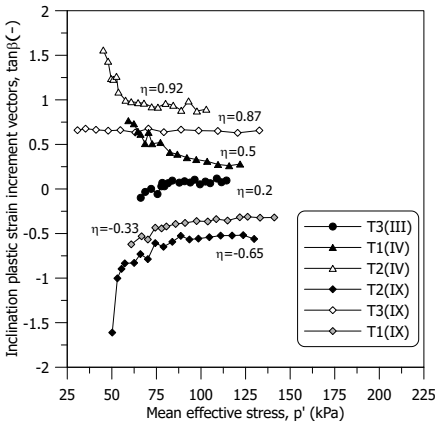

Figure 2.11: Change in the inclination of the plastic strain increment vectors along radial paths

Figure 2.11 shows progressive reorientation of the plastic strain increment vectors along radial paths at constant stress ratios. The magnitude of the rotation depends on the previous stress history and loading direction. For the K_0 compression test on sample T3 (IX), the plastic strain increment vectors do not rotate as a result of the initial alignment of the fabric along the K_0 line.

The experimental evidence in Figure 2.11 justifies adopting an anisotropic stress-dilatancy rule (i.e. anisotropic plastic potential) such as the well-established expression proposed by Dafalias (1986)

$$d = \frac{1}{\tan\beta} = \frac{M_g^2 - \eta^2}{2(\eta - \alpha_g)} \tag{2.6}$$

where d is the dilatancy, M_g is the critical stress ratio, and α_g is a non-dimensional anisotropic variable, which accounts for the deviatoric and volumetric plastic strain rates coupling and introduces the anisotropic response in the plastic deformation mechanism. By integrating equation (2.6), the plastic potential reads:

$$g = (q - p'\alpha_g)^2 + (M_g^2 - \alpha_g^2)p'(p' - p'_g) \tag{2.7}$$

where p'_g is a dummy variable.

As shown in Figure 2.11, with enough straining along radial paths, the inclination of the plastic strain increment vectors reaches a fairly constant value. At this stage, equation (2.6) allows deriving the asymptotic values of α_g called "equilibrium or bounding" values, α_{gb}, for different radial paths (Dafalias and Taiebat, 2013). To account for the different friction angle in triaxial compression and extension observed in Figure 2.7, the experimental data are normalised with the critical stress ratio, $M(\theta)$, corresponding to the Lode angle, θ, of the followed stress path, namely, $M_{g,c}$ for $\eta > 0$ and $M_{g,e}$ for $\eta < 0$. Figure 2.12 shows the comparison between the experimental data and the two analytical expressions proposed in S-CLAY1 (Wheeler et al., 2003) and SANICLAY (Dafalias and Taiebat, 2013). The parameters of the reference analytical expressions were calculated based on the K_0 compression tests as described by Wheeler et al. (2003) and Dafalias et al. (2006). As shown in Figure 2.12, both models fit reasonably well the experimental data in the triaxial compression domain. However, the agreement is not satisfactory in the extension domain, especially at high stress ratios, $\eta/M_{g,e} < -0.5$.

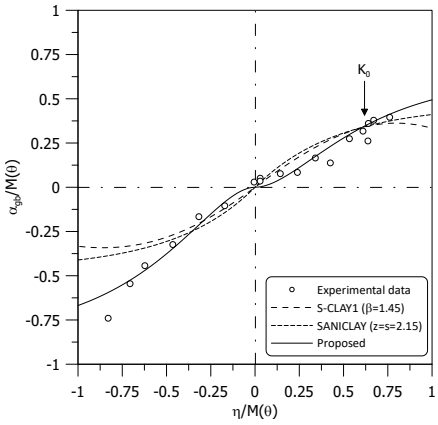

Figure 2.12: Bounding values of α_{gb} for different radial paths

To better fit the new experimental evidence in Figure 2.12, the expression proposed by Dafalias and Taiebat (2013) is amended by weighing the asymptotic behaviour with a strictly positive power coefficient, y, and giving the de-amplification factor, z of the original proposal a dependency on the Lode angle. For triaxial compression and extension, the proposal reads:

$$\alpha_{gb} = \begin{cases} \frac{M_{g,c}}{z_c}\left[1-\exp\left(-s\frac{|\eta|}{M_{g,c}}\right)\right]^y & \text{if } \eta \geq 0 \\ -\frac{M_{g,e}}{z_e}\left[1-\exp\left(-s\frac{|\eta|}{M_{g,e}}\right)\right]^y & \text{if } \eta < 0 \end{cases} \tag{2.8}$$

where s is a positive model constant and z_c, z_e are the values of z over triaxial compression and triaxial extension, respectively. This choice implies that the model can attain different critical state lines in compression and extension paths, as already observed on different types of clays (Yin and Chang, 2009). The experimental data for a wide range of stress ratios were fitted with the proposed equation with $y = 2$, $z_c = 1.6$, $z_e = 1.2$, and $s = 2$, as plotted in Figure 2.12.

It is worth mentioning that the results in Figure 2.12 are derived from experimental results (i.e. plastic strain increment vectors) and theoretical assumptions on the plastic deformation mechanism (i.e. plastic potential as in equation (2.7)). If the information in Figure 2.12 is also used to infer the evolution of anisotropy of the yield surface, equation (2.8) can be adopted in the rotational hardening rule assuming that $\alpha_f = \alpha_g = \alpha$ (Dafalias and Taiebat, 2013; Jiang and Ling, 2010; Jiang et al., 2012).

2.4.5. HARDENING MECHANISM

Critical state models often assume that the current size of the yield surface is controlled solely by plastic volumetric strains, however, information on organic soils is still scarce. Muraro and Jommi (2021) provided evidence that in highly organic peats the hardening mechanism is also ruled by deviatoric plastic strains, likely due to the rearrangement/realignment of the fibres present in the peat fabric. To discriminate between the two hypotheses for the tested material, the results of drained tests are analysed. Figure 2.13 reports the evolution of the pre-consolidation mean effective stress, p'_c, with the volumetric plastic strains, ε_p^p, computed for different radial paths. The current value of p'_c is normalised with the value when the inclination of the yield locus, α, reaches equilibrium along each radial path. This allows isolating the change in the size of the yield locus from its change in inclination.

The evidence in Figure 2.13 supports the assumption that the size of the yield locus for organic clays is ruled solely by the plastic volumetric strains, as opposed to highly organic fibrous soils like peats. All the experimental data align well with the traditional volumetric hardening law (Muir Wood, 1990).

$$\frac{\delta p'_c}{p'_c} = \frac{v}{\lambda - \kappa}\delta\varepsilon_p^p \tag{2.9}$$

A second hardening rule is needed to control the rotation rate of the yield locus produced by plastic straining. As anticipated adhering to a common choice, the rotational rule derived for the plastic potential (equation (2.8)) is also used for the yield locus as proposed by JDafalias and Taiebat (2013), Jiang and Ling (2010), and Jiang et al. (2012).

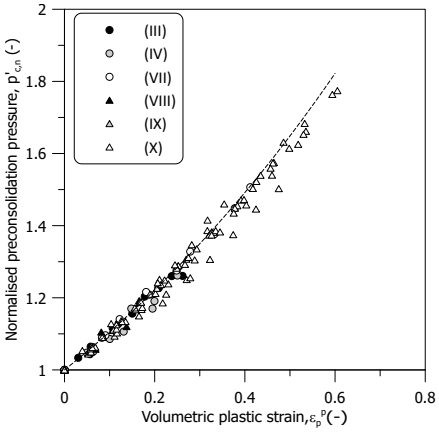

Figure 2.13: Evolution of the pre-consolidation mean effective stress with volumetric plastic strain for different radial stress paths

For the rotation rate, $\delta\alpha = \delta\alpha_g = \delta\alpha_f$, the suggestion by Dafalias and Taiebat (2013) is chosen, with

$$\delta\alpha = \langle L \rangle c p_{\text{atm}} \frac{p'}{p'_c}(\alpha_b - \alpha) \tag{2.10}$$

where the plastic multiplier, L, is enclosed in Macauley brackets $\langle\rangle$ to track plastic loading (i.e. $L > 0$ and $\langle L \rangle = L$) and elastic unloading (i.e. $L \leq 0$ and $\langle L \rangle = 0$), p_{atm} is the atmospheric pressure, p'_c is the pre-consolidation pressure, c is a model parameter controlling the rate of the evolution of α, and α_b is the bounding value of α attained along the reference constant stress ratio path (equation (2.8) and Figure 2.12).

2.5. NUMERICAL CALIBRATION, PREDICTIONS AND VALIDATION

2.5.1. MODEL PARAMETERS

The capabilities of the JMC-clay elastoplastic model built on the previous experimental findings are discussed by simulating the laboratory tests with a single Gauss point scheme. To highlight the benefits of the JMC-clay model over previous formulations, for a few specific tests a simulation with SANICLAY model (Dafalias and Taiebat, 2013), which served as a reference model for this work, is included. Where the simulation with SANICLAY is not reported, the two models perform in an almost identical way.

The model requires calibration of 12 parameters, which can be determined as follows:

- κ^*, λ^* and c are calibrated on isotropic compression test with axial strain and volumetric strain measurements to assess the evolution of deviatoric plastic strain component (i.e. anisotropic response). It is worth reminding that in the JMC-clay model, κ^* and λ^* are defined on the $\ln(v) - \ln(p')$ space;
- ν is estimated from a K_0 unloading path;

- $M_{g,c}$, $M_{g,e}$ are determined from triaxial compression and extension tests;
- z_c, z_e, s and y are defined by fitting equation (8) on at least three triaxial tests: K_0 compression and two radial paths, one in compression and one in extension; if no data is available on the extension side, z_e can be obtained assuming $z_e/z_c = M_{g,e}/M_{g,c}$;
- $M_{f,c}$ and k_f are determined from yielding points along drained stress probe paths; $M_{f,e}$ is obtained assuming $M_{f,e}/M_{f,c} = M_{g,e}/M_{g,c}$.

In the simulation of the tests with the JMC-clay model, the unique set of calibrated parameters collected in Table 2.3 could be used for all groups. For the slope of the compression line and unloading-reloading line, a different strategy was preferred, and specific values were calibrated on each sample group to account for their strong dependence on the organic content reported in Figure 2.5. The ratio κ^*/λ^* was assumed equal to 1/9. The adopted λ^* values are collected in Table 2.4. The calibrated parameters for the SANICLAY model are listed in Table 2.5.

Table 2.3: Model parameters adopted in the JMC-clay simulations

$M_{g,c}$	$M_{g,e}/M_{g,c}$	ν	c	z_c	z_e	s	y	$M_{f,c}$	k_f
1.42	0.74	0.2	50	1.6	1.2	2.2	2	0.99	1.25

Table 2.4: Calibrated values for λ^* for different groups of samples depending on their organic content

Parameter	(III) - (IV)	(VII)	(VIII)	(IX)	(X)
λ^*	0.137	0.085	0.095	0.065	0.140

Table 2.5: Model parameters adopted in the SANICLAY simulations

$M_{g,c}$	$M_{g,e}/M_{g,c}$	ν	c	z	s	$M_{f,c}$	k_f
1.42	0.74	0.2	50	2.15	2.15	0.99	2.0

2.5.2. STRESS STATE INITIALISATION

Three initial state variables are needed for the proposed model, namely the initial void ratio, e_i, corresponding to the initial mean effective stress at the beginning of the triaxial test, p'_i, and the initial inclination of the yield locus and plastic potential, α_i. The latter was determined assuming K_0 conditions when the sample was retrieved from the field:

$$\alpha_i = \frac{B\varepsilon\eta_{K_0}^3 + \eta_{K_0}^2 + \left[2\left(1-\kappa^*/\lambda^*\right) - BM_{g,c}^2\right]\varepsilon\eta_{K_0} - M_{g,c}^2}{2\varepsilon\left(1-\kappa^*/\lambda^*\right)}; B = -\frac{2(1+\nu)}{9(1-2\nu)}\frac{\kappa^*}{\lambda^*} \tag{2.11}$$

where $\varepsilon = \frac{3}{2}$ and η_{K_0} is the stress ratio corresponding to $K_0^{NC} = 0.43$ coming from Jaky's relationship. For normally consolidated conditions, the corresponding initial pre-consolidation

pressure, p'_c, can be computed from equation (2.2) with α_i and the estimated stress state in the field $(p'_{i,f}, q_{i,f})$.

$$p'_{i,f} = \frac{\sigma'_{v,i}(1+2K_0^{NC})}{3}; q_{i,f} = \sigma'_{v,i}(1-K_0^{NC}) \tag{2.12}$$

For over-consolidated conditions, the yield surface is initialised based on the estimated over-consolidation ratio.

2.5.3. EVOLUTION OF THE YIELD SURFACE AND PLASTIC POTENTIAL

The two novel ingredients introduced in the JMC-clay model from the experimental evidence are the flexible shape of the yield locus (equation (2.2)) and the asymptotic relationship for α_{gb} (equation (2.8)). To validate these changes compared to existing models, the model predictions for the yield locus and the evolution of the plastic strain increment vectors are analysed.

Figure 2.14(a) displays the initial yield surface (dashed line) and the subsequent yield locus, expanded and rotated, predicted by the JMC-clay after isotropic compression up to 70 kPa. The predicted yield surface fits very well with experimental yielding points obtained on samples (T3 (III), T1 (IV), T2 (IV), T3 - T4 (VII), T1 – T2 (IX)) after isotropic loading up to 70 kPa, unloading to 40 kPa, and shearing following different probing stress paths. Also, the model demonstrates excellent capability in describing the evolution of the plastic deformation mechanism both in compression and extension as shown in Figure 2.14(b), where the experimental and predicted rotation of the plastic strain increment vectors along radial paths are compared.

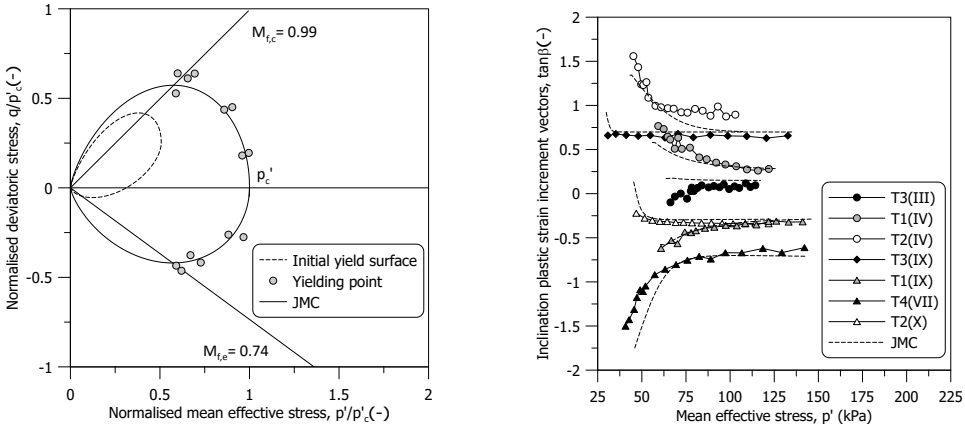

Figure 2.14: Experimental data and numerical prediction for: (a) expanded and rotated yield locus after the first isotropic loading-unloading stage and (b) rotation of the plastic strain increment vectors along radial paths

2.5.4. DRAINED TRIAXIAL TESTS

The comparison between the experimental results and the model simulations is reported in Figure 2.15 for K_0 loading-unloading test and in Figure 2.16 for a multiple drained stress path, which includes p' constant, radial path and p' constant loading-unloading path.

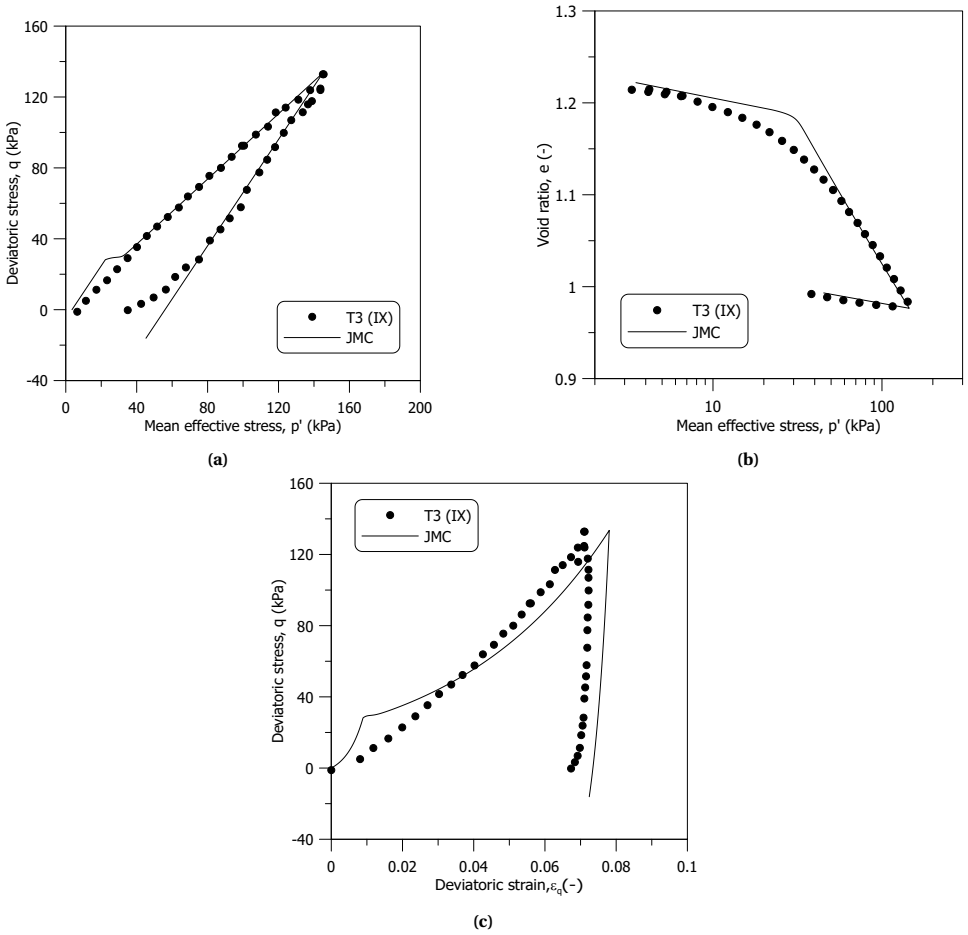

Figure 2.15: Comparison between numerical simulations and experimental data for K_0 loading-unloading on sample T3 (IX)

As expected, the model correctly estimates the final stress path corresponding to the K_0^{NC} state given the calibration of the bounding values α_{gb}. At the beginning of the loading path, the model predicts higher over-consolidation than the one observed experimentally. Upon unloading, the predicted stress path follows the experimental one reasonably well until $p' = 80$ kPa, when the latter deviates, possibly indicating the occurrence of yielding. Both these observations seem to suggest that the shape of the yield locus on the dry side could be slightly narrower than the one adopted in Figure 2.10.

Despite these small differences, the model simulation shows good qualitative and quantitative agreement with the experimental results both in the volumetric and deviatoric response for a wide range of strains. The qualitative and quantitative agreement between the JMC-clay model and the experimental data is also confirmed by the multiple stress path in Figure 2.16.

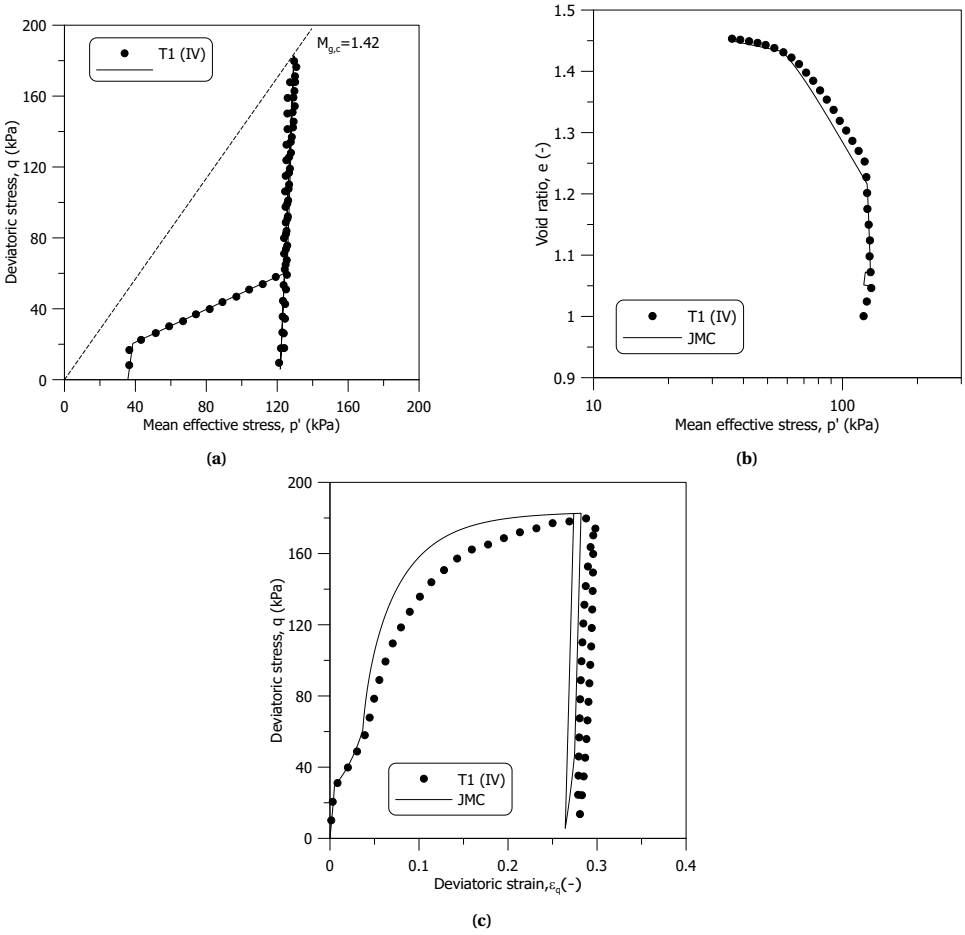

Figure 2.16: Comparison between numerical simulations and experimental data for multiple drained stress paths including p' constant, radial path, and p' constant loading-unloading path on sample T1 (IV)

2.5.5. UNDRAINED TRIAXIAL TESTS: TXCIU

Figure 2.17 shows the comparison between the experimental results and the numerical simulations of undrained triaxial compression tests on normally consolidated and over-consolidated (OCR = 6) samples, starting from isotropic conditions, T1 (III) and T1 (VII) respectively. For the normally consolidated side, the model shows good predictions of the initial stiffness and the overall stress path until the ultimate stress ratio,

$M_{g,c} = 1.42$. After the attainment of $M_{g,c}$, the model shows a hook in the stress path with a further increase in the deviatoric stress, which is not observed in the experimental data. As already discussed by Dafalias and Taiebat (2013), the discrepancy is a consequence of the absence of volumetric plastic strains in the rotation hardening rule (equation (2.10)). However, it is worth mentioning that geometrical effects in the triaxial setup may contribute to the sample ultimate deformation mechanism, as shown by Chao et al. (2023).

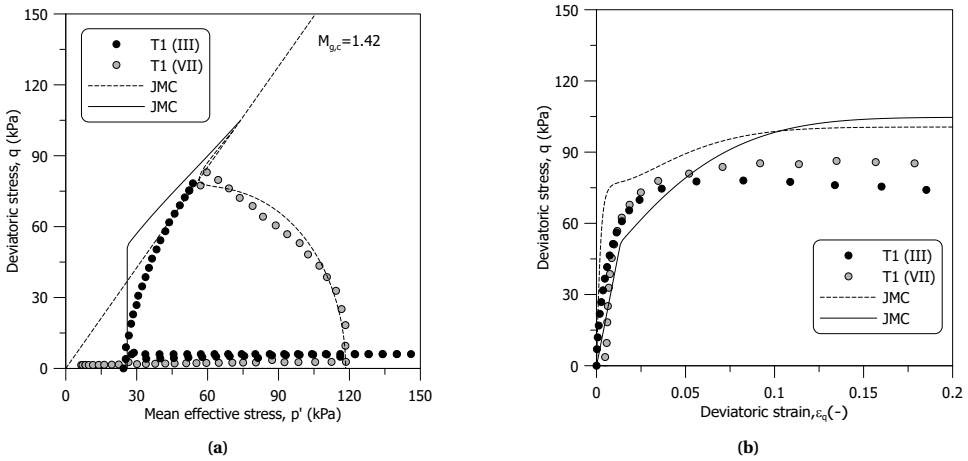

Figure 2.17: Comparison between numerical simulations and experimental data for TxCIU tests on samples T1(III) and T1(VII)

The comparison with the over-consolidated sample T1 (III) highlights the limitations of an elastoplastic model on the dry side. The predicted stress path intercepts the yield locus for a stress ratio above the critical state, while the experimental data show a smoother stress path reaching a lower ultimate deviatoric stress.

2.5.6. UNDRAINED TRIAXIAL TESTS: TXCAU

To better explore the predictive capabilities of the proposed model, Figure 2.18 shows the comparison between numerical simulations and anisotropically consolidated undrained compression tests, which better replicates stress-strain states relevant for field applications. With reference to the normally consolidated sample, T1 (VIII), the model shows very good agreement with the experimental data both in the pre-failure and failure state. Better performance compared to the original SANICLAY is due to the adopted shape of the yield locus, which helps in reproducing the observed stress path more accurately (Figure 2.18(a)). An equally good performance is found for the over-consolidated sample, T3 (IX), except for a slight underestimation of the deviatoric stress at failure mainly due to the predicted elastic response over K_0 unloading (Figure 2.18(c)), as discussed previously.

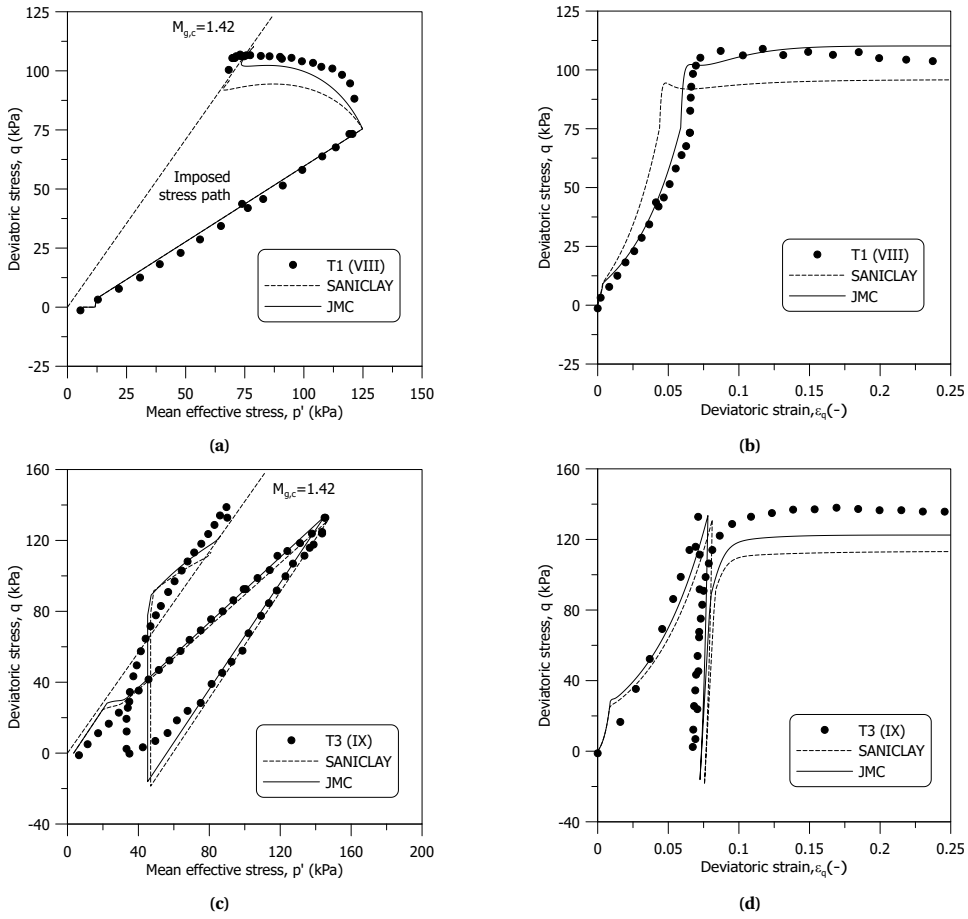

Figure 2.18: Comparison between numerical simulations and experimental data for anisotropic TxCAU tests on samples T1 (VIII) and T3 (IX)

2.5.7. MULTISTAGE DRAINED TRIAXIAL COMPRESSION TESTS

Additional insight into the predictive capabilities of the JMC-clay model is shown on multistage drained compression tests, which included loading and unloading along a variety of stress path directions, as displayed in Figure 2.19.

The comparison in Figure 2.20 shows very good performance of the JMC-clay model on both the volumetric and deviatoric stress-strain response for a wide range of strains up to $\varepsilon_p \approx 0.3$ and $\varepsilon_q \approx 0.15$. It is worth remarking that the data in Figure 2.19 were partially used (i.e. radial paths) to calibrate the bounding values α_{gb}, while all the other paths are predicted by the model.

In spite of the simplicity of the elastoplastic framework, the proposed model appears to be able to describe accurately the pre-failure behaviour of the tested material over a variety of stress paths, which is particularly relevant for field assessment and monitoring.

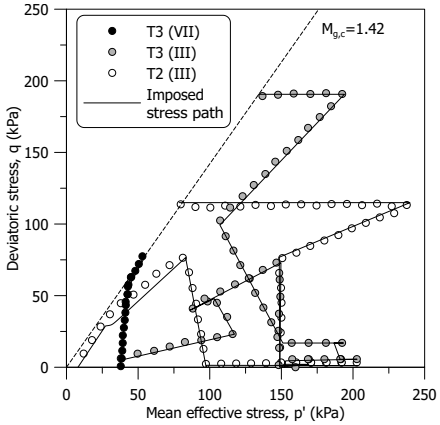

Figure 2.19: Multistage drained triaxial compression tests used to validate the proposed model

2.5.8. DRAINED TRIAXIAL EXTENSION TESTS: SLIGHTLY OVER-CONSOLIDATED SAMPLES

The model capabilities are also evaluated in comparison with drained triaxial extension tests, which include an initial p' constant path followed by a radial path along different stress ratios (Figure 2.21). The samples were first isotropically loaded to $p'_c = 70$ kPa before unloading to $p'_s = 38$ kPa, corresponding to an OCR = 1.8 (Table 2.2).

The comparison in Figure 2.22 shows very good performance of the JMC-clay model on both the volumetric and deviatoric responses along different stress paths. The agreement between the simulations and the data is not surprising, as the radial paths in Figure 2.21 were used to investigate the bounding values α_{gb}. However, it is worth noting that the model performs well in the entire pre-failure domain, showing a remarkable improvement compared to previous models in view of practical applications.

2.5.9. DRAINED TRIAXIAL EXTENSION TESTS OVER-CONSOLIDATED SAMPLES FROM THE FIELD

To better assess the advantages of the model over extension stress paths, the model predictive capabilities are evaluated on the prediction of the extension tests in Figure 2.23, performed on undisturbed samples from the polder side. Differently from the samples in Figure 2.21, these samples were sheared directly starting from the undisturbed state, with an estimated over-consolidation ratio OCR = 3 (Ponzoni, 2017).

Both the JMC-clay and the SANICLAY models show very good quantitative agreement on the volumetric response with the experimental data (Figure 2.24(a)-2.24(c)-2.24(e)). On the contrary, the quantitative agreement on the deviatoric stress-strain response is less satisfactory (Figure 2.24(b)-2.24(d)-2.24(f)). Both models overestimate the deviatoric strain, although the prediction of the new model is improving the one by SANICLAY, thanks to the new calibration of the rotational rule.

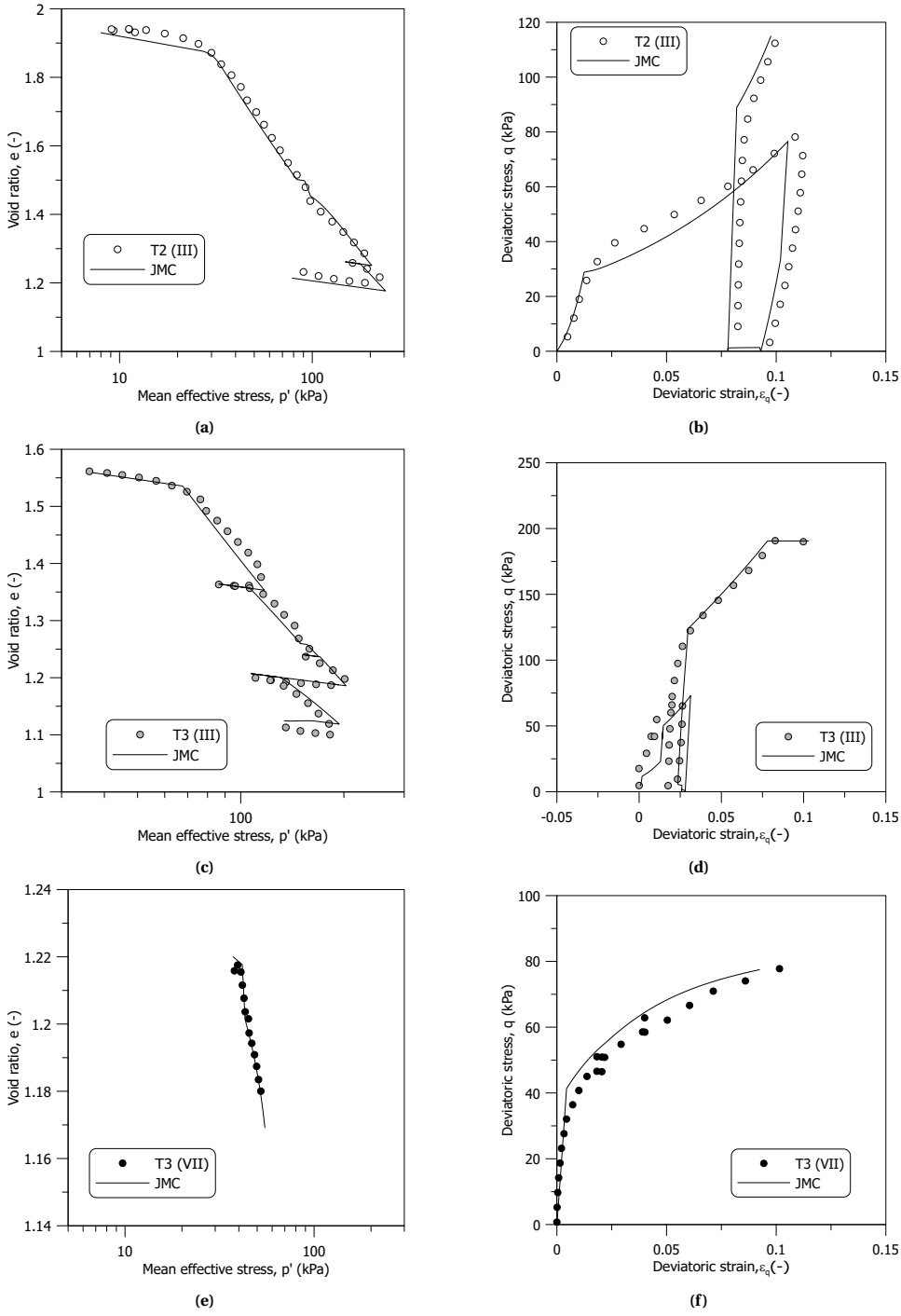

Figure 2.20: Comparison between numerical simulations and experimental data from multistage drained triaxial compression tests on samples T2(III), T3(III) and T3(VII)

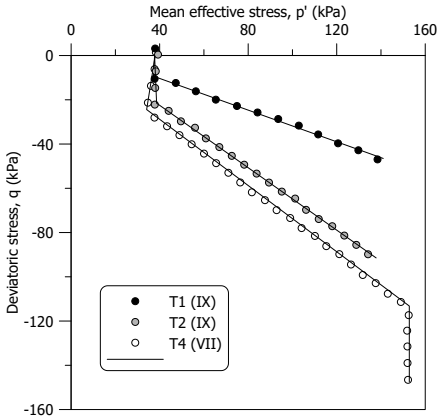

Figure 2.21: Drained triaxial extension tests on samples slightly over-consolidated in the laboratory

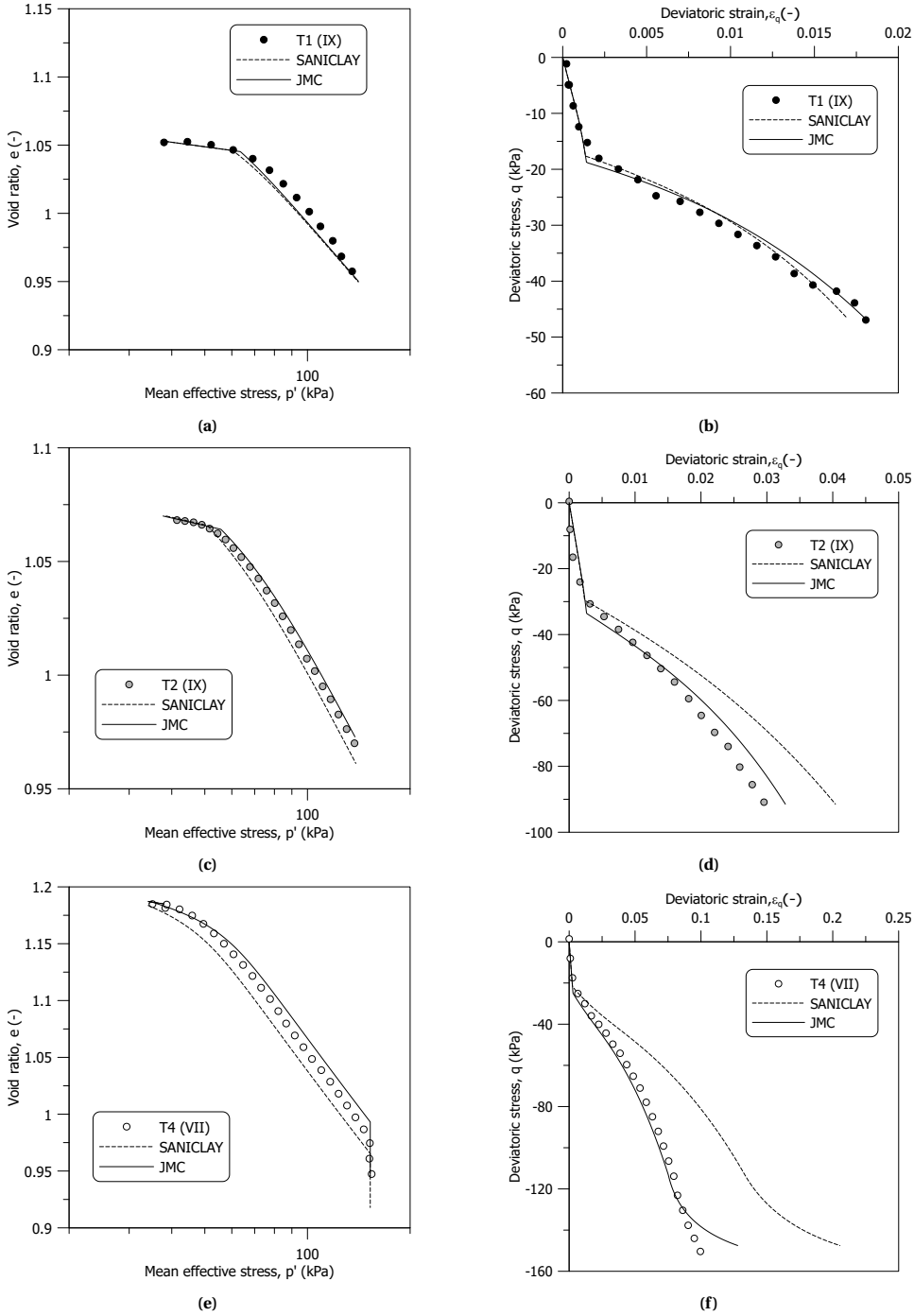

Figure 2.22: Comparison between numerical simulations and experimental data from drained triaxial extension tests on samples T1 (IX), T2 (IX) and T4 (VII)

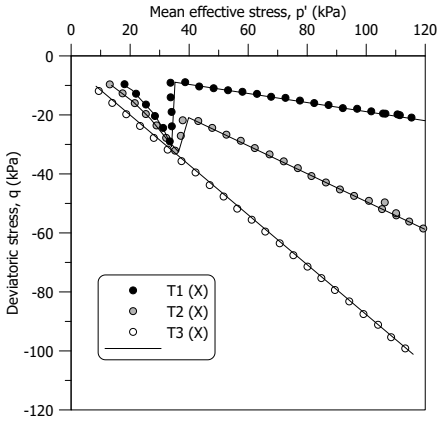

Figure 2.23: Drained triaxial extension tests on over-consolidated samples in the field retrieved from the polder side

2.6. MODEL INITIALISATION

Despite calibration and validation of the JMC-clay model on the new dataset of experimental data, the model predictions in Figure 2.24 show a systematic overestimation of the deviatoric strain along the extension radial path performed on undisturbed samples from the field. The samples were retrieved from the polder side with estimated in-situ vertical effective stress σ'_v of about 15 kPa and estimated OCR = 3. In the previous simulations displayed in Figure 2.24, the initialisation of the hardening variables, p'_c and α_i, followed the assumption of an over-consolidation state caused by 1-D loading/unloading, with a corresponding stress path and initial yield locus as depicted in Figure 2.25(a). However, Ponzoni (2017) observed that the samples retrieved on the polder side were not fully saturated, with an estimated degree of saturation between 0.8 and 0.9. Given the water retention properties of the material, also reported by Ponzoni (2017), this would correspond to a suction stress of about 35 kPa. The latter might have been responsible for apparent over-consolidation, more than purely mechanical loading.

Based on this hypothesis, a different initialisation of the yield surface was attempted, following the stress path history depicted in Figure 2.25(b). The equivalent isotropic suction stress was applied starting from the normally consolidated K_0 state, which overconsolidated the sample and, at the same time, contributed to re-orienting the yield locus around the p'-axis (Romero and Jommi, 2008).

Figure 2.26 shows the influence of the two different initialisation hypotheses on the following deviatoric stress-strain response. The simulation performed after the assumption of suction-induced overconsolidation shows a clear improvement in the deviatoric stress-strain response compared to the mechanical 1-D overconsolidation hypothesis. The results on test T1 (X) improve to a large extent. For test T2 (X) in Figure 2.26(b) the model prediction still shows a small overestimation of the deviatoric strain caused by the proximity of the stress ratio to the critical one in extension, $M_{g,e}$, which reduces the shear stiffness to a greater extent than what observed experimentally.

These results should not be considered proof of the true origin of the observed overconsolidation. They were included in the discussion to clearly highlight that constitutive models built on anisotropic yield surfaces require a robust initialisation strategy to support their reliable use in practical applications.

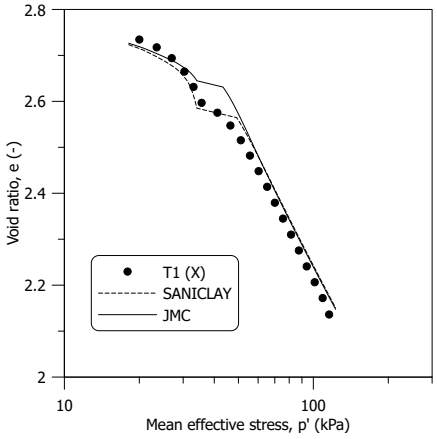

(a)

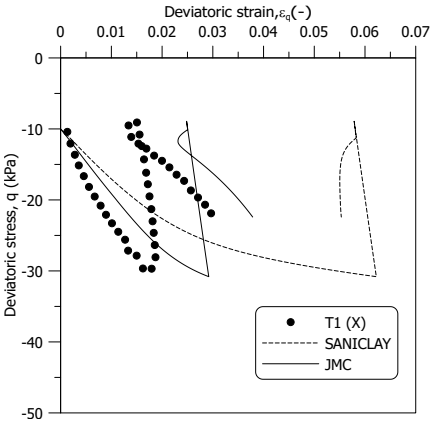

(b)

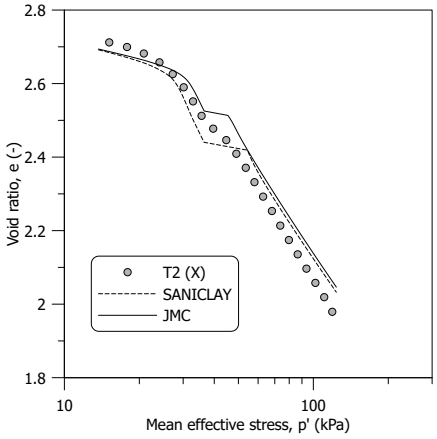

(c)

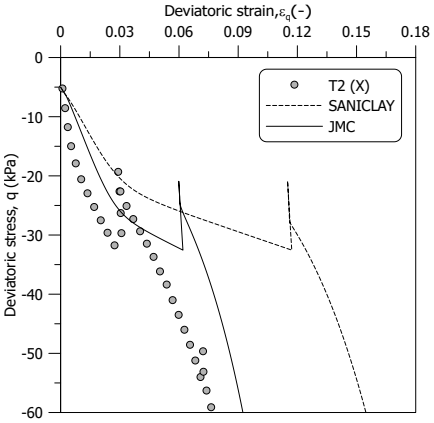

(d)

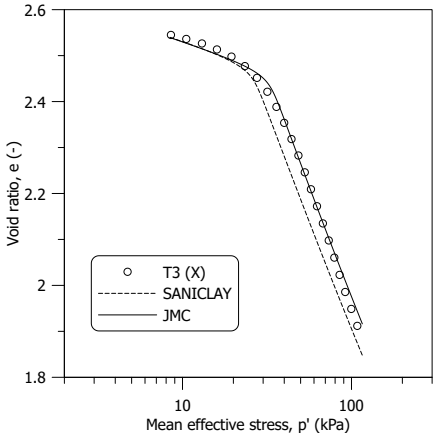

(e)

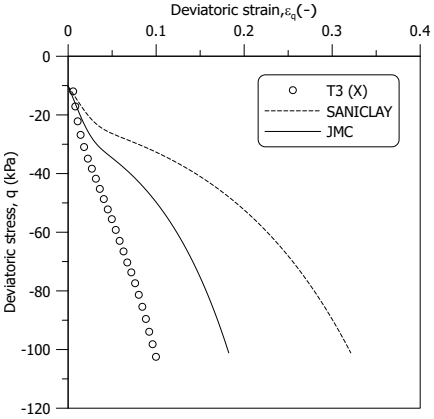

(f)

Figure 2.24: Comparison between numerical simulations and experimental data from drained triaxial extension tests on samples T1 (X), T2(X) and T3 (X)

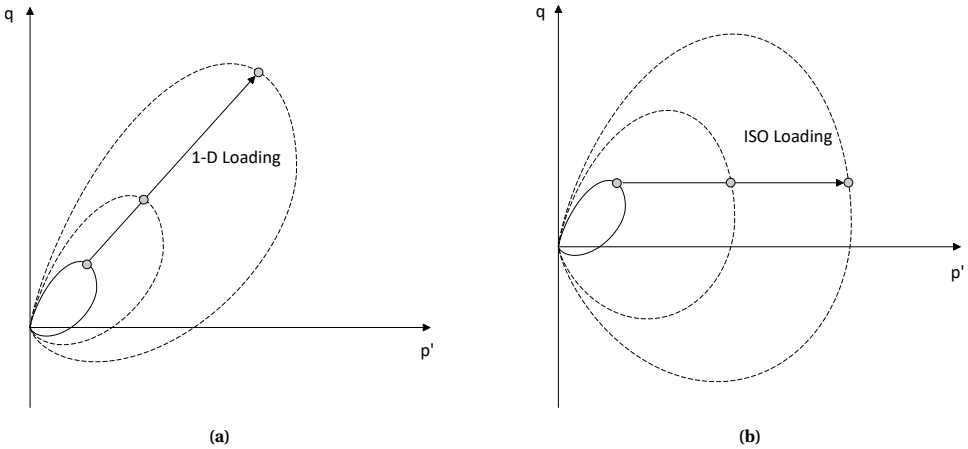

Figure 2.25: Evolution of yield locus under (a) 1-D loading (b) isotropic loading for initialisation of the stress state

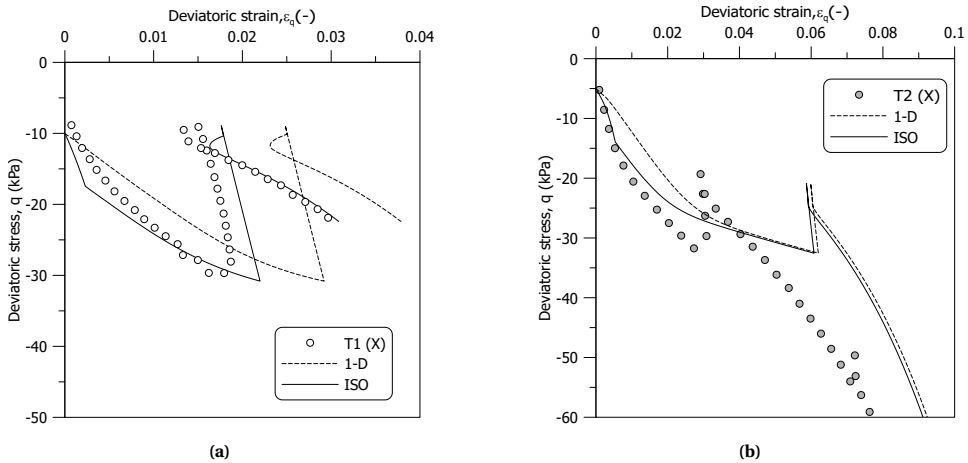

Figure 2.26: Comparison between numerical simulations with two different model initialisation and experimental data: (a) T1(X) and (b) T2(X)

2.7. CONCLUSIONS

Reliability of geotechnical design and assessment stems from advanced constitutive models, capable of modelling both the strength and the pre-failure behaviour of soil. In this work, a typical Dutch soft organic clay was investigated, to provide as thorough as possible insight on its stress-strain response over a variety of triaxial stress paths including extension ones, for which data are still scarce. The results were scrutinised to identify and tune relevant ingredients of an elastic-plastic modelling approach to be used in the practice.

The experimental programme was designed to elucidate compressibility and shear response, anisotropy and hardening of the organic clay. The experimental data show that the compressibility of the material may vary more than other features, depending on the organic content and the presence of diatoms. Over shear, the material displays a friction angle dependent on the Lode angle, based on triaxial compression and extension results. As expected, the depositional fabric is anisotropic and evolves rather quickly depending on the stress path. Careful analysis of drained probes results demonstrates that expansion of the yield locus is solely ruled by volumetric plastic strains, while the evolution of anisotropy depends on the loading direction.

Based on the previous experimental findings, a new constitutive model, JMC-clay is proposed. The model is built up on the SANICLAY framework due to the non-associated flow rule, which was confirmed by the experimental results. The proposal extends the previous formulation, essentially by allowing flexibility to the yield surface shape and improving the rotational hardening rule with a dependence on the Lode angle. The benefits of JMC-clay can be appreciated, especially in the deviatoric stress-strain response, and they become more and more evident at increasing stress ratio in extension.

The numerical simulations show that the proposed model can capture well the pre-failure response over non-monotonic loading and unloading stress paths, which is a crucial need for its implementation in the engineering practice. However, inspection of the limitations in the practical use reveals a very strong dependence of the predicted response on the initialisation of the yield surface inclination, especially at low stresses. The latter observation suggests that the bottleneck in the practical use of this class of models lies more in the initialisation of the current state rather than in calibration, which can follow a rather simple strategy in the laboratory.

BIBLIOGRAPHY

Becker, D., Crooks, J., Been, K., & Jefferies, M. (1987). Work as a criterion for determining in situ and yield stresses in clays. *Canadian Geotechnical Journal*, *24*(4), 549–564.

Bjerrum, L. (1967). Engineering geology of norwegian normally-consolidated marine clays as related to settlements of buildings. *Geotechnique*, *17*(2), 83–118.

Burland, J. (1990). On the compressibility and shear strength of natural clays. *Géotechnique*, *40*(3), 329–378.

Caicedo, B., Mendoza, C., López, F., & Lizcano, A. (2018). Behavior of diatomaceous soil in lacustrine deposits of bogotá, colombia. *Journal of Rock Mechanics and Geotechnical Engineering*, *10*(2), 367–379.

Callisto, L., & Calabresi, G. (1998). Mechanical behaviour of a natural soft clay. *Géotechnique*, *48*(4), 495–513.

Chao, C., Jommi, C., & Muraro, S. (2023). Numerical investigation of the equipment set-up in triaxial testing of soft soils. In *Proceedings 10th numge 2023* (pp. 1–6). GBR.

Cheng, X., Ngan-Tillard, D., & Den Haan, E. (2007). The causes of the high friction angle of dutch organic soils. *Engineering geology*, *93*(1-2), 31–44.

Cheng, X., Janssen, H., & Barends, F. B. (2004). A combination of esem, edx and xrd studies on the fabric of dutch organic clay from oostvaardersplassen (netherlands) and its geotechnical implications. *Applied Clay Science*, *25*(3-4), 179–185.

Coelho, B. Z., Dijkstra, J., & Karstunen, M. (2021). Viscoplastic cyclic degradation model for soft natural soils. *Computers and Geotechnics*, *135*, 104176.

Cotecchia, F., & Chandler, R. (1997). The influence of structure on the pre-failure behaviour of a natural clay. *Géotechnique*, *47*(3), 523–544.

D2974-14. (2014). Standard test methods for moisture, ash, and organic matter of peat and other organic soils. *American Society of Testing and Materials ASTM, PA, USA*.

D5550-14. (2014). Standard test method for specific gravity of soil solids by gas pycnometer. *American Society of Testing and Materials ASTM, PA, USA*.

Dafalias, Y. (1986). An anisotropic critical state soil plasticity model. *Mechanics research communications*, *13*(6), 341–347.

Dafalias, Y., Manzari, M. T., & Papadimitriou, A. G. (2006). Saniclay: Simple anisotropic clay plasticity model. *International Journal for Numerical and Analytical Methods in Geomechanics*, *30*(12), 1231–1257.

Dafalias, Y., & Taiebat, M. (2013). Anatomy of rotational hardening in clay plasticity. *Géotechnique*, *63*(16), 1406–1418.

Den Haan, E. (2003). Sample disturbance of soft organic oostvaardersplassen clay. *Deformation Characterstics of Geomaterials, Di Benedetto et al.(eds)-2003*, 49–55.

Diaz-Rodriguez, J., Leroueil, S., & Aleman, J. (1992). Yielding of mexico city clay and other natural clays. *Journal of geotechnical engineering*, *118*(7), 981–995.

Graham, J., Crooks, J., & Bell, A. L. (1983). Time effects on the stress-strain behaviour of natural soft clays. *Géotechnique*, *33*(3), 327–340.

Hashiguchi, K. (1977). An expression of anisotropy in a plastic constitutive equation of soils. *Constitutive Equations of Soils*, 302–305.

Head, K. H. (1992). *Manual of soil laboratory testing. volume 1. soil classification and compaction tests*.

Hight, D., Bond, A., & Legge, J. (1992). Characterization of the bothkennaar clay: An overview. *Géotechnique*, *42*(2), 303–347.

Huang, M., Liu, Y., & Sheng, D. (2011). Simulation of yielding and stress–stain behavior of shanghai soft clay. *Computers and Geotechnics*, *38*(3), 341–353.

Jiang, J., & Ling, H. I. (2010). A framework of an anisotropic elastoplastic model for clays. *Mechanics Research Communications*, *37*(4), 394–398.

Jiang, J., Ling, H. I., & Kaliakin, V. N. (2012). An associative and non-associative anisotropic bounding surface model for clay. *Journal of Applied Mechanics*, *79*(3).

Jommi, C., Chao, C., Muraro, S., & Zhao, H. (2021). Developing a constitutive approach for peats from laboratory data. *Geomechanics for Energy and the Environment*, *27*, 100220.

Jommi, C., Sterpi, D., de Gast, T., Muraro, S., Ponzoni, E., & van Hemert, H. (2019). Coupled hydro-mechanical analysis of the pre-failure and the failure behaviour of a dyke on soft subsoil: Formulation and synthesis of results. *15th ICOLD International Benchmark Workshop on Numerical Analysis of Dams, ICOLD-BW 2019*, 645–665.

Karstunen, M., Krenn, H., Wheeler, S. J., Koskinen, M., & Zentar, R. (2005). Effect of anisotropy and destructuration on the behavior of murro test embankment. *International Journal of Geomechanics*, *5*(2), 87–97.

Leoni, M., Karstunen, M., & Vermeer, P. (2008). Anisotropic creep model for soft soils. *Géotechnique*, *58*(3), 215–226.

Leroueil, S., & Vaughan, P. (1990). The general and congruent effects of structure in natural soils and weak rocks. *Géotechnique*, *40*(3), 467–488.

Lo, K. Y. (1962). Shear strength properties of a sample of volcanic material of the valley of mexico. *Geotechnique*, *12*(4), 303–318.

Ludwik, P. (1909). *Elemente der technologischen mechanik*. Springer.

Mašín, D. (2005). A hypoplastic constitutive model for clays. *International Journal for numerical and analytical methods in Geomechanics*, *29*(4), 311–336.

Mayne, P. W., & Kulhawy, F. (1982). K-ocr relationships in soil. *International Journal of Rock Mechanics and Mining Sciences and Geomechanics Abstracts*, *20*, A2–A2.

McDowell, G., & Hau, K. (2004). A generalised modified cam clay model for clay and sand incorporating kinematic hardening and bounding surface plasticity. *Granular Matter*, *6*(1), 11–16.

Mesri, G., Rokhsar, A., & Bohor, B. (1975). Composition and compressibility of typical samples of mexico city clay. *Geotechnique*, *25*(3), 527–554.

Muir Wood, D. (1990). *Soil behaviour and critical state soil mechanics*. Cambridge university press.

Muraro, S., & Jommi, C. (2021). Pre-failure behaviour of reconstituted peats in triaxial compression. *Acta Geotechnica*, *16*(3), 789–805.

Newson, T., & Davies, M. (1996). A rotational hardening constitutive model for anisotropically consolidated clay. *Soils and foundations*, *36*(3), 13–20.

Nocilla, A., Coop, M., & Colleselli, F. (2006). The mechanics of an italian silt: An example of 'transitional'behaviour. *Géotechnique*, *56*(4), 261–271.

Parry, R., & Nadarajah, V. (1974). Anisotropy in a natural soft clayey silt. *Engineering Geology*, *8*(3), 287–309.

Pineda, J., Suwal, L., Kelly, R., Bates, L., & Sloan, S. (2016). Characterisation of ballina clay. *Géotechnique*, *66*(7), 556–577.

Ponzoni, E. (2017). *Historical constructions on natural silty soils accounting for the interaction with the atmosphere* [Thesis].

Ponzoni, E., Nocilla, A., Coop, M., & Colleselli, F. (2014). Identification and quantification of transitional modes of behaviour in sediments of venice lagoon. *Géotechnique*, *64*(9), 694–708.

Reina Leal, C. R. (2019). *Influencia del contenido de materia orgánica en el cambio volumétrico de arcillas blandas* [Thesis].

Rezania, M., & Dejaloud, H. (2021). Bs-clay1: Anisotropic bounding surface constitutive model for natural clays. *Computers and Geotechnics*, *135*, 104099.

Rezania, M., Nguyen, H., Zanganeh, H., & Taiebat, M. (2018). Numerical analysis of ballina test embankment on a soft structured clay foundation. *Computers and Geotechnics*, *93*, 61–74.

Rezania, M., Taiebat, M., & Poletti, E. (2016). A viscoplastic saniclay model for natural soft soils. *Computers and Geotechnics*, *73*, 128–141.

Romero, E., & Jommi, C. (2008). An insight into the role of hydraulic history on the volume changes of anisotropic clayey soils. *Water Resources Research*, *44*(5).

Roscoe, K., & Burland, J. (1968). On the generalized stress-strain behaviour of wet clay.

Schmidt, B. (1966). Earth pressures at rest related to stress history. *Canadian Geotechnical Journal*, *3*(4), 239–242.

Seidalinov, G., & Taiebat, M. (2014). Bounding surface saniclay plasticity model for cyclic clay behavior. *International Journal for Numerical and Analytical Methods in Geomechanics*, *38*(7), 702–724.

Sekiguchi, H., & Ohta, H. (1977). Induced anisotropy and time dependancy in clays. *9th ICSMFE. Tokyo*, p163–175.

Sheahan, T. C., Ladd, C. C., & Germaine, J. T. (1996). Rate-dependent undrained shear behavior of saturated clay. *Journal of Geotechnical Engineering*, *122*(2), 99–108.

Shiwakoti, D., Tanaka, H., Tanaka, M., & Locat, J. (2002). Influences of diatom microfossils on engineering properties of soils. *Soils and Foundations*, *42*(3), 1–17.

Sivasithamparam, N., Karstunen, M., & Bonnier, P. (2015). Modelling creep behaviour of anisotropic soft soils. *Computers and Geotechnics*, *69*, 46–57.

Tanaka, H., & Locat, J. (1999). A microstructural investigation of osaka bay clay: The impact of microfossils on its mechanical behaviour. *Canadian Geotechnical Journal*, *36*(3), 493–508.

Tigchelaar, J., Feijter, J. W. d., & Haan, E. J. d. (2001). Shear tests on reconstituted oostvaardersplassen clay. In *Soft ground technology* (pp. 67–81).

Watabe, Y., Tanaka, M., Tanaka, H., & Tsuchida, T. (2003). K0-consolidation in a triaxial cell and evaluation of in-situ k0 for marine clays with various characteristics. *Soils and Foundations*, *43*(1), 1–20.

Wheeler, S. J., Näätänen, A., Karstunen, M., & Lojander, M. (2003). An anisotropic elasto-plastic model for soft clays. *Canadian Geotechnical Journal*, *40*(2), 403–418.

Wong, P., & Mitchell, R. (1975). Yielding and plastic flow of sensitive cemented clay. *Géotechnique*, *25*(4), 763–782.

Yamada, M., Akaishi, M., & Dafalias, Y. (2001). Undrained strain softening behavior of normally consolidated clays and mud rocks. *Doboku Gakkai Ronbunshu*, *2001*(687), 1–8.

Yin, Z.-Y., & Chang, C. S. (2009). Non-uniqueness of critical state line in compression and extension conditions. *International Journal for Numerical and Analytical Methods in Geomechanics*, *33*(10), 1315–1338.

Zdravković, L., Potts, D., & Hight, D. (2002). The effect of strength anisotropy on the behaviour of embankments on soft ground. *Géotechnique*, *52*(6), 447–457.

Zhang, X., Liu, X., Xu, Y., Wang, G., & Ren, Y. (2023). Compressibility, permeability and microstructure of fine-grained soils containing diatom microfossils. *Géotechnique*, 1–15.

3

Slow Cyclic Behaviour: Experimental Analysis and Modelling

The greatest enemy of knowledge is not ignorance, it is the illusion of knowledge.

Stephen Hawking

3.1. INTRODUCTION

Past research has shed light on various aspects of the cyclic response of clays. It is known that cyclic loading tends to deteriorate the soil structure, leading to a propensity for volumetric reduction. In undrained conditions, it causes a corresponding decrease in effective stresses, resulting in a lower cyclic undrained shear strength than the static one (Andersen, 2009). Studies have also found that the cyclic strength of clay reduces with an increase in the initial stress ratio prior to cyclic loading, and the presence of initial shear stresses reduces soil stiffness and increases permanent deformation (Hyodo et al., 1994).

Furthermore, earthquake-induced settlements in clays consist of immediate settlement during cyclic loading and post-cyclic recompression. These are affected by the cyclic amplitude, pre-cyclic initial stress state, and soil compressibility (Yasuhara et al., 2001). Time-dependent behaviour or 'creep' strains in clays have also been identified (Bjerrum, 1967; Graham et al., 1983; and Sheahan et al., 1996). Under cyclic loading, research suggests that increases in loading frequency can reduce excess pore pressure development (Wichtmann and Triantafyllidis, 2018; Tafili et al., 2021) but lead to greater stiffness degradation (Mortezaie and Vucetic, 2013).

Despite these extensive investigations into the dynamic properties, stress-strain behaviour, and post-cyclic responses of clays, research on the specific cyclic behaviour of soft clays, particularly Dutch organic clay, remains scarce. While some studies have examined the cyclic behaviour of soft marine clays (Vucetic, 1988; Hyodo et al., 1999; Wichtmann et al., 2013; Pan et al., 2022), they have often neglected the impact of organic matter on these characteristics. This gap is notable, especially considering the significant influence of organic matter on the monotonic behaviour of soils (Hight et al., 1992; Paul and Barras, 1999). Various researchers have emphasised the significance of the initial stress state preceding cyclic loadings on soils Wichtmann et al., 2013; Wichtmann and Triantafyllidis, 2018; Tafili et al., 2021; Ushev and Jardine, 2020). However, efforts have been limited to characterising the cyclic behaviour under varying initial stress states. This gap in our understanding is particularly relevant because soils in real-world conditions are seldom exposed to isotropic stress states.

This Chapter aims to address these gaps and extend our knowledge by focusing on the cyclic and post-cyclic response of Dutch organic clay. The study involves a comprehensive experimental programme, including strain and stress-controlled cyclic triaxial tests at various amplitudes and frequencies and starting from different initial stress states. This Chapter not only summarises the dynamic properties of Dutch organic clay based on experimental data but also extends the JMC-clay model to characterise its cyclic response. The Chapter concludes with a sensitivity analysis and model validation, comparing experimental data with numerical simulations to demonstrate the capabilities and limitations of the JMC-clay model in capturing various aspects of the cyclic behaviour of Dutch organic clay.

3.2. EXPERIMENTAL INVESTIGATION

3.2.1. MATERIAL DESCRIPTION

The same groups of material used in the experimental investigation in Chapter 2 are chosen to conduct the laboratory test in this Chapter. In addition, samples from two new sample tubes (B101-10 and B101-7) which belong to group (IX) and (X) were also used. Samples from these tubes were retrieved using a 106 mm piston sampler between 3.3 to 3.8 m (B101-7) and 5.0 to 5.5 m (B101-10) below the polder. To reduce biodegradation, the material was stored in a climate-controlled room at 10 ± 1°C and 90% relative humidity. To avoid loss of organic matter, oven-drying for soil classification was performed at 60°C (Head, 1992). The specific gravity of the soil, G_s, was measured with a helium pycnometer (D5550-14, 2014), and the organic content, OC, was assessed by ignition at 440°C (D2974-14, 2014). The material retrieved from the tube B101-10 is a clayey sandy silt with variable organic content ranging around 2%. The material from the tube B101-7 is a silt with a higher clay fraction (38%) and an organic content of about 4%. The tested samples are divided into groups depending on their organic content and sampling location. The particle size distribution from wet-sieving and hydrometer analysis for the tested groups and relevant index properties have been reported in Chapter 2.

3.2.2. TESTING PROGRAMMEME

Undisturbed soil samples of two different sizes were tested using a triaxial apparatus. The majority of the samples had nominal dimensions of 38 mm in diameter and 90 mm in height. For tests that incorporated bender element measurements or optic fibre pore pressure transducers, larger samples with nominal dimensions of 50 mm in diameter and 100 mm in height were used. The experiments were categorised into two groups based on the control mechanism: strain-controlled and stress-controlled tests. In strain-controlled tests, cyclic strain amplitude, $\Delta\varepsilon_{q,\mathrm{cyc}}$, is applied by controlling the axial displacement, as shown in Figure 3.1. In stress-controlled tests, the cyclic stress amplitude, q_{cyc}, is defined as a proportion of the deviatoric stress at critical state stress ratio, q_f, as depicted in Figure 3.1. The stress-controlled is achieved by varying axial load. Table 3.1 collects an indication of the stress path followed on each sample before cyclic shear, the initial void ratio, e_0, and the cyclic shear amplitude. The number of loading cycles applied to samples used for stress-controlled is 100 cycles. The number of loading cycles applied to samples used for strain-controlled is listed in Table 3.2.

Strain-controlled cyclic triaxial tests were performed on natural and reconstituted samples from groups (VII) and (IX). Isotropic or K_0 compression was imposed on samples before the cyclic shearing. Samples from groups (VII), (IX), and (X) were used to conduct stress-controlled cyclic tests. Different loading histories (i.e. isotropic and K_0 compression, radial - $\eta = q/p'$ constant - compression and extension paths) were imposed before cyclic loadings. In some samples, multiple cyclic loading stages were performed, and a resting stage was placed between the cyclic stages to allow excess pore pressure dissipation. If the sample did not reach large deformation or lose controllability, it was brought to failure with standard TxCU or TxEU tests after a post-cyclic recompression stage in which the excess pore pressure fully dissipated.

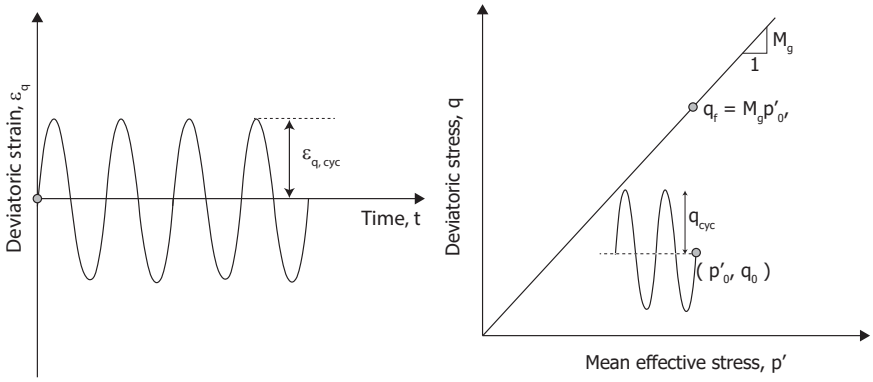

Figure 3.1: Illustration of $\Delta\varepsilon_{q,\text{cyc}}$, q_{cyc}, and q_f

3.2.3. TESTING EQUIPMENT

Two triaxial systems were employed in the experimental programme: the GDS Triaxial Automated System (GDSTAS) and the GDS Quasi Dynamic Triaxial Automated System (QDTAS), as shown in Figure 3.2. The primary distinction between the two lies in their maximum loading frequencies and data acquisition rates. Based on the author's experience, GDSTAS is capable of achieving a maximum loading frequency of 0.005 Hz and a data acquisition rate of 1 Hz. In contrast, QDTAS can apply a loading frequency of 0.1 Hz and a data acquisition rate of 500 Hz. Additionally, QDTAS performs more effectively in stress-controlled tests as its control loop accounts for the approximate stiffness of the sample. Consequently, GDSTAS is utilised for strain-controlled tests, while QDTAS is chosen for stress-controlled tests in this Chapter.

The triaxial system includes a submersible 1 kN load cell, back pressure and cell pressure volume controllers with an accuracy of ±1 kPa on pressure and ±200 mm^3 or ±1000 mm^3 on volume (0.1% full-scale range). In addition, the accuracy and resolution of axial displacement sensors is ±0.035 mm and 8×10^{-4} mm. A suction cap was used to ensure perfect contact between the load cell and the top cap. All the drained stress paths were performed under stress control, assuring a maximum excess pore pressure lower than 3 kPa.

Table 3.1: Initial state and type of stress path followed in the cyclic triaxial tests

Tube	Sample ID	Stress path before the test	OC (%)	Group	e_0 (-)	Cyclic amplitude
B103-14	Cyc T1	Isotropic	2.86	VII	1.61	q_{cyc}/q_f =0.08 and 0.2
	Cyc T2	K_0 and BE	2.86		1.58	$\varepsilon_{q,cyc}$ = 2.5%
	Cyc R1	Isotropic	2.56		1.07	$\varepsilon_{q,cyc}$ = 0.5% (4 stages)
B106-13	Cyc T1	Isotropic	2.3	IX	1.24	$\varepsilon_{q,cyc}$ = 2% and 4%
	Cyc T2	K_0^*	2.2		1.28	$\varepsilon_{q,cyc}$ = 2%
	Cyc R1	Isotropic	2.1		1.28	$\varepsilon_{q,cyc}$ = 2%
	R2	Isotropic	2.1		1.25	-
B101-10	Cyc T3	K_0 and BE**	2.2		1.17	-
B101-8	T1	Constant η***	4.2	X	2.77	q_{cyc}/q_f =0.1 and 0.26
	T2	Constant η	4.5		2.74	q_{cyc}/q_f =0.1 and 0.25
	T3	Constant η	3.8		2.58	q_{cyc}/q_f =0.11 and 0.27
	T4	Constant η	3.5		2.61	q_{cyc}/q_f =0.11 and 0.27
	T5	Constant η	4.6		2.76	q_{cyc}/q_f =0.12 and 0.30
	T6	Constant η	3.7		2.60	q_{cyc}/q_f =0.11 and 0.26
	T7	K_0	3.4		2.35	q_{cyc}/q_f =0.08 and 0.2
	T8	Isotropic	3.2		2.24	q_{cyc}/q_f =0.08 and 0.2
	T9	K_0 and BE	3.2		2.39	q_{cyc}/q_f =0.1 and 0.26
B101-7	Cyc T1	Isotropic	3.9		2.93	q_{cyc}/q_f =0.08 and 0.2

* K_0 triaxial compression at null lateral strain
** BE: bender elements measurement
*** Constant η: stress paths at constant stress ratio (see Chapter 2 for the specific soil samples)

The pseudo-elastic shear modulus, G_{max}, provides valuable soil information relevant to numerous geotechnical engineering applications, particularly in the simplified assessment of soil response under cyclic or dynamic loadings (Lee and Santamarina, 2005). The bender elements are used in the experimental programme to access the pseudo-elastic shear modulus of organic soft clay in this Chapter. The bender elements are combined P and S wave transducers manufactured by GDS Instruments and consist of two element inserts. The S-wave transmitter/P-wave receiver is installed in the top cap, while the P-wave transmitter/S-wave receiver is in the base cap. The S-wave transmitter includes two piezoceramic strips polarised in the same direction. When an excitation voltage is applied, one strip extends, and the other contracts, causing the strips to bend. The two strips in the receiver are polarised by the wave motion in opposite directions, as illustrated in Figure 3.3. The P wave transmitter consists of two piezoceramic strips polarised in opposite directions. When an excitation voltage is applied, both strips extend or contract. The two strips in the receiver are polarised by the wave motion in the same directions, as also depicted in Figure 3.3.

Table 3.2: Number of loading cycles applied to samples used for strain-controlled

Sample ID	Number of Cycles
Cyc T2(VII)	90 cycles
Cyc R1(VII)	48, 46, 32, 50 cycles
Cyc T1(IX)	67 cycles (both stages)
Cyc T2(IX)	67 cycles
Cyc R1(IX)	67 cycles

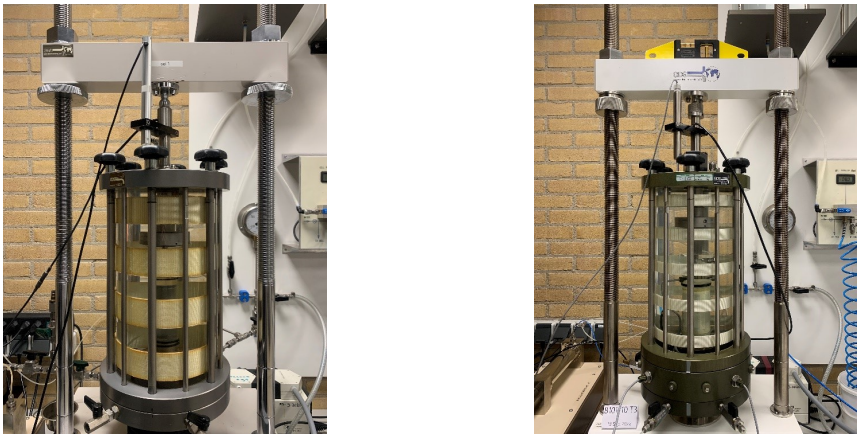

(a) (b)

Figure 3.2: Photo of triaxial system: (a) GDSTAS triaxial system (b) QDTAS triaxial system

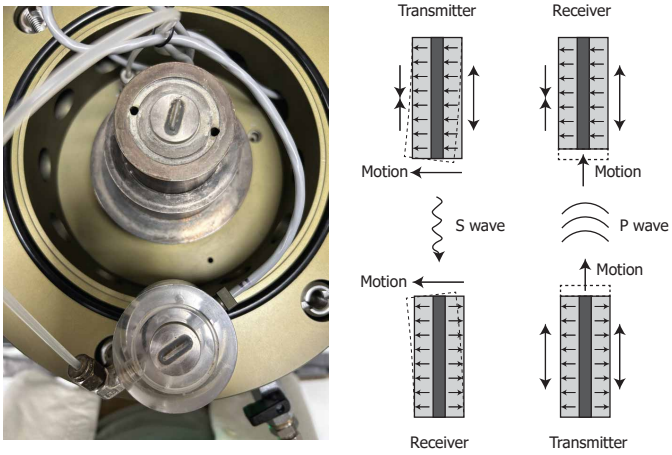

Figure 3.3: Photos and working principle of bender elements (after GDS Bender Elements Hardware Handbook)

3.3. EXPERIMENTAL RESULTS

The triaxial data are elaborated adopting the common triaxial stress-strain variables: mean effective stress p', deviatoric stress q, volumetric strain, ε_p, and deviatoric strain, ε_q. Compressive stresses and strains are assumed to be positive. Natural strains (Ludwik, 1909) are adopted to avoid bias in the data interpretation caused by the large displacements attained by the samples (Jommi et al., 2021).

The volumetric response of soil under cyclic loading can be tracked through the stress path and the development of pore pressure. Figure 3.4(a) illustrates the definition of cyclic excess pore pressure, Δu_{cyc}, and average excess pore pressure, Δu_{avg}, during cyclic loading.

The soil exhibits not only a volumetric response but also a deviatoric response upon cyclic loading. When constant cyclic stress is applied, the deviatoric response mainly involves the accumulation of permanent shear strain, $\varepsilon_{q,\text{per}}$, and an increase in cyclic strain amplitude, $\varepsilon_{q,\text{cyc}}$, under continuous cyclic loading, as shown in Figure 3.4(b). Conversely, if a constant cyclic strain is applied, the deviatoric behaviour is mainly characterised by variations in the secant shear modulus, G_{sec}, and damping ratio, D, as the number of loading cycles increases. The definition and calculation of the secant shear modulus and damping ratio in the cyclic triaxial test is illustrated in Figure 3.5. The subsequent experimental results will focus on the aspects discussed above, including volumetric and deviatoric responses.

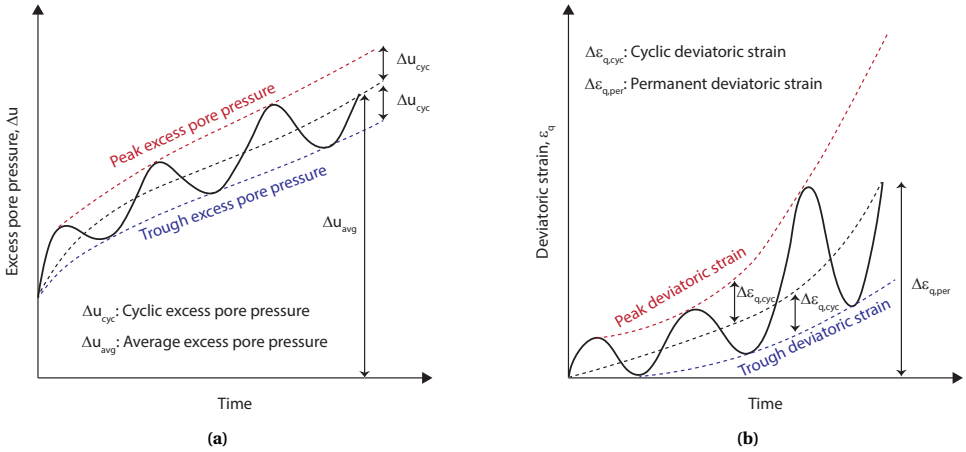

Figure 3.4: Definition of (a) pore pressure generation and (b) permanent deformation during cyclic loading (redrawn after Andersen, 2009)

3.3.1. STRAIN-CONTROLLED TESTS

Strain-controlled cyclic triaxial tests are widely used to study the cyclic behaviour of soils. One advantage of such tests is that they allow for the observation of variations in undrained shear strength during cyclic shearing. Additionally, these tests simplify the calculation of the evolution of the secant shear modulus and damping ratio. Furthermore, strain-controlled tests facilitate the development of constitutive models, as most

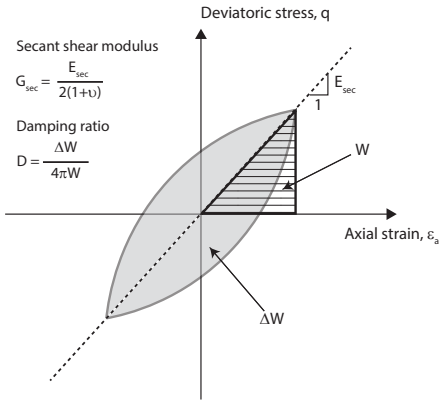

Figure 3.5: Definition of secant shear modulus (G_{sec}) and damping ratio (D) upon cyclic loading (redrawn after Hayashi et al., 2020)

numerical integration algorithms are based on strain increments. Lastly, in investigating the impact of loading frequency on soil response, strain-controlled testing is crucial as it ensures a consistently applied strain rate independent of soil type or sample stiffness. This is particularly important because, in stress-controlled tests, the strain rate can vary depending on the stiffness of the sample and the type of soil being tested.

RATE EFFECT AT LOW FREQUENCY RANGE

To investigate the strain-rate-dependent cyclic behaviour of organic soft clay, a multi-stage, strain-controlled cyclic triaxial test was conducted on remoulded samples Cyc R1(VII). The test employed four different loading frequencies: 0.01, 0.005, 0.001, and 0.0005 Hz, and the strain amplitude is 0.5%. The sample was tested in the GDSTAS equipment, and the equipment is not capable of applying 0.01 Hz of 0.5% strain amplitude. Therefore, the results from this stage are not presented here. The sample was isotropically consolidated to $p' = 115$ kPa before the cyclic shear. Between each cyclic stage, drained resting stages were introduced to facilitate the dissipation of excess pore pressure and to bring the stress state to its initial isotropic consolidation conditions ($p' = 115$ kPa, $q = 0$ kPa). The changes in void ratio observed during these two drained resting stages are below 0.02. Given these minor changes, one can reasonably assume that the influence of the void ratio on the cyclic response is negligible.

Figure 3.6 illustrates the stress paths and stress-strain responses for each stage of the experiment up to 30 cycles. Still, the stage with 0.005 Hz loading frequency reached an amplitude slightly lower than 0.5%, indicating the capability of GDSTAS is limited for a loading rate above 0.001 Hz. The stress paths for all stages appear to stabilise around $p' = 50$ kPa. The stress path during the 30^{th} cycle of each stage, depicted by a red line in the figures, exhibits a butterfly shape. This particular shape, often observed at later stages of cyclic loading in various clays, has been reported in multiple studies (Sheu, 1985; Wichtmann and Triantafyllidis, 2018; Tafili et al., 2021). The phenomenon of dilation-contraction alternations leading to this stress path shape has been attributed to the rearrangement of microstructures resulting from the continuous change in load-

ing direction during cyclic shearing (Oda et al., 2001; Zhao and Guo, 2013; Yu and Yang, 2023). Based on the stress-strain relationship, it is evident that the secant shear modulus diminishes as the number of loading cycles increases. Overall, there appears to be no significant difference in the stress paths and stress-strain responses across different frequencies.

To further explore the impact of loading frequency on soil behaviour, the variations in average excess pore pressure with respect to the loading cycles for each stage are detailed in Figure 3.7. The excess pore pressure plateaus around the 20^{th} cycle, and the magnitude reduces as the loading frequency decreases. The variation of secant shear modulus and damping ratio with number of cycle are presented in Figure 3.8. Both the shear modulus and damping ratio show a decreasing trend as the number of loading cycles increases. Interestingly, the rate of these decreases does not seem to be affected by loading frequency. The secant shear modulus increases at lower loading frequencies, but the impact of loading frequency on the damping ratio is not evident.

Accurately determining the number of loading cycles is challenging in geotechnical engineering due to the irregular nature of cyclic loads. Although methods exist to approximate these loads into equivalent cyclic amplitudes and cycles, it is crucial to consider the effective stress state for a comprehensive analysis of the cyclic behaviour. As illustrated in Figure 3.9, the changes in undrained shear strength, secant shear modulus, and damping ratio during cyclic shearing are plotted against the average mean effective stress, p'_{avg}. The data presented in Figure 3.9 reveal that the undrained shear strength, secant shear modulus, and damping ratio decrease almost linearly as the average mean effective stress diminishes. Intriguingly, the reduction in these properties relative to the average mean effective stress occurs in a parallel manner across different loading frequencies. Additionally, higher values of undrained shear strength and secant shear modulus are observed at stages with lower loading frequencies.

These findings present a contrast with previous research and warrant further investigation. For example, Mortezaie and Vucetic (2013) explored the effects of loading frequencies of 0.001, 0.01, and 0.1 Hz on cyclic degradation and excess pore pressure in remoulded kaolinite clay. They reported a decrease in excess pore pressure with increasing loading frequency and a faster shear modulus degradation at higher frequencies. Similarly, Xiao et al. (2018) observed trends consistent with those of Mortezaie and Vucetic (2013), but at even higher frequencies (0.05, 0.25, and 1 Hz) on remoulded organic soils. It is worth noting that the range of loading frequencies in these prior studies is higher than those examined in the present study. Additionally, some studies demonstrated that both the compression during drained cyclic shearing (Yasuhara, 1994) and the post-cyclic recompression increase the undrained shear strength (Lei et al., 2022). Although the changes in recompression observed during drained resting stages are minor, they might still contribute to the increase in shear stiffness and strength.

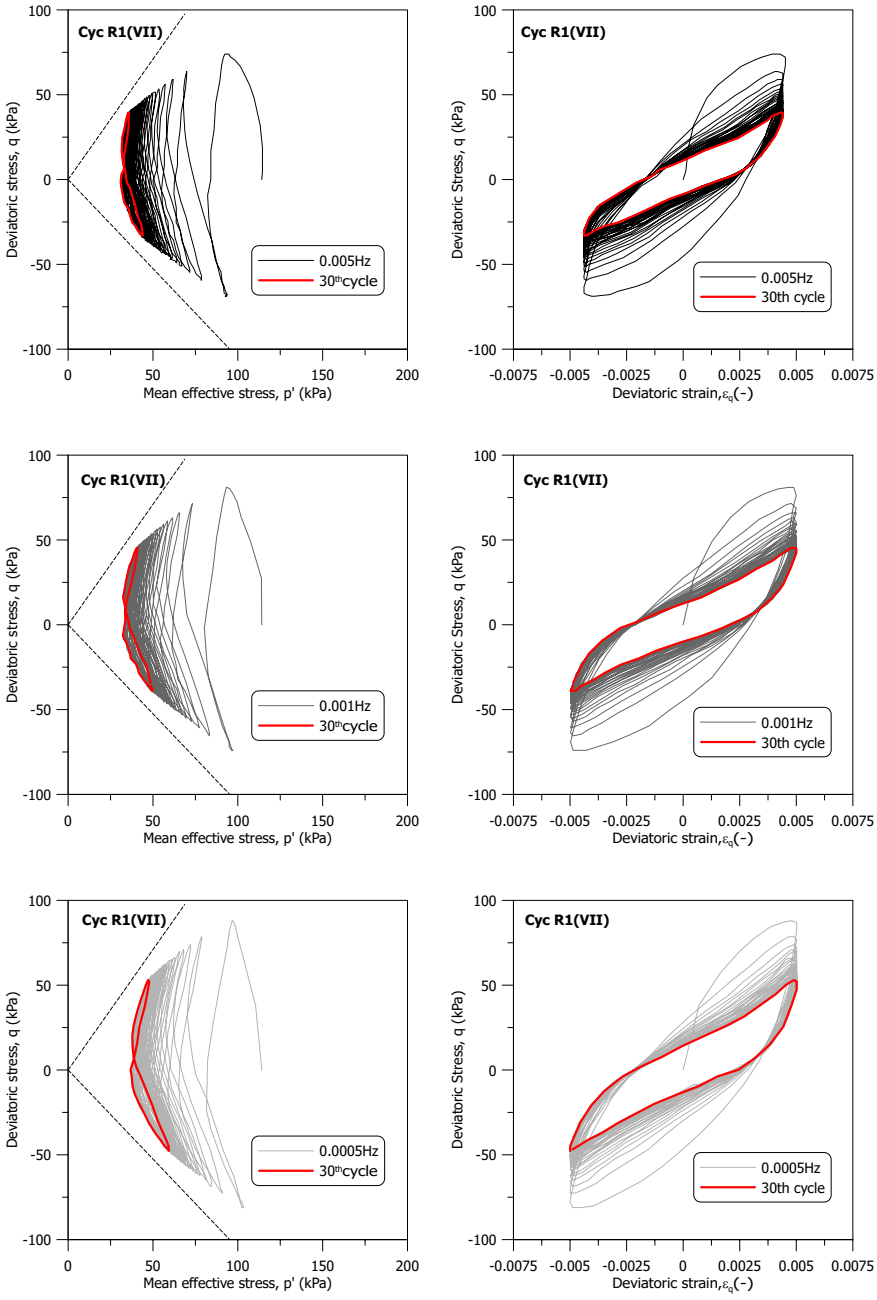

Figure 3.6: Stress paths and stress-strain responses of multi-stage, strain-controlled cyclic triaxial test

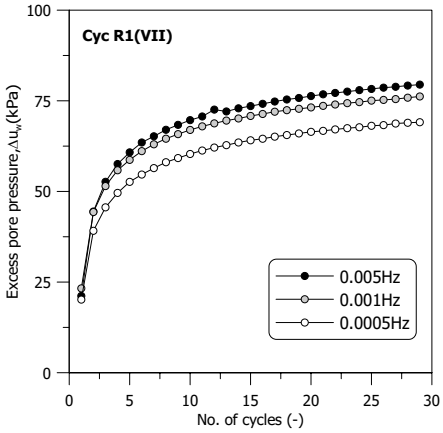

Figure 3.7: Variation of average excess pore pressure with loading cycle

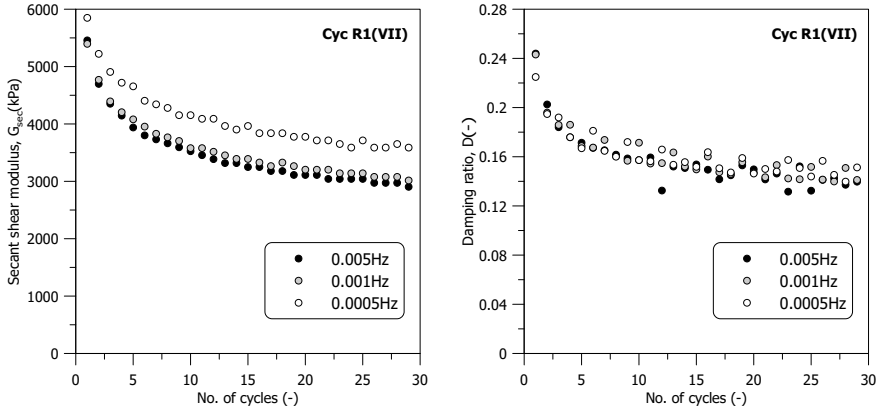

Figure 3.8: Variation of secant shear modulus and damping ratio with loading cycle

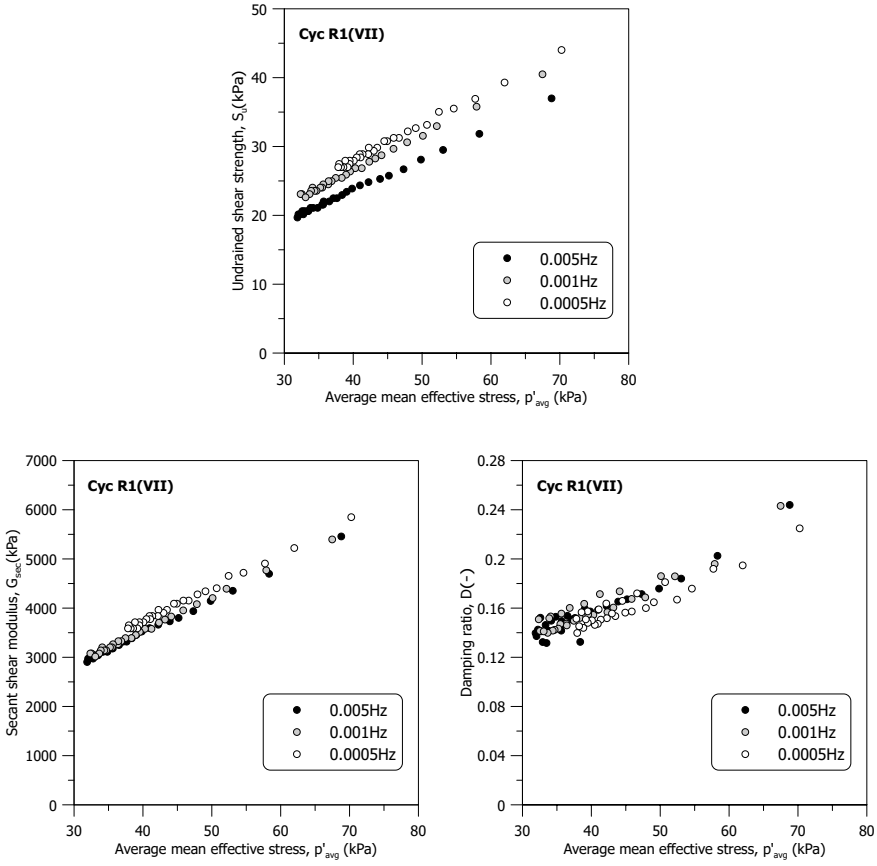

Figure 3.9: Variation of undrained shear strength, secant shear modulus and damping ratio with average mean effective stress

CYCLIC RESPONSE OF NATURAL AND RECONSTITUTED SAMPLE

Several studies have demonstrated that the static and cyclic behaviour of natural soft clay samples exhibits distinct characteristics when compared to reconstituted ones (Burland, 1990; Cotecchia and Chandler, 1997; Hyodo et al., 1999). The investigation of K_0 compression on natural and remoulded Dutch organic clay in Chapter 2 also indicates such a feature under static loading. To explore whether similar differences extend to cyclic behaviour, two cyclic triaxial tests were conducted on group (IX): one on Cyc T1(IX) (natural sample) and another on Cyc R1(IX) (reconstituted sample). GDSTAS setup was used to perform these tests. Both samples were isotropically consolidated to mean effective stress p' = 100 kPa prior to cyclic shearing. The tests employ a strain amplitude of 2% and a loading frequency of 0.001 Hz.

As shown by the stress paths and deviatoric stress-strain responses presented in Figure 3.10 for the first 50 loading cycles, accumulated excess pore pressure and reduced shear stiffness are more evident compared to the sample Cyc R1(VII), on which a smaller cyclic strain amplitude was applied. It should be noted that the data acquisition rate was not fast enough in the first quarter cycle of the sample Cyc R1(IX). The stress path and stress-strain curve of the 50^{th} loading cycle is marked in red, the butterfly-like shape is more distorted as the stress path approaches the origin. Additionally, the 50^{th} stress-strain curve of the remoulded sample is flatter compared to the natural one. It is noteworthy that the stress path of the remoulded sample approaches the origin. However, no significant deformation indicative of liquefaction was observed in the sample. Further scrutiny of the laboratory data reveals that the cell pressure controller in the triaxial setup is not capable of maintaining a constant cell pressure, exhibiting variations of ±4 kPa during the cyclic shearing. This fluctuation could introduce bias into the effective stress calculations. Figure 3.11 presents the variation of average excess pore pressure as a function of the loading cycle. The divergence in excess pore pressure between natural and remoulded samples primarily occurs during the first loading cycle. Subsequently, the rates of excess pore pressure accumulation appear to be similar across subsequent cycles.

Figure 3.12 displays the secant shear modulus and damping ratio from cyclic triaxial tests on both natural and reconstituted samples. The reconstituted sample exhibits a lower secant shear modulus and damping ratio. However, the rates at which the shear modulus and damping ratio decrease do not show a marked difference between the two types of samples. Further insights are provided in Figure 3.13, which illustrates the undrained shear strength, secant shear modulus, and damping ratio for both natural and reconstituted samples, plotted against the average mean effective stress. In both cases, the undrained shear strength, secant shear modulus, and damping ratio decrease as the average mean effective stress decreases. However, the manner in which these properties evolve is different between the natural and reconstituted samples. Particularly, the variation in undrained shear strength, secant shear modulus, and damping ratio with respect to average mean effective stress in the natural sample is not linear, unlike in the reconstituted sample. The natural sample exhibits higher shear stiffness, lower excess pore pressure development, and a slower reduction in undrained shear strength during cyclic loading. This suggests that the cyclic strength of the natural sample is greater than that of the reconstituted one, a finding that is consistent with Hyodo et al. (1999), who stud-

ied eight different marine clays. In agreement with existing literature, the secant shear modulus is significantly impacted by strain amplitude. This is exemplified by sample Cyc R1(VII), which displays a substantially higher secant shear modulus than that of samples Cyc T1(IX) and Cyc R1(IX) despite the minimal differences in their soil properties.

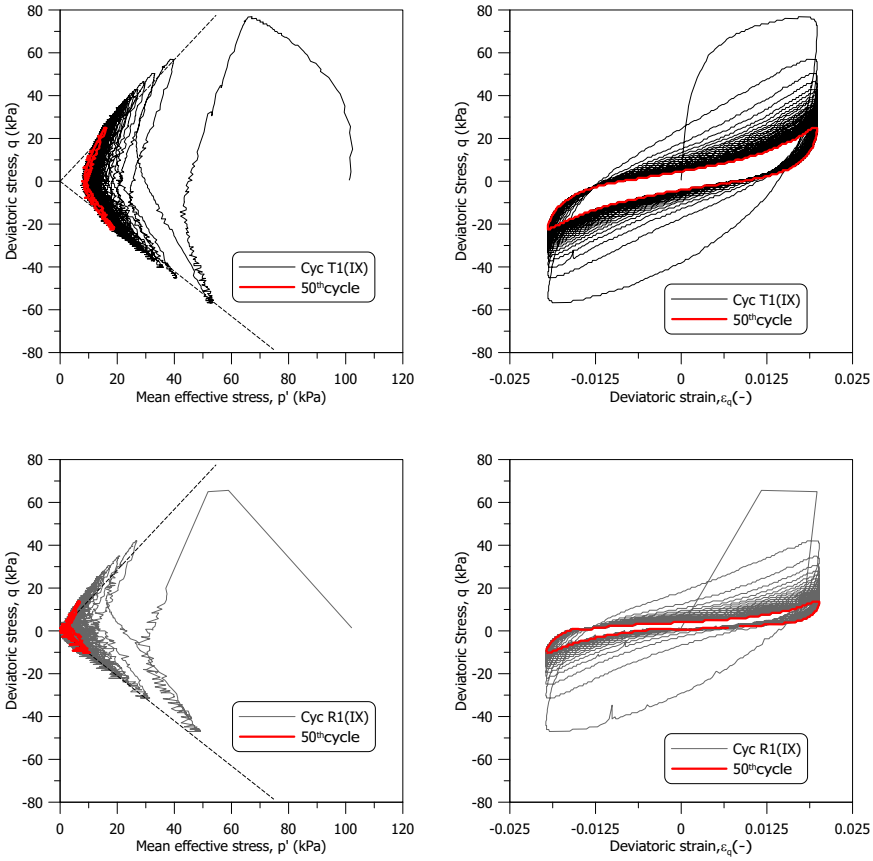

Figure 3.10: Stress paths and stress-strain responses of cyclic triaxial test on natural and reconstituted sample

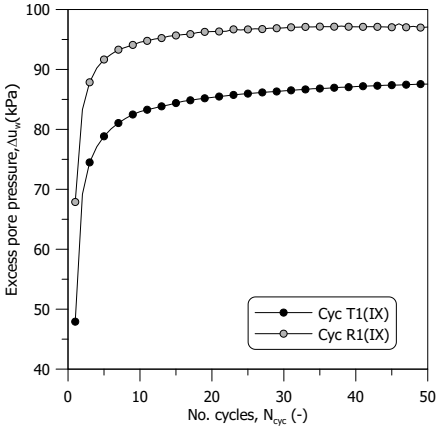

Figure 3.11: Average excess pore pressure of cyclic triaxial test on natural and reconstituted sample

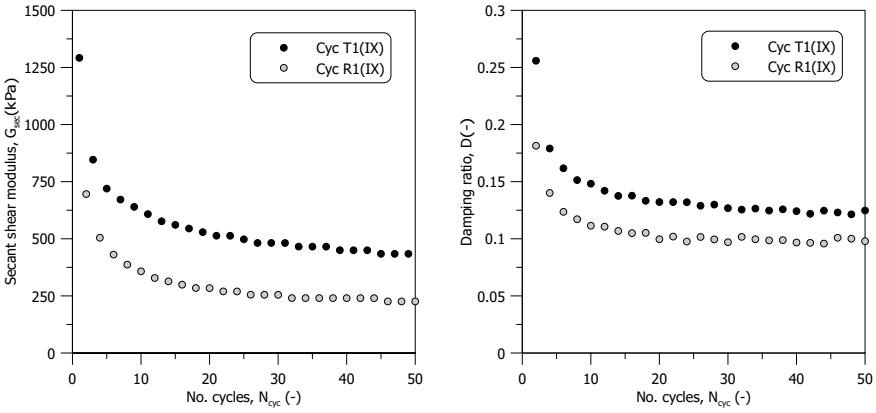

Figure 3.12: Secant shear modulus and damping ratio of cyclic triaxial test on natural and reconstituted sample with loading cycle

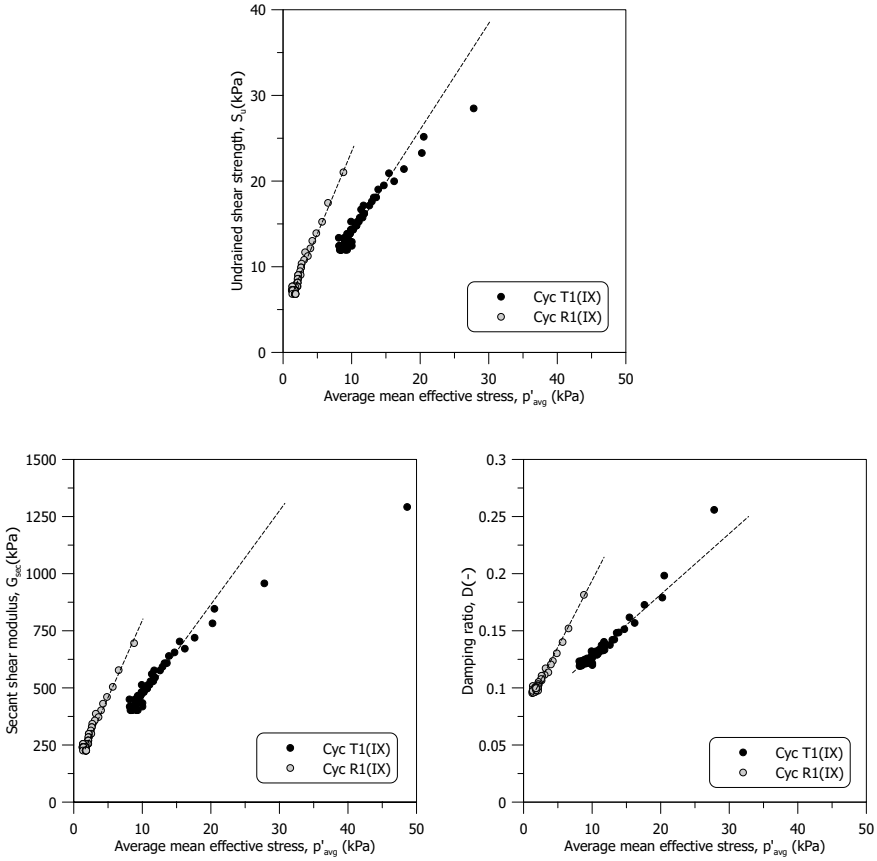

Figure 3.13: Undrained shear strength, secant shear modulus and damping ratio of cyclic triaxial test on natural and reconstituted sample with average mean effective stress

INFLUENCE OF INITIAL STRESS STATE

All previously presented strain-controlled cyclic triaxial tests were initiated from isotropic conditions. However, the initial stress state in field conditions is seldom isotropic. Additionally, several studies have demonstrated the impact of pre-shearing stress state on cyclic behaviour (Hyodo et al., 1994; Wichtmann and Triantafyllidis, 2018; Ushev and Jardine, 2020). To address this, a strain-controlled test was also performed on a K_0 consolidated sample Cyc T2(IX), the most commonly observed initial stress state in the field. The test reached the same mean effective stress $p' = 100$ kPa prior to cyclic shearing and employed a strain amplitude of 2% at a loading frequency of 0.001 Hz. The cyclic responses originating from different initial stress states are compared and discussed.

Figure 3.14 depicts the stress paths and stress-strain curves for selected cycles: 1^{st}, 2^{nd}, 5^{th}, 10^{th}, 25^{th}, and 50^{th} cycle. In both the isotropic and K_0-consolidated tests, the stress paths shift toward the left during the initial ten cycles and subsequently stabilise, exhibiting a butterfly-shaped pattern. The stress path of the test commencing from isotropic conditions displays greater symmetry along the horizontal axis, while the K_0-consolidated test appears symmetric along the η_{K_0} line. This asymmetry is also reflected in the stress-strain curves originating from K_0 conditions. Furthermore, the stress path of the isotropic test closely surpasses critical state stress ratios on both the compression and extension sides. In contrast, the K_0-consolidated test surpasses the critical state stress ratio on the compression side and remains below it on the extension side. To further investigate whether the anisotropic response of sample Cyc T2(IX) is specific to the sample or is a material behaviour, additional cyclic tests were conducted on samples Cyc T2(VII) using a strain amplitude of 2.4%. The stress path and stress-strain curve for these tests are presented in Figure 3.15. The anisotropic response can still be observed in the first ten loading cycles. However, the line of symmetry appears to shift towards the isotropic line at later loading cycles, and the stress path surpasses critical state stress ratios on both the compression and extension sides. Given the strain amplitudes used in test Cyc T2(VII) and Cyc T2(IX) are quite similar, it is reasonable to infer that the anisotropic response is specific to the sample Cyc T2(IX).

Figure 3.16 demonstrates that the test initiated from isotropic conditions exhibits higher average pore pressure in each cycle. This is attributed to its symmetrical behaviour along the horizontal axis, leading to a more pronounced movement of the average pore pressure toward the left on the meridian plane. In contrast, the stress path in the K_0-consolidated test, due to its asymmetrical stress path, shows a less dramatic shift toward the left on the meridian plane. Additionally, as observed from Figure 3.16, sample Cyc T2(VII) exhibits slightly higher excess pore pressure compared to sample Cyc T2(IX), a result of a more symmetrical stress path evolution.

Figure 3.17 presents the secant shear modulus and damping ratio of samples Cyc T1(IX), Cyc T2(IX), and Cyc T2(VII) in relation to the number of loading cycles. It is observed that sample Cyc T2(IX) exhibits the highest secant shear modulus and sample Cyc T1(IX) the lowest in the first cycle. Conversely, the damping ratio trend in the first loading cycle is inverse to that of the secant shear modulus. This difference aligns with the anisotropic behaviour of organic soft clays discussed in Chapter 2.

Interestingly, the secant shear modulus and damping ratio variations in sample Cyc T2(VII) tend to converge towards those of Cyc T1(IX) as the number of loading cycles

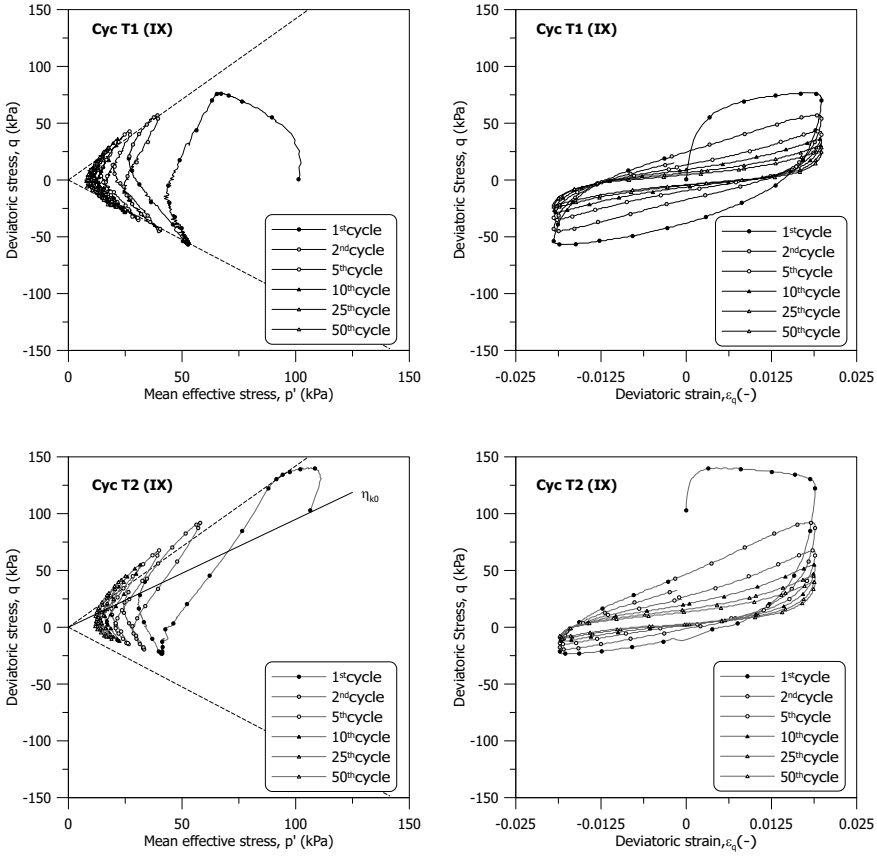

Figure 3.14: Stress paths and stress-strain responses of cyclic triaxial test starting from different initial stress state

increases. This phenomenon becomes more apparent in Figure 3.18, which plots the undrained shear strength, secant shear modulus, and damping ratio against the average mean effective stress. Initially, the secant shear modulus and damping ratio for sample Cyc T2(VII) are close to those of Cyc T2(IX), but they gradually align with the values of Cyc T1(IX) at an average mean effective stress of approximately 15-17 kPa. Specifically, the response of sample Cyc T2(VII) appears to transition from anisotropic to isotropic with increasing loading cycles, suggesting the erasing of stress-induced anisotropy during cyclic loading. Furthermore, it verifies the inherent anisotropy of sample Cyc T2(IX).

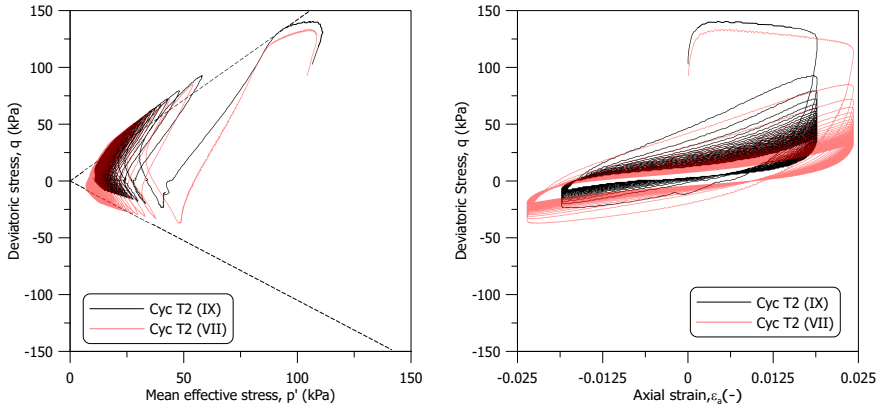

Figure 3.15: Stress paths and stress-strain responses of cyclic triaxial tests starting from K_0 stress state

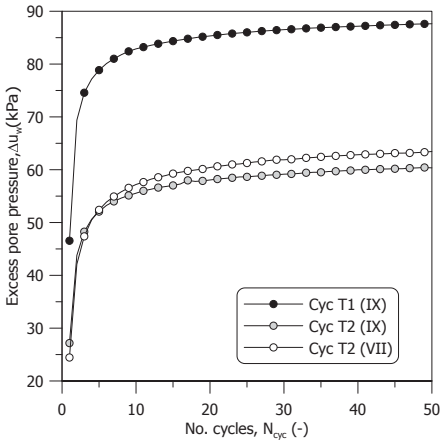

Figure 3.16: Average excess pore pressure of cyclic triaxial test starting from different initial stress state with loading cycle

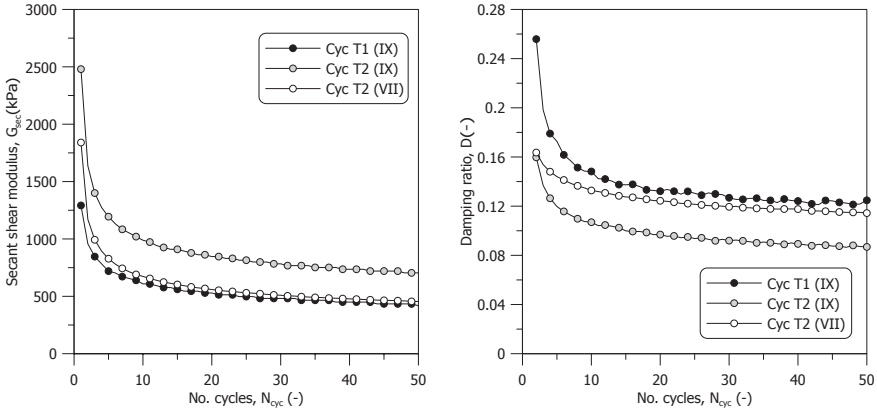

Figure 3.17: Secant shear modulus and damping ratio of cyclic triaxial test starting from different initial stress state with loading cycle

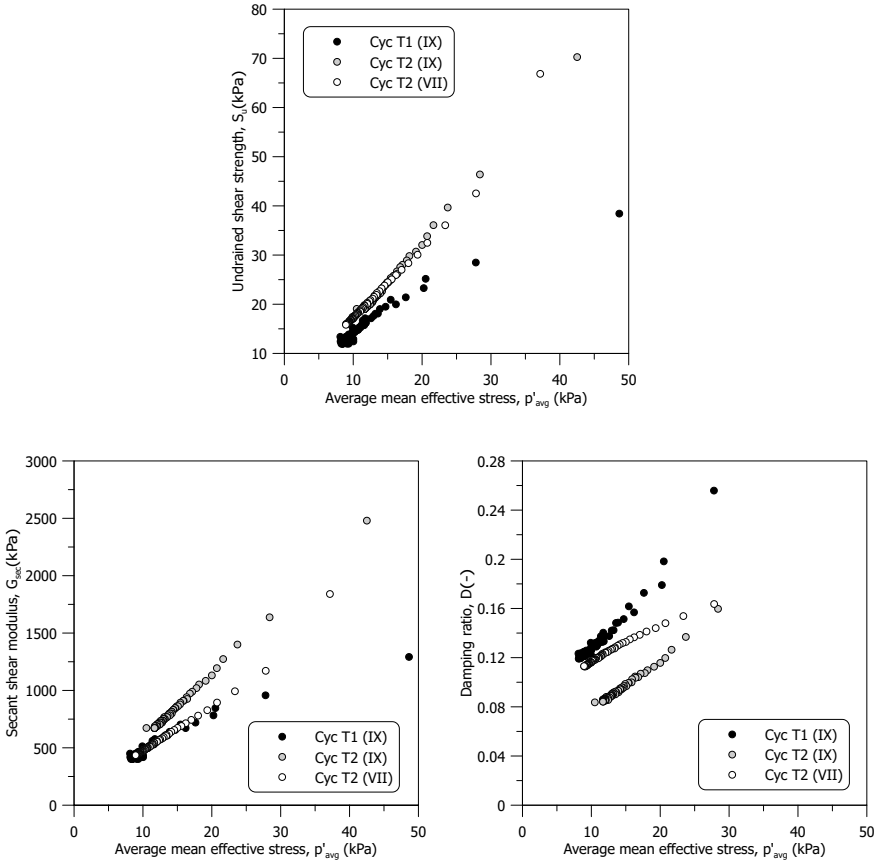

Figure 3.18: Undrained shear strength, secant shear modulus and damping ratio of cyclic triaxial test starting from different initial stress state with average mean effective stress

POST-CYCLIC UNDRAINED SHEAR STRENGTH

Upon completion of the cyclic shearing, drainage was allowed to enable the dissipation of excess pore pressure. After the drainage stage, the samples underwent either undrained compression or extension tests. Figure 3.19 delineates both the stress paths and the stress-strain curves for two different samples: the first is subjected to shearing directly following isotropic consolidation, whereas the second is sheared after the complete dissipation of excess pore pressure subsequent to two cyclic loading stages. When compared to a sample that did not undergo cyclic loading, the post-cyclic undrained shear strength, S_u, experiences a significant increase, surging from 35 kPa to 120 kPa—a nearly four-fold enhancement. This finding aligns with the literature (Yasuhara et al., 1992). In relation to critical state stress ratios, a comparison between the results depicted in Figure 3.20 and the experimental data on the same material, as presented in Chapter 2, suggests that cyclic shearing does not appear to modify the critical state stress ratios of the material under investigation.

POST-CYCLIC DEFORMATION

In strain-controlled cyclic shearing tests, the post-cyclic undrained shear strength of the samples is higher than the static shear strength. While the soil's strength is crucial for stability analysis, the permanent deformation resulting from cyclic loading is often more pertinent for serviceability assessments, particularly given the higher number of events of induced seismicity compared to natural earthquakes.

Figure 3.21 illustrates the variations in void ratio, excess pore pressure, volumetric strain, and axial strain during the two-stage strain-controlled cyclic test, Cyc T1(IX), alongside the isotropic compression stage. The data reveal that both permanent volumetric and axial strains are generated after cyclic loading. Notably, the permanent volumetric strain after the two recompression stages is approximately 10%, nearly identical to the strain observed during the isotropic consolidation stage. On the other hand, the permanent axial strain after the two cyclic and resting stages is about 4%, higher than that recorded during isotropic consolidation.

It can be seen that the slope of the post-cyclic recompression curve is higher than the slope of the reloading curve, Yasuhara and Andersen (1991) noted that the post-cyclic recompression index, $C_{r,cy}$, is approximately 1.5 times the ordinary recompression index, C_r. Interestingly, the permanent volumetric and axial strains from the first and second cyclic shearing stages are very similar, despite the strain amplitude in the second stage being twice as high as in the first stage. Yasuhara et al. (2001) indicates that post-earthquake recompression settlement is highly related to cyclic-induced excess pore pressure. Since maximum average excess pore pressures for these two stages are similar, as also shown in Figure 3.21, the same magnitude of post-cyclic recompression between the two stages is observed.

To explore the impact of the initial stress state on post-cyclic permanent deformation, Figure 3.22(a) and Figure 3.22(b) present the variations in void ratio, volumetric strain, and axial strain during the resting stages of two strain-controlled cyclic tests, Cyc T1(IX) and Cyc T2(IX). These are plotted alongside data from the consolidation stages. During the post-cyclic recompression stages, both samples are brought to an isotropic stress state of p' = 100 kPa. In the test that starts from isotropic conditions, the permanent volumetric strain measures 4.5%, while it is 4.1% in the K_0 test. For axial strain, the

isotropic test exhibits about 2%, and the K_0 test shows about 1%. Turning our attention to Figure 3.16, the peak average excess pore pressures in the cyclic tests amount to 86 kPa for isotropic and 58 kPa for K_0 conditions.

An initial comparison suggests that a straightforward relationship between excess pore pressure and permanent volumetric strain may not exist. However, upon closer scrutiny of sample compressibility, the K_0-consolidated sample turns out to be more compressible. The slopes of the normal compression lines, denoted as λ, for the isotropic and K_0-consolidated samples are 0.125 and 0.165 on the $e - \ln(p')$ plane. When normalised by λ, the permanent volumetric strains for the isotropic and K_0 conditions become 0.36 and 0.25. The ratio between these normalised strains is 1.44, close to the 1.48 ratio between the peak average excess pore pressures.

This indicates that the degree of permanent volumetric strain is dictated by both the sample compressibility and the excess pore pressure generated, given the same post-cyclic recompression stress path. In terms of axial strain, the K_0-consolidated sample exhibits a similar strain to its isotropic counterpart, hinting that the recompression stress path instead of the consolidation one has a more significant influence on this metric. Nevertheless, further investigation is needed on this aspect.

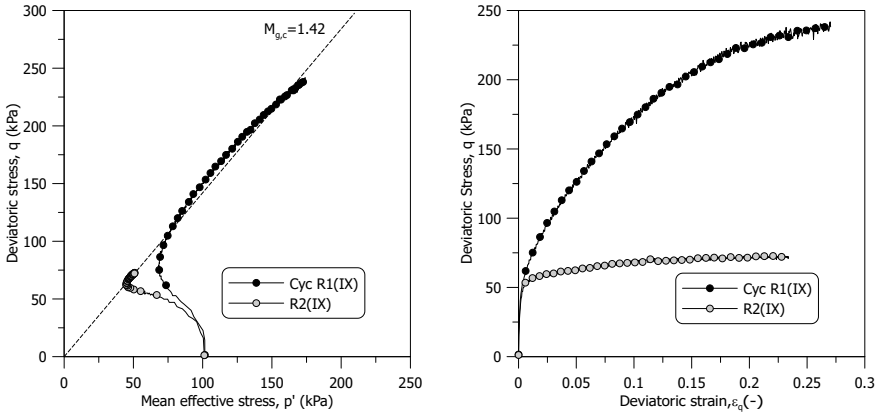

Figure 3.19: TxCU results on samples with and without experiencing cyclic loading

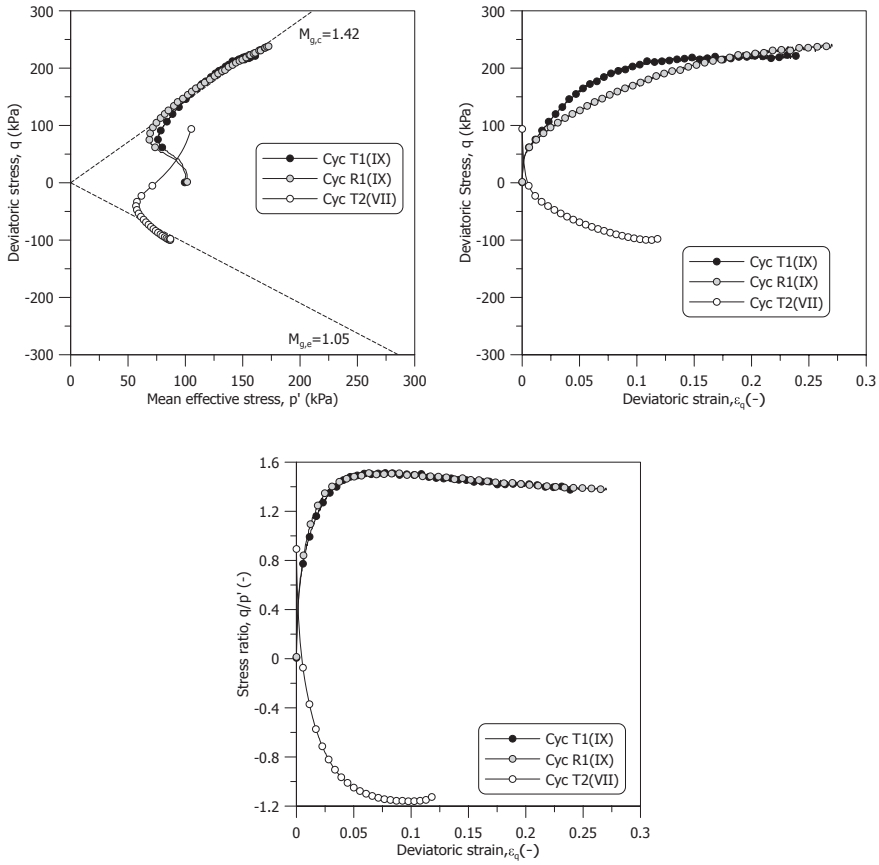

Figure 3.20: TxCU and TxEU results on samples after cyclic loading

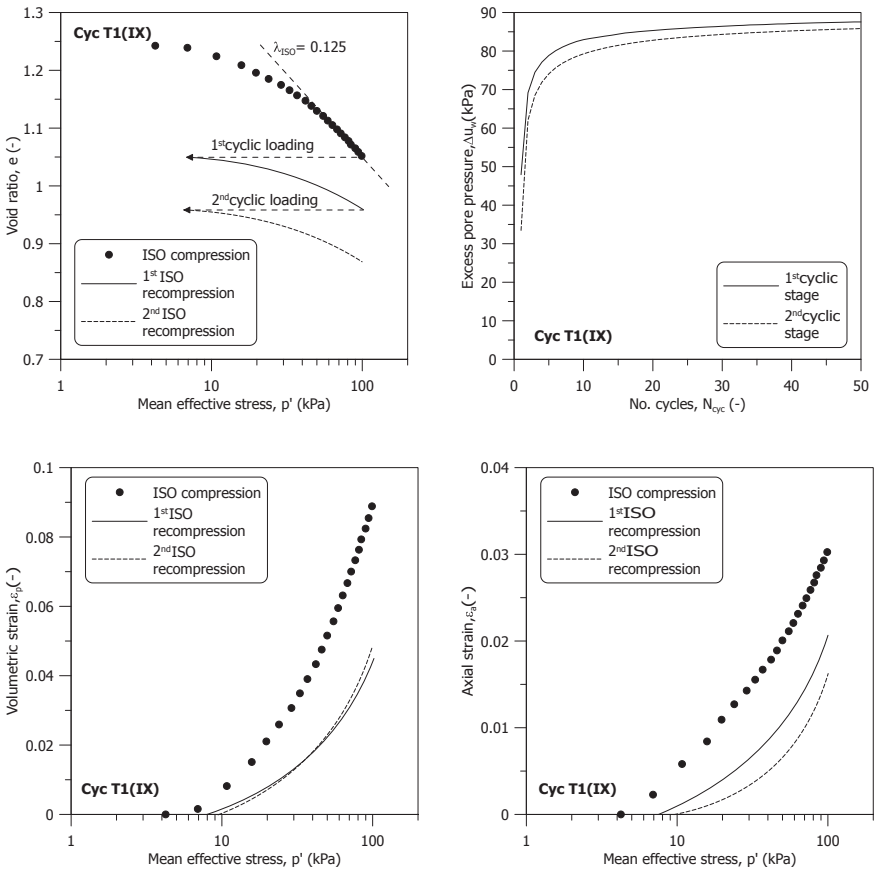

Figure 3.21: Variation of void ratio, excess pore pressure, and strains of two-stages cyclic triaxial test

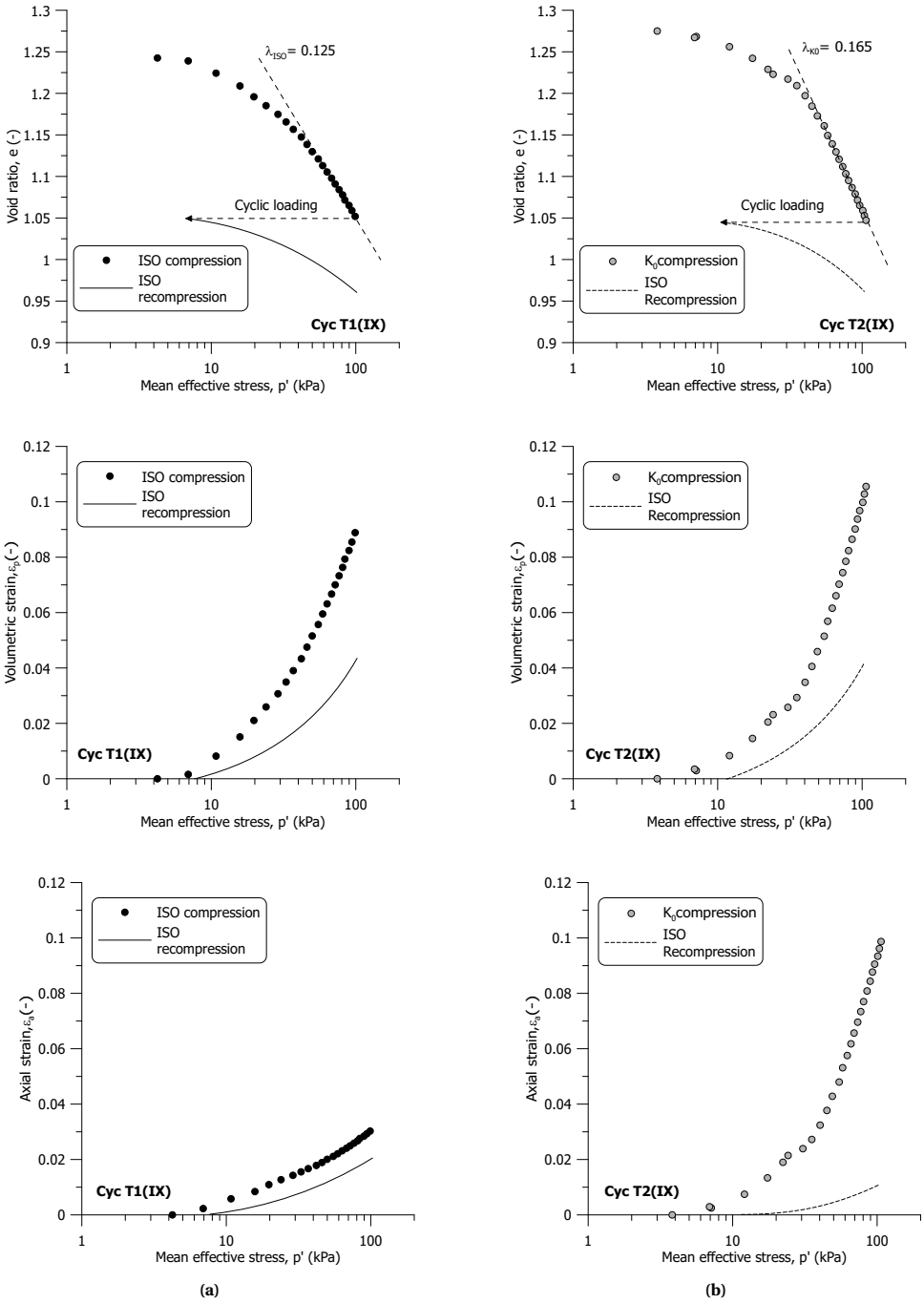

Figure 3.22: Variation of void ratio and strains of cyclic triaxial tests starting from different initial stress state

3.3.2. STRESS-CONTROLLED TESTS

In many earthquake engineering applications, field-measured acceleration or loading time histories are transformed into equivalent stress time histories and cycle counts. This conversion enables conventional laboratory investigations such as cyclic triaxial or cyclic direct simple shear tests to be more feasibly conducted (Seed, 1975; Liu et al., 2001). While strain-controlled cyclic tests are invaluable for a fundamental understanding of the soil's cyclic response and are convenient for constitutive model development, stress-controlled tests provide practical insights into how soil behaves under specific stress conditions. Because most geotechnical infrastructures are designed to meet particular stress conditions, many design references are based on the magnitude of cyclic stress encountered (Andersen, 2015). Therefore, stress-controlled tests have become a key component of experimental programmes for many researchers exploring the cyclic behaviour of soils.

INFLUENCE OF INITIAL STRESS STATE

In the preceding section, the influences of the initial stress state on cyclic response are examined through strain-controlled cyclic tests, focusing on isotropic and K_0 conditions. However, it is worth noting that the initial stress state in the field can vary and may not necessarily be a K_0 condition. To extend our understanding of how the initial stress state impacts cyclic behaviour, two-stage stress-controlled cyclic tests were conducted on samples from the group (X) with varying initial stress ratios after radial probe stress paths.

Figure 3.23 illustrates the stress paths during the cyclic stages for all tests. All samples were consolidated along a constant stress ratio radial path to mean effective stress, p' of 120 kPa. Specifically, samples T1(X)–T3(X) began on the extension side prior to the cyclic stages, whereas samples T4(X)–T6(X) and T9(X) started on the compression side. If the excess pore pressure was above 5kPa during the first cyclic stage, a recompression stage was introduced between the cyclic stages to allow for the dissipation of excess pore pressure.

For the first cyclic stage, the stress amplitude was around 12% of the deviatoric stress at critical state stress ratio, q_f with p' = 120 kPa. This translates to 18 kPa on the compression side and 13.2 kPa on the extension side. During the second cyclic stage, the stress amplitude was around 27% of the q_f at p' = 120 kPa, corresponding to 45 kPa on the compression side and 33 kPa on the extension side. A loading frequency of 0.1 Hz was used in these tests, and the tests ran for up to 100 cycles on the QDTAS equipment.

The sample designated T5(X) presents a unique case: it did not achieve a mean effective stress p' = 120 kPa prior to the cyclic stages. This deviation is due to the radial path being along a high stress ratio, which results in significant axial displacement. To preserve the measurement range of the axial position sensor, the cyclic shearing for this particular sample started from a slightly lower mean effective stress, p'. Additionally, for sample T5(X), significant softening occurred during the initial loading cycle of the second stage, rendering the apparatus unable to maintain control due to the abrupt change in sample stiffness. On the other hand, sample T3(X) exhibited a maximum axial strain of 5% at the 83^{rd} cycle, accompanied by substantial softening. As a result, the tests were halted before completing the planned 100 cycles.

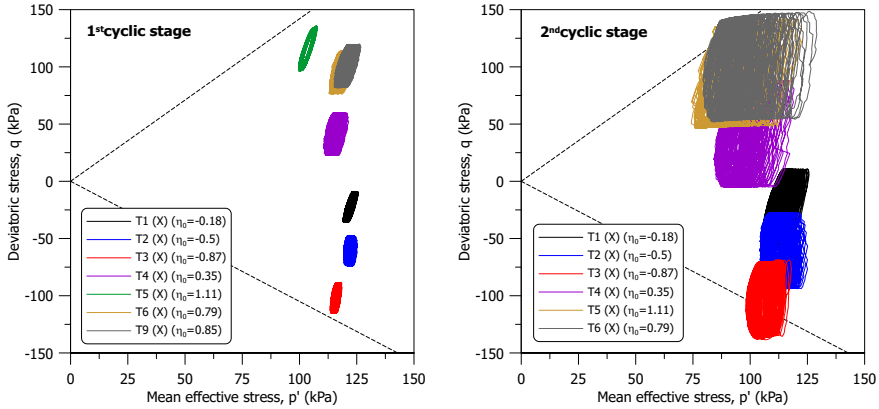

Figure 3.23: Stress path of two-stage stress-controlled cyclic triaxial tests

The detailed stress paths for these tests are illustrated in Figures 3.24 and 3.25, with the final stage stress path marked in red. The test on sample T9(X) is not included here as its results closely resemble those of T6(X), which is expected given their similar initial stress ratios. As Figure 3.24 shows, all samples exhibit a contractive response over 100 cycles. The shift in mean effective stress towards the left for all tests ranges from 5 to 10 kPa. Generally, tests initiated from the compression side show a more pronounced contractive response, except for sample T5(X), where minimal stress path shift occurs in the first 50 cycles.

Interestingly, the first cyclic stage stress paths for all samples display a lens-like shape from the initial loading cycle. Wichtmann and Triantafyllidis (2018) observed similar lens-shaped stress paths in remoulded kaolin samples as the excess pore pressure reaches a stabilisation phase. They also noted the consistent stress path inclination on both compression and extension sides as indicative of pronounced inherent anisotropy. However, the variation in lens thickness with the initial stress ratio does not follow a discernible pattern from the tests conducted.

Figure 3.25 depicts the detailed stress paths for the second cyclic stage. As in the first stage, all samples demonstrate a contractive response during cyclic shearing, with more pronounced contraction in samples starting from higher absolute stress ratios, particularly on the compression side. For the two tests with high absolute stress ratios, the stress paths surpass the critical state stress ratio. Especially for samples T2(X) and T3(X), the inclination of the stress path diminishes in the second stage, suggesting that inherent anisotropy is altered at higher stress amplitudes. Additionally, the lens thickness for all samples increases with higher stress amplitude.

Xu et al. (2020) and Ushev and Jardine (2020) show that a lens-like stress path shape is also observed in over-consolidated clays and glacial till samples. With pre-consolidation pressures in the field around 30-40 kPa for the tested samples (Ponzoni, 2017), and after consolidation to a mean effective stress of 120 kPa, the samples should be in a normally consolidated state before cyclic shearing. A detailed investigation is required to understand the reasons behind this particular stress path evolution fully.

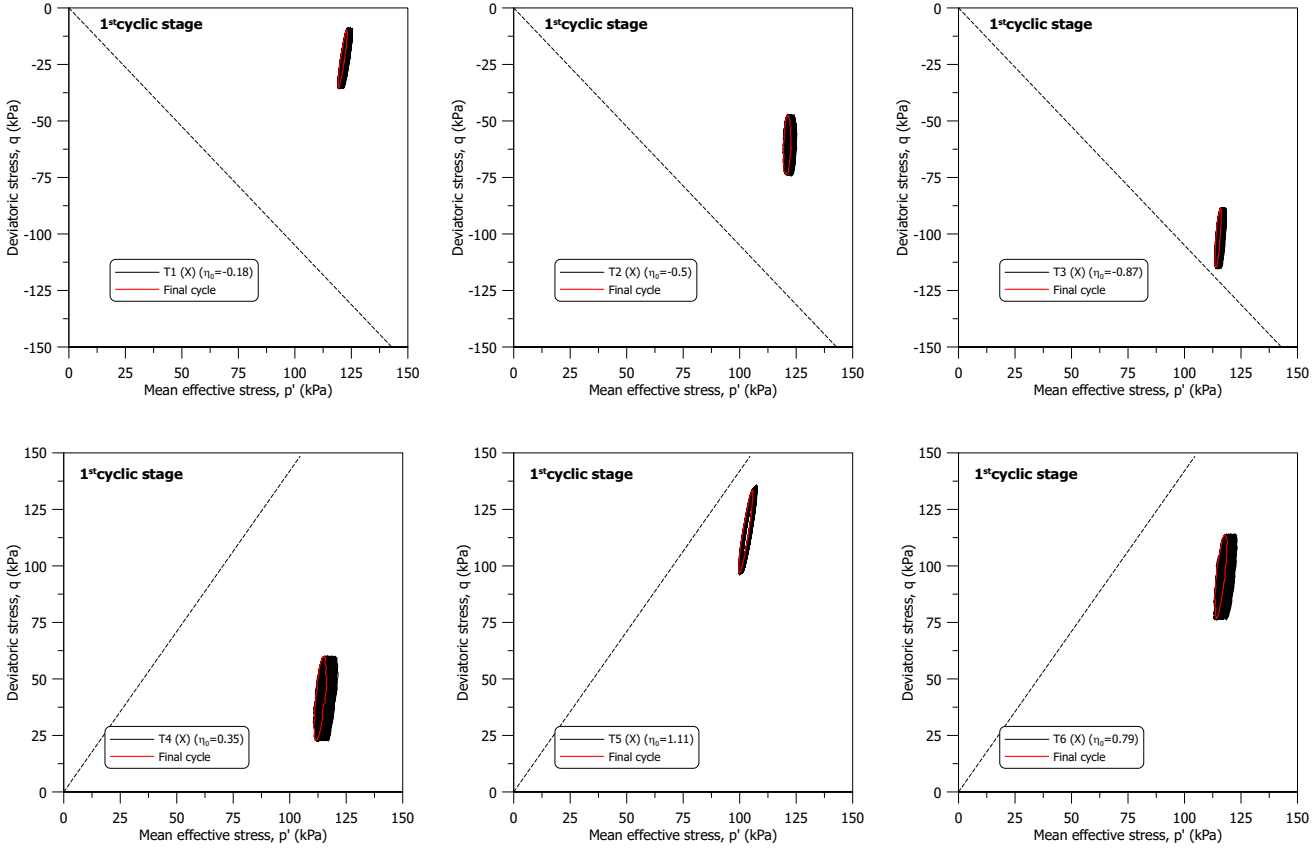

Figure 3.24: Stress path of stress-controlled cyclic triaxial tests starting from different initial stress states (fist cyclic stage)

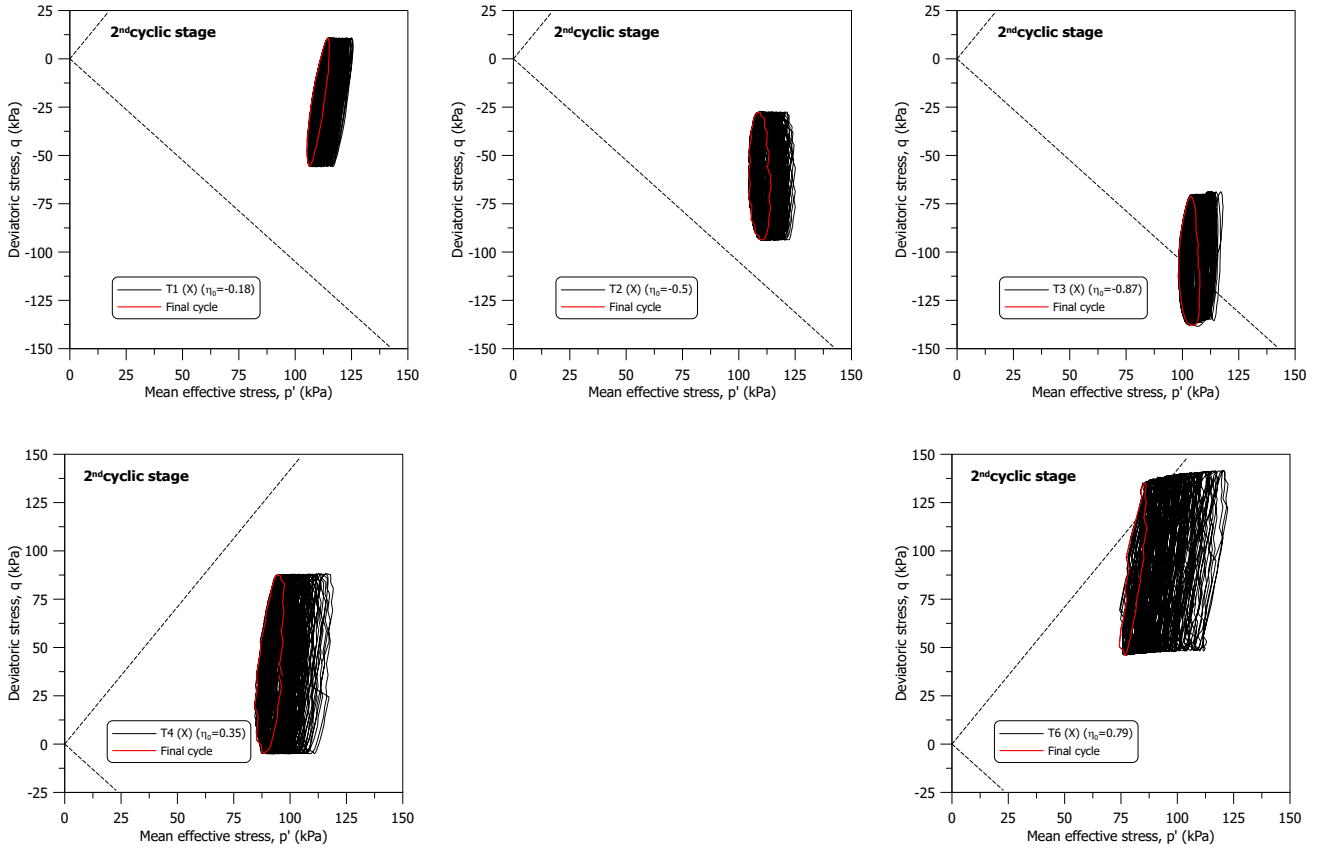

Figure 3.25: Stress path of stress-controlled cyclic triaxial tests starting from different initial stress states (second cyclic stage)

The stress-strain curves are depicted in Figures 3.26 and 3.27. In the first cyclic stage, irrecoverable deviatoric strain is mostly absent, with the notable exception of sample T5(X). The magnitude of permanent deviatoric strain increases with the absolute stress ratio. Samples initiated from the compression side develop permanent deviatoric strain in compression, whereas those initiated from the extension side do so in extension. Additionally, the slope of the stress-strain curves remains almost constant across increasing cycle numbers in this first stage. However, as the cyclic stress amplitude escalates in the second stage, a more pronounced development of permanent deviatoric strain is observed. Furthermore, the stress-strain curve slopes become progressively less steep with each additional loading cycle. Interestingly, the rate of permanent deviatoric strain development is slower on the extension side.

Figure 3.28 presents the variation in secant shear modulus across loading cycles during stress-controlled cyclic triaxial tests starting from different initial stress states. A minor reduction in secant shear modulus is observed during the first cyclic loading stage, corroborating the findings from Figure 3.26. Yet, as the cyclic stress amplitude increases in the second stage, the secant shear modulus exhibits a decrease with an increasing number of loading cycles. Generally, tests initiated from the extension side show a higher shear modulus compared to those from the compression side, which correlates with lower permanent deviatoric strain development. Moreover, a higher initial stress ratio prior to cyclic shearing leads to a lower secant shear modulus, a trend that becomes more evident in the second cyclic stage.

Plotting the variation of secant shear modulus across loading cycles offers insights into how shear stiffness evolves under stress-controlled cyclic loading. However, it is important to note that the shear modulus of soil is influenced by both strain amplitude and mean effective stress. Since both factors vary during stress-controlled cyclic loading, the observed changes in secant shear modulus across loading cycles reflect the combined effects of strain amplitude and mean effective stress on the cyclic response. Figure 3.29 illustrates the variation in secant shear modulus in relation to the average mean effective stress, p'_{avg}. Consistent with observations from strain-controlled tests, the secant shear modulus decreases as the average mean effective stress reduces. Furthermore, it appears that the rate of shear modulus reduction in relation to p'_{avg} is not influenced by the initial stress ratio. To highlight the impact of strain amplitude on the secant shear modulus variation, Figure 3.30 presents changes in the secant shear modulus across the cyclic deviatoric strain, $\Delta\varepsilon_{q,\text{cyc}}$. Intriguingly, in either cyclic shearing stage, the variations in secant shear modulus can be categorised into two distinct groups: tests initiated from either the compression or extension side. This observation contrasts with what is depicted in Figure 3.28, the secant shear modulus is lower for tests starting from the extension side. However, the lower strain amplitudes result in an apparently higher shear modulus for extension-side tests in Figure 3.28. While the trend is less pronounced, a higher absolute initial stress ratio generally corresponds to a lower secant shear modulus at the same cyclic deviatoric strain.

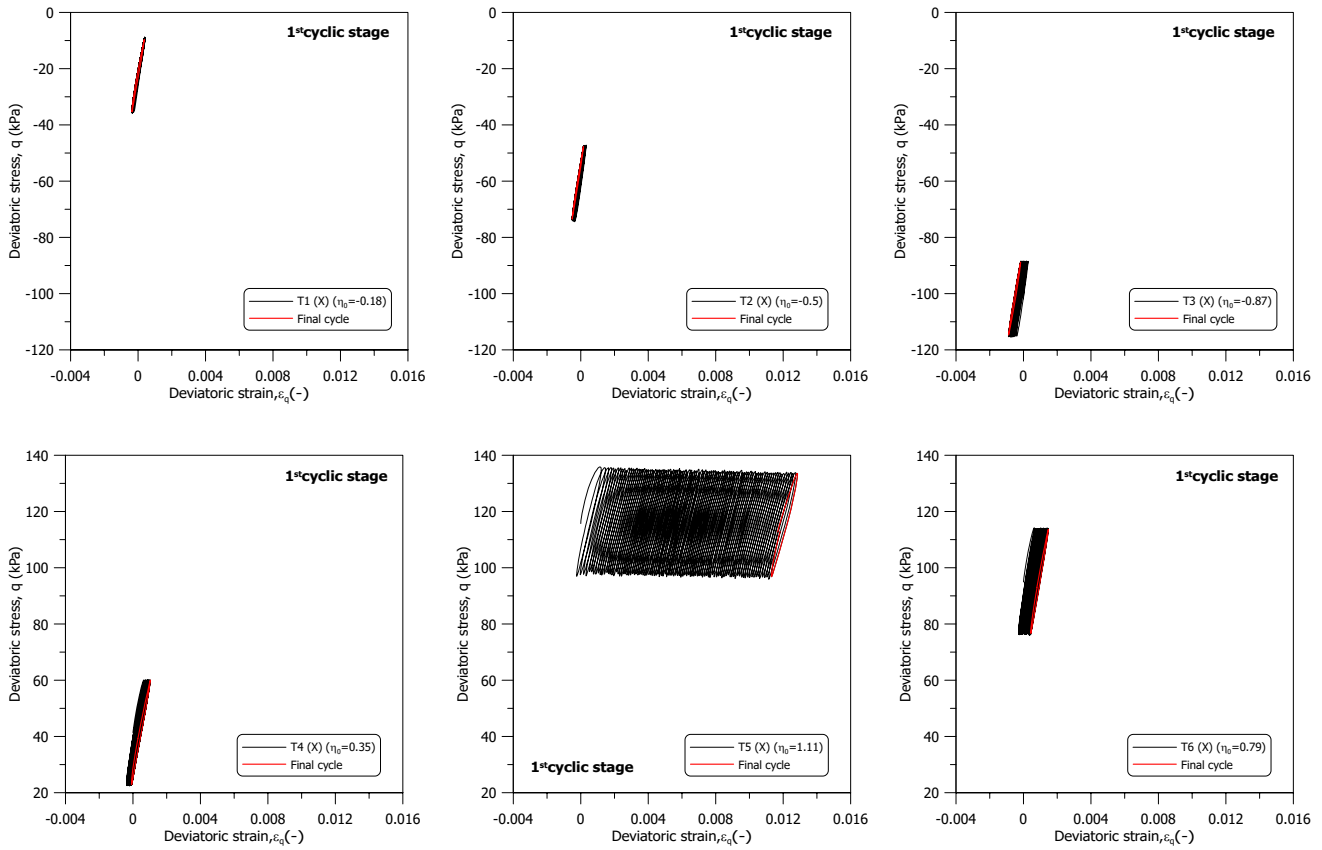

Figure 3.26: Stress-strain curve of stress-controlled cyclic triaxial tests starting from different initial stress states (fist cyclic stage)

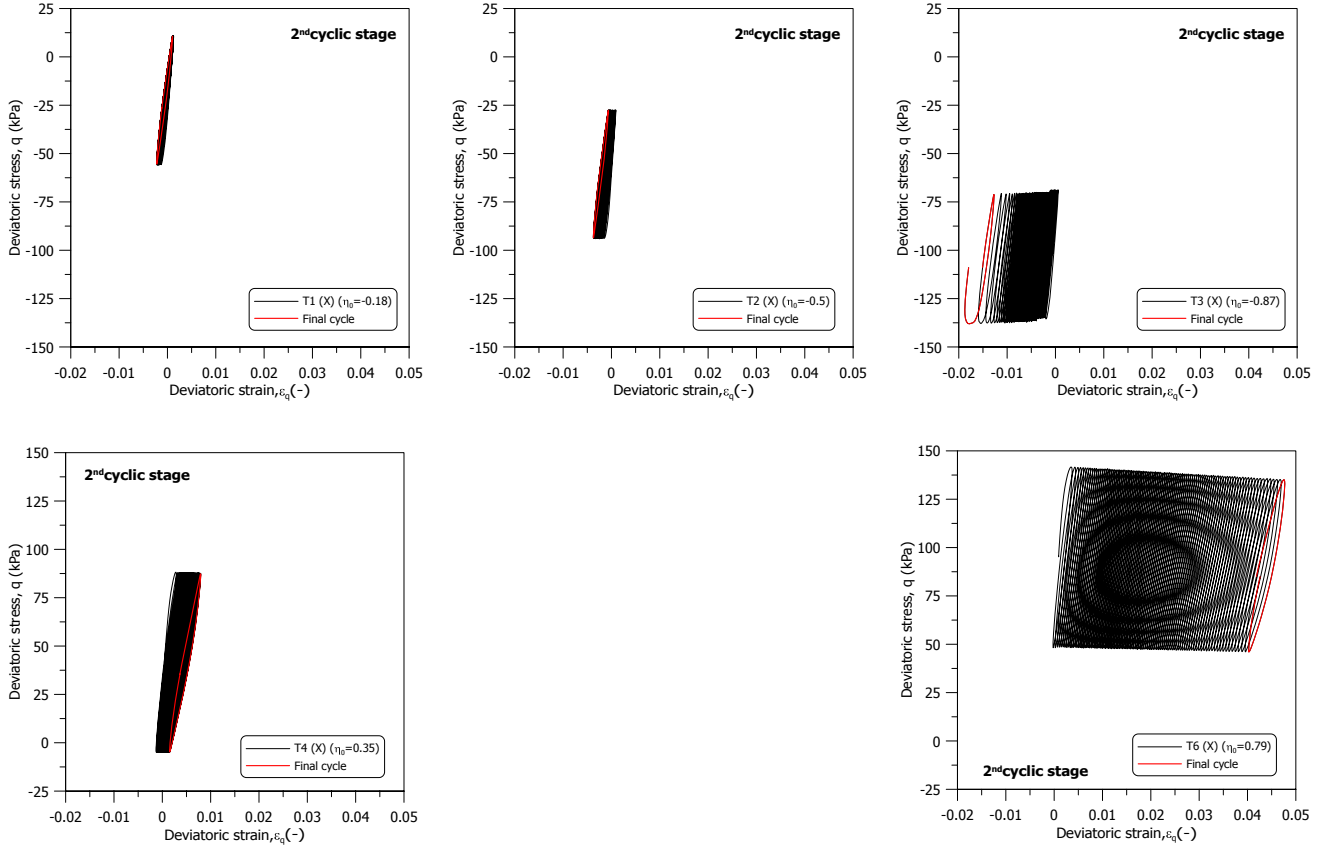

Figure 3.27: Stress-strain curve of stress-controlled cyclic triaxial tests starting from different initial stress states (second cyclic stage)

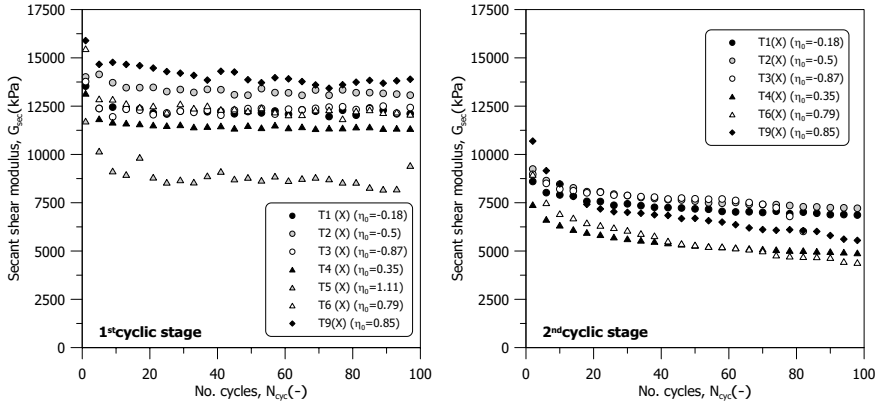

Figure 3.28: Secant shear modulus of stress-controlled cyclic triaxial tests starting from different initial stress states (with respect to loading cycle)

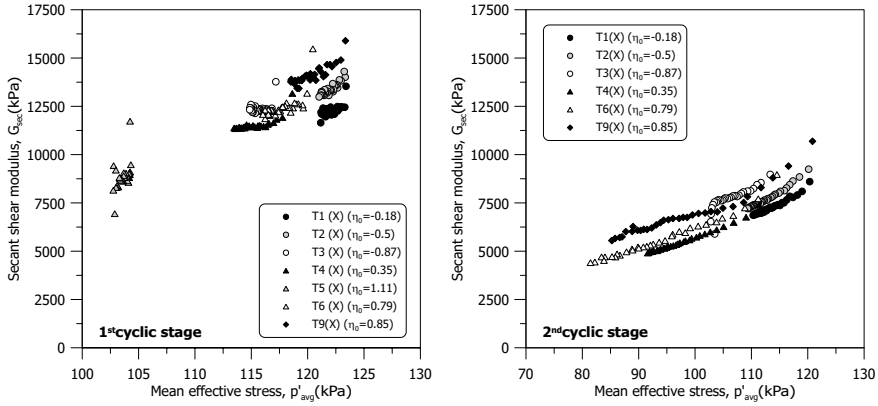

Figure 3.29: Secant shear modulus of stress-controlled cyclic triaxial tests starting from different initial stress states (with respect to p'_{avg})

Figure 3.31 presents the behaviour of average excess pore pressure in relation to both loading cycles and cyclic deviatoric strain. During the first stage, all samples exhibit an increase in average excess pore pressure ranging from 1 to 6 kPa. Generally, tests initiated from the extension side show a lower magnitude of excess pore pressure. Moreover, there is no distinct correlation between average excess pore pressure and cyclic deviatoric strain during this stage. In the second stage, however, the average excess pore pressure escalates significantly, reaching levels five to six times higher than those in the first stage, despite the stress amplitude only increasing by 2.5 times. At this stage, the relationship between average excess pore pressure and cyclic deviatoric strain becomes more evident. On the compression side, samples with a higher initial stress ratio exhibit a more rapid increase in excess pore pressure relative to the cyclic deviatoric strain. On the extension side, it is observed that a higher absolute initial stress ratio leads to a quicker escalation of excess pore pressure in relation to cyclic deviatoric strain.

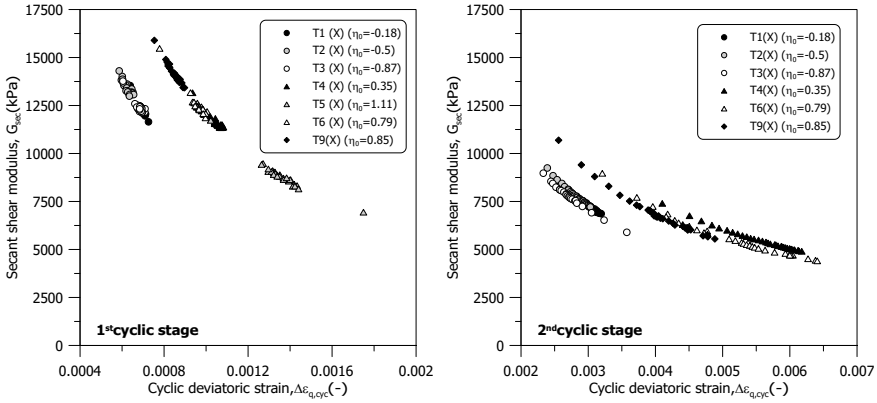

Figure 3.30: Secant shear modulus of stress-controlled cyclic triaxial tests starting from different initial stress states (with respect to $\Delta\varepsilon_{q,\text{cyc}}$)

Figure 3.32 displays the trend of permanent deviatoric strain across each cycle. During the first stage, there is a consistent relationship between a larger stress ratio magnitude and a higher permanent deviatoric strain. Sample T5(X) demonstrates an axial strain accumulation of approximately 1.2% in this stage, which is markedly higher than the less than 0.1% seen in other samples. Additionally, tests that commence from the compression side result in an accumulation of compressive deviatoric strain, while tests that begin on the extension side show extensive deviatoric strain. In the second stage, the pattern of permanent deviatoric strain generally aligns with what was observed in the first stage. Specifically, higher initial stress ratios are linked to greater permanent deviatoric strain. For samples where the stress path exceeds the critical stress ratio and moves into the 'dry' side of critical (e.g., samples T3(X), T6(X), and T9(X)), the rate of axial strain accumulation accelerates sharply, implying that these samples are nearing the point of failure under the given cyclic shearing conditions.

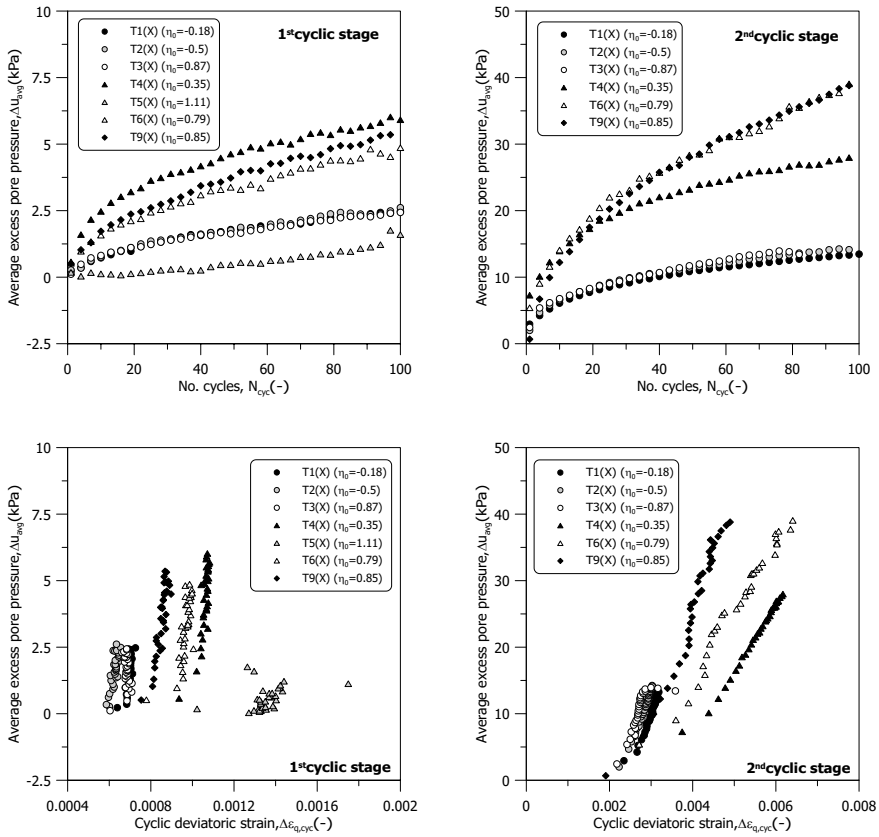

Figure 3.31: Average excess pore pressure of stress-controlled cyclic triaxial tests starting from different initial stress states

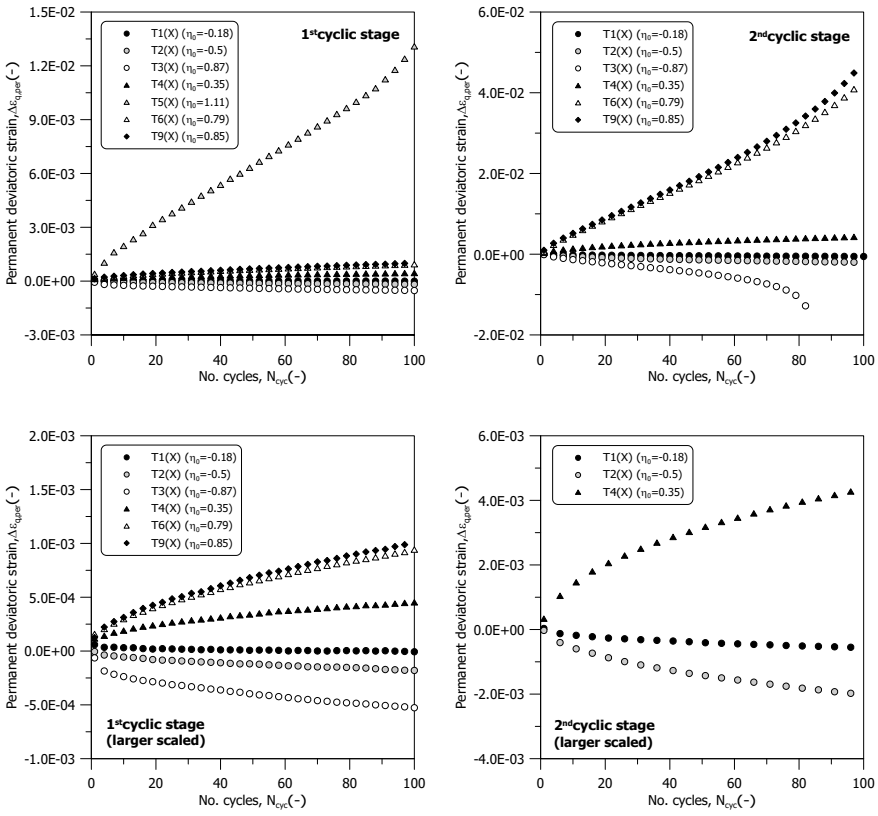

Figure 3.32: Permanent deviatoric strain of stress-controlled cyclic triaxial tests starting from different initial stress states

INFLUENCE OF CYCLIC STRESS AMPLITUDE

To further investigate the influence of cyclic stress amplitude on soil response, cyclic shearing was applied to two samples, T7(X) and T9(X), which exhibit similar compressibility and start from the same initial stress state facilitating a more direct comparison, as depicted in Figure 3.33. Prior to cyclic loading, both samples were K_0-consolidated. Due to differing mean effective stresses, p', at the end of consolidation, the experimental results presented are normalised with the mean effective stress at the end of consolidation, p'_0. The cyclic stress amplitudes, q_{cyc}/q_f, applied to T7(X) and T9(X) during the first cyclic stage, are 0.08 and 0.1, respectively. In the second cyclic stage, the amplitudes are increased to 0.2 and 0.25, respectively. The stress paths of these two tests are also illustrated in Figure 3.33; the higher the amplitude, the more pronounced the shift of the stress path towards the left on the $p' - q$ plane. It can be seen more clearly in Figure 3.34, which highlights the stress path of the final cycle. As seen in the previous section, the first cyclic stage stress paths for both samples display a lens-like shape. For the second cyclic stage, the stress paths of T9(X) surpass the critical state stress ratio. Additionally, the inclination of the stress path loop diminishes for T9(X) in the second stage, suggesting that the higher stress amplitude has reduced inherent anisotropy.

Figure 3.35 displays the stress-strain curves for samples T7(X) and T9(X), demonstrating that both tests accumulate permanent deviatoric strain towards the compression side. As expected, higher cyclic amplitudes lead to a faster accumulation of permanent strain.

The K_0 compression curves reveal that the stiffness of both samples follows a log-linear relationship. Considering the different mean effective stress levels from which samples T7(X) and T9(X) were initiated, the secant shear modulus is normalised against the logarithmic of mean effective stress at the end of consolidation, denoted as $\log p'_0$.

Figure 3.36 illustrates the normalised secant shear modulus in relation to the number of loading cycles, average mean effective stress, and cyclic deviatoric strain. Consistent with earlier findings, there is no substantial stiffness degradation in relation to the loading cycle during the first loading stage. However, during the second loading stage, both samples exhibit noticeable stiffness degradation as the number of loading cycles increases. The test with higher amplitude shows a more rapid stiffness reduction within the first twenty cycles. Despite T7(X) stabilising at a higher mean effective stress, the variation in normalised secant shear modulus with respect to average mean effective stress exhibits a similar trend between the two samples. Intriguingly, even though T7(X) and T9(X) have comparable compressibility, T7(X) demonstrates a higher normalised secant shear modulus. A closer examination of the normalised secant shear modulus in relation to cyclic deviatoric strain indicates that the greater shear stiffness of T7(X) is due to its smaller cyclic deviatoric strain. Specifically, in the second loading stage, the data from both tests converge at a cyclic deviatoric strain of around 0.25%.

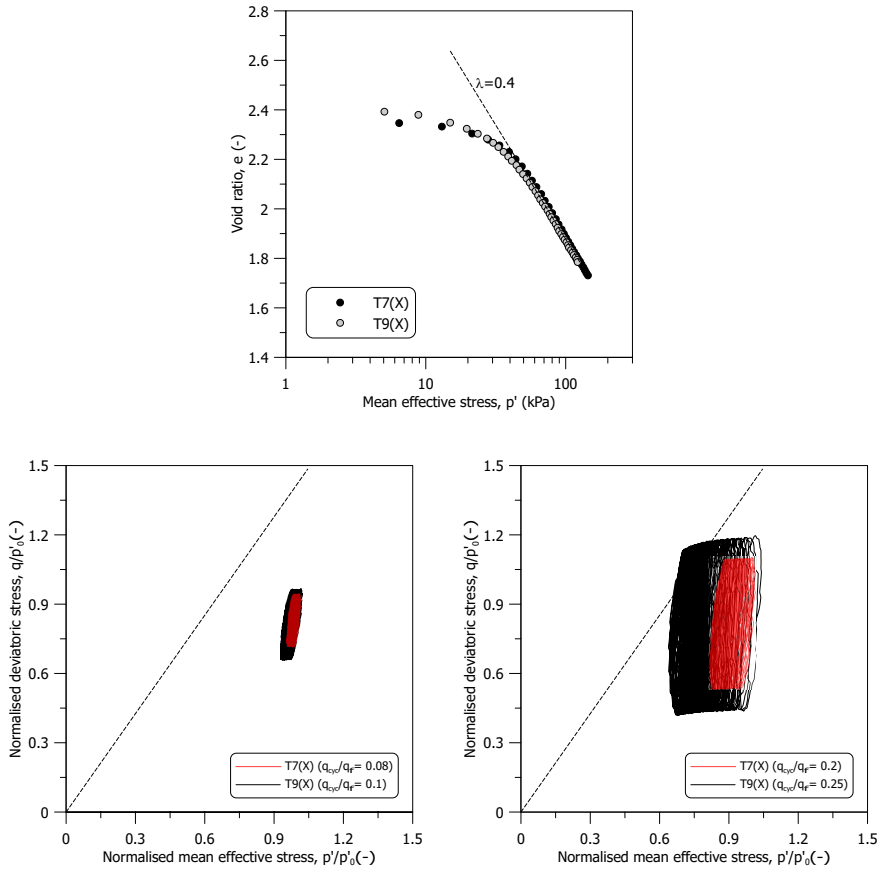

Figure 3.33: K_0 compression curve and stress path of stress-controlled cyclic triaxial tests with different stress amplitudes

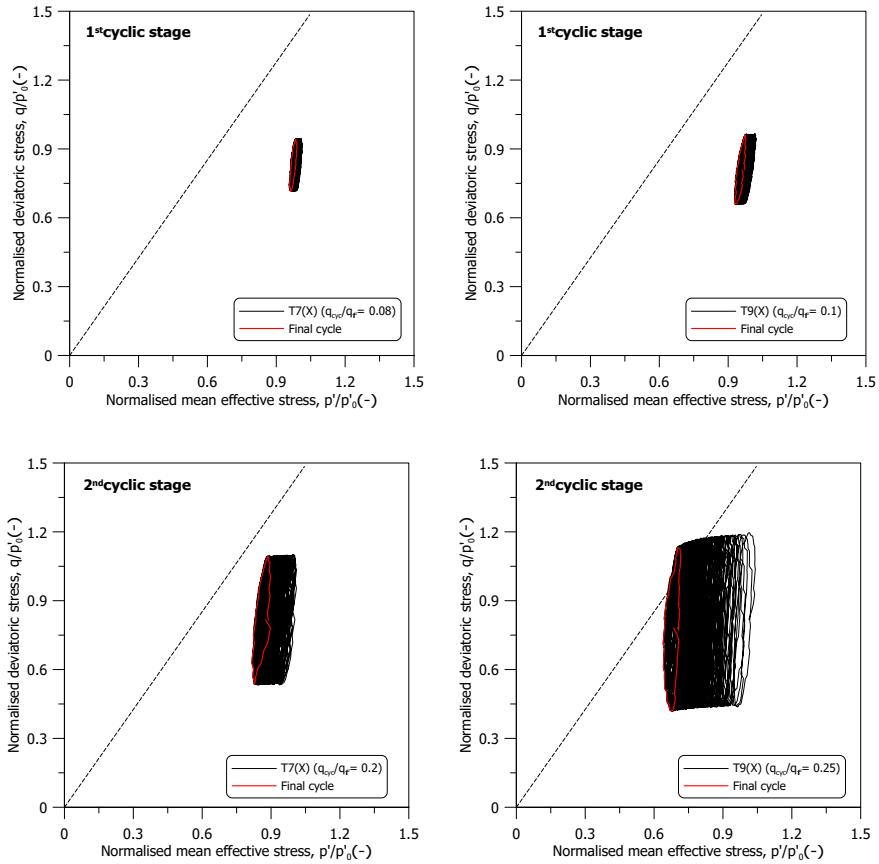

Figure 3.34: Stress path of stress-controlled cyclic triaxial tests with different stress amplitudes

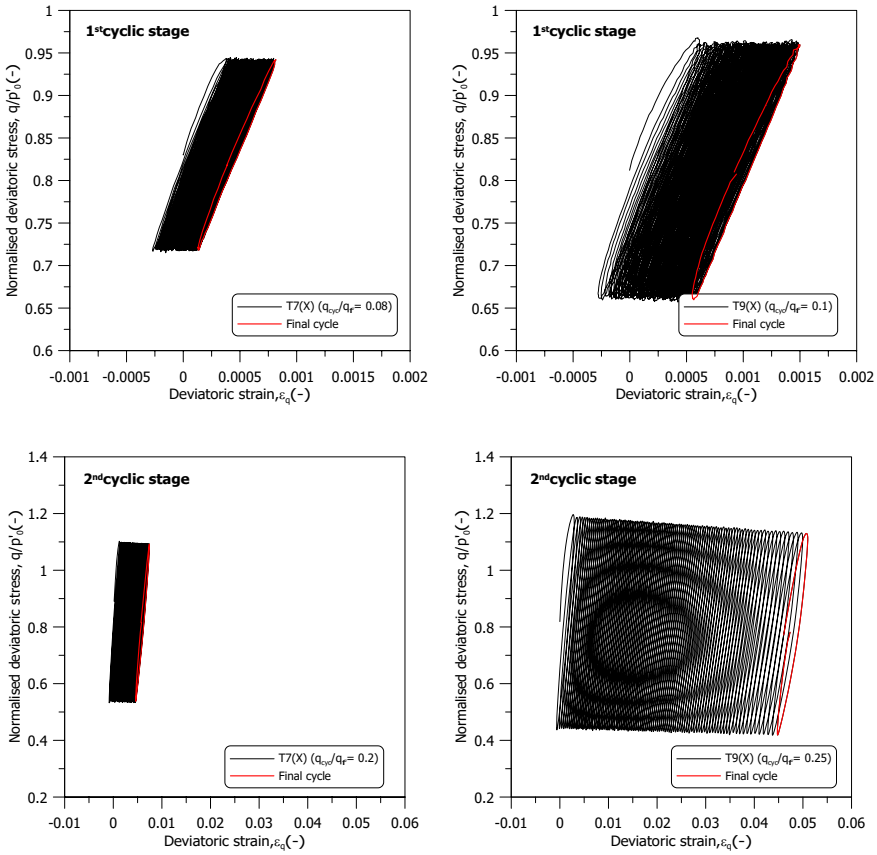

Figure 3.35: Stress-strain curve of stress-controlled cyclic triaxial tests with different stress amplitudes

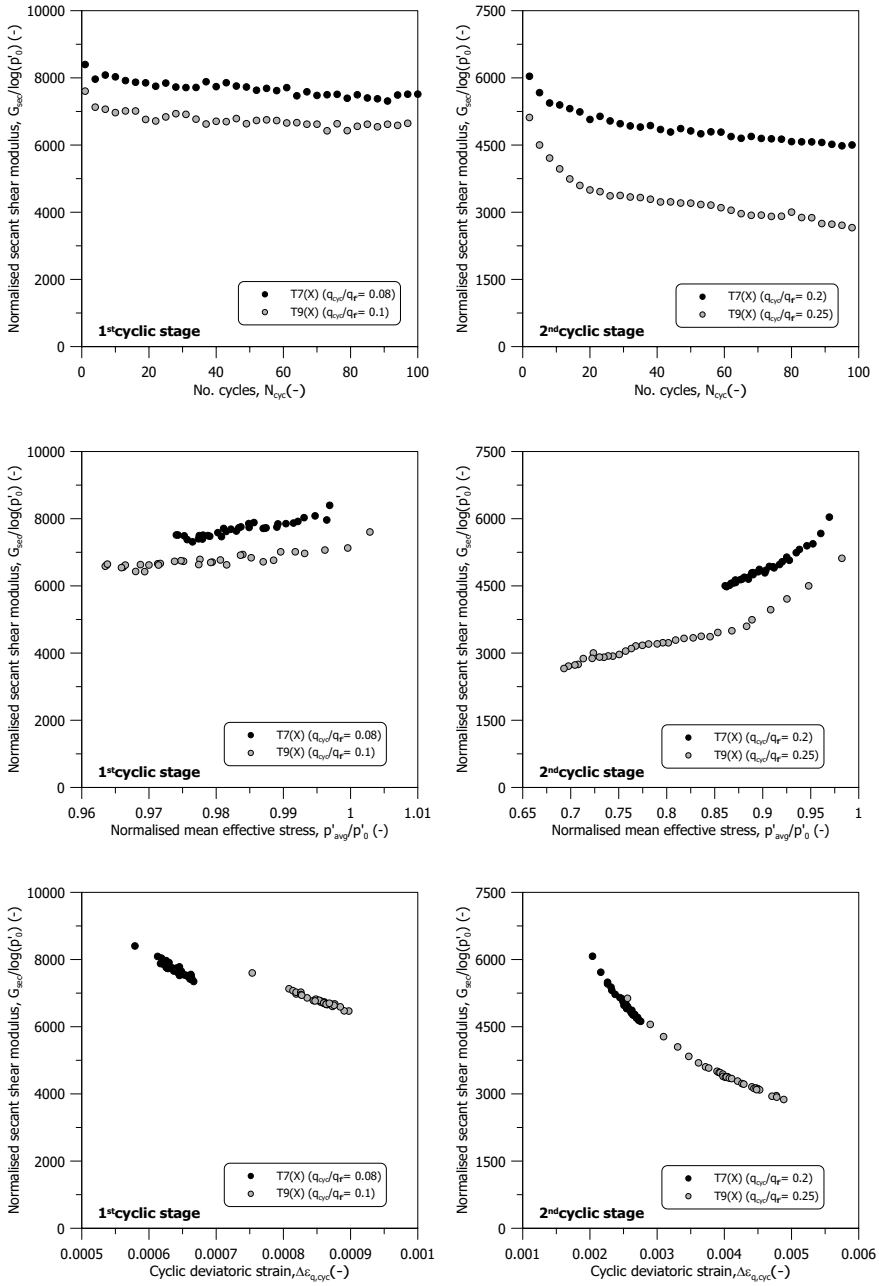

Figure 3.36: Secant shear modulus of stress-controlled cyclic triaxial tests with different stress amplitudes (with respect to loading cycle, p'_{avg}, and $\Delta\varepsilon_{q,\mathrm{cyc}}$)

Figure 3.37 displays the normalised average excess pore pressure in relation to the loading cycle and cyclic deviatoric strain. The higher stress amplitude applied to T9(X) leads to a more significant development of excess pore pressure with the loading cycle. Interestingly, the rate of excess pore pressure increase in relation to cyclic deviatoric strain is faster for sample T7(X). This observation is consistent with the trend noted in Figure 3.31, where the higher stress amplitude in T9(X), resulting in a lower stress ratio on the compression side, is associated with a slower increase in excess pore pressure relative to the cyclic deviatoric strain. Figure 3.38 illustrates the development of permanent deviatoric strain in samples T7(X) and T9(X). Here, it is evident that higher stress amplitudes lead to a quicker accumulation of permanent deviatoric strain. In the second cyclic stage of T9(X), there is an accelerated increase in permanent deviatoric strain after 60 cycles, suggesting that the sample was nearing failure.

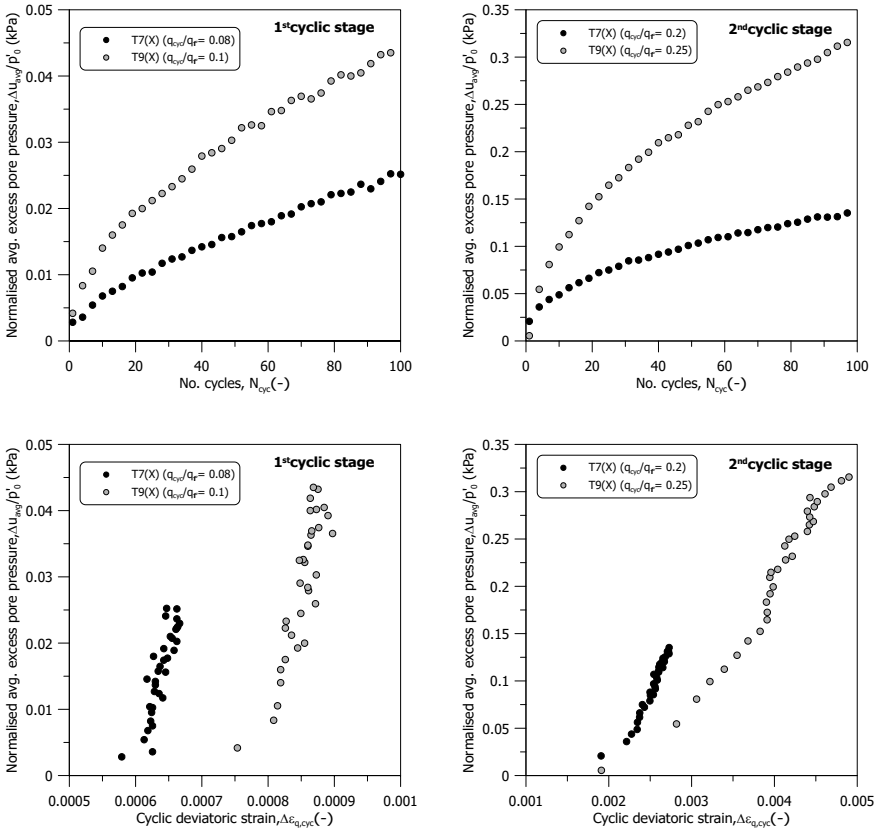

Figure 3.37: Average excess pore pressure of stress-controlled cyclic triaxial tests with different stress amplitudes

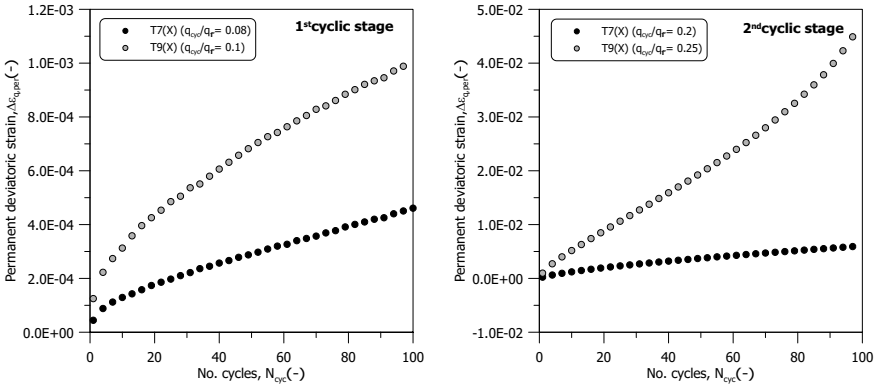

Figure 3.38: Permanent deviatoric strain of stress-controlled cyclic triaxial tests with different stress amplitudes

INFLUENCE OF CLAY AND ORGANIC CONTENT

In Chapter 2, experimental results highlighted that the primary effect of organic matter on the behaviour of Dutch organic clays is on the compressibility. Additionally, a notable distinction between group (X) and other groups lies in the clay content. Several studies have investigated the impact of clay content on the cyclic behaviour of sand or silt (Guo and Prakash, 1999; Boulanger and Idriss, 2006; Chang and Hong, 2008). For instance, Guo and Prakash (1999) observed that even a slight increase in the clay content of silt-clay mixtures enhances the rate of excess pore pressure development due to reduced hydraulic conductivity. However, when the plasticity index exceeds 10%, the liquefaction resistance of these mixtures increases with clay content.

To explore the influence of clay and organic content on cyclic response, two-stage stress-controlled cyclic tests were conducted on three isotropically consolidated samples differing in their clay and organic content. Figure 3.39 shows the change in void ratio during the isotropic compression stage, with the slope of the isotropic compression line annotated. Sample Cyc T1(VII) contains 4% clay and 2.8% organic content, while samples T8(X) and Cyc T1(X) have similar clay contents of 38%, but different organic contents of 3.2% and 3.9%, respectively. The plasticity index for groups (VII) and *X) is 20% and 61%, respectively. All samples were isotropically consolidated to a mean effective stress (p') of 120 kPa. The stress amplitudes for the first and second stages were set at 13.2 kPa ($0.08q_f$) and 33 kPa ($0.2q_f$), respectively, with all tests conducted at a frequency of 0.1 Hz for up to 100 cycles.

Figure 3.39 also presents the stress paths during the cyclic stages. The sample with the lowest compressibility shifts the most towards the left on the p'-q plane, while those with higher compressibility exhibit a less pronounced shift. The stress paths are more clearly depicted in Figure 3.40. The stress paths of samples T8(X) and Cyc T1(X) are less inclined than those of sample Cyc T1(VII), indicating varying degrees of anisotropy. Figure 3.41 presents the stress-strain curves, with the final loading cycle highlighted in red. Both stages show irrecoverable deviatoric strain during shearing cycles, with the first stage maintaining a nearly constant slope across increasing cycle numbers. However, in the second stage, as cyclic stress amplitude increases, the slope of the stress-strain

curves gradually decreases with each subsequent cycle. Additionally, sample Cyc T1(X) accumulates permanent deviatoric strain towards the compression side in the second cyclic stage, unlike the other sample.

Figure 3.42 displays the secant shear modulus across loading cycles, average mean effective stress, and cyclic deviatoric strain for the three samples. Sample Cyc T1(VII) has the highest secant shear modulus, while the other two samples show similar moduli. During the first cyclic loading stage, the reduction in secant shear modulus is negligible. However, in the second stage, which involves higher cyclic stress amplitude, the secant shear modulus for all samples progressively degrades with the number of loading cycles. For sample Cyc T1(VII), with less clay and organic content, the shear modulus degrades more rapidly, consistent with the conclusion of Vucetic and Dobry (1991) that shear modulus degradation accelerates as the plasticity index decreases. However, no clear difference is observed in the rate of secant shear modulus reduction between samples T8(X) and Cyc T1(X). When examining the variation of secant shear modulus in relation to average mean effective stress, all samples exhibit a similar reduction rate as mean effective stress decreases. The more rapid degradation rate with the loading cycle observed in sample Cyc T1(VII) results from a faster reduction in average mean effective stress with each cycle. Additionally, the change in secant shear modulus in relation to cyclic deviatoric strain suggests that the trends of samples T8(X) and Cyc T1(X) are almost identical. It appears that sample Cyc T1(VII) will converge to the trend of samples T8(X) and Cyc T1(X), suggesting that the secant shear modulus for the tested Dutch organic clays is dominated by cyclic deviatoric strain. Nonetheless, further investigation is needed to confirm this aspect.

Figure 3.43 reveals the average excess pore pressure in relation to the loading cycle and cyclic deviatoric strain. The group (X) samples exhibit much lower excess pore pressure development compared to sample Cyc T1(VII). Additionally, the rate of excess pore pressure development in relation to cyclic deviatoric strain is the fastest for sample Cyc T1(VII). Vucetic and Dobry (1991) mentioned that soils with higher plasticity consist of tiny particles with a high surface area per unit weight, leading to strong electrical, chemical bonds and repulsion forces, which are significant compared to the particles' weight. Consequently, high plasticity soils behave like flexible linear springs, enduring large shear strains before permanent displacement and stiffness degradation occur. It can be inferred that a more flexible microstructure results in a higher capacity to adapt to applied cyclic loading, thus exhibiting lower excess pore pressure development. However, the excess pore pressure responses of the other two samples are quite similar, indicating a lesser influence of organic content on excess pore pressure development. Figure 3.44 illustrates the development of permanent deviatoric strain with the number of loading cycles. No unique trend is observed among the three samples. Considering the results presented in Figure 3.32, it appears that the initial stress ratio has a more significant impact on permanent deviatoric strain development during cyclic loading.

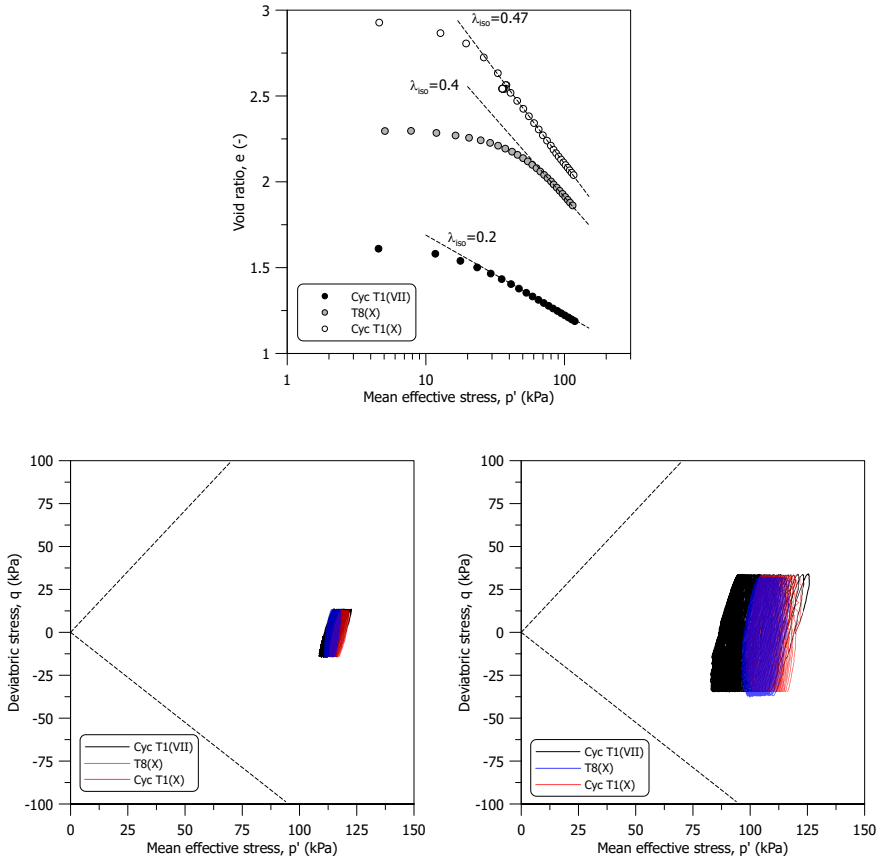

Figure 3.39: Isotropic compression curve and stress path of stress-controlled cyclic triaxial tests with different clay and organic content

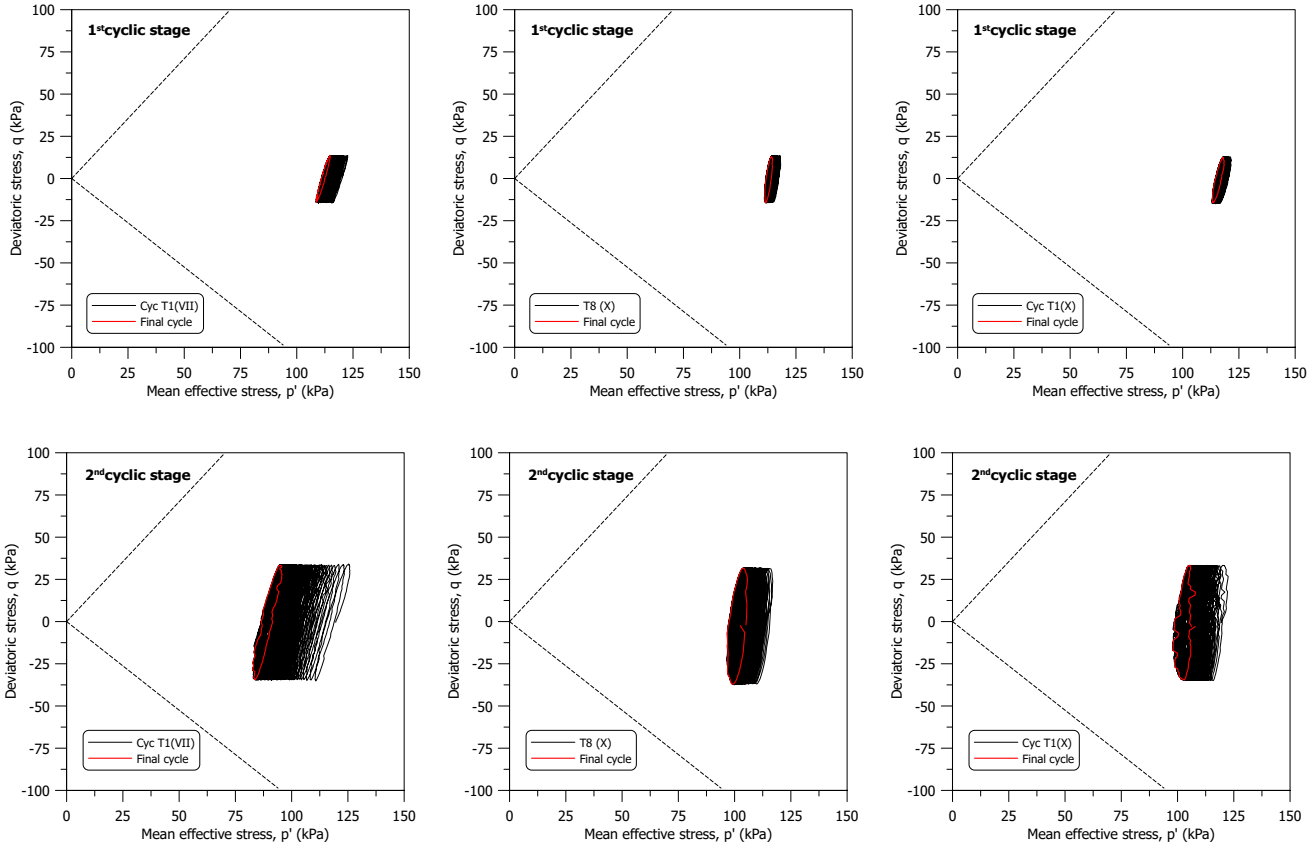

Figure 3.40: Stress path of stress-controlled cyclic triaxial tests with different clay and organic content

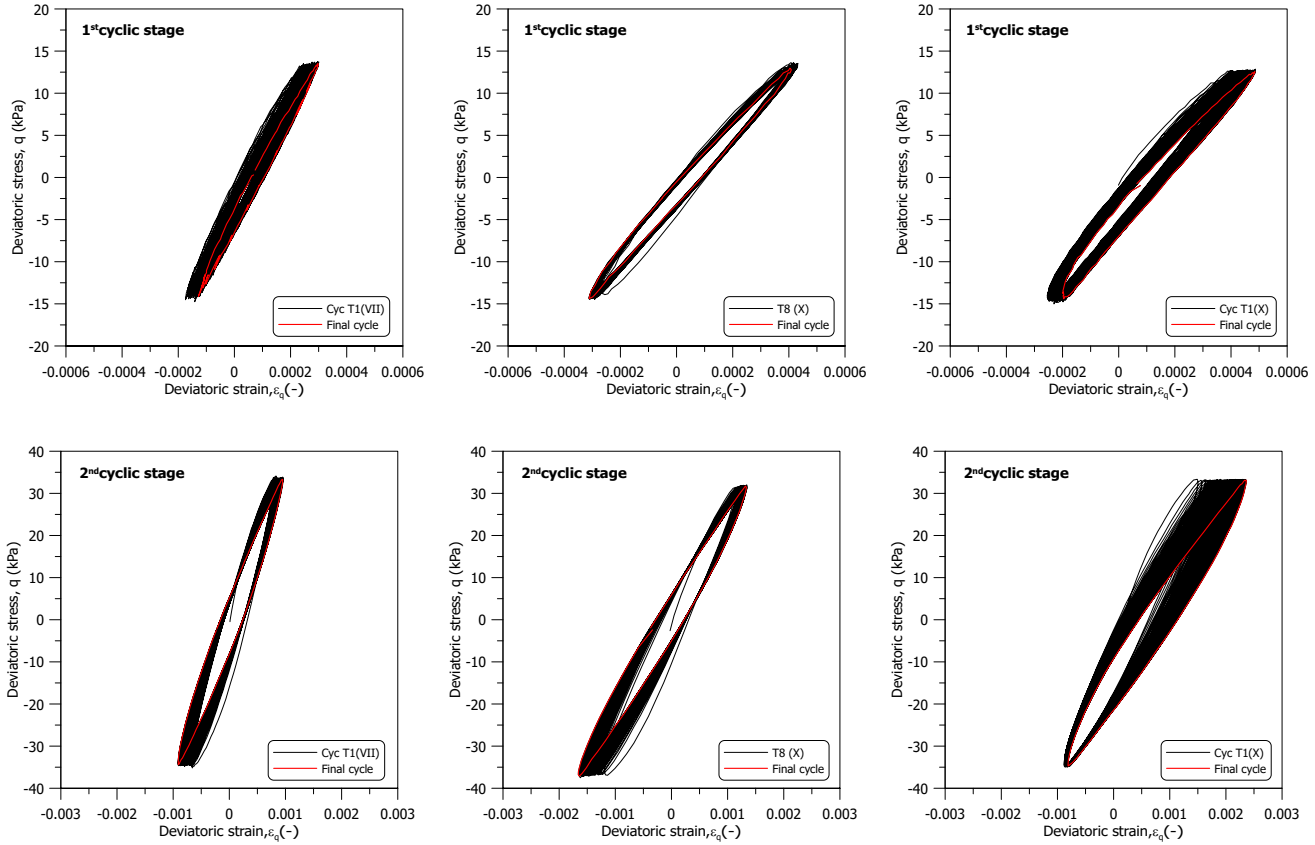

Figure 3.41: Stress-strain curve of stress-controlled cyclic triaxial tests with different clay and organic content

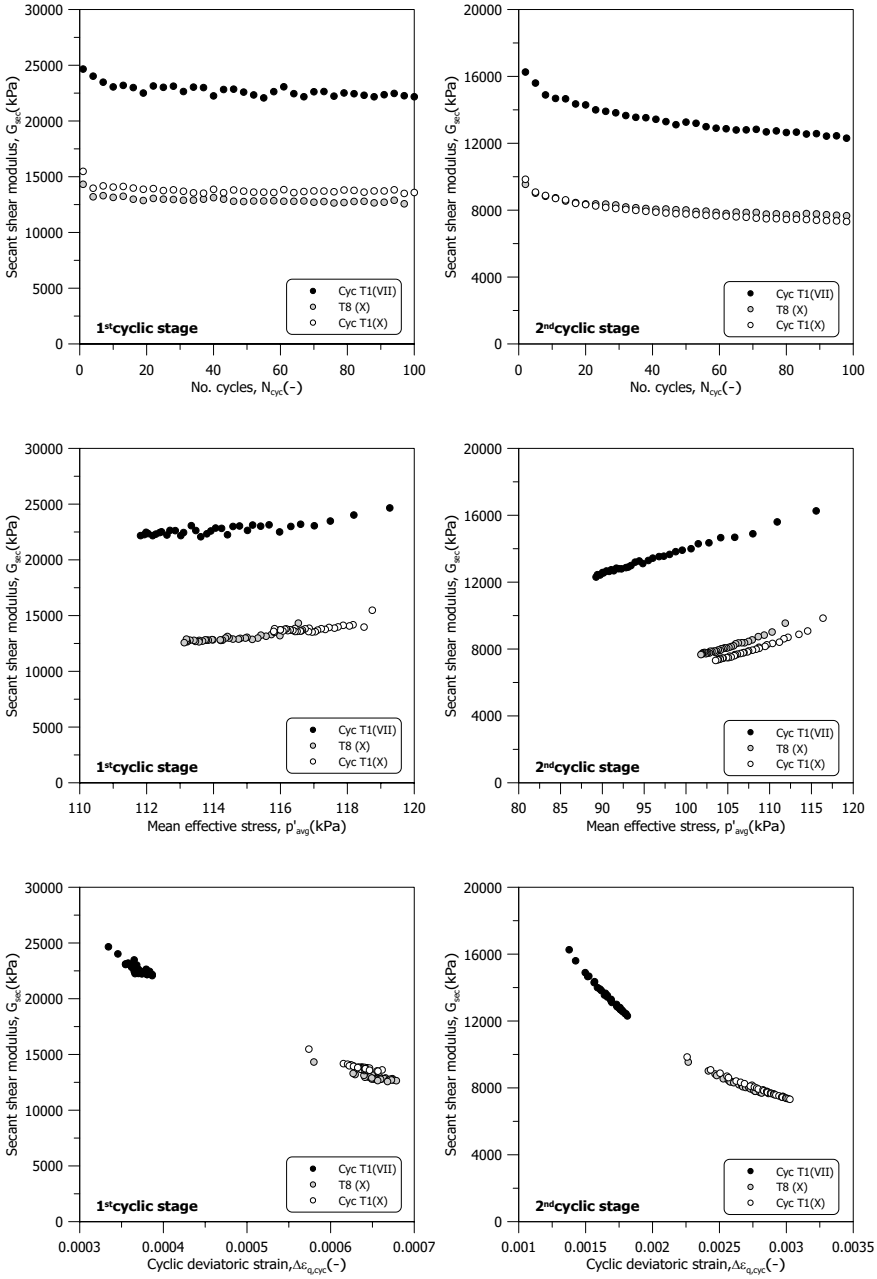

Figure 3.42: Secant shear modulus of stress-controlled cyclic triaxial tests with different clay and organic content (with respect to loading cycle, p'_{avg}, and $\Delta\varepsilon_{q,\mathrm{cyc}}$)

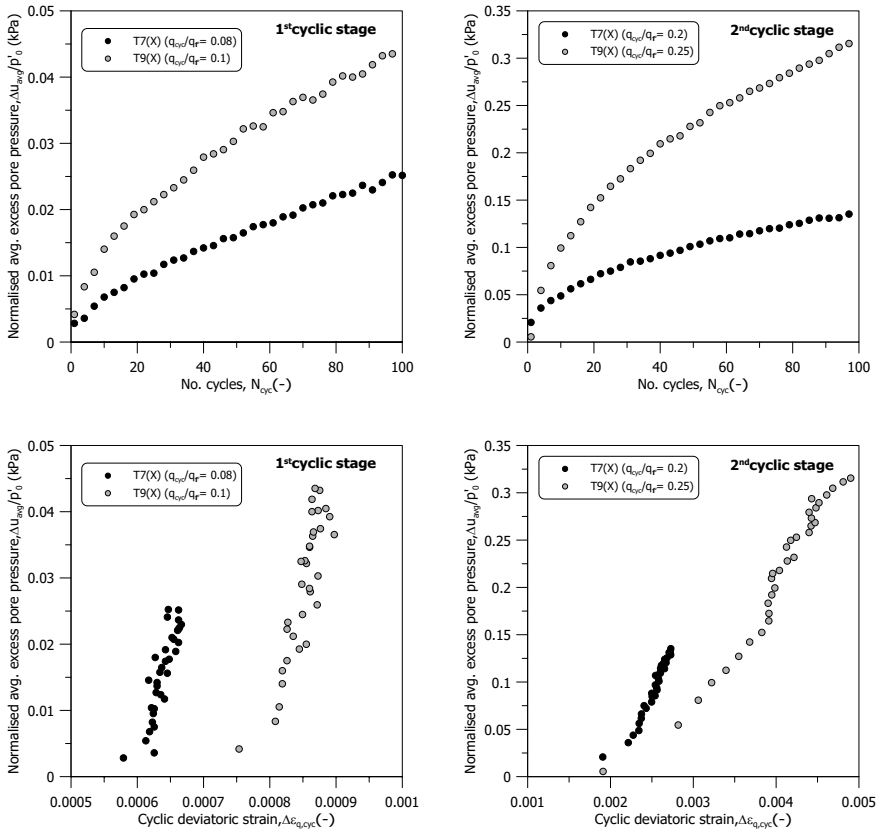

Figure 3.43: Average excess pore pressure of stress-controlled cyclic triaxial tests with different clay and organic content

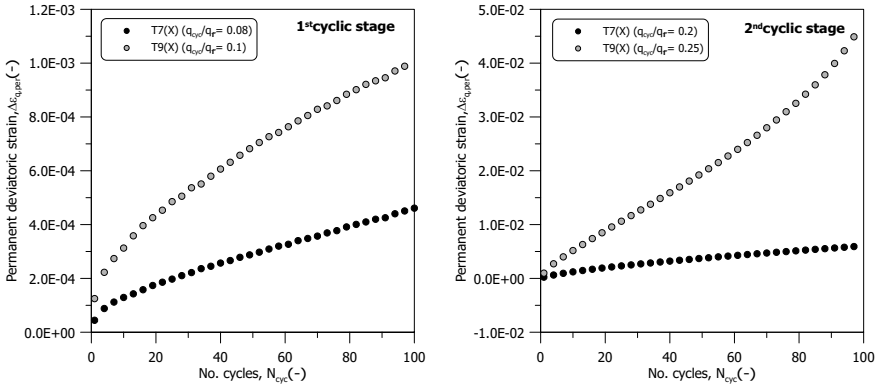

Figure 3.44: Permanent deviatoric strain of stress-controlled cyclic triaxial tests with different clay and organic content

POST-CYCLIC SHEAR STRENGTH AND DEFORMATION

If the samples did not fail during the second cyclic stage, undrained compression or extension was applied to the samples after a post-cyclic recompression state to investigate the post-cyclic shear strength. Figure 3.45 illustrates the stress paths, strain-stress and strain-stress ratio evolution of the monotonic undrained shearing stage. When plotted with the experimental data for the same material, as detailed in Chapter 2, it is reiterated that cyclic shearing seemingly does not alter the critical state stress ratios of the examined material.

During the post-cyclic recompression stage, the dissipation of excess pore pressure induces volumetric and axial strain development, as depicted in Figure 3.46 together with average excess pore pressure in the second cyclic stage. Data are plotted until the excess pore pressure falls below 0.1kPa to minimise the contribution of creep strain, given that post-cyclic volumetric and axial strains are considerably smaller than those observed in strain-controlled tests. For samples Cyc T1(X) and T9(X), the time span of the recompression stage was reduced because double drainage was permitted. In general, higher excess pore pressure during cyclic shearing correlates with larger post-cyclic strains. However, no clear trend is discernible.

Building on observations from strain-controlled tests, volumetric strain is normalised using the slope of the compression line. Simultaneously, the maximum average excess pore pressure is normalised with the mean effective stress at the onset of cyclic loading, as shown in Figure 3.47(a). A reasonably linear correlation emerges between post-cyclic volumetric strain and maximum average excess pore pressure. This relationship suggests that post-cyclic volumetric strain depends solely on soil compressibility and the amount of excess pore pressure, essentially mirroring a consolidation process. Hyodo et al. (1994) found a unique relation between post-cyclic volumetric strain and normalised peak excess pore pressure at the end of cyclic shearing on initially isotropic and anisotropic consolidated samples, as shown in equation 3.1:

$$\varepsilon_p = \frac{C_r}{1+e_0} \log\left(\frac{1}{1-\frac{\Delta u_p}{p_0'}}\right) \tag{3.1}$$

where C_r, e_0, Δu_p, and p_0' are coefficient of recompression, initial void ratio, peak excess pore pressure and mean effective stress before cyclic shearing, respectively.

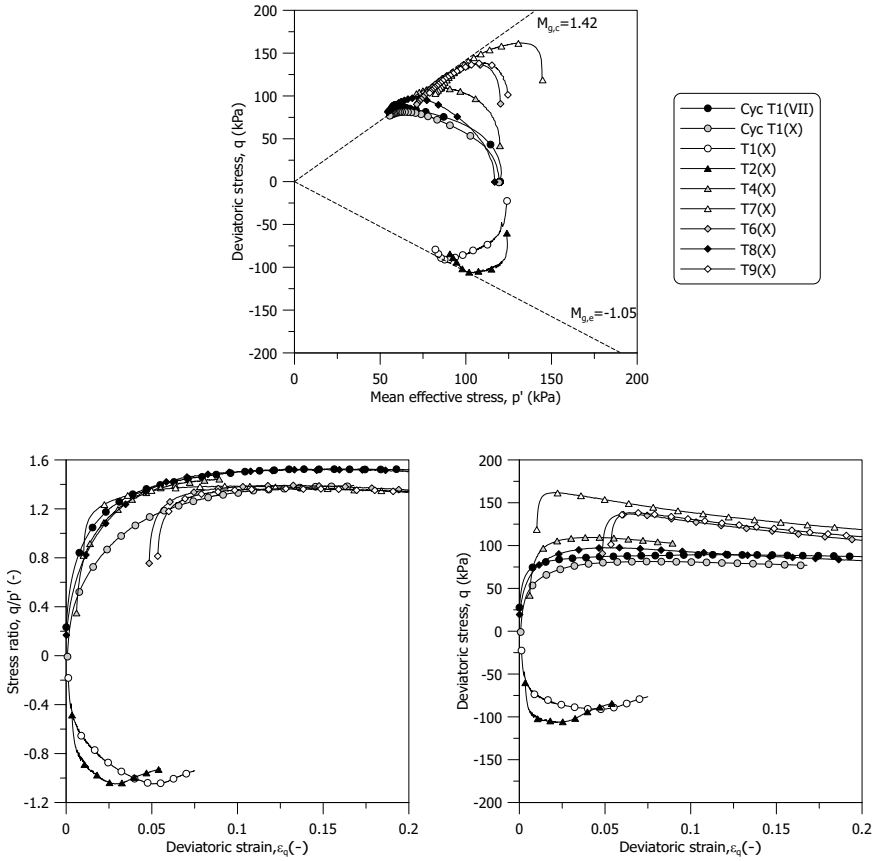

Figure 3.45: TxCU and TxEU results on samples after cyclic loading

The predicted volumetric strain from equation 3.1 is plotted against the measured volumetric strain in Figure 3.47(b), a good linear relation can be found. However, the measured volumetric strain is almost two times higher than the predicted one. According to the experimental observation on Drammen clay under cyclic direct simple shearing, the coefficient of post-cyclic recompression is around 1.5 times of the static one (Yasuhara et al., 1992). A higher magnitude of post-cyclic recompression is observed on Dutch organic clay. Regarding post-cyclic axial strain, its relationship with normalised maximum average excess pore pressure and normalised stress ratio at the recompression stage is presented in Figure 3.48. The post-cyclic axial strain seems to be more influenced by the amount of excess pore pressure than by the stress state during the resting stage.

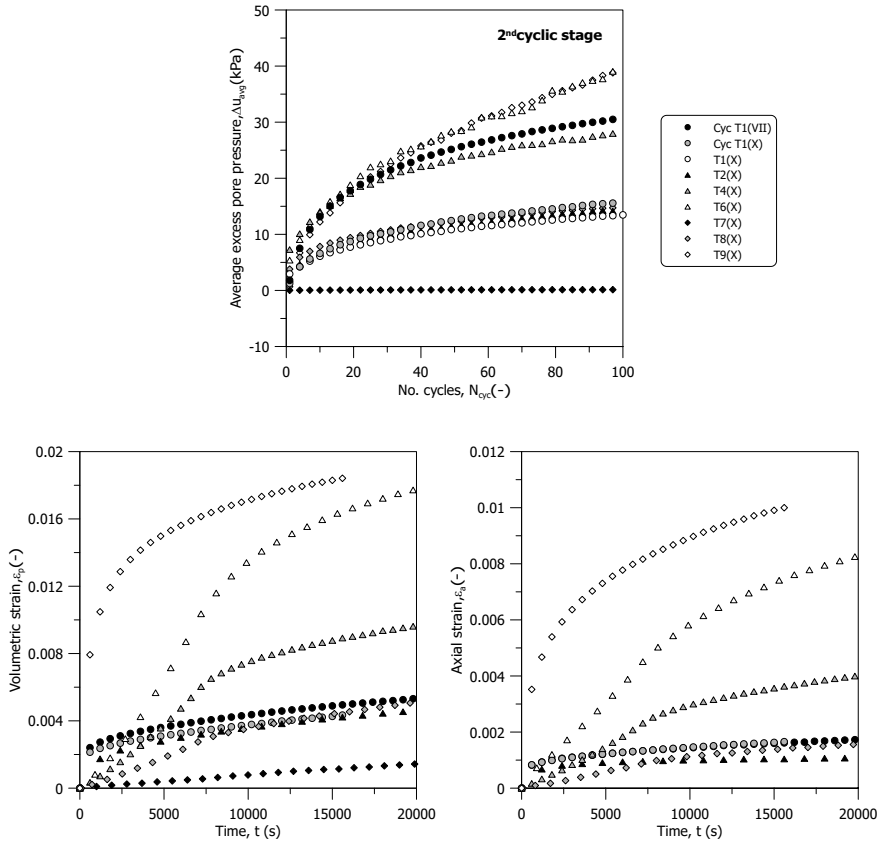

Figure 3.46: Development of excess pore pressure during cyclic shearing and post-cyclic strains

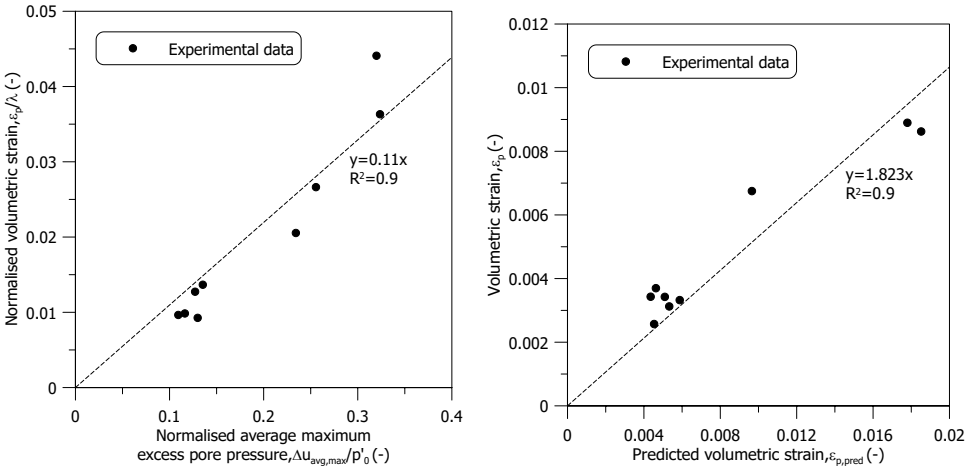

Figure 3.47: Relation between (a) normalised average maximum excess pore pressure and normalised post-cyclic volumetric strain (b) predicted and measured post-cyclic volumetric strain

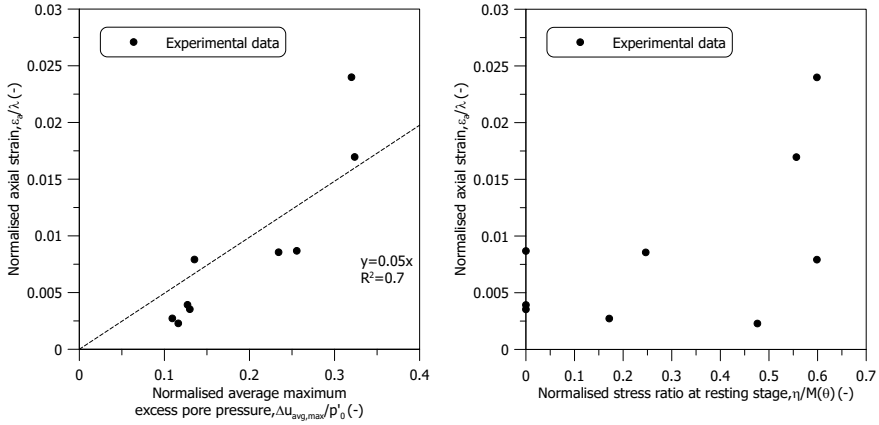

Figure 3.48: Normalised post-cyclic axial strain with respect to normalised average maximum excess pore pressure and normalised stress ratio

3.3.3. BENDER ELEMENTS MEASUREMENT

To investigate the small-strain behaviour of Dutch organic clay, bender element measurements are conducted on samples during K_0 consolidation. Using the obtained shear wave velocity, the pseudo-elastic shear modulus (Shibuya et al., 1997) can be calculated based on the theory of shear wave propagation in an elastic medium. The bender elements were inserted 3.65 mm into the soil sample from each side. The transmitter, mounted on the top cap, was activated using a sine wave with a period of 0.2 ms. The travel distance for the shear wave was measured as the tip-to-tip distance between the bender elements, and takes the sample height change into account. The travel time inside the bender elements is obtained and used for travel time correction. Additionally, the shear wave arrival time is determined based on the point of the first inversion of the received signal (Viggiani and Atkinson, 1995), as illustrated in Figure 3.49.

The stress path, void ratio change, shear wave velocity, and pseudo-elastic shear modulus of samples under K_0 consolidation are presented in Figure 3.50. Since these three samples have a very similar critical state stress ratio, they follow almost the same stress path during K_0 consolidation. However, the samples do have quite different compressibility. The evolution of shear wave velocity with the mean effective stress, p', for the sample with the highest compressibility, seems to be linear, while for the other two samples, shear wave velocity increases as a power of the mean effective stress. In addition, the rate of shear wave velocity increase with the mean effective stress, p', is slower for the most compressible sample, while the other two samples increase at a similar but faster rate. Equation 3.2 is adopted to convert the shear wave velocity to the pseudo-elastic shear modulus, in which ρ is the density of the soil. The pseudo-elastic shear modulus of samples increases linearly with mean effective stress, p'.

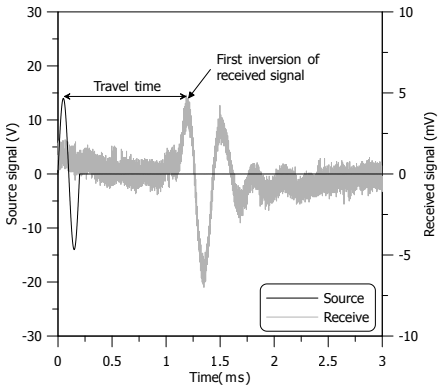

Figure 3.49: Determination of the shear wave arrival time

$$G_{max} = \rho V_s^2 \tag{3.2}$$

Hardin and Black (1968) performed resonant-column tests on normally consolidated kaolinite under various anisotropic stress states to obtain pseudo-elastic shear modulus; it was demonstrated that the pseudo-elastic shear modulus is dependent on mean effective stress, void ratio for remoulded samples. The authors also proposed the following

relation to estimate pseudo-elastic shear modulus for normally consolidated soils with void ratio and mean effective stress:

$$G_{\max} = \frac{3270 \cdot (2.97 - e)^2}{1 + e} \cdot \sqrt{p'} (\text{unit:kPa}) \tag{3.3}$$

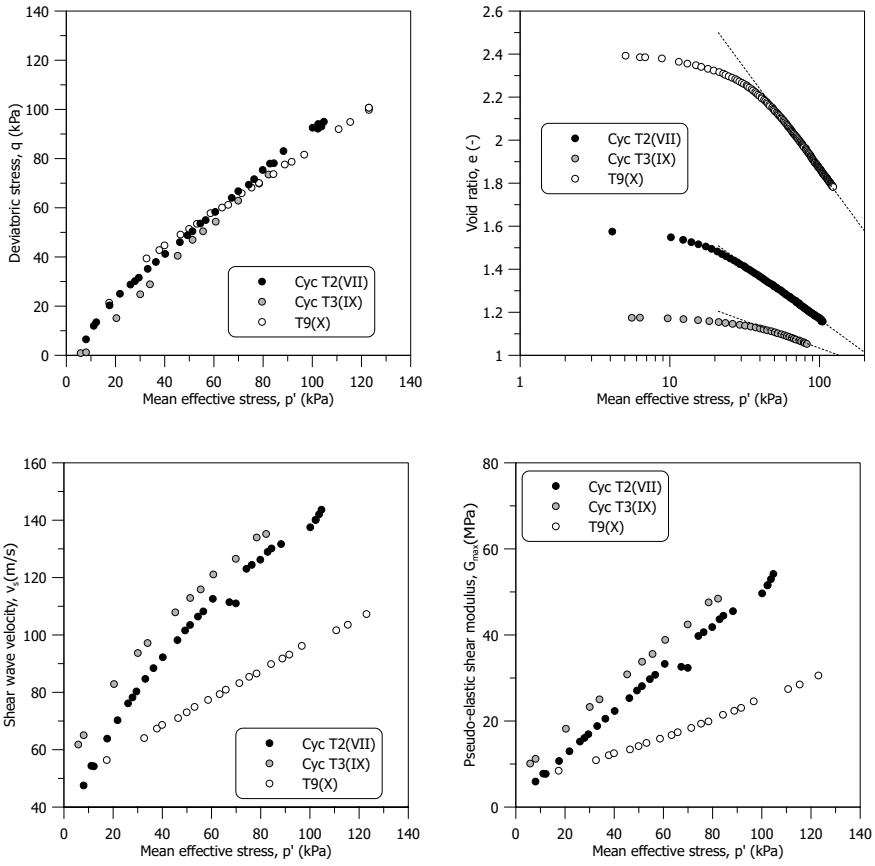

Figure 3.50: Stress path, void ratio change, shear wave velocity, and pseudo-elastic shear modulus of samples under K_0 consolidation

Figure 3.51 showcases the comparison between the pseudo-elastic shear modulus of tested Dutch organic clay and the empirical relation proposed by Hardin and Black (1968). The predicted values align well with the experimental data of samples Cyc T2(VII) and Cyc T3(IX). However, the empirical relation significantly underestimates the pseudo-elastic shear modulus sample T9(X). Hardin and Black (1968) indicated that there is a secondary increase of the pseudo-elastic shear modulus with time in situ at constant effective stress, which is not accounted for in Equation 3.3. Nevertheless, this additional stiffness is sensitive to particle disturbance and can be partially or totally destroyed by disturbance. Based on this, it can be inferred that the sample disturbance on Cyc T2(VII) and Cyc T3(IX) might result in better alignment with the relation based on data of remoulded samples.

A generalised relationship is proposed by Shibuya and Tanaka (1996) to estimate the pseudo-elastic shear modulus of soft clay layer with void ratio and vertical effective stress, with data from a series of in-situ seismic cone tests, as presented in Equation 3.4. The comparison between the pseudo-elastic shear modulus of tested Dutch organic clay and the empirical relation proposed by Shibuya and Tanaka (1996) is also shown in Figure 3.51. Good alignment can be found for all tested Dutch organic clay samples, suggesting that typical empirical relations for pseudo-elastic shear modulus can provide a reasonable estimation of the pseudo-elastic shear modulus of Dutch organic clay.

$$G_{\max} = 5000e^{-1.5}\sqrt{\sigma'_v}(\text{unit:kPa}) \tag{3.4}$$

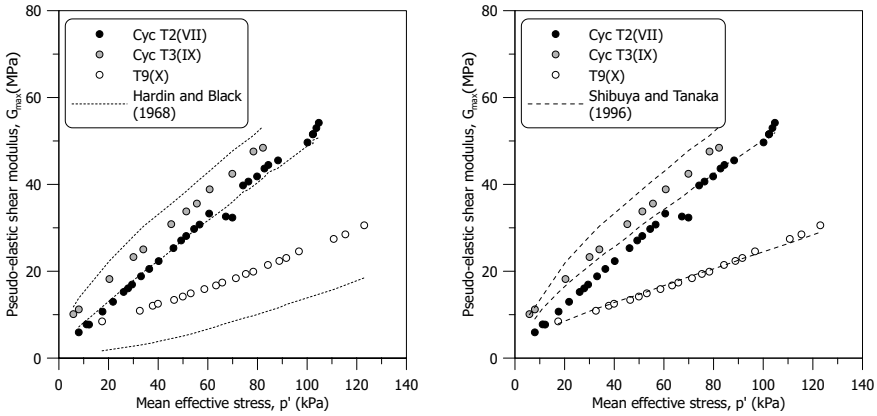

Figure 3.51: Comparison between pseudo-elastic shear modulus of Dutch organic clay and pseudo-elastic shear modulus from empirical relations in literature

3.4. EXTENDING JMC-CLAY MODEL TO BOUNDING SURFACE FORMULATION

As demonstrated in Chapter 2, the JMC-clay model effectively captures both the monotonic and non-monotonic static responses of Dutch soft organic clay. Constructed within an elastoplastic framework, the JMC-clay model predicts only elastic strains for stress states that lie within the yield locus. However, actual soil behaviour is rarely purely elastic, even when the stress states are within the yield locus. As illustrated in Figure 3.52, which compares experimental data with model predictions for sample Cyc R1(VII), the elastoplastic model predicts only elastic strain and generates no additional excess pore pressure after the tenth cycle. In terms of the stress-strain relationship, the model captures only the loading phase of the first cycle.

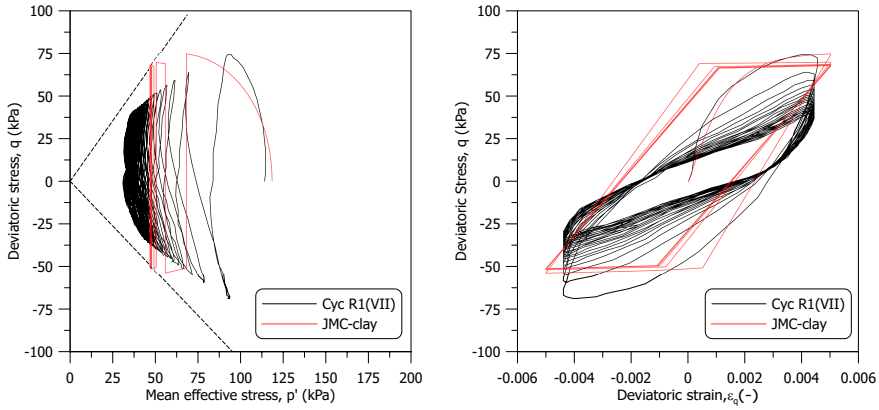

Figure 3.52: Experimental and modelling results of cyclic triaxial test on sample B103-14 Cyc R1

Owing to its mathematical simplicity, bounding surface plasticity has been adopted by several researchers to predict the cyclic behaviour of clay (Rezania et al., 2014; Seidalinov and Taiebat, 2014). The presence of a robust elastoplastic formulation makes the extension to cyclic response relatively straightforward. By incorporating the concept of the bounding surface along with a radial mapping rule, the model allows for plastic strains even when the stress states are within the bounding surface. This enhancement improves the model's capability to better represent cyclic responses. The bounding surface concept within the JMC-clay model is illustrated in Figure 3.53. Additionally, the expression for this bounding surface can be reformulated from the JMC-clay yield locus as follows:

$$F = \left(\bar{q} - \bar{p}'\alpha_f\right)^2 + \frac{M_f^2 - \alpha_f^2}{k_f - 1}\bar{p}'^2 - \frac{M_f^2 - \alpha_f^2}{k_f - 1}p_0'^2\left(\frac{\bar{p}'}{p_0'}\right)^{\frac{2}{k_f}} \tag{3.5}$$

where $\bar{p}'$ represents the image mean effective stress and $\bar{q}$ signifies the image deviatoric stress on the bounding surface. The parameter α_f defines the inclination of the bounding surface, while M_f and k_f control its shape. Finally, p_0' determines the size of the bounding surface.

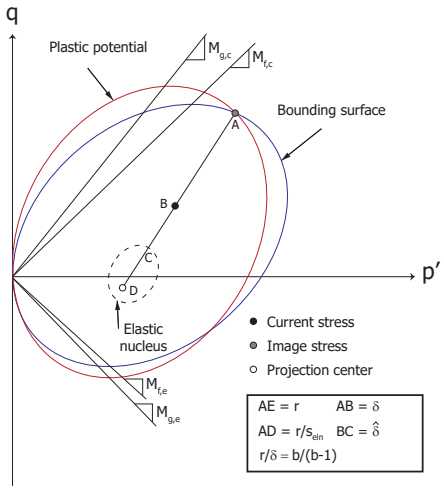

Figure 3.53: Sketch of elastoplastic bounding surface concept

For the extension of the JMC-clay bounding surface, the radial mapping rule proposed by Seidalinov (2018) is utilised. The image stresses $(\bar{p}', \bar{q})$ are associated with the current stresses (p', q) via the similarity ratio b and the projection centre (p'_c, q_c). This relationship can be expressed as:

$$\bar{p}' = p'_c + b \cdot (p' - p'_c); \bar{q} = q'_c + b \cdot (q - q'_c) \tag{3.6}$$

The plastic potential reads:

$$G = \left(\bar{q} - \bar{p}'\alpha_g\right)^2 + \left(M_g^2 - \alpha_g^2\right)\bar{p}'(\bar{p}' - p'_g) \tag{3.7}$$

where parameter α_g defines the inclination of the plastic potential, while M_g is the critical state stress ratio. Finally, p_g is a dummy variable to determine the size of the plastic potential.

The core of the bounding surface concept is the projection centre evolution. For models that incorporate rotational hardening, the projection centre has to evolve to maintain its relative position within the dynamically changing bounding surface (Seidalinov, 2018). Moreover, in line with existing constitutive models and experimental observation, the projection centre has to be updated at every stress reversal. The necessity of updating the projection centre upon stress reversals is demonstrated in Figure 3.54. The initial position of the projection centre is $(p'_c = 1\text{kPa}, q_c = 0\text{kPa})$.

The plastic modulus K_p for any stress state (p, q) is related to a bounding plastic modulus $\bar{K}_p$ at the corresponding image stress $(\bar{p}', \bar{q})$ by means of the Euclidean distances δ (between image stress and current stress state), and r (between image stress and projection centre) in the following formulations:

$$\frac{r}{\delta} = \frac{b}{(b-1)} \tag{3.8}$$

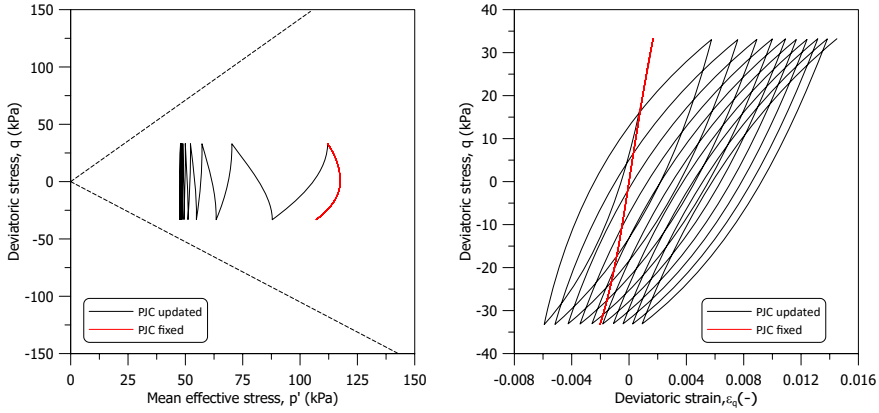

Figure 3.54: Necessity of projection centre update at last stress reversal for cyclic response prediction

$$K_p = \bar{K_p} + \frac{h{p'_0}^3\delta}{\langle r - s\delta\rangle} = \bar{K_p} + \frac{hp'_0}{\langle \frac{b}{b-1} - s_{\text{eln}}\rangle}\left(\frac{p'_0}{p'_{\text{ref}}}\right)^2 \tag{3.9}$$

$$\bar{K_p} = -\left(\frac{\partial F}{\partial p'_0}p'_0 + \frac{\partial F}{\partial \alpha}\alpha\right) \tag{3.10}$$

where h serves as a positive shape hardening variable. The parameter s_{eln} controls the relative size of the elastic nucleus. Specifically, when $s_{\text{eln}} = 1$, the elastic nucleus is reduced to a single point located at the projection centre. Additionally, p_{ref} acts as the reference pressure, ensuring unit consistency. The plastic modulus K_p is defined in line with the consistency condition of the bounding surface, expressed as $\dot{F} = 0$.

To accurately model the continuous evolution of stress-strain curves and the corresponding cyclic degradation/shakedown observed during cyclic loading in the laboratory, the shape hardening parameter h can evolve with an internal variable d to reproduce cyclic degradation/shakedown caused by the accumulation of plastic deviatoric strain. This damage parameter a_d, first introduced by Seidalinov and Taiebat (2014), is pivotal in capturing the reduction of secant shear modulus with the number of loading cycles. Shi et al. (2018) modified this formulation to also describe cyclic shakedown. This thesis adopts the formulation by Shi et al. (2018) to maintain the flexibility of the model for both cyclic degradation ($a_d \geq 0$) and cyclic shakedown ($a_d < 0$).

$$h = \frac{h_0}{1+d} \tag{3.11}$$

$$\delta d = \begin{cases} a_d(1+d)|\delta\varepsilon_q^p|, & \text{if } a_d < 0 \\ a_d|\delta\varepsilon_q^p|, & \text{if } a_d \geq 0 \end{cases} \tag{3.12}$$

where h_0 and a_d are model parameters.

When the bulk modulus is dependent on the mean effective stress p', there are two options: a 'variable' or a constant shear modulus. Practically, a value for the shear modulus can be derived from the bulk modulus by assuming a specific value for Poisson's ratio. Alternatively, using a constant shear modulus would imply a varying Poisson's ratio. Although choosing a constant Poisson's ratio implies hypo-elastic formulation and energy conservation during cyclic loading is not complied (Zytynski et al., 1978), they offer a straightforward platform to capture small strains stiffness properties within the bounding surface framework (Shi et al., 2018). Therefore, a hypo-elastic formulation with a constant Poisson's ratio is adopted when extending the JMC-clay to a bounding surface framework.

The early stabilisation of the stress path in the model prediction is triggered when the image stress reaches the critical state stress ratio, rendering no plastic volumetric strain. Shi et al. (2018) proposed the concept of the hybrid flow rule, in which the volumetric plastic strain increment is not solely dependent on the image stress state. Instead, it is contributed by both current stress and image stress as follows:

$$\frac{\partial G_{\text{hyb}}}{\partial p'_{\text{hyb}}} = \frac{\partial G_{\text{img}}}{\partial \bar{p}'} \cdot x + \frac{\partial G_{\text{cur}}}{\partial p'} \cdot (1 - x) \tag{3.13}$$

where subscripts img and cur denote the plastic potential defined at the image and current stress state. x is a variable that controls the contribution of the flow rule from the image stress state and current stress state; its evolution is defined as

$$x = (1/b)^w \tag{3.14}$$

where b is the similarity ratio; w is a model parameter, and the image stress flow rule is regained when $w = 0$. The deviatoric plastic increment is only contributed by the image stress.

$$\frac{\partial G_{\text{hyb}}}{\partial q_{\text{hyb}}} = \frac{\partial G_{\text{img}}}{\partial \bar{q}} \tag{3.15}$$

3.4.1. SENSITIVITY ANALYSIS OF THE MODEL PREDICTION

By extending JMC-clay towards a bounding surface framework, the total number of model parameters increases from 12 to 16. This increase is from the four parameters of the adopted bounding surface formulation (h_0, a_d, s_{eln}, and w). Following the calibration procedure presented in Chapter 2, the parameters of the elastoplastic (EP) JMC-clay model can be calibrated from experimental data. As the bounding surface extension primarily aims to better represent various aspects of cyclic response in clays, necessitating a comprehensive sensitivity analysis for effective model calibration and practical application.

Preliminary sensitivity analysis on the anisotropic bounding surface model has been performed by Seidalinov (2018) to showcase the constitutive features of the SANICLAY-B model. Additionally, Kancharla (2019) conducted a parametric study on the SANICLAY-B model, focusing on its predictive capabilities regarding the cyclic behaviour of kaolin clay. However, detailed investigations into the impacts of parameters such as s_{eln}, w,

and the over-consolidation ratio (OCR) on model predictions remain sparse. Therefore, the influence of newly introduced parameters associated with the bounding surface formulation will be investigated in the following section. The subsequent sensitivity analysis will investigate the predicted responses of the soil to cyclic loading, focusing on the aspects previously discussed in the experimental result, including volumetric and deviatoric responses. Additionally, simulations of different loading amplitudes will be discussed.

PARAMETERS SELECTION, STATE VARIABLES INITIALISATION, AND TEST TYPE OF SENSITIVITY ANALYSIS

The calibrated JMC-clay (EP) parameters for Dutch organic clay are adopted for sensitivity analysis, as listed in Table 3.3 and Table 3.4. A cyclic triaxial test is selected for the sensitivity analysis. The simulation initiates from an isotropic stress state, with a mean effective stress (p') of 5 kPa and the initial size ($p_{0,i}$) and inclination ($\alpha_{0,i}$) of the bounding surface set to 40 kPa and 0.5, respectively. In the isotropic consolidation stage, (p') is incrementally increased to 100 kPa for simulations starting from a normally consolidated state. For over-consolidated states, the simulation reaches a predetermined mean effective stress and then unloads to 100 kPa.

The subsequent cyclic stage involves up to 10 cycles of either stress- or strain-controlled loading. This cyclic loading follows a triangular wave pattern. In the strain-controlled simulation, a cyclic strain amplitude (ε_{cyc}) of 0.01 was applied. For the stress-controlled simulations, two distinct stress amplitudes (q_{cyc}) are used: $0.15p'_i$ and $0.30p'_i$, where p'_i is the mean effective stress after consolidation.

Table 3.3: Model parameters adopted for sensitivity analysis (inherent from original JMC-clay)

$M_{g,c}$	$M_{g,e}/M_{g,c}$	ν	c	z_c	z_e	s	y	$M_{f,c}$	k_f
1.42	0.74	0.2	50	1.6	1.2	2.2	2	0.99	1.25

Table 3.4: Model parameters adopted for sensitivity analysis(κ^* and λ^*)

λ^*	κ^*
0.1	0.011

SUMMARY OF SENSITIVITY ANALYSIS

To facilitate a comprehensive understanding, the detailed sensitivity analysis of the model parameters is thoroughly presented in Appendix B. The following section will summarise the simulation results, with a primary focus on two critical aspects of cyclic response. These include the volumetric response, which covers the evolution of the stress path and the development of pore pressure, and the deviatoric response, comprising the stress-strain curve, shear stiffness, damping ratio, and permanent deformation. Additionally, the influence of cyclic amplitude on the model's predictions will be briefly discussed.

In summary, an increase in the h_0 value increases the plastic modulus within the bounding surface. This leads to a stiffer compression curve during the consolidation

stage, coupled with a more pronounced transition in stiffness. In the context of cyclic loading, higher h_0 values correlate with reduced excess pore pressure development, increased secant shear modulus, and diminished permanent deviatoric strain.

The parameter a_d primarily influences the deviatoric aspects of the cyclic response, including peak deviatoric stress, secant shear modulus, and permanent deviatoric strain. However, the significant rise or reduction in plastic modulus during cyclic loading with extreme a_d values can also impact other facets of the cyclic response. For example, a very high positive a_d value can alter the pattern of stress path evolution and the development of excess pore pressure. Additionally, a very low negative a_d value results in a rapid increase in plastic modulus, leading to a viscoelastic response. Therefore, while the direct effects of a_d are observed in deviatoric responses, its broader impact extends to influencing the overall cyclic behaviour prediction.

A larger elastic nucleus size leads to a bigger elastic range within the bounding surface. Its impact on the compression curve is not evident from the conducted simulation. In terms of volumetric response, a larger elastic nucleus size reduces the development of excess pore pressure. As for the deviatoric response, a higher s_{eln} value leads to a higher peak deviatoric stress, secant shear modulus, and damping ratio. Additionally, when the elastic nucleus is active ($s_{\text{eln}} > 1$), the permanent deviatoric strain develops towards the extension side.

The hybrid flow rule parameter w is initially introduced to better capture the development of pore pressure during cyclic loading. However, w also alters cyclic deviatoric responses. For example, as stiffness is dependent on mean effective stress, higher w values lead to a more rapid reduction in mean effective stress. This, in turn, results in a quicker decrease in shear stiffness, as evidenced by lower peak deviatoric stress and secant shear modulus observed after the first loading cycle. Additionally, w influences the development of permanent deviatoric strain. This is due to the variation in deviatoric plastic strain increment that occurs when implementing the hybrid flow rule, allowing the image stress to evolve towards the dry side of the critical state and consequently reducing the deviatoric plastic strain increment.

As the OCR increases, the predicted response changes from contractive behaviour (positive excess pore pressure) to dilative behaviour (negative excess pore pressure). In terms of peak deviatoric stress and secant shear modulus, higher OCR values result in higher moduli. For low OCR values (OCR ≤ 2), a reduction in modulus with an increasing number of loading cycles is observed. The damping ratio tends to decrease as OCR values decrease; however, the difference is not evident. Additionally, higher OCR values lead to less permanent deviatoric strain.

Lastly, the influence of stress amplitude on the predicted cyclic response is straightforward. Specifically, higher stress amplitudes result in greater development of excess pore pressure and an increase in permanent deviatoric strain.

3.5. NUMERICAL CALIBRATION, PREDICTIONS AND VALIDATION

3.5.1. MODEL CALIBRATION AND STRESS STATE INITIALISATION

The 12 JMC-clay (EP) parameters can be calibrated using static laboratory tests as described in Chapter 2. The calibration procedure of bounding surface related parameters (h_0, a_d, s_{eln}, and w) will be described in this section.

To calibrate the bounding surface-related parameters, data from cyclic triaxial tests are needed. Ideally, these tests should include one sample initially in an isotropic state and another initially consolidated under K_0 conditions. Reflecting on the sensitivity analysis discussed in the previous section and referring to the literature that adopts bounding surface formulations, default values for these parameters are suggested to facilitate the calibration process. These default values are described below:

- Set s_{eln} equal to one by default. It can be adjusted for the best fit to the stress path and stress-strain curve evolution observed in both initially isotropic and K_0 consolidated cyclic triaxial tests.
- Set h_0 to 50 by default and select values that best fit the static compression and the cyclic triaxial stress-strain curves.
- Set a_d to zero by default and adjust a_d to best match the secant shear modulus reduction or the development of permanent deviatoric strain with the number of loading cycles.
- Set w to one by default and adjust it for the best fit to the stress path and excess pore pressure development in both initially isotropic and K_0 consolidated cyclic triaxial tests.

To effectively calibrate all model parameters, a minimum of six distinct tests are required, as summarised below:

- K_0 loading-unloading: active K_0 consolidation achieved by back volume or direct radial strain measurement.
- Isotropic loading-unloading: isotropic compression test with axial strain and volumetric strain measurements.
- Drained stress probe paths (two tests): one in compression and one in extension, the samples are brought to failure with undrained triaxial compression (TxCU) or undrained triaxial extension (TxEU) after stress probe path.
- Cyclic triaxial tests (two tests): including one test with an initially isotropic consolidated sample and another with an initially K_0 consolidated sample.

Five initial state variables are needed for the proposed model, namely the initial void ratio, e_i, the initial stress state at the beginning of the test (p'_i, q_i), the initial size of the bounding surface, $p'_{0,i}$, the initial inclination of the bounding surface and plastic potential, α_i, and the initial location of projection centre, (p'_c, q_c). The initialisation of

both $p'_{0,i}$ and α_i has been described in Chapter 2. The initial location of the projection centre is set at ($p'_c = 1kPa$, $q_c = 0kPa$).

Following the calibration procedure, the first ten cycles of samples Cyc T1(XI) and Cyc T2(XI) are selected to calibrate the model parameters related to bounding surface formulation. All calibrated model parameters are outlined in Tables 3.5, 3.6, and 3.7. The simulation with calibrated parameters and the test results are presented in Figure 3.55. In general, the model depicts the volumetric response well, except for the overestimated excess pore pressure in the first loading cyclic. Although the model underestimates the peak deviatoric stress in the first cycle of Cyc T2(XI), the model reasonably captures the stress path and stress-strain curve evolution. Additionally, the model shows a deviation in the evolution of deviatoric stress on the extension side, tending towards a more negative side compared to test Cyc T2(XI). This discrepancy might be due to the inherent anisotropy of the tested sample discussed previously. Moreover, while the model successfully captures the decrease in deviatoric stress with an increasing number of cycles on the compression side, it underestimates the reduction of deviatoric stress on the extension side.

Table 3.5: Calibrated original JMC-clay model parameters

$M_{g,c}$	$M_{g,e}/M_{g,c}$	ν	c	z_c	z_e	s	y	$M_{f,c}$	k_f
1.42	0.74	0.2	50	1.6	1.2	2.2	2	0.99	1.25

Table 3.6: Calibrated model parameters (bounding surface related)

h_0	a_d	s_{eln}	w
50	10	1	3

Table 3.7: Calibrated values for κ^* and λ^* for Cyc T1(IX) and Cyc T2(IX)

Parameter	Cyc T1(IX)	Cyc T2(IX)
κ^*	0.006	0.008
λ^*	0.055	0.070

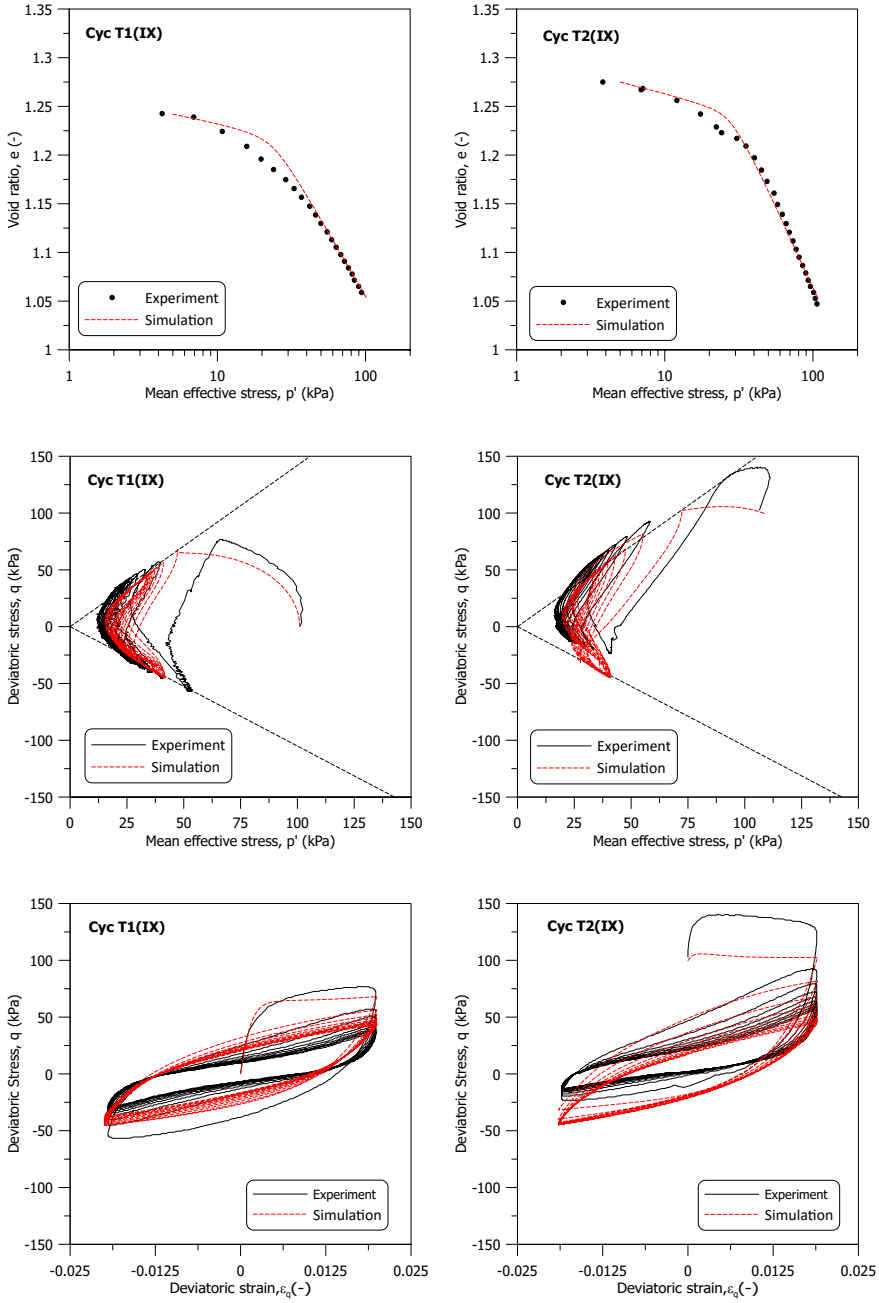

Figure 3.55: Simulation and experimental results of Cyc T1(IX) and Cyc T2(IX)

To assess the performance of the JMC-clay bounding surface (BS) model, static tests were simulated, and the results were compared to those obtained using the elastoplastic (EP) version of the model in Chapter 2. The calibrated values for κ^* and λ^* employed for the static test simulations are presented in Table 3.8.

Table 3.8: Calibrated values for κ^* and λ^* for different static tests samples

Parameter	T1(III)	T1(VII)	T1(VIII)	T3(IX)
κ^*	0.015	0.009	0.011	0.007
λ^*	0.137	0.085	0.095	0.065

The predictive capabilities of the JMC-clay (BS) model are further validated through test Cyc T2(VII), which entails strain-controlled cyclic shearing at a frequency of 0.001Hz and an amplitude of 2.4% on an initially K_0-consolidated sample. The calibrated values for κ^* and λ^* employed in the simulation are presented in Table 3.9. Stress-controlled cyclic test (0.1 Hz) from isotropic and K_0 are also simulated. Table 3.10 present calibrated values for κ^* and λ^* used in the stress controlled cyclic test simulation.

Table 3.9: Calibrated values for κ^* and λ^* for Cyc T2(VII)

Parameter	Cyc T2(VII)
κ^*	0.085
λ^*	0.009

Table 3.10: Calibrated values for κ^* and λ^* for T8(X) and T9(X)

Parameter	T8(X)	T9(X)
κ^*	0.013	0.014
λ^*	0.120	0.125

3.5.2. MODEL VALIDATION

The experimental data and simulation outcomes for the static tests are depicted in Figure 3.56 and 3.57. It can be observed that the JMC-clay (BS) model yields a smoother response compared to the JMC-clay (EP) model, particularly for samples in the over-consolidated state. This is attributed to the gradual transition of plastic modulus within the bounding surface.

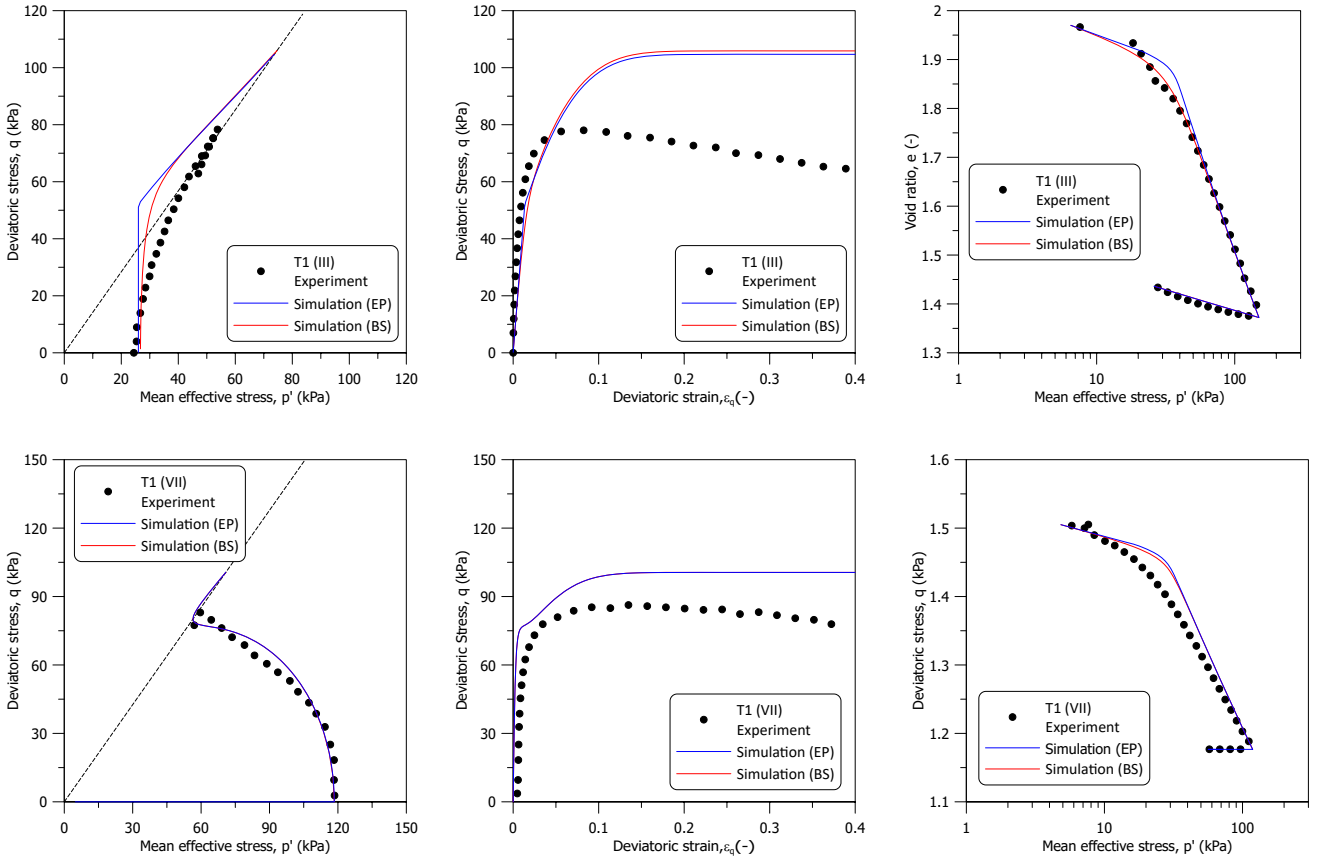

Figure 3.56: Experimental data and simulation results of static tests on group (III) and (VII)

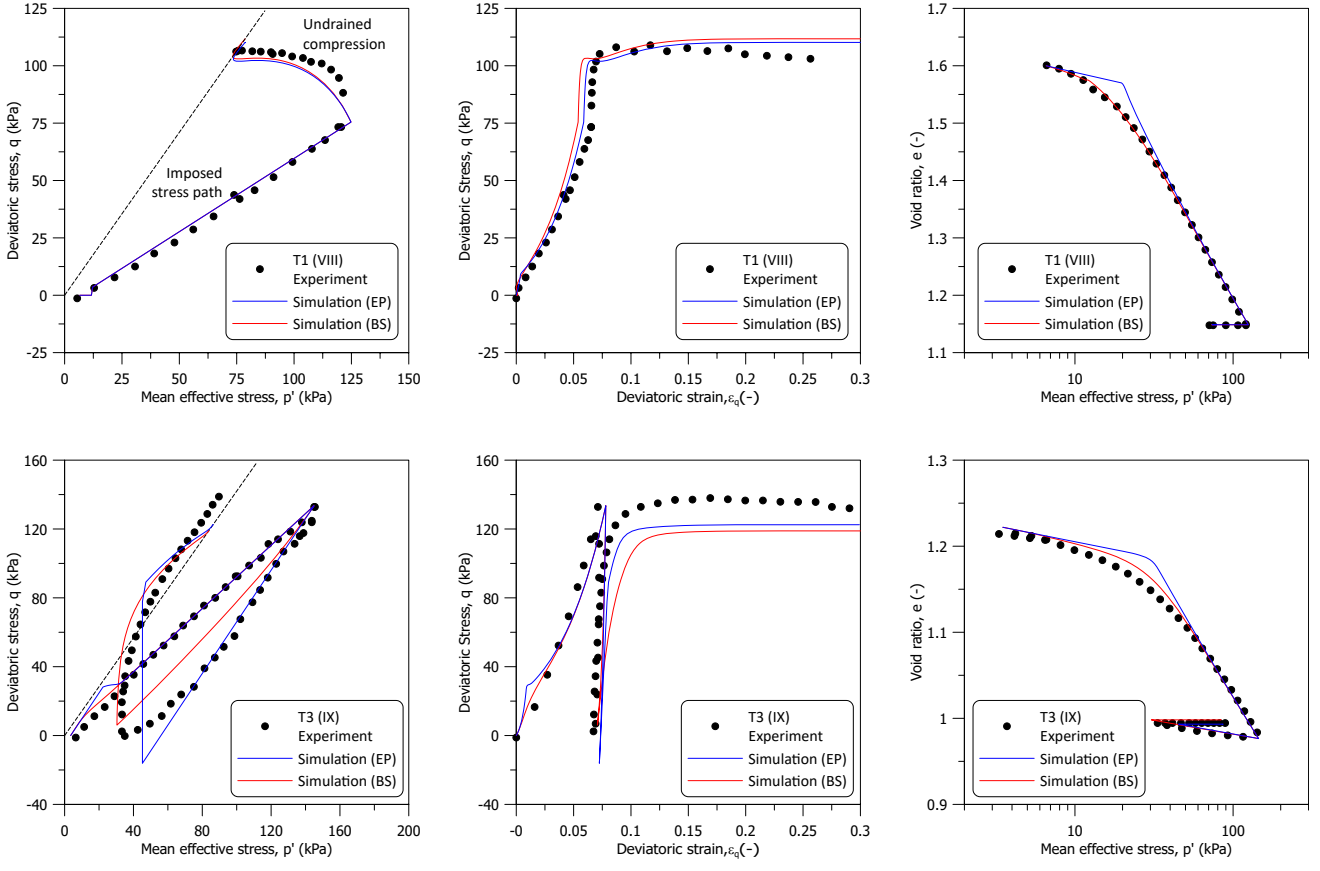

Figure 3.57: Experimental data and simulation results of static tests on group (VIII) and (IX)

To validate the predictive capability of the proposed model upon cyclic loading, the experimental results and simulation of test Cyc T2(VII) are analysed. Figure 3.58 displays the comparison between the experimental results and the numerical simulations for Cyc T2(VII). As depicted in the figure, the model predictions closely match the experimental data along K_0 consolidation. The model also reasonably predicts the cyclic volumetric response, as evidenced by the stress path evolution and excess pore pressure development. Regarding the deviatoric response, while the model underestimates the peak deviatoric stress during the first cycle, it captures well with the laboratory data in subsequent cycles. This better consistency is observed in deviatoric stress evolution on the extension side, compared to the one in the simulation of Cyc T2(IX).

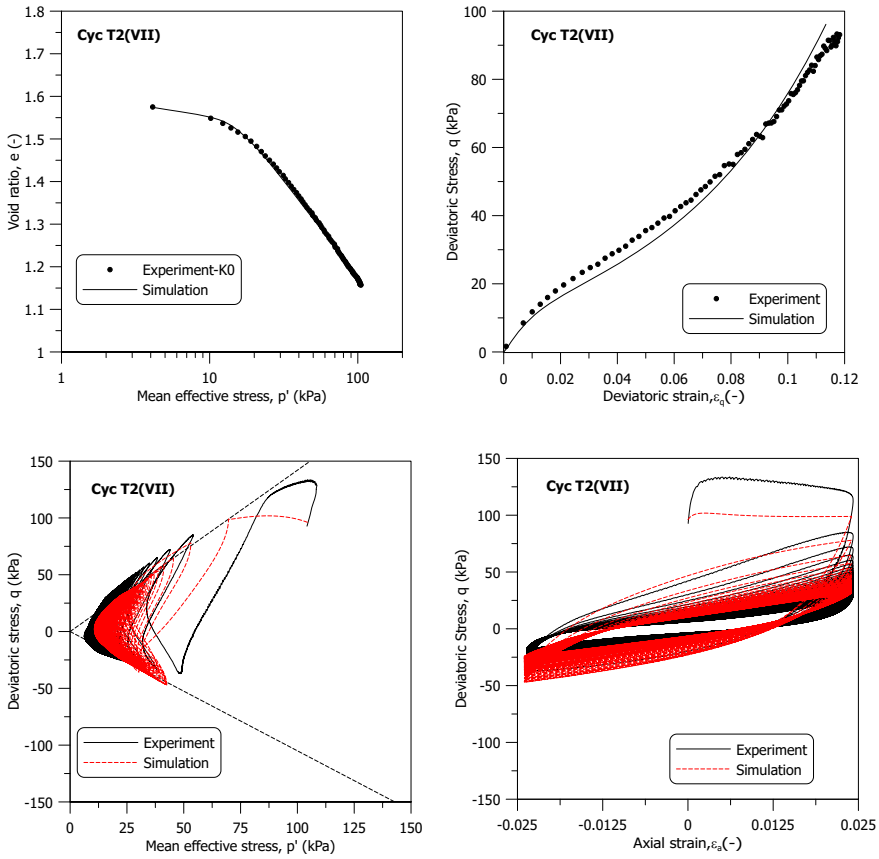

Figure 3.58: Simulation and experimental results of Cyc T2(VII)

ISSUES IN MODEL VALIDATION ON GROUP (X) SAMPLES

The simulation and experimental results for sample T8(X) are illustrated in Figure 3.59. The model accurately predicts the isotropic consolidation phase, but encounters challenges upon cyclic loading, significantly overestimating both the contractive response and the development of excess pore pressure. Additionally, there is a tendency within the model to overpredict deviatoric strain while underpredicting shear stiffness. For sample T9(X), as shown in Figure 3.60, the model offers a reasonable prediction of the K_0 consolidation path. However, it exhibits the same issues identified in the simulation of T8(X), with the added challenge that the model prediction does not achieve the peak deviatoric stress observed in laboratory tests.

The analysis of experimental data suggests that the higher clay content in group (X) samples leads to a different response under cyclic loading. These samples exhibit lower excess pore pressure compared to those in group (VII) when subjected to the same cyclic load. An explanation for this observation is that the increased clay content contributes to a more flexible microstructure, enhancing the material's ability to accommodate applied cyclic loading. Given the insights from the proposed modelling framework, it is logical to conclude that the size of the elastic nucleus should be configured to a larger value. The simulations for samples T8(X) and T9(X), with the elastic nucleus size parameter (s_{eln}) set to 2, are shown in Figures 3.61 and 3.62. An improvement in the model predictions is observed in the first cyclic stage for sample T8(X). However, for the remaining simulations, the model still fails to capture the experimental observations accurately. Although increasing the size of the elastic nucleus may enhance the model prediction for T8(X), the issue of underpredicting the peak deviatoric stress in T9(X) persists.

Within the current modelling framework, the only possibility of reaching peak deviatoric stress in T9(X) is to increase the size of the bounding surface, which has an over-consolidated state before cyclic shearing. A preliminary check is performed by increasing the size of the bounding surface p'_0 two times after the consolidation stage. For sample T8(X), the size of the bounding surface is increased from 121 kPa to 242 kPa. For sample T9(X), the size of the bounding surface is increased from 140 kPa to 280 kPa (keeping the same inclination). The size of the elastic nucleus is set at 1.5. The simulation results are presented together with experimental data in Figure 3.63 and Figure 3.64. The pore pressure prediction of the model is now much closer to the experimental observation. For the deviatoric stress-strain behaviour, the model can reach the peak deviatoric stress observed in the laboratory, but it still provides a softer response compared to the test. A more advanced elastic law might improve the model performance at the small strain range.

Initial evaluations indicate that a larger bounding surface, characterised by a higher over-consolidation ratio (OCR), might be necessary to align the model predictions with experimental observations. Specifically, it appears that the bounding surface at the end of consolidation is larger than what would be expected from a purely elastoplastic response, suggesting the occurrence of creep. This creep-induced over-consolidation could be one reason for the model underperformance in accurately predicting the behaviour of group (X) samples. Another potential explanation for this discrepancy might be the rate dependency of soil behaviour, considering that the loading frequency applied to group (X) samples is 100 times higher than that applied to samples from other groups.

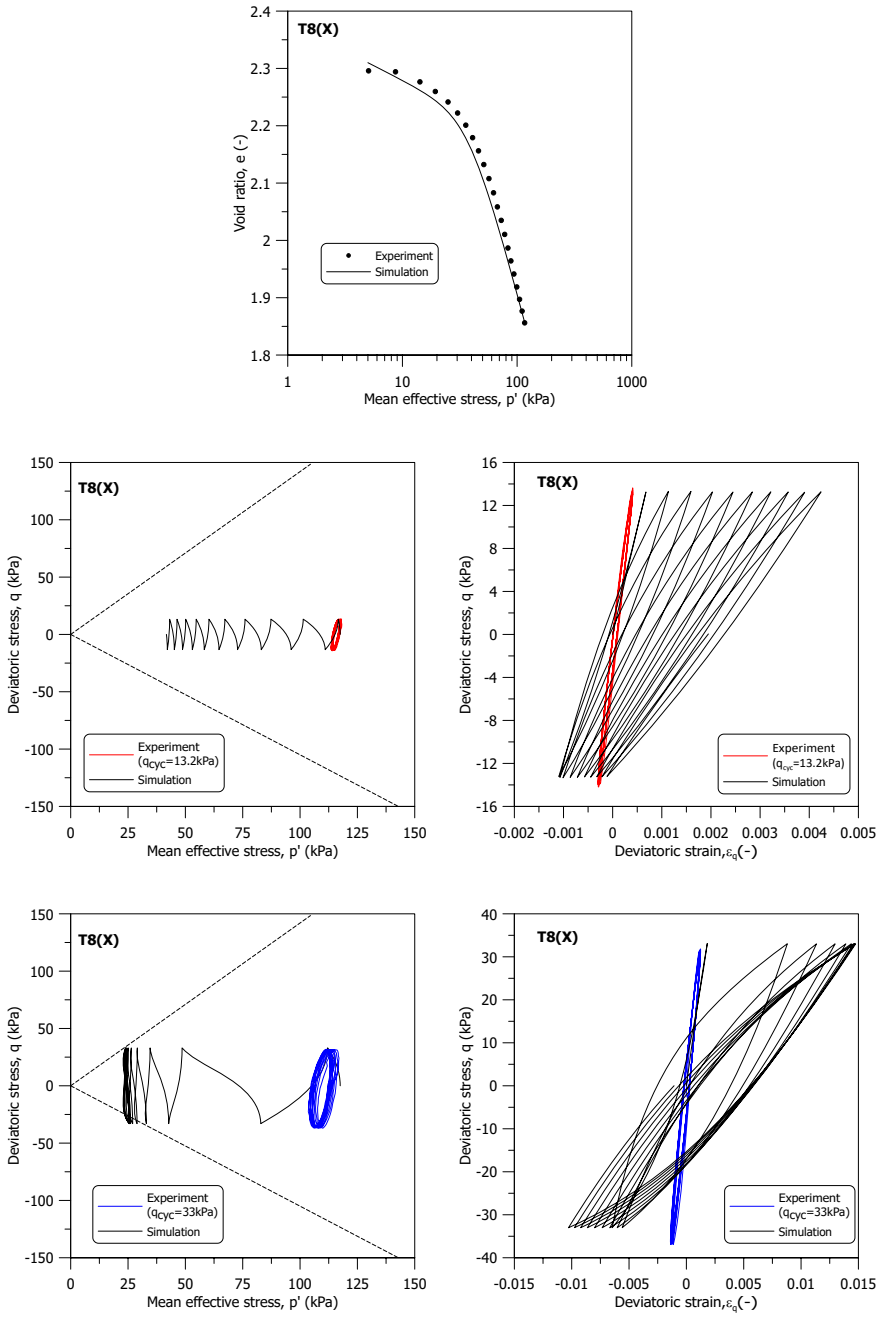

Figure 3.59: Simulation and experimental results of T8(X)

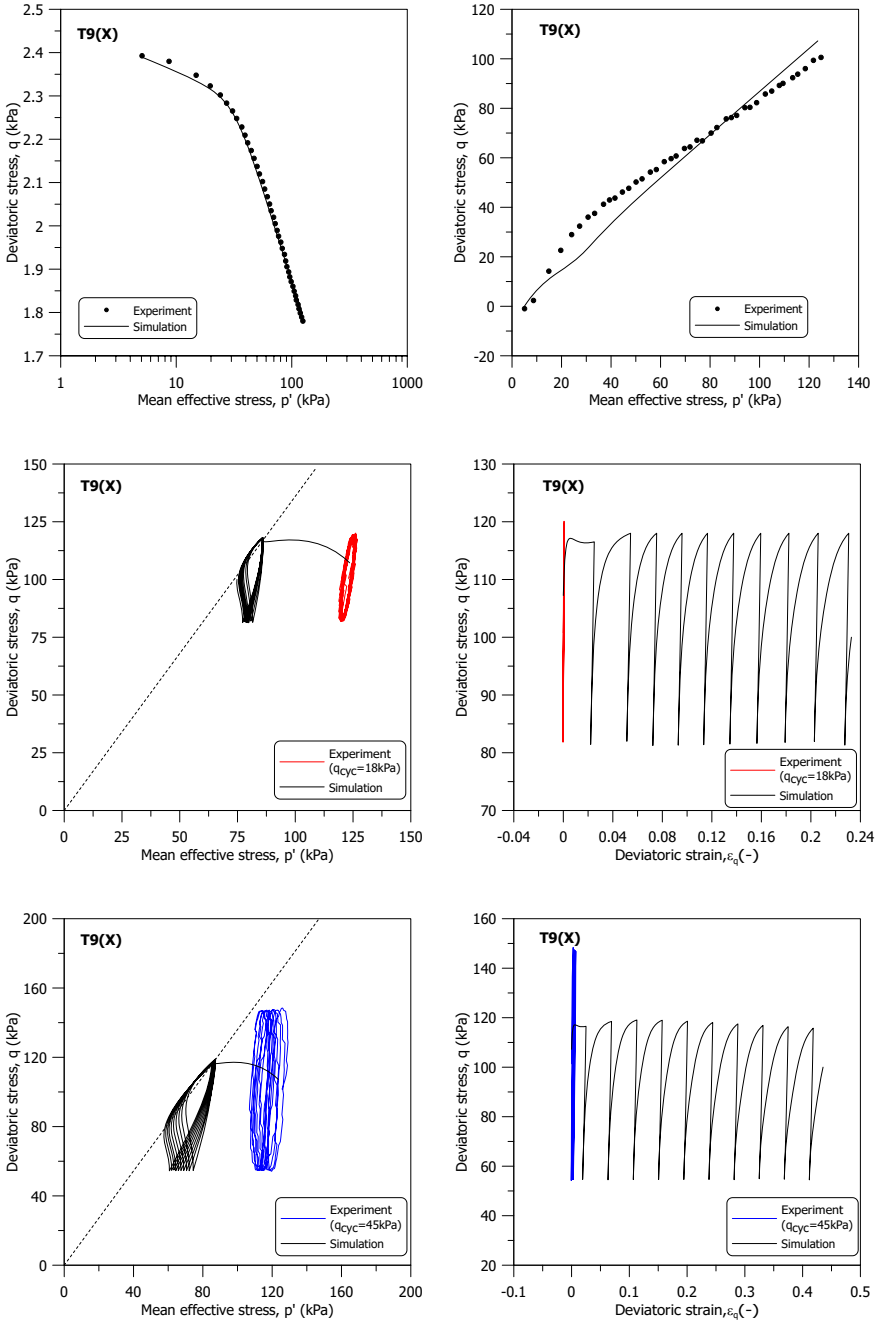

Figure 3.60: Simulation and experimental results of T9(X)

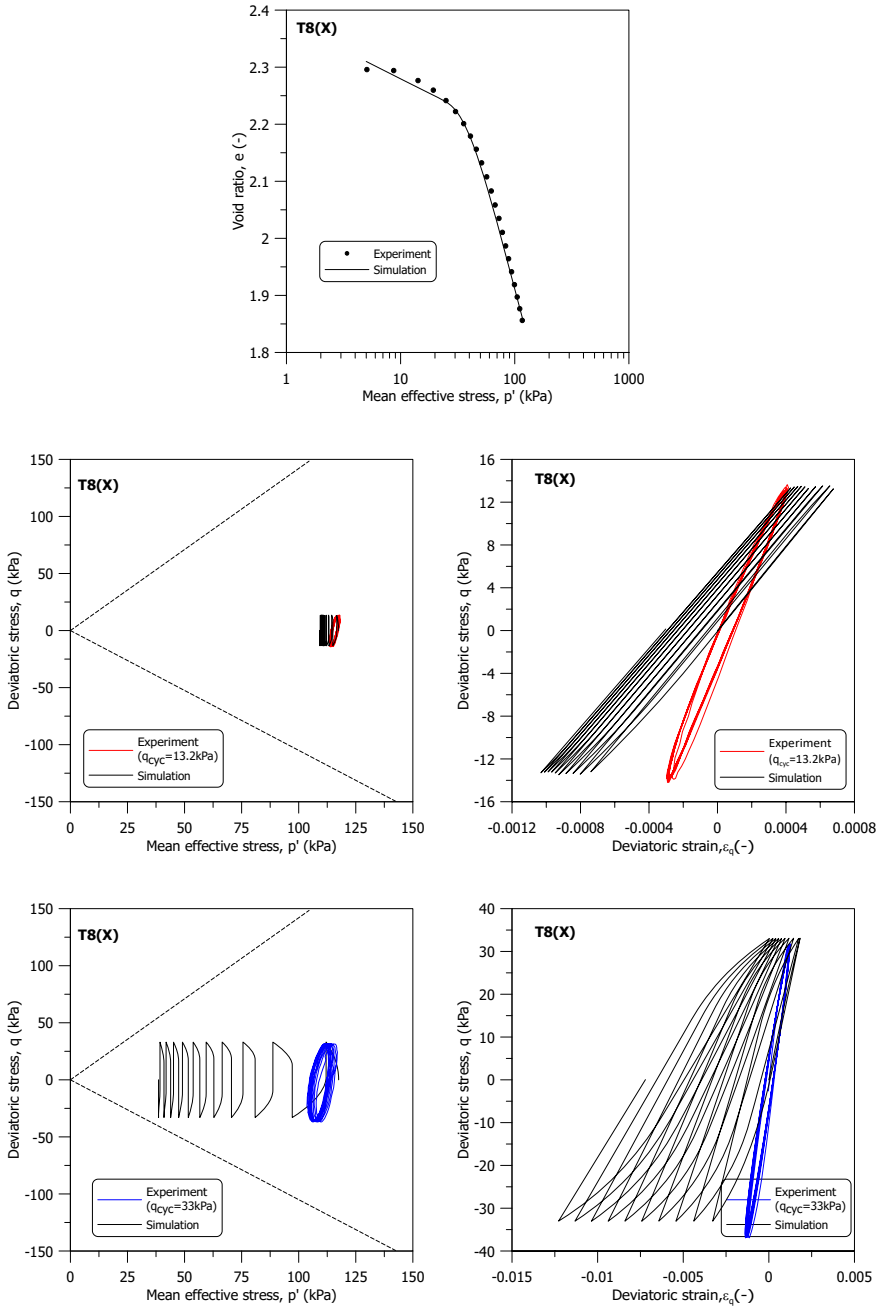

Figure 3.61: Simulation and experimental results of T8(X) with s_{eln} set to 2

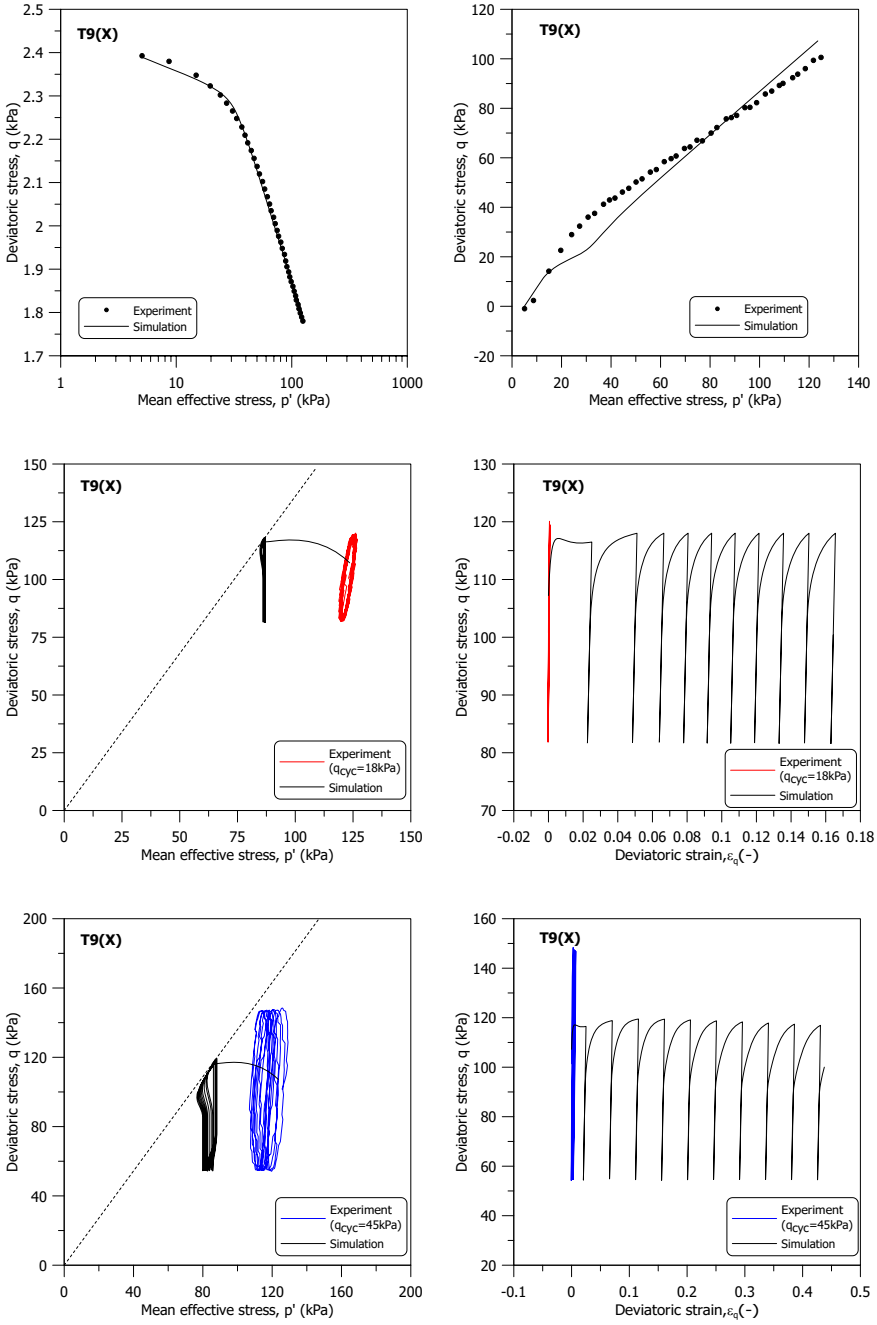

Figure 3.62: Simulation and experimental results of T9(X) with s_{eln} set to 2

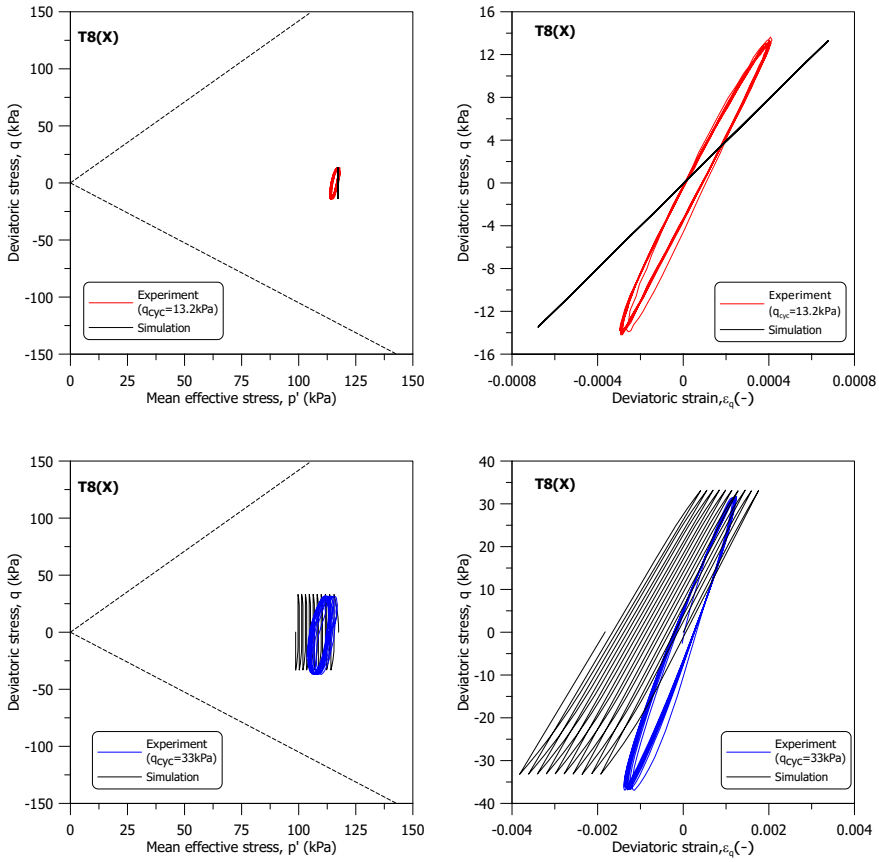

Figure 3.63: Simulation and experimental results of T8(X) with p'_0 set to 242 kPa and s_{eln} set to 1.5

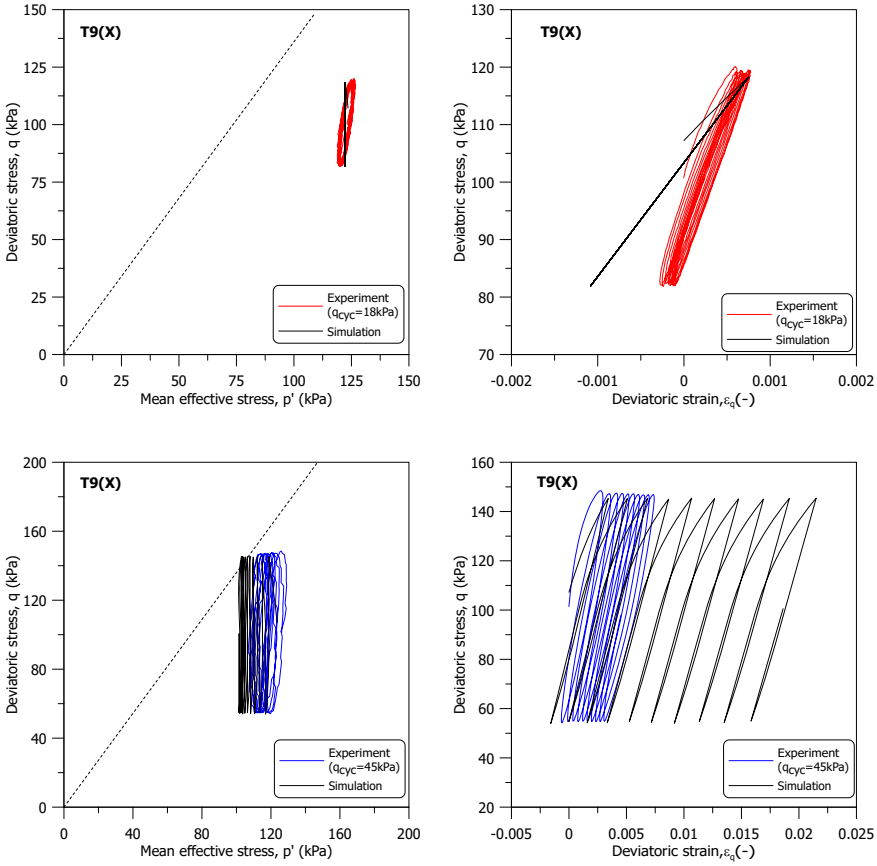

Figure 3.64: Simulation and experimental results of T9(X) with p'_0 set to 280 kPa and s_{eln} set to 1.5

3.6. DISCUSSIONS AND CONCLUSIONS

In this Chapter, a thorough investigation into the slow cyclic response of Dutch organic clay through experimental studies and constitutive modelling is presented, aiming to demystify the complex behaviour of Dutch organic clay under cyclic loading conditions. The approach adopted herein has unearthed insight regarding the influence of loading frequency, the contrasting responses between natural and reconstituted samples, the significance of the initial stress state, the impact of the cyclic stress amplitude, the role of clay and organic content, and the crucial aspect of post-cyclic undrained shear strength and recompression.

A noteworthy discovery is the dependency of the soil cyclic response on the amplitude of cyclic strain. This relationship is essential for grasping the fundamental mechanics of soil behaviour under cyclic loading, as it directly influences shear stiffness, strength, and the development of excess pore pressure.

The detailed comparative analysis between natural and reconstituted samples has highlighted substantial differences in their responses to cyclic loading, thereby emphasising the critical role of soil structure and composition. It is observed that natural samples demonstrate higher shear stiffness and less development of excess pore pressure, which accentuates the impact of the soil's inherent characteristics on its cyclic behaviour.

Moreover, the exploration into the effects of the initial stress state offers deeper insights into the anisotropic nature of soil behaviour and its sensitivity to pre-cyclic stress conditions. This Chapter underscores how the initial stress state can affect excess pore pressure development, influence the accumulation of permanent strain, and dictate the cyclic strength of Dutch organic clay. These findings highlight the need for more sophisticated models that can accurately represent anisotropy and stress history.

The influence of clay and organic content on the cyclic response of Dutch organic clay further elucidates the impact of soil composition on its mechanical properties under cyclic loading. This revelation also carries profound implications for the development of advanced soil models.

The extension of the JMC-clay model to include cyclic behaviour, incorporating bounding surface plasticity, offers a more accurate and predictive framework for modelling soil behaviour under cyclic loading conditions, despite the encountered challenges in model validation.

This Chapter progresses our understanding of the slow cyclic response of Dutch organic clay, particularly highlighting the crucial role of cyclic strain amplitude. The experimental and modelling efforts have shed light on the intricate factors that influence soil behaviour under cyclic loading, providing nuanced insights that augment both the theoretical and practical comprehension of soil cyclic responses.

BIBLIOGRAPHY

Andersen, K. H. (2009). Bearing capacity under cyclic loading—offshore, along the coast, and on land. the 21st bjerrum lecture presented in oslo, 23 november 2007. *Canadian Geotechnical Journal*, *46*(5), 513–535.

Andersen, K. H. (2015). Cyclic soil parameters for offshore foundation design. *Frontiers in offshore geotechnics III*, *5*.

Bjerrum, L. (1967). Engineering geology of norwegian normally-consolidated marine clays as related to settlements of buildings. *Geotechnique*, *17*(2), 83–118.

Boulanger, R. W., & Idriss, I. (2006). Liquefaction susceptibility criteria for silts and clays. *Journal of geotechnical and geoenvironmental engineering*, *132*(11), 1413–1426.

Burland, J. (1990). On the compressibility and shear strength of natural clays. *Géotechnique*, *40*(3), 329–378.

Chang, W.-J., & Hong, M.-L. (2008). Effects of clay content on liquefaction characteristics of gap-graded clayey sands. *Soils and foundations*, *48*(1), 101–114.

Cotecchia, F., & Chandler, R. (1997). The influence of structure on the pre-failure behaviour of a natural clay. *Géotechnique*, *47*(3), 523–544.

D2974-14. (2014). Standard test methods for moisture, ash, and organic matter of peat and other organic soils. *American Society of Testing and Materials ASTM, PA, USA*.

D5550-14. (2014). Standard test method for specific gravity of soil solids by gas pycnometer. *American Society of Testing and Materials ASTM, PA, USA*.

Graham, J., Crooks, J., & Bell, A. L. (1983). Time effects on the stress-strain behaviour of natural soft clays. *Géotechnique*, *33*(3), 327–340.

Guo, T., & Prakash, S. (1999). Liquefaction of silts and silt-clay mixtures. *Journal of Geotechnical and Geoenvironmental Engineering*, *125*(8), 706–710.

Hardin, B. O., & Black, W. L. (1968). Vibration modulus of normally consolidated clay. *Journal of the Soil Mechanics and Foundations Division*, *94*(2), 353–369.

Hayashi, H., Hatakeyama, O., Hashimoto, H., & Yamaki, M. (2020). Shear modulus and damping of peat subjected to overconsolidation stress history. *Geotechnical and Geological Engineering*, *38*(6), 6421–6430.

Head, K. H. (1992). *Manual of soil laboratory testing. volume 1. soil classification and compaction tests*.

Hight, D., Bond, A., & Legge, J. (1992). Characterization of the bothkennaar clay: An overview. *Géotechnique*, *42*(2), 303–347.

Hyodo, M., Hyde, A. F., Yamamoto, Y., & Fujii, T. (1999). Cyclic shear strength of undisturbed and remoulded marine clays. *Soils and Foundations*, *39*(2), 45–58.

Hyodo, M., Yamamoto, Y., & Sugiyama, M. (1994). Undrained cyclic shear behaviour of normally consolidated clay subjected to initial static shear stress. *Soils and Foundations*, *34*(4), 1–11.

Jommi, C., Chao, C., Muraro, S., & Zhao, H. (2021). Developing a constitutive approach for peats from laboratory data. *Geomechanics for Energy and the Environment*, *27*, 100220.

Kancharla, V. (2019). A parametric study on the bounding surface sanicaly model for cyclic behaviour of kaolin clay.

Lee, J.-S., & Santamarina, J. C. (2005). Bender elements: Performance and signal interpretation. *Journal of geotechnical and geoenvironmental engineering*, *131*(9), 1063–1070.

Lei, J., Wang, Y., Zhang, B., Li, F., & Liu, C. (2022). Cyclic and post-cyclic characteristics of marine silty clay under the multistage cycling-reconsolidation conditions. *Ocean Engineering*, *258*, 111803.

Liu, A. H., Stewart, J. P., Abrahamson, N. A., & Moriwaki, Y. (2001). Equivalent number of uniform stress cycles for soil liquefaction analysis. *Journal of Geotechnical and Geoenvironmental Engineering*, *127*(12), 1017–1026.

Ludwik, P. (1909). *Elemente der technologischen mechanik*. Springer.

Mortezaie, A. R., & Vucetic, M. (2013). Effect of frequency and vertical stress on cyclic degradation and pore water pressure in clay in the ngi simple shear device. *Journal of Geotechnical and Geoenvironmental Engineering*, *139*(10), 1727–1737.

Oda, M., Kawamoto, K., Suzuki, K., Fujimori, H., & Sato, M. (2001). Microstructural interpretation on reliquefaction of saturated granular soils under cyclic loading. *Journal of Geotechnical and Geoenvironmental Engineering*, *127*(5), 416–423.

Pan, K., Yuan, Z., Zhao, C., Tong, J., & Yang, Z. (2022). Undrained shear and stiffness degradation of intact marine clay under monotonic and cyclic loading. *Engineering Geology*, *297*, 106502.

Paul, M., & Barras, B. (1999). Role of organic material in the plasticity of bothkennar clay. *Géotechnique*, *49*(4), 529–535.

Ponzoni, E. (2017). *Historical constructions on natural silty soils accounting for the interaction with the atmosphere* [Thesis].

Rezania, M., Dejaloud, H., & Nezhad, M. M. (2014). Sclay1s-bs: An anisotropic model for simulation of cyclic behaviour of clays. In *Geomechanics from micro to macro* (pp. 670–675). CRC Press.

Seed, H. B. (1975). *Representation of irregular stress time histories by equivalent uniform stress series in liquefaction analyses*. National Technical Information Service.

Seidalinov, G. (2018). *Constitutive and numerical modeling of clay subjected to cyclic loading* [Thesis].

Seidalinov, G., & Taiebat, M. (2014). Bounding surface saniclay plasticity model for cyclic clay behavior. *International Journal for Numerical and Analytical Methods in Geomechanics*, *38*(7), 702–724.

Sheahan, T. C., Ladd, C. C., & Germaine, J. T. (1996). Rate-dependent undrained shear behavior of saturated clay. *Journal of Geotechnical Engineering*, *122*(2), 99–108.

Sheu, W.-Y. (1985). Modeling of stress-strain-strength behavior of a clay under cyclic loading. *Dissertation Abstracts International Part B: Science and Engineering[DISS. ABST. INT. PT. B- SCI. & ENG.]*, *45*(9).

Shi, Z., Finno, R. J., & Buscarnera, G. (2018). A hybrid plastic flow rule for cyclically loaded clay. *Computers and Geotechnics*, *101*, 65–79.

Shibuya, S., Hwang, S., & Mitachi, T. (1997). Elastic shear modulus of soft clays from shear wave velocity measurement. *Géotechnique*, *47*(3), 593–601.

Shibuya, S., & Tanaka, H. (1996). Estimate of elastic shear modulus in holocene soil deposits. *Soils and foundations*, *36*(4), 45–55.

Tafili, M., Wichtmann, T., & Triantafyllidis, T. (2021). Experimental investigation and constitutive modeling of the behaviour of highly plastic lower rhine clay under monotonic and cyclic loading. *Canadian Geotechnical Journal*, *58*(9), 1396–1410.

Ushev, E., & Jardine, R. (2020). The behaviour of bolders bank glacial till under undrained cyclic loading. *Géotechnique*, 1–19.

Viggiani, G., & Atkinson, J. (1995). Interpretation of bender element tests. *Geotechnique*, *45*(1), 149–154.

Vucetic, M. (1988). Normalized behavior of offshore clay under uniform cyclic loading. *Canadian Geotechnical Journal*, *25*(1), 33–41.

Vucetic, M., & Dobry, R. (1991). Effect of soil plasticity on cyclic response. *Journal of geotechnical engineering*, *117*(1), 89–107.

Wichtmann, T., Andersen, K., Sjursen, M., & Berre, T. (2013). Cyclic tests on high-quality undisturbed block samples of soft marine norwegian clay. *Canadian Geotechnical Journal*, *50*(4), 400–412.

Wichtmann, T., & Triantafyllidis, T. (2018). Monotonic and cyclic tests on kaolin: A database for the development, calibration and verification of constitutive models for cohesive soils with focus to cyclic loading. *Acta Geotechnica*, *13*(5), 1103–1128.

Xiao, W., Gui, Y., & Xu, G.-Z. (2018). Effect of organic content and frequency on degradation and pore pressure in marine organic soils. *Marine Georesources & Geotechnology*, *36*(1), 108–122.

Xu, Z., Pan, L., Gu, C., Wang, J., & Cai, Y. (2020). Deformation behavior of anisotropically overconsolidated clay under one-way cyclic loading. *Soil Dynamics and Earthquake Engineering*, *129*, 105943.

Yasuhara, K. (1994). Postcyclic undrained strength for cohesive soils. *Journal of geotechnical engineering*, *120*(11), 1961–1979.

Yasuhara, K., & Andersen, K. H. (1991). Recompression of normally consolidated clay after cyclic loading. *Soils and Foundations*, *31*(1), 83–94.

Yasuhara, K., Hirao, K., & Hyde, A. F. (1992). Effects of cyclic loading on undrained strength and compressibility of clay. *Soils and Foundations*, *32*(1), 100–116.

Yasuhara, K., Murakami, S., Toyota, N., & Hyde, A. F. (2001). Settlements in fine-grained soils under cyclic loading. *Soils and Foundations*, *41*(6), 25–36.

Yu, Y., & Yang, Z. (2023). Bounding surface plasticity model for clay under cyclic loading conditions considering fabric anisotropy. *Journal of Engineering Mechanics*, *149*(9), 04023067.

Zhao, J., & Guo, N. (2013). Unique critical state characteristics in granular media considering fabric anisotropy. *Géotechnique*, *63*(8), 695–704.

Zytynski, M., Randolph, M., Nova, R., & Wroth, C. (1978). On modelling the unloading-reloading behaviour of soils. *International Journal for Numerical and Analytical Methods in Geomechanics*, *2*(1), 87–93.

4

Rate Dependency in Modelling Cyclic Behaviour: An Elastoplastic-Viscoplastic Framework

Success is not final, failure is not fatal: It is the courage to continue that counts.

Winston Churchill

4.1. INTRODUCTION

In Chapter 3, simulations demonstrate that the bounding surface version of JMC-clay inadequately represents the cyclic response of soft organic clay, especially for the samples of the group (X). The preliminary check suggests that a larger bounding surface (with a higher over-consolidation ratio, OCR) is required to align with experimental observations. In other words, at the end of consolidation, the bounding surface is larger than expected for a purely elastoplastic response, which suggests that creep is occurring. This is in line with findings by Bjerrum (1967), Graham et al. (1983), and Sheahan et al. (1996), who observed that soft soils exhibit time-dependent, or 'creep' strains, necessitating an enlarged bounding surface in constitutive modelling. The elastoplastic-viscoplastic approach, widely referenced in the literature, effectively describes the time-dependent behaviour of soils (Zienkiewicz et al., 1975; Rezania et al., 2016). Additionally, a few researchers incorporate the elastoplastic-viscoplastic approach into the bounding surface framework to model monotonic and cyclic response (Kaliakin and Dafalias, 1990a; Kaliakin and Dafalias, 1990b; Jiang et al., 2017; Nieto-Leal and Kaliakin, 2021).

In this chapter, the JMC-clay model is extended toward an elastoplastic-viscoplastic bounding surface formulation, termed JMC-clay BSEVP. The elastoplastic-viscoplastic bounding surface model is central to the 'overstress function' evolution. The parameters controlling this 'overstress function', as proposed by Kaliakin and Dafalias (1990a), have not been thoroughly investigated. This chapter aims to first systematically elucidate the influence of viscoplastic-related parameters on the 'overstress function'. Subsequently, a comprehensive sensitivity analysis will be conducted. This analysis will clarify the impact of these newly introduced model parameters, in conjunction with those related to the bounding surface, on the predicted cyclic response.

The integration of bounding surface and elastoplastic-viscoplastic formulations into the JMC-clay model introduces a total of 19 parameters. This chapter outlines the calibration process for the JMC-clay BSEVP model. Drawing on the sensitivity analysis presented in the chapter and relevant literature on elastoplastic-viscoplastic coupling frameworks, default values for several parameters are suggested. These defaults aim to simplify the calibration process or serve as substitutes when experimental data is unavailable.

The efficacy of the JMC-clay BSEVP model is validated using static tests on Dutch organic clay, as presented in Chapter 2, and cyclic tests on Dutch organic clay, as detailed in Chapter 3. Comparisons between experimental data and numerical simulations highlight the JMC-clay BSEVP model capability in predicting various aspects of cyclic behaviour. These aspects include cyclic recompression and post-cyclic shear. Specifically, the model performance on samples from the group (X) is investigated in detail. Lastly, the rate-dependency features of the model are illustrated with typical aspects considered in practical geotechnical design, such as shear modulus reduction and damping curves, as well as the number of loading cycles to failure at a given stress amplitude.

4.2. ELASTOPLASTIC-VISCOPLASTIC BOUNDING SURFACE FORMULATION

Building upon the foundational structure proposed by Kaliakin and Dafalias (1990a), the JMC-clay is extended to encompass an elastoplastic-viscoplastic bounding surface formulation (JMC-clay BSEVP), as illustrated in Figure 4.1. Adopting Perzyna's overstress theory (Perzyna, 1966) necessitates the definition of a corresponding overstress reference surface. The overstress reference surface mirrors the shape of the bounding surface, as well as the elastic nucleus, and its size is defined by the model parameter, s_v. Inside the overstress reference surface and outside the elastic nucleus, the response is elastoplastic. As the stress point moves out of the reference surface, the viscoplastic strain rate is correlated with the 'distance' from the overstress reference surface to the current stress point.

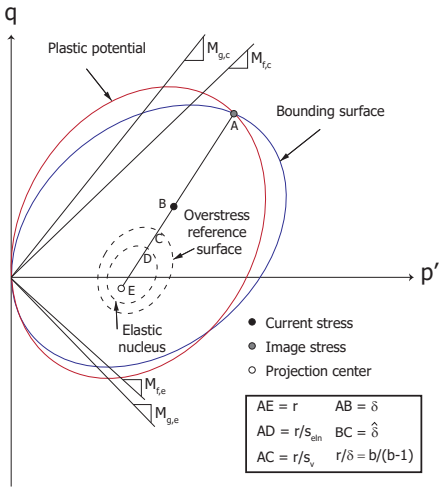

Figure 4.1: Sketch of elastoplastic-viscoplastic bounding surface concept

Given a generic stress state, σ, the 'normalised overstress', according to Kaliakin and Dafalias (1990a), is delineated as follows:

$$\Delta\hat{\sigma} = \frac{\hat{\delta}}{r - \frac{r}{s_v}} \tag{4.1}$$

where $\hat{\delta}$ is the distance from the current stress state to the overstress reference surface, and r is the distance from the image stress to the projection centre. Figure 4.1 shows that the following relation holds:

$$\hat{\delta} = \frac{r}{s_v} - \delta \tag{4.2}$$

where δ is the distance from the current stress state to the image stress. Adopting the similarity ratio introduced in equation 3.8 in Chapter 3, equation 4.1 and 4.2 allow rewriting the normalised overstress as a function of s_v and b:

$$\Delta\hat{\sigma} = \frac{s_v}{b(s_v - 1)} - 1 \tag{4.3}$$

Viscoplastic strains are generated if $\Delta\hat{\sigma}$ is greater than zero. The minimum similarity ratio, $b_{\min}$, for which this condition is met depends on s_v, as plotted in Figure 4.2.

The magnitude of the viscoplastic strain is controlled by the overstress function, denoted as Φ, following Perzyna's approach (Perzyna, 1966), Kaliakin and Dafalias (1990a) defined the latter as:

$$\Phi = \frac{1}{V} \exp\left(\frac{q}{M_g p'}\right) (\Delta\hat{\sigma})^n \tag{4.4}$$

where V and n are new model parameters.

The viscoplastic strain can be calculated as follows:

$$\varepsilon_v^{vp} = \langle\Phi\rangle \frac{\partial g}{\partial(p')} \left| \frac{\partial g}{\partial(p')} \right|^{-1} \tag{4.5}$$

$$\varepsilon_q^{vp} = \langle\Phi\rangle \frac{\partial g}{\partial(q)} \left| \frac{\partial g}{\partial(q)} \right|^{-1} \tag{4.6}$$

According to Kaliakin (1991), for relatively small values of V, the response exhibits almost inviscid characteristics throughout the loading history, meaning the viscous response occurs very rapidly. Conversely, with large V values, the viscoplastic strain is substantially reduced, leading to minimal change in the overall response over time. Similarly, increases in the exponent term n affect the response in a manner akin to increases in V, particularly on the initial slope of the response curves.

To facilitate practical calibration of the model, it is essential to explore the influence of the three viscoplastic-related parameters: s_v, V, and n. This exploration will help achieve better model predictions.

The parameter n determines the exponent for the 'normalised overstress', denoted as $\Delta\hat{\sigma}$. Its impact on the viscoplastic response varies with the value of $\Delta\hat{\sigma}$. Specifically:

- When $\Delta\hat{\sigma}$ is less than 1, an increase in n results in a decrease in the overstress function, Φ.
- If $\Delta\hat{\sigma}$ equals 1, the value of n does not affect Φ.
- When $\Delta\hat{\sigma}$ exceeds 1, a higher n value leads to an increase in Φ.

The 'normalised overstress' $\Delta\hat{\sigma}$ is a function of s_v and similarity ratio b. For a given s_v value, the following equations define the ranges of the similarity ratio that correspond to the three circumstances previously mentioned.

$$\begin{cases} \Delta\hat{\sigma} > 1, & b < \frac{s_v}{2(s_v-1)} \\ \Delta\hat{\sigma} = 1, & b = \frac{s_v}{2(s_v-1)} \\ \Delta\hat{\sigma} < 1, & b > \frac{s_v}{2(s_v-1)} \end{cases} \tag{4.7}$$

Figure 4.3 illustrates how the parameter n affects the overstress function Φ for three different s_v values: 1.5, 2, and 2.5. The parameters V and n are fixed at 5×10^7 kPa·min and 4, respectively. A stress ratio $\eta = \frac{q}{p'}$ of 0.5 is adopted for plotting the results. For s_v = 1.5, the critical similarity ratio b is 1.5 ($\Delta\hat{\sigma} = 1$), meaning that $\Delta\hat{\sigma}$ is less than one above this ratio and greater than one below it. This indicates that increasing n can positively, neutrally, or negatively impact Φ, depending on the stress state (reflected by different similarity ratios b, as shown in Figure 4.3). As s_v increases to 2, the critical similarity ratio becomes 1, suggesting that increasing n can either neutrally or negatively influence Φ. When s_v is 2.5, any increase in n will only have a negative effect on Φ.

The influence of the parameter V is relatively distinct: the higher the V value, the lower the overstress function Φ, as illustrated in Figure 4.4, with $s_v = 2$ and $n = 4$. Equation 4.4 shows that the overstress function Φ also depends on the stress ratio η. Figure 4.5 illustrates how Φ varies with different stress ratios, assuming $M_g = 1.42$, $s_v = 2$, $V = 5 \times 10^7$ kPa·min, and $n = 4$. It is observed that Φ increases as the stress ratio increases.

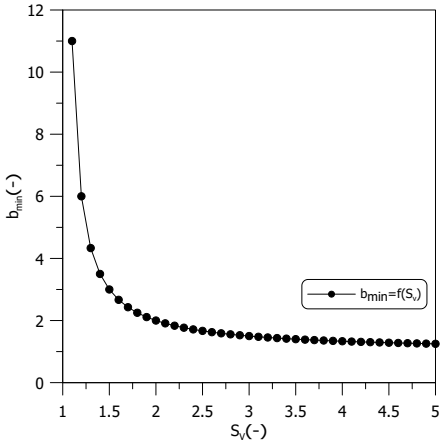

Figure 4.2: Corresponding $b_{\min}$ value for different s_v values

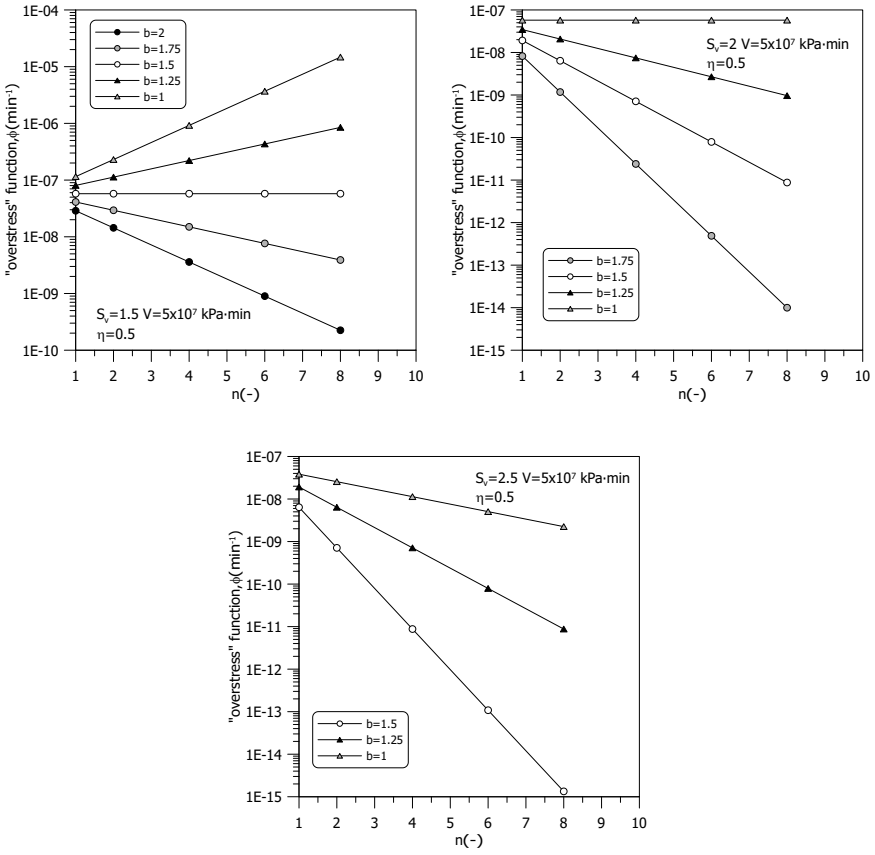

Figure 4.3: Influence of model parameter n on viscoplastic response for different s_v value

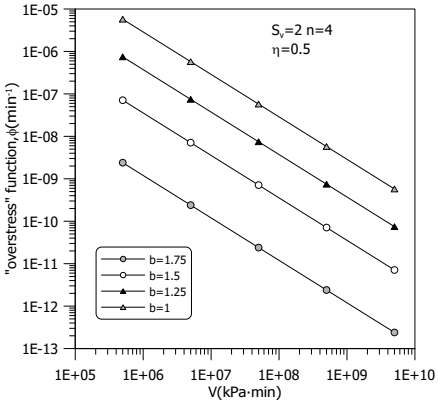

Figure 4.4: Influence of model parameter V on viscoplastic response

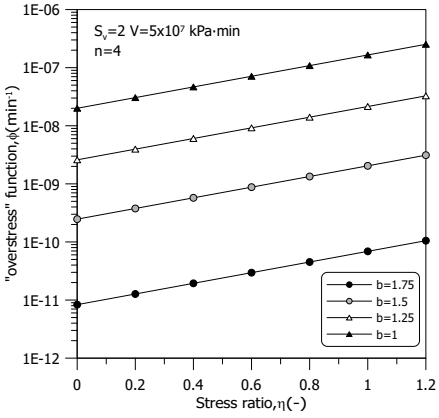

Figure 4.5: Influence of stress ratio η on viscoplastic response

4.3. SENSITIVITY ANALYSIS OF THE MODEL PREDICTION

By incorporating bounding surface and elastoplastic-viscoplastic formulations into JMC-clay, the total number of model parameters increases from 12 to 19. This increase includes four parameters from the bounding surface formulation (h_0, a_d, s_eln, and w) and three from the elastoplastic-viscoplastic formulation (s_v, V, and n). Table 4.1 presents the definition and the reasonable range of these parameters for organic soils. The twelve parameters of the elastoplastic (EP) JMC-clay model are relatively straightforward and can be rather easily calibrated from experimental data. The additional parameters introduced through the bounding surface and elastoplastic-viscoplastic formulations aim to capture varied aspects of rate-dependent and cyclic response. The impact of parameters associated with the bounding surface formulation was preliminarily investigated in Chapter 3. While the impact of parameters s_v, V, and n on the overstress function has been demonstrated in the previous section, their overall contribution to model prediction remains ambiguous. In the following section, a comprehensive sensitivity analysis will be conducted to elucidate the influence of these newly introduced model parameters on the predicted cyclic response.

Table 4.1: Definition and suggested range of model parameters

Parameters	Definition	Reasonable Range
$M_{g,c}$	Ultimate stress ratio in triaxial compression	0.8 – 1.75
$M_{g,e}$	Ultimate stress ratio in triaxial extension	0.6 – 1.2
ν	Poisson's ratio	0.15 – 0.35
c		5 – 200
z_c		1 – 5
z_e	Coefficients of the rotational hardening rule	1 – 5
s		0.5 – 5.0
y		0.5 – 5.0
$M_{f,c}$	Shape coefficients for the yield locus	$0.65M_{g,c}$–$1.0M_{g,c}$
k_f		0.75 – 3
λ^*	Slope of the normal compression line on the $\ln(v) - \ln(p')$	0.05 – 0.2
κ^*	Slope of the unloading-reloading line on the $\ln(v) - \ln(p')$	$0.1\lambda^*$–$0.15\lambda^*$
h_0	Plastic shape hardening parameter	25 – 300
a_d	Damage parameter	-25 – 25
s_{eln}	Size of elastic nucleus	1 – 2.5
w	Hybrid flow rule parameter	0 – 10
s_v	Size of viscoplastic nucleus	> 1 and $\geq s_{eln}$
V	Viscoplastic rate parameter	$5 \times 10^6 - 1 \times 10^8$ kPa·min
n	Viscoplastic slope parameter	1 – 6

4.3.1. COMPRESSION BEHAVIOUR WHEN ACCOUNTING ELASTOPLASTIC-VISCOPLASTIC RESPONSE

In the JMC-clay model (EP and BS), the compression behaviour is characterised by two key parameters: the slope of the normal compression line in the $\ln(v) - \ln(p')$ space, denoted as λ^*, and the slope of the unloading-reloading line in the same space, represented by κ^*. Given that the compression behaviour of soft soils is time-dependent and under the elastoplastic-viscoplastic framework, λ^* actually encapsulates both time-dependent and time-independent responses. Consequently, the selection of λ^* value should consider the time-dependent response of the soil.

In the context of the elastoplastic-viscoplastic framework introduced in this chapter, the predicted compression behaviour is influenced by the parameters s_v, V, and n. Figure 4.6 illustrates the effect of the parameter s_v and the size of the elastic nucleus, s_{eln}, on predicted volumetric response along isotropic compression, with λ^* and κ^* set at 0.1 and 0.011, respectively. For this analysis, the viscoplastic-related parameters used are $V = 5 \times 10^7$ kPa·min and $n = 4$. The isotropic compression spans a time interval of 10,800 minutes. The other model parameters adopted when plotting the results are reported in Table 4.2 and Table 4.3.

It is observed that the apparent slope of the normal compression line varies from 0.1 to 0.13 as s_v decreases from 2.5 to 1.25. The size of the bounding surface at the end of isotropic compression increases, and the apparent pre-consolidation pressure decreases as the value of s_v decreases. Additionally, Figure 4.6 demonstrates that the model predictions are insensitive to values of $s_v \geq 2$ for all the elastic nucleus sizes investigated.

Table 4.2: Model parameters adopted for plotting Figure 4.6 (inherent from JMC-clay (EP))

$M_{g,c}$	$M_{g,e}/M_{g,c}$	ν	c	z_c	z_e	s	y	$M_{f,c}$	k_f
1.42	0.74	0.2	50	1.6	1.2	2.2	2	0.99	1.25

Table 4.3: Model parameters adopted for plotting Figure 4.6 (bounding surface related)

h_0	a_d	s_{eln}	w
50	0	1	0

4.3.2. PARAMETERS SELECTION, STATE VARIABLES INITIALISATION, AND TEST TYPE OF SENSITIVITY ANALYSIS

The subsequent sensitivity analysis will investigate the predicted responses of the soil to cyclic loading, focusing on the aspects previously discussed in Chapter 3, including cyclic volumetric and deviatoric responses. As demonstrated by the experimental data in Chapter 3, the soil behaviour under cyclic loading is very dependent on the pre-cyclic shearing stress state and loading amplitude. To thoroughly assess this, the analysis will encompass both isotropic and anisotropic initial stress states. Additionally, simulations of different loading amplitudes will be discussed.

Considering the more apparent influence of the bounding surface parameters h_0 and s_{eln}, which has already been investigated in Chapter 3, along with the impact of OCR, a_d,

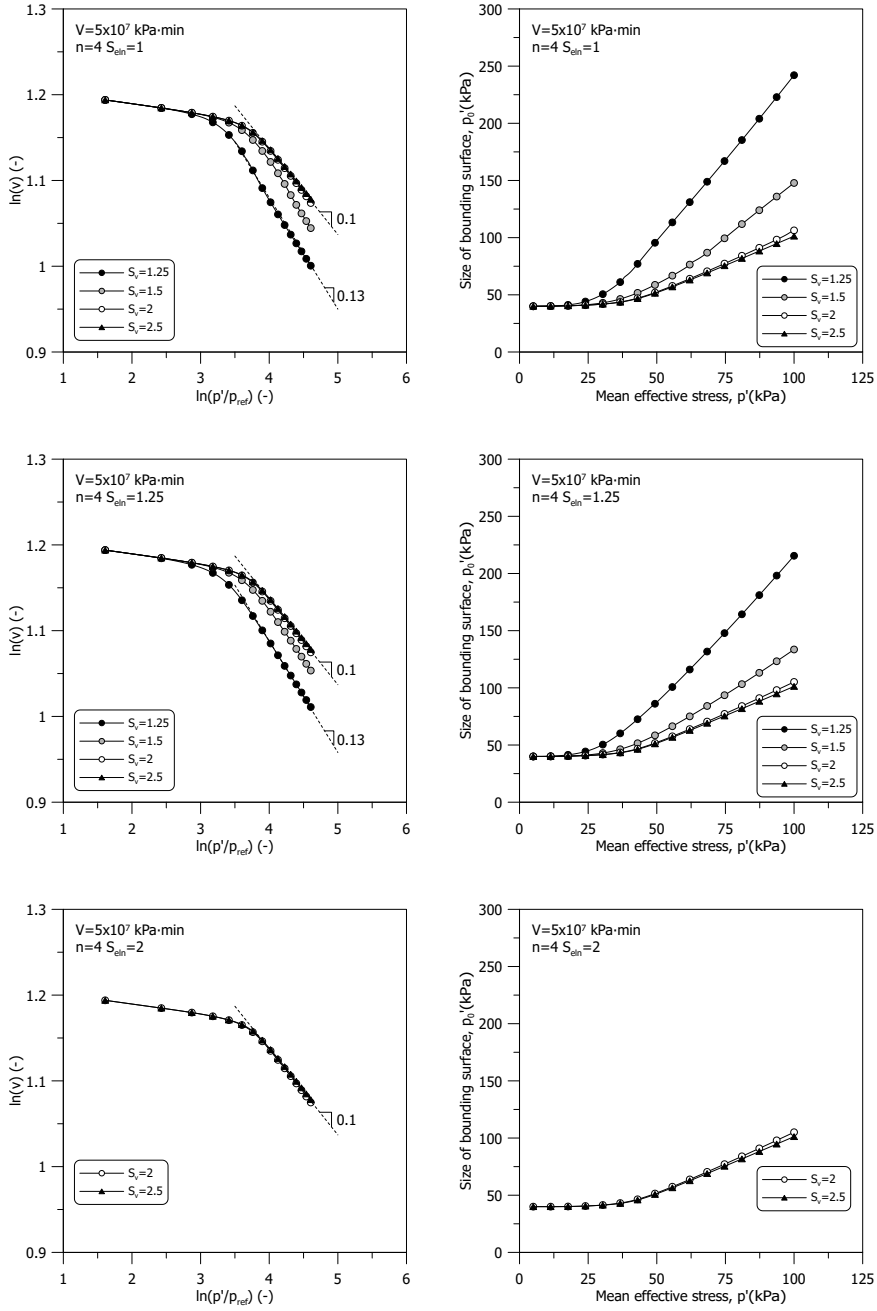

Figure 4.6: Influence of parameter s_v on predicted isotropic compression behaviour for different elastic nucleus size

and w on cyclic response, this section will concentrate on viscoplastic related parameters s_ν, V, and n. Additionally, their interaction with the bounding surface parameters a_d and w will be investigated.

As previously mentioned, the predicted compression behaviour is influenced by the viscoplastic parameters s_ν, V, and n. Consequently, to derive a unique compression curve on the $\ln(v) - \ln(p')$ plane, it is necessary to select specific values for λ^* and the initial bounding surface size, $p'_{0,i}$, based on the selected viscoplastic parameters. Figure 4.7(a) demonstrates that a unique isotropic compression curve can be obtained for varying s_ν values with appropriately chosen λ^* and $p'_{0,i}$. The consolidation stage spans a time interval of 10,800 minutes, and the other two viscoplastic parameters adopted are: $V = 5 \times 10^7$ kPa·min and $n = 4$. Here, λ^* is adjusted from 0.1 to 0.078 as s_ν changes from 2.5 to 1.25, while $p'_{0,i}$ increases from 40 kPa to 70 kPa for the same range of s_ν values. The same procedure applied to isotropic consolidation is also performed for K_0 consolidation, with the results presented in Figure 4.7(b). In the case of K_0 compression, λ^* is adjusted from 0.1 to 0.078 as the s_ν value decreases from 2.5 to 1.25. Similarly, $p'_{0,i}$ increases from 40 kPa to 77 kPa across this range of s_ν values. Therefore, the values for λ^* and the initial bounding surface size, $p'_{0,i}$, are selected based on the viscoplastic parameters to be used in the forthcoming sensitivity analysis. The other model parameters adopted for sensitivity analysis are listed in Table 4.4 and Table 4.5.

The cyclic triaxial test is selected for the sensitivity analysis. The simulation initiates from an isotropic stress state, with a mean effective stress (p') of 5 kPa and an initial inclination of the bounding surface ($\alpha_{0,i}$) set to $\alpha_{K_0} = 0.5$. During the consolidation stage, the process is either isotropic or follows a K_0 condition, escalating the mean effective stress before the cyclic stage (p'_i) up to 100 kPa. Following the consolidation stage, the simulation proceeds to a cyclic stage, which is controlled by either stress or strain, and includes up to 10 cycles. This cyclic loading follows a triangular wave pattern with a frequency of 0.1 Hz.

In the strain-controlled simulation, a cyclic strain amplitude, ε_{cyc}, of 0.01 is applied. For the stress-controlled simulations, two distinct stress amplitudes, q_{cyc}, are used: $0.15p'_i$ and $0.30p'_i$.

Table 4.4: Model parameters adopted for sensitivity analysis (inherent from JMC-clay (EP))

$M_{g,c}$	$M_{g,e}/M_{g,c}$	ν	c	z_c	z_e	s	y	$M_{f,c}$	k_f
1.42	0.74	0.2	50	1.6	1.2	2.2	2	0.99	1.25

Table 4.5: Model parameters adopted for sensitivity analysis (bounding surface related)

h_0	s_{eln}
50	1

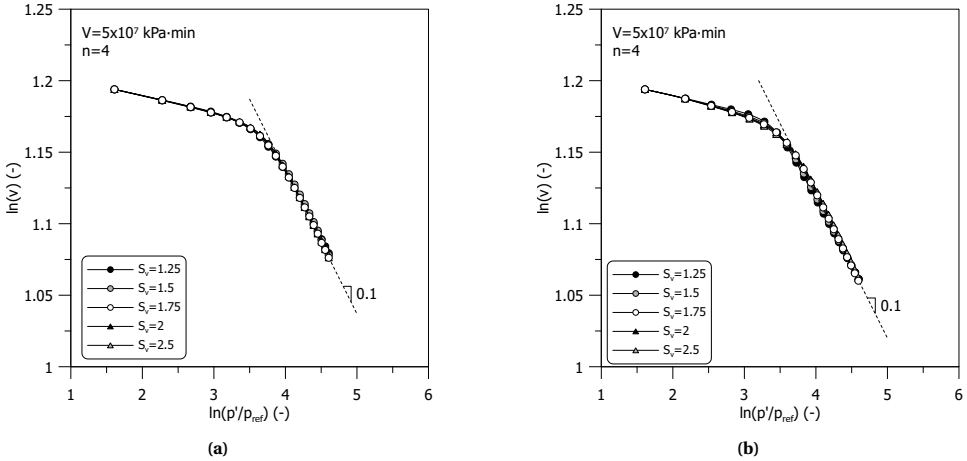

Figure 4.7: (a) Isotropic (b) 1D compression curves obtained for different s_v with selected λ^* and $p'_{0,i}$

4.3.3. SUMMARY OF SENSITIVITY ANALYSIS

To facilitate a comprehensive understanding, the detailed sensitivity analysis of the model parameters is thoroughly presented in Appendix C. The following section will discuss selected simulation results, with a primary focus on two critical aspects of cyclic response. These include the volumetric response, which covers the evolution of the stress path and the development of pore pressure, and the deviatoric response, comprising the stress-strain curve, shear stiffness, damping ratio, and permanent deformation. Additionally, the discussion will delve into the effects of the initial stress state prior to cyclic loading and the influence of cyclic amplitude on the model's predictions.

According to the sensitivity analysis, the volumetric response to cyclic shearing is influenced by nearly all the examined model parameters, except for the damage parameter, a_d. Among the viscoplastic parameters — s_v, V, and n — s_v emerges as the most significant. It alters the size of the viscoplastic zone within the bounding surface, significantly affecting both the initial size of this surface at the end of the consolidation stage and its rate of change under cyclic loading. Decreasing the s_v value leads to an increase in the bounding surface size at the consolidation stage within the same time frame. Consequently, as illustrated in Figure 4.8, the stress path evolution shifts from contractive to dilative behaviour. Simultaneously, excess pore pressure is transitioned from positive to negative.

Kaliakin (1991) noted that parameters V and n influence the viscoplastic response by altering the evolution rate and initial slope of the overstress function. While reducing V has a similar effect to decreasing s_v, the predicted response to changes in V is more log-linear, as depicted in Figure 4.9. The effect of n, though somewhat analogous to s_v and V, is more complex. Its specific impact depends on the selected s_v value and the stress path's nature during the consolidation stage. As an exponent in the 'normalised overstress', $\Delta\hat{\sigma}$, its influence on the overstress function, Φ, varies. It can be positive, neutral, or negative when the n value exceeds 1. This variability affects the evolution

rate of the overstress function and, consequently, the model prediction. As shown in Figure 4.10(a) for $s_v = 1.5$, increasing n reduces contractive behaviour and excess pore pressure development in initially isotropic consolidated states. Conversely, it enhances these responses in initially K_0 consolidated states, as indicated in Figure 4.10(b). Given that the influence of n is akin to that of s_v and V, a default value of 1 for n could simplify model calibration, unless specific experimental data suggest otherwise.

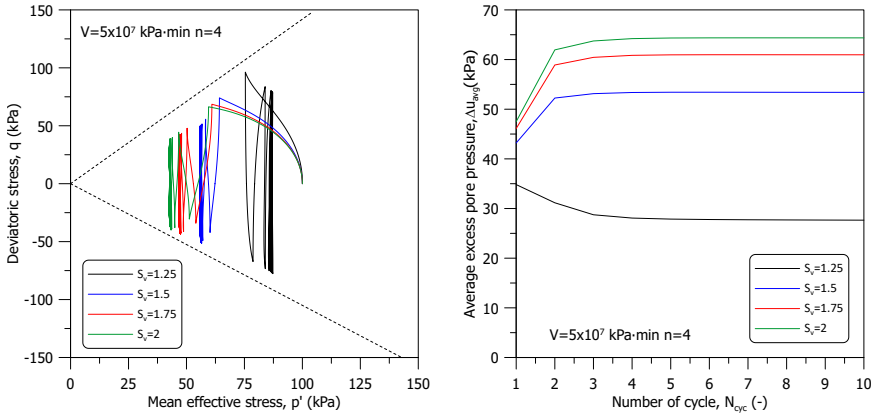

Figure 4.8: Stress path and development of excess pore pressure of strain-controlled cyclic shearing stage for different s_v value

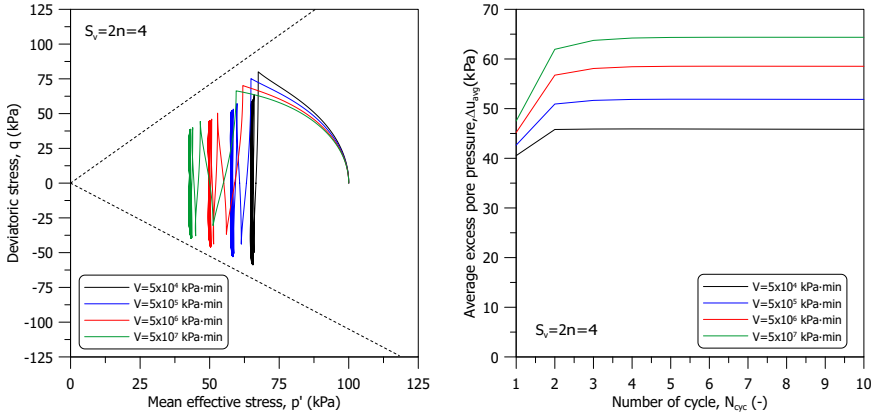

Figure 4.9: Stress path and development of excess pore pressure of strain-controlled cyclic shearing stage for different V value

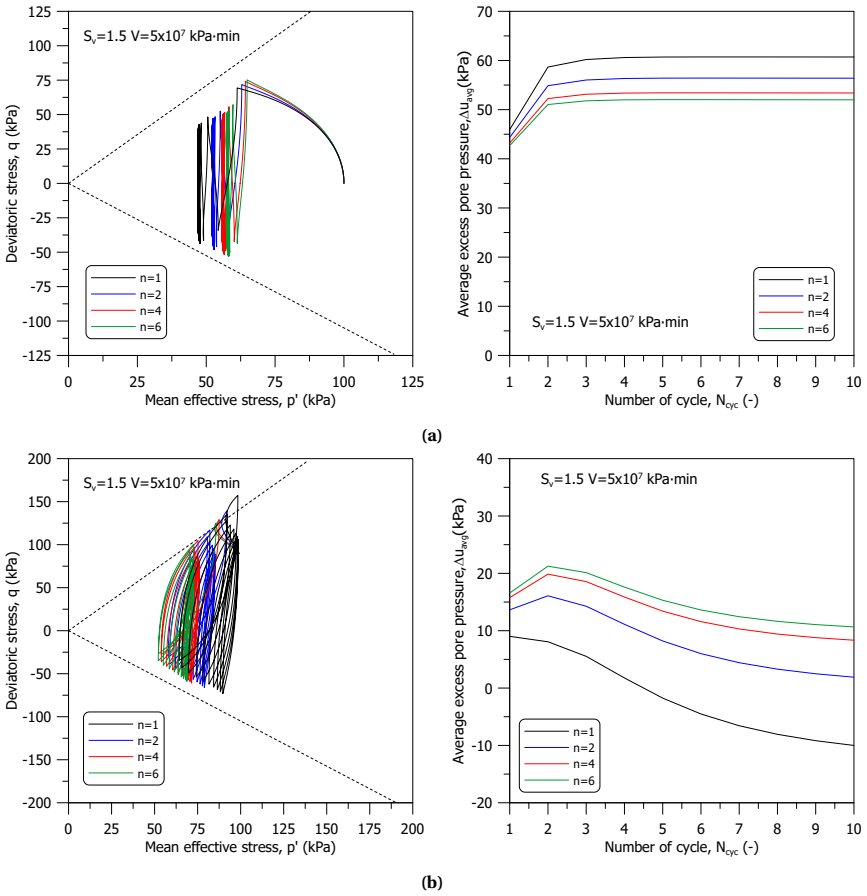

Figure 4.10: Stress path and development of excess pore pressure of strain-controlled cyclic shearing stage for different n value (a) initially isotropic consolidated (b) initially K_0 consolidated

The proposed model includes the hybrid flow rule parameter, w, to specifically address the early stabilisation or 'freezing' observed in both stress paths and excess pore pressure development. The influence of w on the volumetric response is straightforward and illustrated in Figure 4.11: as w increases, the model predicts a more contractive response and greater development of positive excess pore pressure when the current stress state lies on the wet side of the critical state.

When it comes to the sensitivity analysis of the deviatoric response, all investigated parameters significantly influence model predictions. A decrease in s_v values, lower values of λ^* adopted, and the larger bounding surface size results in higher peak/trough deviatoric stress and secant shear modulus under strain-controlled conditions and a reduction in permanent deviatoric strain $\varepsilon_{q,\text{per}}$ under stress-controlled conditions, as illustrated in Figure 4.12 and Figure 4.13. Similarly, reducing V values leads to analogous effects, as depicted in Figure 4.14 and Figure 4.15.

The effect of n on the deviatoric response is similar to that of s_v and V. However, its specific impact is contingent on the chosen s_v value and the nature of the stress path during the consolidation stage, as previously discussed. For instance, with s_v set at 1.5 and in simulations of initially isotropic consolidated conditions, an increase in n value intensifies peak/trough deviatoric stress and secant shear modulus under strain-controlled scenarios and diminishes permanent deviatoric strain $\varepsilon_{q,\text{per}}$ under stress-controlled conditions, as shown in Figure 4.16 and Figure 4.17.

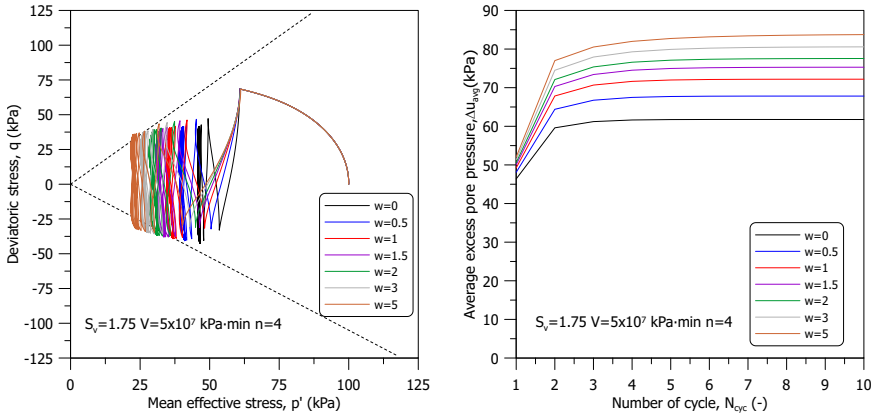

Figure 4.11: Stress path and development of excess pore pressure of strain-controlled cyclic shearing stage for different w value

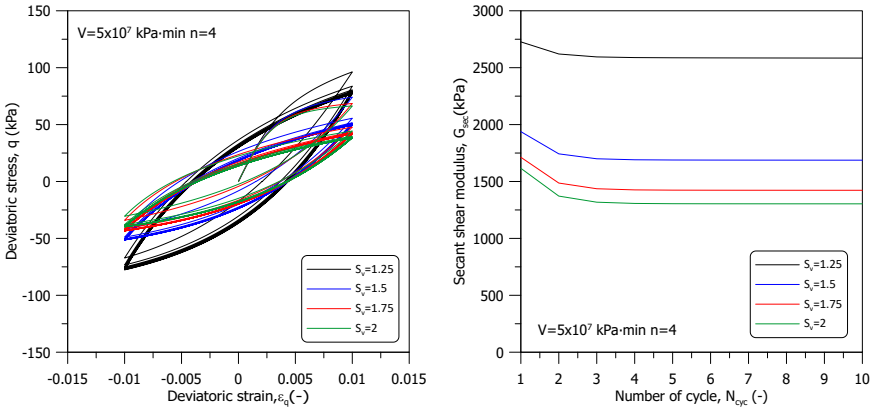

Figure 4.12: Stress-strain curve and secant shear modulus of strain-controlled cyclic shearing stage for different s_v value

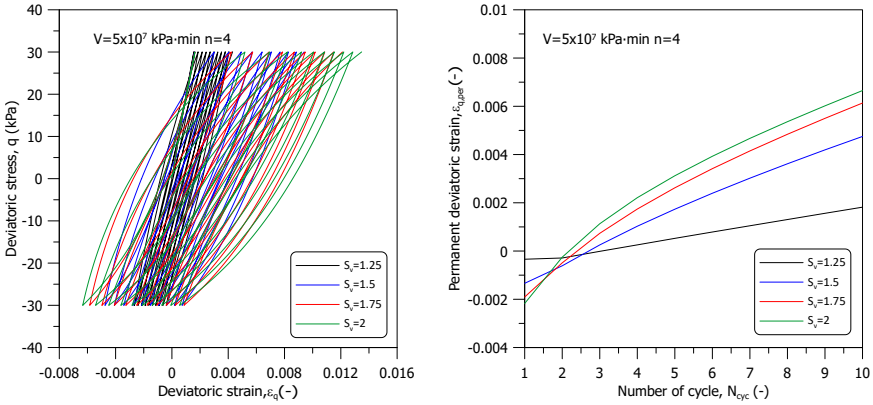

Figure 4.13: Stress-strain curve and permanent deviatoric strain of stress-controlled cyclic shearing stage for different s_v value ($q_{cyc} = 0.30p'_i$)

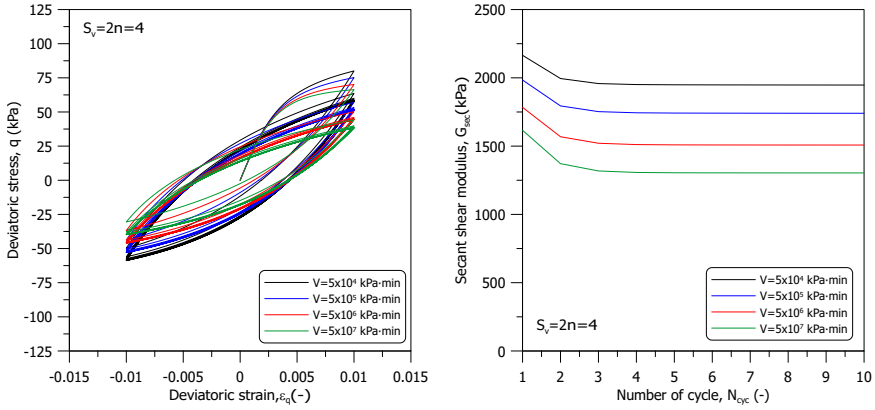

Figure 4.14: Stress-strain curve and secant shear modulus of strain-controlled cyclic shearing stage for different V value

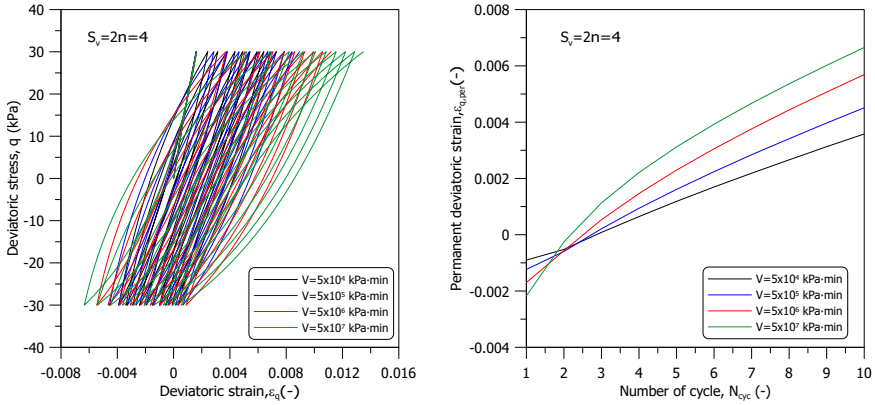

Figure 4.15: Stress-strain curve and permanent deviatoric strain of stress-controlled cyclic shearing stage for different V value ($q_{\text{cyc}} = 0.30p'_i$)

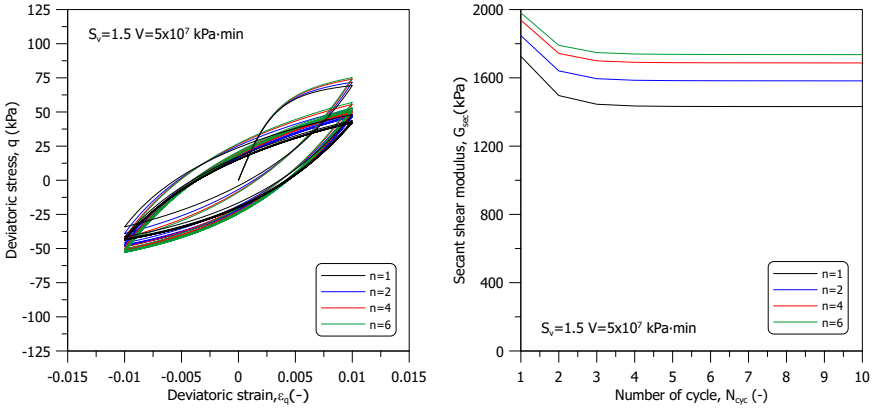

Figure 4.16: Stress-strain curve and secant shear modulus of strain-controlled cyclic shearing stage for different n value

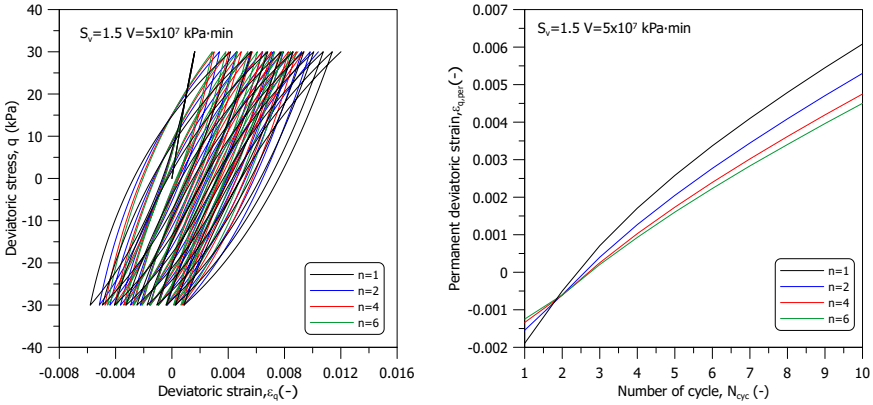

Figure 4.17: Stress-strain curve and permanent deviatoric strain of stress-controlled cyclic shearing stage for different n value ($q_{cyc} = 0.30p'_i$)

As indicated in Chapter 3, the hybrid flow rule parameter w also alters cyclic deviatoric responses. For example, as stiffness is dependent on mean effective stress, higher w values lead to a more rapid reduction in mean effective stress. This, in turn, results in a quicker decrease in shear stiffness, as evidenced by lower peak deviatoric stress and secant shear modulus observed after the first loading cycle, as shown in Figure 4.18. Additionally, as depicted in Figure 4.19, w influences the development of permanent deviatoric strain. This is due to the variation in deviatoric plastic strain increment that occurs when implementing the hybrid flow rule, allowing the image stress to evolve towards the dry side of the critical state and consequently reducing the deviatoric plastic strain increment.

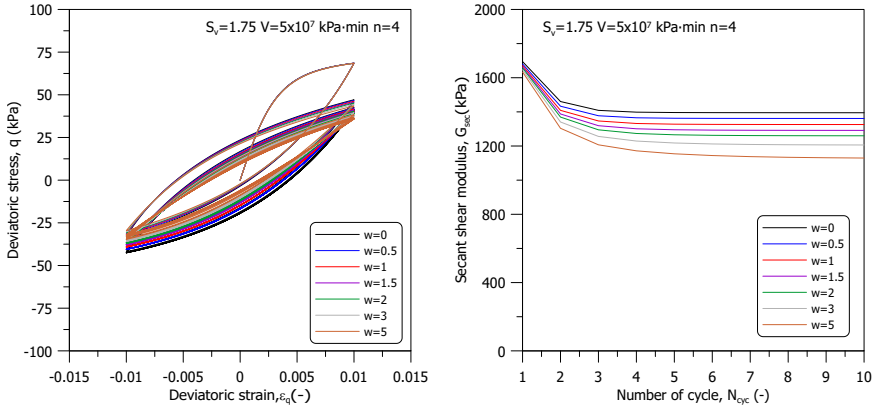

Figure 4.18: Stress-strain curve and secant shear modulus of strain-controlled cyclic shearing stage for different w value

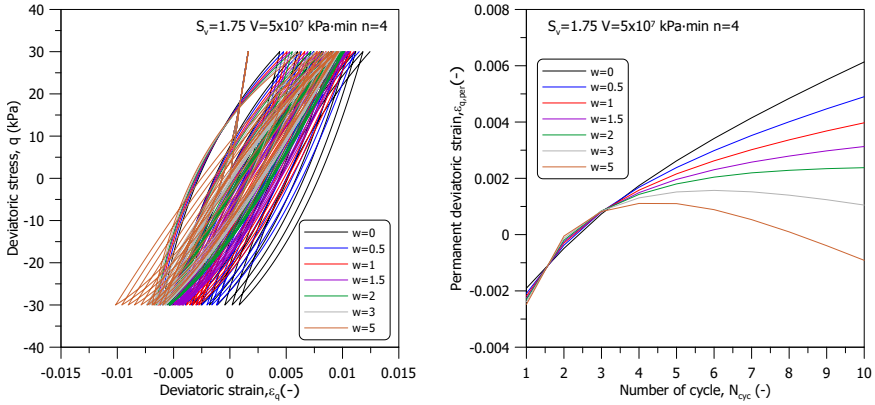

Figure 4.19: Stress-strain curve and permanent deviatoric strain of stress-controlled cyclic shearing stage for different w value ($q_{\text{cyc}} = 0.30\,p'_i$)

In summary, the parameter a_d significantly influences the deviatoric aspects of the cyclic response, including peak deviatoric stress, secant shear modulus, and permanent deviatoric strain, as shown in Figure 4.20 and Figure 4.21. An increase in positive a_d value enhances the reduction in peak deviatoric stress and secant shear modulus with each loading cycle, as evidenced in Figure 4.20. Simultaneously, a higher positive a_d value accelerates the development of permanent deviatoric strain, depicted in Figure 4.21. However, a substantial positive a_d value ($a_d \geq 50$) can also significantly reduce the plastic modulus during cyclic loading. This reduction might intensify rotational hardening, leading to quicker changes in the inclination of the bounding surface during cyclic shearing. Such alterations can affect the stress path evolution and excess pore pressure development, as shown in Figure 4.22. Thus, while a positive a_d value directly affects deviatoric responses, its broader influence encompasses the entire cyclic behaviour of the soil. When introducing positive a_d values to match cyclic degradation observed in experimental data, it is crucial to ensure realistic predictions across all aspects of the cyclic response.

Conversely, a negative a_d value leads to an increase in peak deviatoric stress and secant shear modulus with each loading cycle, as illustrated in Figure 4.23. However, when the a_d value falls below -25, there is a significant rise in the plastic modulus during cyclic loading, affecting other cyclic response aspects. For instance, with a_d at -25 and -50, the model predicts a viscoelastic response and an increase in the damping ratio after several loading cycles, as depicted in Figure 4.23. Additionally, decreasing the negative a_d value reduces the development of permanent deviatoric strain, as shown in Figure 4.24. Therefore, while incorporating negative a_d values to reflect cyclic shakedown seen in experimental data, it is essential to ensure that the model also provides realistic predictions in other cyclic response aspects.

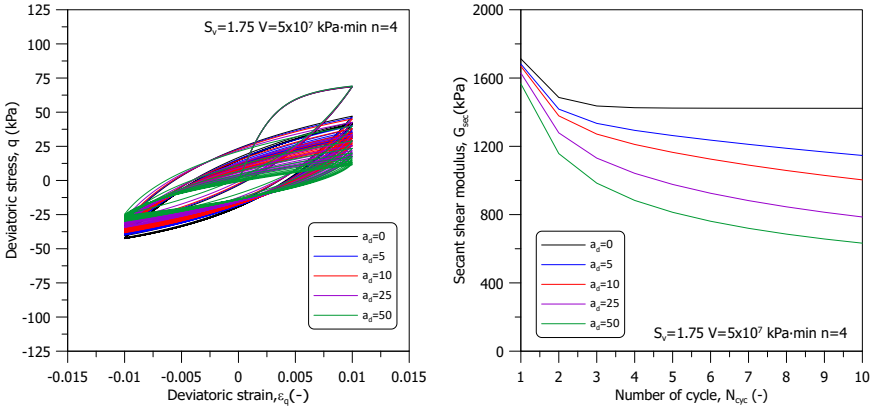

Figure 4.20: Stress-strain curve and secant shear modulus of strain-controlled cyclic shearing stage for different positive a_d value

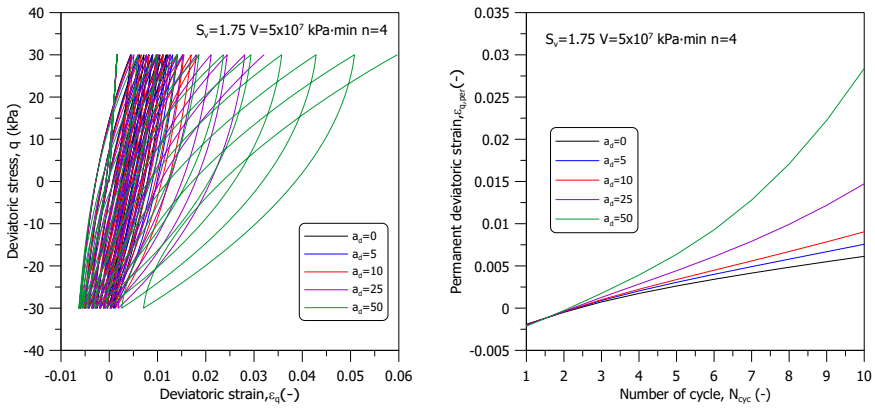

Figure 4.21: Stress-strain curve and permanent deviatoric strain of stress-controlled cyclic shearing stage for different positive a_d value ($q_{cyc} = 0.30p_i'$)

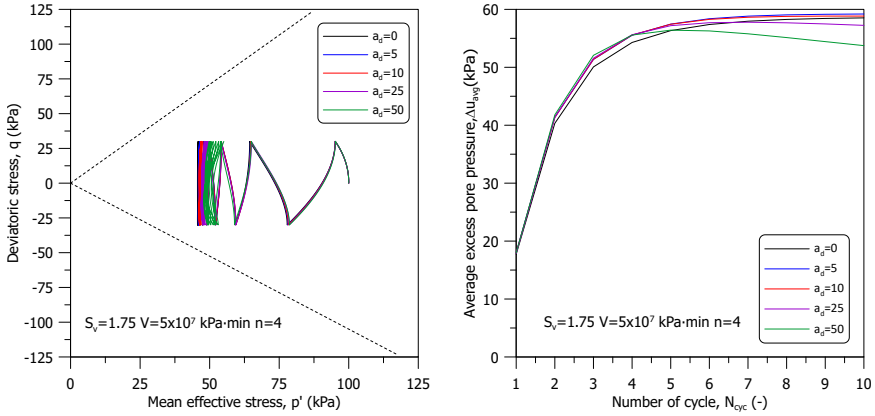

Figure 4.22: Stress path and development of excess pore pressure of strain-controlled cyclic shearing stage for different positive a_d value

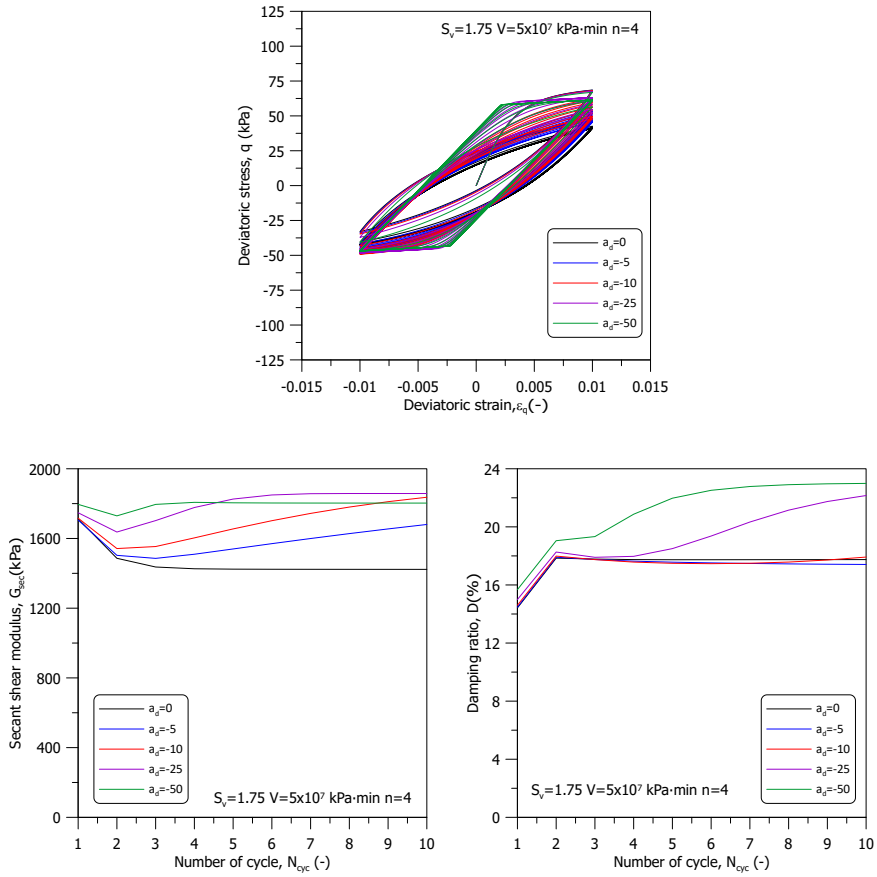

Figure 4.23: Stress-strain curve, secant shear modulus, and damping ratio of strain-controlled cyclic shearing stage for different negative a_d value

Interestingly, as shown in Figure 4.25(a), the damping ratio upon cyclic loading appears to be only affected by the hybrid flow rule parameter, w. This dependence arises because an increase in w not only reduces the contribution of the plastic volumetric increment at the image stress state but also slows the increase in image stress weighting for similarity ratios lower than 1.5 (equivalent to $1/b \approx 0.7$, as shown in Figure 4.25(b)). This leads to a lower plastic modulus and a slower variation in predicted shear stiffness, thereby reducing the area in the hysteresis loop and resulting in a lower damping ratio.

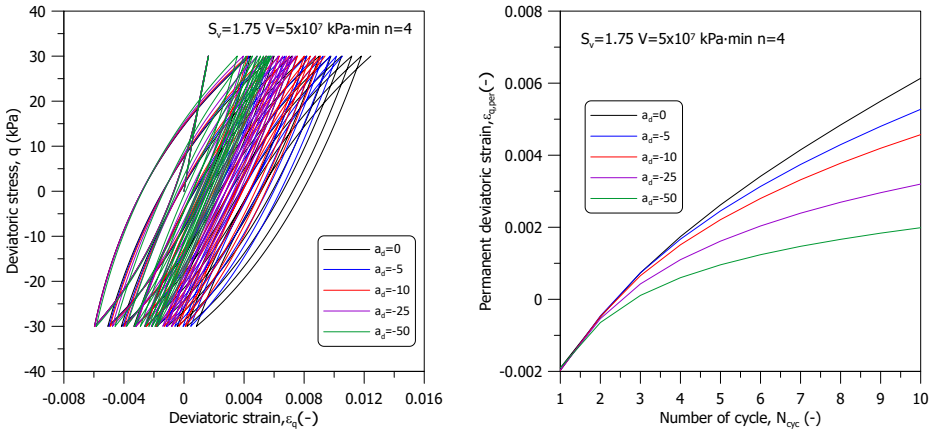

Figure 4.24: Stress-strain curve and permanent deviatoric strain of stress-controlled cyclic shearing stage for different negative a_d value ($q_{\text{cyc}} = 0.30p'_i$)

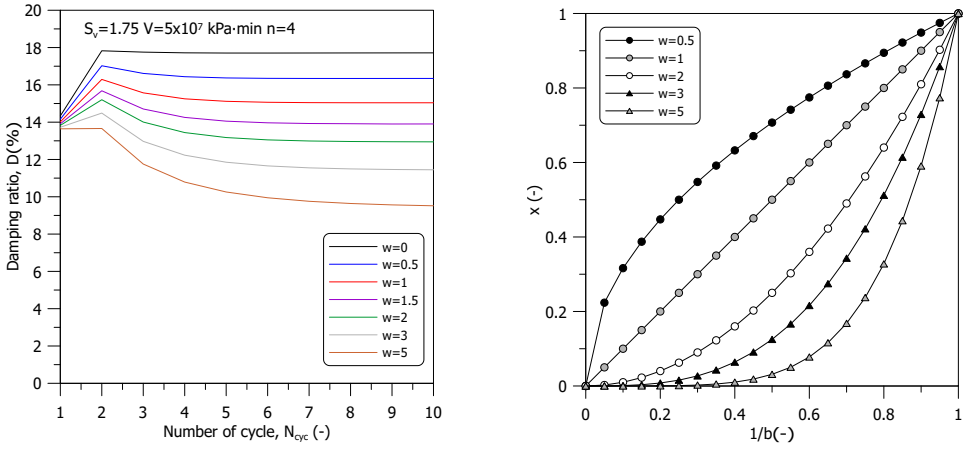

Figure 4.25: (a) Damping ratio of strain-controlled cyclic shearing stage for different w value (b) Variation of image stress weighting x with different hybrid flow rule parameter w and similarity ratio b

Besides the model parameters, cyclic amplitude also influences the predicted response. Generally, higher amplitudes result in greater excess pore pressure development, as well as increased cyclic and permanent deviatoric strain, as demonstrated in Figure 4.26, which shows simulations conducted without the hybrid flow rule activated ($w = 0$). Additionally, the impact of the initial stress state is depicted in Figure 4.27, also under conditions with the hybrid flow rule deactivated. These simulations reveal that starting from an isotropic stress state leads to higher excess pore pressure but lower cyclic and permanent deviatoric strain compared to a K_0 stress state. Concerning shear modulus, simulations originating from a K_0 stress state exhibit higher shear stiffness and a marginally quicker reduction in stiffness as the number of loading cycles increases. Regarding the damping ratio, the response from an isotropic stress state remains stable after the initial cycle, whereas it gradually increases with more loading cycles in a K_0 stress state.

These predicted responses to different cyclic amplitudes and initial stress states are in good agreement with the experimental observations presented in Chapter 3. Beyond these factors, other crucial elements affect model predictions, including the evolution of anisotropy (rotational hardening), updates to the projection centre, and the Lode angle dependency of the critical state stress ratio.

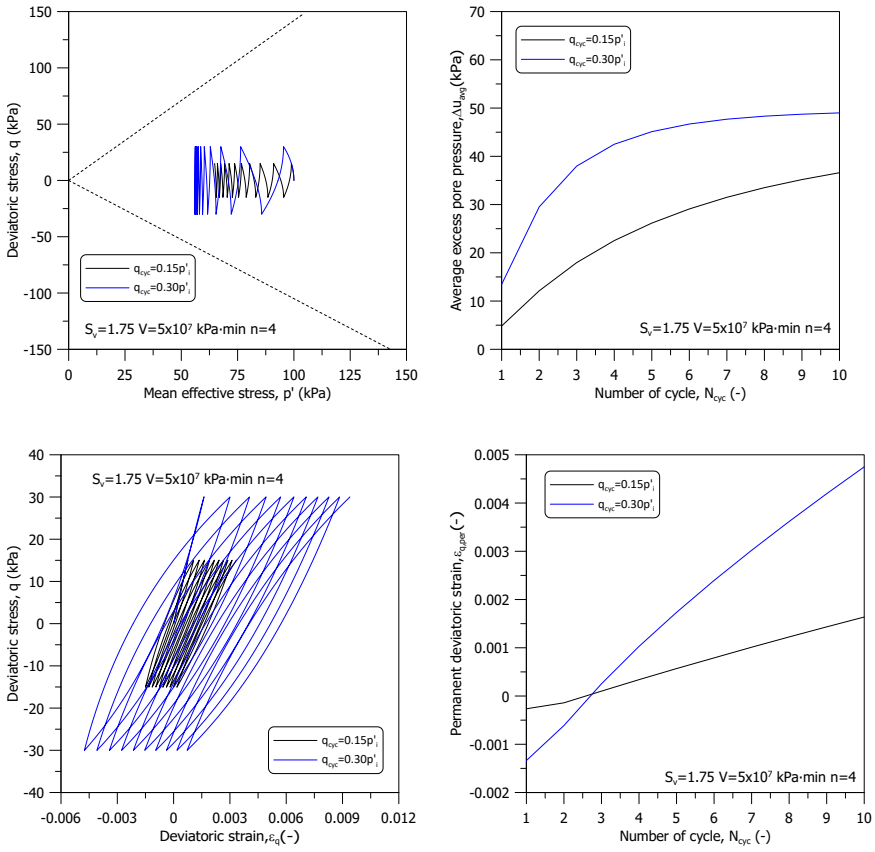

Figure 4.26: Influence of cyclic amplitude, q_{cyc} on stress path, development of excess pore pressure, stress-strain curve, and permanent deviatoric strain

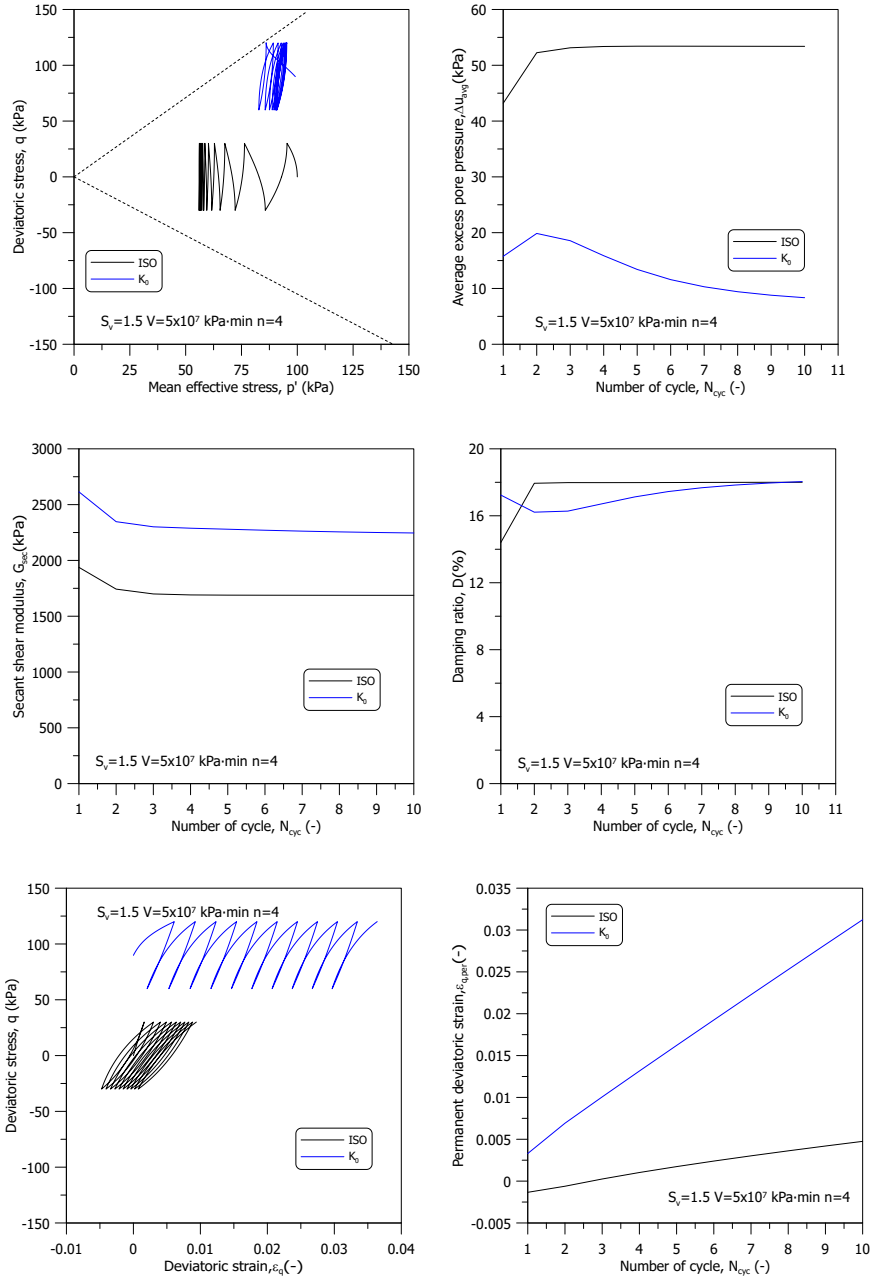

Figure 4.27: Influence of initial stress state on stress path, development of excess pore pressure, secant shear modulus, damping ratio, stress-strain curve, and permanent deviatoric strain

4.4. NUMERICAL CALIBRATION, PREDICTIONS AND VALIDATION

4.4.1. MODEL CALIBRATION

The elastoplastic-viscoplastic coupling framework shows strain-rate 'saturation' when predicting strain-rate effects (Kaliakin and Dafalias, 1990a; Kaliakin and Dafalias, 1990b). Essentially, this means that under sufficiently rapid loading conditions, the model predicts a rate-independent response. This is illustrated in Figure 4.28, where the predicted undrained triaxial compression response aligns with the predictions of a rate-independent model when the axial strain rate exceeds 0.1%, given the set of model parameters used. Owing to the coupling between elastoplasticity and viscoplasticity in the model, a rate-independent response is predicted when the strain rate surpasses a certain 'saturation' threshold. Beyond this saturation value, elastoplasticity becomes the dominant mechanism for predicting material response. Consequently, the model parameters should be calibrated using the fastest experimental data available.

Incorporating bounding surface and elastoplastic-viscoplastic formulations into the JMC-clay model results in a total of 19 parameters. These include 12 parameters from the JMC-clay (EP), four from the bounding surface formulation (h_0, a_d, s_{eln}, and w), and three from the elastoplastic-viscoplastic formulation (s_v, V, and n). The 12 JMC-clay (EP) parameters are mostly rate-insensitive, allowing them to be calibrated using static laboratory tests as described in Chapter 2. For drained tests, the loading rate typically ranges between 0.007 and 0.01 kPa/min to prevent the development of excess pore pressure. For undrained tests, the strain rate is usually set between 0.012 and 0.015 %/min. The slopes of the normal compression line and the unloading-reloading line in $\ln(v) - \ln(p')$ space are defined from these static tests as $\lambda^*_{\text{static}}$ and κ^*_{static}, respectively. The calibration process for the JMC-clay (EP) parameters using static tests is outlined as follows:

- κ^*_{static}, $\lambda^*_{\text{static}}$, and c are calibrated on isotropic compression tests with axial strain and volumetric strain measurements to assess the evolution of the deviatoric plastic strain component (i.e., anisotropic response). κ^*_{static} and $\lambda^*_{\text{static}}$ are defined in the $\ln(v) - \ln(p')$ space.
- ν is estimated from a K_0 unloading path.
- $M_{g,c}$ and $M_{g,e}$ are determined from triaxial compression and extension tests.
- z_c, z_e, s, and y are defined by fitting equation 2.8 in Chapter 2 on at least three triaxial tests: K_0 compression and two radial paths, one in compression and one in extension; if no data is available on the extension side, z_e can be obtained assuming $z_e/z_c = M_{g,e}/M_{g,c}$.
- $M_{f,c}$ and k_f are determined from yielding points along drained stress probe paths; $M_{f,e}$ is obtained assuming $M_{f,e}/M_{f,c} = M_{g,e}/M_{g,c}$.

To calibrate the remaining seven model parameters – four from the bounding surface formulation (h_0, a_d, s_{eln}, and w) and three from the elastoplastic-viscoplastic formulation (s_v, V, and n) – data from the fastest cyclic triaxial tests are needed. These tests should ideally include one initially isotropic and one initially K_0 consolidated sample.

Reflecting on the sensitivity analysis discussed in the previous section and drawing upon literature that utilises the elastoplastic-viscoplastic coupling framework, default values for several parameters are proposed to facilitate the calibration process. These default values are described below:

- V is set within the typical range of 5×10^6 - 5×10^8 kPa·min, by default, a value of 5×10^7 kPa·min can be adopted.
- The default setting for n is 1.
- Initially, set s_v to 1.5. λ^* and κ^* should be set to $0.85\lambda^*_{\text{static}}$ and $1/9\lambda^*$, respectively. These parameters can then be adjusted to best fit the evolution of the stress path and stress-strain curve during cyclic shearing.
- Set s_{eln} equal to s_v by default. It can be adjusted for the best fit to the stress path and stress-strain curve evolution observed in both initially isotropic and K_0 consolidated cyclic triaxial tests.
- Initial size of the bounding surface, $p'_{0,i}$ and plastic shape parameter,h_0: Set h_0 to 50 by default and select values that best fit the static compression curves.
- Set a_d to zero by default and adjust a_d to best match the secant shear modulus reduction or the development of permanent deviatoric strain with the number of loading cycles.
- Set w to one by default and adjust it for the best fit to the stress path and excess pore pressure development in both initially isotropic and K_0 consolidated cyclic triaxial tests.

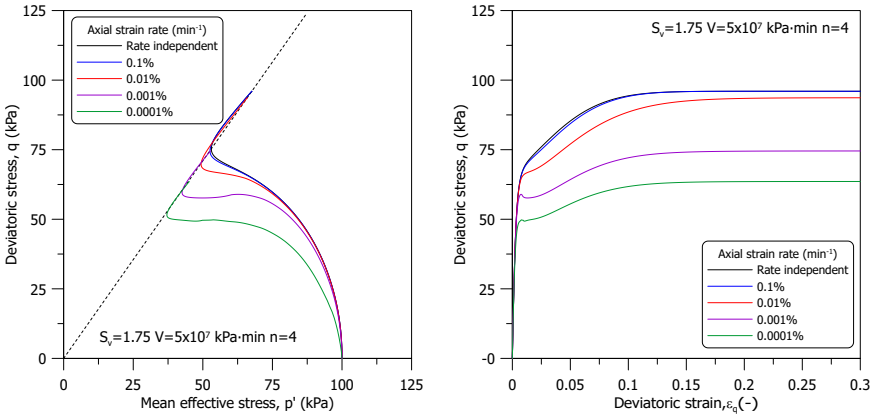

Figure 4.28: Effect of rate of strain on predicted undrained triaxial compression test

To effectively calibrate the 19 model parameters, a minimum of six distinct tests are required, as summarised in Table 4.6:

- K_0 loading-unloading: active K_0 consolidation achieved by back volume or direct radial strain measurement.
- Isotropic loading-unloading: isotropic compression test with axial strain and volumetric strain measurements.
- Drained stress probe paths (two tests): one in compression and one in extension, the samples are brought to failure with undrained triaxial compression (TxCU) or undrained triaxial extension (TxEU) after the stress probe path.
- Cyclic triaxial tests (two tests): including one test with an initially isotropic consolidated sample and another with an initially K_0 consolidated sample.

Furthermore, Table 4.6 also summarises the default values for the model parameters. These defaults can facilitate the calibration process or be used when experimental data is unavailable.

Table 4.6: Test type required to calibrate model parameters and default values for model parameters

Parameters	Test Type	Default Value
$M_{g,c}$	Undrained triaxial compression (TxCU)	-
$M_{g,e}$	Undrained triaxial extension (TxEU)	-
ν	K_0 loading-unloading	-
c		-
z_c	Isotropic compression test	-
z_e		$z_e/z_c = M_{g,e}/M_{g,c}$
s	K_0 compression and two stress probe paths	-
y		2.0
$M_{f,c}$	Drained stress probe paths (two tests)	-
k_f	TxCU and TxEU after drained stress probe path	-
λ^*	Isotropic compression test	$0.85\lambda^*_{\text{static}}$
κ^*	Isotropic compression test	$1/9\lambda^*$
h_0	Isotropic compression test	50
a_d	Cyclic triaxial tests	0
s_{eln}	Cyclic triaxial tests	equals to s_ν
w	Cyclic triaxial tests	1
s_ν	Cyclic triaxial tests	1.5
V	Cyclic triaxial tests	5×10^7 kPa·min
n	Cyclic triaxial tests	1

The following section demonstrates the calibration procedure using samples from the group (IX). Chapter 2 has already detailed the calibration process for the 12 JMC-clay (EP) model parameters, and the calibrated JMC-clay (EP) model parameters are presented in Table 4.7. The focus here will be specifically on calibrating the additional parameters from the bounding surface formulation (h_0, a_d, s_{eln}, and w) and the elastoplastic-viscoplastic formulation (s_v, V, and n). As presented in Chapter 3, the fastest cyclic tests in this group are the strain-controlled cyclic test at a loading rate of 0.001 Hz, starting from isotropic stress state (Cyc T1(IX)) and K_0 stress state (Cyc T2(IX)).

Table 4.7: Calibrated JMC-clay (EP) model parameters for the group (IX)

$M_{g,c}$	$M_{g,e}/M_{g,c}$	ν	c	z_c	z_e	s	y	$M_{f,c}$	k_f
1.42	0.74	0.2	50	1.6	1.2	2.2	2	0.99	1.25

4

PARAMETER s_v, V, AND n

The calibration process for parameters s_v, V, and n aims to optimally fit the evolution of the stress path and stress-strain curve during the first ten cycles of cyclic shearing. The previously suggested default values are adopted as starting points: s_v at 1.5, V at 5×10^7 kPa·min, and n at 1. Additionally, the initial trial uses s_{eln} at 1.5, h_0 at 50, a_d at 0, w at 1, λ^* at $0.85\lambda^*_{\text{static}}$, and κ^* at $1/9\lambda^*$. The simulation results, compared with the experimental data from Cyc T1(IX) and Cyc T2(IX), are presented in Figure 4.29. While the model accurately captures the first cycle of the test starting from the isotropic stress state, it significantly overestimates the deviatoric stress in the test beginning from the K_0 stress state, particularly on the extension side. Notably, the model predicts an elastic response upon stress reversal, which is not observed in the experiments.

Based on these observations, the second trial of simulations adjusts s_v to 1.75 and s_{eln} to 1, while keeping the other parameters constant. Figure 4.30 shows the updated model predictions alongside laboratory data. Although the response upon stress reversal is better captured, the model still overpredicts the deviatoric stress on the extension side for the test starting from a K_0 stress state. In the third trial, the parameter V is increased to 5×10^8 kPa·min, with the rest of the parameters remaining unchanged. This adjustment, as shown in Figure 4.31, reasonably mitigates the overprediction of deviatoric stress for the initially K_0 consolidated test. Further improvements can be expected with subsequent calibration of the damage parameter, a_d.

PARAMETER h_0

The calibration of parameter h_0 was conducted using the experimental results from the isotropic and K_0 consolidation stages of tests Cyc T1(IX) and Cyc T2(IX), respectively. The model predictions with h_0 set to 50 showed a reasonable match with the K_0 consolidation results, as illustrated in Figure 4.32. However, for isotropic consolidation, even a reduced h_0 value of 25 resulted in a stiffer response than what was observed experimentally. Given the close agreement between the model prediction and test Cyc T2(IX), the discrepancy in the isotropic consolidation response of sample Cyc T1(IX) could be due to sample disturbance. Therefore, h_0 is calibrated at a value of 50 to better represent the behaviour observed in the majority of the tests.

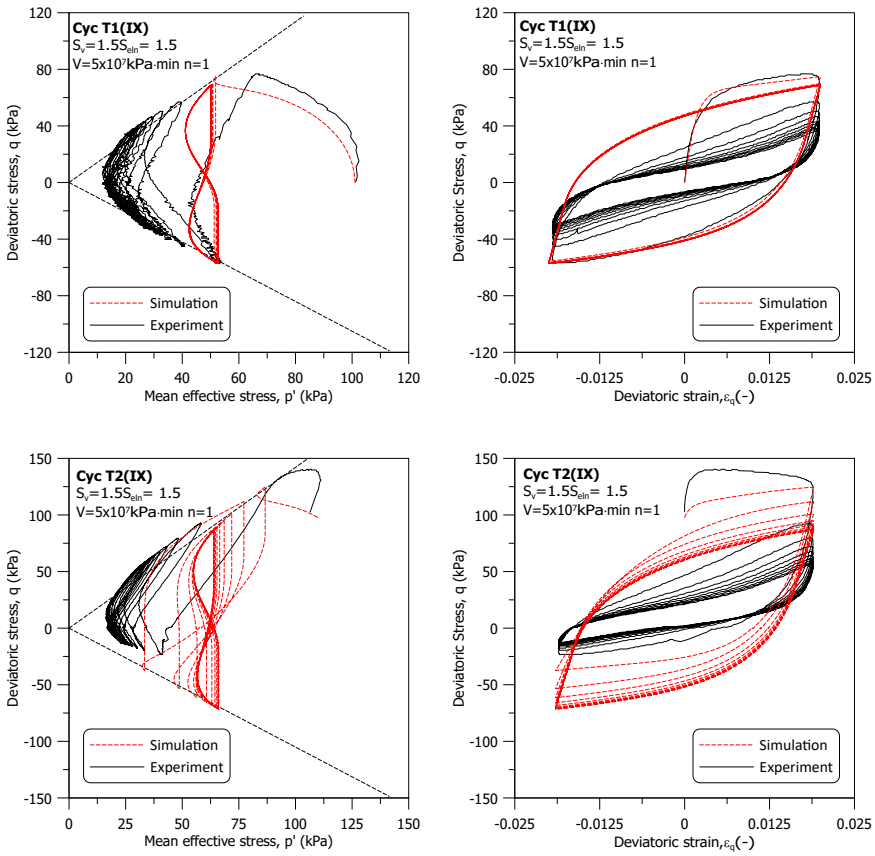

Figure 4.29: Parameter s_v, V, and n calibration with cyclic triaxial tests on group (IX) (first trial)

PARAMETER a_d

The calibration of parameter a_d was specifically focused on the reduction of secant shear modulus during the first ten cycles of cyclic shearing in tests Cyc T1(IX) and Cyc T2(IX). Setting a_d to 10, as illustrated in Figure 4.33, resulted in a good match with the test results. However, it is important to note that the model generally tends to underpredict the secant shear moduli, particularly during the first loading cycle. The calibrated stress paths and stress-strain curves, obtained with a_d set to 10, are presented in Figure 4.34. These calibrated results provide a better representation of the observed behaviour in the tests and demonstrate the effectiveness of adjusting the parameter a_d to capture the reduction in secant shear modulus during cyclic shearing.

PARAMETER w

The calibration of parameter w was focused on two key aspects: the development of average excess pore pressure and the evolution of secant shear modulus and damping ratio during the first ten cycles of cyclic shearing in tests Cyc T1(IX) and Cyc T2(IX). Setting w to 3 yielded model predictions that align well with the test results, as shown in

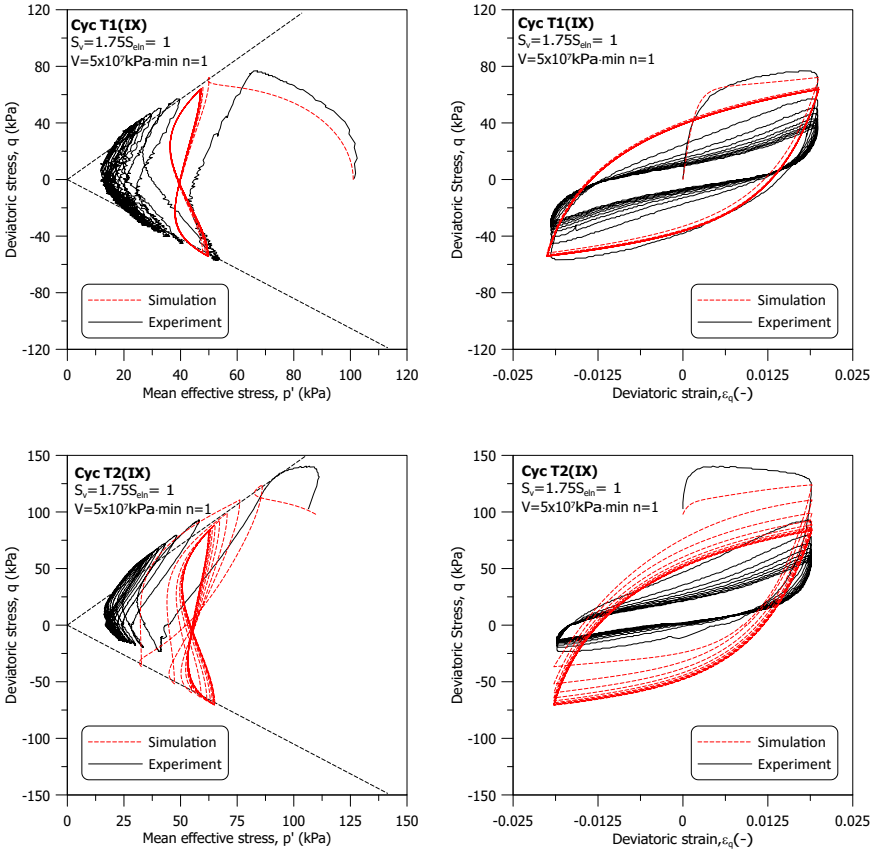

Figure 4.30: Parameter s_v, V, and n calibration with cyclic triaxial tests on group (IX) (second trial)

Figure 4.35. However, it is notable that the model tends to overestimate the damping ratio. Additionally, the model predicts slightly higher average excess pore pressure in the first three loading cycles. The stress paths and stress-strain curves, reflecting the calibrated value of w, are presented in Figure 4.36. These calibrated results provide improved agreement with the observed behaviour in the tests and demonstrate the effectiveness of adjusting the parameter w to capture the development of average excess pore pressure and the evolution of secant shear modulus and damping ratio during cyclic shearing.

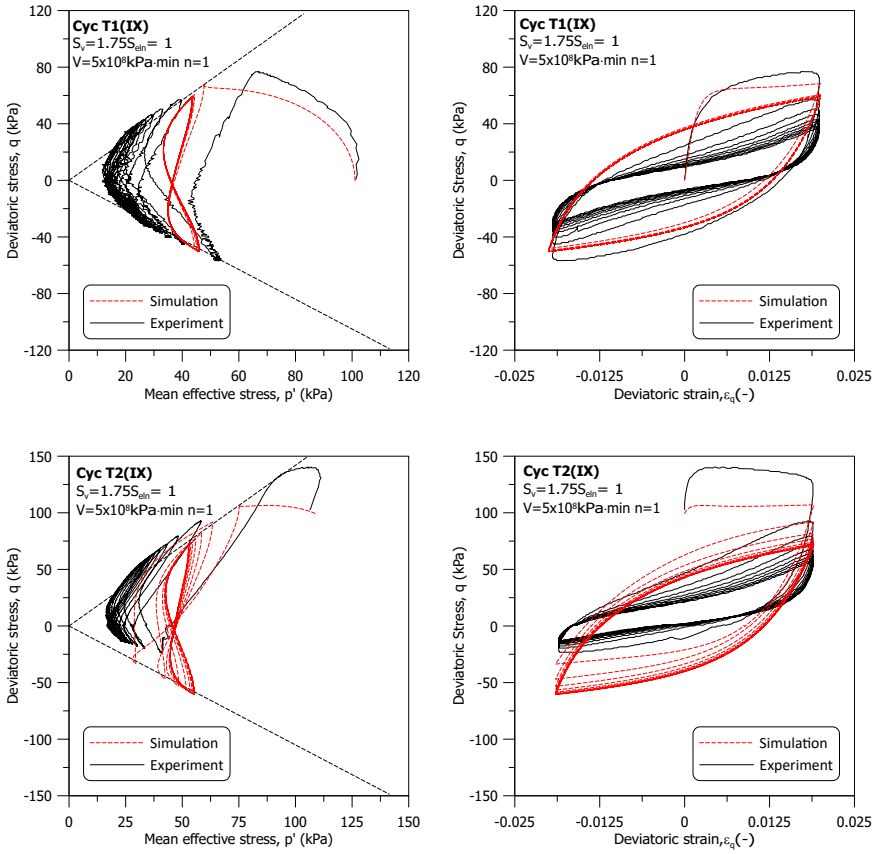

Figure 4.31: Parameter s_v, V, and n calibration with cyclic triaxial tests on group (IX) (third trial)

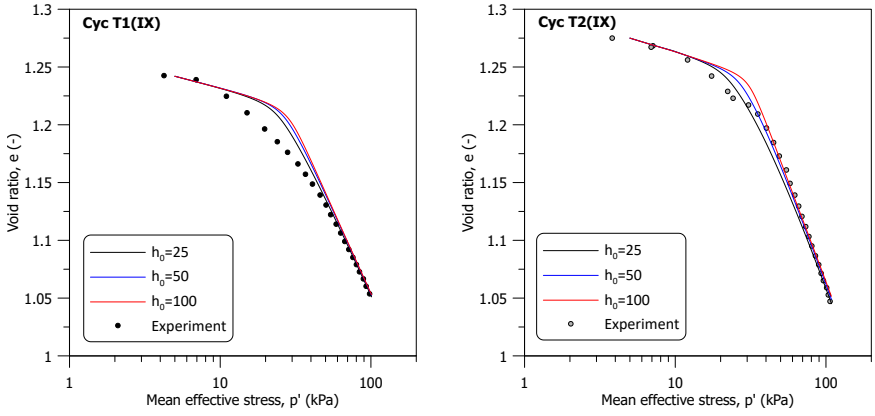

Figure 4.32: Parameter h_0 calibration with cyclic triaxial tests on group (IX)

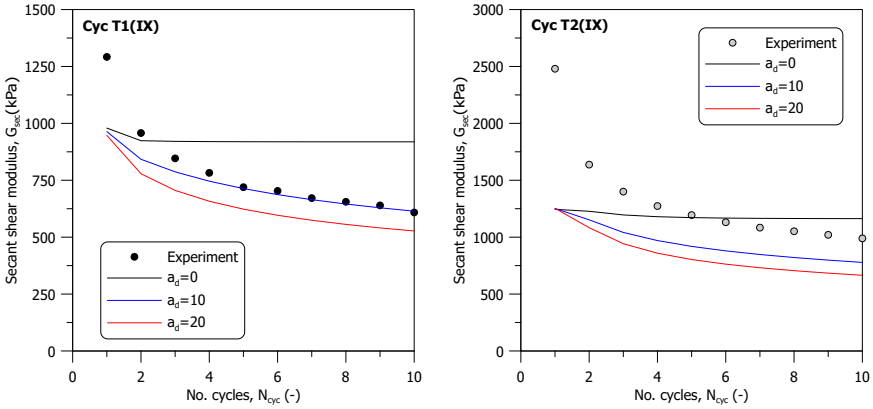

Figure 4.33: Parameter a_d calibration with cyclic triaxial tests on group (IX) (secant shear modulus reduction)

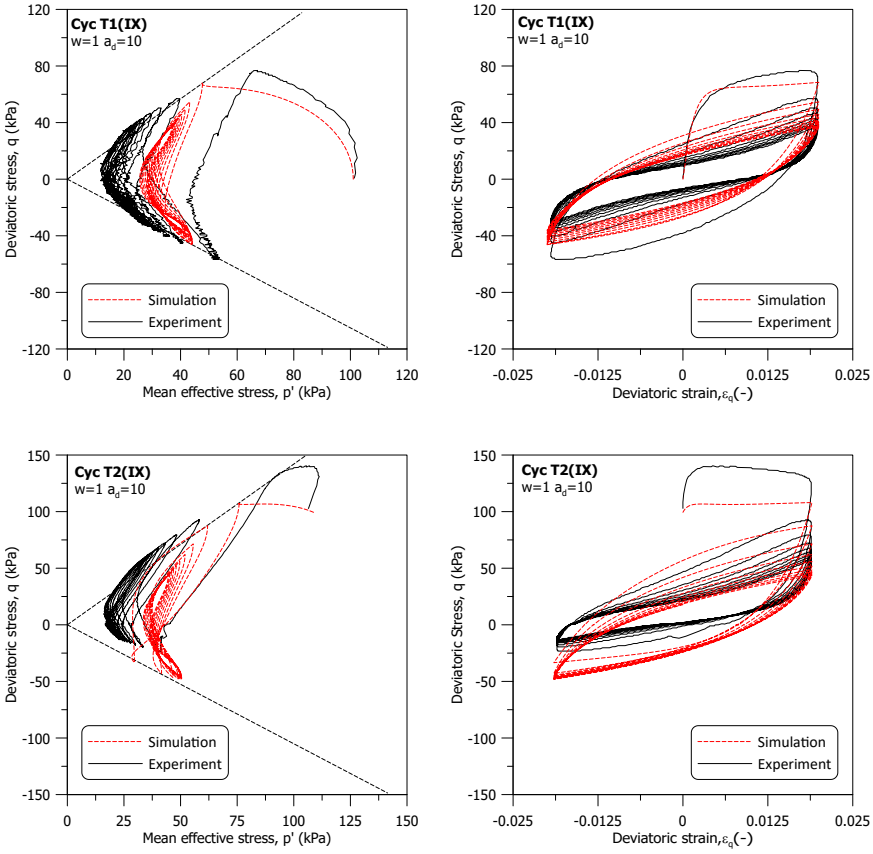

Figure 4.34: Parameter a_d calibration with cyclic triaxial tests on group (IX) (stress path and stress-strain curve)

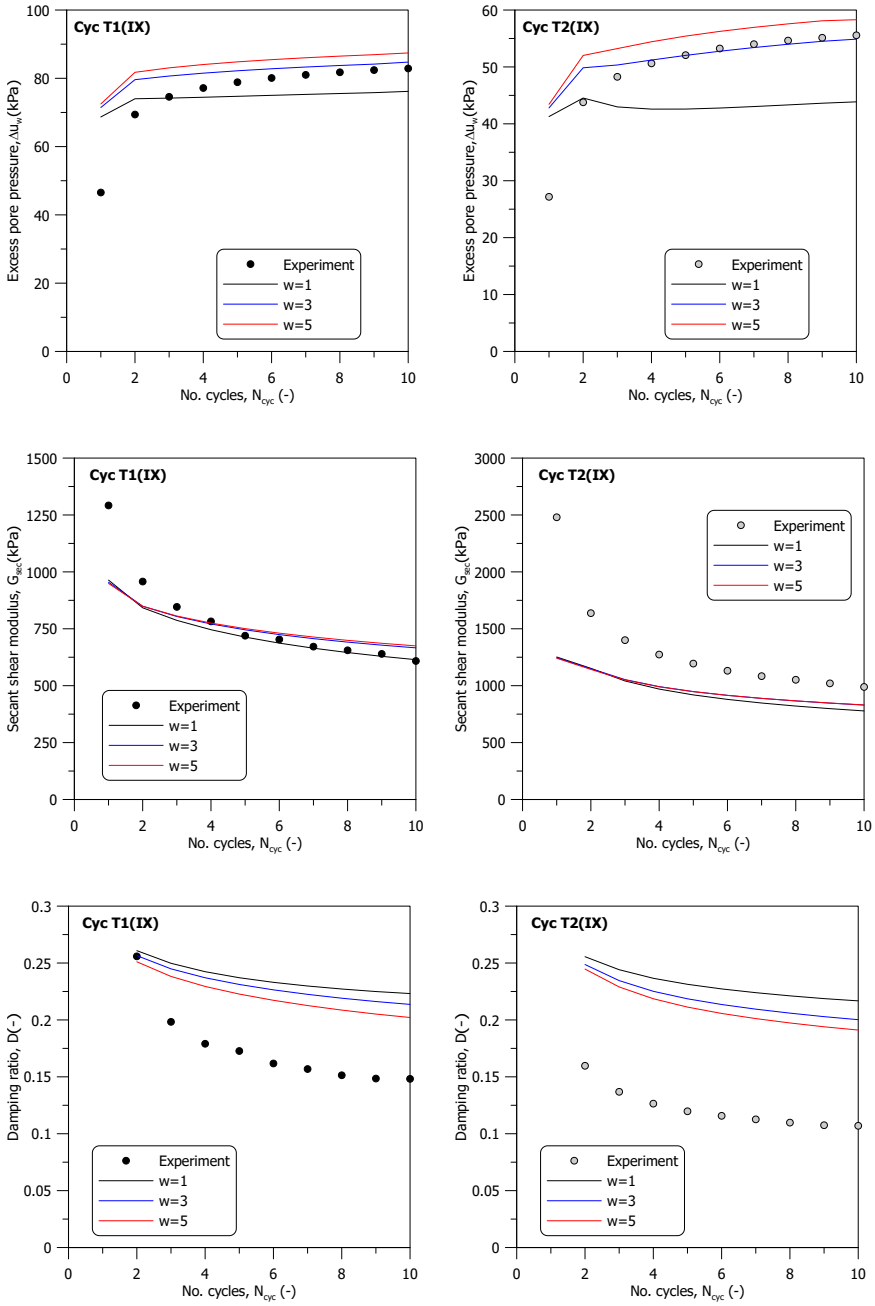

Figure 4.35: Parameter w calibration with cyclic triaxial tests on group (IX) (excess pore pressure, secant shear modulus, and damping ratio reduction)

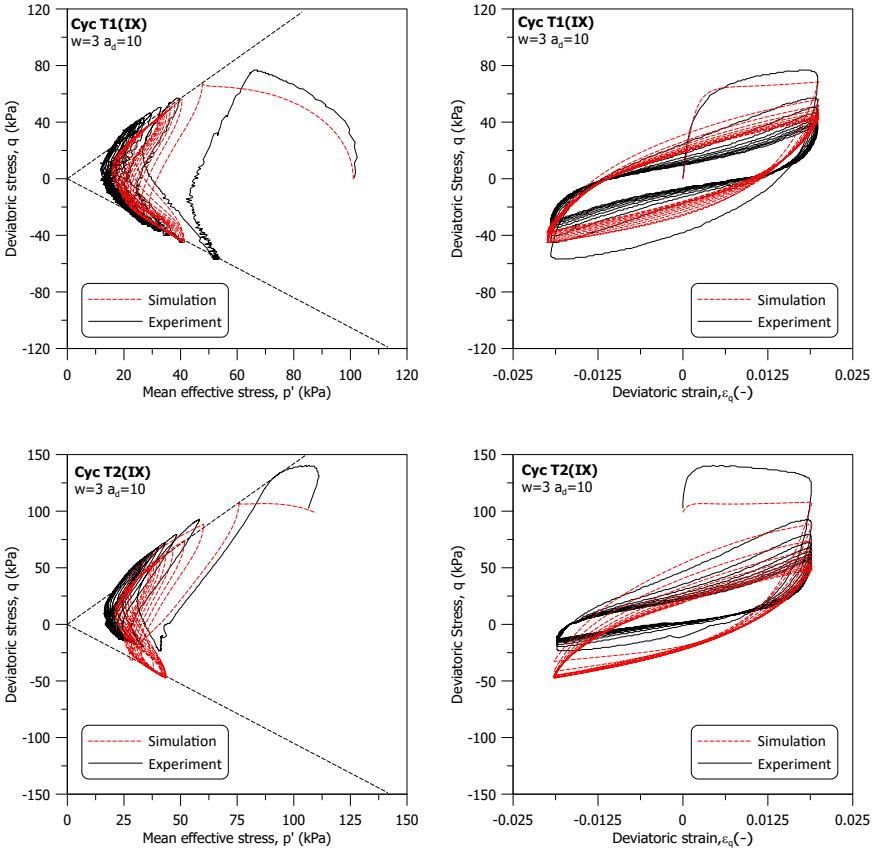

Figure 4.36: Parameter w calibration with cyclic triaxial tests on group (IX) (stress path and stress-strain curve)

4.4.2. MODEL PARAMETER

The calibrated parameters for the bounding surface and elastoplastic-viscoplastic formulations for samples from group (IX) are summarised in Table 4.8. Following the same calibration procedure, the calibrated parameters for samples from the group (X) are detailed in Table 4.9. In addition, the calibrated λ^* for group (IX) and (X) are $0.85\lambda^*_{\text{static}}$ and $0.8\lambda^*_{\text{static}}$, respectively. The κ^* is $1/9\lambda^*$ for both groups. It is important to note a key distinction: for the group (X), the a_d value is calibrated using the development of permanent deviatoric strain, $\varepsilon_{q,\text{per}}$ from stress-controlled cyclic triaxial tests. Apart from the initial size of the bounding surface, $p'_{0,i}$, three initial state variables are needed for the proposed model, namely the initial void ratio, e_i, corresponding to the initial mean effective stress at the beginning of the triaxial test, p'_i, the initial inclination of the bounding surface and plastic potential, α_i, and the initial location of projection centre, (p'_c, q_c). The initialisation of these state variables has been described in Chapter 2 and 3.

Table 4.8: Calibrated model parameters for group (IX) (bounding surface and elastoplastic-viscoplastic related)

h_0	s_{eln}	a_d	w	s_v	V	n
50	1.0	10	3	1.75	5×10^8kPa·min	1

Table 4.9: Calibrated model parameters for group (X) (bounding surface and elastoplastic-viscoplastic related)

h_0	s_{eln}	a_d	w	s_v	V	n
200	1.2	-10	1	1.2	5×10^7 kPa·min	1

Figure 4.37 and Figure 4.38 provide the void ratio, stress paths, and stress-strain curves from the first ten cycles of the tests conducted on the group (X), which were utilised for calibrating the model parameters. Additionally, these figures include the outcomes of simulations performed using these calibrated parameters. The model underestimates the shear stiffness at smaller cyclic amplitudes, ranging from 13.2 to 18 kPa. At higher cyclic amplitudes (33 to 45 kPa), the model predicts a slightly less stiff response for samples initially consolidated isotopically. In addition, for these higher amplitudes, the model slightly overestimates the excess pore pressure in the initially isotropic consolidated sample. However, it is noteworthy that the model depicts both the stress-strain curve and the development of excess pore pressure well for the samples that are initially K_0 consolidated.

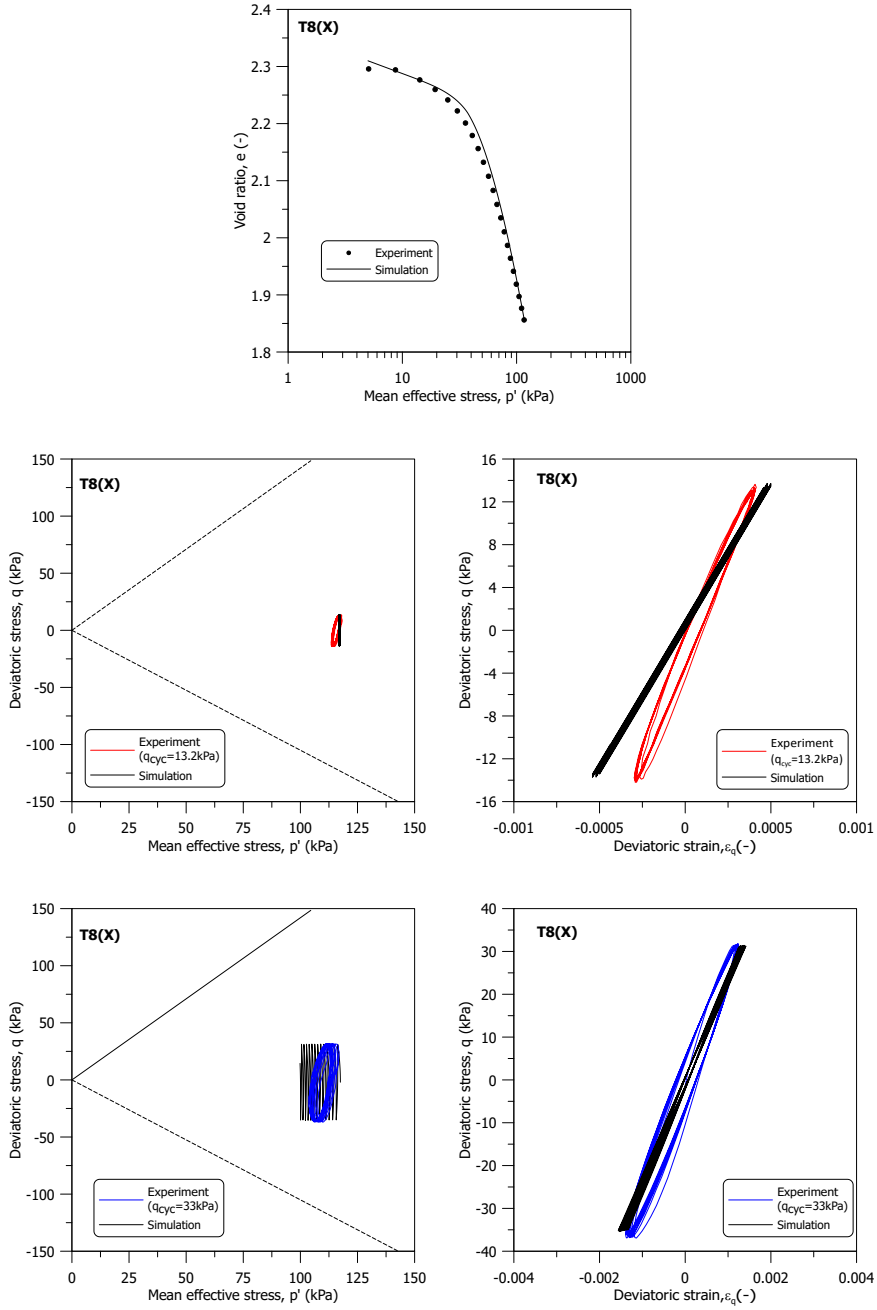

Figure 4.37: Simulation and experimental results of cyclic triaxial test on T8(X) (with calibrated parameters)

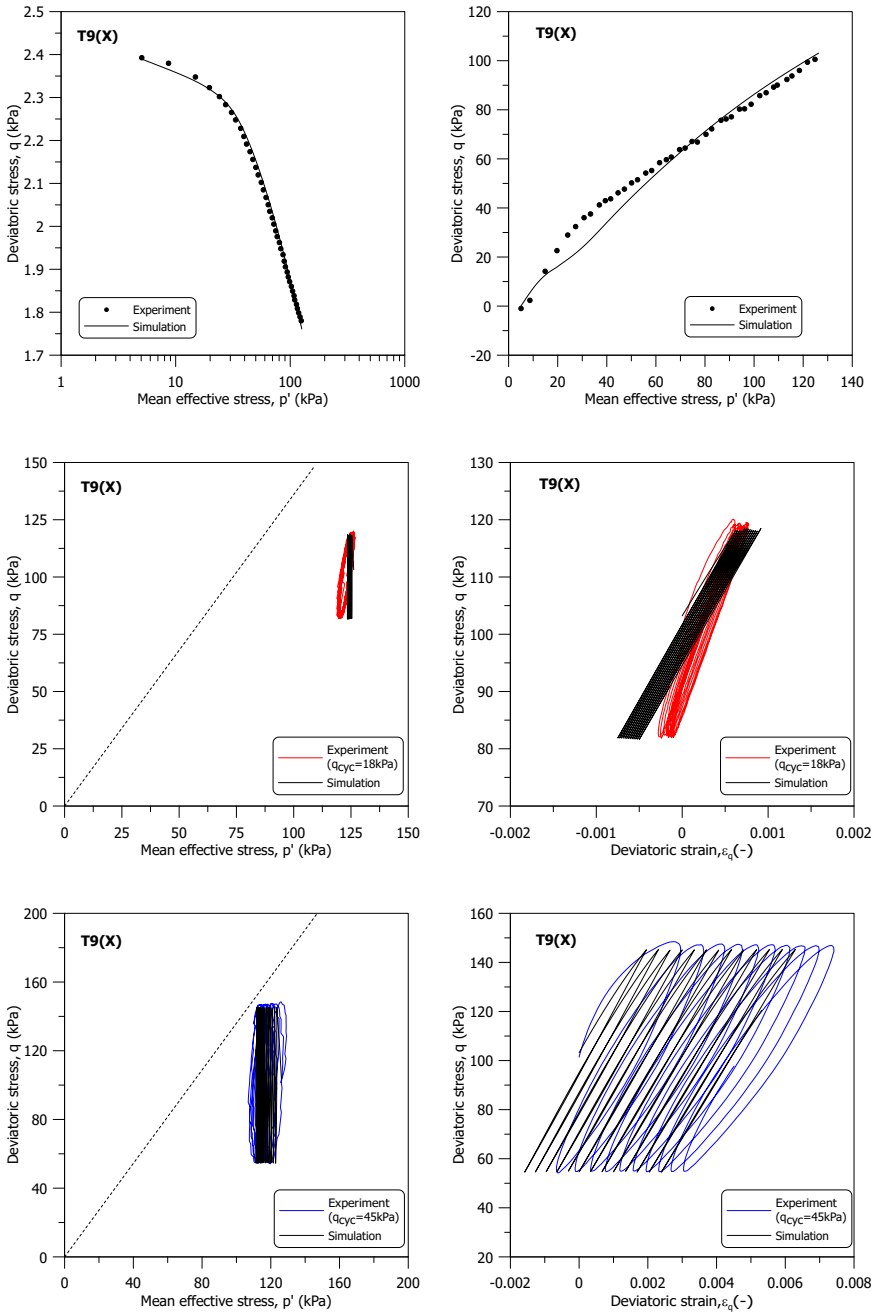

Figure 4.38: Simulation and experimental results of cyclic triaxial test on T9(X) (with calibrated parameters)

Although groups (IX) and (X) share the same JMC-clay (EP) model parameters, as listed in Table 4.7, their calibrated parameters for the bounding surface and elastoplastic-viscoplastic formulations are different. This variation can be attributed to the differences in soil properties between the two groups. As outlined in Chapter 2, the group (X) has a higher clay content and plasticity index PI, impacting various aspects of the cyclic response, as discussed in the literature (Dobry, 1987; Vucetic and Dobry, 1991) and Chapter 3.

Furthermore, the insights into the K_0 compression response, discussed in Chapter 2, reveal that the void index, I_v for group (X) samples, according to Burland (1990), lies well above the intrinsic compression line (ICL). In contrast, samples from the group (IX) are closer to the ICL, indicating differences in soil structure. Environmental Scanning Electron Microscope (ESEM) photomicrographs of group (VIII) (which is materially similar to group (IX)) as shown in Figure 4.39, depict a more open structure compared to that of group (X). The influence of soil structure on rate-dependent response has been highlighted by several researchers (Vaid and Finn, 1979; Leroueil et al., 1985). Sheahan (2005) introduced a framework to predict the rate dependence of soils based on the void index. This framework utilises a 'structure number', SN to quantify the structural state of the soil. A lower SN value indicates a soil structure closer to the intrinsic compression line (ICL), and soils with lower SN values exhibit less rate dependency. This concept correlates well with the calibration results for groups (IX) and (X), where higher values of s_v and V are observed. The higher s_v value indicates a smaller viscoplastic zone within the bounding surface, while the higher V value suggests a slower rate of viscoplastic response.

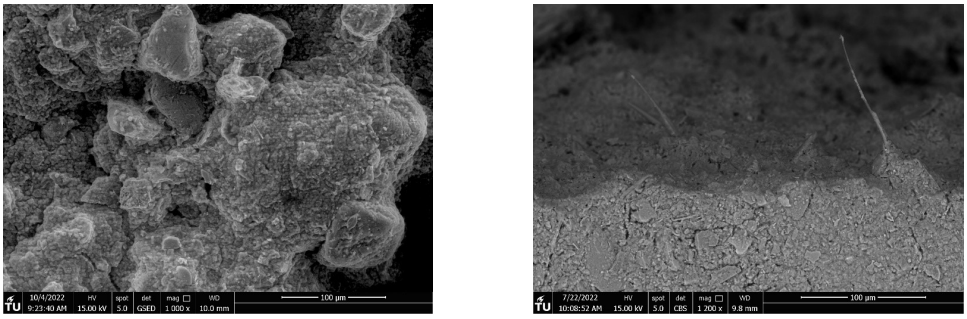

(a) (b)

Figure 4.39: ESEM photomicrographs of the material from (a) group (VIII) and (b) group (X)

4.4.3. MODEL PREDICTION AND VALIDATION ON GROUP (III), (VII), (VIII), AND (IX)

The performance of the JMC-clay BSEVP model on samples from group (III) to (IX) is first evaluated using static tests detailed in Chapter 3, specifically to assess the effectiveness of the JMC-clay BS component. The outcomes are compared with those from the elastoplastic (EP) and bounding surface (BS) versions of the model. The parameters used for these simulations are listed in Table 4.7 and Table 4.8. Figure 4.40 and Figure 4.41 present both the experimental data and the simulation results for these tests.

From this comparison, it is evident that the JMC-clay BSEVP model yields a response similar to that of the JMC-clay BS model. Notably, using the JMC-clay BSEVP model seems to enhance predictive accuracy along the undrained compression path following K_0 unloading. However, in other undrained compression paths, the JMC-clay BSEVP model predicts a marginally higher peak deviatoric stress. This difference can be attributed to the calibration of the model parameters, which was based on tests with a cyclic loading frequency of 0.001Hz and a loading amplitude of 2%, corresponding to an average axial strain rate of 0.48%/min. In contrast, the average axial strain rate used in the static tests during undrained shearing is approximately 0.015%/min.

The first ten loading cycles of tests Cyc T1(IX) and T2 are utilised to calibrate the model parameters. To validate the predictive capability of the proposed model, the subsequent loading cycles of these tests are analysed. Figure 4.42 and Figure 4.43 display the comparison between the experimental results and the numerical simulations for Cyc T1(IX) and T2.

In Figure 4.42, the model prediction of the stress path evolution aligns well with the experimental observations, as corroborated by the excess pore pressure development shown in Figure 4.43. The model accurately reflects the variation in the secant shear modulus after the initial cycle. However, for test Cyc T2(IX), the model predicts a deviation in the evolution of deviatoric stress on the extension side, tending towards a less negative side compared to the laboratory data. This discrepancy might be due to the inherent anisotropy of the tested sample, as the implementation of Lode angle dependency in the parameter h_0, suggested by Shi et al. (2018), did not reproduce the observed laboratory trend, as evidenced in Figure 4.44.

Regarding the damping ratio evolution, the model captures the overall trend across the number of loading cycles but predicts higher values than those observed in the tests. This discrepancy is also illustrated in Figure 4.42, where the stress-strain loops from the laboratory data exhibit a flatter shape compared to the model predictions.

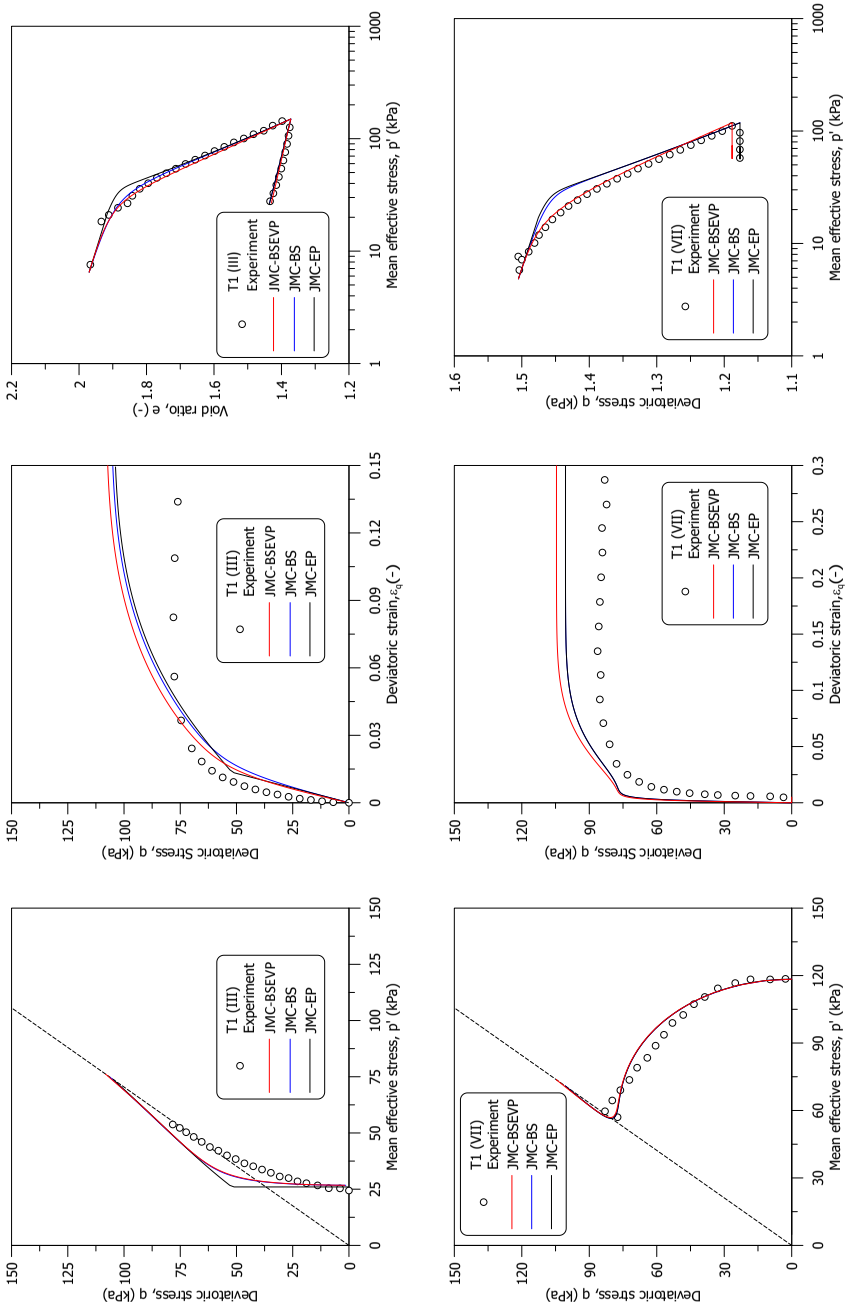

Figure 4.40: Experimental data and simulation results of static tests on group (III) and (VII)

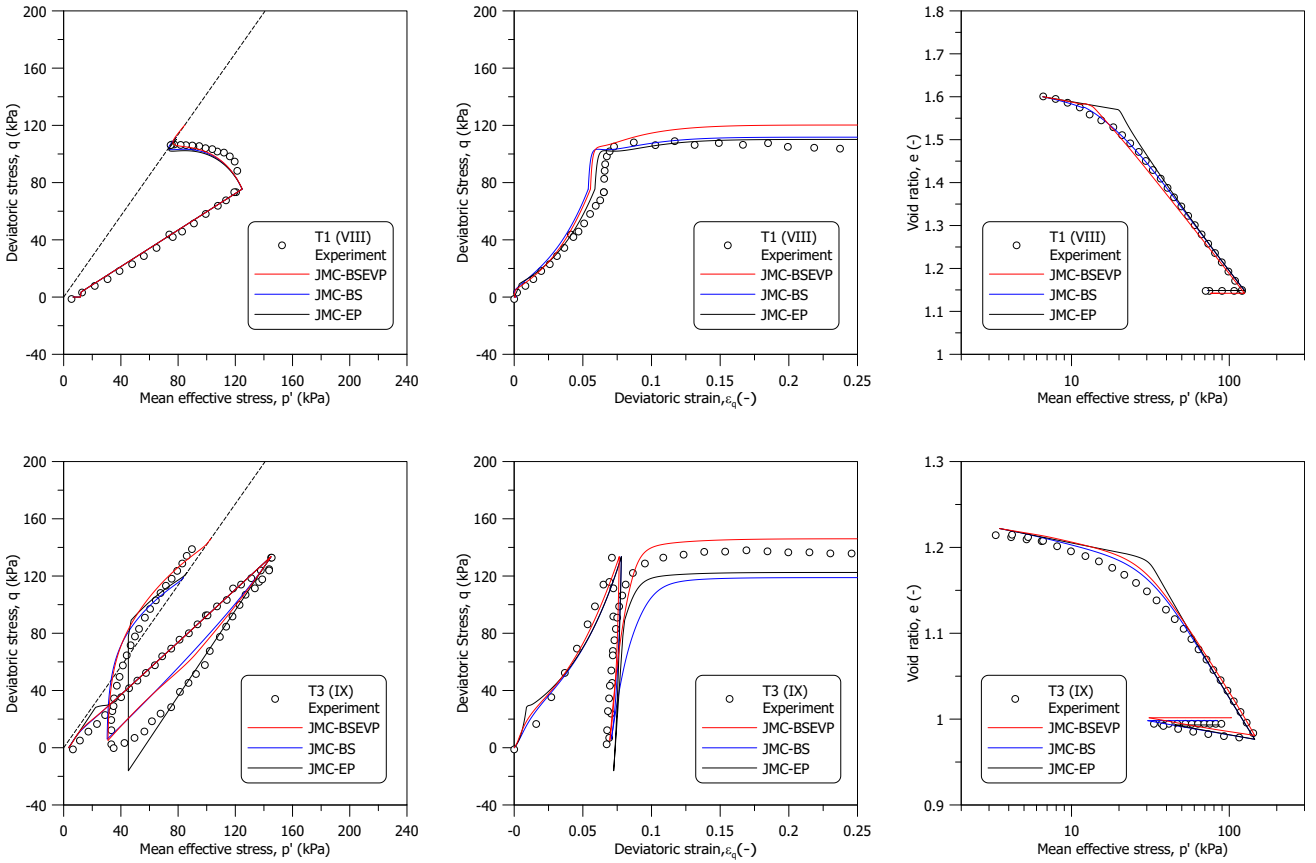

Figure 4.41: Experimental data and simulation results of static tests on group (VIII) and (IX)

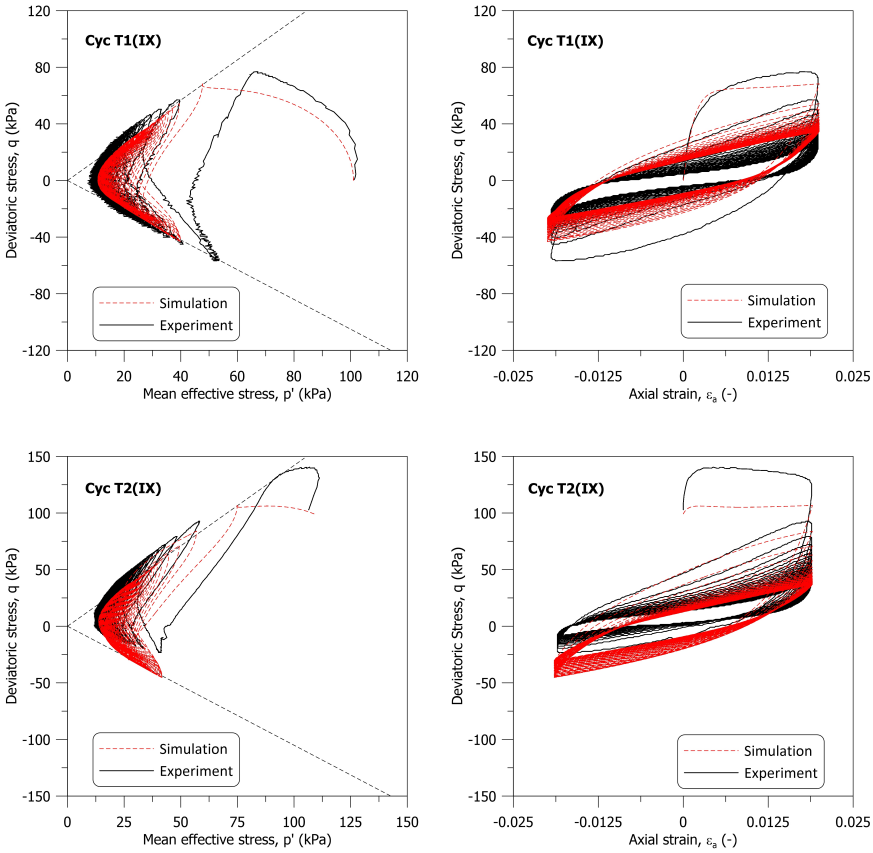

Figure 4.42: Comparison between numerical simulations and experimental data for strain-controlled cyclic shearing on samples Cyc T1(IX) and T2(IX) (stress path and stress-strain curve)

The predictive capabilities of the proposed model are further validated through test Cyc T2(VII), which entails strain-controlled cyclic shearing at a frequency of 0.001Hz and an amplitude of 2.4% on a K_0 consolidated sample. Figure 4.45 to Figure 4.47 present the comparison between the experimental results and the model simulations for this test.

As depicted in Figure 4.45, the model predictions closely match the experimental K_0 data. The model also accurately predicts the cyclic volumetric response, as evidenced by the stress path evolution and excess pore pressure development. Regarding the deviatoric response, while the model slightly underestimates the peak deviatoric stress during the first cycle, it aligns well with the laboratory data in subsequent cycles. This consistency in deviatoric stress evolution, especially on the extension side, again suggests that the divergent trend observed in test Cyc T2(IX) could be attributed to the inherent anisotropy of that sample.

Additionally, the model predictions for secant shear modulus and damping ratio reduction across loading cycles are quite accurate. The model indicates a slightly higher secant shear modulus, but the overall trend matches the experimental data well. No-

tably, the issues observed in damping ratio prediction for other tests are not evident in test Cyc T2(VII); in fact, the model predictions here align quite closely with the experimental results.

In addition to the cyclic shearing stage, the model performance is also assessed during the post-cyclic recompression phase and subsequent undrained triaxial extension. The results of this assessment, including a comparison between the experimental data and model simulations, are detailed in Figure 4.48. During the post-cyclic recompression phase, the model predicts a lower recompression than what is observed experimentally. There are two primary reasons for this discrepancy:

- Recompression index: Yasuhara and Andersen (1991) noted that the post-cyclic recompression index, $C_{r,cy}$, is approximately 1.5 times the ordinary recompression index, C_r. Additionally, as demonstrated in Chapter 3, the post-cyclic recompression of Dutch organic clay is almost two times higher than the empirical relation. This aspect is not incorporated into the proposed model.

- Excess pore pressure: The model also predicts lower excess pore pressure development during cyclic shearing compared to experimental observations. Yasuhara et al. (2001) indicates that post-earthquake recompression settlement increases with higher cyclic-induced excess pore pressure. Therefore, the underestimation of excess pore pressure during shearing could lead to underprediction of post-cyclic recompression.

Lastly, the model performs well in simulating the post-cyclic undrained triaxial extension. It captures the general behaviour with a slight overprediction in deviatoric stress and a marginal underprediction of excess pore pressure.

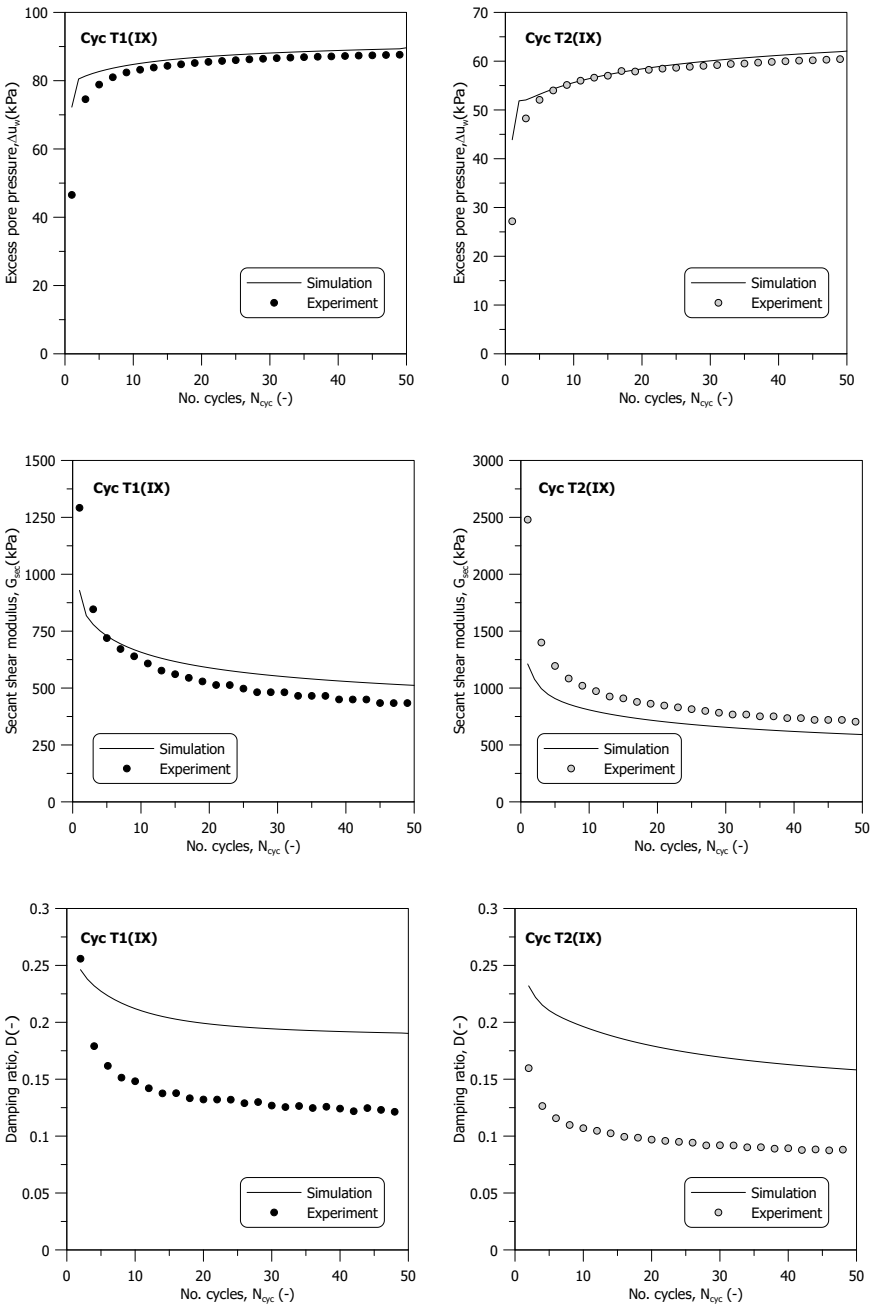

Figure 4.43: Comparison between numerical simulations and experimental data for strain-controlled cyclic shearing on samples Cyc T1(IX) and T2(IX) (average excess pore pressure, secant shear modulus, and damping ratio)

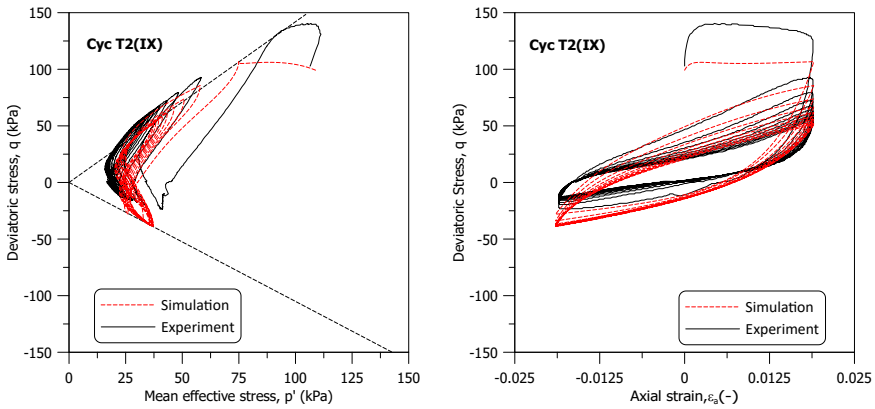

Figure 4.44: Comparison between numerical simulations (with Lode angle dependency in h_0)and experimental data for strain-controlled cyclic shearing Cyc T2(IX)

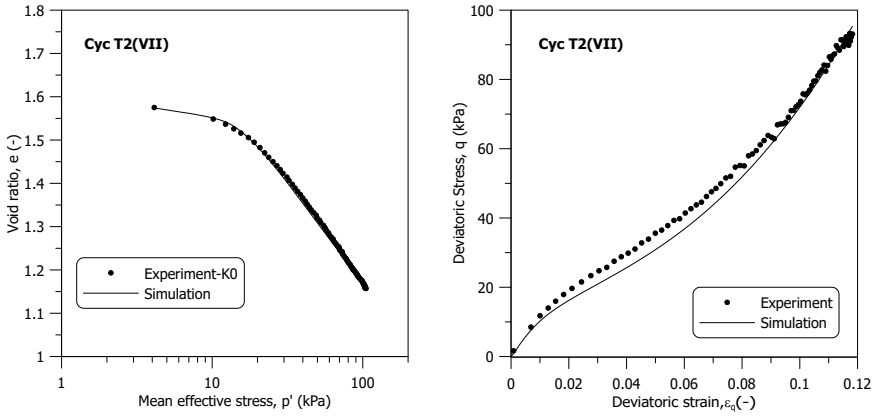

Figure 4.45: Comparison between numerical simulations and experimental data for K_0 consolidation on sample Cyc T2(VII)

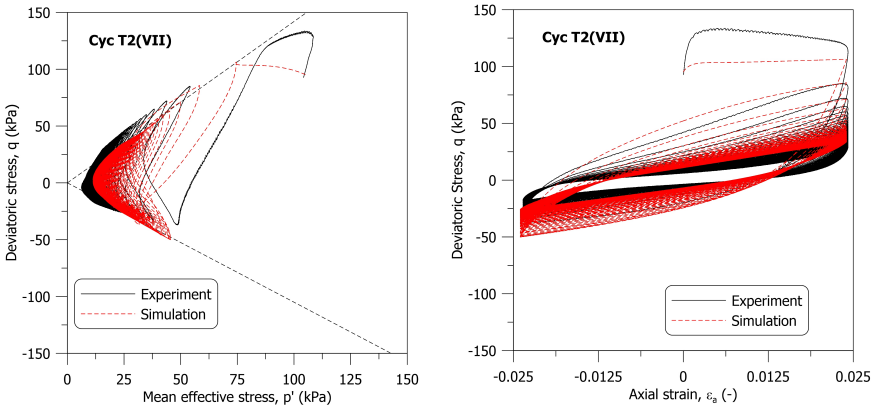

Figure 4.46: Comparison between numerical simulations and experimental data for strain-controlled cyclic shearing on sample Cyc T2(VII) (stress path and stress-strain curve)

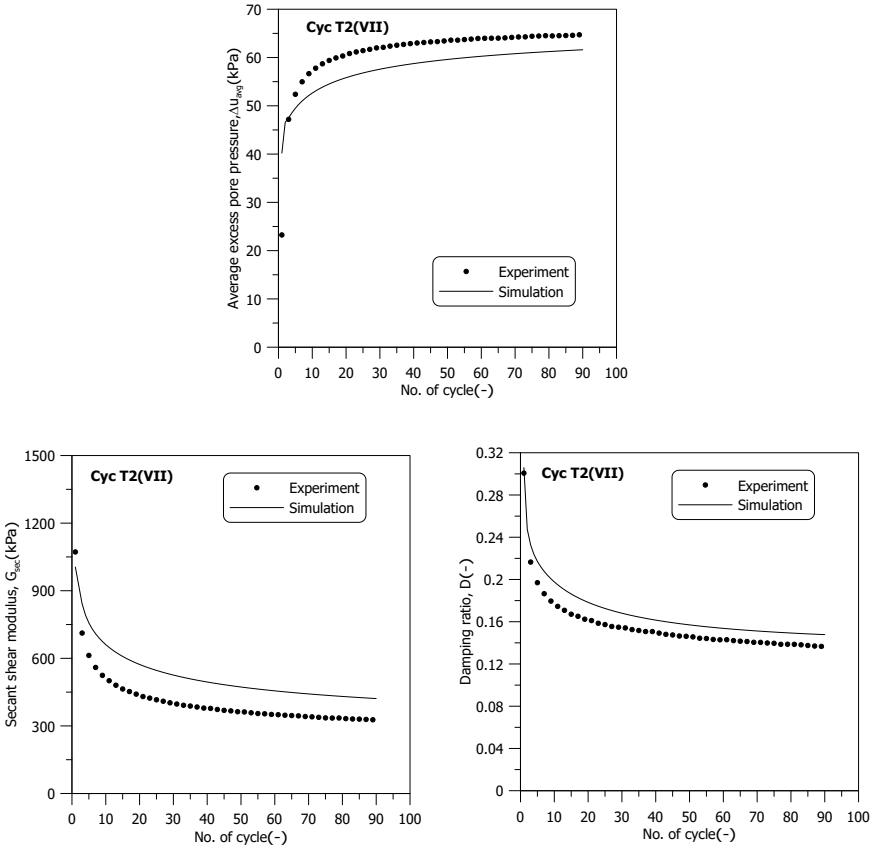

Figure 4.47: Comparison between numerical simulations and experimental data for strain-controlled cyclic shearing on sample Cyc T2(VII) (average excess pore pressure, secant shear modulus, and damping ratio)

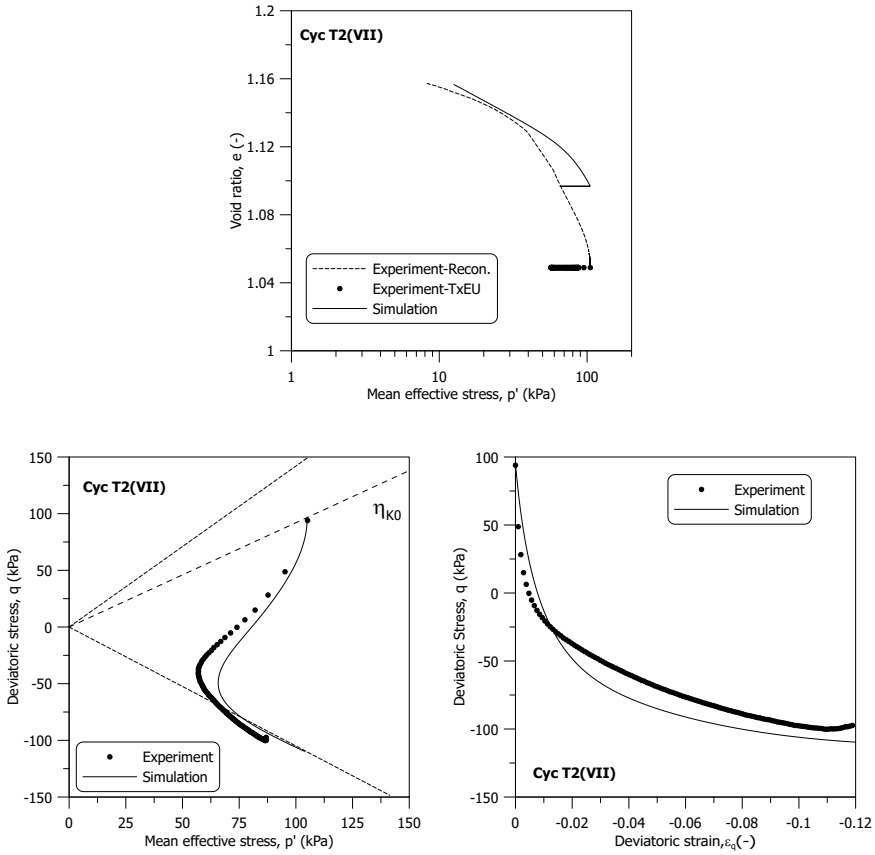

Figure 4.48: Comparison between numerical simulations and experimental data for post-cyclic recompression and triaxial undrained extension on sample Cyc T2(VII)

4.4.4. MODEL PREDICTION AND VALIDATION ON GROUP (X)

The model performance of JMC-clay BSEVP is also assessed using static probe paths before cyclic shearing on samples from the group (X), as described in Chapters 2 and 3. For samples T1(X) and T2(X), the outcomes are compared with those from the elasto-plastic (JMC-EP) version of the model. The parameters for these static test simulations are listed in Table 4.7 and Table 4.9. Figure 4.49, Figure 4.50, and Figure 4.51 display both the experimental data and the simulation results for these static probe paths.

In Figure 4.51, the JMC-clay BSEVP model demonstrates the ability to predict the change in loading rate during unloading and reloading, particularly for sample T1(X). However, the model appears to overestimate the deviatoric strain when compared to the JMC-EP model, likely due to its calibration based on tests with a fast cyclic loading frequency of 0.1Hz.

The model parameters are calibrated using isotropic and K_0 consolidated samples, and this is reflected in Figure 4.50 and Figure 4.51. The model shows better performance for stress probe paths close to isotropic and K_0 stress states, as seen in samples T4(X), T5(X), and T6(X). Conversely, for T3(X), which follows a stress path at a stress ratio close to the critical one on the extension side $M_{g,e}$, which reduces the model-predicted shear stiffness and thus overestimates deviatoric strain.

The model performance is further evaluated using two-stage stress-controlled cyclic tests on group (X) samples, where each stage involved 100 loading cycles. While data from the initial ten cycles of tests T8(X) and T9(X) are used for model calibration, the subsequent cycles offer an opportunity for model validation. Figure 4.52 to Figure 4.55 compare the experimental results with the numerical simulations for tests T8(X) and T9(X), the evolution direction of the simulations is indicated in the figures.

For sample T8(X), the model tends to underestimate the shear stiffness at a smaller cyclic amplitude of 13.2 kPa, as seen in Figure 4.52 and Figure 4.53. Additionally, the model predicts an average excess pore pressure that is slightly higher (by about 2 kPa) than the experimental observation at this smaller amplitude. On the other hand, at higher cyclic amplitudes (33 kPa), the model more accurately captures the shear stiffness. However, the predicted continuous reduction in secant shear modulus is not observed in the test, even with a negative a_d value adopted. This discrepancy might be related to the overestimation of excess pore pressure development, which in turn reduces the mean effective stress. As a constant Poisson's ratio is adopted for the elastic rule, the shear modulus decreases with the mean effective stress reduction.

Furthermore, while negligible permanent deviatoric strain was recorded during the test at the smaller cyclic amplitude (13.2 kPa), the model predicts an accumulation of deviatoric strain, particularly towards the extension side. In contrast, at the higher cyclic amplitude (33 kPa), the model predicts permanent deviatoric strain with satisfactory accuracy. In summary, the model tends to better capture the volumetric response at smaller cyclic amplitudes, whereas the deviatoric response is more accurately predicted at higher amplitudes.

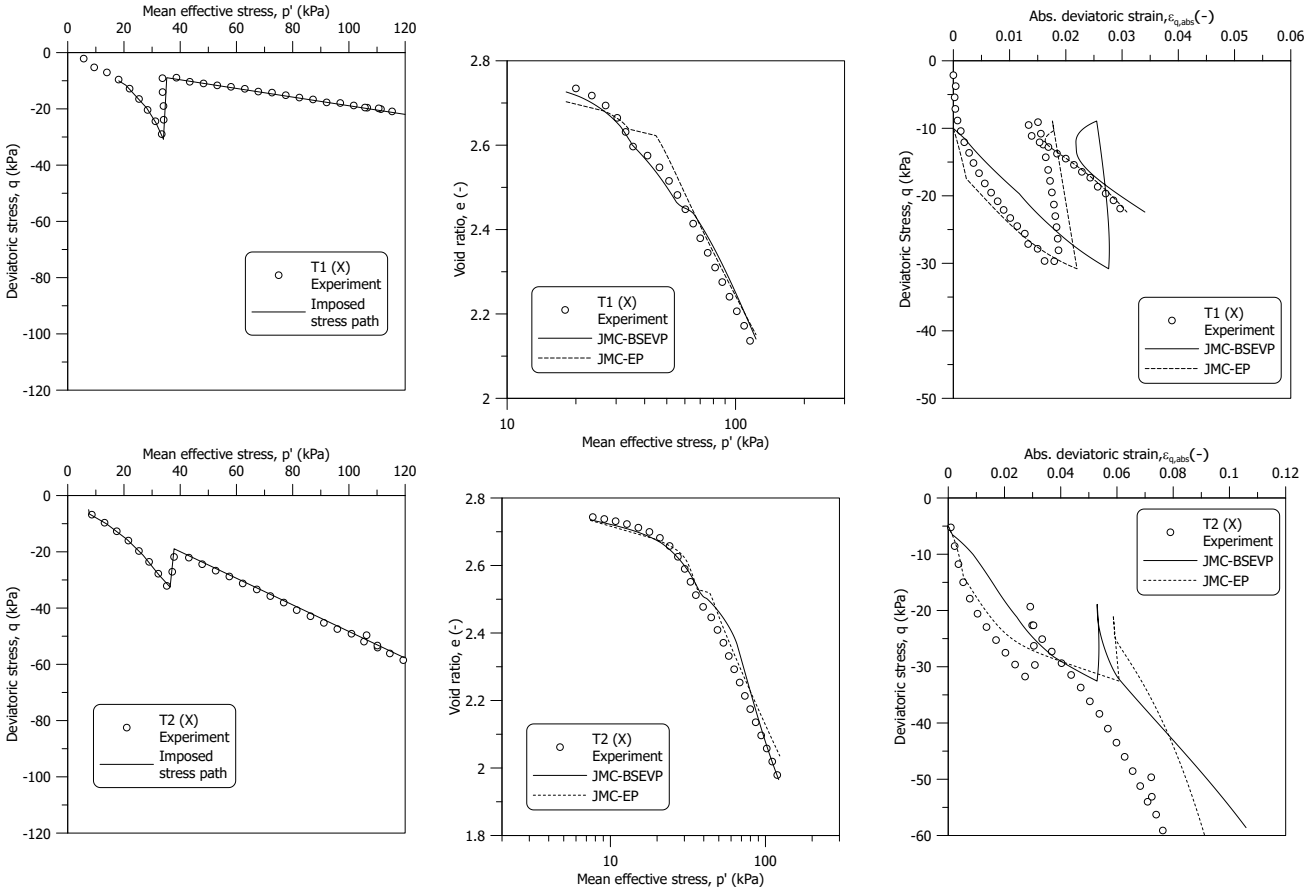

Figure 4.49: Experimental data and simulation results of static tests of T1(X) and T2(X)

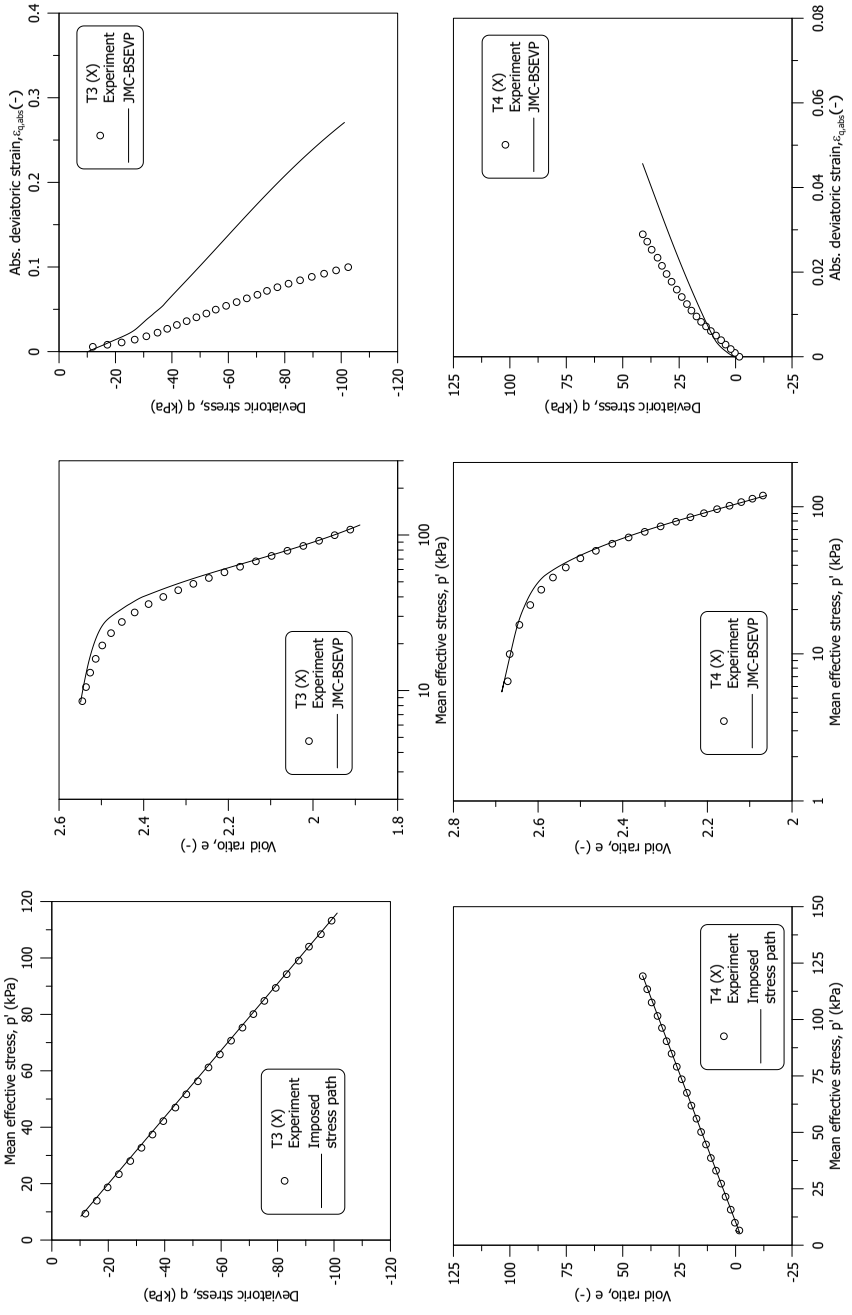

Figure 4.50: Experimental data and simulation results of static tests of T3(X) and T4(X)

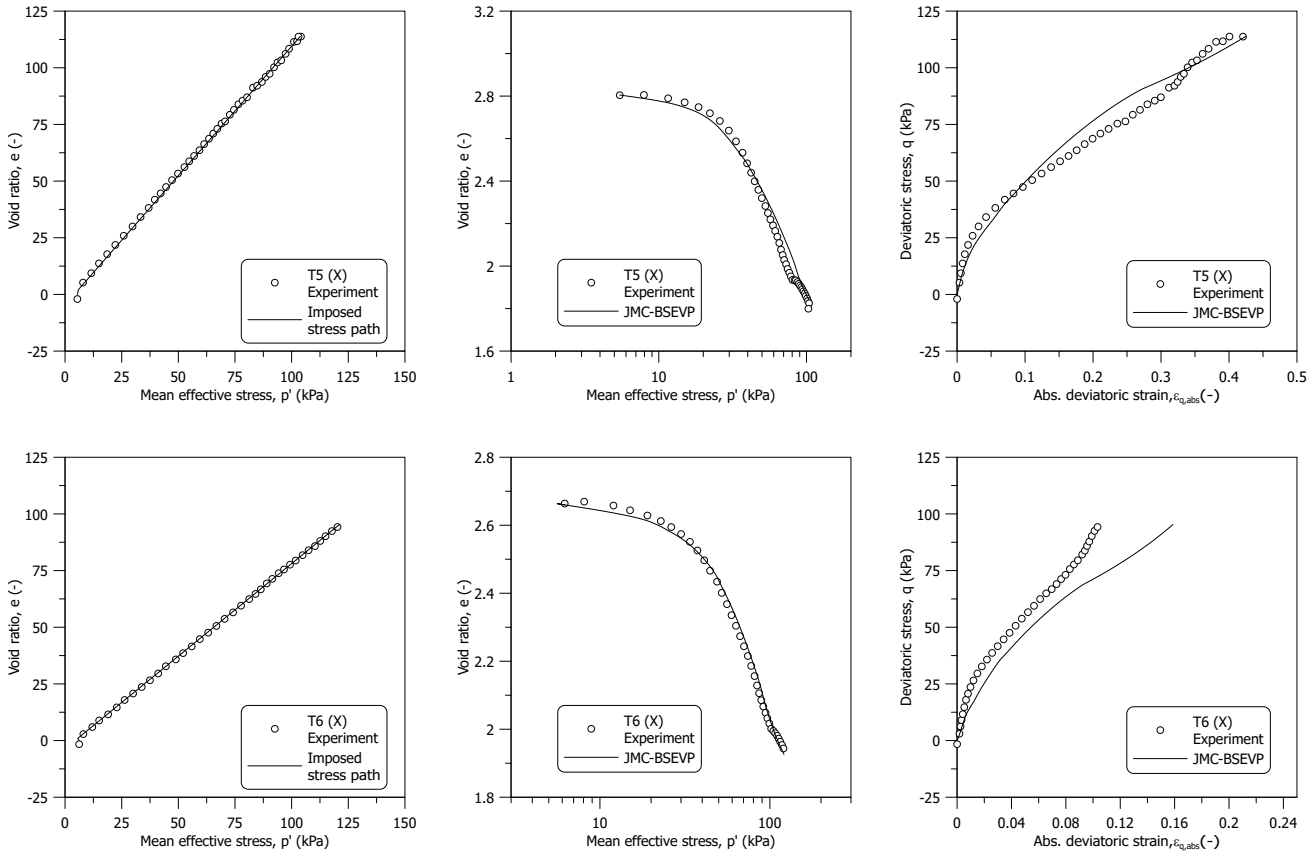

Figure 4.51: Experimental data and simulation results of static tests of T5(X) and T6(X)

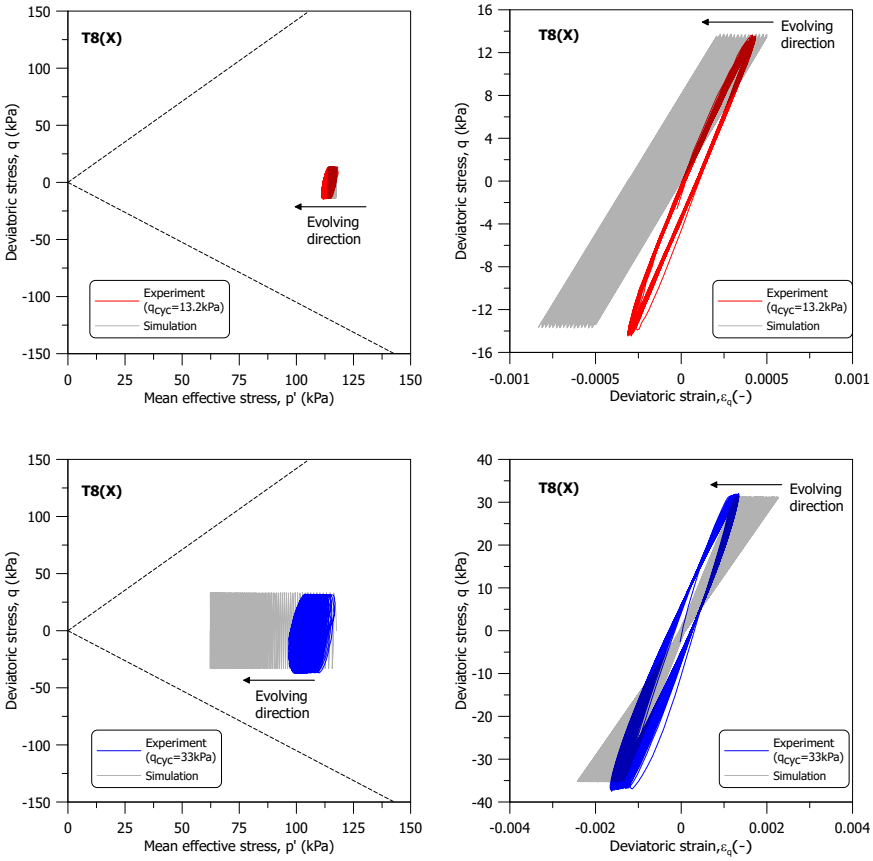

Figure 4.52: Comparison between numerical simulations and experimental data for strain-controlled cyclic shearing on T8(X) (stress path and stress-strain curve)

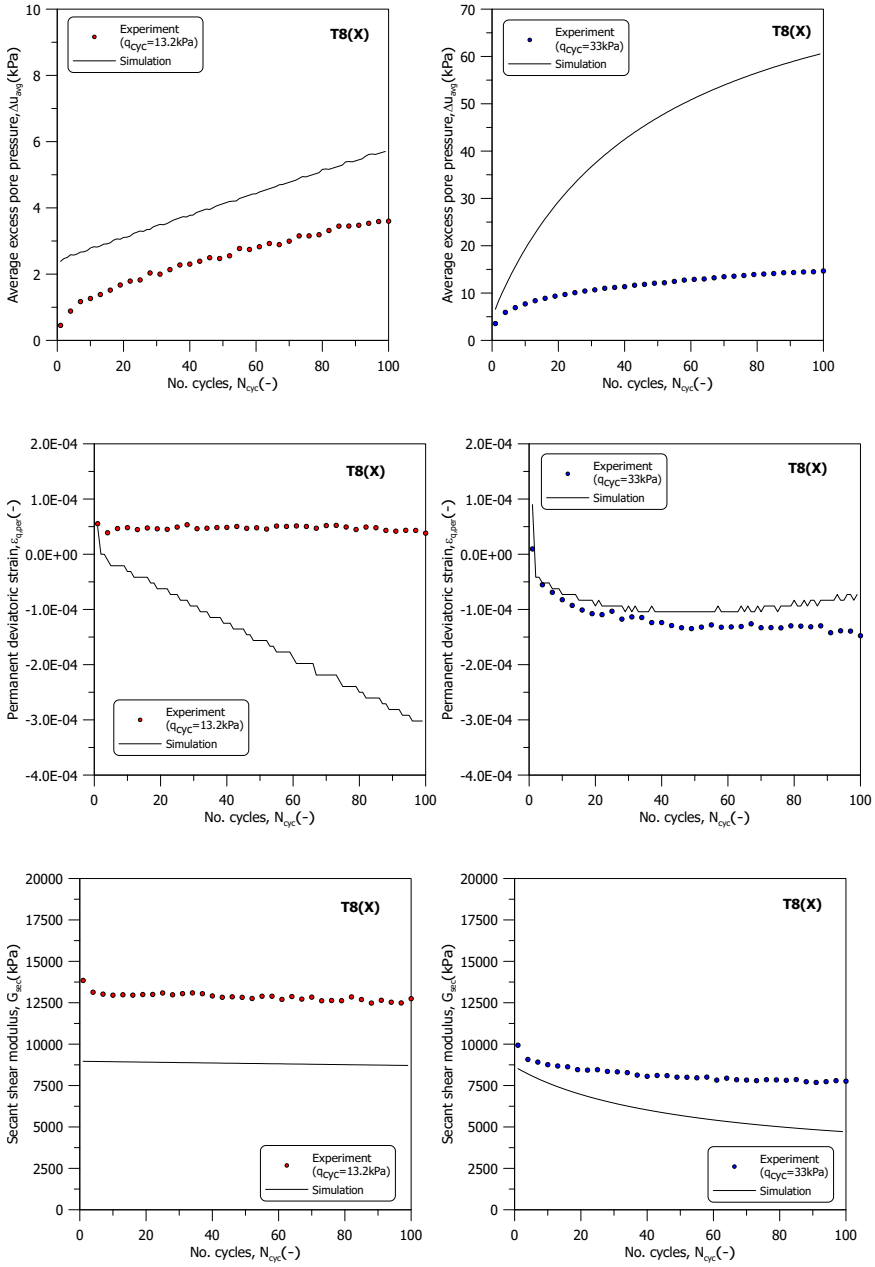

Figure 4.53: Comparison between numerical simulations and experimental data for strain-controlled cyclic shearing on T8(X) (average excess pore pressure, permanent deviatoic strain, and secant shear modulus)

When examining cyclic loading from a K_0 stress state, the model accurately captures the development of excess pore pressure in the initial cycles. However, as indicated in Figure 4.54 and Figure 4.55, it tends to overestimate and underestimate the excess pore pressure in subsequent cycles for smaller (18 kPa) and larger (45 kPa) amplitudes, respectively. Regarding shear stiffness, the model consistently predicts a lower secant shear modulus than observed in experiments for the smaller amplitude, while it overestimates the shear stiffness for the larger amplitude.

Contrary to the observations in sample T8(X), the model effectively mirrors the trend of secant shear modulus evolution across loading cycles in sample T9(X). Notably, both the permanent deviatoric strain and secant shear modulus evolve differently after the 70^{th} cycle at the higher amplitude. This happens when the experimental stress path surpasses the critical state stress ratio and moves into the dry side, leading to an accelerated accumulation of permanent deviatoric strain and a more rapid reduction in the secant shear modulus. However, the stress path predicted by the model tends to stabilise around the critical state stress ratio. Adjusting the hybrid flow rule parameter, w, could potentially address this stabilisation, but it might also negatively impact the model performance for sample T8(X), particularly given the current overestimation of excess pore pressure with the adopted w value. Furthermore, for smaller amplitudes, the model begins to overestimate permanent deviatoric strain after the 30^{th} cycle, highlighting another area where the model prediction diverges from experimental observations.

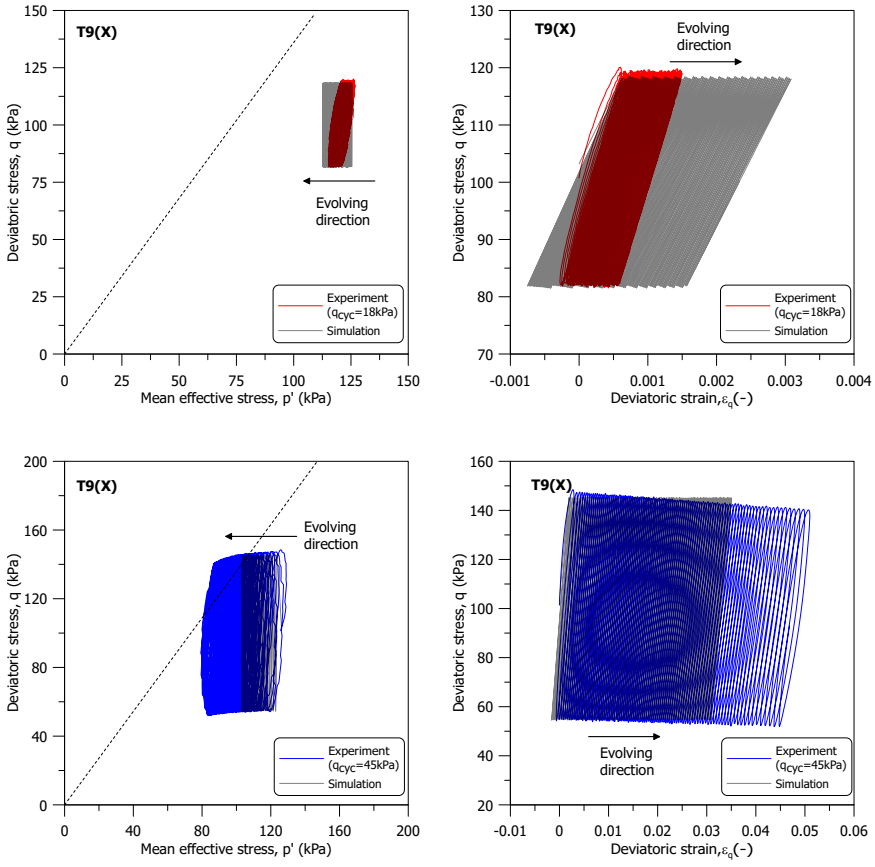

Figure 4.54: Comparison between numerical simulations and experimental data for strain-controlled cyclic shearing on T9(X) (stress path and stress-strain curve)

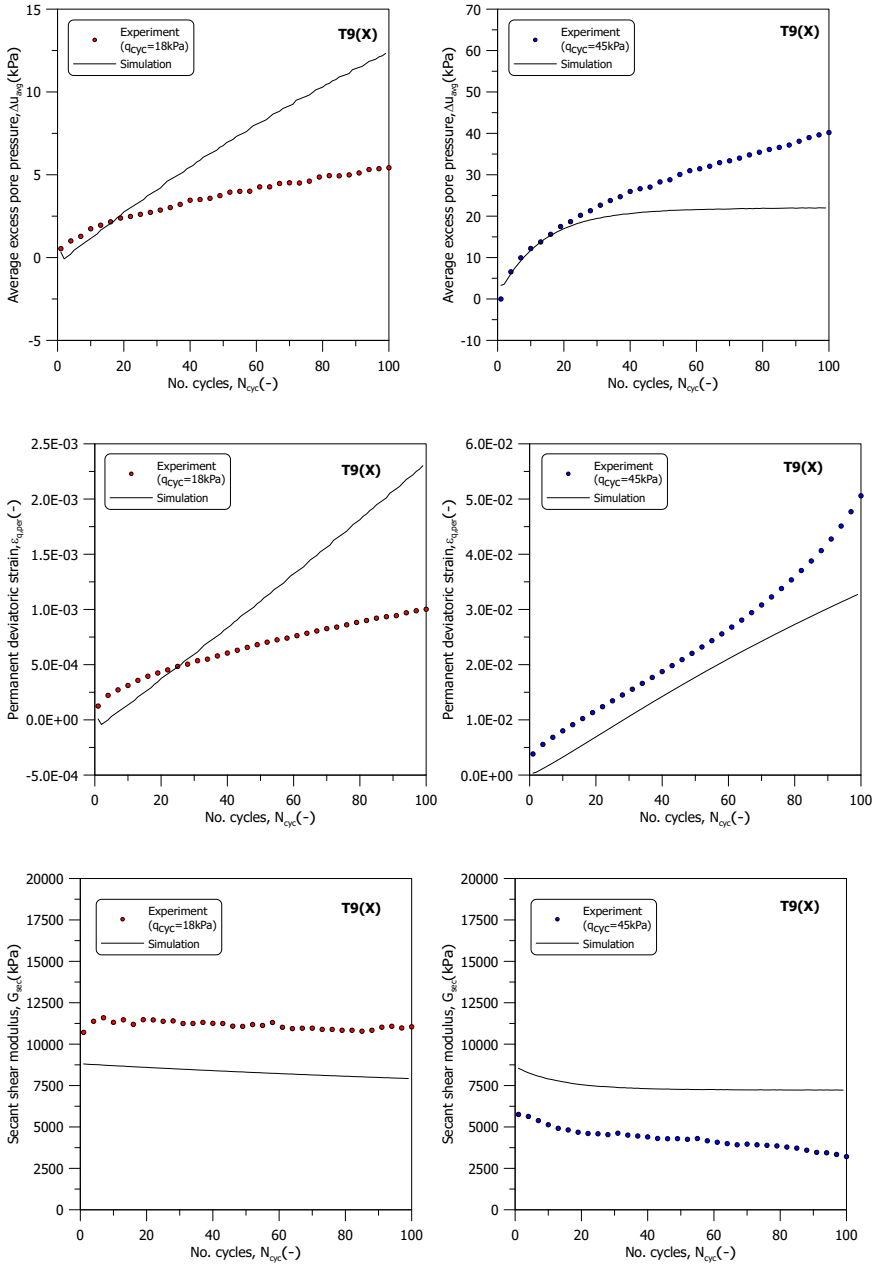

Figure 4.55: Comparison between numerical simulations and experimental data for strain-controlled cyclic shearing on T9(X) (average excess pore pressure, permanent deviatoic strain, and secant shear modulus)

The model performance is further assessed with stress-controlled cyclic tests on samples from the group (X), starting from varying initial stress states. This section will primarily focus on tests initiated on the extension side of the $p' - q$ plane.

- Sample T1(X) ($\eta_0 = -0.18$): Figure 4.56 and Figure 4.57 showcase the experimental results and numerical simulations. The model underestimates shear stiffness at a smaller cyclic amplitude (13.2 kPa) and slightly underpredicts average excess pore pressure by about 1 kPa. At higher cyclic amplitudes (33 kPa), while the secant shear modulus magnitude is well captured, the overestimated excess pore pressure leads to a faster reduction rate in the secant shear modulus. The model predicts an accumulation of deviatoric strain towards the extension side, which is also observed experimentally, particularly at the smaller amplitude. Nevertheless, the model fails to capture the evolution rate.

- Sample T2(X) ($\eta_0 = -0.5$): As depicted in Figure 4.58 and Figure 4.59, the model shows similar tendencies as observed in T1(X), underestimating shear stiffness at smaller amplitudes (13.2 kPa) but accurately capturing the accumulation of permanent deviatoric strain. At larger amplitudes (33 kPa), the model overpredicts permanent deviatoric strain after the 40^{th} cycle, although it successfully captures the excess pore pressure development for both amplitudes.

- Sample T3(X) ($\eta_0 = -0.87$): In this case, illustrated in Figure 4.60 and Figure 4.61, the model consistently underestimates excess pore pressure at both smaller and larger amplitudes. For the smaller amplitude, the predicted excess pore pressure is nearly zero, and for the larger amplitude, it incorrectly predicts negative excess pore pressure, in contrast to the positive development observed in the experiment. Shear stiffness is consistently underestimated at smaller amplitudes, while at larger amplitudes, the model overestimates the secant shear modulus, which increases with each loading cycle. This overestimation correlates with the large cyclic deviatoric strain observed in the test and the negative a_d value adopted in the simulation. Furthermore, while the model captures the general trend of deviatoric strain accumulation well before the sample loses controllability in the test, it underpredicts the permanent deviatoric strain for both cyclic amplitudes.

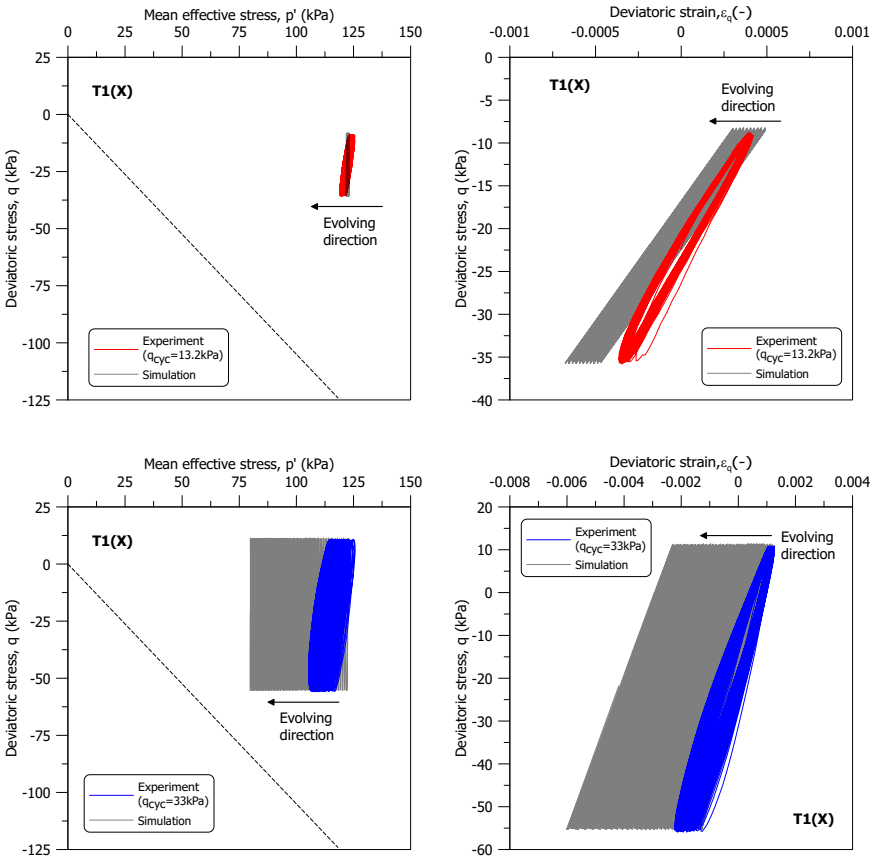

Figure 4.56: Comparison between numerical simulations and experimental data for strain-controlled cyclic shearing on T1(X) (stress path and stress-strain curve)

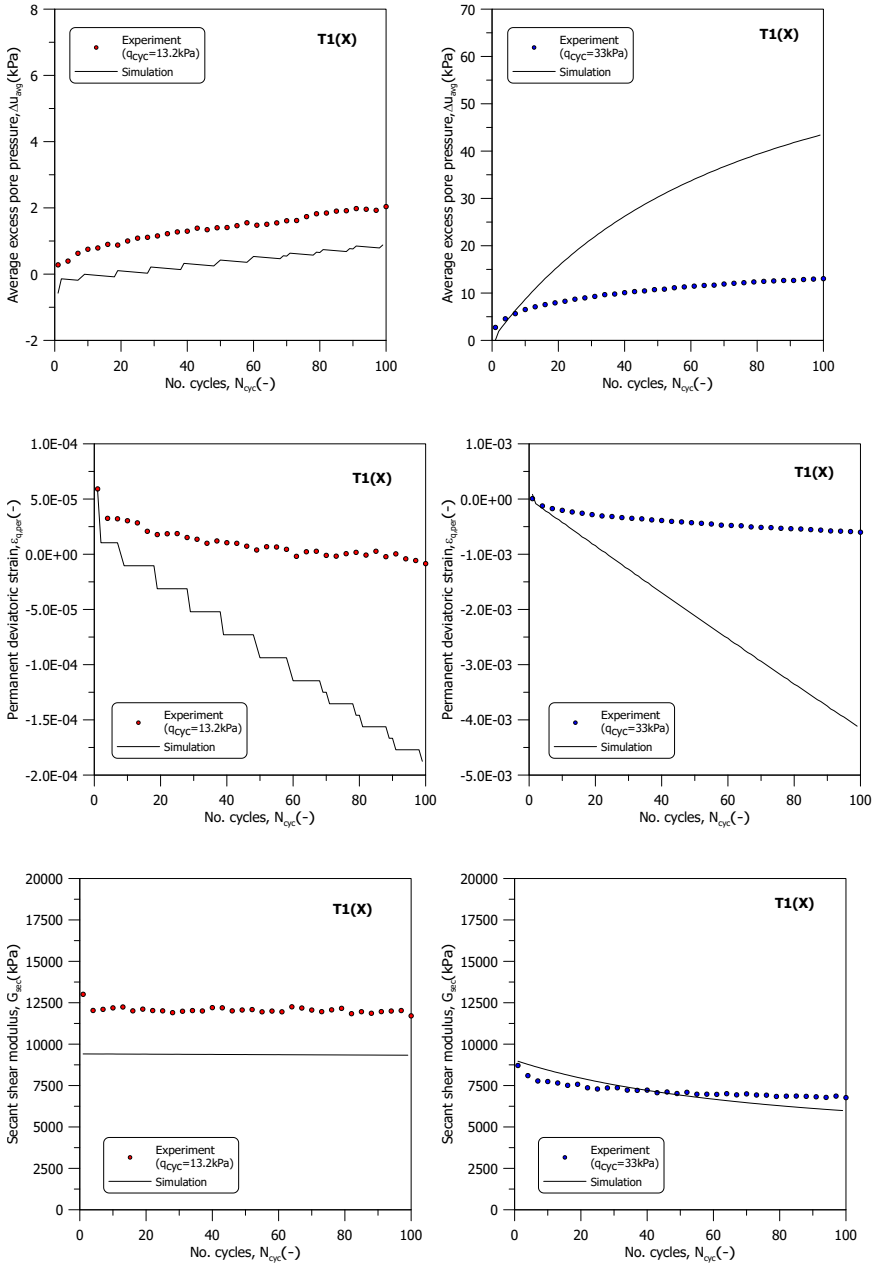

Figure 4.57: Comparison between numerical simulations and experimental data for strain-controlled cyclic shearing on T1(X) (average excess pore pressure, permanent deviatoic strain, and secant shear modulus)

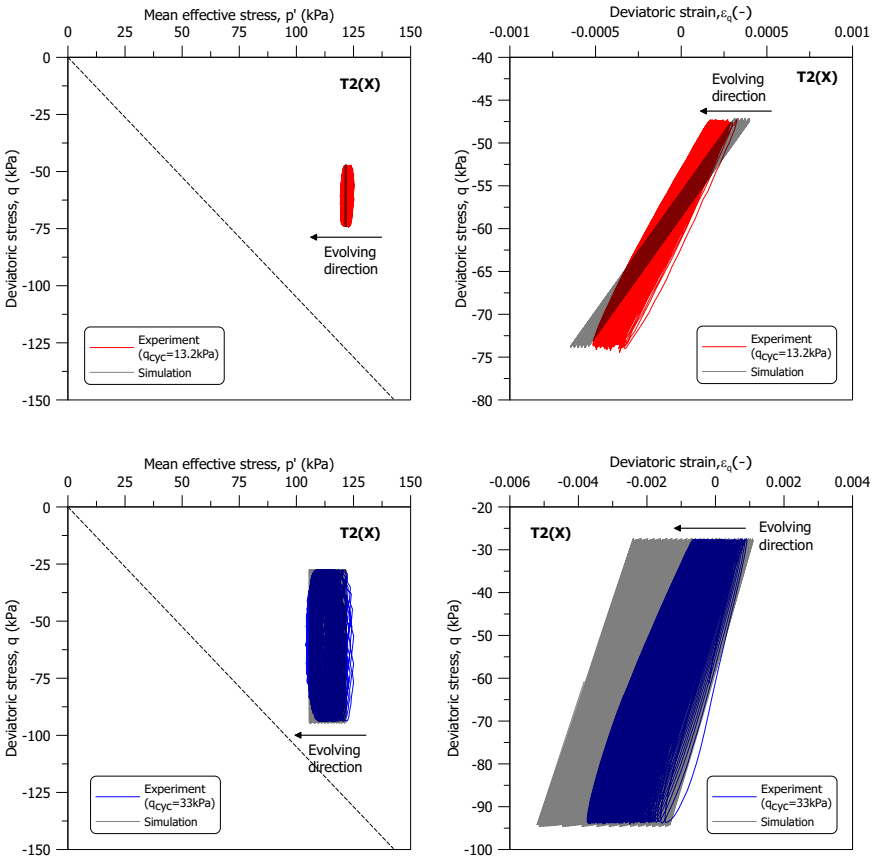

Figure 4.58: Comparison between numerical simulations and experimental data for strain-controlled cyclic shearing on T2(X) (stress path and stress-strain curve)

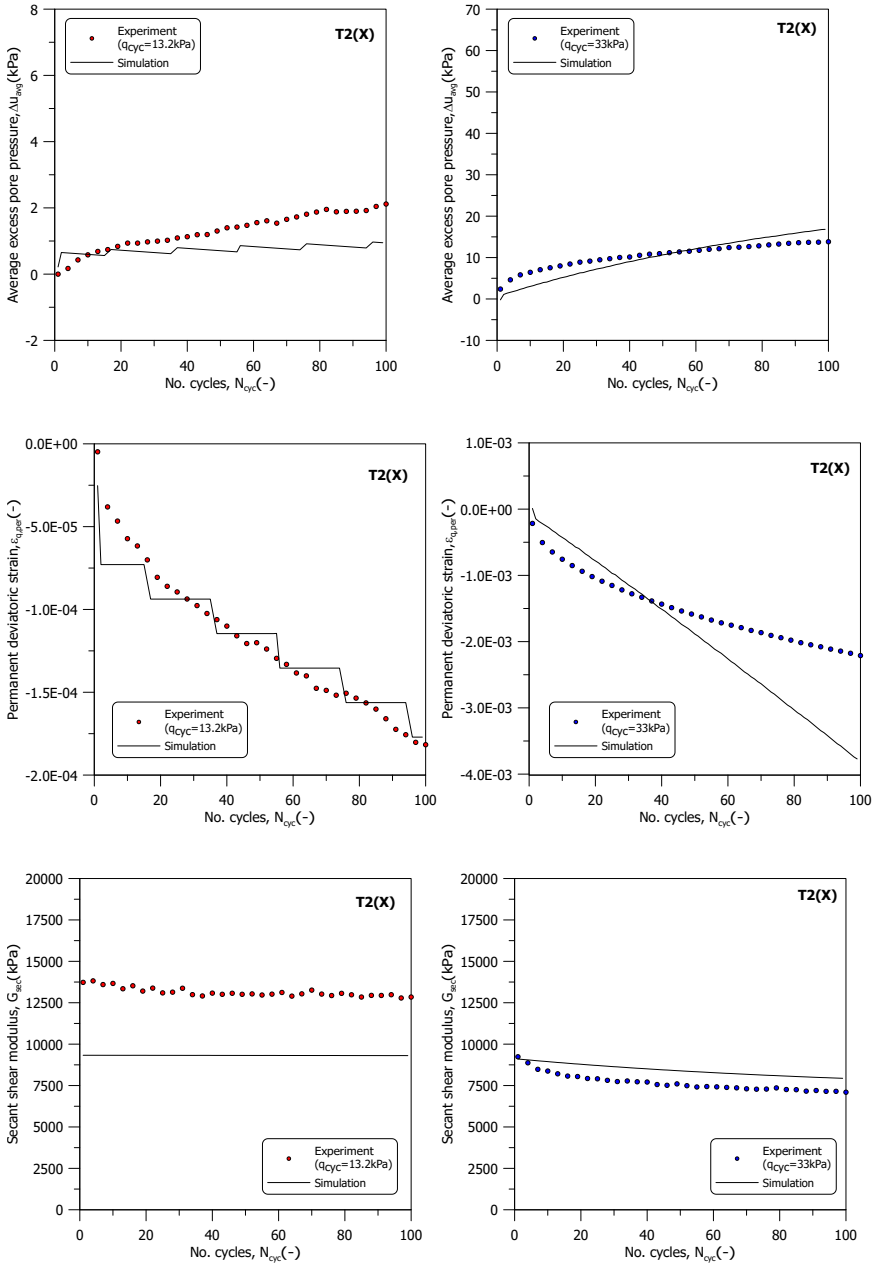

Figure 4.59: Comparison between numerical simulations and experimental data for strain-controlled cyclic shearing on T2(X) (average excess pore pressure, permanent deviatoic strain, and secant shear modulus)

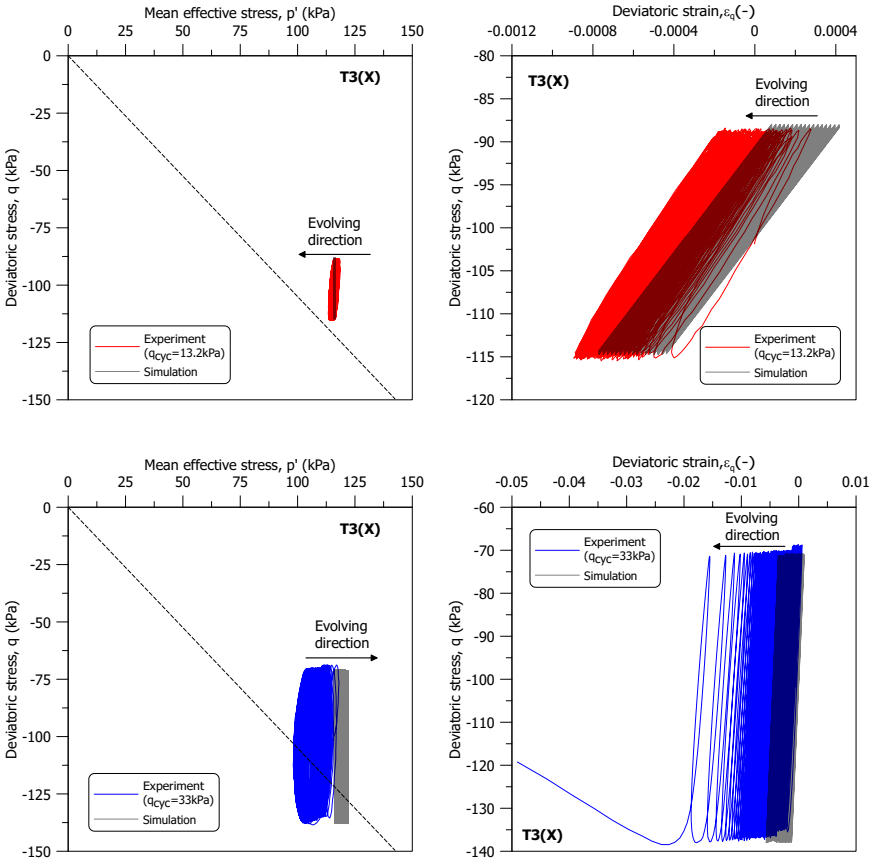

Figure 4.60: Comparison between numerical simulations and experimental data for strain-controlled cyclic shearing on T3(X) (stress path and stress-strain curve)

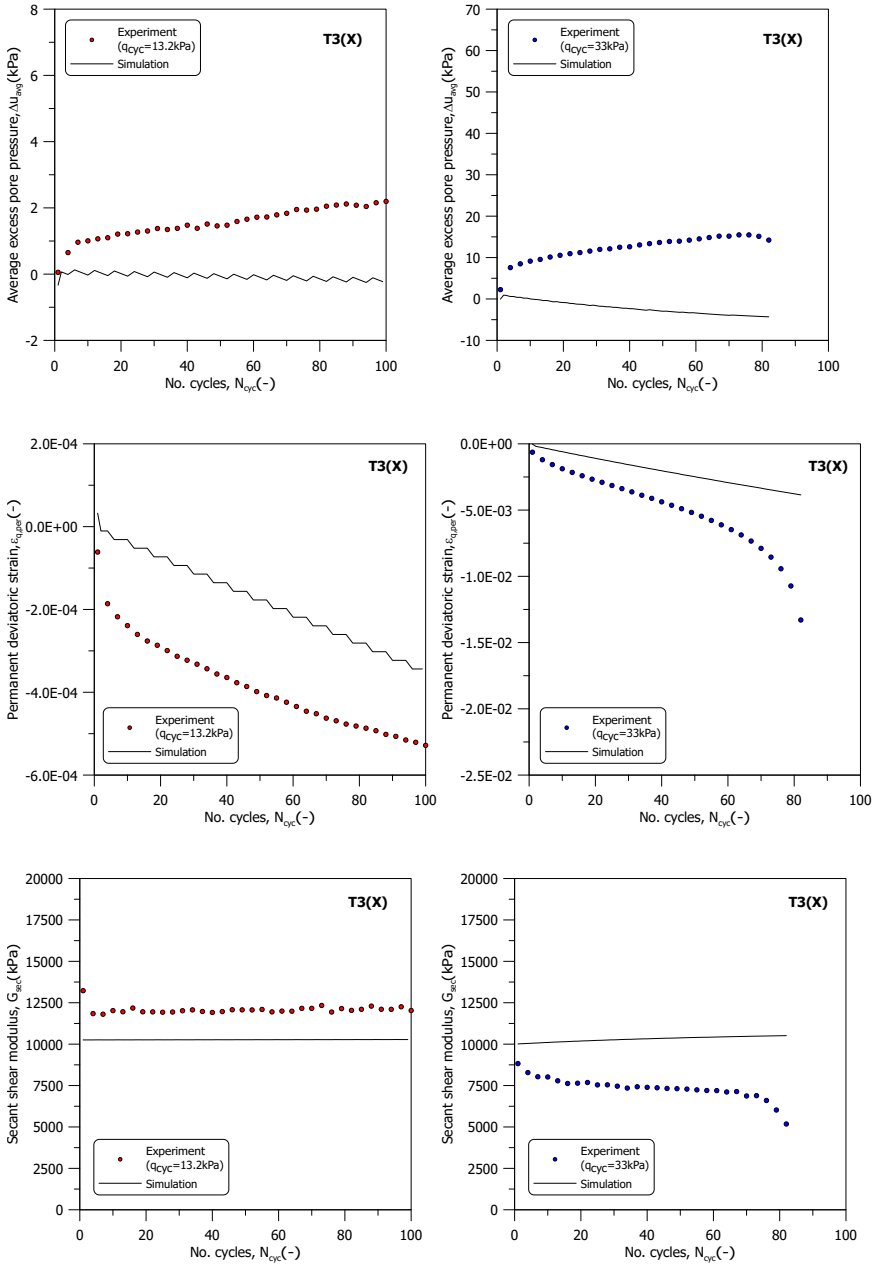

Figure 4.61: Comparison between numerical simulations and experimental data for strain-controlled cyclic shearing on T3(X) (average excess pore pressure, permanent deviatoic strain, and secant shear modulus)

In the subsequent section, the model is validated with other tests starting on the compression side of the $p' - q$ plane.

- Sample T4(X) ($\eta_0 = 0.35$): Figure 4.62 and Figure 4.63 present the experimental results and numerical simulations. The model underestimates shear stiffness at a smaller cyclic amplitude (18 kPa) and underpredicts the average excess pore pressure by about 1 kPa. At higher amplitudes (45 kPa), while the secant shear modulus evolution is well captured, the model overestimates both the excess pore pressure and permanent deviatoric strain. However, at the smaller amplitude, the model successfully depicts the trend of permanent deviatoric strain accumulation.

- Sample T5(X) ($\eta_0 = 1.11$): As shown in Figure 4.64 and Figure 4.65, the model exhibits similar behaviour to previous tests, underestimating shear stiffness at smaller amplitudes (18 kPa), but accurately capturing the excess pore pressure. The permanent deviatoric strain is significantly underpredicted, likely due to the stress state being closer to the critical state stress ratio line in triaxial compression.

- Sample T6(X) ($\eta_0 = 0.79$): Illustrated in Figure 4.66 and Figure 4.67, the model consistently underestimates excess pore pressure at both smaller (18 kPa) and larger amplitudes (45 kPa). For the smaller amplitude, the predicted excess pore pressure is nearly zero. The model also underestimates shear stiffness at smaller amplitudes, while at larger amplitudes, it overestimates the secant shear modulus, with almost no reduction across loading cycles. This discrepancy is linked to the large cyclic deviatoric strain observed in the test and the adoption of a negative a_d value in the simulation. Additionally, the model significantly underestimates deviatoric strain accumulation for both amplitudes.

To sum up, when subjected to various initial stress states, the model tends to underestimate certain characteristics, such as shear stiffness and deviatoric strain accumulation while overestimating others, like excess pore pressure and secant shear modulus at specific amplitudes. It is fairly accurate in predicting trends, but there are discrepancies in specific quantitative responses.

In addition to assessing the model's performance during the cyclic shearing stage, its efficacy is also evaluated during the post-cyclic recompression and subsequent undrained triaxial compression/extension stages for group (X) samples, provided they did not fail during the experiment. A detailed comparison between the experimental data and model simulations is presented in Figure 4.68.

During the post-cyclic recompression stage, the model consistently predicts lower recompression compared to experimental observations for all samples. These discrepancies are likely due to the under-prediction or over-prediction of excess pore pressure development during cyclic shearing, as well as uncertainties related to the post-cyclic recompression index.

The validity of the model is further tested through simulations of post-cyclic undrained triaxial compression or extension. For all tests, the peak deviatoric stress predicted by the model exceeds that of the experimental data. The simulations for samples T2(X), T4(X), T6(X), and T9(X) indicate an initially elastic response, suggesting that the pre-undrained shear stress state is within the elastic nucleus. In addition, these tests show the model

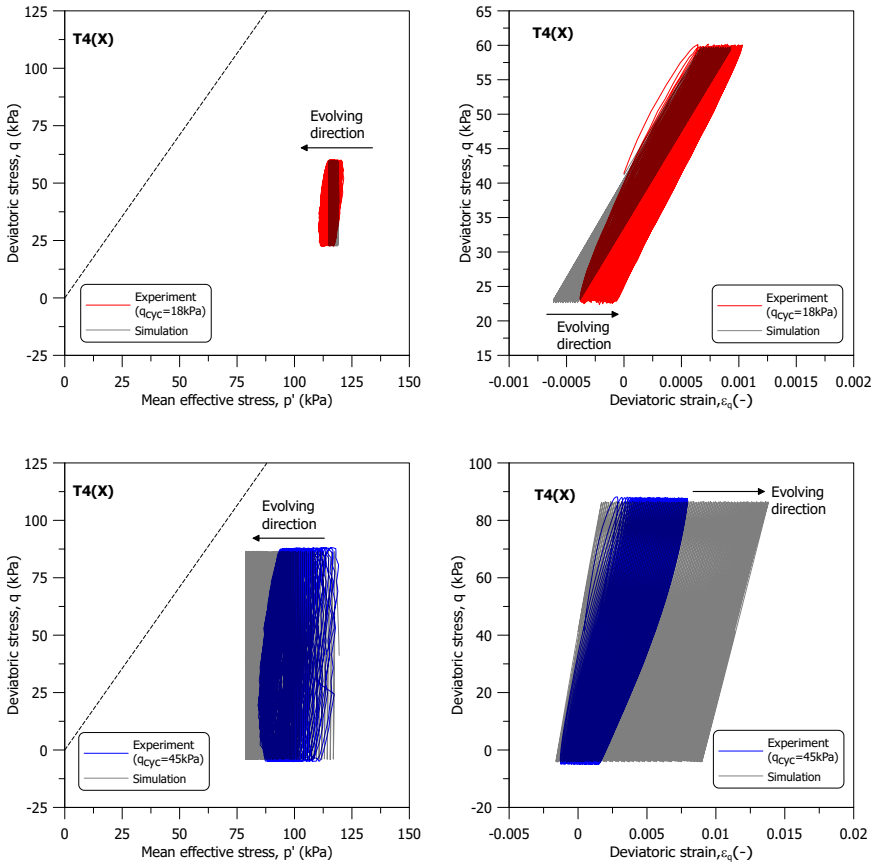

Figure 4.62: Comparison between numerical simulations and experimental data for strain-controlled cyclic shearing on T4(X) (stress path and stress-strain curve)

predicting a more dilative response, in contrast to the contractive response observed in laboratory experiments. A closer examination of samples T1(X) and T8(X), in which the undrained shearing stage is better captured, reveals an overestimation of excess pore pressure development during cyclic shearing. Following Seidalinov and Taiebat (2014), the proposed model incorporates an update to the projection centre position at every stress reversal to better capture cyclic responses. Overestimation in excess pore pressure suggests a projection centre location closer to the origin.

To the author's knowledge, the bounding surface model has not been previously validated with post-cyclic responses. A crucial aspect of the bounding surface formulation is the evolution of the projection centre position. Predicting post-cyclic responses with this model hinges critically on the stress state at the last stress reversal. An extreme case highlighting the significant impact of the projection centre position on post-cyclic response prediction is presented below.

Figure 4.69 displays both experimental data and model simulations with the projec-

tion centre positioned at the origin during the post-cyclic recompression and undrained shearing simulations. The model satisfactorily captures post-cyclic undrained behaviour; however, discrepancies exist. The peak deviatoric stress occurs earlier in the model predictions than in the experimental data, along with a slight underprediction of excess pore pressure development. Specifically, for sample T6(X), the model predicts a stiffer response compared to the test result, likely due to a larger predicted bounding surface size at the end of the cyclic shearing stage.

For sample T6(X), the model still underpredicts recompression during the post-cyclic stage. These discrepancies are attributed to both the underpredicted excess pore pressure development and a larger bounding surface. Nonetheless, the model prediction of post-cyclic response, particularly in the undrained shearing stage, shows evident improvement.

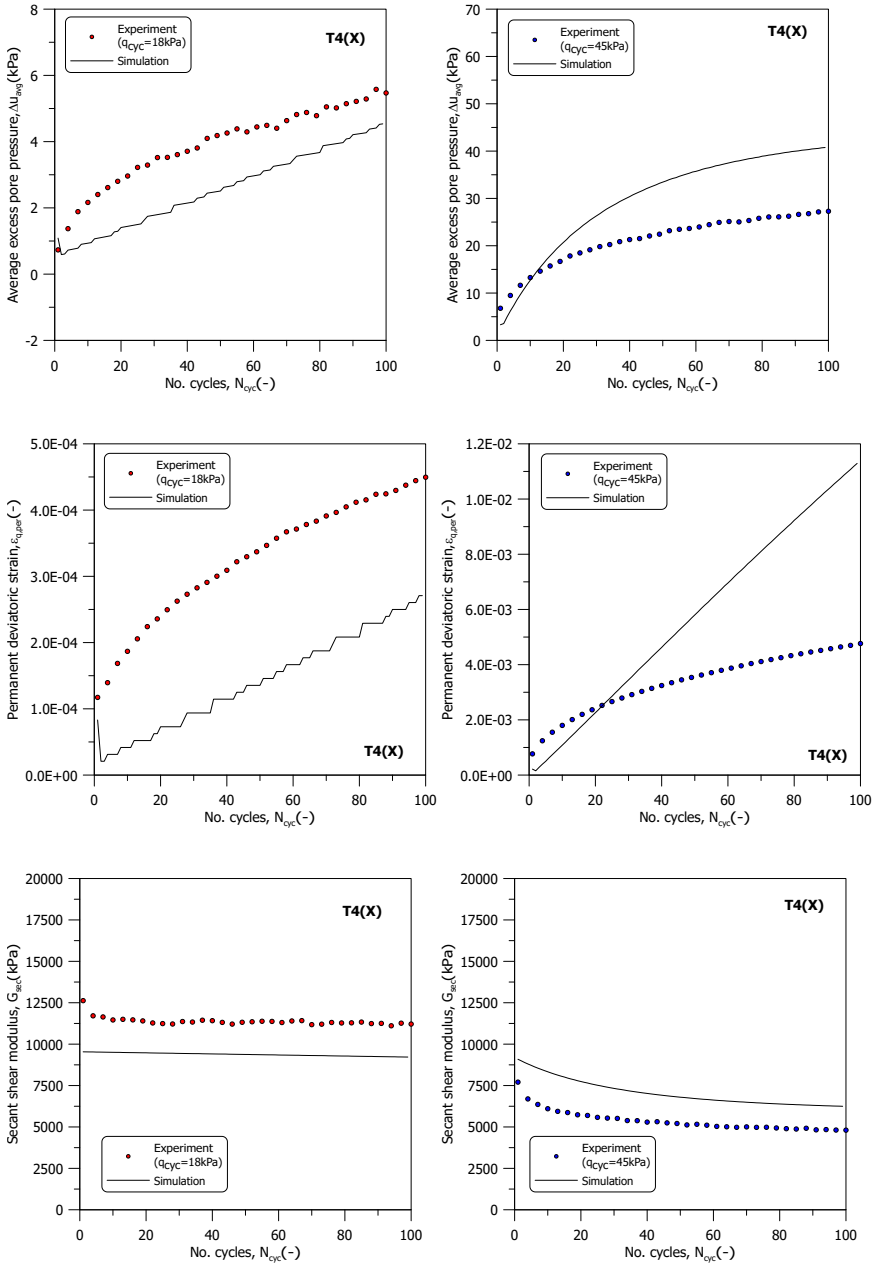

Figure 4.63: Comparison between numerical simulations and experimental data for strain-controlled cyclic shearing on T4(X) (average excess pore pressure, permanent deviatoic strain, and secant shear modulus)

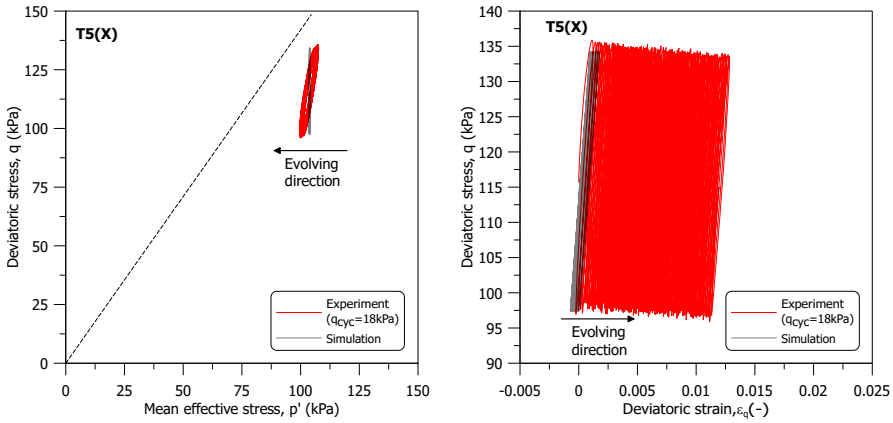

Figure 4.64: Comparison between numerical simulations and experimental data for strain-controlled cyclic shearing on T5(X) (stress path and stress-strain curve)

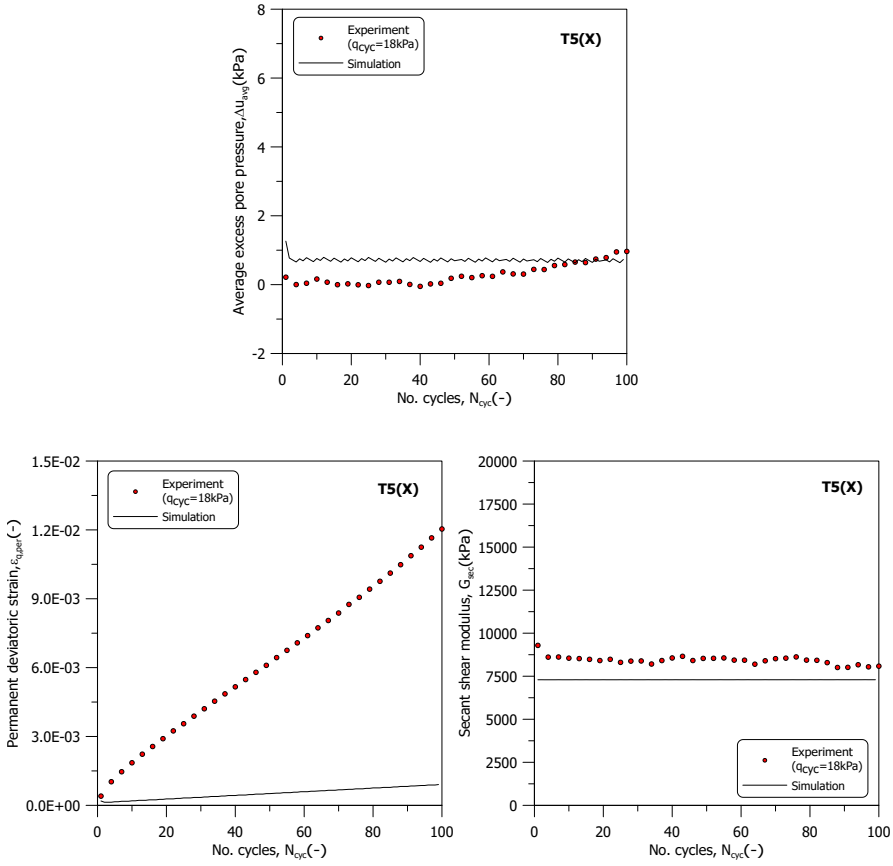

Figure 4.65: Comparison between numerical simulations and experimental data for strain-controlled cyclic shearing on T5(X) (average excess pore pressure, permanent deviatoic strain, and secant shear modulus)

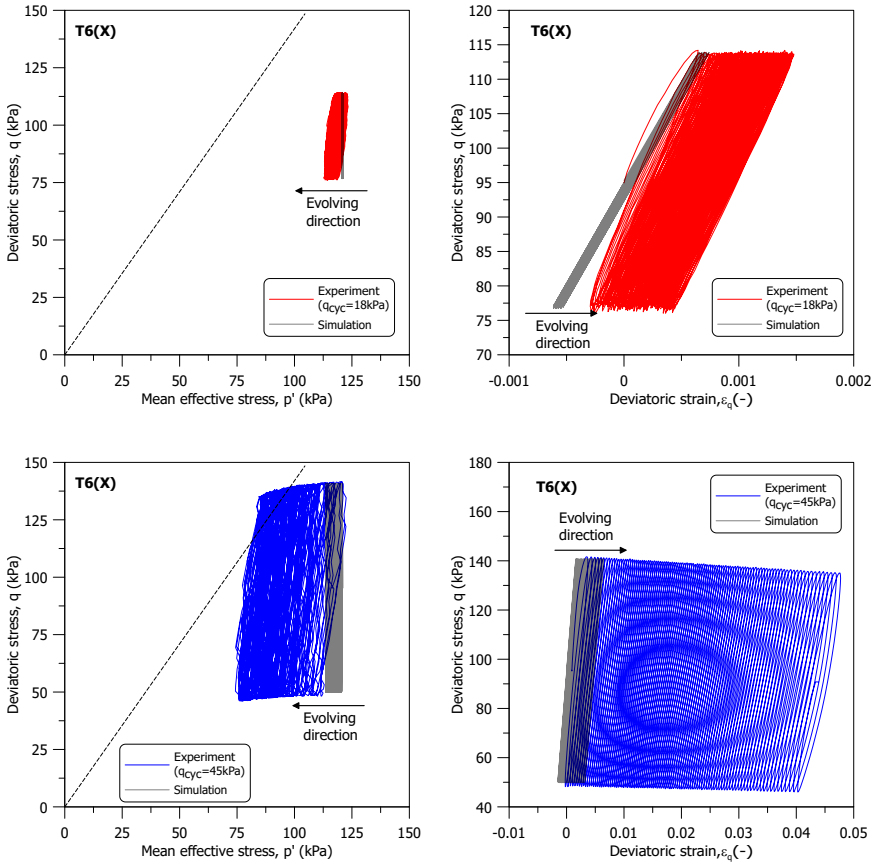

Figure 4.66: Comparison between numerical simulations and experimental data for strain-controlled cyclic shearing on T6(X) (stress path and stress-strain curve)

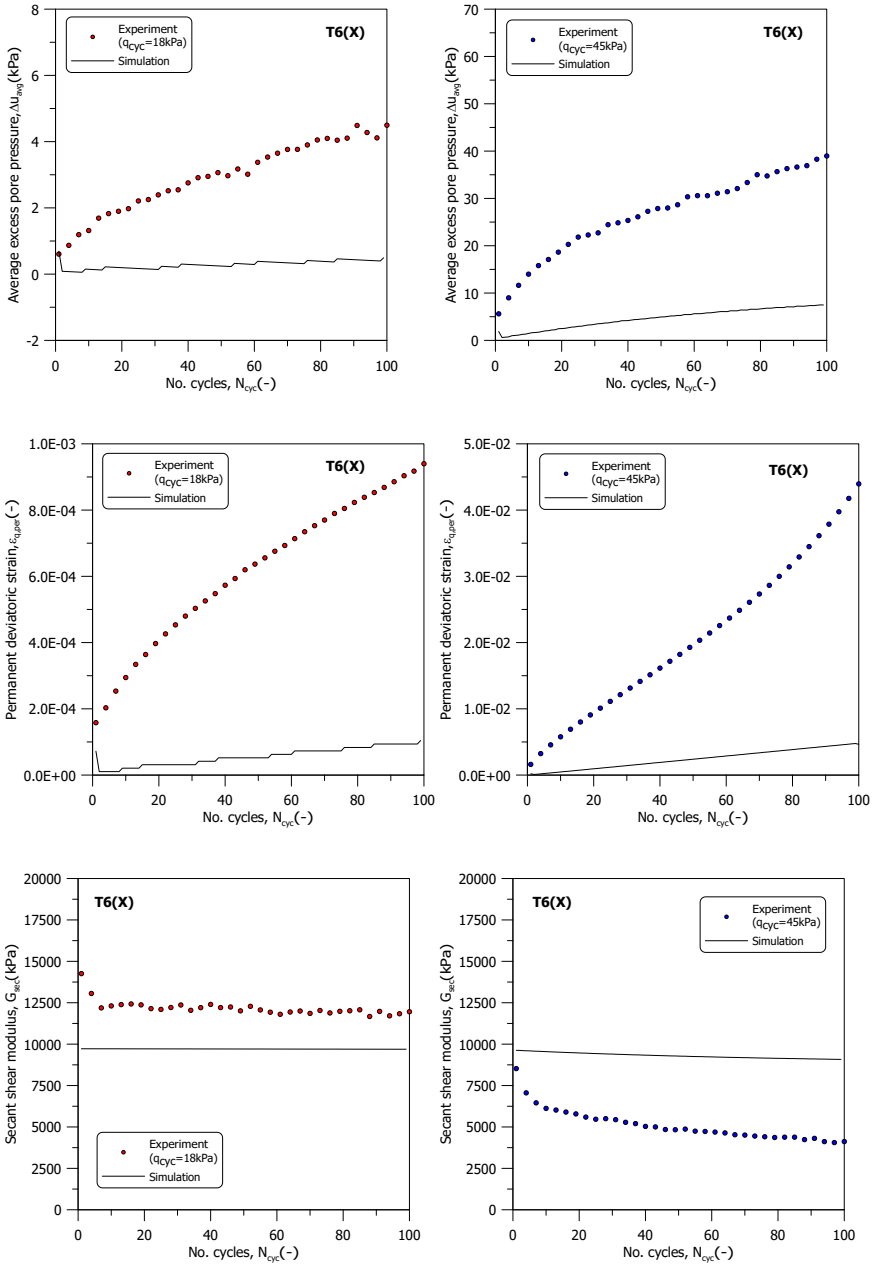

Figure 4.67: Comparison between numerical simulations and experimental data for strain-controlled cyclic shearing on T6(X) (average excess pore pressure, permanent deviatoic strain, and secant shear modulus)

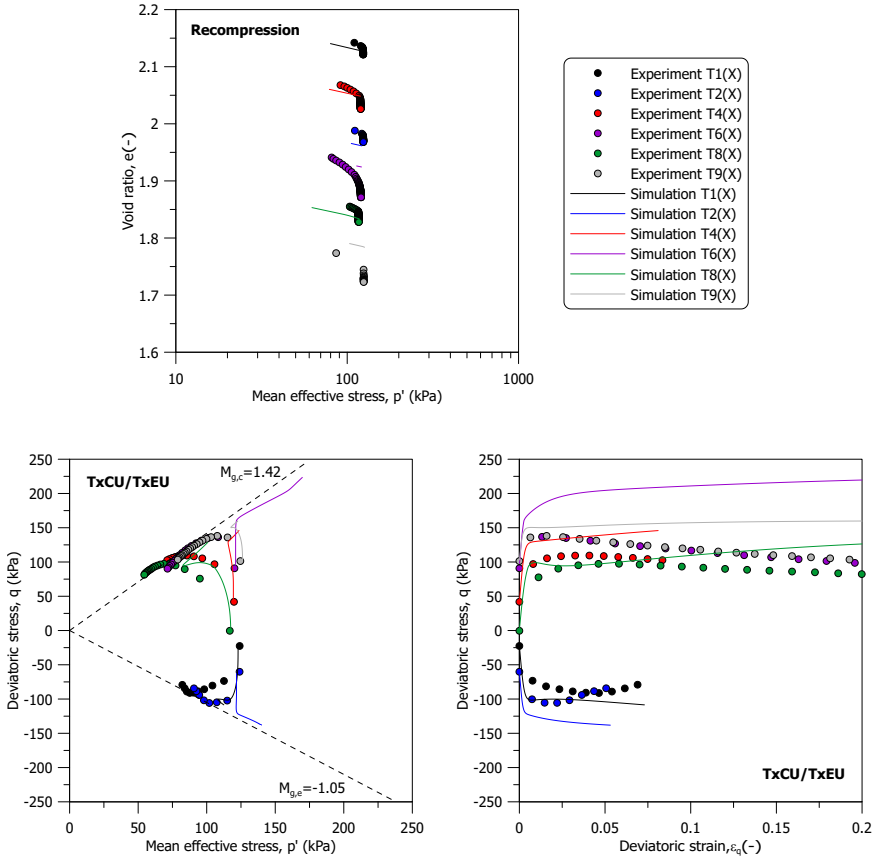

Figure 4.68: Comparison between numerical simulations and experimental data for post-cyclic recompression and triaxial undrained shearing on group (X) samples (projection centre at last stress reversal)

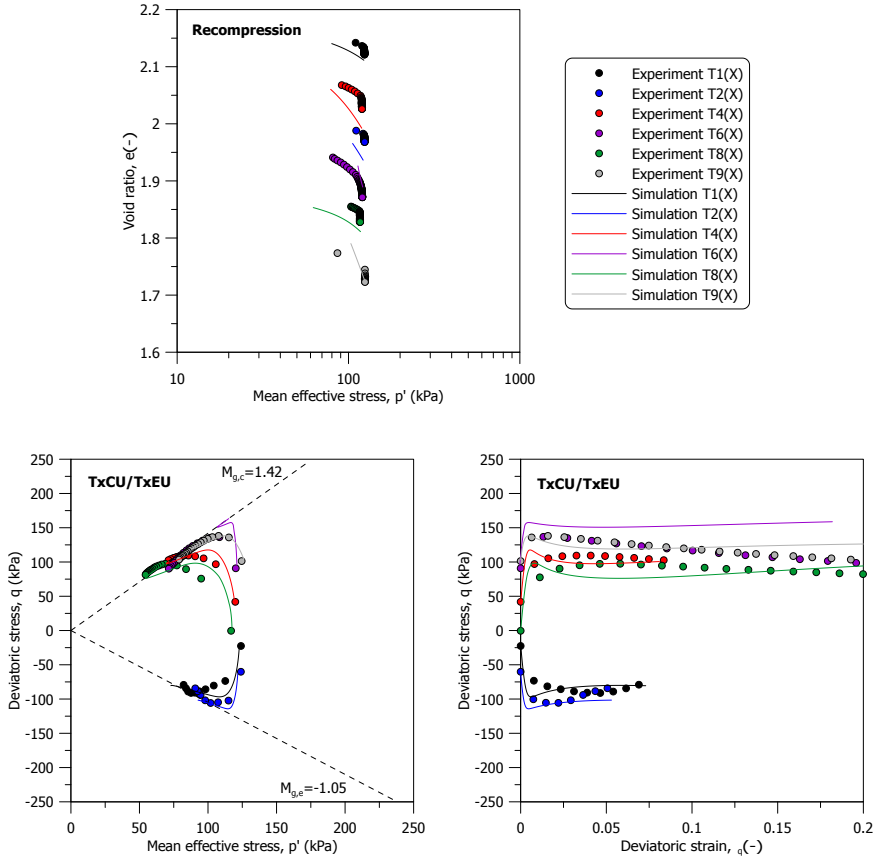

Figure 4.69: Comparison between numerical simulations and experimental data for post-cyclic recompression and triaxial undrained shearing on group (X) samples (projection centre at origin)

4.5. RATE-DEPENDENCY FEATURES OF THE MODEL FOR PRACTICAL USE

The integration of bounding surface and elastoplastic-viscoplastic formulations in the model enables it to account for rate-dependent soil behaviour. In the following section, the rate-dependency features of the model are illustrated, focusing on aspects critical to practical geotechnical design upon cyclic loadings. This includes shear modulus reduction and damping curves, which are commonly utilised in equivalent linear site-response analysis and seismic microzonation. Moreover, the model's ability to predict the number of cycles to failure at a given stress amplitude is of particular importance. This aspect serves as a vital reference for geotechnical engineers when considering cyclic loads in their designs. Typically, the determination of the number of cycles to failure is based on the magnitude of either cyclic or permanent shear strain, depending on the specific failure modes involved. The predicted cyclic or permanent shear strain by the proposed model will be presented and discussed in detail, highlighting its practical implications to estimate the number of cycles to failure.

Vucetic and Dobry (1991) developed seminal reference curves for shear modulus reduction and damping ratios applicable to both normally and over-consolidated clays, drawing on a wide range of experimental data. One critical factor influencing these curves' evolution and positioning is the plasticity index, PI. For clays with a higher plasticity index, the shear modulus reduction curves are positioned higher and exhibit a slower degradation rate in the plot. Conversely, damping ratio curves for clays with a higher plasticity index start lower and increase at a slower rate.

To showcase the JMC-clay BSEVP model capabilities, shear modulus reduction and damping ratio curves are generated based on the 5^{th} cycle loading, following the approach of Seed et al. (1986). The test type simulated is the strain-controlled cyclic triaxial test starting from an isotropic stress state. Figure 4.70 demonstrates these curves for five different h_0 values. The trends predicted by the model align closely with the findings of Vucetic and Dobry (1991). For higher h_0 values, the shear modulus reduction curves are positioned higher and degrade more slowly, while the damping ratio curves start lower and rise more gradually.

As Andersen (2015) highlights, both permanent and cyclic shear strains are crucial considerations in geotechnical design dealing with cyclic loads. The capability of the model to predict permanent and cyclic shear strains is assessed using stress-controlled cyclic triaxial tests, which also start from an isotropic stress state. Figure 4.71 illustrates the permanent and cyclic deviatoric strains as predicted by the proposed model for various h_0 values. It should be noted that the cyclic deviatoric strain is computed as the average of the peak and trough cyclic deviatoric strains within each cycle. Consistent with expectations, the results show that both permanent and cyclic deviatoric strains increase as the h_0 values decrease.

A key feature of the proposed model is its rate-dependency. The shear modulus reduction and damping ratio curves generated under various loading frequencies are demonstrated in Figure 4.72. With increasing loading frequencies, the shear modulus reduction curves are positioned higher, and the damping ratio curves start lower, rising more gradually. However, the rate of shear modulus reduction across different loading

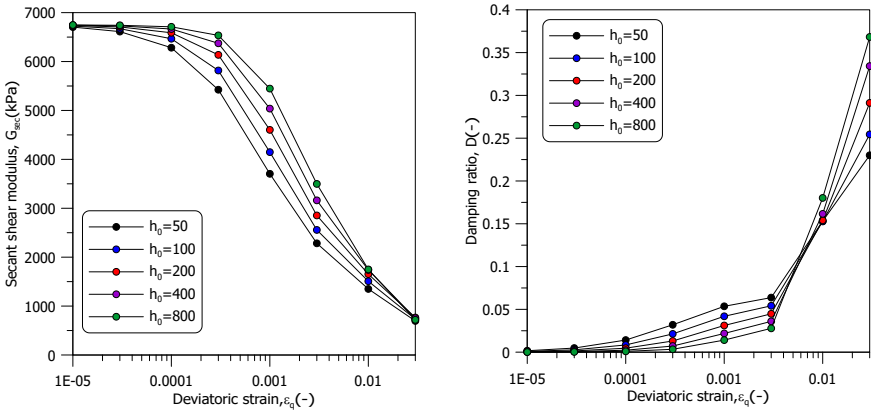

Figure 4.70: Secant shear modulus and damping ratio curves predicted by the proposed model for different h_0 values

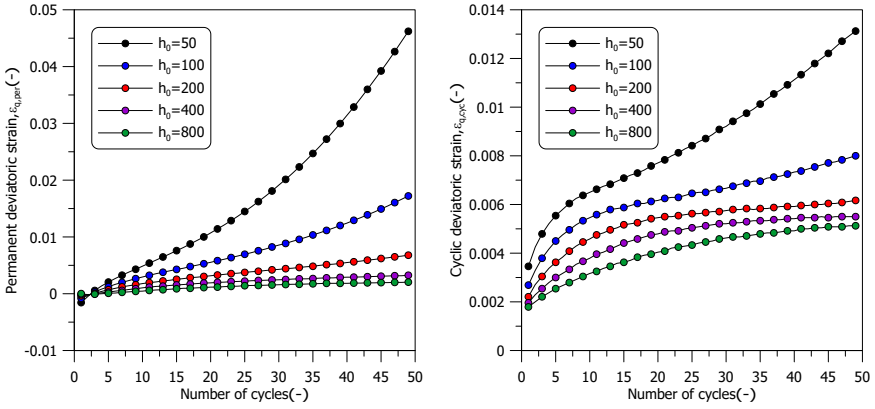

Figure 4.71: Permanent and cyclic deviatoric strain predicted by proposed model for different h_0 values

frequencies is not markedly pronounced. Additionally, the differences between the shear modulus reduction and damping ratio curves for loading frequencies above 0.001Hz are relatively minor, which can be attributed to the strain-rate 'saturation' phenomenon previously mentioned.

The rate-dependency of permanent and cyclic shear strains is further illustrated in Figure 4.73. Interestingly, the permanent deviatoric strain decreases with lower loading frequencies, while the cyclic deviatoric strain increases under these conditions. This observation is in line with findings from Li et al. (2011), who reported an increase in single amplitude deviatoric strain with reduced loading frequency in cyclic triaxial tests on K_0 consolidated natural marine clay. A closer examination of the peak and trough deviatoric strains predicted by the proposed model for different loading frequencies, as shown in Figure 4.74, reveals that while the permanent deviatoric strain is lower at a 10^{-5} Hz loading frequency, the amplitude of cyclic shear strains is higher. This can be explained by

the reduced shear modulus at lower loading rates. Huang et al. (2022) observed a similar trend in the evolution of cyclic deviatoric strain in their simulation of undrained cyclic triaxial tests on marine clays, although their findings on permanent deviatoric strain development contrast with the predictions of the proposed model.

It is important to note that the experimental programme by Li et al. (2011) and Huang et al. (2022) focused on one-way cyclic triaxial tests, whereas the results from the proposed model are based on two-way cyclic triaxial tests. In practice, the number of cycles to failure is typically determined when the permanent or cyclic shear strain exceeds a certain threshold. According to the model predictions in Figure 4.73, failure at high loading rates is predominantly governed by permanent shear strain, while at low loading rates, failure may be more triggered by cyclic shear strain. However, the impact of loading frequency on permanent and cyclic shear strains, considering different cyclic shearing modes and pre-shearing stress states, warrants further investigation.

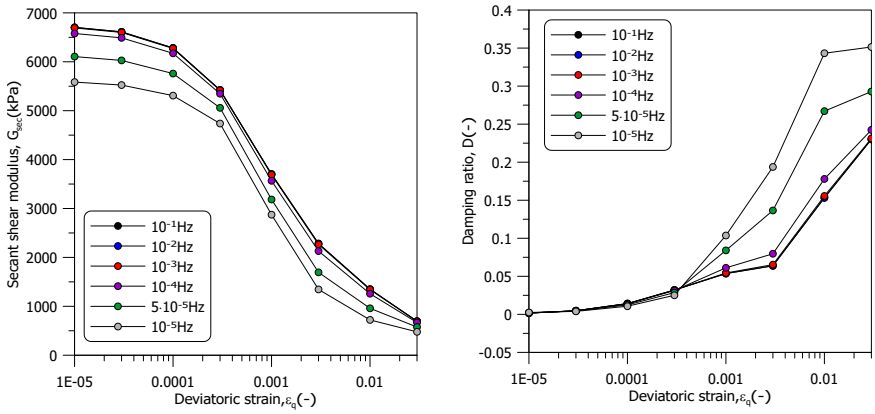

Figure 4.72: Secant shear modulus and damping ratio curves predicted by the proposed model for different loading frequencies

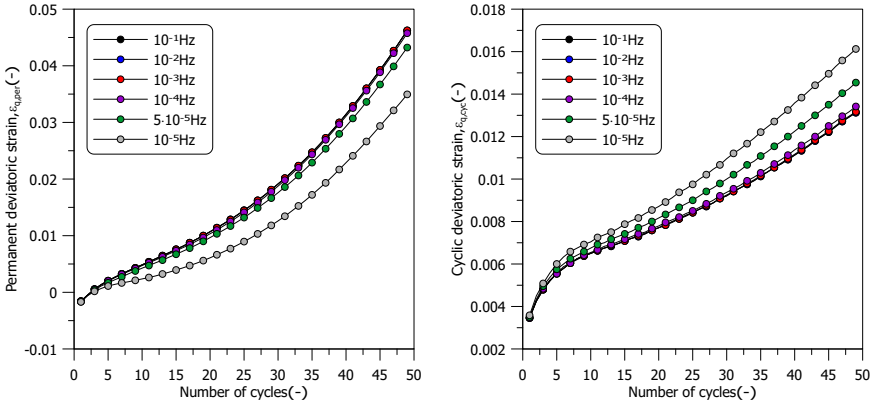

Figure 4.73: Permanent and cyclic deviatoric strain predicted by the proposed model for different loading frequencies

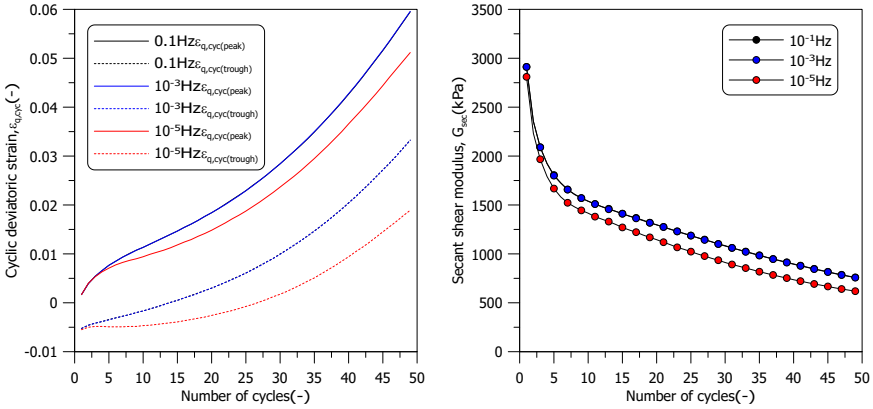

Figure 4.74: Cyclic deviatoric strain and secant shear modulus predicted by the proposed model for different loading frequencies

4.6. DISCUSSION AND CONCLUSIONS

The core of the proposed JMC-clay elastoplastic-viscoplastic model is the evolution of the overstress function. The influence of parameters s_v and V on the overstress function is direct; reducing either parameter increases the function's magnitude. However, the parameter n, which determines the exponent for the 'normalised overstress' ($\Delta\sigma^*$), has a variable impact on the viscoplastic response depending on the value of $\Delta\sigma^*$. As n increases, its effect on the overstress function's magnitude can be positive, neutral, or negative. This complicates the model calibration, as the contribution of n is stress path dependent. Based on the sensitivity analysis performed on cyclic response prediction, a default value of 1 is suggested for the parameter n. However, further experimental investigation is needed to study its role when adopting Perzyna's approach for rate-dependent soil behaviour modelling.

By integrating elastoplastic-viscoplastic bounding surface formulations into the JMC-clay model, the total parameter count rises from 12 to 19, including four from bounding surface formulation (h_0, a_d, s_{eln}, and w), and three from elastoplastic-viscoplastic formulation (s_v, V, and n). The JMC-clay (EP) parameters, which are relatively insensitive to rate, are calibrated using static laboratory tests. Fast cyclic triaxial tests are essential for the additional parameters, including both isotropic and K_0 consolidated samples. The default values for several parameters to facilitate initial calibration are proposed. A minimum of six specific tests are recommended for comprehensive calibration. The model calibration involves iterative parameter adjustments to closely match experimental observations of stress paths, stress-strain curves, secant shear modulus, and excess pore pressure development.

A comprehensive sensitivity analysis clarifies the impact of the new model parameters, including those related to the bounding surface, on the predicted cyclic response. This analysis underlines the significance of viscoplastic parameters, particularly s_v, in defining the viscoplastic zone size and bounding surface evolution. The choice of viscoplastic parameters also affects the apparent slope of the normal compression line and the apparent pre-consolidation pressure. Therefore, the selection of λ^* should account for the time-dependent response of soil. The hybrid flow rule parameter w is crucial for addressing early stabilisation in stress paths and excess pore pressure development. However, its selection should match experimental observation, as it also changes the predicted deviatoric response. The damage parameter a_d significantly influences deviatoric responses, affecting peak deviatoric stress and shear modulus reduction. Extreme values of a_d should be avoided as they induce unrealistic model prediction. This analysis also examines the effects of cyclic stress amplitude and initial stress state on soil behaviour. As the level of stress increases, there is a corresponding increase in both the permanent deviatoric strain and excess pore pressure. Based on the simulation results, tests starting from a K_0 stress state show a lower average excess pore pressure but a higher permanent deviatoric strain. These findings are in line with experimental data. Additionally, the evolution of anisotropy, updates to the projection centre, and Lode angle dependency are also shown to be crucial in model predictions.

The difference in calibrated BSEVP parameters between the soil of groups (IX) and (X) emphasises the relatively strong influence of differing soil properties, such as clay content and plasticity index. These variations significantly impact cyclic response char-

acteristics, corroborating previous literature. The 'structure number' (SN) concept, correlating with rate-dependence in soil behaviour, further supports these findings.

The JMC-clay BSEVP model evaluation on samples from groups (III) to (IX) shows advancements in predictive accuracy, particularly in simulating the cyclic behaviour of organic clay. Key successes include accurate predictions of stress path evolution, excess pore pressure, and secant shear modulus variations, validated through tests Cyc T1(IX), Cyc T2(IX), and Cyc T2(VII). However, the model slightly overestimates peak deviatoric stress in static tests and diverges in stress-strain response for Cyc T2(IX), possibly due to sample anisotropy. The model performance in predicting damping ratio evolution and secant shear modulus magnitude suggest areas for refinement. Discrepancies observed in the post-cyclic recompression phase, attributed to factors like the recompression index uncertainty and underestimation of excess pore pressure, indicate a need for model adjustments to more accurately incorporate these aspects.

Evaluating the JMC-clay BSEVP model on group (X) samples offers insights into its predictive capabilities and limitations. In static probe paths, the model effectively captures changes in loading rate during unloading and reloading, especially as seen in sample T1(X). However, it tends to overestimate deviatoric strain, likely influenced by its calibration based on specific cyclic loading frequencies. The model performance varies across different stress probe paths and cyclic loading conditions, showing better accuracy for stress states close to isotropic and K_0 conditions, which are the ones selected for calibration.

The model response on group (X) samples is nuanced: it underestimates shear stiffness at smaller cyclic amplitudes but predicts the secant shear modulus more accurately at higher amplitudes. Additionally, discrepancies in permanent deviatoric strain and excess pore pressure development are evident, particularly for those starting at an initial stress ratio far from K_0 and isotropic conditions. Key areas for refinement include:

- Strain-amplitude dependent shear modulus: The model reasonably captures shear stiffness at higher amplitude, but it tends to underestimate the shear modulus compared to experimental observations. It suggests that strain-amplitude dependency is needed.

- Overstress function: The predicted response is significantly affected by the evolution of the overstress function, requiring further investigation and refinement, especially for different initial stress states.

- Hybrid flow rule: The excess pore pressure prediction relates to the parameter w, which is currently constant in the model. The dependency of w on the stress path or current stress state needs further study. Including the deviatoric component of the current stress state in the hybrid flow rule might improve model predictions of deviatoric response.

The model exhibits efficacy in simulating the cyclic behaviour of group (X) samples, yet it shows discrepancies with experimental results in the post-cyclic recompression and undrained shearing stages. These discrepancies likely stem from the underprediction of excess pore pressure development during cyclic shearing, the uncertainty in the

post-cyclic compression index, and the evolution of the projection centre position. Improved predictions with the projection centre at the origin for post-cyclic stages suggest a need to further investigate and refine the projection centre evolution.

The proposed model is able to generate typical shear modulus reduction and damping curves, as reported in the literature, which is crucial for engineering practice. The model displays rate-dependent characteristics when generating these curves under different loading frequencies. Given the coupled elastoplastic-viscoplastic framework, minor differences in the curves are observed at frequencies above 0.001Hz, likely due to strain-rate saturation. However, further experimental validation is needed at higher loading frequencies to ascertain if this saturation is a limitation of the constitutive framework or a characteristic of soil behaviour.

The model ability to predict both cyclic and permanent shear strains at varying loading frequencies is another critical aspect. The parameters and pre-shearing stress state adopted for demonstration indicate that at high loading rates, failure is predominantly governed by permanent shear strain, while at low loading rates, failure is more likely due to cyclic shear strain. This highlights the need for further research into the impact of loading frequency on these strains under different cyclic shearing modes and pre-shearing stress states.

This chapter not only outlines the current capabilities and limitations of the proposed model in capturing soil behaviour under static, cyclic, and post-cyclic loading but also sets the stage for further refinement. By addressing identified gaps, particularly in small strain stiffness, stress-state dependency of the overstress function, the hybrid flow rule, and projection centre positioning, future work can enhance the model's accuracy and reliability for practical applications in geotechnical engineering. This research contributes valuable insights into the model's validity and provides a foundation for continued development and validation against a broader range of experimental data.

BIBLIOGRAPHY

Andersen, K. H. (2015). Cyclic soil parameters for offshore foundation design. *Frontiers in offshore geotechnics III*, *5*.

Bjerrum, L. (1967). Engineering geology of norwegian normally-consolidated marine clays as related to settlements of buildings. *Geotechnique*, *17*(2), 83–118.

Burland, J. (1990). On the compressibility and shear strength of natural clays. *Géotechnique*, *40*(3), 329–378.

Dobry, R. (1987). Dynamic properties and seismic response of soft clay deposits. *Proc. Int. Symp. on Geotech. Engrg. of Soft Soils*, *2*, 51–87.

Graham, J., Crooks, J., & Bell, A. L. (1983). Time effects on the stress-strain behaviour of natural soft clays. *Géotechnique*, *33*(3), 327–340.

Huang, Z., Shi, L., Sun, H., & Cai, Y. (2022). A simple bounding surface elasto-viscoplasticity model for marine clays under monotonic and cyclic loading. *Ocean Engineering*, *266*, 113129.

Jiang, J., Ling, H. I., Kaliakin, V. N., Zeng, X., & Hung, C. (2017). Evaluation of an anisotropic elastoplastic–viscoplastic bounding surface model for clays. *Acta Geotechnica*, *12*, 335–348.

Kaliakin, V. N. (1991). Application of the elastoplastic-viscoplastic bounding surface model to cyclic loading.

Kaliakin, V. N., & Dafalias, Y. (1990a). Theoretical aspects of the elastoplastic-viscoplastic bounding surface model for cohesive soils. *Soils and foundations*, *30*(3), 11–24.

Kaliakin, V. N., & Dafalias, Y. (1990b). Verification of the elastoplastic-viscoplastic bounding surface model for cohesive soils. *Soils and Foundations*, *30*(3), 25–36.

Leroueil, S., Kabbaj, M., Tavenas, F., & Bouchard, R. (1985). Stress–strain–strain rate relation for the compressibility of sensitive natural clays. *Géotechnique*, *35*(2), 159–180.

Li, L.-L., Dan, H.-B., & Wang, L.-Z. (2011). Undrained behavior of natural marine clay under cyclic loading. *Ocean Engineering*, *38*(16), 1792–1805.

Nieto-Leal, A., & Kaliakin, V. N. (2021). Additional insight into generalized bounding surface model for saturated cohesive soils. *International Journal of Geomechanics*, *21*(6), 04021068.

Perzyna, P. (1966). Fundamental problems in viscoplasticity. *Advances in applied mechanics*, *9*, 243–377.

Rezania, M., Taiebat, M., & Poletti, E. (2016). A viscoplastic saniclay model for natural soft soils. *Computers and Geotechnics*, *73*, 128–141.

Seed, H. B., Wong, R. T., Idriss, I., & Tokimatsu, K. (1986). Moduli and damping factors for dynamic analyses of cohesionless soils. *Journal of geotechnical engineering*, *112*(11), 1016–1032.

Seidalinov, G., & Taiebat, M. (2014). Bounding surface saniclay plasticity model for cyclic clay behavior. *International Journal for Numerical and Analytical Methods in Geomechanics*, *38*(7), 702–724.

Sheahan, T. C. (2005). A soil structure index to predict rate dependence of stress-strain behavior. In *Geomechanics: Testing, modeling, and simulation* (pp. 81–97).

Sheahan, T. C., Ladd, C. C., & Germaine, J. T. (1996). Rate-dependent undrained shear behavior of saturated clay. *Journal of Geotechnical Engineering*, *122*(2), 99–108.

Shi, Z., Finno, R. J., & Buscarnera, G. (2018). A hybrid plastic flow rule for cyclically loaded clay. *Computers and Geotechnics*, *101*, 65–79.

Vaid, Y. P., & Finn, W. L. (1979). Static shear and liquefaction potential. *Journal of the Geotechnical Engineering Division*, *105*(10), 1233–1246.

Vucetic, M., & Dobry, R. (1991). Effect of soil plasticity on cyclic response. *Journal of geotechnical engineering*, *117*(1), 89–107.

Yasuhara, K., & Andersen, K. H. (1991). Recompression of normally consolidated clay after cyclic loading. *Soils and Foundations*, *31*(1), 83–94.

Yasuhara, K., Murakami, S., Toyota, N., & Hyde, A. F. (2001). Settlements in fine-grained soils under cyclic loading. *Soils and Foundations*, *41*(6), 25–36.

Zienkiewicz, O. C., Humpheson, C., & Lewis, R. (1975). Associated and non-associated visco-plasticity and plasticity in soil mechanics. *Geotechnique*, *25*(4), 671–689.

5

BEYOND CONVENTIONAL TESTING: A NOVEL CYCLIC MULTIDIRECTIONAL SHEAR DEVICE

If I had asked people what they wanted, they would have said faster horses.

Henry Ford

Part of this chapter was published as a paper in the Journal of Physics: Conference Series (Vol. 2647, No. 14, p. 142006) entitled "Development of an earthquake simulator for soft soils: Multidirectional Shear Testing Device".

5.1. ABSTRACT

Testing soils for earthquake and dynamic loads requires advanced equipment able to assess the effects of hydro-mechanical coupling on the soil response. The majority of laboratory element tests are either 'slow tests', which intend to approach drained conditions throughout the soil sample in order to obtain reliable pore water pressure measurements, or 'fast undrained tests', where non-uniform pore pressure distribution appears. However, many natural loads, including earthquakes, impose a wide range of high loading frequencies, typically triggering a partially drained response in the field. Although the rate effect plays an important role in soil behaviour, its investigation is hindered by the limitations of existing equipment. In addition, the ability to apply multidirectional loading to soil elements in the laboratory is important to fully understand the soil response under earthquakes. Currently, multidirectional simple shear devices are used to study the soil behaviour under earthquake loadings. Nevertheless, many shear devices experience non-uniformities in stresses and strains. These non-uniformities arise from imperfect boundary conditions in the experimental setup (e.g., rough porous stone), large deformations, and hydro-mechanical coupling under cyclic loading, which can potentially lead to misinterpretation of data and hinder the development of constitutive models. This Chapter presents an innovative multidirectional shear device developed in the Geo-engineering section at TU Delft, which can apply higher loading frequencies compared to previous equipment and a wider variety of multidirectional cyclic loading patterns. The apparatus is equipped with several advanced sensors, also developed at TU Delft, to capture the local response of specimens. The sensors are installed to reduce a priori assumptions on the soil response, better interpret the element experimental results and further investigate the rate effect of applied loading. Preliminary performance test results are provided to illustrate the complex load conditions which can be achieved. Lastly, validation tests on Dutch organic clay samples are presented to demonstrate the capabilities and limitations of the new equipment.

5.2. INTRODUCTION

In the Netherlands, the Groningen gas field has been a source of induced seismic activity, with the highest recorded magnitude reaching M_L 3.6 at Huizinge. Although the magnitudes of these induced earthquakes are relatively low compared to natural events, they can still cause significant damage to buildings and infrastructure. This is due to their shallow depths and the high site amplification in areas with soft soils (van Thienen-Visser and Breunese, 2015). To precisely assess the risks associated with these recurring, low-magnitude induced seismic events—which are characterised by a higher frequency content compared to the natural ones (as shown in Figure 5.1)—it is crucial to deepen our understanding of the behaviour of soft soils under such conditions. Gathering reliable experimental data is key for studying soil response to induced seismicity and for developing accurate constitutive models. Advanced testing equipment capable of assessing hydro-mechanical coupling effects on soil response is essential for these investigations.

Triaxial devices are frequently employed in these types of studies, mainly due to the ease of sample preparation, direct pore pressure measurement, and the ability to control both vertical and horizontal stresses, allowing for a wide range of stress paths prior to cyclic shearing. However, these devices are limited in that they only apply cyclic loads in the vertical direction, which may not fully capture the complexities of real-world earthquake loading scenarios. For a more comprehensive understanding, it is vital to consider the effects of multidirectional loading. Numerous studies have shown that soil response is influenced by loading from multiple directions (Rutherford, 2012; Matsuda et al., 2013; Matsuda et al., 2016; Nhan and Matsuda, 2016; Yang et al., 2016).

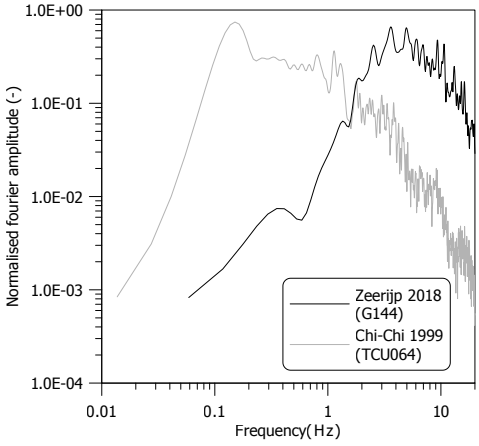

Figure 5.1: Fourier response spectrum of induced (Zeerijp 2018) and natural (Chi-Chi 1999) earthquake

Direct simple shear (DSS) equipment is also frequently used to study soil behaviour under cyclic and dynamic loading. The design of DSS devices inherently allows for multidirectional loading capabilities. Several multidirectional DSS systems have been developed to investigate soil behaviour under seismic loads. The initial results were not completely satisfactory due to various difficulties encountered in the development of the equipment. Jaime (1975) highlighted the overestimation of the shear strains in a two-directional cyclic simple shear because of mechanical compliances. Ishihara and Yamazaki (1980) introduced a multidirectional simple shear apparatus with cell pressure and back pressure control, which allows direct pore pressure measurement. These authors encountered issues related to top cap rocking and significant mechanical friction. Boulanger et al. (1993) designed and fabricated the UCB-2D apparatus, which significantly reduced the mechanical compliances. In addition, the machine adopted high-capacity pneumatic servo valves to provide quick response to control signals. Duku et al. (2007) described a servo-hydraulic, digitally controlled multidirectional simple shear device, able to reproduce realistic earthquake histories with a strain-controlled procedure and were able to minimise the cross-coupling effect between the two horizontal loading axes. However, the installation of a dual-axis load cell to obtain post-friction force measurement was found to increase mechanical compliance. Rutherford and Biscontin (2013) developed a multidirectional simple shear system together with a multi-axis load cell. The system allows back pressure saturation and can apply complicated loading pattern such as circular or eight-shaped.

Since then, several commercial multidirectional simple shear equipment have been made available (Rudolph et al., 2014; Li et al., 2017), however, they are typically limited to a range of frequencies with a maximum of 5 Hz. Shafiee et al. (2017) improved the apparatus built by Duku et al. (2007) so that the device can apply realistic earthquake loadings with stress controlled. Recently, Bhaumik et al. (2023) presented a new multidirectional simple shear device based on the design of Rutherford and Biscontin (2013). The major advantages over the previous systems are the capability of imposing real-time, not scaled-down, realistic earthquake loadings and the possibility of measuring shear wave velocity with bender elements.

The limitations of simple shear devices are inherited by the previous multidirectional simple shear equipment (Lucks et al., 1972; Shen et al., 1978; Vucetic and Lacasse, 1982; Saada et al., 1983; Budhu, 1984; Budhu, 1985; Budhu and Britto, 1987; DeGroot et al., 1994; Reyno et al., 2005). The primary drawback of these devices is the inability to control the shear stress acting on the specimen lateral side, which prevents a uniform stress/strain state, despite the common assumption. Considering the higher compressibility of soft soils, stress and strain non-uniformities are anticipated to be more pronounced. Figure 5.2 presents a monotonic direct simple shear (DSS) simulation performed in ABAQUS, using the JMC-clay model calibrated for Dutch organic soft clay. The results clearly demonstrate strain localisation. Moreover, in traditional simple shear apparatus, an equivalent 'constant volume' condition is adopted by constraining the lateral boundary using stacked rings or reinforced membranes and maintaining the sample height to reproduce undrained conditions (Vaid and Finn, 1979). The equivalent pore pressure is derived from changes in applied total vertical stress. Dyvik et al. (1987) concluded that the equivalent 'constant volume' produces results akin to truly undrained

tests on normally consolidated Drammen clay. However, a recent study on sand suggests that the conventional approach for determining equivalent pore pressure in constant volume tests conflicts with the fact that pore pressure is isotropic (Ghafghazi et al., 2023). Additionally, conventional setups cannot measure lateral stresses, leaving a gap in knowledge regarding the stress state and stress path of the sample.

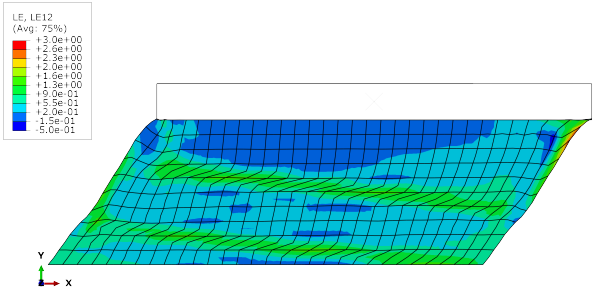

Figure 5.2: Strain localisation in DSS simulation on Dutch organic soft soil

Accurate measurement of pore water pressure is crucial in testing soils, due to the need of evaluating the hydro-mechanical coupling soils response. With a traditional setups, pore water pressure is obtained through either the change of vertical stress in constant height tests (direct simple shear device) or by using a pressure transducer installed at the bottom of the sample (triaxial apparatus). To ensure a uniform distribution and reliable measurement of pore water pressure, tests must be conducted at a sufficiently slow pace (Boulanger and Idriss, 2004). The specific speed depends on the hydraulic conductivity and the size of the sample being tested, as per the assumptions of an element test. However, recent studies have shown that equalisation of pore water pressure may be very difficult to achieve in soft soils, even under a monotonic loading programme (Jommi et al., 2021). This is a significant concern, particularly given the high loading frequency of earthquakes, under which rate effects play an important role on the response of soft soils (Bjerrum, 1967; Graham et al., 1983; Sheahan et al., 1996). To fully understand the cyclic behaviour of organic soft soils, 'fast' tests are also crucial.

The limitations of existing cyclic shearing systems and the importance of understanding soft soils behaviour under cyclic/dynamic conditions, have led to the design and manufacturing of a new cutting-edge dynamic equipment to investigate the multidirectional hydro-mechanical coupled response of the soft soils found in the Netherlands' deltaic regions. Considering the high compressibility of soft soils, as well as the added complexities due to multidirectional cyclic loading, achieving uniform strain, stress states, and pore water pressure presents a formidable challenge. This makes it difficult, if not impossible, to adhere to the conventional assumption of treating the sample as an element test. To address these challenges, this thesis introduces a new concept for apparatus design. The aim is to minimise the influence of the experimental setup as much as possible, while maximizing data collection from the tested sample. Advanced numerical back-analysis methods are then employed to recover the true material behaviour. This concept is illustrated in Figure 5.3.

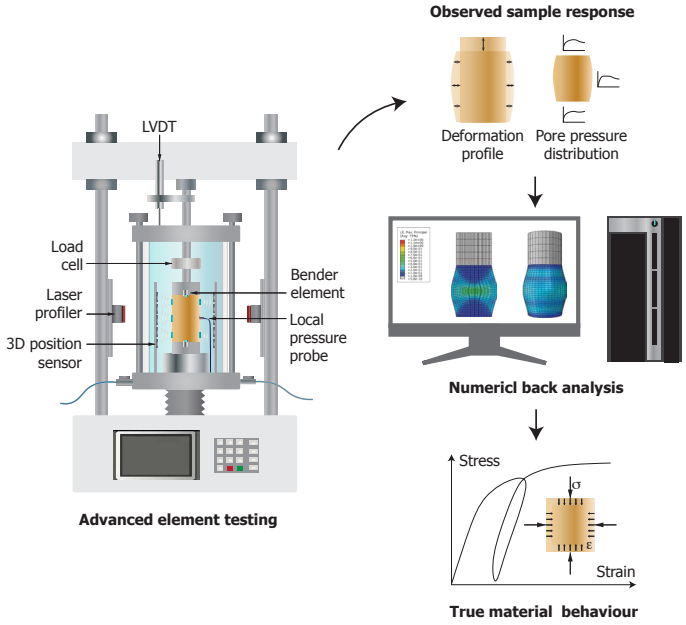

Figure 5.3: Design concept of the new apparatus.

The newly developed apparatus, termed CYC-DoSS (Cyclic-Dynamic Shearing System for Organic Soft Soils), aims to overcome the limitations inherent in existing cyclic shearing systems. These systems typically suffer from mechanical compliance and limited capabilities in capturing fast phenomena. CYC-DoSS allows for higher loading frequencies of up to 20 Hz and provides precise measurements of stress, strain, and pore water pressure. These measurements are achieved under a range of loading rates, from slow to fast, thanks to advanced sensors that are custom-built in-house. This Chapter presents the innovative multidirectional shear testing device developed in the Geo-engineering section at TU Delft, which has the following features:

1. digitally controlled, servo-hydraulic actuators in the x, y, and z axis
2. capability to reproduce the real-time history of earthquakes
3. automatic control of cell and back pressure, enabling versatile stress paths
4. in-house developed local response sensors providing comprehensive information on the hydro-mechanical coupled response
5. *P*-wave and *S*-wave bender element measurement, to complement the information on the small-strain response.

5.3. DESCRIPTION OF THE EARTHQUAKE SIMULATOR FOR SOFT SOILS

The impact of bidirectional shaking on the settlement of dry sands was assessed by Pyke et al. (1975). In the study, the authors used a small shaking table placed horizontally atop a larger one. This design remains a crucial reference point for apparatus involving multidirectional simple shear loading. The CYC-DoSS adopts the same mechanical layout for its simplicity and effectiveness. The CYC-DoSS apparatus consists of six main subsystems, including (1) loading and mechanical components; (2) hydraulic power supply unit; (3) cell pressure and back pressure controllers; (4) control and data acquisition units; (5) bender elements unit; and (6) local response sensors. The primary loading and mechanical components of the CYC-DoSS device are illustrated in Figure 5.4.

The pressure chamber houses a horizontal shaking table at its bottom, connected to two horizontal hydraulic actuators. A vertical actuator links to the top cap within the chamber. The hydraulic power supply unit boasts a maximum output of 45 kW, and its oil tank has a capacity of 150 litres, enabling a stable working pressure of 25 MPa to be supplied to the actuators.

Control of cell pressure is managed by a pneumatic pressure controller, while back pressure/volume within the soil sample is regulated via a water pressure/volume controller. The control and data acquisition units feature a computer, microcontrollers for hydraulic servo valves, and a data acquisition device with analogue output capabilities.

Additionally, the setup incorporates a bender elements unit, comprising a master signal conditioner integrated with an oscilloscope, as well as two bender elements located in the top and bottom caps. Local response sensors within the CYC-DoSS system include fibre optic pore pressure transducers, accelerometers, and contactless displacement sensors.

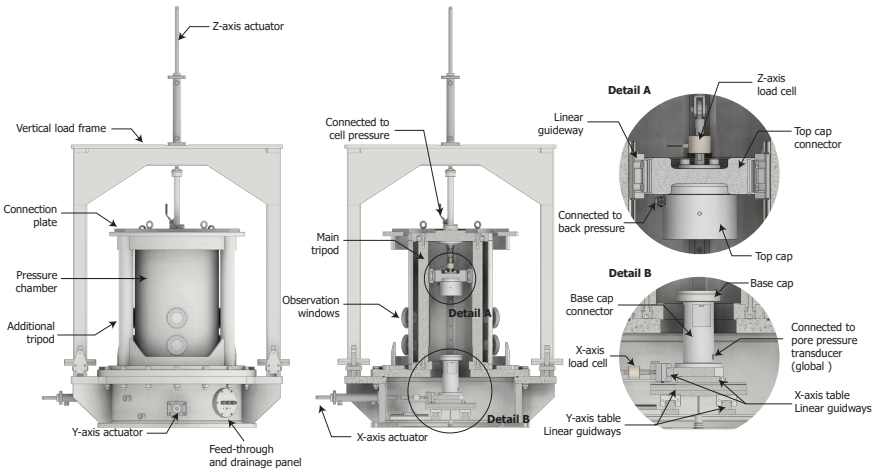

Figure 5.4: Illustration of the loading and mechanical components of CYC-DoSS

5.3.1. LOADING AND MECHANICAL SYSTEM

The loading and mechanical system consists of two primary components: the vertical load frame and the horizontal shaking platform. A Z-axis actuator with a cross-sectional area of 290 mm^2 is mounted on top of the load frame and can apply a vertical force of up to 7.2 kN to the soil sample through a top cap connector (refer to Detail A in Figure 5.4). This top cap connector assembly is linked to low-friction linear guideways situated on the main tripod (also see Detail A in Figure 5.4). The main tripod is interconnected with an additional tripod via a top connection plate, a design that enhances rotational stiffness and reduces the likelihood of lateral movement and top cap rocking.

The actuator possesses a total stroke of 200 mm (±100 mm), allowing for the accommodation of a sample up to 250 mm in height, making the device suitable for use as a cyclic triaxial device. Driven by a hydraulic servo valve (HSV-1) with a 40 L/min flow rate, the limiting factors of the actuators at high loading frequencies (> 15 Hz) are the hydraulic pump pressure capacity and the mass of the moving assembly (Duku et al., 2007). Consequently, the top cap assembly is composed of aluminium to reduce the mass. In addition, a miniature submersible load cell with a capacity of ±5 kN is employed for the Z-axis load cell. This load cell, weighing approximately 0.07 kg, is significantly lighter than traditional submersible load cells (~ 1 kg). To mitigate the impact of lateral forces on the load cell reading, a pin connector is employed to link the load cell to both the top cap assembly and the load ram. The load cell accuracy is ±0.5% of full scale, equivalent to ±3.18 kPa for a 100 mm diameter sample. Compared to the values reported by other researchers (Boulanger et al., 1993; Bhaumik et al., 2023), this error margin is larger. To improve the accuracy, either a load cell with a lower capacity or a calibration for a specific loading range can be employed. The Z-axis displacement is measured by a potentiometer with a 200 mm range and an accuracy of 0.05%.

The horizontal forces are applied with two hydraulic actuators, which are perpendicular to each other. They have the same cross-section area and maximum capacity as the Z-axis one. The actuators with a stroke of 100 mm (±50 mm) are controlled by two independent hydraulic servo valves with 40 L/min flow rate (HSV-2 and HSV-3). The Y-axis actuator is connected to the lower table and is lying on low-friction guideways. On top of the Y-axis table, the X-axis table is mounted on another set of low-friction guideways, as shown in Figure 5.5. Two independent servo valves allow moving the shaking platform to any position on the horizontal plane. The shaking platform is connected to the base cap. The specification of the two horizontal load cells is the same as the vertical one. Pin connectors are also used to connect the load cells to shaking tables, thereby minimising the influence of off-axis forces on the load cell readings. The X and Y axis displacements are measured by a potentiometer with a 100 mm range and an accuracy of 0.07%.

The friction forces of the guideways in the X, Y, and Z axis, without the sample mounted, are around 9 N, 12 N, and 7 N, equivalent to 1.15 kPa, 1.53 kPa, and 0.89 kPa on a 100 mm diameter sample. The friction calibration allows load readings correction when testing at low stress levels. As an alternative, a multi-axis load cell mounted above/below the sample could have been adopted to obtain post-friction loads (Duku et al., 2007; Rutherford and Biscontin, 2013; Bhaumik et al., 2023). Nevertheless, calibration of the friction load was preferred to the latter solution because of the increased mechanical compliance observed with a multi-axis load cell (Duku et al., 2007).

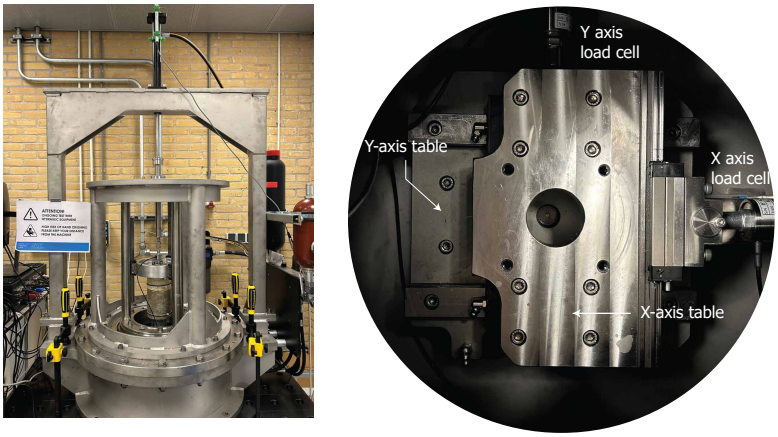

Figure 5.5: CYC-DoSS device and shaking platform of CYC-DoSS device

The cross-coupling effect in multidirectional shear devices refers to the impact of movement along one axis on the movement occurring along another axis (Duku et al., 2007). To assess the cross-coupling effect in CYC-DoSS, two harmonic waves were used to investigate different motion effects. The first harmonic wave featured a 5 mm amplitude at a frequency of 0.5 Hz to study the effects of slow yet high-amplitude motion. The second wave had a 1 mm amplitude at a 10 Hz frequency to explore the implications of fast yet low-amplitude motion.

For the slow-motion case, results are presented in Figure 5.6(a) and 5.6(b). When the X-axis table was moved, no noticeable impact was observed on the Y-axis displacement and load readings. Conversely, when the Y-axis table was moved, almost no displacement was measured on the holding axis. However, a 3 N variation was recorded in the X-axis load reading, which is logical given that the X-axis table is mounted on the Y-axis table.

For the fast-motion case, results are shown in Figure 5.7(a) and 5.7(b). Similar to the slow-motion case, no noticeable impact on the Y-axis displacement and load readings was observed when the X-axis table was moved. However, a 2 N variation was recorded in the X-axis load reading when the Y-axis table was moved, suggesting that this variation is related to the displacement amplitude of the motion. These observations collectively indicate that the CYC-DoSS system exhibits minimal cross-coupling effects.

5.3.2. CELL PRESSURE AND BACK PRESSURE CONTROLLER

The CYC-DoSS provides control over both cell and back pressures by means of a pressure chamber. The pressure chamber, constructed from stainless steel, has a maximum design pressure of 500 kPa. It is filled with water, and air pressure is applied on top of the cell using a pneumatic controller (GDSPPC) from GDS Instruments. The compressibility of air serves to minimise fluctuations in cell pressure as the load rams reciprocate during testing. Additionally, the more rapid response time of the pneumatic controller, compared to that of a water pressure controller, enables the application of

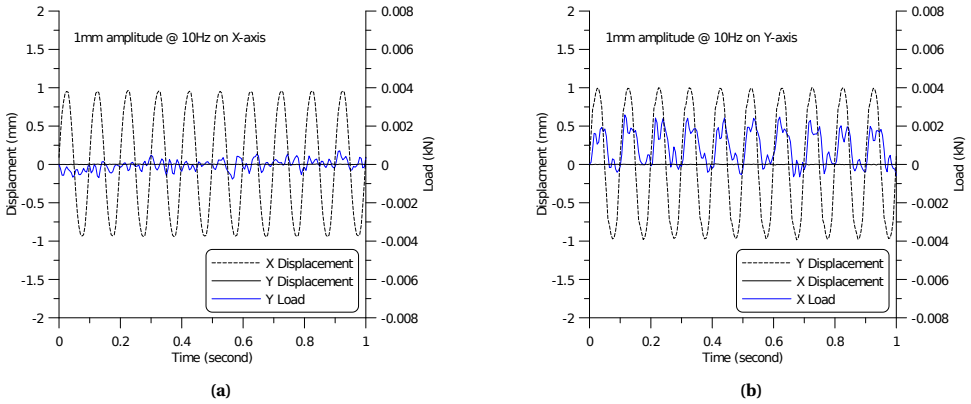

Figure 5.6: Displacement and load measured during the slow motion of (a)X axis (b)Y axis

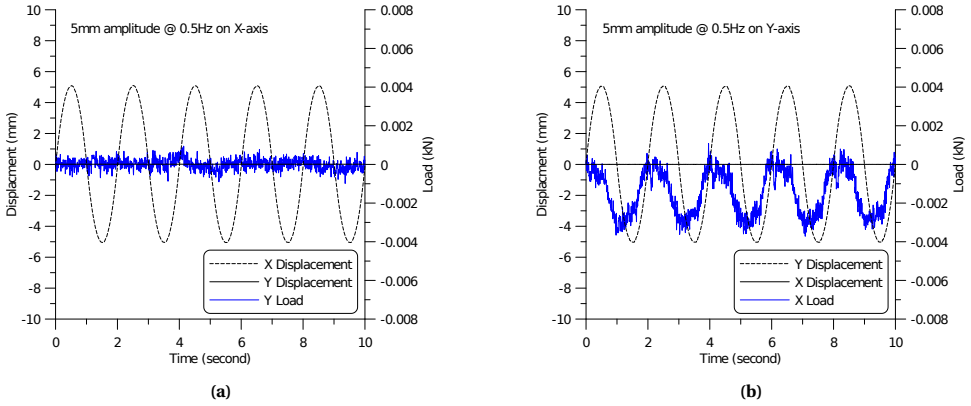

Figure 5.7: Displacement and load measured during the fast motion of (a)X axis (b)Y axis

cyclic cell pressure. A pressure transducer is integrated into the pneumatic controller to measure and regulate cell pressure throughout the testing process. The transducer's accuracy is rated at 0.1%.

The CYC-DoSS is equipped with an advanced water pressure/volume controller (AD-VDPC) also from GDS Instruments, which offers back pressure and back volume control and measurement. The back water pressure/volume controller has a maximum pressure and volume capacity of 1 MPa and 1000 cm^3, respectively. The accuracy of the water pressure controller is 0.1% for both pressure and volume.

The advantage of having cell and back pressure control is that it allows for the conducting of genuinely undrained tests. Additionally, by using cell pressure and back pressure, the CYC-DoSS system offers the flexibility to follow versatile stress paths and achieve back pressure saturation. This sets it apart from existing devices that can only initiate cyclic shearing from a K_0 condition. The system also enables the determination of lateral stress. It is capable of performing zero lateral strain (constant average area) cyclic shear-

ing tests—akin to those conducted with conventional cyclic simple shear devices on saturated samples—by maintaining constant height and preventing drainage (Boulanger et al., 1993). As a result, there is no need for rigid lateral support to constrain the sample's lateral strain development. The specimen can be simply enclosed in a standard latex membrane. The layout of the cell and back pressure control system is shown in Figure 5.8.

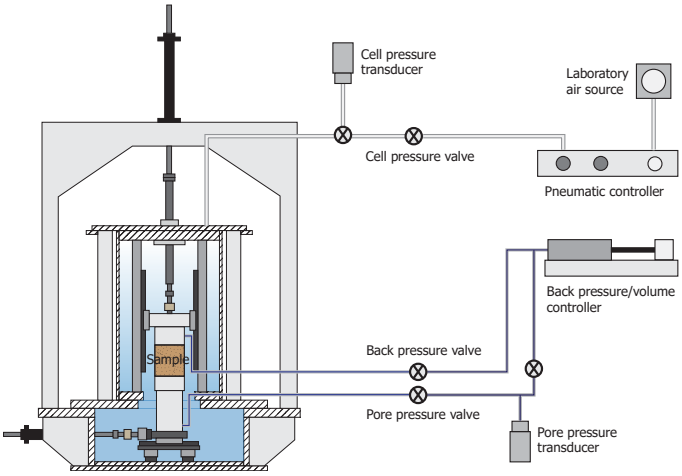

Figure 5.8: Illustration of the cell and back pressure systems

5.3.3. SPECIMENS, DRAINAGE LINES AND SIGNAL CABLES

The CYC-DoSS is designed to offer the flexibility to conduct various types of shearing tests through the use of interchangeable sample holder modules. It can accommodate samples with maximum dimensions of 250 mm in height and 150 mm in diameter. The CYC-DoSS is capable of performing both cyclic triaxial and direct simple shear tests. There are five distinct sets of sample holder modules available: two sets with diameters of 70 mm and 100 mm that are without bender element measurements, and three sets with diameters of 50 mm, 70 mm, and 100 mm that include bender element measurements. As illustrated in Figure 5.9, the sample is equipped with drainage lines at both the top and bottom sample holders, enabling double drainage to expedite the consolidation process—particularly for samples exceeding 70 mm in diameter. The inner diameter of these drainage lines is 6 mm. The top sample holder's drainage line is directly connected to the back pressure controller via the feedthrough module, while the drainage line from the bottom sample holder first connects to a pressure transducer via the feedthrough module and then to the back pressure controller. During undrained cyclic shearing tests, the valve situated between the pressure transducer and the back pressure controller can be closed. This arrangement allows for the capture of any potential pressure gradient, as evidenced by the readings from both the back pressure and the pressure transducer. The signal cables of load cells, bender elements, and local response sensors are connected to servo valve controllers and the data acquisition system via the feedthrough module.

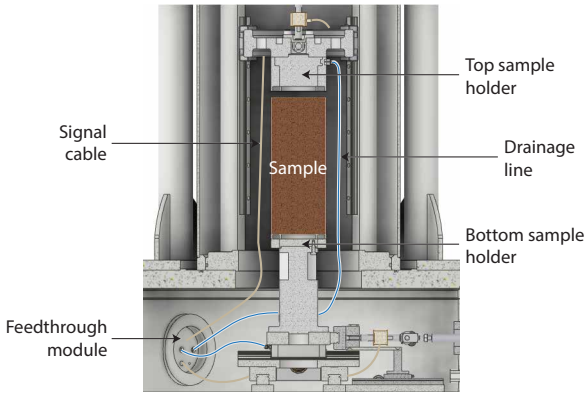

Figure 5.9: Sketch of the sample holders, drainage lines, and feedthrough module

5.3.4. SERVO VALVE CONTROLLERS, DATA ACQUISITION SYSTEM, AND SOFTWARE

The servo valves serve as the heart of the CYC-DoSS system. They are integral to the CYC-DoSS system, regulating the hydraulic oil flow based on feedback from various sensors, including position sensors, load cells, and cell and back pressure/volume sensors. This allows actuators on the X, Y, and Z-axes to achieve either targeted positions or loads. As depicted in Figure 5.10, the control and data acquisition systems are streamlined for clarity, with only one actuator illustrated. The same controller is used for the remaining two actuators. Conventional PC-based control systems using PID algorithms can experience latency issues, affecting high-frequency loading performance (Duku et al., 2007). To overcome this, the CYC-DoSS employs a high-speed Teensy 3.6 microcontroller board for real-time control. The system implements a PID control algorithm, with a theoretical maximum internal feedback loop sampling rate of up to 100 kHz. The eight-channel, 16-bit analogue-to-digital converter (ADC) acts as a bridge, converting the analogue input signals and delivering them to the microcontroller as feedback for the PID algorithm. This includes signals for load, displacement, and user-defined waveform. The ADC offers 16 effective bits of resolution (250 kS/s rate, ±10V), significantly outperforming the built-in ADC of the Teensy 3.6. The position sensors and load cells are powered and regulated through signal conditioners.

The microcontroller's built-in function generator supports four waveform functions: ramp, square, triangle, and sine. Additionally, an automated testing algorithm enables versatile stress path applications based on measurements of cell pressure, back pressure, and back volume. For data recording, a USB-6343 device from National Instruments is employed. It features 32 analogue input channels with a maximum sampling rate exceeding 15 kHz and is equipped with four analogue output channels. These output channels can be configured to generate user-defined waveforms, as illustrated in Figure 5.10. Taking into account the high-frequency capabilities of the CYC-DoSS, the device can also simulate the real-time history of an earthquake through user-defined waveform functions linked to the microcontroller.

The functionalities described above are incorporated into an in-house developed

software suite, called MP3. This software features four main windows: three dedicated to controlling the hydraulic actuators (via servo valves), and one for data recording and generating user-defined waveform signals. As demonstrated in Figure 5.11, the window allows users to control the actuator in either position or load modes, using various waveform options such as ramp, sine, triangle, and square. Arrow buttons are included to enable fine adjustments of the position or load settings. Calibration factors for all sensors can be input through this window, as indicated in Figure 5.111. Additionally, PID control parameters can be adjusted here, as shown in Figure 5.11.

Figure 5.12 showcases the data acquisition window within the MP3 software. This interface allows users to configure real-time tables and plots for data visualisation. The calibration factors of each sensor can be set up by clicking the designated button (specified as "Data acquisition channels settings"), as presented in Figure 5.12. Data recording can be set up by clicking the designated button (specified as "Data recording settings"), as seen in Figure 5.12. Additionally, user-defined waveform signals can be sent to the hydraulic actuator controllers by pressing another specified button (also denoted as "User-defined waveform settings").

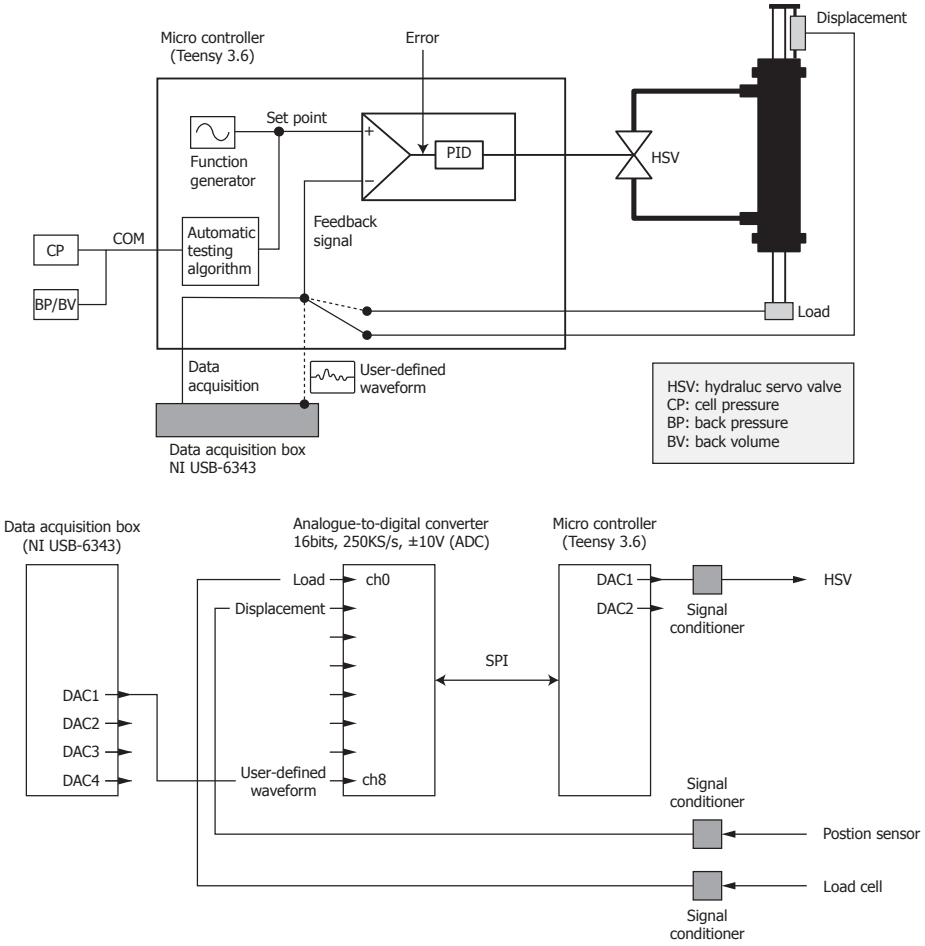

Figure 5.10: Illustration of the control and data acquisition system of CYC-DoSS

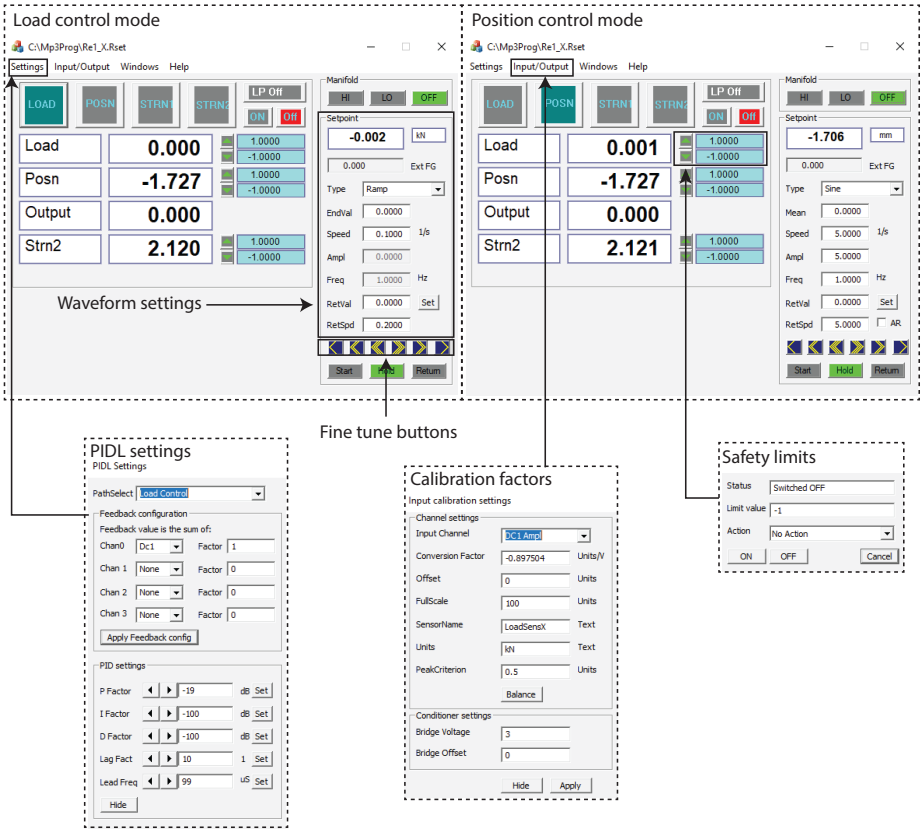

Figure 5.11: MP3 software window for controlling the hydraulic actuators

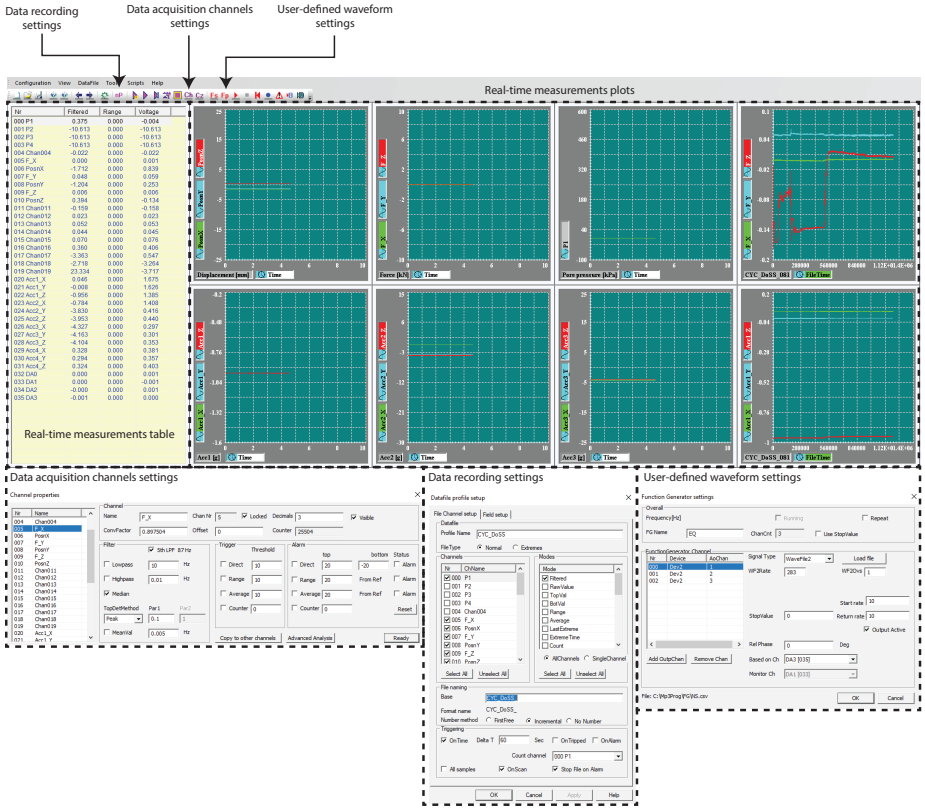

Figure 5.12: MP3 software window for recording test data and generating user-defined waveform signals

5.3.5. BENDER ELEMENTS

The pseudo-elastic shear modulus, G_{max}, provides valuable soil information relevant to numerous geotechnical engineering applications, particularly in simplified assessment of soil response under cyclic or dynamic loadings (Tokimatsu and Uchida, 1990). In the laboratory, G_{max} can be obtained from shear wave velocity measurements using bender elements. Moreover, shear wave velocity allows for a more direct comparison of laboratory and field soil states (Bhaumik et al., 2023).

A bender element is a two-layer piezoelectric transducer made of two conductive outer electrodes, two piezoceramic sheets, and a conductive metal shim at the centre (Lee and Santamarina, 2005). An excitation voltage produces a displacement in the source transducer, sending a wave through the sample. This wave generates a displacement in the receiver, inducing a voltage that can be measured. The bender elements installed in CYC-DoSS are combined P and S wave transducers manufactured by GDS Instruments and consist of two element inserts. The S-wave transmitter/P wave receiver is installed in the top cap, while the P-wave transmitter/S-wave receiver is in the base cap.

The S-wave transmitter includes two piezoceramic strips polarised in the same direction. When an excitation voltage is applied, one strip extends and the other contracts, causing the strips to bend. The two strips in the receiver are polarised by the wave motion in opposite directions, as illustrated in Figure 5.13. The P-wave transmitter consists of two piezoceramic strips polarised in opposite directions. When an excitation voltage is applied, both strips extend or contract. The two strips in the receiver are polarised by the wave motion in the same directions, as also depicted in Figure 5.13.

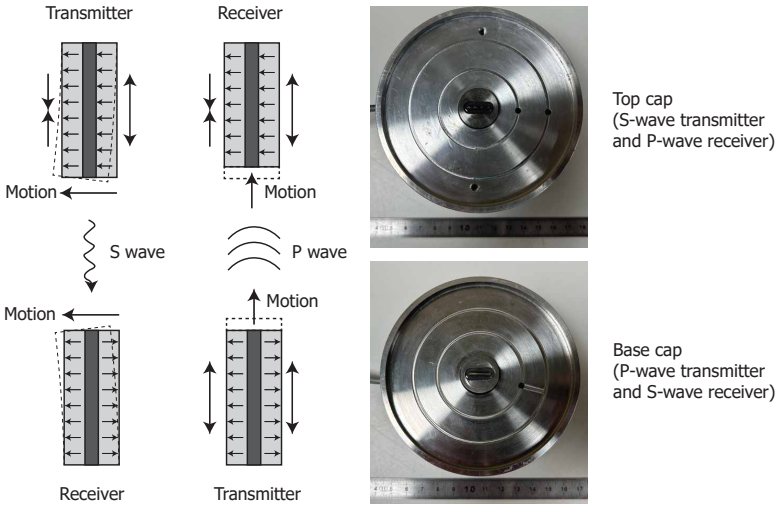

Figure 5.13: Working principle of bender elements (after GDS Bender Elements Hardware Handbook) and top/base cap of CYC-DoSS with element inserts

5.3.6. LOCAL RESPONSE SENSORS

The studies on monotonic soil behaviour have shown that stresses, strain, and pore pressure are seldom uniform within the specimen during element testing, particularly in soft soils (Jommi et al., 2021; Muraro and Jommi, 2019). Non-uniformities can become more significant during multidirectional loading, and pore pressure equalisation within the specimen may not be achieved at high loading frequencies. To improve the understanding of element experimental results and further explore the hydro-mechanical coupling response under multidirectional cyclic loading, advanced sensors have been developed at TU Delft.

Local displacement and pore pressure sensors have been employed in triaxial shear apparatus to enhance the interpretation of laboratory experimental observations (Fourie and Xiaobi, 1991; Yimsiri et al., 2005; Ackerley et al., 2016). In simple shear devices, the limitation of unknown horizontal stresses can be partially addressed using special wire-reinforced membranes or null pressure sensors (Ghafghazi et al., 2023; Dyvik et al., 1981). To the authors' knowledge, local response sensors have not yet been implemented in multidirectional cyclic shear devices, with a key challenge being the presence of stacked rings or wire-reinforced membranes.

The CYC-DoSS device offers fully controlled cell pressure and back pressure/volume, along with an automatic testing algorithm, allowing the maintenance of K0 conditions during both consolidation and undrained cyclic shear stages. As a result, tests can be conducted without stacked rings or wire-reinforced membranes, enabling the installation of local response sensors. Nevertheless, it should be noted that the K0 condition in CYC-DoSS is achieved under zero "average" lateral strain.

FIBRE OPTIC PORE PRESSURE TRANSDUCERS

Local measurement of pore pressure is crucial to understand the soil response under multidirectional cyclic loading. By obtaining pore pressure information not only at the boundaries but also within the sample, experimental results can be interpreted more effectively using numerical back-analysis. Consequently, achieving pore pressure equalisation throughout the entire sample may not be necessary, as the detailed pore pressure data allows for a more comprehensive analysis of soil behaviour.

The CYC-DoSS system incorporates the FOP-M fibre optic pressure sensor from FISO for local pore pressure sensing. Utilising White-Light Fabry-Pérot Interferometry technology, the sensor measures the pressure based on the deflection of a silicon diaphragm. The adopted model can provide stable and accurate readings under several adverse conditions like temperature fluctuations, electromagnetic interference, humidity, and vibration. The sensor is attached to the specimen using a silicone rubber connector, as illustrated in Figure 5.14.

CONTACTLESS DISPLACEMENT SENSORS

An advanced displacement sensing unit has been developed to track and record the lateral strain of specimens during testing. The unit comprises a laser distance sensor and a 3D Hall effect sensor.

The 3D Hall effect sensor employed is the TMAG 5273 from Texas Instruments, as illustrated in Figure 5.15(a). Its flux density varies with the distance between the sensor

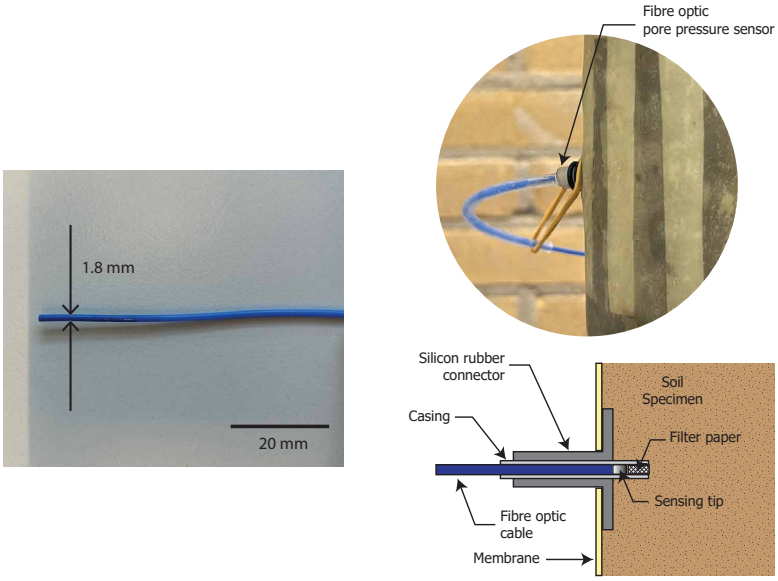

Figure 5.14: Fibre optic pressure sensor and installation principle

and the magnetic source. By analysing the measured flux density, the X, Y, and Z positions can be determined.

Laser distance sensors, as illustrated in Figure 5.15(b), are also employed in the CYC-DoSS device to measure lateral deformation. These sensors offer several advantages over Hall effect sensors, such as a higher sampling rate and greater accuracy. However, they are limited in that they cannot provide 3D position information. The incorporation of both types of sensors in CYC-DoSS ensures more robust and reliable lateral strain measurements.

ACCELEROMETERS

In addition to local displacement and pore pressure sensors, MEMS accelerometers have also been incorporated into the CYC-DoSS system to measure acceleration during multidirectional cyclic tests. Given the placement of the load cells—situated between the load rams and shaking tables or the top sample holder—it becomes imperative to correct the load cell readings using both the mass and the measured acceleration. Further, the inclusion of accelerometers opens the door for acceleration-controlled tests. Such tests are considered better approaches for mimicking real loading conditions that arise during seismic events such as earthquakes.

The Adafruit breakout board, fitted with the ADXL335 analogue MEMS accelerometer ($\pm 3g$ full scale) is selected. Figure 5.16 showcases the accelerometer prior to its encasement in a waterproof shell. Theoretical acceleration values corresponding to diverse static positions are also depicted in the same figure. For example, an acceleration reading of -1 g is recorded when the positive axis of the device is oriented towards the Earth's crust.

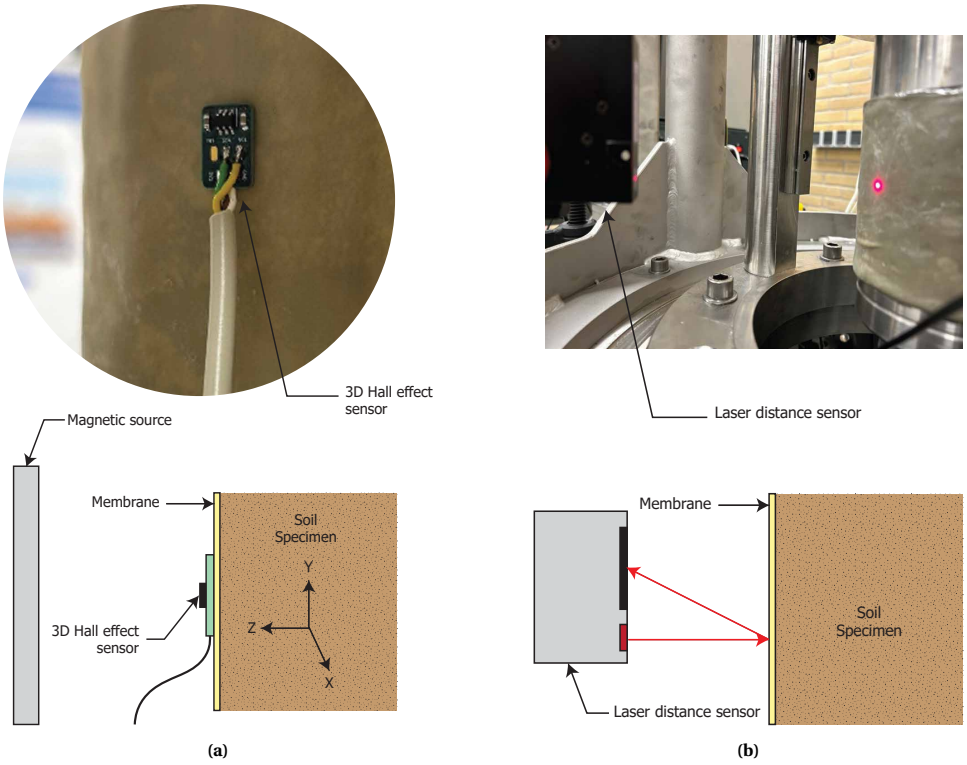

Figure 5.15: Photo and illustration of (a) 3D hall effect sensor (b) laser distance sensor

5.4. SENSORS CALIBRATION AND PROOF OF CONCEPT

Sensors in the CYC-DoSS play a pivotal role by converting physical parameters into electronic signals, facilitating both apparatus control and sample response recording. To guarantee their accuracy and reliability, these sensors undergo a calibration process, ensuring their outputs accurately represent the physical quantities they measure. This calibration is crucial for the overall precision of the system. Additionally, proof-of-concept tests are presented to further validate the operational feasibility of in-house developed sensors.

5.4.1. POSITION SENSORS

Position sensors have been incorporated into the CYC-DoSS to capture displacements along the X, Y, and Z axes. The system employs the GEFRAN PY1-C-100 linear transducer (±50 mm stroke) for the horizontal axes and the PZ12-S-200 (±100 mm stroke) for the vertical axis. The sensor's output voltage varies based on its current position. This relationship between the output voltage and position underwent calibration employing a micrometer device, characterised by a 0.01mm resolution.

Figure 5.17 captures both the calibration procedure and the resultant data for all axes. A good linearity is discernible between the output voltage and displacement. Sub-

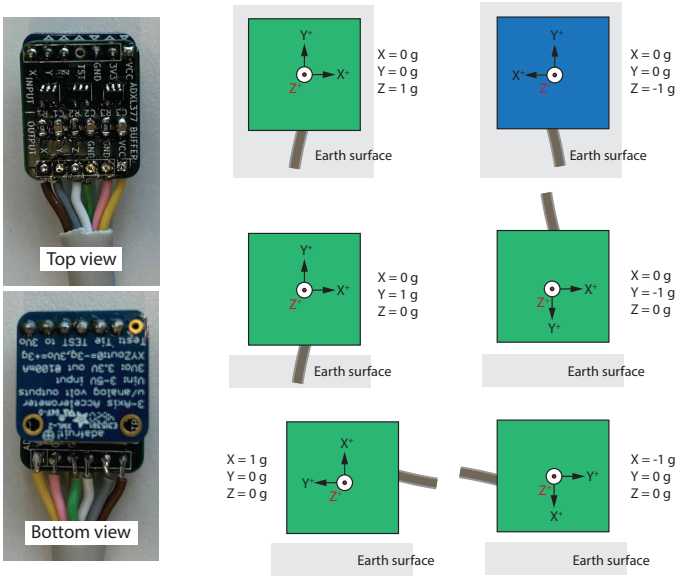

Figure 5.16: Photo of accelerometer and illustration of theoretical acceleration readings at different static positions

sequently, these conversion constants were integrated into both the servo valve control mechanism and the data acquisition software known as MP3.

5.4.2. LOAD CELLS

Load cells, integral to the CYC-DoSS setup, measure forces along the X, Y, and Z axes of the specimen using the ALF255-5kN model from Althen Sensors & Controls. Adapted for submersion, they withstand pressures up to 500 kPa, adjusting their output voltage in response to applied forces. Calibration, aiming to map output voltage to the applied load, utilised a precision 5kN load cell from GDS Instruments, noted for its accuracy below 0.1%. This process involved aligning both load cells in series within a hydraulic jack and applying force through the jack's activation.

Figure 5.18 details the calibration process and its outcomes for each axis, highlighting the linear relationship between output voltage and force. These calibration results were then integrated into the servo valve control system and the MP3 data acquisition software, enhancing measurement accuracy.

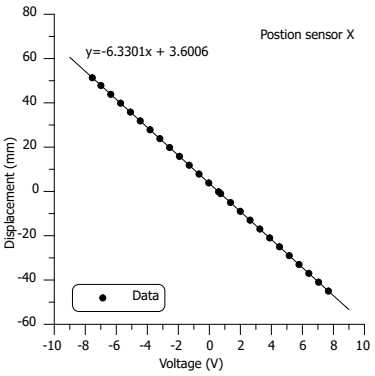

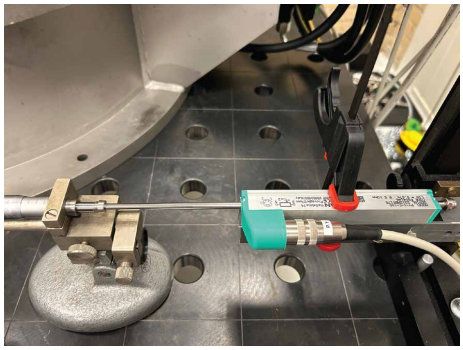

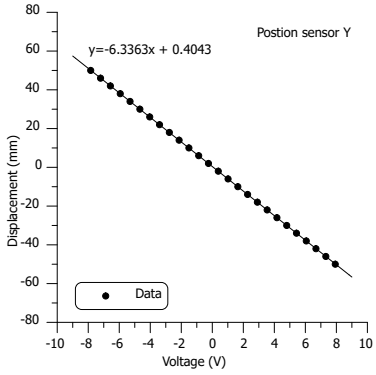

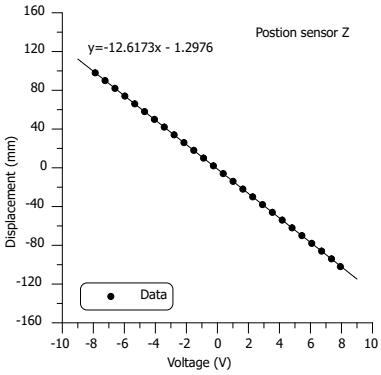

Figure 5.17: Photos and results of position sensors calibration

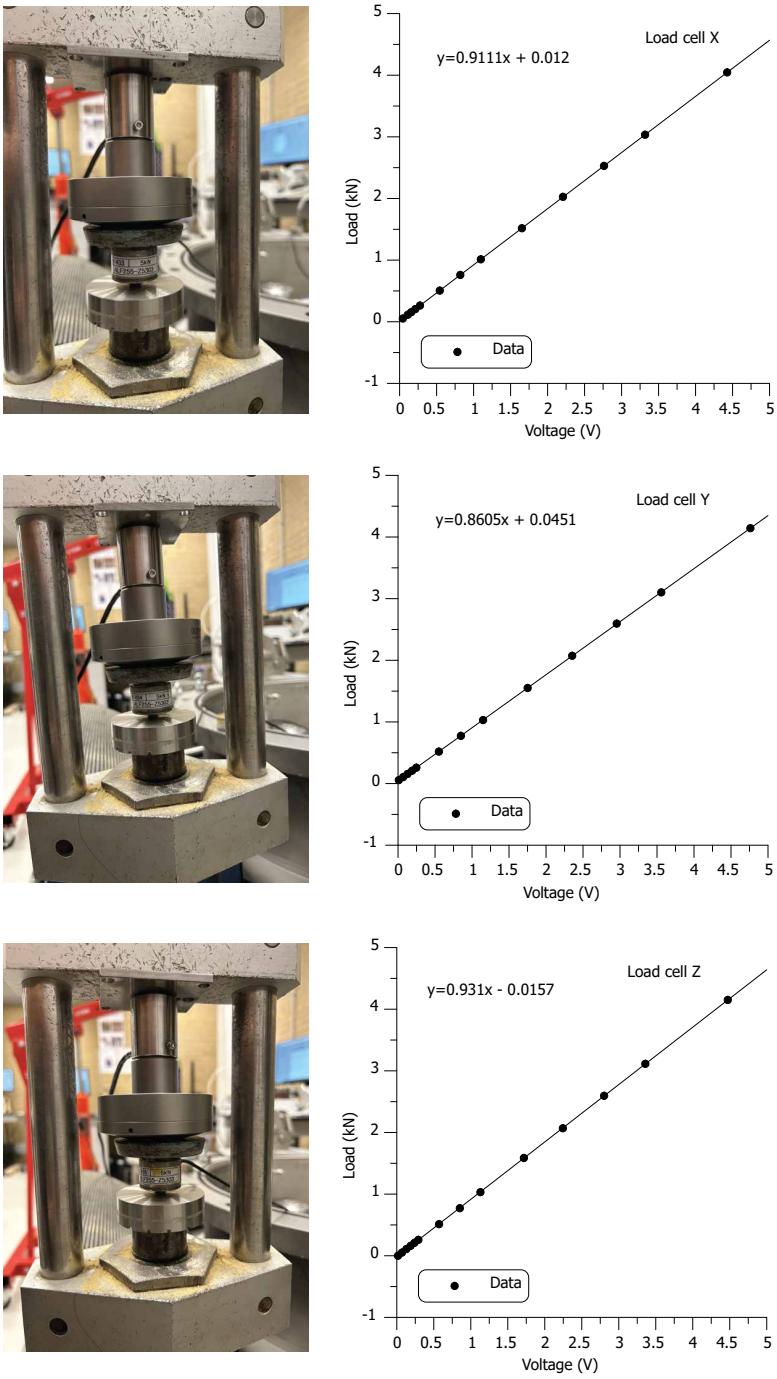

Figure 5.18: Photos and results of load cells calibration

5.4.3. PORE PRESSURE TRANSDUCER

Pore pressure transducers, connected to the sample's base via a drainage line, play a crucial role in measuring the pore water pressure. The specific transducer from GDS Instruments comes with a deairing block and has a capability of up to 1MPa. While it arrives calibrated by the manufacturer, the conversion factor depends on the particular data acquisition system used. Therefore, it was connected to the CYC-DoSS data acquisition system and recalibrated using a volume/pressure controller from GDS Instruments, known for its accuracy of better than 0.1% error over full range.

Figure 5.19 provides a detailed view of the relationship between output voltage and reference pressure, explored through both increasing and decreasing pressure up to 500 kPa. Alongside, an error analysis compared to the reference pressure is offered, revealing a consistent linearity in the transducer's output with a negligible average error of about 0.2 kPa.

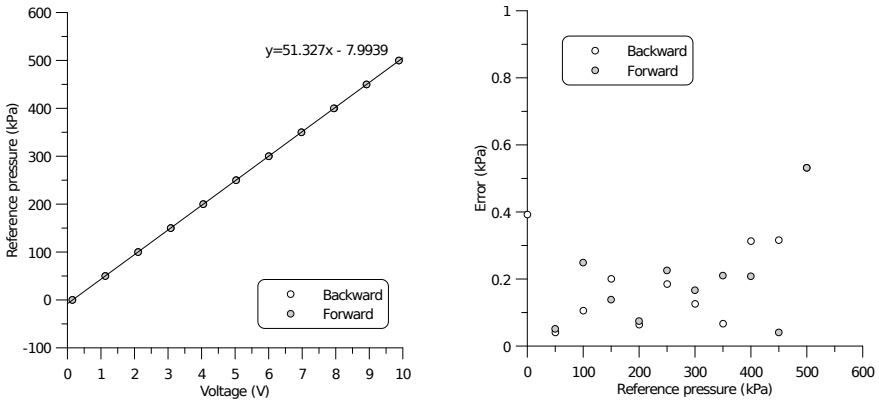

Figure 5.19: Results of GDS pore pressure transducer calibration

5.4.4. FIBRE OPTIC PRESSURE TRANSDUCER

The FOP-M-R2 Pressure Sensor from FISO, integrated into the CYC-DoSS, plays a vital role in continuously monitoring the sample's local hydro-mechanical behaviour during experiments. Designed to measure pressures up to 345kPa with an accuracy of 1.72 kPa, its recalibration was necessary to extend its range beyond 345 kPa to match the CYC-DoSS's capability of handling pressures up to 500 kPa. This recalibration was precisely conducted using a volume/pressure controller from GDS Instruments, known for its accuracy of better than 0.1%. Unlike traditional transducers that output voltage readings, this fibre optic model provides direct pressure values.

Figure 5.20 presents a detailed comparison of the results against reference pressure standards, showcasing the transducer's high precision, with an accuracy of around 1.5 kPa for measurements up to 650 kPa. The derived conversion factor enables accurate interpretation of the pressure readings from the fibre optic transducer in later data analysis phases.

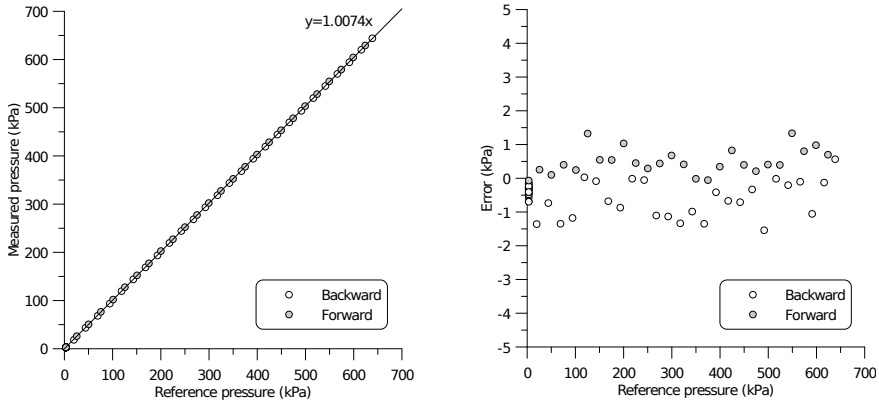

Figure 5.20: Results of fibre optic pressure transducer calibration

5.4.5. 3D HALL EFFECT SENSOR (PROOF OF CONCEPT TEST)

Hall effect sensors delineate a progressive, non-intrusive methodology for the meticulous monitoring of sample deformation. The magnitude of the total magnetic field, denoted as $|B|$, is conceived from the cumulative contributions emanating from the X, Y, and Z axes as depicted in Equation (5.1). When the sensor harmoniously aligns with the cylindrical magnet's central axis, the proximity of the magnet, represented as d, can be inferred by scrutinising the magnitude of the magnetic field, $|B|$, as elucidated in Equation (5.2). In this context, B_r signifies the magnet's remnant, a consistent value that inherently varies based on the magnet's dimensions, aspect ratio, and material composition. Meanwhile, r denotes the magnet's radius, and T represents its thickness.

$$|B| = \sqrt{B_x^2 + B_y^2 + B_z^2} \tag{5.1}$$

$$|B| = \frac{B_r}{2}\left(\frac{d+T}{\sqrt{r^2+(d+T)^2}} - \frac{d}{\sqrt{r^2+d^2}}\right) \tag{5.2}$$

By analysing the magnet's proximity, the positions on the X, Y, and Z axes, labelled as d_X, d_Y, and d_Z, can be determined by comparing the ratio of magnitudes along the three axes B_X, B_Y, and B_Z. This method, especially relevant for the YZ-plane, is depicted in Figure 5.21. It is important to note that Equation (5.2) applies accurately only when the sensor is aligned with the cylindrical magnet's central axis. As a result, the calculated positions must be adjusted based on the angle ϕ_{zy}.

An initial test was conducted to verify this concept, where the magnetic source was held steady while the Hall effect sensor was moved in various patterns to simulate possible test conditions. Both the calibration process and its results are illustrated in Figure 5.21. These results demonstrate the sensor's capability to accurately detect movement across the X, Y, and Z axes with a maximum deviation of 1mm. However, it is critical to point out that this level of precision is based on theoretical analysis. Implementing a detailed calibration routine can enhance this accuracy even further.

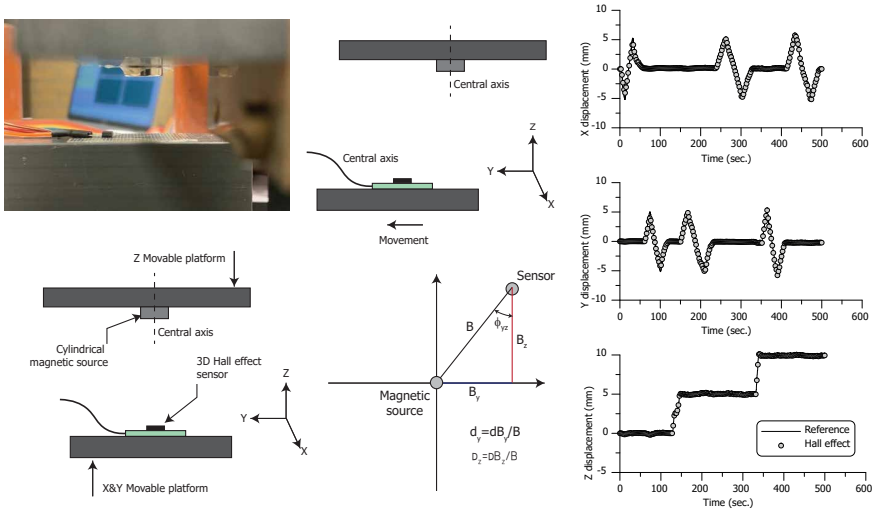

Figure 5.21: 3D hall effect sensor proof of concept test

5.4.6. ACCELEROMETER (CALIBRATION AND PROOF OF CONCEPT TEST)

For calibration, a straightforward yet effective method is used. The accelerometer is oriented in six primary positions as described in Figure 5.16. An in-house built buffer board is paired with the accelerometer, serving as a critical component in reducing signal noise and enhancing the quality of the measurements. To evaluate the module's performance, it is attached to the Z-axis actuator. Following this, tests are conducted with sinusoidal waves of 10mm amplitude at a frequency of 1Hz and a smaller 2mm at a higher frequency of 10Hz. Using the amplitude, A, and frequency, f of the applied sine wave, one can derive the theoretical acceleration time history with equation 5.3. Additionally, the acceleration can be calculated directly from the imposed displacement history.

$$a(t) = -4A\pi^2 f^2 \sin(2\pi f t) \tag{5.3}$$

Figure 5.22 displays the applied displacement history alongside a comparison between theoretical acceleration, imposed acceleration, and actual recorded data by accelerometer. In the trial featuring a 10mm amplitude at a frequency of 1Hz, the theoretical and the imposed acceleration trend is discernible, yet the imposed one is characterised by high peak noises. This phenomenon is attributed to the fact that the sinusoidal wave applied was not perfect. However, the measured and the imposed acceleration align quite well.

In the trial with a 2mm amplitude at a frequency of 10Hz, the measured and the imposed acceleration values more closely match the theoretical expectations. Still, the applied acceleration does not form a perfect sinusoidal wave. The first sudden change is related to the jump in displacement in the first quarter cycle. For the other ones, closer examination reveals that this abrupt shift coincides with the displacement reaching a zero value. Considering the accelerometer is connected to the data acquisition system via a relatively heavy cable, in comparison to the accelerometer's self-weight, it is plau-

sible that the sudden change results from the cable's swinging motion induced by directional changes in displacement.

Additionally, it is important to note that the Adafruit breakout board, equipped with an analogue MEMS accelerometer, includes 0.1 μF capacitors combined with a 32 kΩ output resistance. This configuration forms a low-pass filter with a 50 Hz cut-off frequency. As a result, there is a 10% attenuation at 10 Hz, which can also affect test results at that frequency.

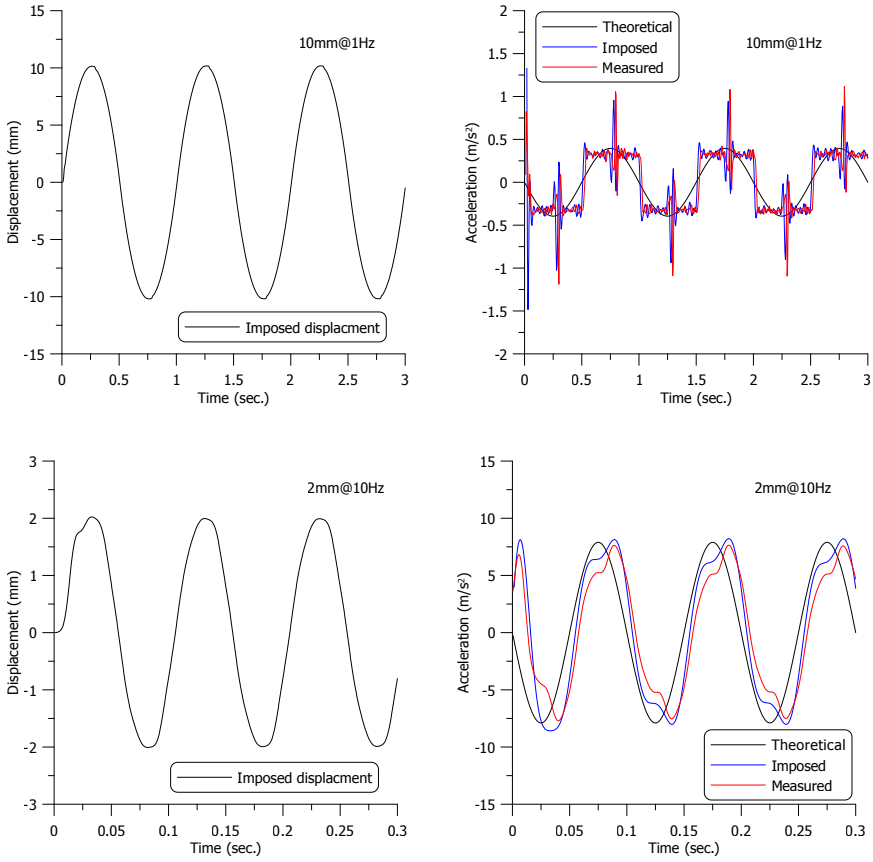

Figure 5.22: Accelerometer proof of concept test

5.4.7. OFFSET OF THE SYSTEM AND CALIBRATION RAMP

All pressure transducers, placed at various locations within the system, align in their readings. To ensure uniformity, the readings are synchronised to a commonly agreed reference level: the sample's mid-height. With the system's baseline offset established, a calibration test is conducted without the sample. The cell pressure is increased to 350kPa, allowing for a thorough check of all pressure transducers. Figure 5.23 shows readings from various instruments, including the cell pressure transducer, back pressure transducer, pore pressure transducer, and the innovative fibre optic pressure sensors. The consistent alignment of these readings confirms the accuracy and effectiveness of the calibration process.

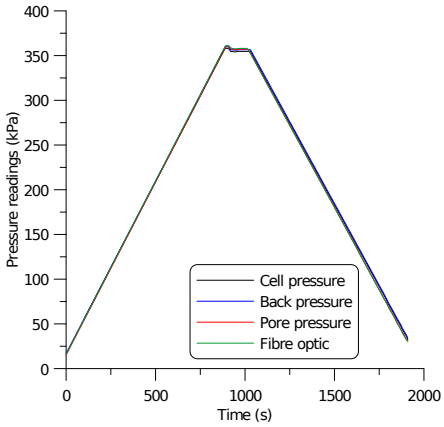

Figure 5.23: Pressure readings during the calibration ramp.

During the calibration ramp, it was observed that cell pressure noticeably affected the load cell readings. This interaction is due to the lack of a pressure compensation mechanism in the load cell, which is a trade-off made to reduce its size and weight. Figure 5.24 illustrates this relationship, showing a linear increase in readings as cell pressure rises. A consistent drift in the load cells was identified, measured at approximately 0.0002kN/kPa. This amount of drift is carefully corrected in the load cell readings for all axes.

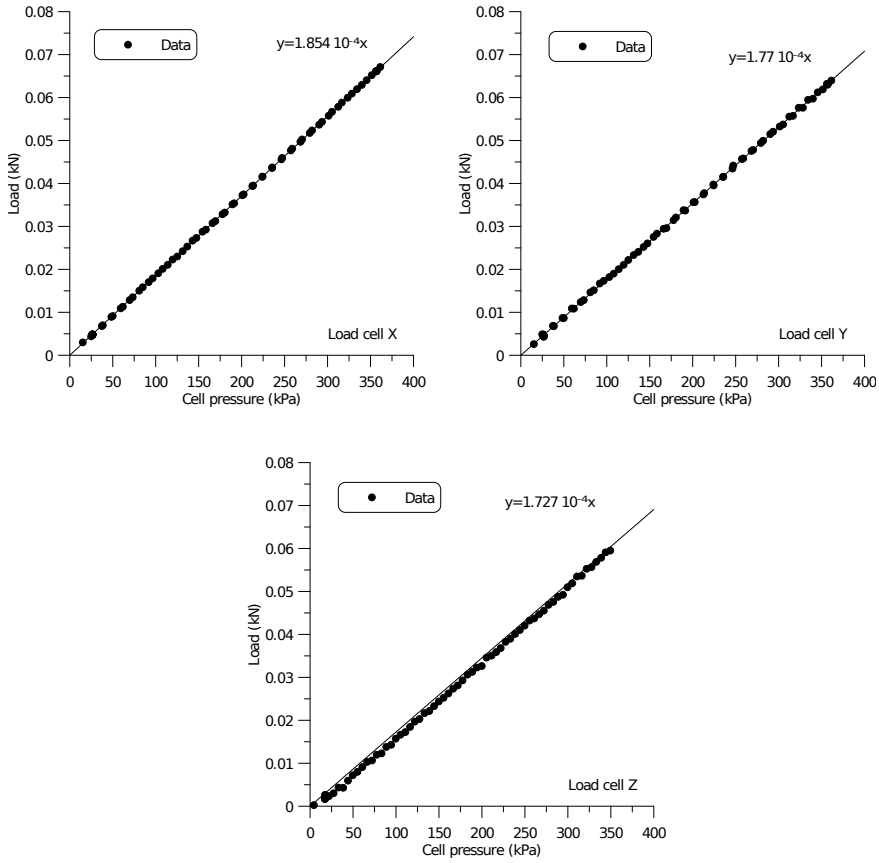

Figure 5.24: The influence of cell pressure on load cell readings

5.5. EXPERIMENTAL EVALUATIONS INTO CYC-DOSS CAPABILITIES

5.5.1. CYCLIC CELL PRESSURE

The adoption of a pneumatic controller in the system affords a quicker response time compared to the water pressure controller, primarily because the volume of the pressure chamber in the CYC-DoSS is substantially larger than in traditional triaxial cells. Furthermore, the rapid responsiveness of air pressure facilitates the execution of a cyclic cell pressure test programme.

To assess the efficacy of the CYC-DoSS in managing cyclic cell pressure, an experiment was conducted wherein a cyclic cell pressure with a period of 900 seconds and an amplitude of 50 kPa. This was done in the absence of a mounted sample. A back pressure controller, connected to the pressure chamber, served to monitor the cell pressure at the base of the chamber. This monitoring was essential to ascertain whether the chamber's internal pressure could achieve equilibrium even under cyclic conditions.

Figure 5.25 presents the pressure readings from this experiment. The data conclusively shows that the pressures at both the top and the bottom of the chamber remain in equilibrium. This successfully validates the capability of the CYC-DoSS to handle cyclic cell pressure efficiently.

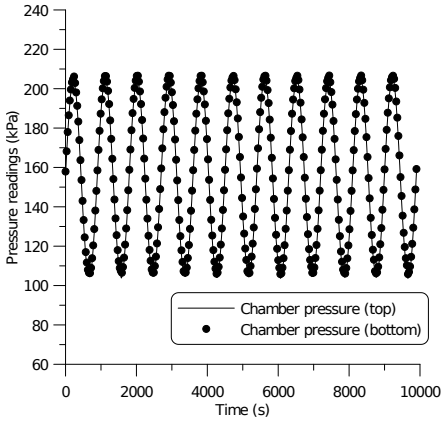

Figure 5.25: Cell pressure variation during cyclic cell pressure test

5.5.2. MULTIDIRECTIONAL CYCLIC LOADING

The CYC-DoSS device's capabilities were assessed using a soft organic soil sample. Notably, the sample was mounted without employing cell and back pressure and was subjected to diverse loading conditions. Throughout the tests, the Z-axis actuator's displacement was consistently held constant. Additionally, the hydraulic pump operated at half its maximum pressure, and the PID parameters were optimised for a loading frequency of 1 Hz.

Figure 5.26 illustrates the displacement-time history, as well as the X versus Y displacement for three distinct loading patterns: circular, 8-shaped, and butterfly-shaped. The circular pattern was realised with a 2 mm amplitude and a 1 Hz frequency, introducing a phase shift of 90 degrees between the horizontal actuators (X and Y). This pattern manifested effective actuator control. In contrast, the butterfly-shaped pattern was implemented with a 2 mm amplitude, operating at frequencies of 1 Hz for the X-axis and 0.5 Hz for the Y-axis. This, too, yielded satisfactory outcomes. The 8-shaped pattern was executed by simply reversing the loading frequencies of the X and Y axes from the butterfly pattern, as detailed in Figure 5.26.

5.5.3. HIGH FREQUENCIES CYCLIC SHEARING

To assess higher loading frequency performance, a 25 Hz loading with 0.7 mm amplitude is applied to the X-axis actuator without a sample mounted. The results in Figure 5.27(a) are less satisfactory compared to those at lower frequencies. However, considering the hydraulic pressure is at half capacity and the PID parameters are not tuned for high loading frequencies, it is expected that the performance will improve with full pressure and optimal tuning of PID parameters.

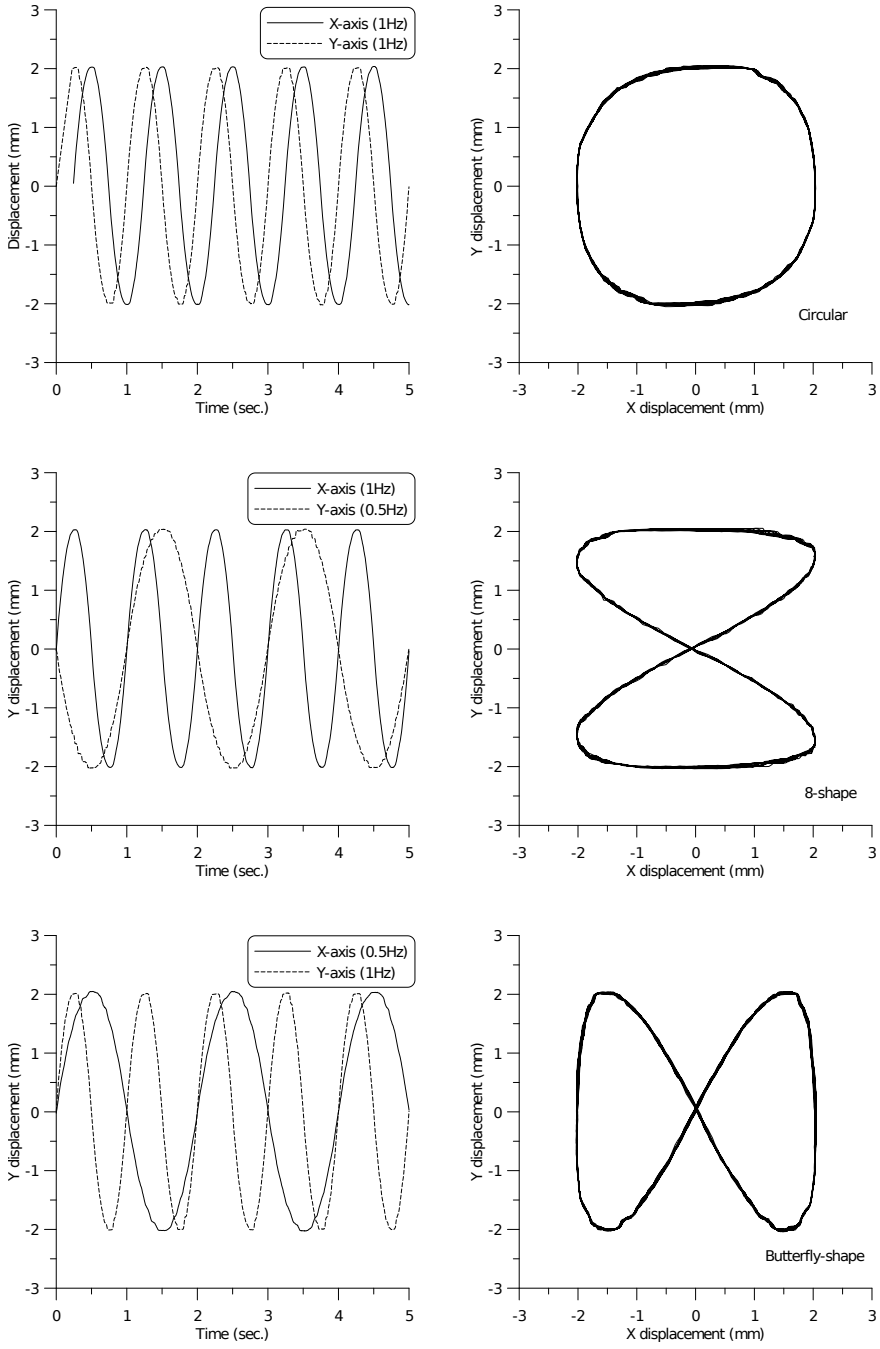

Figure 5.26: Displacements time history and X versus Y displacement of multidirectional cyclic loading

Upon a detailed examination of the load depicted in Figure 5.27(b) during the test, a variation of ±0.15 kN is observed, even in the absence of a mounted sample. Given the positioning of the load cells — between the load rams and either the shaking table or the top sample container assembly — their readings are influenced by the inertia of these mechanical components. Consequently, there is a pressing need to adjust these load readings by taking into account the mass of the mechanical components and their acceleration.

The X-axis actuator moves a mass of 8.61 kg. Using the amplitude, A, and frequency, f of the applied sine wave, one can derive the theoretical acceleration time history as represented previously by equation 5.3. Furthermore, the load in need of correction can be computed using equation 5.4, where m denotes the mass being shifted by the actuator. The updated load readings, shown in Figure 5.27(b), reveal a minimised variation of 0.02 kN. This is closely aligned with the magnitude of mechanical friction, substantiating the effectiveness of inertia-based load correction. It is pertinent to mention that a more accurate correction could be achieved by using acceleration data sourced from an accelerometer.

$$F_{\text{inertia}}(t) = ma(t) = -4mA\pi^2 f^2 \sin(2\pi f t) \tag{5.4}$$

5.5.4. REAL-TIME EARTHQUAKE LOADINGS

One of the most important design goals of CYC-DoSS is to reproduce the real-time earthquake loadings. In order to evaluate whether CYC-DoSS is able to simulate the time history of a real earthquake, the time history of Meinong Earthquake in 2016 recorded at CHY063 station is scaled to a peak amplitude of 2.4 mm and 4.2mm for X and Y direction, respectively. The scaled time history is used as an input for the servo-valve controllers via a user-defined waveform function in MP3. Figure 5.28 presented the input waveforms and the measured displacements of both axes. A very good alignment between them can be observed, indicating the CYC-DoSS is capable of reproducing the real-time earthquake loadings accurately. The X versus Y displacement is also plotted in Figure 5.28, further demonstrating the phase difference between the two axes is also well captured by CYC-DoSS.

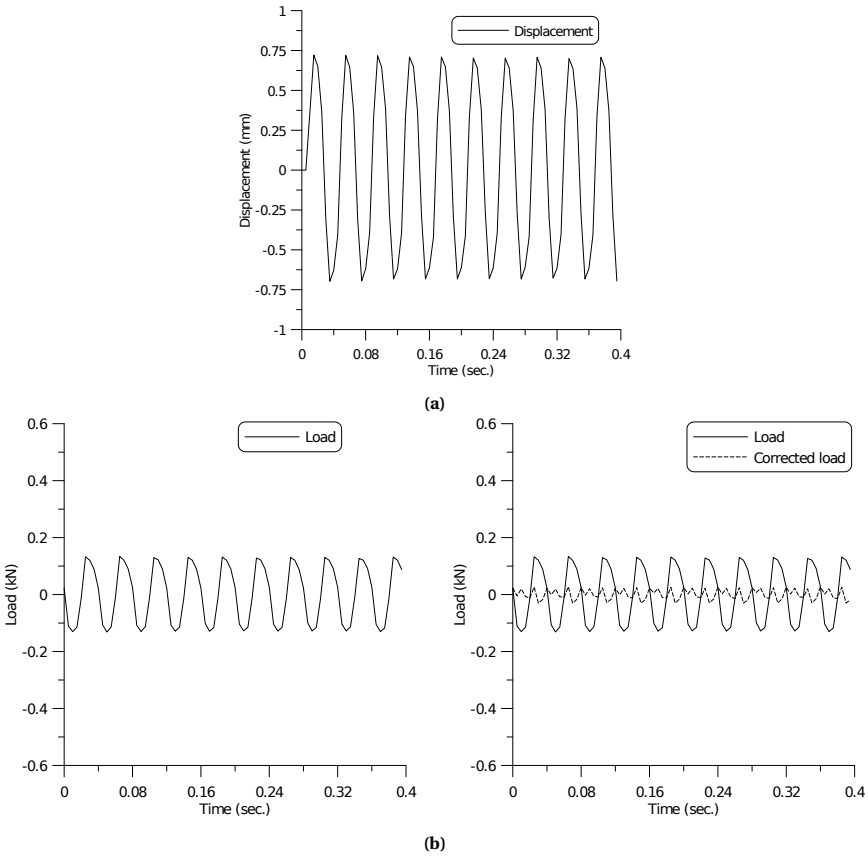

Figure 5.27: (a) Displacements (b) load and corrected load time history of a 25 Hz loading

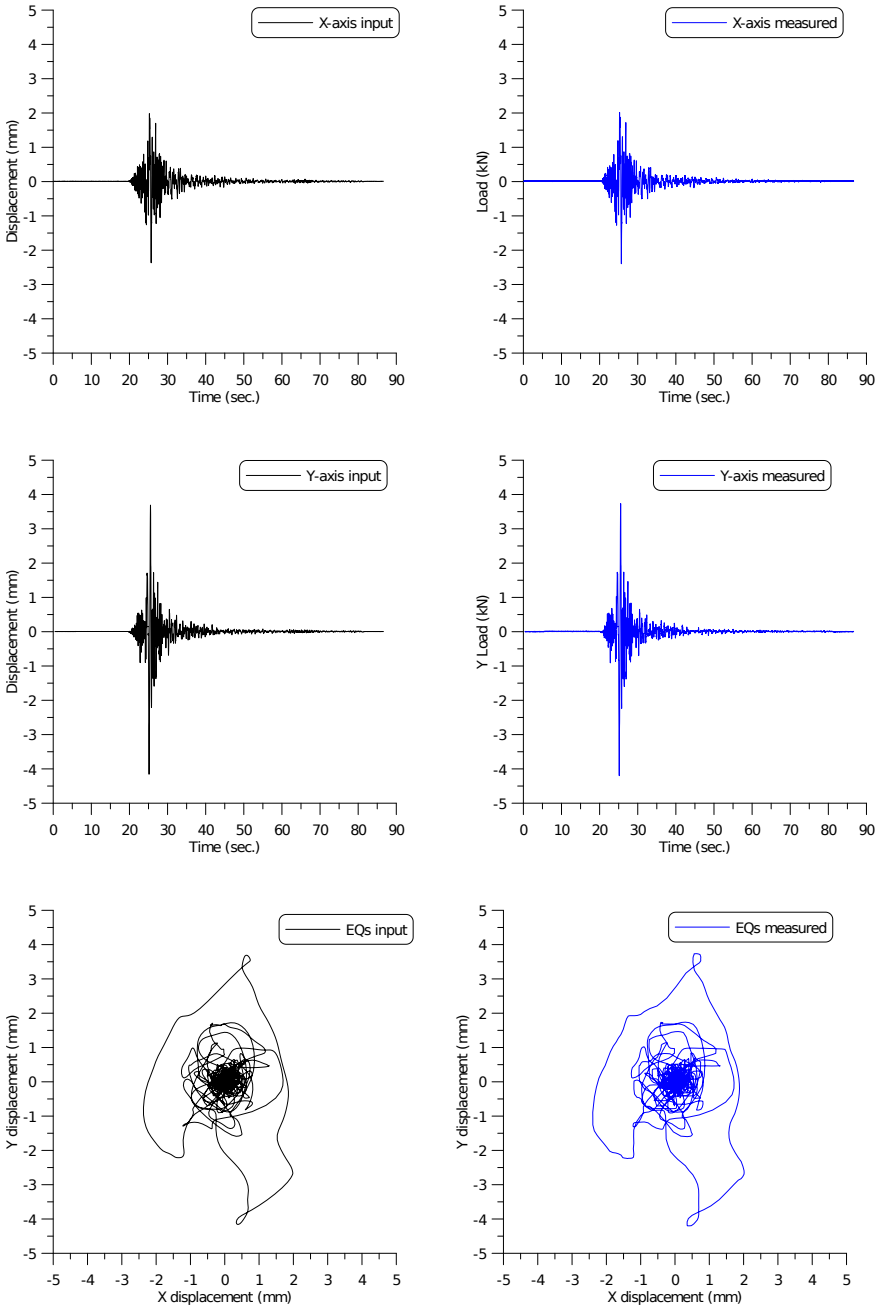

Figure 5.28: Displacements time history, and X versus Y displacement of real-time earthquake loadings

5.5.5. VALIDATION TESTS WITH SOFT ORGANIC CLAY

All evaluations discussed previously were conducted without mounting an actual soil sample in the CYC-DoSS apparatus. To assess the capability of CYC-DoSS for testing soft organic soils, validation cyclic triaxial tests have been carried out. The QDTAS system from GDS Instruments, known for its performance and reliability in soil testing, served as the reference equipment. However, it is important to note that the fastest achievable loading frequency of QDTAS is limited to 0.1Hz. For these validation tests, undisturbed Dutch organic soil samples with 100mm in height and 50mm in diameter, taken from specific depths in a sampling tube, were utilised. Prior to cyclic shearing, the samples underwent isotropic consolidation to mean effective stress of 100 kPa. Figure 5.29 illustrates the compression curves and variations in pore pressure at the samples' base. The observed differences in compression curves can be attributed to the varying initial void ratios of the natural material samples. Throughout the entire consolidation stage, the pore pressure between the two samples remained almost identical.

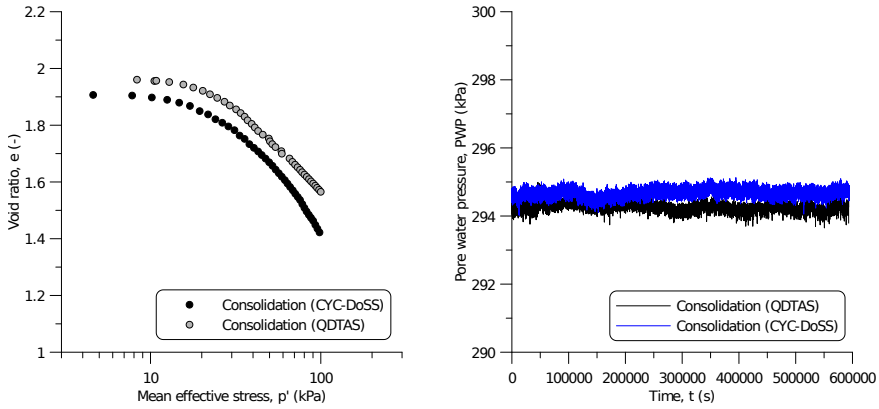

Figure 5.29: Compression curves and the pore water pressure variation during isotropic compression of validation tests

Following consolidation, strain-controlled cyclic triaxial tests were conducted with a sinusoidal wave application of 2% strain amplitude and 0.1Hz frequency. The axial load readings during cyclic shearing, as shown in Figure 5.30, reveal that QDTAS provides smooth load readings, benefitting from its load cell positioning which captures post-friction load effectively. In contrast, the CYC-DoSS load readings exhibit fluctuations around 20N (±10N). A closer examination of CYC-DoSS identified a misalignment between the vertical load ram and the hydraulic actuator, significantly increasing friction. This issue was not apparent in previous friction determination due to a much slower displacement rate.

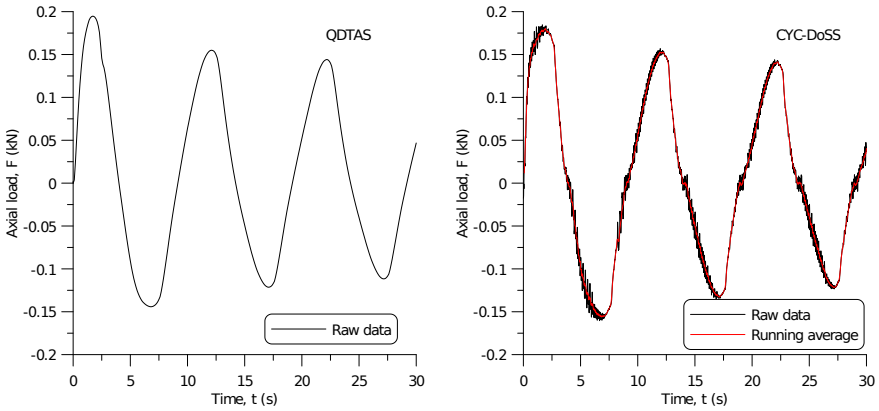

Figure 5.30: Axial load readings during cyclic shearing of validation tests

Moreover, a delay in load reading is observed as the load nears zero. The CYC-DoSS's multi-axial shearing design incorporates pin connectors to link load cells with load rams and hydraulic actuators, mitigating potential bending moments and side forces. However, these commercially manufactured pin connectors have a tolerance of ±0.008mm, allowing for movement when not under load, hence the observed delay in load readings at load reversal points.

To account for these observations, especially given the ten times higher sampling rate of CYC-DoSS compared to QDTAS, a running average has been applied to the CYC-DoSS load readings for better data interpretation, as also depicted in Figure 5.30.

Figure 5.31 presents the stress paths, stress-strain curves, and variations in deviatoric stress from both tests. The results from CYC-DoSS are characterised by a sawtooth pattern throughout the test and a flatter response around the neutral load, attributed to fluctuations and delays in load readings. Despite these discrepancies, the deviatoric responses of the two tests are relatively similar. However, the stress path in QDTAS shifts more rapidly to the left, suggesting a quicker development of excess pore pressure.

Pore water pressure during cyclic loading is measured at the top and bottom boundaries of the sample in QDTAS, and at the top, middle, and bottom in CYC-DoSS, as shown in Figure 5.32. QDTAS exhibits a higher variation in pore water pressure during cyclic shearing, although the average pressures recorded by both systems are comparable. The variation in CYC-DoSS is significantly less, shedding light on the divergent stress path evolution between the two tests. Upon dismounting the CYC-DoSS sample, trapped air was discovered in the water pipes connected to the top and bottom caps. The presence of air, due to its high compressibility and the rapid loading rate, likely contributed to the smaller observed variation in pore pressure, as it hindered the system from reaching equilibrium.

This theory is further corroborated by the results of subsequent monotonic undrained shearing after cyclic loading, depicted in Figure 5.33. Although the CYC-DoSS results show higher deviatoric stress, the differences between the two tests are minimal. Moreover, when shearing occurs at a significantly slower rate, the pore water pressure measurements from both systems align more closely, indicating that the CYC-DoSS system eventually allows the pore pressure to reach an equilibrium state.

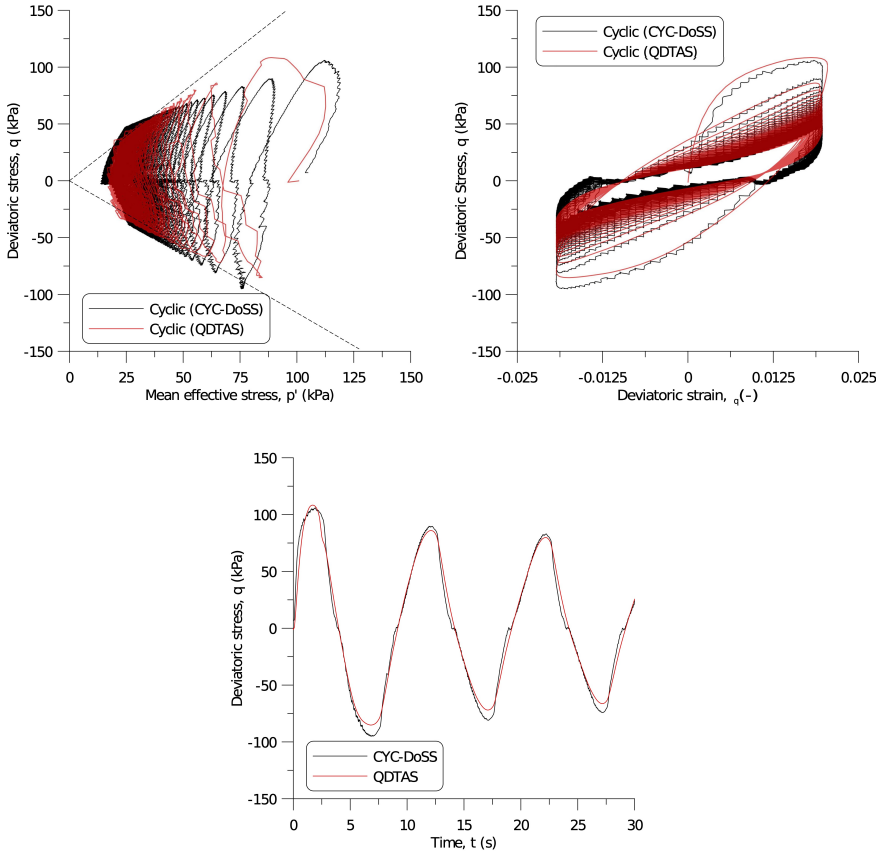

Figure 5.31: Stress paths, stress-strain curves and variation of deviatoric stress of validation tests

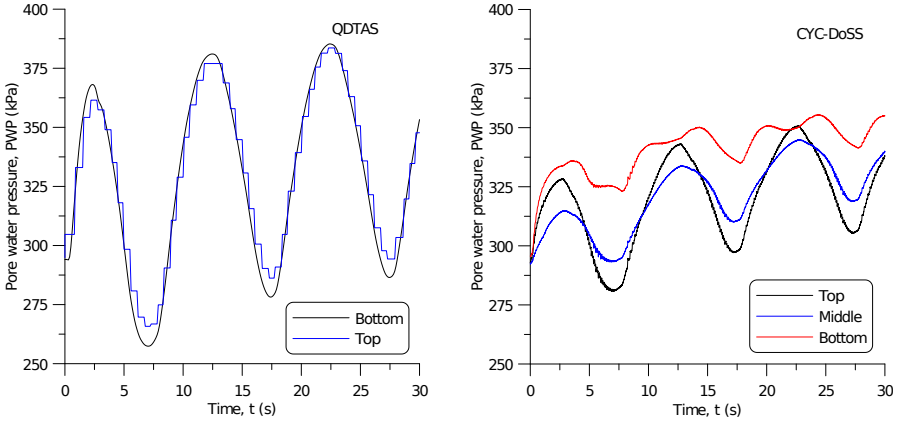

Figure 5.32: Pore water pressure measurements of validation tests

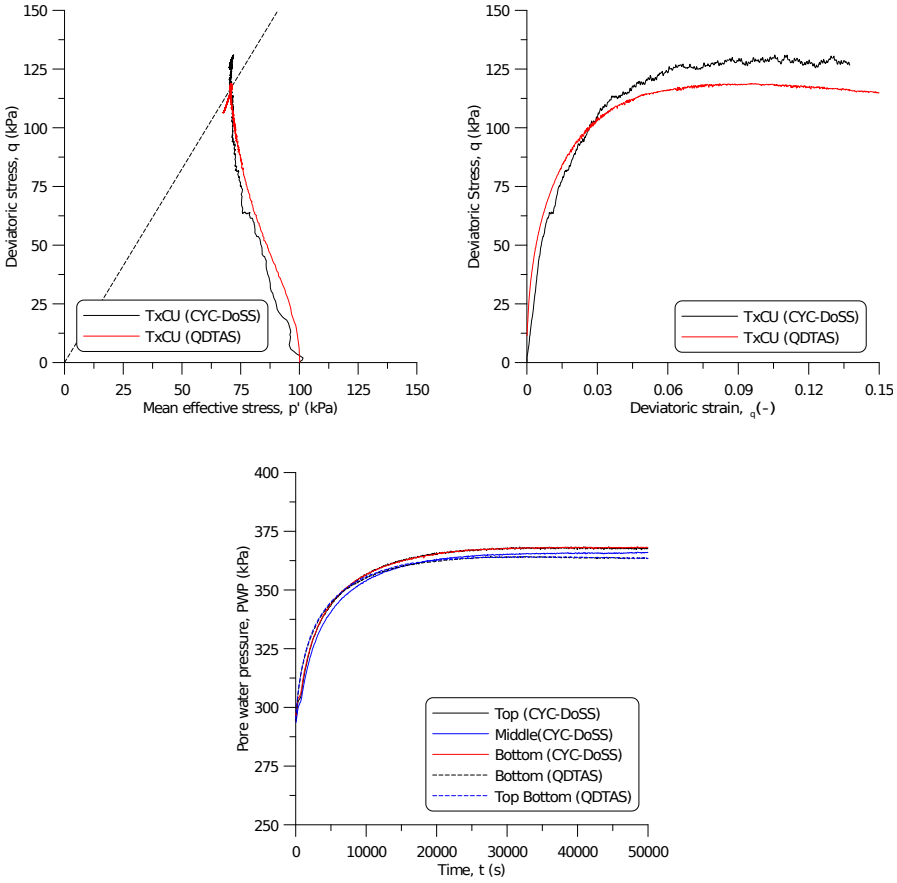

Figure 5.33: Stress paths, stress-strain curves, and pore water pressure measurements during monotonic undrained shearing

5.6. LIMITATIONS AND FUTURE IMPROVEMENTS

The experimental evaluations of CYC-DoSS underscore its proficiency in handling diverse loading scenarios such as cyclic cell pressure, multidirectional cyclic loading, high-frequency loading, and real-time earthquake simulations. However, these evaluations primarily attest to the mechanical and electrical design's capability without delving into the performance nuances with soft organic clay samples, where current limitations become apparent. A significant issue is the misalignment between the vertical load ram and the hydraulic actuator, which escalates friction and undermines precise load measurements. Furthermore, mechanical compliance from commercially manufactured pin connectors introduces a delay in load readings upon load reversal. Addressing the former requires the accurate repositioning of the vertical hydraulic actuator. The latter issue may be mitigated through the utilisation of custom-built rod connectors or those with an alternative mechanism.

Another challenge arises from the presence of trapped air within the system, skewing pore water pressure measurements under cyclic loading conditions. Given that CYC-DoSS is engineered to accommodate samples up to 150mm in diameter and 250mm in height, water pipes of 6mm in diameter were chosen for connectivity during validation test with a much smaller sample. This setup necessitates the introduction of changeable fittings to facilitate the use of water pipes with varying diameters, tailored to the size of the sample at hand. Moreover, the design and installation process of the top cap complicates the thorough deairing of the system. Improving the mounting procedure/deairing procedure has been considered, but it is most worthwhile after the compliance issues above have been resolved. As such, it was decided not to run additional tests at improved deaired conditions at this stage.

For the moment, the PID control parameters are tuned specifically for half the capacity of the hydraulic actuator system and are optimised for displacement control. This configuration contributes to less satisfactory performance during high-frequency loading, stemming from the limited scope of the current tuning. To achieve optimal system performance across its full capacity, it is imperative to adjust the PID control parameters accordingly. The challenges identified in previous validation tests, particularly the misalignment and compliance issues, further complicate the fine-tuning of PID control parameters for stress-controlled operations. These mechanical limitations inherently restrict the precision and effectiveness of any control parameter adjustments. Consequently, addressing the misalignment and mechanical compliance is a prerequisite for refining the PID control parameters for stress-controlled scenarios.

To enhance our understanding of element experimental outcomes and delve deeper into the hydro-mechanical coupling response under cyclic loading, this chapter introduces advanced sensors developed in-house. Among these innovations, only the fibre optic pressure transducer was utilised in tests with soil samples. For the 3D Hall effect sensors, a preliminary proof of concept test has been conducted. It is crucial to emphasise that the precision levels achieved by these sensors are currently based solely on analytical considerations. Introducing a specialised calibration routine presents an opportunity to significantly improve this accuracy, making the sensors suitable for deployment on soil samples.

Upon closer inspection of the accelerometer, it becomes evident that noise levels are

particularly pronounced at low loading frequencies. While the accelerometer demonstrates improved performance at higher frequencies, its readings are adversely affected by sudden changes attributed to the cable's motion, which swings due to directional changes in displacement. To mitigate these issues, the implementation of a filter or the selection of an accelerometer with a lower range, coupled with the use of a lightweight cable, is anticipated to enhance its performance. Moreover, the laser sensor, while promising in its precision and utility, requires modification to be made submersible for application in real tests.

Lastly, the positioning of the load cells in CYC-DoSS streamlines the mechanical layout and simplifies maintenance procedures. However, at high frequencies, the load readings require correction due to the influence of inertia. Additionally, this arrangement of load cells also captures the frictional forces of the system, though these can be calibrated out. The adoption of a multi-axis load cell, placed below the bottom cap, could potentially diminish the complexity involved in data correction and system calibration. Nevertheless, the cross-coupling effect of the multi-axis load cell and the feasibility of its maintenance must be further examined.

5.7. SUMMARY AND CONCLUSIONS

The Chapter presents the conceptual design and the electro-mechanical development of a cutting-edge earthquake simulator for soft soils, named the CYC-DoSS device. The design of the apparatus augments rotational stiffness while simultaneously minimising lateral movement and top cap rocking, achieved through the implementation of a robust double-tripod system. The device is equipped with digitally controlled, servo-hydraulic actuators in the x, y, and z axes to be capable of replicating real-time histories of earthquakes. The CYC-DoSS device overcomes certain limitations inherent in traditional simple shear apparatus, such as unreliable pore pressure measurement and indeterminate lateral stresses, thanks to an automatically controlled cell and back pressure system.

The novel concept relies on the incorporation of in-house developed local response sensors, able to collect comprehensive data on the coupled hydro-mechanical response of the soil sample. This includes information such as deformation, pore pressure and acceleration, an insight which was unavailable in earlier devices. To further enrich the data collected on the small-strain response and to bridge the gap between laboratory and field observations, P-wave and S-wave bender element measurements were incorporated into the CYC-DoSS device.

This Chapter not only highlights the adaptability and range of CYC-DoSS in simulating complex loading conditions, but also candidly acknowledges the system's current limitations when tested with soft organic clay samples. Addressing these challenges through strategic design and procedural modifications will enhance the precision and reliability of CYC-DoSS, paving the way for its broader application in geotechnical research and practice.

BIBLIOGRAPHY

Ackerley, S., Standing, J., & Hosseini Kamal, R. (2016). A system for measuring local radial strains in triaxial apparatus. *Géotechnique*, *66*(6), 515–522.

Bhaumik, L., Rutherford, C. J., Olson, S. M., Hashash, Y. M., Numanoglu, O. A., Cerna-Diaz, A. A., & Weaver, T. (2023). A multidirectional cyclic direct simple shear device for characterizing dynamic soil behavior. *Geotechnical Testing Journal*, *46*(2).

Bjerrum, L. (1967). Engineering geology of norwegian normally-consolidated marine clays as related to settlements of buildings. *Geotechnique*, *17*(2), 83–118.

Boulanger, R. W., Chan, C. K., Seed, H. B., Seed, R. B., & Sousa, J. B. (1993). A low-compliance bi-directional cyclic simple shear apparatus. *Geotechnical Testing Journal*, *16*(1), 36–45.

Boulanger, R. W., & Idriss, I. M. (2004). *Evaluating the potential for liquefaction or cyclic failure of silts and clays*. Citeseer.

Budhu, M. (1984). Nonuniformities imposed by simple shear apparatus. *Canadian Geotechnical Journal*, *21*(1), 125–137.

Budhu, M. (1985). Lateral stresses observed in two simple shear apparatus. *Journal of Geotechnical Engineering*, *111*(6), 698–711.

Budhu, M., & Britto, A. (1987). Numerical analysis of soils in simple shear devices. *Soils and Foundations*, *27*(2), 31–41.

DeGroot, D. J., Germaine, J. T., & Ladd, C. C. (1994). Effect of nonuniform stresses on measured dss stress-strain behavior. *Journal of geotechnical engineering*, *120*(5), 892–912.

Duku, P. M., Stewart, J. P., Whang, D. H., & Venugopal, R. (2007). Digitally controlled simple shear apparatus for dynamic soil testing. *Geotechnical Testing Journal*, *30*(5), 368–377.

Dyvik, R., Berre, T., Lacasse, S., & Raadim, B. (1987). Comparison of truly undrained and constant volume direct simple shear tests. *Geotechnique*, *37*(1), 3–10.

Dyvik, R., Floess, C., & Zimmie, T. (1981). *Lateral stress measurements in direct simple shear device*. ASTM International.

Fourie, A., & Xiaobi, D. (1991). Advantages of midheight pore pressure measurements in undrained triaxial testing. *Geotechnical Testing Journal*, *14*(2), 138–145.

Ghafghazi, M., Talesnick, M., & Givi, F. (2023). The full state of stress in monotonic simple shear tests on sand. *Géotechnique*, 1–30.

Graham, J., Crooks, J., & Bell, A. L. (1983). Time effects on the stress-strain behaviour of natural soft clays. *Géotechnique*, *33*(3), 327–340.

Ishihara, K., & Yamazaki, F. (1980). Cyclic simple shear tests on saturated sand in multi-directional loading. *Soils and Foundations*, *20*(1), 45–59.

Jaime, A. (1975). A two-direction cyclic shear apparatus. *5th Pan American Conference on Soil Mechanics and Foundation Engineering, Buenos Aires, Argentina*, *2*, 395–402.

Jommi, C., Chao, C., Muraro, S., & Zhao, H. (2021). Developing a constitutive approach for peats from laboratory data. *Geomechanics for Energy and the Environment*, *27*, 100220.

Lee, J.-S., & Santamarina, J. C. (2005). Bender elements: Performance and signal interpretation. *Journal of geotechnical and geoenvironmental engineering*, *131*(9), 1063–1070.

Li, Y., Yang, Y., Yu, H.-S., & Roberts, G. (2017). Monotonic direct simple shear tests on sand under multidirectional loading. *International Journal of Geomechanics*, *17*(1), 04016038.

Lucks, A. S., Christian, J. T., Brandow, G. E., & Höeg, K. (1972). Stress conditions in ngi simple shear test. *Journal of the Soil Mechanics and Foundations Division*, *98*(1), 155–160.

Matsuda, H., Nhan, T. T., & Ishikura, R. (2013). Prediction of excess pore water pressure and post-cyclic settlement on soft clay induced by uni-directional and multi-directional cyclic shears as a function of strain path parameters. *Soil Dynamics and Earthquake Engineering*, *49*, 75–88.

Matsuda, H., Nhan, T. T., & Sato, H. (2016). Estimation of multi-directional cyclic shear-induced pore water pressure on clays with a wide range of plasticity indices. *Proceedings of the second international conference on civil, structrual and transportation engineering*, 1–8.

Muraro, S., & Jommi, C. (2019). Implication of end restraint in triaxial tests on the derivation of stress–dilatancy rule for soils having high compressibility. *Canadian Geotechnical Journal*, *56*(6), 840–851.

Nhan, T., & Matsuda, H. (2016). A development of pore water pressure model for multi-directional cyclic shearing on normally consolidated clays. *Proceedings of the sixty nineth Canadian geotechnical conference, Vancouver, BC, Canada*, 8.

Pyke, R. M., Chan, C. K., & Seed, H. B. (1975). Settlement of sands under multidirectional shaking. *Journal of the Geotechnical Engineering Division*, *101*(4), 379–398.

Reyno, A., Airey, D., & Taiebat, H. (2005). Influence of height and boundary conditions in simple shear tests. *International Symposium on Frontiers in Offshore Geotechnics*.

Rudolph, C., Grabe, J., & Albrecht, I. (2014). Simple shear tests with a varying shearing direction during cyclic shearing. *Géotechnique Letters*, *4*(2), 102–107.

Rutherford, C. J., & Biscontin, G. (2013). Development of a multidirectional simple shear testing device. *Geotechnical Testing Journal*, *36*(6), 858–866.

Rutherford, C. J. (2012). *Development of a multi-directional direct simple shear testing device for characterization of the cyclic shear response of marine clays*. Texas A&M University.

Saada, A. S., Fries, G., & Ker, C.-C. (1983). Stress induced in short cylinders subjected to axial deformation and lateral pressures. *Soils and Foundations*, *23*(1), 114–118.

Shafiee, A., Stewart, J., Venugopal, R., & Brandenberg, S. (2017). Adaptation of broadband simple shear device for constant volume and stress-controlled testing. *Geotechnical Testing Journal*, *40*(1), 15–28.

Sheahan, T. C., Ladd, C. C., & Germaine, J. T. (1996). Rate-dependent undrained shear behavior of saturated clay. *Journal of Geotechnical Engineering*, *122*(2), 99–108.

Shen, C., Sadigh, K., & Herrmann, L. (1978). An analysis of ngi simple shear apparatus for cyclic soil testing. In *Dynamic geotechnical testing*. ASTM International.

Tokimatsu, K., & Uchida, A. (1990). Correlation between liquefaction resistance and shear wave velocity. *Soils and foundations*, *30*(2), 33–42.

Vaid, Y. P., & Finn, W. L. (1979). Static shear and liquefaction potential. *Journal of the Geotechnical Engineering Division*, *105*(10), 1233–1246.

van Thienen-Visser, K., & Breunese, J. (2015). Induced seismicity of the groningen gas field: History and recent developments. *The Leading Edge*, *34*(6), 664–671.

Vucetic, M., & Lacasse, S. (1982). Specimen size effect in simple shear test. *Journal of the Geotechnical Engineering Division*, *108*(12), 1567–1585.

Yang, M., Taiebat, M., & Vaid, Y. (2016). Bidirectional monotonic and cyclic shear testing of soils: State of knowledge. *Proceedings of the sixty nineth Canadian geotechnical conference, Vancouver, BC, Canada*.

Yimsiri, S., Soga, K., & Chandler, S. (2005). Cantilever-type local deformation transducer for local axial strain measurement in triaxial test. *Geotechnical Testing Journal*, *28*(5), 445–451.

6

CONCLUSIONS AND RECOMMENDATIONS

6.1. OBSERVATIONS AND CONCLUSIONS

This thesis tackles the understudied aspects of Dutch soft organic clay behaviour under static and cyclic loads, with a focus on mitigating the seismic hazards induced by activities in the Groningen gas field. Recognising the gaps in our understanding of the static response of these clays—particularly concerning organic content, stress-induced anisotropy, and behaviours beyond triaxial compression—a rigorous experimental programme was initiated. This programme explored both monotonic and non-monotonic stress paths, encompassing compression and extension scenarios. The experimental observations and analyses have illuminated pathways for refining the existing constitutive models, enhancing their precision in capturing the pre-failure behaviour of Dutch soft organic clays.

Extending beyond static behaviours, the research delved into the dynamics of 'slow' cyclic loading, intentionally excluding the effects of non-uniform pore pressure distribution. Through detailed experimental and modelling efforts, critical insights into the slow cyclic response were uncovered. These include the effects of loading frequency, the distinct behaviours of natural versus reconstituted samples, and the significant roles of initial stress states, cyclic stress amplitudes, clay and organic content, and post-cyclic undrained shear strength and recompression. The adaptation of the JMC-clay model to include cyclic behaviours, through the introduction of bounding surface plasticity (JMC-clay BS), represents a leap towards a more predictive modelling framework for cyclic loading conditions. However, challenges in validating the JMC-clay BS model have led to further enhancements, incorporating time-dependent strains through an elastoplastic-viscoplastic bounding surface formulation (JMC-clay BSEVP). This model's effectiveness, validated against static and slow cyclic tests on Dutch organic clay, underscores its strengths and limitations in reflecting soil behaviour under various loading conditions and sets the stage for future refinements.

Additionally, the thesis identifies the limitations of existing shear testing systems and the imperative to understand the 'fast' cyclic and dynamic behaviours of Dutch organic soft soils. This need inspired the development of a novel dynamic testing apparatus, CYC-DoSS, equipped with advanced local response sensors. The apparatus achieved high rotational stiffness, minimised lateral movement, and reduced top cap rocking through a robust double-tripod system. The device is equipped with digitally controlled, servo-hydraulic actuators in the x, y, and z axes to be capable of applying multidirectional loading up to 20Hz and replicating real-time histories of earthquakes. With an automatically controlled cell and back pressure system, the CYC-DoSS device provides reliable pore pressure measurement, determinate lateral stresses, and flexible stress paths. While highlighting CYC-DoSS's adaptability and potential, the thesis also acknowledges its current limitations with soft organic clay samples. Issues with the current system include misaligned load ram and hydraulic actuator, which cause friction and inaccurate measurements; commercially manufactured pin connectors, which cause delays in force measurement; and trapped air, which affects the accuracy of pore water pressure measurements. PID control parameters are optimised for displacement control and half-capacity of the hydraulic actuator system, potentially leading to less satisfied performance during high-frequency loading. Future enhancements through design and procedural adjustments are anticipated to improve the apparatus's precision

and reliability, contributing significantly to geotechnical research and practice.

6.1.1. STATIC BEHAVIOUR AND MODELLING OF DUTCH ORGANIC CLAY

Driven by the objective to fill knowledge gaps in the static behaviour of Dutch organic clay, this investigation delved into the roles of organic content, stress-induced anisotropy, and behaviours beyond triaxial compression across varying stress paths. The analysis aimed at refining the modelling approach by identifying and tuning essential components.

- The compressibility of Dutch organic clay was found to significantly vary, influenced by organic content and the presence of diatoms. The friction angle changes with the Lode angle, showcasing a complex behaviour under shear. Notably, the depositional fabric exhibits clear anisotropy that evolves swiftly with stress path changes. Drained test analyses revealed that yield locus expansion is governed by volumetric plastic strains, whereas anisotropy evolution is closely tied to the loading direction.

- Based on the experimental insights, the JMC-clay model was formulated. Incorporating a non-associated flow rule, the model refines the yield locus formulation, enhancing the yield surface shape's flexibility and introducing a Lode angle-dependent rotational hardening rule. The JMC-clay model's strengths are particularly noticeable in the deviatoric stress-strain response, becoming increasingly important as the stress ratio in extension increases.

- Numerical simulations validated the JMC-clay model's capability to accurately capture the pre-failure response across diverse loading and unloading stress paths, a vital attribute for its application in engineering practice. However, a critical examination of its practical limitations highlighted a significant sensitivity to the initialisation of the yield surface inclination, particularly at lower stress levels. This finding suggests that the primary challenge in applying this model category in practical scenarios lies in the initial state's accurate representation, rather than model calibration.

6.1.2. SLOW CYCLIC BEHAVIOUR OF DUTCH ORGANIC CLAY

This research extends into 'slow' cyclic loading dynamics of Dutch organic clay, deliberately omitting non-uniform pore pressure distribution effects. The study unveils significant insights into the slow cyclic response, emphasising the influence of loading frequency, comparison between natural and reconstituted samples, and the importance of initial stress states, cyclic stress amplitudes, clay and organic content, and post-cyclic properties.

- It is observed that reconstituted samples exhibit a lower secant shear modulus and damping ratio. However, the rate at which the shear modulus and damping ratio decrease with the increase in the number of cycles does not show a marked difference between the two types of samples. Further insights are provided by plotting the undrained shear strength, secant shear modulus, and damping ratio for both

natural and reconstituted samples against the average mean effective stress. The manner in which these properties evolve differs between the natural and reconstituted samples. Particularly, the variation in undrained shear strength, secant shear modulus, and damping ratio with respect to average mean effective stress in the natural sample is nonlinear, unlike in the reconstituted sample. The natural sample exhibits higher shear stiffness, lower excess pore pressure development, and a slower reduction in undrained shear strength during cyclic loading. This suggests that the cyclic strength of the natural sample is greater than that of the reconstituted one.

- Both the induced and inherent anisotropy affect the soil response upon cyclic loadings. The butterfly-shape stress path observed at later stages in the strain-controlled cyclic triaxial tests is related to the dilation-contraction alternations, which have been attributed to the rearrangement of microstructures resulting from the continuous change in loading direction during cyclic shearing. Additionally, the consistent stress path inclination on both compression and extension sides in the strain-controlled cyclic triaxial tests is an indication of pronounced inherent anisotropy. Furthermore, the inherent anisotropy of sample Cyc T2(IX) results in a more asymmetrical stress path evolution. The test initiated from isotropic conditions exhibits higher average pore pressure in each cycle. This is attributed to its symmetrical behaviour along the horizontal axis, leading to a more pronounced movement of the stress path toward the left on the meridian plane. In contrast, the stress path in the K_0-consolidated test, due to its asymmetrical stress path, shows a less shift toward the left on the meridian plane. Interestingly, the secant shear modulus and damping ratio variations in K_0-consolidated samples tend to converge towards those of isotropic-consolidated samples as the average mean effective stress decreases. Such a transition from anisotropic to isotropic during cyclic loading suggests the erasing of stress-induced anisotropy during cyclic loading.

- In engineering practice, accurately determining the exact number of loading cycles can be challenging, particularly because most cyclic loads encountered in geotechnical engineering designs are irregular and characterised by variable amplitudes and frequencies. Thanks to the contributions of numerous researchers, methods have been developed to translate these irregular cyclic loads into sets of equivalent cyclic amplitudes and loading cycles. However, it is important to remem- ber that soil behaviour is dependent on the effective stress state and strain level. Therefore, when investigating the cyclic behaviour of soils, it is essential to anal- yse and interpret experimental data in the context of both effective stress state and strain level, in addition to considering the number of loading cycles. The changes in undrained shear strength, secant shear modulus, and damping ratio during cyclic shearing with respect to the average mean effective stress, p'_{avg}, reveal that the undrained shear strength, secant shear modulus, and damping ratio tend to decrease almost linearly as the average mean effective stress diminishes. Furthermore, it appears that the rate of shear modulus reduction in relation to p'_{avg} is not influenced by the initial stress ratio. Intriguingly, in both smaller and higher cyclic shearing stages, the variations in secant shear modulus can be categorised

into two distinct groups: tests initiated from either the compression or extension side. This observation contrasts with the observation when plotting the secant shear modulus with respect to loading cycles. This is due to the lower strain amplitudes, which result in an apparently higher shear modulus for extension-side tests. While the trend is less pronounced, a higher absolute initial stress ratio generally corresponds to a lower secant shear modulus at the same cyclic deviatoric strain.

- The stress-ratio dependency of excess pore pressure development becomes evident when analysing with cyclic deviatoric strain. On the compression side, samples with a higher initial stress ratio exhibit a more rapid increase in excess pore pressure relative to the cyclic deviatoric strain. On the extension side, it is observed that a higher absolute initial stress ratio leads to a quicker escalation of excess pore pressure in relation to cyclic deviatoric strain. There is a consistent relationship between larger stress ratio magnitude and higher permanent deviatoric strain. Additionally, tests that commence from the compression side result in an accumulation of compressive deviatoric strain, while tests that begin on the extension side show extensive deviatoric strain. Intriguingly, for samples where the stress path exceeds the critical stress ratio and moves into the 'dry' side of critical, the rate of axial strain accumulation accelerates sharply. This implies that these samples are nearing the point of failure under the given cyclic shearing conditions.

- Regarding the impact of cyclic stress amplitude, the test with higher amplitude shows a more rapid stiffness reduction in the early cyclic stage. The sample with lower amplitude stabilising at a higher mean effective stress, the variation in normalised secant shear modulus with respect to average mean effective stress exhibits a similar trend between the two samples. A closer examination of the normalised secant shear modulus in relation to cyclic deviatoric strain indicates that the greater shear stiffness of the sample with lower amplitude is due to its smaller cyclic deviatoric strain. The higher stress amplitude leads to a more significant development of excess pore pressure with the loading cycle. Interestingly, the rate of excess pore pressure increase in relation to cyclic deviatoric strain is slower for the sample with higher amplitude. This observation is consistent with a lower stress ratio on the compression side achieved by higher stress amplitude, is associated with a slower increase in excess pore pressure relative to the cyclic deviatoric strain. The higher stress amplitudes lead to a quicker accumulation of permanent deviatoric strain.

- The impact of organic and clay content on the cyclic response is investigated. For samples with less clay and organic content, the shear modulus degrades more rapidly. However, no clear difference is observed in the rate of secant shear modulus reduction between samples with different organic content but similar clay content. When examining the variation of secant shear modulus in relation to average mean effective stress, all samples exhibit a similar reduction rate as mean effective stress decreases. The more rapid degradation rate with the loading cycle observed in samples with less clay and organic content results from a faster reduction in average mean effective stress with each cycle. Additionally, the change

in secant shear modulus in relation to cyclic deviatoric strain suggests that the secant shear modulus for the tested Dutch organic clays is dominated by cyclic deviatoric strain. Nonetheless, further investigation is needed to confirm this aspect. The rate of excess pore pressure development in relation to cyclic deviatoric strain is fastest for samples with less clay and organic content. Soils with higher plasticity have a more flexible microstructure and result in a higher capacity to adapt to applied cyclic loading, thus exhibiting lower excess pore pressure development. However, the excess pore pressure responses of samples with different organic content but similar clay content are quite similar, indicating a lesser influence of organic content on excess pore pressure development.

- Regarding the cyclic and post-cyclic undrained shear strength, compared to a sample that did not undergo cyclic loading, the post-cyclic undrained shear strength, S_u, experiences a significant increase—a nearly four-fold enhancement. In relation to critical state stress ratios, cyclic shearing does not appear to modify the critical state stress ratios of the material under investigation. As for post-cyclic deformation, the degree of post-cyclic deformation is dictated by both the sample compressibility and the excess pore pressure generated. A good linear relation can be found between the predicted post-cyclic volumetric strain with empirical relation and the measured one. However, the measured post-cyclic volumetric strain is almost two times higher than the predicted one. A higher magnitude of post-cyclic recompression is observed in Dutch organic clay. The post-cyclic axial strain seems to be more influenced by the amount of excess pore pressure than by the stress path during the recompression stage.

- The comparison between the pseudo-elastic shear modulus of tested Dutch organic clay and the empirical relation based on remoulded samples indicates that the empirical relation could underestimate the pseudo-elastic shear modulus of Dutch organic clay. The sample with more disturbance might result in better alignment with the relation based on data from remoulded samples. A generalised relationship based on a series of in-situ seismic cone tests is also compared with experimental data. Good alignment can be found for all tested Dutch organic clay samples, suggesting that typical empirical relations for pseudo-elastic shear modulus can provide a reasonable estimation of the pseudo-elastic shear modulus of Dutch organic clay.

6.1.3. SLOW CYCLIC MODELLING OF DUTCH ORGANIC CLAY

The thesis introduces the JMC-clay BSEVP model, a novel advancement in modelling soil behaviour under cyclic loads. It delves into the sensitivity analysis of key parameters within an elastoplastic-viscoplastic bounding surface framework, aiming to facilitate model calibration and enhance predictive accuracy. The calibration procedure and suggested parameter values are outlined. Lastly, the potential of the model for practical geotechnical applications is underscored.

- The essence of the proposed model lies in the advancement of the elastoplastic-viscoplastic framework, with a particular focus on the evolution of the overstress

function. The parameters governing this function are meticulously examined. The impact of the parameters s_v and V on the overstress function is immediate; however, the parameter n, which defines the exponent for the 'normalised overstress' $\Delta\sigma^*$, exhibits a varying influence on the viscoplastic response, contingent on the value of $\Delta\sigma^*$. By integrating the bounding surface and elastoplastic-viscoplastic theories into the JMC-clay model, the total number of parameters increases from 12 to 19. This thesis summaries definitions and suggests reasonable ranges for these parameters when applied to organic soils, which facilitates model calibration. The selection of viscoplastic parameters critically affects the slope of the normal compression line and the apparent pre-consolidation pressure, indicating that the choice of λ^* should consider the soil's time-dependent behaviour.

- A thorough sensitivity analysis highlights the influence of the new model parameters, including those associated with the bounding surface, on the model's ability to predict cyclic responses. This analysis emphasises the importance of viscoplastic parameters, especially s_v, in determining the size of the viscoplastic zone and the evolution of the bounding surface. The parameter w, indicative of the hybrid flow rule, is pivotal in addressing initial stabilisation in stress paths and the development of excess pore pressure. The damage parameter a_d plays a significant role in the deviatoric responses, influencing peak deviatoric stress and the reduction of shear modulus. The consideration of anisotropy evolution, adjustments to the projection centre, and Lode angle dependency also prove essential in model predictions.

- The model calibration process derives from the sensitivity analysis, with calibration of the JMC-clay EP parameters achievable through static laboratory tests. Calibration of additional parameters necessitates rapid cyclic triaxial tests, including isotropic and K_0 consolidated samples, with default parameter values provided to aid initial calibration efforts. A minimum of six distinct tests is advised for a comprehensive calibration, involving iterative adjustments to parameters to align closely with observed experimental outcomes, such as stress paths, stress-strain curves, secant shear modulus, and excess pore pressure development.

- Evaluation of the JMC-clay BSEVP model on samples from groups (III) to (IX) demonstrates improvements in predictive accuracy, notably in simulating the cyclic behaviour of organic clay. The model successfully predicts stress path evolution, excess pore pressure, and variations in secant shear modulus, though it slightly overestimates peak deviatoric stress in static tests. Model performance in predicting damping ratio evolution and a slight overprediction of secant shear modulus indicate areas for further refinement. Observed discrepancies in the post-cyclic recompression phase point to the need for model adjustments to reflect aspects more accurately, such as the recompression index uncertainty and underestimation of excess pore pressure.

- Applying the JMC-clay BSEVP model to group (X) samples provides insights into its predictive capabilities and limitations. The model effectively captures changes in loading rate during the unloading and reloading phases in static probe paths.

The model tends to overestimate deviatoric strain in the static probe stage, a likely consequence of calibration based on specific cyclic loading frequencies. Its performance varies across different stress probe paths and cyclic loading conditions, showing improved accuracy for stress states close to isotropic and K_0 conditions. In cyclic tests, the model response is nuanced, underestimating shear stiffness at lower cyclic amplitudes while accurately predicting secant shear modulus at higher amplitudes. Discrepancies in permanent deviatoric strain and excess pore pressure development, especially in tests starting from initial stress ratios far from the ones adopted for calibration, are notable. Despite reasonable efficacy in simulating the cyclic behaviour of group (X) samples, the model exhibits significant discrepancies with experimental results in post-cyclic recompression and undrained shearing stages, stemming from underprediction of excess pore pressure development during cyclic shearing, the uncertainty in the post-cyclic compression index, and the evolution of the projection centre position. Improvements with the projection centre at the origin for post-cyclic stages highlight the necessity of further investigation and refinement of the projection centre evolution.

- An achievement of the model is its capacity to produce shear modulus reduction and damping curves, as reported in the literature, which is crucial for engineering practice. The model demonstrates rate-dependent characteristics in generating these curves across different loading frequencies. With the coupled elastoplastic-viscoplastic framework, minor discrepancies in the curves are observable at frequencies above 0.001Hz, likely attributable to strain-rate saturation. The model proficiency in predicting both cyclic and permanent shear strains across various loading frequencies underscores its critical aspect. Based on the parameters and pre-shearing stress state employed for demonstration, the model demonstration indicates that at high loading rates, failure predominantly results from permanent shear strain, whereas at lower loading rates, failure is more likely attributed to cyclic shear strain.

6.1.4. DEVELOPMENT OF CYC-DOSS

The thesis unveils the conceptual design and electro-mechanical development of a cutting-edge earthquake simulator for soft soils, termed the CYC-DoSS device. This innovative device addresses and overcomes certain limitations found in traditional equipment. Its novel approach is characterised by the integration of in-house developed local response sensors, which are capable of collecting comprehensive data on the coupled hydro-mechanical response of soil samples.

- The cross-coupling effect in multidirectional shear devices describes the influence of movement along one axis on the movements occurring along another axis. To evaluate this effect within the CYC-DoSS system, two harmonic waves were employed to explore different motion effects. In the slow-motion scenario, movement of the X-axis table showed no significant impact on the Y-axis displacement and load measurements. In contrast, movement of the Y-axis table resulted in negligible displacement on the holding axis, yet a 3N variation in the X-axis load reading was noted. This outcome is consistent with the mechanical configuration, as the

X-axis table is mounted atop the Y-axis table. During fast-motion testing, similar observations were made, with no substantial impact on Y-axis displacement and load readings when the X-axis table was moved. However, a 2N variation in the X-axis load was observed upon movement of the Y-axis table, likely attributable to the displacement amplitude of the motion. These findings collectively suggest that the CYC-DoSS system demonstrates minimal cross-coupling effects, underscoring its effectiveness in isolating directional movements.

- The incorporation of cell and back pressure control within the CYC-DoSS system enables the execution of authentic undrained tests, distinguishing it from traditional shearing devices. This capability not only allows for the application of cell and back pressure to follow versatile stress paths but also facilitates back pressure saturation, enhancing the system's versatility beyond the limitations of existing devices, which typically commence cyclic shearing from an isotropic or a K_0 condition. Moreover, the CYC-DoSS system supports the determination of lateral stress and allows for the performance of zero lateral strain (constant average area) cyclic shearing tests. These tests are comparable to those conducted with conventional cyclic simple shear devices on saturated samples, achieved by maintaining constant height and preventing drainage, thereby eliminating the need for rigid lateral support to control the sample's lateral strain. Instead, the specimen is simply enclosed in a standard latex membrane, simplifying the setup while maintaining test integrity.

- In the CYC-DoSS, $G_{\max}$ is determined through shear wave velocity measurements via bender elements, providing a direct method for comparing laboratory and field soil states. Non-uniformities and challenges in achieving pore pressure equalisation within the specimen become more pronounced under multidirectional loading at high frequencies. To advance the understanding of experimental results and the hydro-mechanical coupling response under such conditions, this thesis has led to the development of advanced sensors. Specifically, the CYC-DoSS incorporates the FOP-M fibre optic pressure sensor. This technology allows stable and accurate pressure measurement despite adverse conditions such as temperature fluctuations, electromagnetic interference, humidity, and vibration. An advanced displacement sensing unit has also been developed, equipped with a laser distance sensor and a 3D Hall effect sensor, to meticulously track and record the lateral strain of specimens during testing. This dual-sensor approach enhances the robustness and reliability of lateral strain measurements within the CYC-DoSS system. Furthermore, the integration of MEMS accelerometers facilitates the measurement of acceleration during cyclic tests, necessitating the correction of load cell readings based on both mass and measured acceleration. This inclusion not only enhances the accuracy of the system but also enables acceleration-controlled tests, broadening the scope of experimental possibilities.

- The experimental evaluations conducted without a soil sample have showcased the CYC-DoSS's capabilities in handling cyclic cell pressure, multidirectional cyclic shearing, high-frequency cyclic loading, and real-time earthquake loadings. These tests effectively demonstrate the mechanical and electrical design's robustness.

However, they stopped short of assessing the system performance with soft organic clay samples, where specific limitations became evident. One notable issue is the misalignment between the vertical load ram and the hydraulic actuator, which increases friction and compromises the accuracy of load measurements. Additionally, mechanical compliance introduced by commercially manufactured pin connectors results in a delay in load readings following load reversal. Compounding these challenges is the presence of trapped air within the system, which distorts pore water pressure measurements under cyclic loading, highlighting areas for further refinement to enhance the system efficacy with actual soil samples. These aspects warrant attention and improvements in the continued development of CYC-DoSS.

6.2. LIMITATIONS

While every effort was made to ensure the robustness and validity of the research, certain constraints inherent to the experimental design, scope, and resources have influenced the outcomes. Acknowledging these limitations is crucial for understanding the context and scope of the thesis conclusions.

- The experimental tests conducted are confined to axisymmetric stress states, which do not fully encompass the range of possible stress-strain paths encountered in field conditions. Moreover, the direction of loading remains singular, limiting the scope of simulated loading conditions and their corresponding effects on soil behaviour. This restriction highlights the need for further development and testing methodologies that can more accurately replicate the complex and multidirectional stress-strain paths typical of real-world scenarios.
- In cyclic triaxial testing, a sinusoidal waveform is commonly used to apply cyclic strain or stress amplitudes. However, it is important to note that adopting a sinusoidal waveform results in a non-constant strain rate. Furthermore, in stress-controlled cyclic triaxial tests, establishing a constant strain rate is crucial to isolate the influence of varying strain rates that arise from differences in stiffness among samples. This approach ensures that the effects observed are attributable to the stress conditions being investigated, rather than artefacts of varying strain rates.
- The misalignment between the vertical load ram and the hydraulic actuator exacerbates friction, which in turn compromises the accuracy of load measurements. Additionally, mechanical compliance inherent in commercially manufactured pin connectors contributes to a delay in load readings following load reversal.
- Currently, the PID control parameters have been specifically tuned for operations at half the capacity of the hydraulic actuator system and optimised for displacement control. This limits loading rates and the rate at which setup can follow changes in load direction without overshoot.
- Among all in-house developed local sensors, only the fibre optic pressure transducer was utilised in tests with soil samples. Other sensors needed additional cali-

bration and optimisation in waterproofing before test runs could be attempted on soil samples.

- The proposed model is only evaluated with cyclic triaxial tests up to a loading frequency of 0.1Hz. The model validation at higher loading frequencies was not possible due to lacking experimental data on Dutch organic clay at higher loading rates.

6.3. FUTURE RECOMMENDATIONS

This section presents recommendations and aims to inspire further exploration and refinement in this field, addressing unanswered questions and exploring new avenues that have emerged from this research.

- Despite the well-acknowledged rate-dependency of soft soils, the exploration of this property is limited by the challenges in reliably measuring pore water pressure during 'fast' loading scenarios. The advent of the CYC-DoSS system, equipped with innovative sensor technology, introduces the capability to conduct 'fast' loading tests. This development allows for the validation of experimental results against the proposed model, enhancing our understanding of soil behaviour under seismic conditions.

- For a comprehensive understanding of soil response under seismic events, it is crucial to consider the impact of multidirectional loading. Numerous studies have highlighted that soil behaviour is significantly influenced by loading from multiple directions, underscoring the importance of incorporating multidirectional loading scenarios in experimental designs and theoretical models.

- A major limitation in the practical application of the proposed class of models is rooted in the initialisation of the current state. This emphasises the critical need for a robust strategy to ensure reliable initialisation of constitutive models for practical applications. Developing such a strategy is essential to enhance the model effectiveness and reliability.

- Applying the JMC-clay BSEVP model to group (X) samples has shed light on both its predictive strengths and areas needing improvement. The model reveals a tendency to underestimate shear stiffness at lower cyclic amplitudes, while its predictions for secant shear modulus at higher amplitudes are more accurate. This discrepancy highlights the need to incorporate a strain-amplitude dependent shear modulus into the model to enhance its accuracy across a broader range of cyclic conditions. Furthermore, significant discrepancies were observed in the prediction of permanent deviatoric strain and excess pore pressure development, particularly in tests initiated from initial stress ratios far from those calibrated ones. These findings point to the critical influence of the overstress function and hybrid flow rule on the model response, underscoring the need for further research and refinement, especially concerning different initial stress states. While the model demonstrates a reasonable ability to simulate the cyclic behaviour of group (X)

samples, it significantly diverges from experimental results in the post-cyclic re-compression and undrained shearing stages. A demonstration by setting the projection centre at the origin for post-cyclic stages suggests a clear path for future enhancements by focusing on the projection centre evolution.

A

CALIBRATION OF TRIAXIAL EQUIPMENT

A

A.1. CALIBRATION OF TRIAXIAL EQUIPMENT

The triaxial equipment used in this thesis is calibrated every two months or before each experimental campaign to ensure the accuracy of the experimental program. The calibration procedure involves offsetting the pressure readings of pressure/volume controllers and pressure transducers at the half height of the sample, as shown in Figure A.1, and checking the alignment between pressure readings with a calibration ramp up to 600 kPa (both forward and backwards).

Four triaxial systems are used in this thesis for laboratory testing: GDSTAS Cell 1, GDSTAS Cell 2, QDTAS Cell 1 and QDTAS Cell 2. GDSTAS Cell 1 and GDSTAS Cell 2 are used to perform quasi-static tests and slow cyclic tests up to 0.001Hz loading frequency, while QDTAS Cell 1 and QDTAS Cell 2 are used to perform slow cyclic tests up to 0.1Hz and validation tests for CYC-DoSS. For clarity, one calibration result is presented for each equipment.

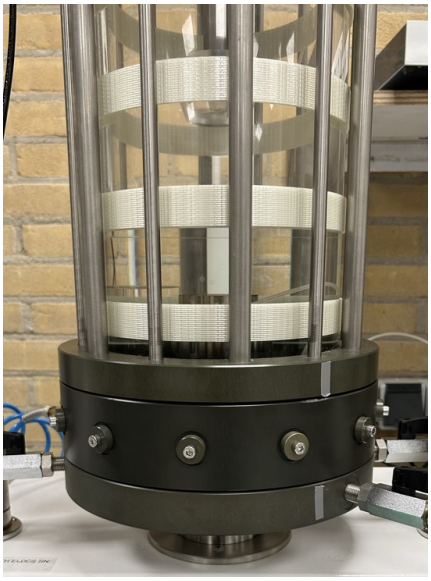

Figure A.1: Offsetting the pressure readings of pressure/volume controllers and pressure transducers at the half height of the sample

A.1.1. CALIBRATION OF GDSTAS CELL 1

On August 31st, 2021, the GDSTAS Cell 1 was calibrated before slow cyclic triaxial tests up to 0.001Hz. Figure A.2 presents the pressure readings from the cell, back pressure/volume controllers, and the pore pressure transducer during the forward and backward pressure ramp without a sample. The pressure differences of cell pressure, back pressure, and pore pressure transducers during the calibration ramp are also reported in Figure A.2. The difference between the pressure readings is less than 2kPa.

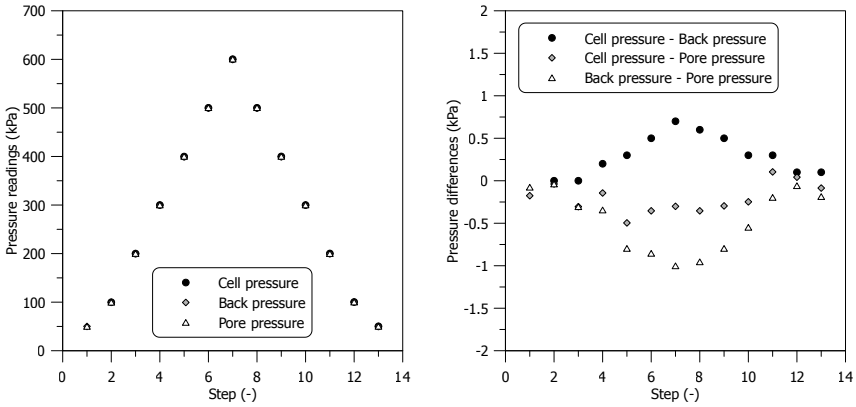

Figure A.2: Offsetting the pressure readings of pressure/volume controllers and pressure transducers at the half height of the sample

A.1.2. CALIBRATION OF GDSTAS CELL 2

On August 31st, 2021, the GDSTAS Cell 2 was calibrated before slow cyclic triaxial tests up to 0.001Hz. Figure A.3 presents the pressure readings from the cell, back pressure/volume controllers, and the pore pressure transducer during the forward and backward pressure ramp without a sample. The pressure differences of cell pressure, back pressure, and pore pressure transducers during the calibration ramp are also reported in Figure A.3. The difference between the pressure readings is less than 2kPa.

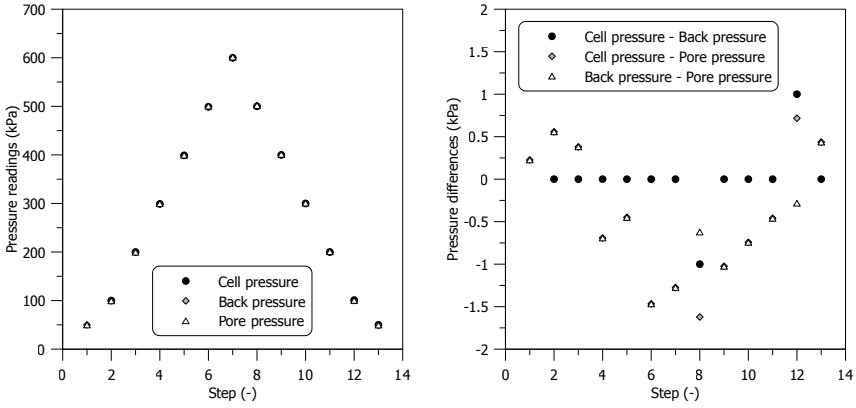

Figure A.3: Pressure readings and pressure differences of cell pressure, back pressure, and pore pressure transducers during calibration ramp

A.1.3. CALIBRATION OF QDTAS CELL 1

On August 2nd, 2022, the GDSTAS Cell 1 was calibrated before slow cyclic triaxial tests started at 0.1Hz. Figure A.4 presents the pressure readings from the cell, back pressure/volume controllers, and the pore pressure transducer during the forward and back-

ward pressure ramp without a sample. The pressure differences of cell pressure, back pressure, and pore pressure transducers during the calibration ramp are also reported in Figure A.4. The difference between the pressure readings is less than 2kPa.

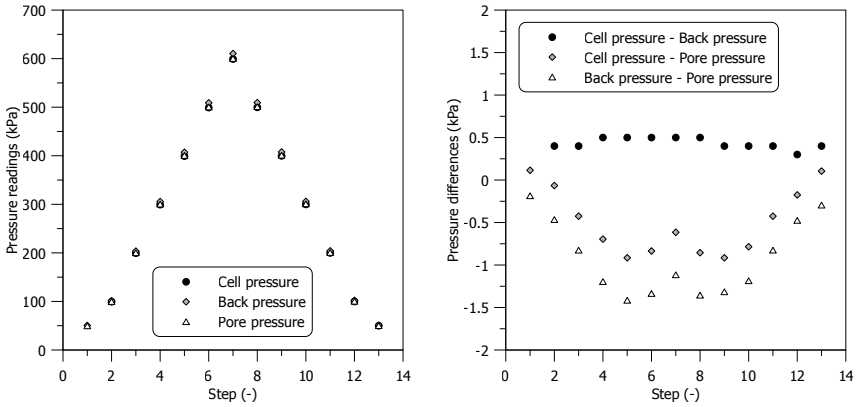

Figure A.4: Pressure readings and pressure differences of cell pressure, back pressure, and pore pressure transducers during calibration ramp

A.1.4. CALIBRATION OF QDTAS CELL 2

On August 2nd, 2022, the QDTAS Cell 2 was calibrated before slow cyclic triaxial tests started at 0.1Hz. Figure A.5 presents the pressure readings from the cell, back pressure/volume controllers, and the pore pressure transducer during the forward and backward pressure ramp without a sample. The pressure differences of cell pressure, back pressure, and pore pressure transducers during the calibration ramp are also reported in Figure A.5. The difference between the pressure readings is less than 2kPa.

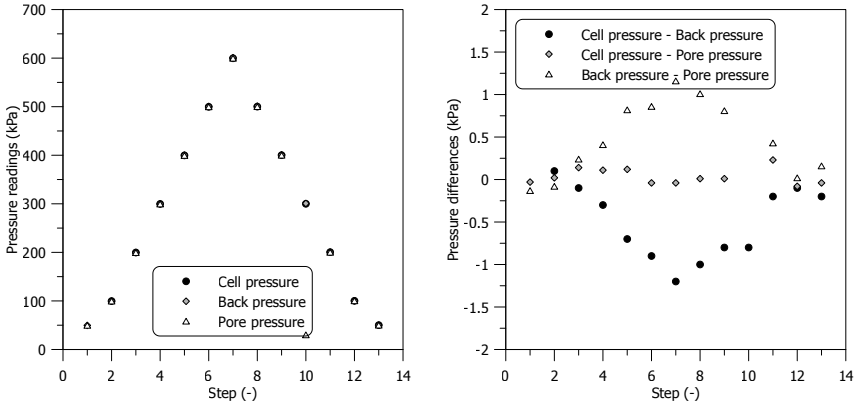

Figure A.5: Pressure readings and pressure differences of cell pressure, back pressure, and pore pressure transducers during calibration ramp

B

Sensitivity Analysis of JMC-Clay Elastoplastic Bounding Surface Model Parameters

B

B.1. INFLUENCE OF PARAMETER h_0 ON THE CYCLIC RESPONSE

The impact of the parameter h_0 on cyclic response is examined using strain-controlled cyclic shearing, with a cyclic strain amplitude, ε_{cyc} set at 0.01. For this sensitivity analysis, four distinct h_0 values are considered. Model parameters are listed in Chapter 3 and Table B.1. The simulation process comprises two stages: an isotropic consolidation stage followed by a cyclic shearing stage.

Table B.1: Model parameters adopted in sensitivity analysis

a_d	s_{eln}	w
0	1	0

Figure B.1 depicts the evolution of void ratio throughout both the consolidation and strain-controlled cyclic shearing stages. A lower h_0 value leads to an earlier change from stiff to less stiff compression response. As the value increases, such a transition is more evident.

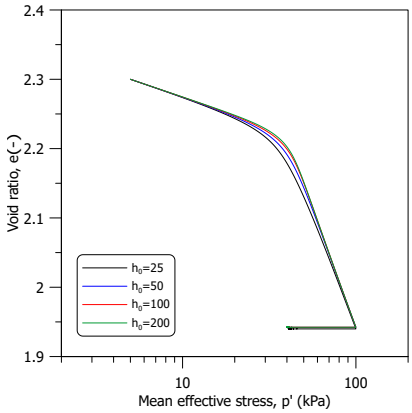

Figure B.1: Variation of void ratio during consolidation and strain-controlled cyclic shearing stage for different h_0 value

Figure B.2 further illustrates the stress path and the average excess pore pressure during cyclic shearing. It is observed that higher h_0 values are associated with higher peak deviatoric stresses attained during cyclic loading. For all investigated h_0 values, the stress paths tend to move leftward during cyclic loading. This leftward movement indicates contractive behaviour and the development of positive excess pore pressure. In general, a larger h_0 value results in slightly more excess pore pressure development (at same ε_{cyc}).

Strain-controlled cyclic shearing enables the analysis of the evolution of shear stiffness and damping ratio during cyclic loading. Figure B.3 displays the deviatoric stress-strain curve, as well as the development of the secant shear modulus and damping ratio for various h_0 values. Consistent with the stress path observations, the larger h_0 values correlate with higher peak deviatoric stresses during cyclic shearing. Regarding the secant shear modulus, larger h_0 values result in higher moduli, which slightly decrease as

the number of loading cycles increases. The damping ratio generally increases as h_0 values decrease in the first two loading cycles, although the differences among various h_0 values are relatively minor. Additionally, the variation in damping ratio with increasing loading cycles is not pronounced.

To further investigate various aspects of the predicted cyclic response, a sensitivity analysis is also conducted using stress-controlled cyclic shearing. Two different cyclic stress amplitudes, q_{cyc} ($0.15p'_i$ and $0.30p'_i$, with $p'_i = 100\,\text{kPa}$), were chosen to assess the impact of loading magnitude. Figure B.4 presents the stress path and average excess pore pressure observed during stress-controlled cyclic shearing. Consistently, across all h_0 values, the stress paths show a leftward movement during cyclic loading, leading to the development of positive excess pore pressure. Additionally, it is observed that higher cyclic stress amplitudes and lower h_0 values result in greater excess pore pressure development.

Figure B.5 illustrates the accumulation of permanent deviatoric strain, denoted as $\varepsilon_{q,\text{per}}$, during cyclic shearing. It is observed that lower h_0 values lead to larger developments of $\varepsilon_{q,\text{per}}$. Additionally, there is a correlation between the increase in permanent deviatoric strain and the rise in stress amplitude. Although the cyclic stress amplitude is symmetrical along the mean effective stress axis, for some h_0 values, $\varepsilon_{q,\text{per}}$ initially accumulates towards the extension side during the first 2 to 3 cycles, and then shifts towards the compression side, with the magnitude of this shift decreasing alongside h_0 values. This asymmetrical response can be attributed to three key factors: (1) the Lode angle dependency of the critical state stress ratio, (2) the Lode angle dependency of anisotropy evolution, as governed by the rotational hardening rule, and (3) the updating of the projection centre upon stress reversal.

An increase in the h_0 value increases the plastic modulus within the bounding surface. This leads to a stiffer compression curve during the consolidation stage, coupled with a more pronounced transition in stiffness. In the context of cyclic loading, higher h_0 values correlate with reduced excess pore pressure development (at same q_{cyc}), increased secant shear modulus, and diminished permanent deviatoric strain. Furthermore, higher stress amplitudes result in greater development of excess pore pressure and an increase in permanent deviatoric strain.

B

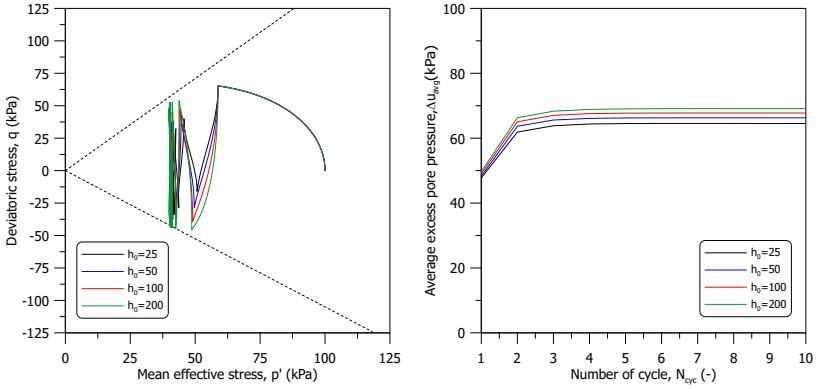

Figure B.2: Stress path and development of excess pore pressure of strain-controlled cyclic shearing stage for different h_0 value

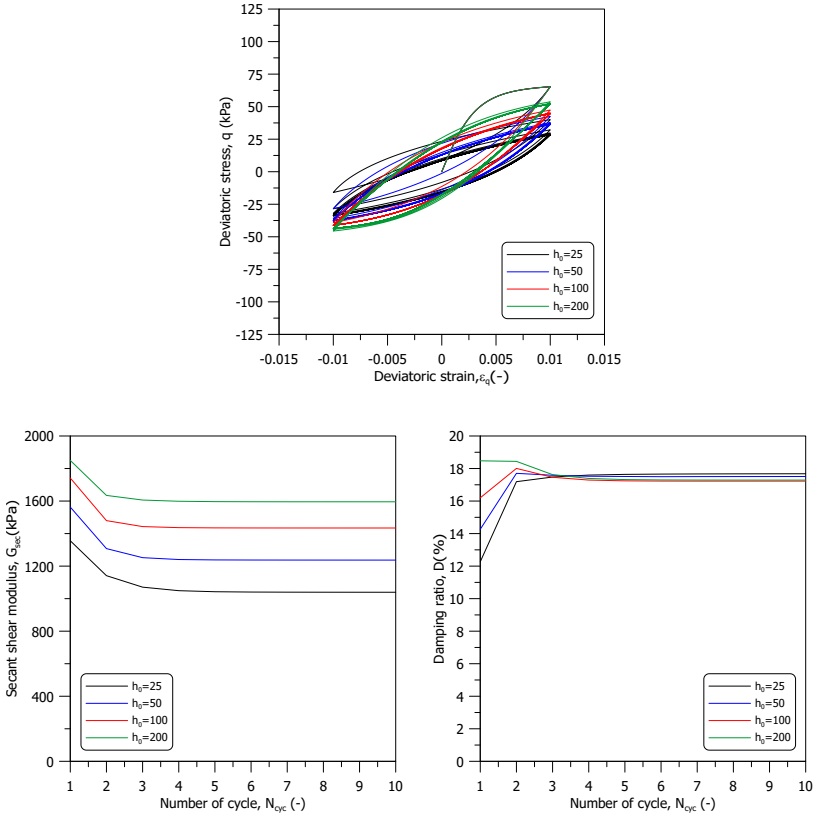

Figure B.3: Stress-strain curve, secant shear modulus, and damping ratio of strain-controlled cyclic shearing stage for different h_0 value

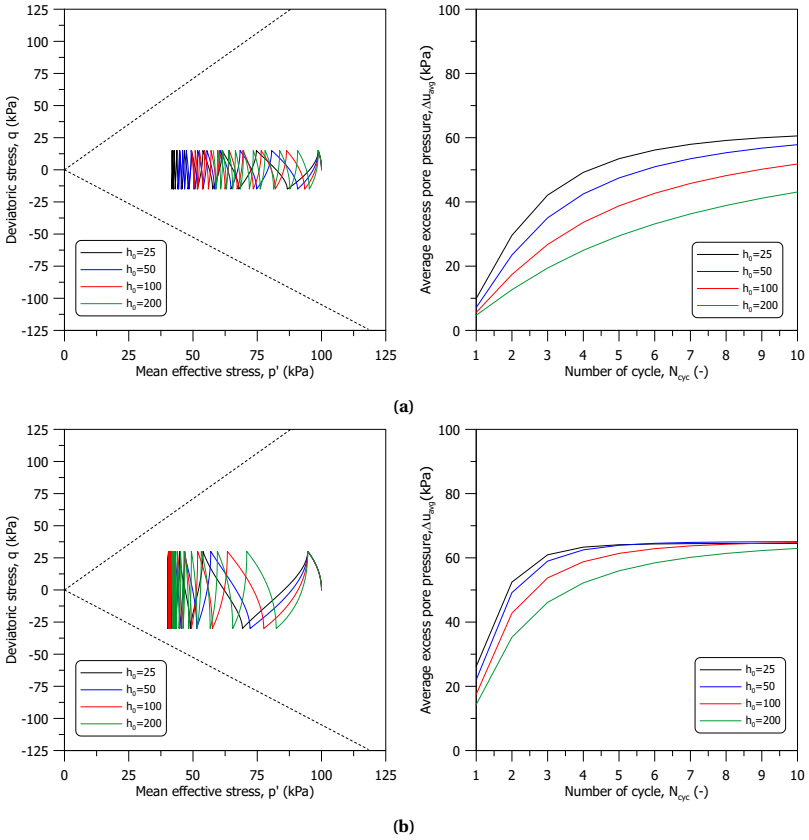

Figure B.4: Stress path and development of excess pore pressure of stress-controlled cyclic shearing stage for different h_0 values: (a) $q_{cyc} = 0.15p'_i$ and (b) $q_{cyc} = 0.30p'_i$

B

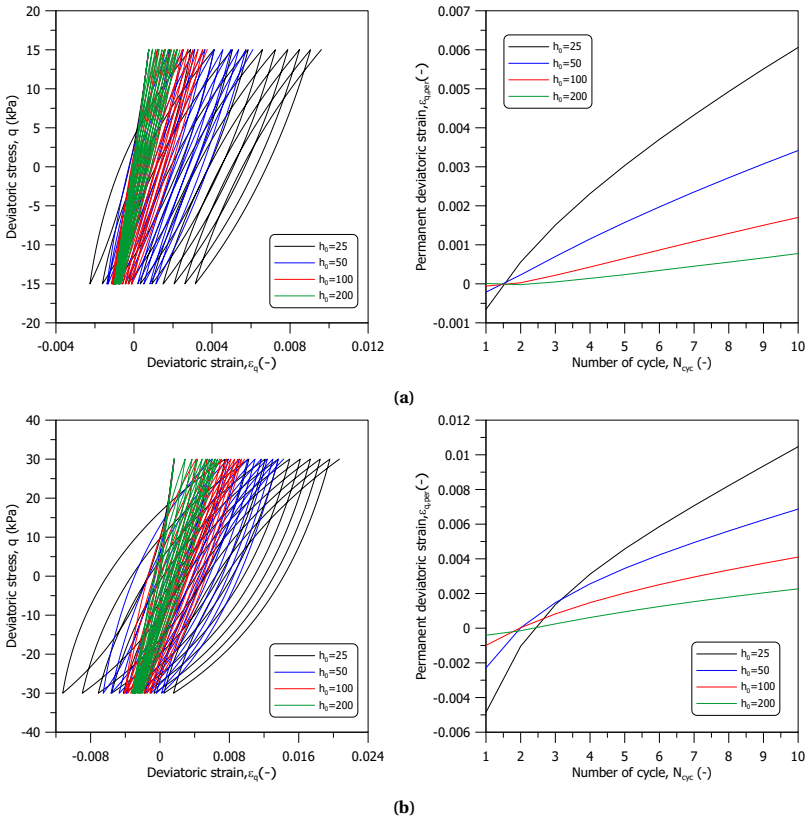

Figure B.5: Stress-strain curve and permanent deviatoric strain of stress-controlled cyclic shearing stage for different h_0 values: (a) $q_{cyc} = 0.15p'_i$ and (b) $q_{cyc} = 0.30p'_i$

B.2. INFLUENCE OF PARAMETER a_d ON THE CYCLIC RESPONSE ($a_d > 0$)

The impact of the positive damage parameter ($a_d > 0$) on cyclic response is explored using strain-controlled cyclic shearing, with the cyclic strain amplitude, ε_{cyc} set at 0.01. For this sensitivity analysis, four a_d values are considered. Model parameters can be found in Chapter 3 and Table B.2. The simulation includes two stages: firstly, an isotropic consolidation stage, and secondly, a cyclic shearing stage.

Table B.2: Model parameters adopted in sensitivity analysis

h_0	s_{eln}	w
50	1	0

Figure B.6 showcases the variation of void ratio during both the consolidation and strain-controlled cyclic shearing stages, and it suggests that there is almost no influence on the compression curve when parameter $a_d > 0$.

Figure B.7 presents the stress path and average excess pore pressure during cyclic shearing. For all a_d values, the simulations attain the same peak deviatoric stress in the first loading cycle. However, this peak deviatoric stress degrades more rapidly with increasing a_d values. In all simulations, the stress paths exhibit a consistent leftward movement during cyclic loading, suggesting contractive behaviour and the development of positive excess pore pressure. Furthermore, a minor reduction in excess pore pressure with an increase in a_d value is observed.

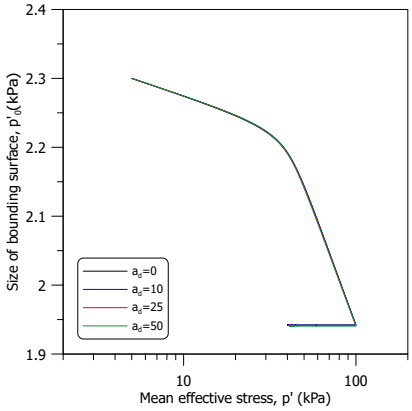

Figure B.6: Variation of void ratio during consolidation and strain-controlled cyclic shearing stage for different a_d value

Figure B.8 presents the deviatoric stress-strain curve, along with the development of the secant shear modulus and damping ratio for a range of a_d values. In alignment with the stress path observations, smaller a_d values are associated with a slower degradation of peak deviatoric stresses during cyclic shearing. When it comes to the secant shear modulus, lower a_d values lead to higher moduli and a more gradual reduction in mod-

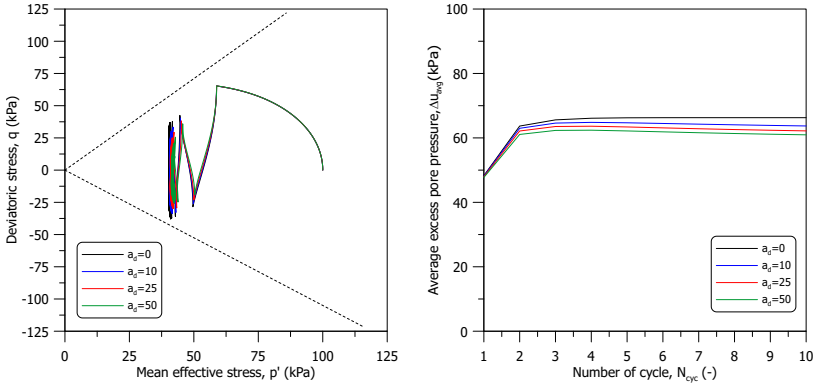

Figure B.7: Stress path and development of excess pore pressure of strain-controlled cyclic shearing stage for different a_d value

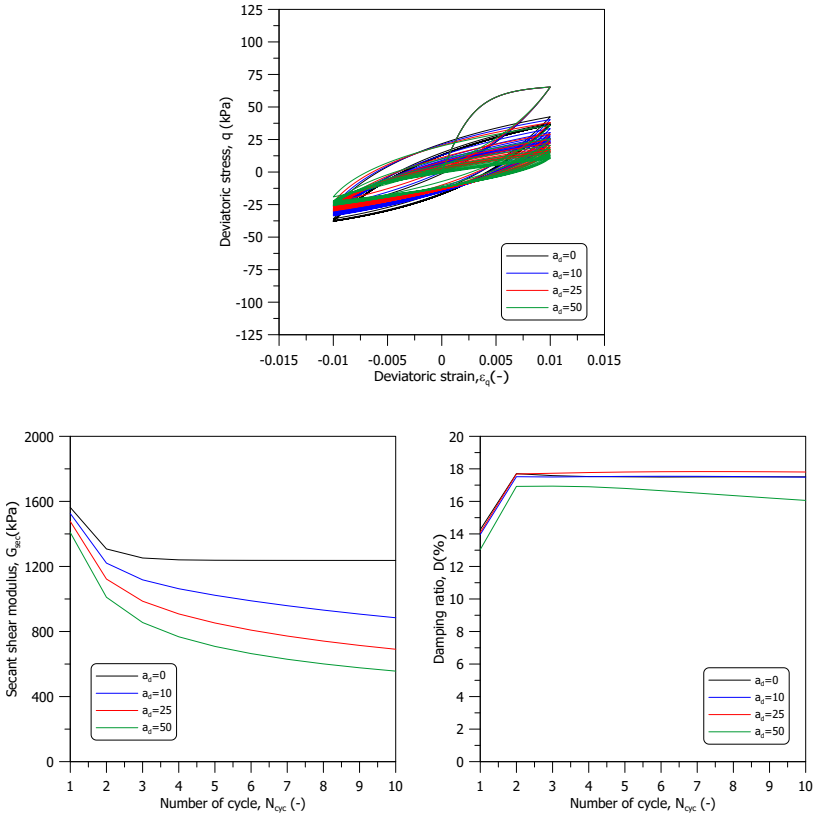

Figure B.8: Stress-strain curve, secant shear modulus, and damping ratio of strain-controlled cyclic shearing stage for different a_d value

ulus as the number of loading cycles increases. The damping ratio tends to decrease as a_d values increase, though the differences among various a_d values are not significant. However, a decreasing trend in the variation of damping ratio with increasing loading cycles is observed for a_d value equals to 50.

To further investigate various aspects of the predicted cyclic response, a sensitivity analysis was also conducted using stress-controlled cyclic shearing. Two different cyclic stress amplitudes, q_{cyc} ($0.15p'_i$ and $0.30p'_i$, with $p'_i = 100\,\text{kPa}$), were chosen to assess the impact of loading magnitude. Figure B.9 illustrates the stress path and average excess pore pressure during stress-controlled cyclic shearing. Consistently, for all a_d values, the simulations predict contractive behaviour and development of positive excess pore pressure. There is a direct correlation between higher a_d values and slightly increased excess pore pressure development. Furthermore, the simulations reveal that higher cyclic stress amplitudes lead to greater development of excess pore pressure. It is important to note that in the simulation with a cyclic stress amplitude of $q_{\text{cyc}} = 0.30p'_i$, an interesting phenomenon is observed. For a_d values greater than 25, the stress paths exhibit a scimitar shape, and the excess pore pressure shows a decreasing trend. This difference is attributed to the drastically reduced plastic modulus during cyclic loading with higher damage parameters. As a result, rotational hardening is intensified, leading to a much faster change in the inclination of the bounding surface during cyclic shearing.

Figure B.10 depicts the accumulation of permanent deviatoric strain, represented as $\varepsilon_{q,\text{per}}$, during cyclic shearing. Despite similar levels of permanent deviatoric strain in the initial cycle across all simulations, higher a_d values are observed to result in larger accumulations of $\varepsilon_{q,\text{per}}$ as the shearing progresses. Additionally, a correlation is evident between the increase in permanent deviatoric strain and higher stress amplitudes.

B

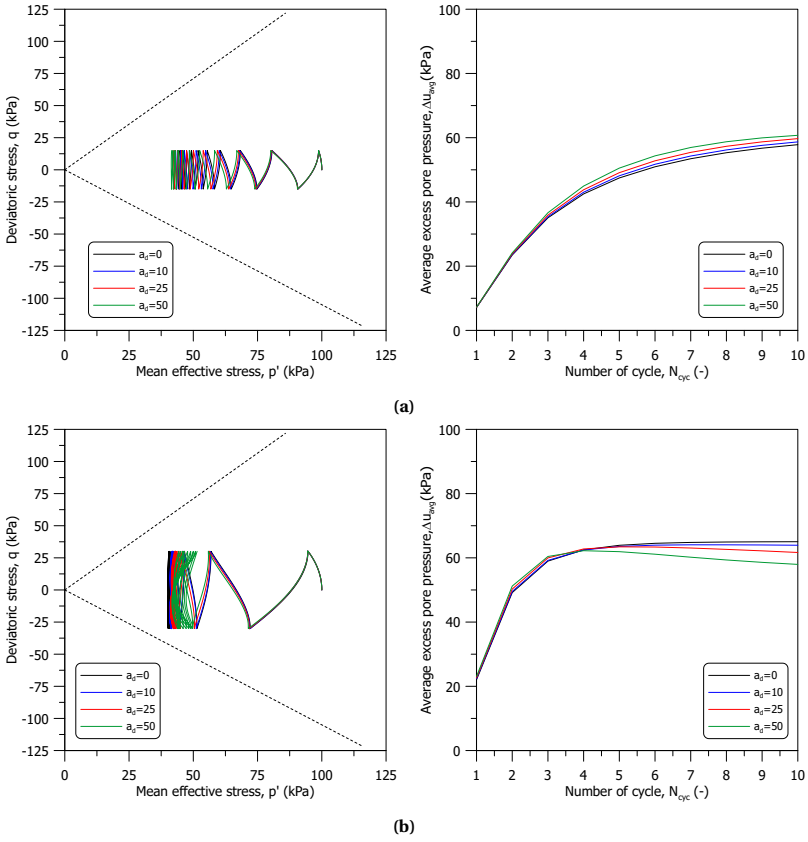

Figure B.9: Stress path and development of excess pore pressure of stress-controlled cyclic shearing stage for different a_d values: (a) $q_{\text{cyc}} = 0.15p'_i$ and (b) $q_{\text{cyc}} = 0.30p'_i$

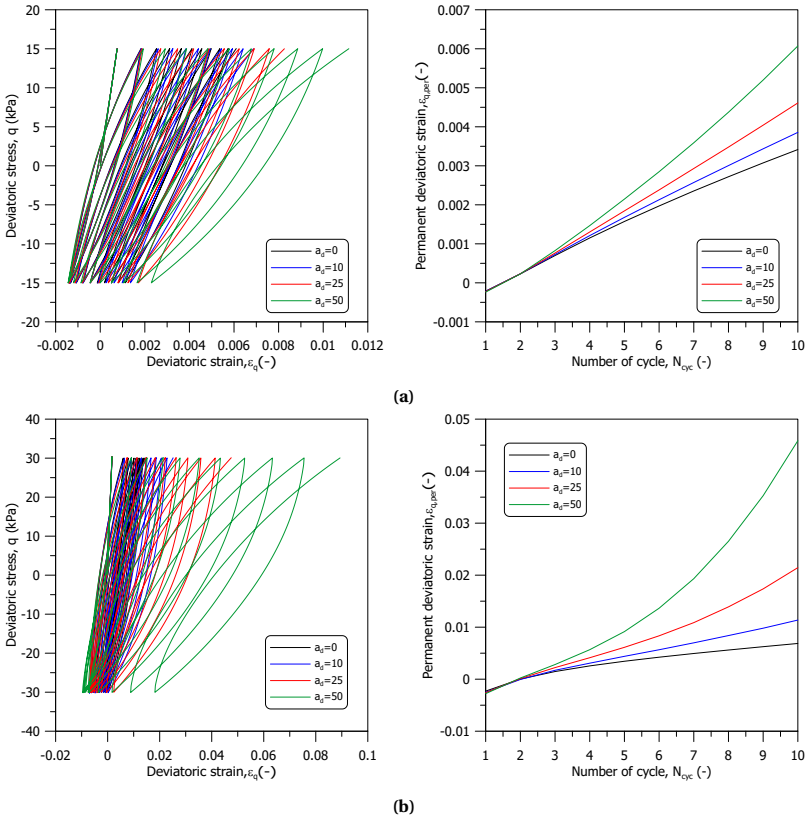

Figure B.10: Stress-strain curve and permanent deviatoric strain of stress-controlled cyclic shearing stage for different a_d values: (a) $q_{\text{cyc}} = 0.15p'_i$ and (b) $q_{\text{cyc}} = 0.30p'_i$

B.3. INFLUENCE OF PARAMETER a_d ON THE CYCLIC RESPONSE ($a_d < 0$)

In the previous sections, the sensitivity analysis was conducted for the positive damage parameter ($a_d > 0$). The next section will be dedicated to the sensitivity analysis of the negative damage parameter a_d ($a_d < 0$), aiming to elucidate its influence within the proposed model framework.

The impact of the negative damage parameter ($a_d < 0$) on cyclic response is explored using strain-controlled cyclic shearing, with the cyclic strain amplitude, ε_{cyc} set at 0.01. For this sensitivity analysis, four a_d values are considered. Model parameters can be found in Chapter 3 and Table B.3. The simulation process includes two stages: firstly, an isotropic consolidation stage, and secondly, a cyclic shearing stage.

Table B.3: Model parameters adopted in sensitivity analysis

h_0	s_{eln}	w
50	1	0

Figure B.11 showcases the variation of void ratio during both the consolidation and strain-controlled cyclic shearing stages, and it also indicates that there is no influence on the compression curve when the parameter $a_d < 0$.

Figure B.12 presents the stress path and average excess pore pressure during cyclic shearing. For all a_d values, the simulations again attain the same peak deviatoric stress in the first loading cycle, but the peak deviatoric stress in the subsequent cycles increases as a_d value reduces. Additionally, the stress paths exhibit contractive behaviour and the development of positive excess pore pressure. Furthermore, a minor increase in excess pore pressure with a lower a_d value is observed, attributing this to the higher peak deviatoric stress with a lower a_d value.

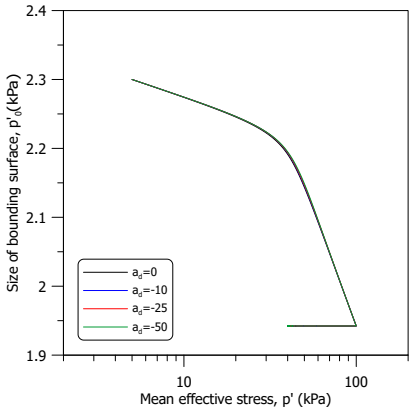

Figure B.11: Variation of void ratio during consolidation and strain-controlled cyclic shearing stage for different a_d value

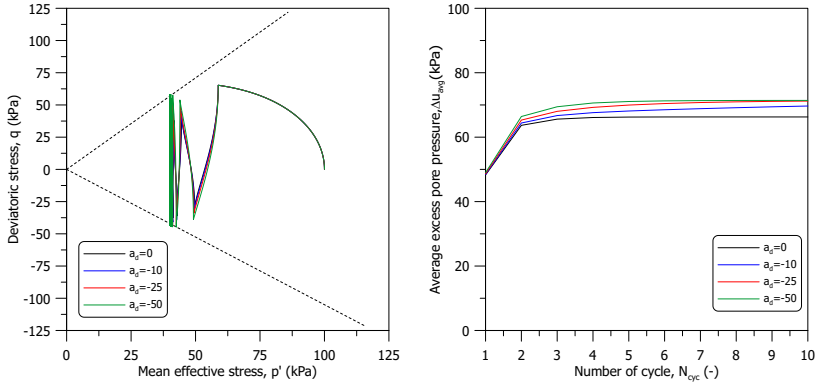

Figure B.12: Stress path and development of excess pore pressure of strain-controlled cyclic shearing stage for different a_d value

Figure B.13 presents the deviatoric stress-strain curve, along with the development of the secant shear modulus and damping ratio for a range of a_d values. In alignment with the stress path observations, smaller a_d values are associated with higher peak deviatoric stresses during cyclic shearing. When it comes to the secant shear modulus, except for $a_d = -50$, lower a_d values lead to higher moduli and a more gradual increase in modulus as the number of loading cycles increases. As for the damping ratio, the differences for a_d values larger than -25 are relatively minor. The damping ratio increases with the loading cycle for simulations with a_d values lower than -25. This is attributed to the drastic increase in plastic modulus with loading cycle, rendering stiffer stress-strain curves and higher loop area. Additionally, an increasing trend in the damping ratio with a rising number of loading cycles is noted for a_d values below -25. It is important to highlight that at an a_d value of -50, a rapid increase in plastic modulus occurs, leading to a viscoelastic response. This suggests that a reasonable range for the a_d value should be set above -50 to ensure a more accurate and realistic prediction of soil behaviour.

To further investigate various aspects of the predicted cyclic response, a sensitivity analysis was also conducted using stress-controlled cyclic shearing. Two different cyclic stress amplitudes, q_{cyc} ($0.15p'_i$ and $0.30p'_i$, with $p'_i = 100\,\text{kPa}$), were chosen to assess the impact of loading magnitude. Figure B.14 illustrates the stress path and average excess pore pressure during stress-controlled cyclic shearing. The simulations reveal that higher cyclic stress amplitudes and a_d values lead to greater development of excess pore pressure. Figure B.15 depicts the accumulation of permanent deviatoric strain, represented as $\varepsilon_{q,\text{per}}$, during cyclic shearing. Despite similar levels of permanent deviatoric strain in the initial cycle across all simulations, lower a_d values result in smaller accumulations of $\varepsilon_{q,\text{per}}$ as the shearing progresses. Additionally, the permanent deviatoric strain increases with stress amplitude.

The parameter a_d primarily influences the deviatoric aspects of the cyclic response, including peak deviatoric stress, secant shear modulus, and permanent deviatoric strain. However, the significant rise or reduction in plastic modulus during cyclic loading with extreme a_d values can also impact other facets of the cyclic response. For example, a

B

very high positive a_d value can alter the pattern of stress path evolution and the development of excess pore pressure. Additionally, a very low negative a_d value results in a rapid increase in plastic modulus, leading to a viscoelastic response. Therefore, while the direct effects of a_d are observed in deviatoric responses, its broader impact extends to influencing the overall cyclic behaviour of the soil.

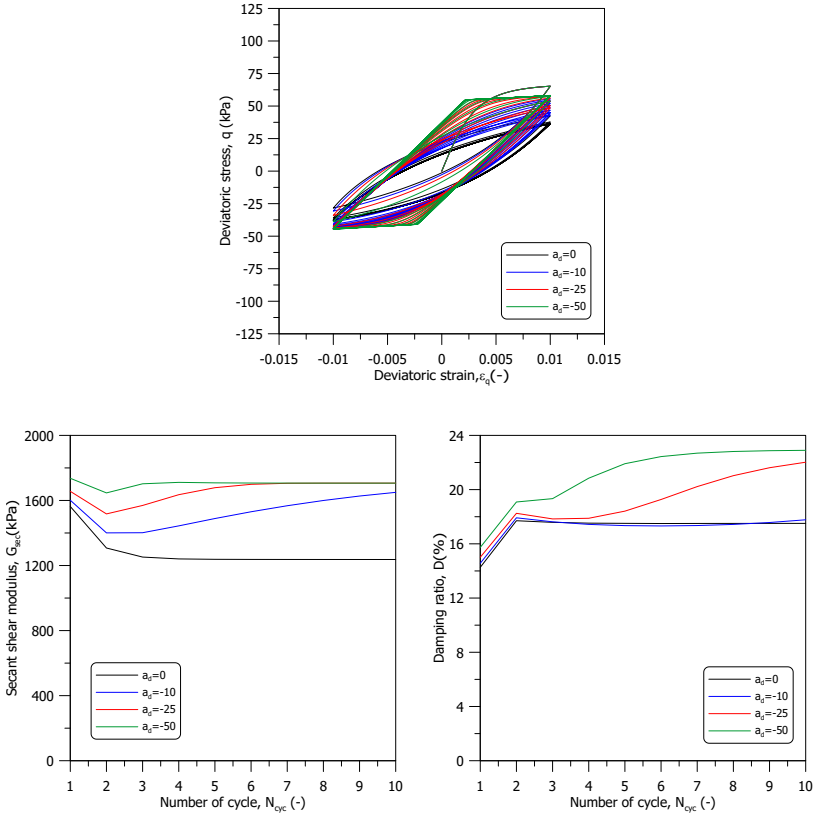

Figure B.13: Stress-strain curve, secant shear modulus, and damping ratio of strain-controlled cyclic shearing stage for different a_d value

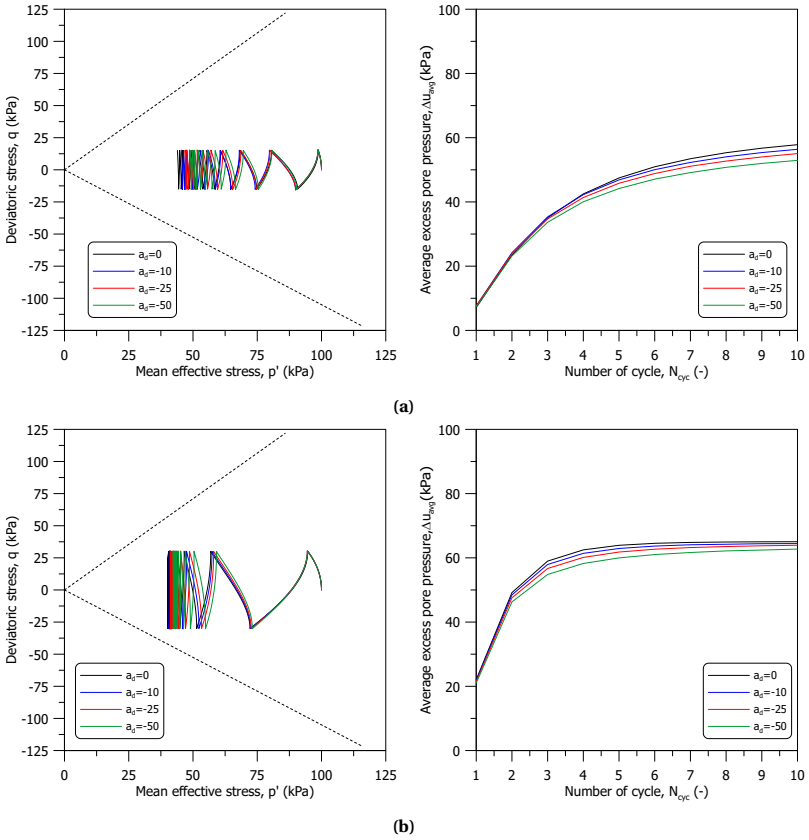

Figure B.14: Stress path and development of excess pore pressure of stress-controlled cyclic shearing stage for different a_d values: (a) $q_{\text{cyc}} = 0.15p'_i$ and (b) $q_{\text{cyc}} = 0.30p'_i$

B

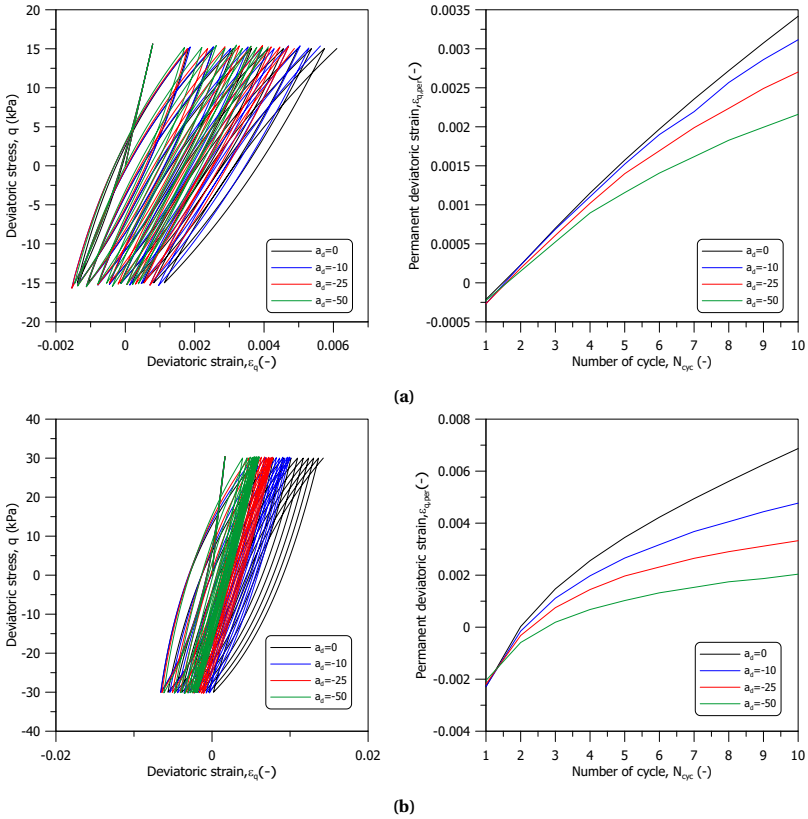

Figure B.15: Stress-strain curve and permanent deviatoric strain of stress-controlled cyclic shearing stage for different a_d values: (a) $q_{\text{cyc}} = 0.15p'_i$ and (b) $q_{\text{cyc}} = 0.30p'_i$

B.4. INFLUENCE OF ELASTIC NUCLEUS SIZE s_{ELN} ON THE CYCLIC RESPONSE

The impact of the elastic nucleus size s_{eln} on cyclic response is initially examined using strain-controlled cyclic shearing, with a cyclic strain amplitude, ε_{cyc} set at 0.01. For this sensitivity analysis, four distinct s_{eln} values are considered. Model parameters are listed in Chapter 3 and Table B.4. The simulation process comprises two stages: a consolidation stage followed by a cyclic shearing stage.

Table B.4: Model parameters adopted in sensitivity analysis

h_0	a_d	w
50	0	0

Figure B.16 depicts the evolution of void ratio throughout both the consolidation and strain-controlled cyclic shearing stages. Although it is not so evident, a small elastic nucleus size (smaller s_{eln}) leads to an earlier change from stiff to less stiff compression response.

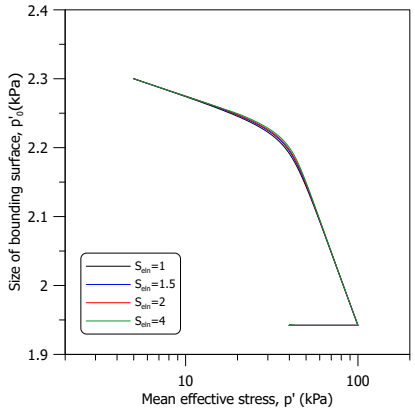

Figure B.16: Variation of void ratio during consolidation and strain-controlled cyclic shearing stage for different s_{eln} value

Figure B.17 further illustrates the stress path and the average excess pore pressure during cyclic shearing. It is observed that larger elastic nucleus sizes (higher s_{eln}) are associated with higher peak deviatoric stresses attained during cyclic loading. For all simulations, the leftward movement indicates contractive behaviour and the development of positive excess pore pressure. The excess pore pressure also slightly increases for larger elastic nucleus sizes (higher s_{eln}).

Figure B.18 displays the deviatoric stress-strain curve, as well as the development of the secant shear modulus and damping ratio for various s_{eln} values. Consistent with the stress path observations, the higher s_{eln} values correlate with higher peak deviatoric stresses during cyclic shearing. Regarding the secant shear modulus, higher s_{eln} values result in higher moduli, which slightly decrease as the number of loading cycles

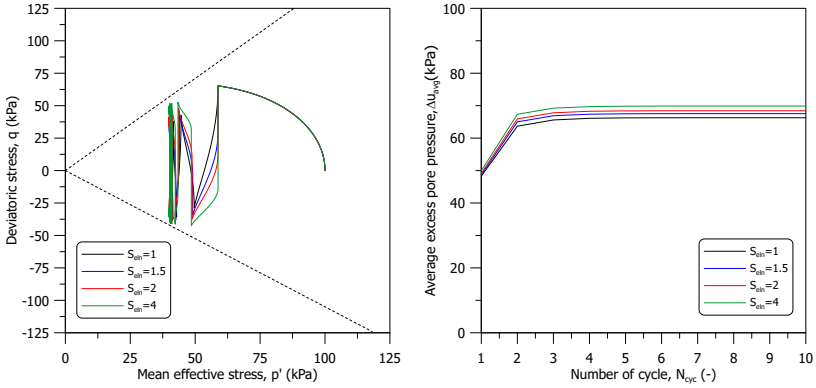

Figure B.17: Stress path and development of excess pore pressure of strain-controlled cyclic shearing stage for different s_{eln} value

increases. The damping ratio generally increases as s_{eln} values increase, aligning with a larger elastic range within the bounding surface. Additionally, the variation in damping ratio with increasing loading cycles is not pronounced.

To further investigate various aspects of the predicted cyclic response, a sensitivity analysis was also conducted using stress-controlled cyclic shearing. Two different cyclic stress amplitudes, q_{cyc} ($0.15p'_i$ and $0.30p'_i$, with $p'_i = 100\,\text{kPa}$), were chosen to assess the impact of loading magnitude. Figure B.19 presents the stress path and average excess pore pressure observed during stress-controlled cyclic shearing. Consistently, across all s_{eln} values, the development of positive excess pore pressure is observed. Additionally, higher cyclic stress amplitudes result in greater excess pore pressure development.

Figure B.20 illustrates the accumulation of permanent deviatoric strain, denoted as $\varepsilon_{q,\text{per}}$, during cyclic shearing. It is observed that higher s_{eln} values lead to a smaller magnitude of $\varepsilon_{q,\text{per}}$. Additionally, there is a correlation between the increase in permanent deviatoric strain and the rise in stress amplitude. It is worth noting that when the elastic nucleus is active ($s_{\text{eln}} > 1$), the permanent deviatoric strain develops towards the extension side. This can be attributed to two factors: (1) the Lode angle dependency of the critical state stress ratio, rendering a smaller elastic range towards the extension side and (2) the updating of the projection centre upon stress reversal, resulting in the movement of the elastic nucleus.

The impact of elastic nucleus size on the compression curve is not evident from the conducted simulation. In terms of volumetric response, a larger elastic nucleus size reduces the development of excess pore pressure. As for the deviatoric response, a higher s_{eln} value leads to higher peak deviatoric stress, secant shear modulus, and damping ratio. Additionally, when the elastic nucleus is active ($s_{\text{eln}} > 1$), the permanent deviatoric strain develops towards the extension side.

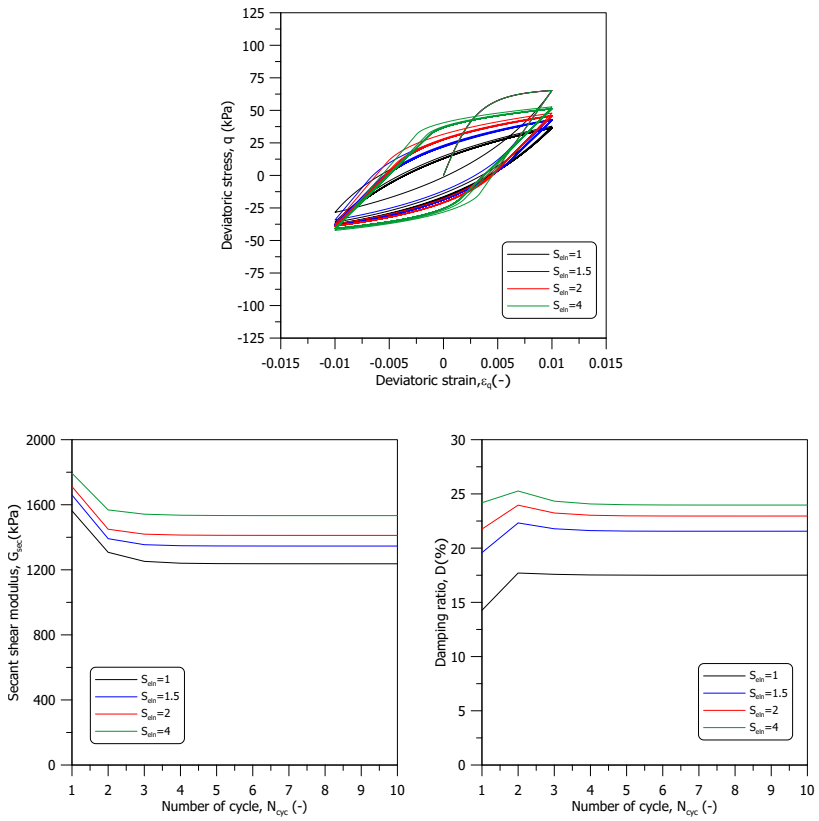

Figure B.18: Stress-strain curve, secant shear modulus, and damping ratio of strain-controlled cyclic shearing stage for different s_{eln} value

B

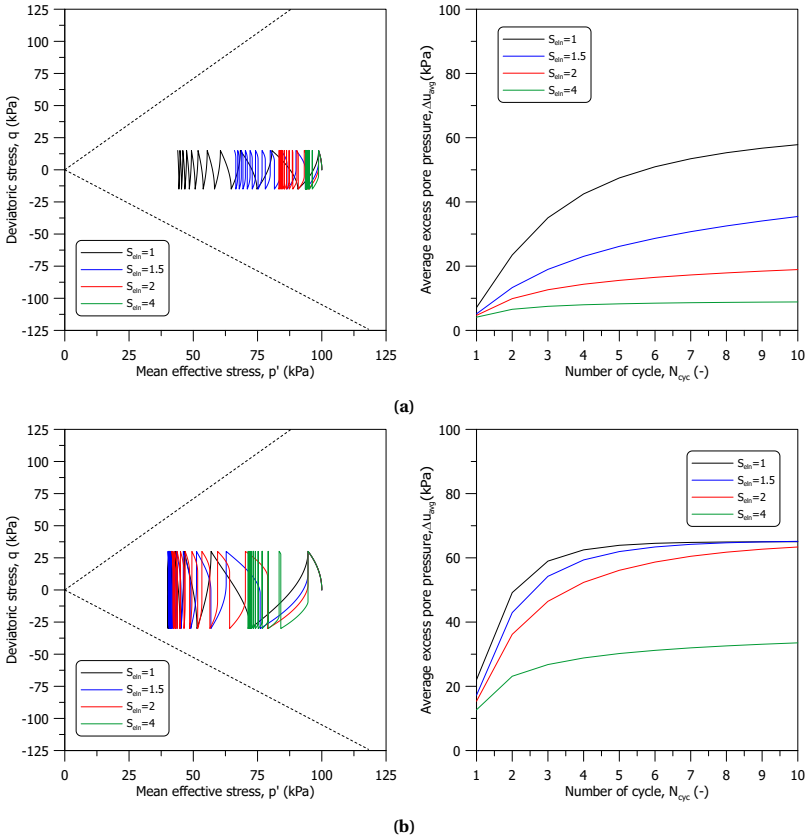

Figure B.19: Stress path and development of excess pore pressure of stress-controlled cyclic shearing stage for different s_{eln} values: (a) $q_{\text{cyc}} = 0.15p'_i$ and (b) $q_{\text{cyc}} = 0.30p'_i$

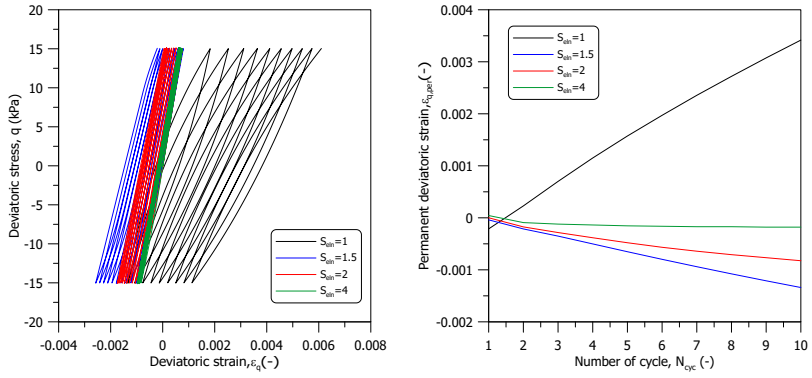

(a)

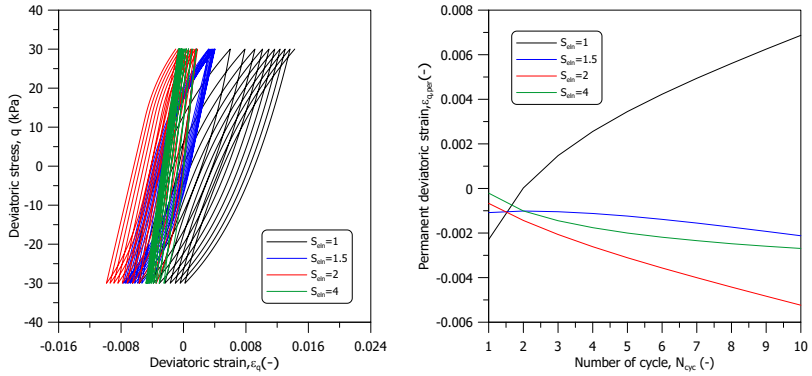

(b)

Figure B.20: Stress-strain curve and permanent deviatoric strain of stress-controlled cyclic shearing stage for different s_{eln} values: (a) $q_{\text{cyc}} = 0.15p'_i$ and (b) $q_{\text{cyc}} = 0.30p'_i$

B.5. INFLUENCE OF PARAMETER w ON THE CYCLIC RESPONSE

In the subsequent section, a sensitivity analysis of the hybrid flow rule parameter w is conducted. The impact of the hybrid flow rule parameter w on cyclic response is explored using strain-controlled cyclic shearing, with the cyclic strain amplitude, ε_{cyc} set at 0.01. For this sensitivity analysis, four w values are considered. Model parameters can be found in Chapter 3 and Table B.5. The simulation process includes two stages: firstly, an isotropic consolidation stage, and secondly, a cyclic shearing stage.

Table B.5: Model parameters adopted in sensitivity analysis

h_0	a_d	s_{eln}
50	0	1

Figure B.21 showcases the variation of void ratio during both the consolidation and strain-controlled cyclic shearing stages, and it indicates that the influence of parameter w on the compression curve is minor.

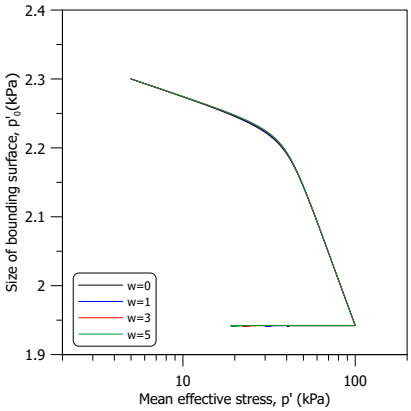

Figure B.21: Variation of void ratio during consolidation and strain-controlled cyclic shearing stage for different w value

Figure B.22 depicts the stress path and average excess pore pressure observed during cyclic shearing. Across all w values, the simulations consistently achieve similar peak deviatoric stress levels during cyclic loading. In each simulation, the stress paths show contractive behaviour and development of positive excess pore pressure. Furthermore, an increase in the w value leads to greater excess pore pressure development under cyclic loading. As expected, the simulation with a w value of zero shows stabilisation in both the stress path and pore pressure development.

Figure B.23 illustrates the deviatoric stress-strain curve, along with the development of the secant shear modulus and damping ratio for a range of w values. There is a trend of reduction in peak deviatoric stress after the first loading cycle as the w value increases. In terms of the secant shear modulus, lower w values result in higher moduli and a lesser reduction in modulus with an increasing number of loading cycles. Regarding the damping ratio, it tends to decrease as w values increase, and the differences among various w

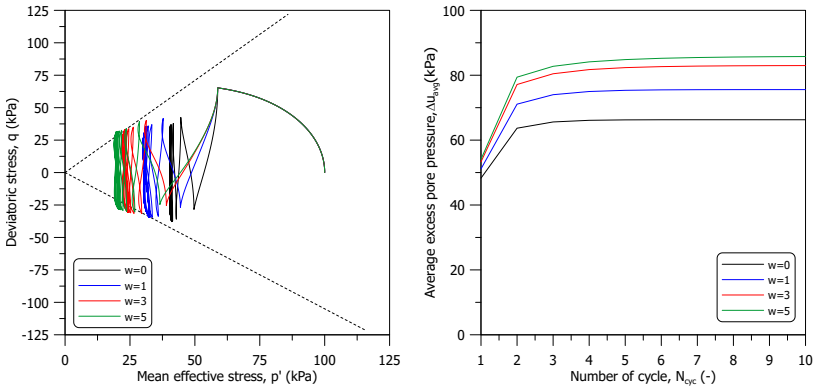

Figure B.22: Stress path and development of excess pore pressure of strain-controlled cyclic shearing stage for different w value

values are quite noticeable. Additionally, for w values other than zero, there is a discernible decreasing trend in the variation of the damping ratio with increasing loading cycles.

The sensitivity analysis was extended to include stress-controlled cyclic shearing, utilising two distinct cyclic stress amplitudes, q_{cyc} ($0.15p'_i$ and $0.30p'_i$, with $p'_i = 100\,\text{kPa}$), to determine the impact of loading magnitude. Figure B.24 illustrates the stress path and average excess pore pressure during stress-controlled cyclic shearing. There is a direct correlation between higher w values and increased excess pore pressure development. Furthermore, the simulations reveal that higher cyclic stress amplitudes lead to greater development of excess pore pressure.

Figure B.25 demonstrates the accumulation of permanent deviatoric strain, represented as $\varepsilon_{q,\text{per}}$, during cyclic shearing. In simulations with a cyclic stress amplitude of $q_{\text{cyc}} = 0.15p'_i$, higher w values lead to greater accumulations of $\varepsilon_{q,\text{per}}$ up to the 9^{th} loading cycle. Conversely, for $q_{\text{cyc}} = 0.30p'_i$, all w values result in similar accumulations of $\varepsilon_{q,\text{per}}$ up to the 3^{rd} loading cycle. Intriguingly, for w values above 3, $\varepsilon_{q,\text{per}}$ begins to decrease after the 3^{rd} loading cycle, while it continues to increase for w values below 3. This pattern is attributed to the variation in the deviatoric plastic strain increment. When w equals zero, the deviatoric plastic strain increment reaches its maximum as the image stress reaches and stabilises at the critical state stress ratio. However, with the adoption of the hybrid flow rule, the image stress can evolve towards the dry side of the critical state, leading to a reduction in the deviatoric plastic strain increment.

The hybrid flow rule parameter w is initially introduced to better capture cyclic volumetric responses, w also significantly alters cyclic deviatoric responses. For example, as stiffness is dependent on mean effective stress, higher w values lead to a more rapid reduction in mean effective stress. This, in turn, results in a quicker decrease in shear stiffness, as evidenced by lower peak deviatoric stress and secant shear modulus observed after the first loading cycle.

B

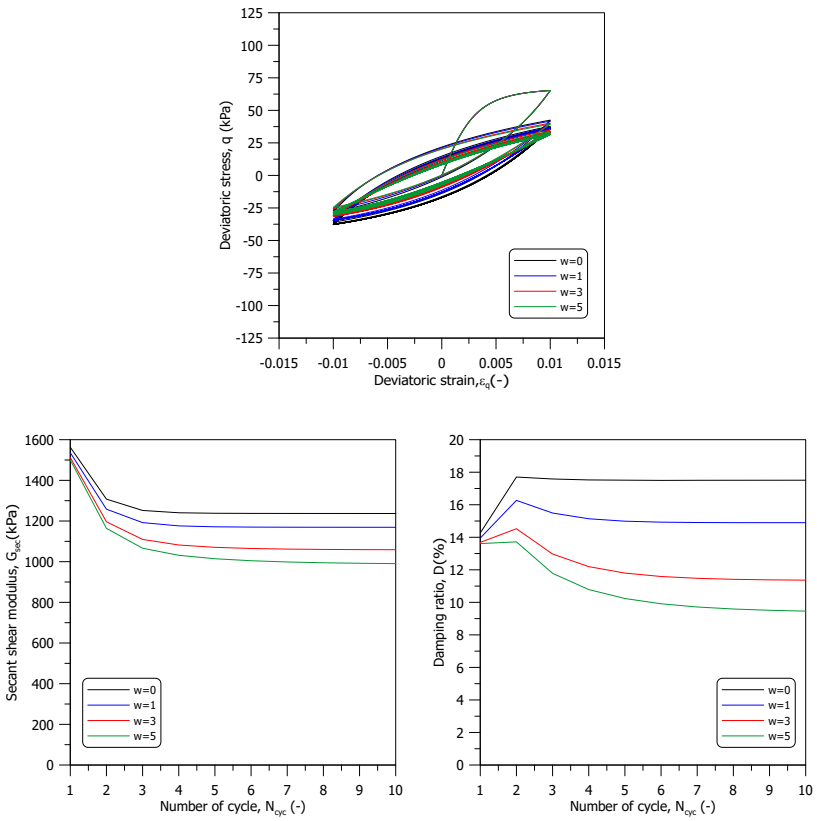

Figure B.23: Stress-strain curve, secant shear modulus, and damping ratio of strain-controlled cyclic shearing stage for different w value

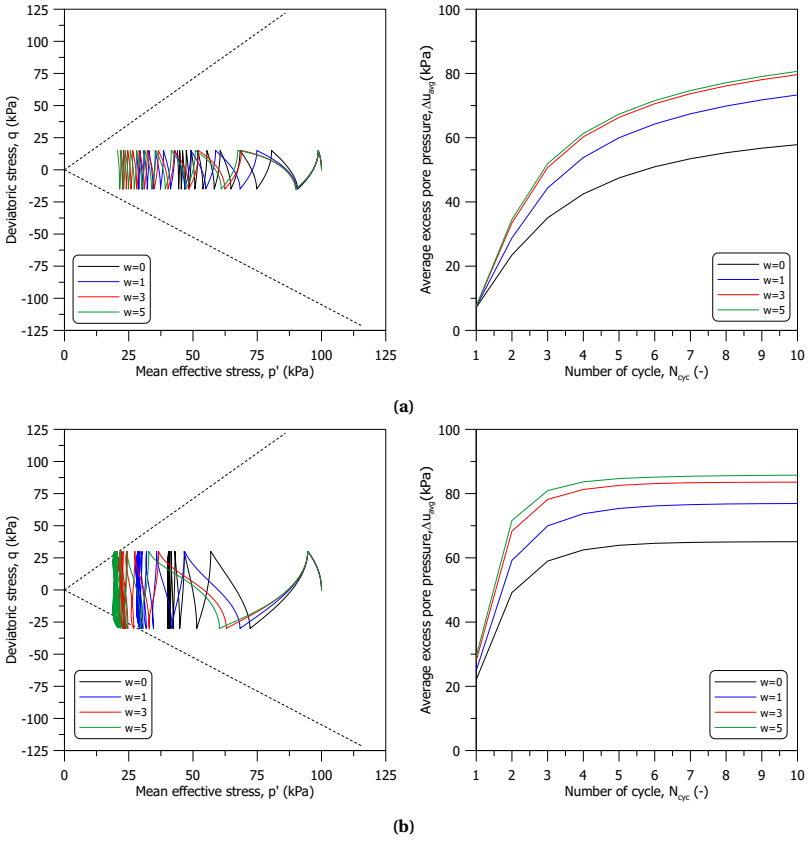

Figure B.24: Stress path and development of excess pore pressure of stress-controlled cyclic shearing stage for different w values: (a) $q_{\text{cyc}} = 0.15p'_i$ and (b) $q_{\text{cyc}} = 0.30p'_i$

B

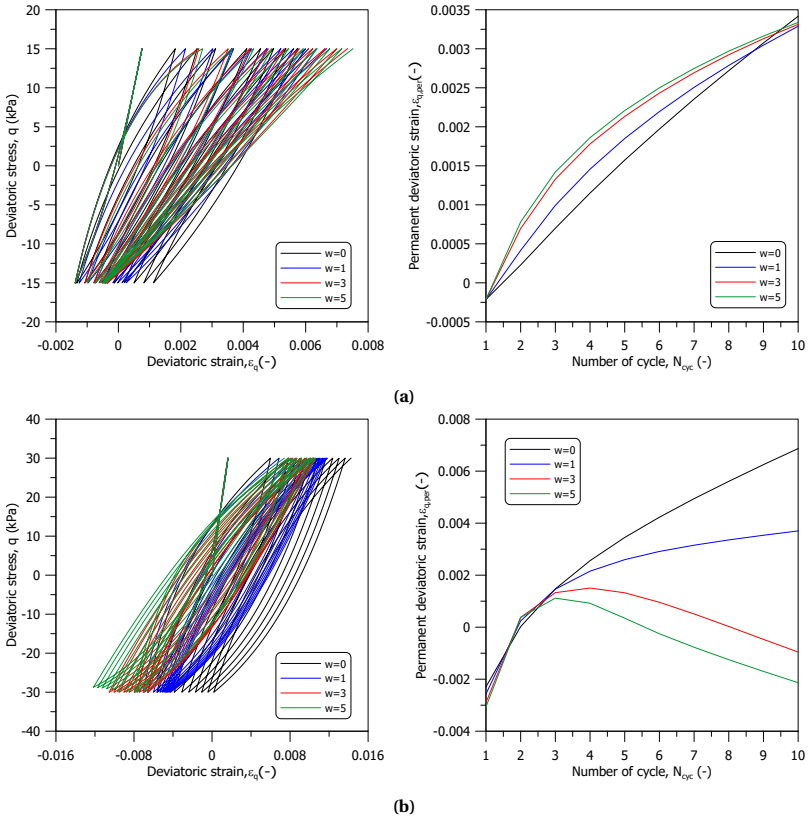

Figure B.25: Stress-strain curve and permanent deviatoric strain of stress-controlled cyclic shearing stage for different w values: (a) $q_{cyc} = 0.15p'_i$ and (b) $q_{cyc} = 0.30p'_i$

Additionally, w influences the development of permanent deviatoric strain. This is due to the variation in deviatoric plastic strain increment that occurs when implementing the hybrid flow rule, allowing the image stress to evolve towards the dry side of the critical state and consequently reducing the deviatoric plastic strain increment.

Interestingly, the damping ratio upon cyclic loading appears to be highly dependent on the hybrid flow rule parameter. This dependence arises because an increase in w not only reduces the contribution of the plastic volumetric increment at the image stress state but also slows the increase in image stress weighting for similarity ratios lower than 1.5 (equivalent to $1/b \approx 0.7$, as shown in Figure B.26). This leads to a lower plastic modulus and a slower variation in predicted shear stiffness, thereby reducing the area in the hysteresis loop and resulting in a lower damping ratio.

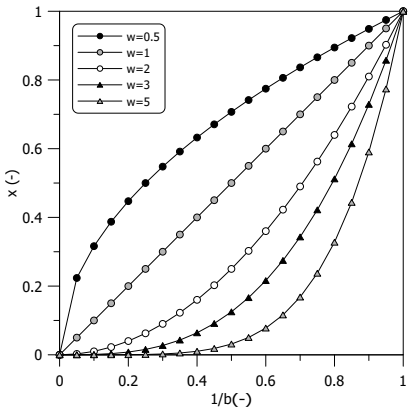

Figure B.26: Variation of image stress weighting x with different hybrid flow rule parameter w and similarity ratio b.

B.6. INFLUENCE OF OVER-CONSOLIDATION RATIO (OCR) ON THE CYCLIC RESPONSE

It is well-known that the over-consolidation ratio (OCR) has a significant impact on the static behaviour of soil. The impact of the over-consolidation ratio (OCR) on cyclic response is initially examined using strain-controlled cyclic shearing, with a cyclic strain amplitude, ε_{cyc} set at 0.01. For this sensitivity analysis, four distinct OCRs are considered. Model parameters are listed in Chapter 3 and Table B.6. The simulation process comprises two or three stages: a consolidation stage, an unloading stage (for OCR > 1), and followed by a cyclic shearing stage.

Table B.6: Model parameters adopted in sensitivity analysis

h_0	a_d	s_{eln}	w
50	0	1	0

Figure B.27 illustrates the stress path and the average excess pore pressure during cyclic shearing. It is observed that higher OCR values are associated with higher peak deviatoric stresses attained during cyclic loading. Additionally, as the OCR increases, the predicted response changes from contractive behaviour (positive excess pore pressure) to dilative behaviour (negative excess pore pressure).

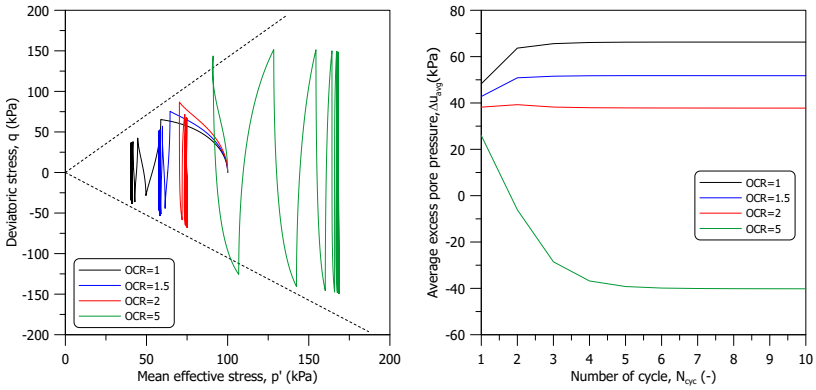

Figure B.27: Stress path and development of excess pore pressure of strain-controlled cyclic shearing stage for different OCR

Figure B.28 illustrates the deviatoric stress-strain curve, along with the development of the secant shear modulus and damping ratio for a range of OCR. Aligning with the stress path observations, peak deviatoric stress increases as OCR increases. In terms of the secant shear modulus, higher OCR values result in higher moduli. Besides the simulation with an OCR of five, a reduction in modulus with an increasing number of loading cycles is observed. The damping ratio tends to decrease as OCR values decrease, but the difference is not significant.

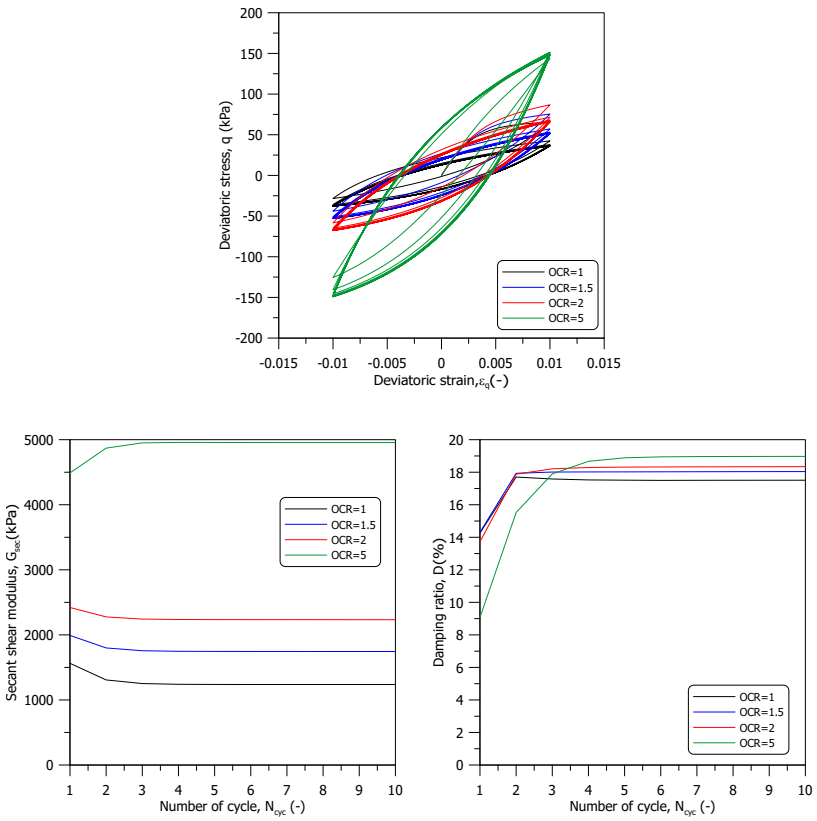

Figure B.28: Stress-strain curve, secant shear modulus, and damping ratio of strain-controlled cyclic shearing stage for different OCR value

The sensitivity analysis was extended to include stress-controlled cyclic shearing, utilising two distinct cyclic stress amplitudes, q_{cyc} ($0.15p'_i$ and $0.30p'_i$, with $p'_i = 100\,\text{kPa}$), to determine the impact of loading magnitude.

Figure B.29 illustrates the stress path and average excess pore pressure during stress-controlled cyclic shearing. For all OCR values below five, the stress paths exhibit a leftward movement during cyclic loading, indicative of contractive behaviour and the consequent development of positive excess pore pressure. Furthermore, the simulations reveal that higher cyclic stress amplitudes lead to greater development of excess pore pressure.

Figure B.30 demonstrates the accumulation of permanent deviatoric strain, represented as $\varepsilon_{q,\text{per}}$, during cyclic shearing. In all simulations, higher OCR values lead to smaller accumulations of $\varepsilon_{q,\text{per}}$. Additionally, higher cyclic stress amplitudes lead to a larger accumulation of permanent deviatoric strain.

As the OCR increases, the predicted response changes from contractive behaviour (positive excess pore pressure) to dilative behaviour (negative excess pore pressure). In terms of the peak deviatoric stress and secant shear modulus, higher OCR values result in higher moduli. For low OCR values (OCR ≤ 2), a reduction in modulus with an increasing number of loading cycles is observed. The damping ratio tends to decrease as OCR values decrease, however, the difference is not evident. Additionally, higher OCR values lead to less permanent deviatoric strain. For all OCR values, higher cyclic stress amplitudes lead to a greater magnitude of excess pore pressure and accumulations of $\varepsilon_{q,\text{per}}$.

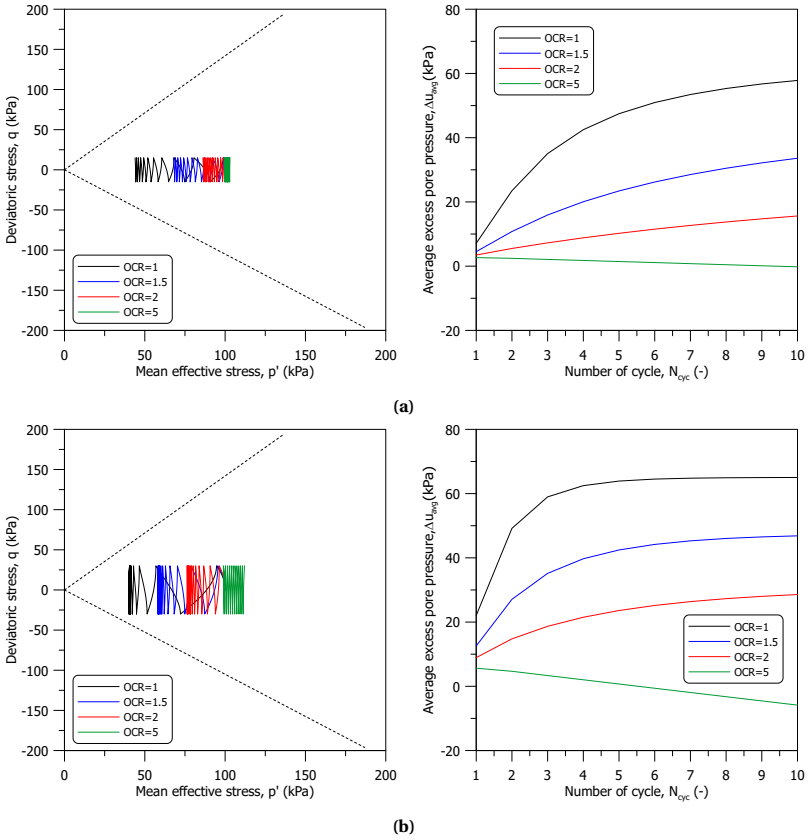

Figure B.29: Stress path and development of excess pore pressure of stress-controlled cyclic shearing stage for different OCR values: (a) $q_{\text{cyc}} = 0.15p'_i$ and (b) $q_{\text{cyc}} = 0.30p'_i$

B

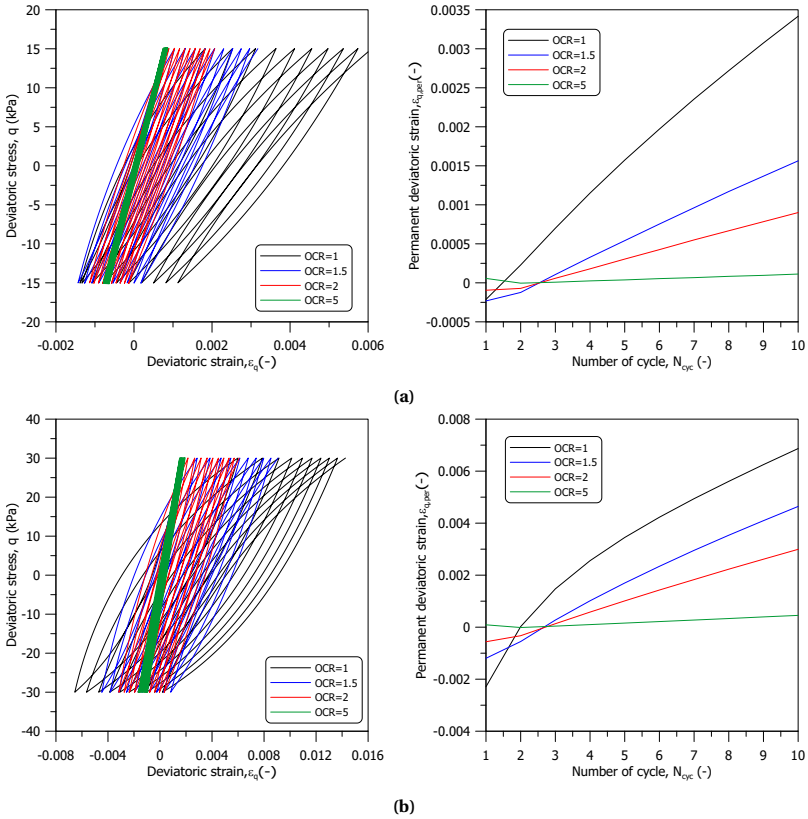

Figure B.30: Stress-strain curve and permanent deviatoric strain of stress-controlled cyclic shearing stage for different OCR values: (a) $q_{cyc} = 0.15p'_i$ and (b) $q_{cyc} = 0.30p'_i$

C

Sensitivity Analysis of JMC-Clay Elastoplastic-Viscoplastic Bounding Surface Model Parameters

C.1. INFLUENCE OF PARAMETERS s_ν ON THE CYCLIC RESPONSE

C.1.1. ISOTROPIC INITIAL STRESS STATE

The impact of the viscoplastic parameter s_ν on cyclic response is initially examined using strain-controlled cyclic shearing, with a cyclic strain amplitude, ε_{cyc} set at 0.01. For this sensitivity analysis, four distinct s_ν values are considered. Model parameters not detailed in Chapter 4 are listed in Table C.1. The simulation process comprises two stages: a consolidation stage followed by a cyclic shearing stage. The consolidation stage is conducted over a period of 10,800 minutes, the cyclic loading frequency and waveform adopted are reported in Chapter 4.

Table C.1: Model parameters adopted in sensitivity analysis

V	n	a_d	w
5×10^7 kPa·min	4	0	0

Figure C.1 depicts the evolution of the bounding surface size throughout both the consolidation and strain-controlled cyclic shearing stages. A lower s_ν value leads to a faster change in the bounding surface size.

Figure C.2 illustrates the stress path and the average excess pore pressure during cyclic shearing. It is observed that smaller s_ν values are associated with higher peak deviatoric stresses attained during cyclic loading. Except for the simulation where the s_ν value is equal to 1.25, the stress paths tend to move leftward during cyclic loading. This leftward movement indicates contractive behaviour and the development of positive excess pore pressure. Conversely, in the simulation with a s_ν value of 1.25, the soil exhibits contractive behaviour in the first cycle followed by dilative behaviour in subsequent cycles, as evidenced by the pattern of excess pore pressure development.

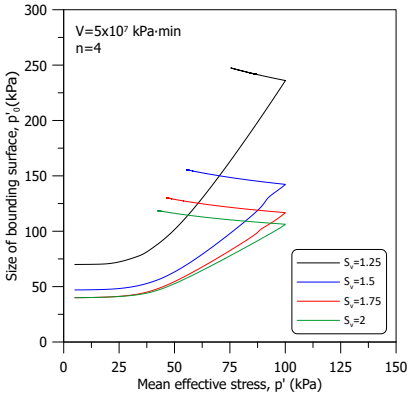

Figure C.1: Evolution of the size of bounding surface during consolidation and strain-controlled cyclic shearing stage for different s_ν value

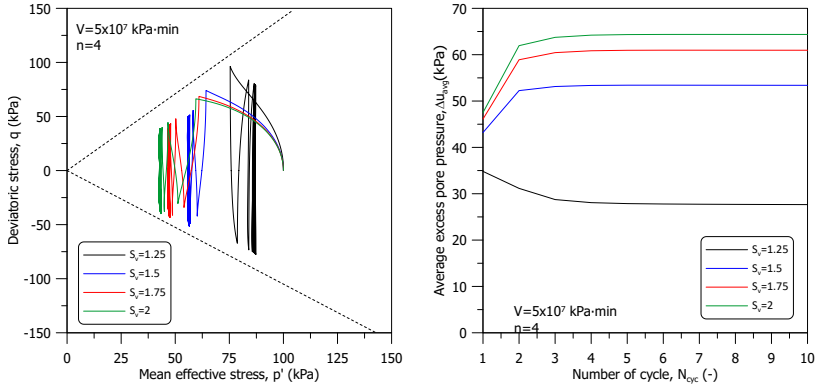

Figure C.2: Stress path and development of excess pore pressure of strain-controlled cyclic shearing stage for different s_ν value

Strain-controlled cyclic shearing enables the analysis of the evolution of shear stiffness and damping ratio during cyclic loading. Figure C.3 displays the deviatoric stress-strain curve, as well as the development of the secant shear modulus and damping ratio for various s_ν values. Consistent with the stress path observations, the smaller s_ν values correlate with higher peak deviatoric stresses during cyclic shearing. This correlation is also evident in the deviatoric stress-strain evolution. Regarding the secant shear modulus, lower s_ν values result in higher moduli, which slightly decrease as the number of loading cycles increases. The damping ratio generally increases as s_ν values decrease, although the differences among various s_ν values are relatively minor. Additionally, the variation in damping ratio with increasing loading cycles is not pronounced.

To further investigate various aspects of the predicted cyclic response, a sensitivity analysis was also conducted using stress-controlled cyclic shearing. Two different cyclic stress amplitudes, q_{cyc} ($0.15p'_i$ and $0.30p'_i$, with $p'_i = 100\,\text{kPa}$), were chosen to assess the impact of loading magnitude. Figure C.4 displays the evolution of the bounding surface size during both the consolidation and stress-controlled cyclic shearing stages. Similar to the strain-controlled simulations, a lower s_ν value results in a quicker change in the bounding surface size.

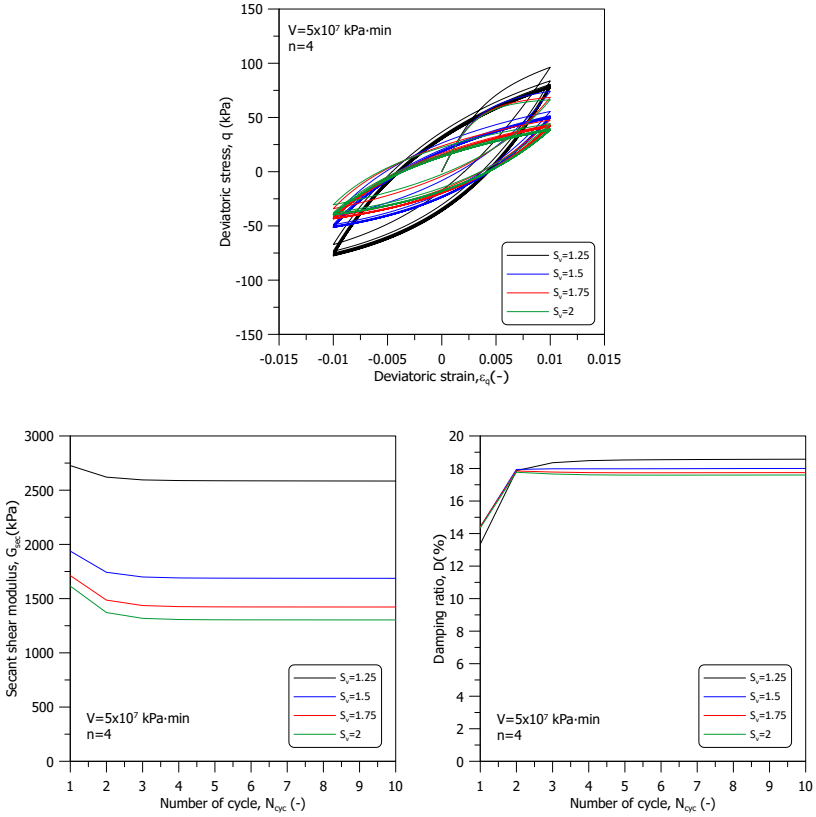

Figure C.3: Stress-strain curve, secant shear modulus, and damping ratio of strain-controlled cyclic shearing stage for different s_v value

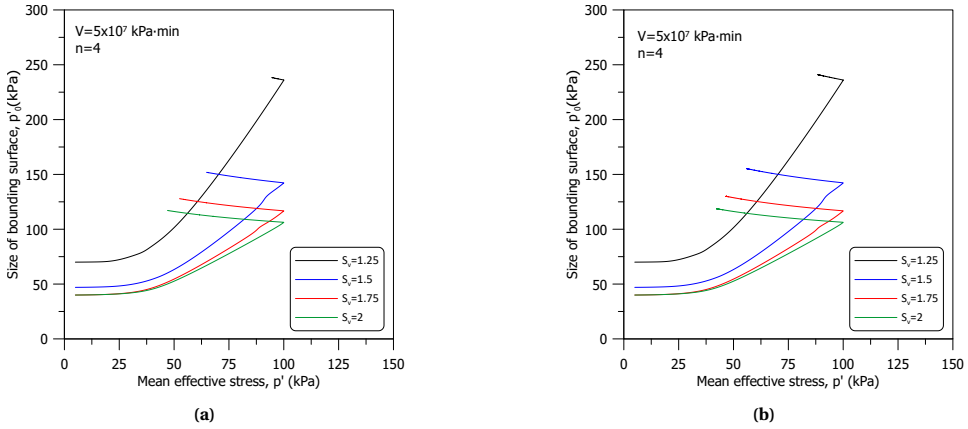

Figure C.4: Evolution of the size of bounding surface during consolidation and stress-controlled cyclic shearing stage for different s_v value : (a) $q_{\text{cyc}} = 0.15p'_i$ and (b) $q_{\text{cyc}} = 0.30p'_i$

Figure C.5 presents the stress path and average excess pore pressure observed during stress-controlled cyclic shearing. Consistently, across all s_v values, the stress paths show a leftward movement during cyclic loading, leading to the development of positive excess pore pressure. Additionally, it is observed that higher cyclic stress amplitudes result in greater excess pore pressure development.

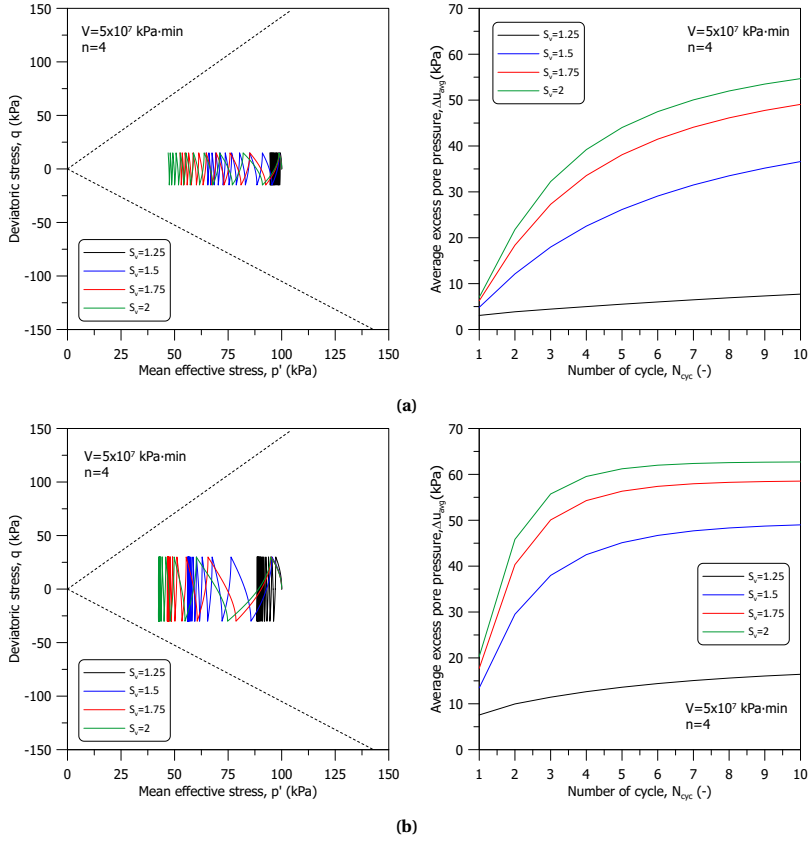

Figure C.5: Stress path and development of excess pore pressure of stress-controlled cyclic shearing stage for different s_v value : (a) $q_{\text{cyc}} = 0.15p'_i$ and (b) $q_{\text{cyc}} = 0.30p'_i$

Figure C.6 illustrates the accumulation of permanent deviatoric strain, denoted as $\varepsilon_{q,\text{per}}$, during cyclic shearing. It is observed that higher s_v values lead to larger developments of $\varepsilon_{q,\text{per}}$. Additionally, there is a significant correlation between the increase in permanent deviatoric strain and the rise in stress amplitude. Although the cyclic stress amplitude is symmetrical along the mean effective stress axis, for all s_v values, $\varepsilon_{q,\text{per}}$ initially accumulates towards the extension side during the first 2 to 3 cycles, and then shifts towards the compression side. As discussed in Appendix B, this asymmetrical response can be attributed to three key factors: (1) the Lode angle dependency of the critical state stress ratio, (2) the Lode angle dependency of anisotropy evolution, as governed by the rotational hardening rule, and (3) the updating of the projection centre upon stress reversal.

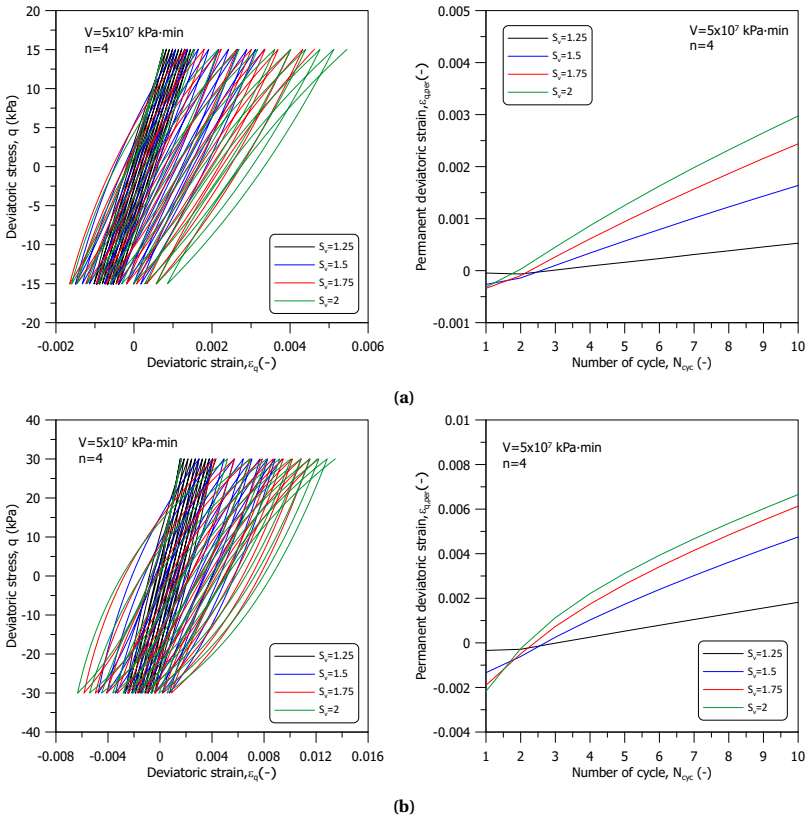

Figure C.6: Stress-strain curve and permanent deviatoric strain of stress-controlled cyclic shearing stage for different s_v value : (a) $q_{\text{cyc}} = 0.15p'_i$ and (b) $q_{\text{cyc}} = 0.30p'_i$

C.1.2. K_0 INITIAL STRESS STATE

Experimental observations presented in Chapter 3, along with several research studies, have highlighted the significant influence of the initial stress state on cyclic response. Building upon these insights, the impact of the viscoplastic parameter s_v on cyclic behaviour is investigated, starting from a K_0 stress state, using strain-controlled cyclic shearing. The chosen cyclic strain amplitude is $\varepsilon_{cyc} = 0.01$, and four distinct s_v values are considered for this analysis. The model parameters not presented in Chapter 4 are listed in Table C.1. The simulation encompasses two stages: a K_0 consolidation stage, followed by a cyclic shearing stage. The consolidation stage spans 10,800 minutes, and the details of the cyclic loading frequency and waveform are provided in Chapter 4.

Figure C.7 illustrates the evolution of bounding surface size during both the K_0 consolidation and strain-controlled cyclic shearing stages. In alignment with results from simulations starting from an isotropic stress state, a lower s_v value results in a more rapid change in the bounding surface size.

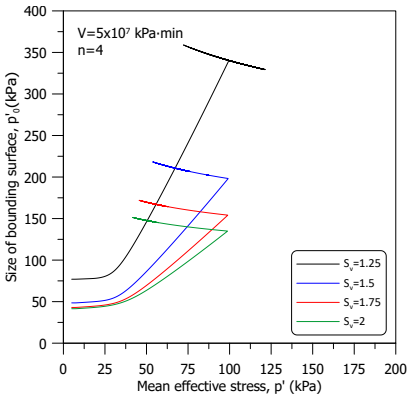

Figure C.7: Evolution of the size of bounding surface during consolidation and strain-controlled cyclic shearing stage for different s_v value

Figure C.8 showcases the stress path and the average excess pore pressure during cyclic shearing. A notable observation is that smaller s_v values correlate with higher peak deviatoric stresses during cyclic loading. The stress path for a s_v value of 1.25 moves above the critical state stress ratio in the first three loading cycles. This is attributed to a substantially larger bounding surface size after the consolidation stage, leaving the image stress on the dry side of the critical stress state. For simulations with s_v values other than 1.25, the average excess pore pressure initially increases in the first three cycles and then decreases. This behaviour is linked to the image stress being on the dry side, a result of the increased bounding surface size, the inclination of the bounding surface, and the updating of the projection centre. In contrast, the simulation with a s_v value of 1.25, having a much larger bounding surface size, exhibits a monotonic reduction in excess pore pressure.

Figure C.9 presents the deviatoric stress-strain curve along with the development of the secant shear modulus and damping ratio for different s_v values. In line with the sensitivity analysis results from the isotropic stress state, smaller s_v values are associated

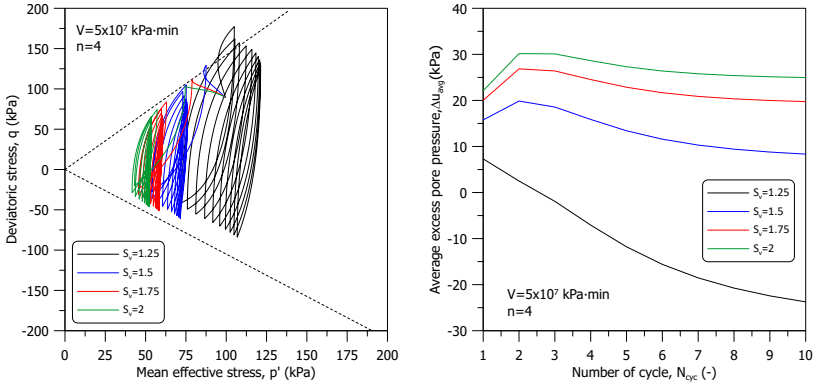

Figure C.8: Stress path and development of excess pore pressure of strain-controlled cyclic shearing stage for different s_v value

with higher peak deviatoric stresses during cyclic shearing, a trend also visible in the deviatoric stress-strain evolution. With regard to the secant shear modulus, for s_v values larger than 1.25, lower s_v values result in higher moduli, which tend to slightly decrease as the number of loading cycles increases. For the simulation with $s_v = 1.25$, the secant shear modulus exhibits a slight decrease in the second cycle, followed by a slight increase from the 4^{th} to 7^{th} cycles, and then a reduction in subsequent cycles. This initial increase is attributed to the rise in mean effective stress, p', while the later decrease correlates with the reduction in bounding surface size. Regarding the damping ratio, it generally shows an increase as s_v values decrease; however, the differences between various s_v values are relatively minor. Moreover, the variation in damping ratio across increasing loading cycles shows an increasing trend.

Continuing with the sensitivity analysis, stress-controlled cyclic shearing was also employed to delve deeper into different aspects of the predicted cyclic response. Two distinct cyclic stress amplitudes, q_{cyc} ($0.15p'_i$ and $0.30p'_i$, with $p'_i = 100\,\text{kPa}$), were utilised to determine the impact of loading magnitude. Figure C.10 illustrates the evolution of bounding surface size through both the K_0 consolidation and stress-controlled cyclic shearing stages. Mirroring the strain-controlled simulations, the size of the bounding surface at the end of the consolidation stage increases with s_v value. It is important to highlight that in simulations with higher cyclic stress amplitudes, a reduction in excess pore pressure is observed after the second cycle. This behaviour can be attributed to the adopted rotational hardening rule and the subsequent increase in bounding surface size during cyclic loading.

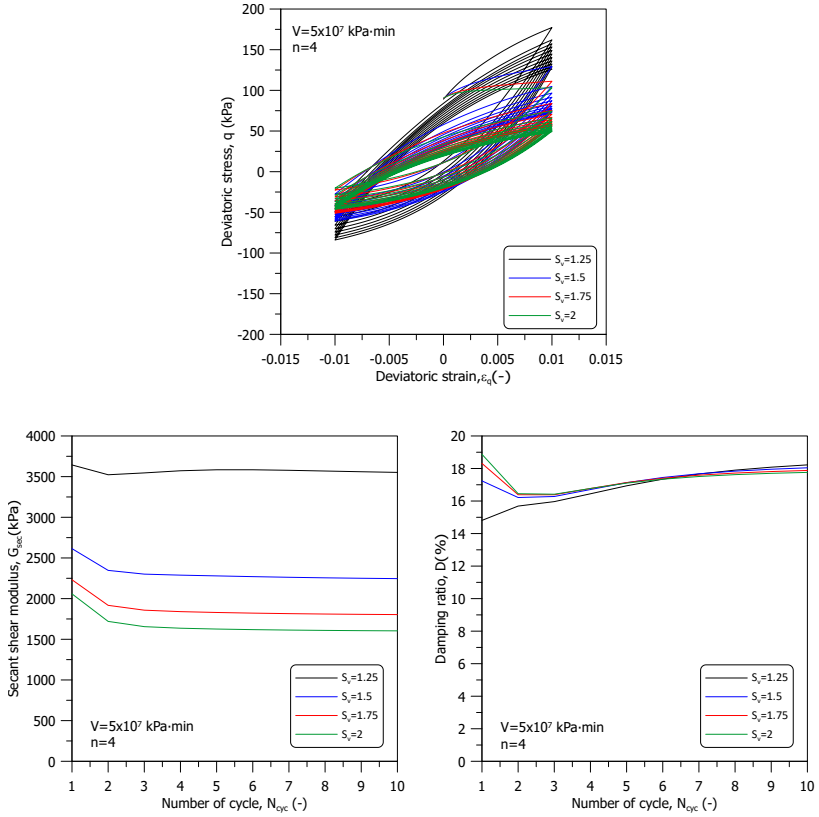

Figure C.9: Stress-strain curve, secant shear modulus, and damping ratio of strain-controlled cyclic shearing stage for different s_v value

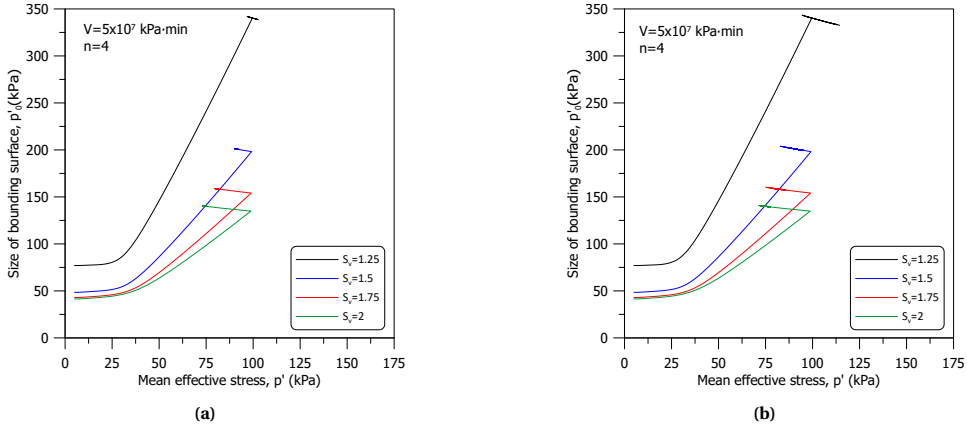

Figure C.10: Evolution of the size of bounding surface during consolidation and stress-controlled cyclic shearing stage for different s_v value : (a) $q_{\text{cyc}} = 0.15p'_i$ and (b) $q_{\text{cyc}} = 0.30p'_i$

Figure C.11 displays the stress path and average excess pore pressure during stress-controlled cyclic shearing. For s_v values greater than 1.25, the stress paths exhibit a leftward movement during cyclic loading, resulting in the development of positive excess pore pressure. In contrast, the simulation with a s_v value of 1.25 initially shows positive excess pore pressure in the first three cycles, followed by negative excess pore pressure in subsequent cycles. Lastly, higher cyclic stress amplitudes lead to more pronounced positive or negative excess pore pressure development.

Figure C.12 demonstrates the accumulation of permanent deviatoric strain, $\varepsilon_{q,\text{per}}$, during cyclic shearing. Consistent with results from simulations starting from an isotropic stress state, higher s_v values are associated with larger accumulations of $\varepsilon_{q,\text{per}}$. There is also a marked correlation between the increase in permanent deviatoric strain and higher stress amplitudes. For all s_v values, $\varepsilon_{q,\text{per}}$ predominantly accumulates on the compression side, with the extent of accumulation rising in tandem with s_v values. Notably, the accumulated permanent deviatoric strain is significantly greater compared to simulations originating from an isotropic stress state.

In terms of volumetric response, including the evolution of the stress path and the development of excess pore pressure, the dominant factor is the size of the bounding surface at the end of the consolidation stage. This size significantly influences the behaviour during cyclic shearing. Regarding the deviatoric response, lower values of λ^* and the larger bounding surface size are associated with increased secant shear modulus and reduced permanent deviatoric strain, $\varepsilon_{q,\text{per}}$, as s_v values decrease. However, the reduction in secant shear modulus and variations in damping ratio appear less influenced by s_v values. Beyond the s_v parameter, other critical model ingredients affecting model predictions include the evolution of anisotropy (rotational hardening), updates to the projection centre, and the Lode angle dependency of the critical state stress ratio.

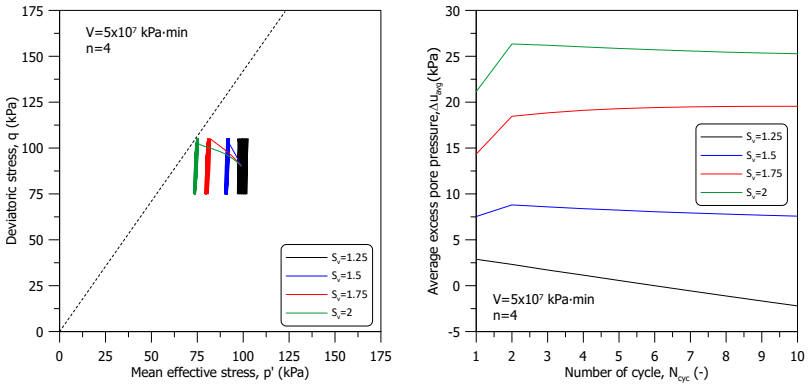

(a)

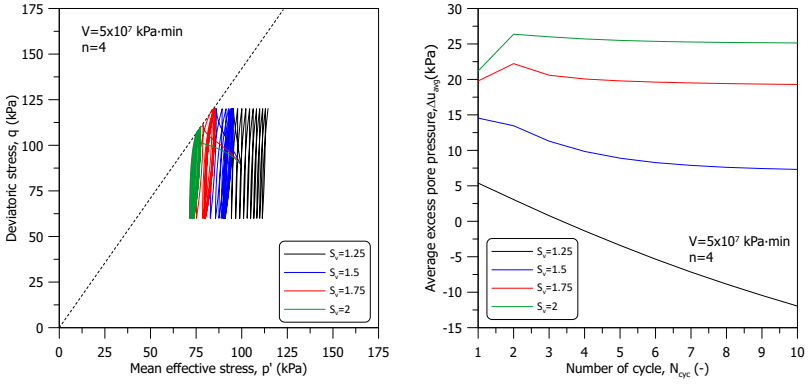

(b)

Figure C.11: Stress path and development of excess pore pressure of stress-controlled cyclic shearing stage for different s_v value : (a) $q_{\text{cyc}} = 0.15p_i'$ and (b) $q_{\text{cyc}} = 0.30p_i'$

C

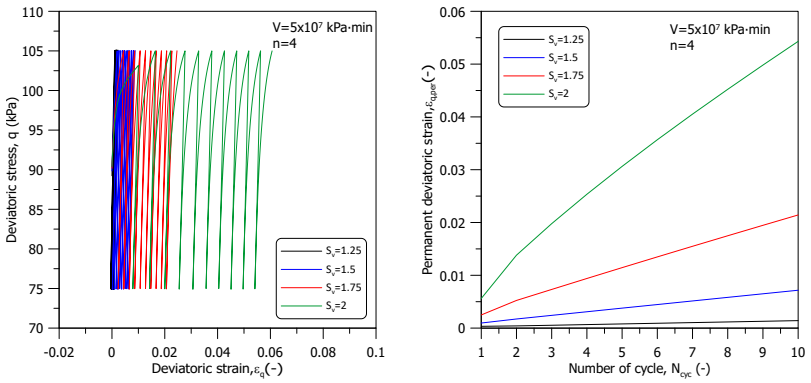

(a)

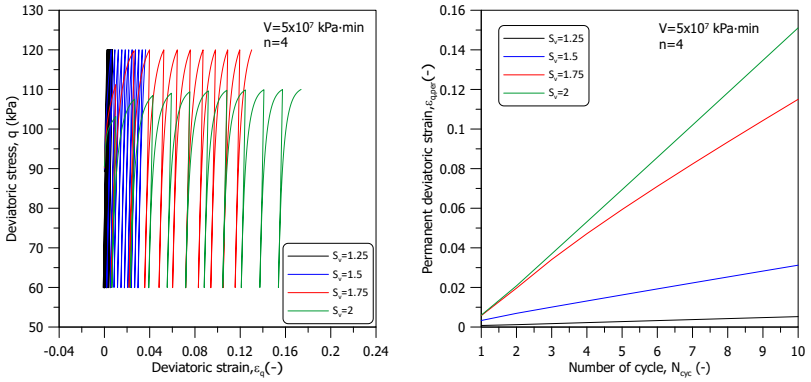

(b)

Figure C.12: Stress-strain curve and permanent deviatoric strain of stress-controlled cyclic shearing stage for different s_ν value : (a) $q_{\text{cyc}} = 0.15p'_i$ and (b) $q_{\text{cyc}} = 0.30p'_i$

C.2. INFLUENCE OF PARAMETERS V ON THE CYCLIC RESPONSE

C.2.1. ISOTROPIC INITIAL STRESS STATE

The sensitivity analysis for the viscoplastic parameter V also utilises strain-controlled cyclic shearing, with the cyclic strain amplitude, ε_{cyc} set to 0.01. In this analysis, four distinct V values are examined. Model parameters that are not detailed in Chapter 4 can be found in Table C.2. The simulation process includes two stages: firstly, a consolidation stage, and secondly, a cyclic shearing stage. The consolidation stage spans a duration of 10,800 minutes. Details regarding the cyclic loading frequency and waveform used in this analysis are provided in Chapter 4.

Table C.2: Model parameters adopted in sensitivity analysis

s_v	n	a_d	w
2	4	0	0

Figure C.13 illustrates the evolution of bounding surface size during both the consolidation and strain-controlled cyclic shearing stages. A key observation is that lower V values result in a more rapid change in the bounding surface size, demonstrating a notable trend. Interestingly, the relationship between the bounding surface size evolution and V value appears more log-linear compared to the relationship observed with s_v values.

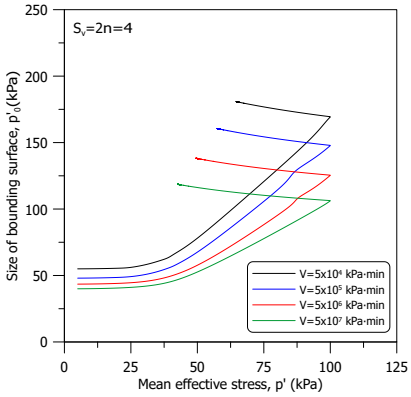

Figure C.13: Evolution of the size of bounding surface during consolidation and strain-controlled cyclic shearing stage for different V value

Figure C.14 presents the stress path and average excess pore pressure observed during cyclic shearing. It shows that lower V values correlate with higher peak deviatoric stresses attained during cyclic loading. Across all investigated V values, the stress paths exhibit a consistent leftward movement during cyclic loading. This movement towards the left signifies contractive behaviour and is associated with the development of positive excess pore pressure. Furthermore, it is observed that the magnitude of excess pore pressure increases as V values increase, indicating a direct relationship between V and the extent of pore pressure development.

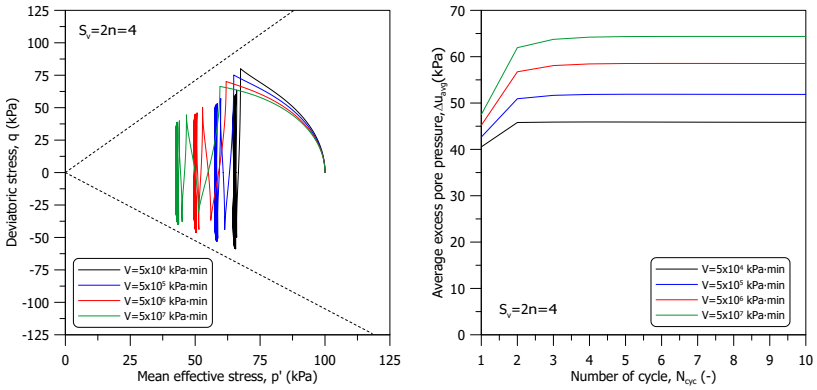

Figure C.14: Stress path and development of excess pore pressure of strain-controlled cyclic shearing stage for different V value

Figure C.15 shows the deviatoric stress-strain curve along with the variation of the secant shear modulus and damping ratio for a range of V values. In line with the stress path observations, lower V values are associated with higher peak deviatoric stresses during cyclic shearing. When it comes to the secant shear modulus, smaller V values lead to higher moduli, which exhibit a slight decrease as the number of loading cycles increases. As for the damping ratio, it generally tends to increase as V values decrease. However, the differences among various V values are relatively minor. Additionally, there is no pronounced variation in damping ratio with an increase in loading cycles.

The sensitivity analysis was extended to include stress-controlled cyclic shearing, utilising two different cyclic stress amplitudes, q_{cyc} ($0.15p'_i$ and $0.30p'_i$, with $p'_i = 100\,\text{kPa}$), to determine the impact of loading magnitude. Figure C.16 illustrates the evolution of bounding surface size during both the consolidation and stress-controlled cyclic shearing stages. Echoing the results from the strain-controlled simulations, lower V values are associated with a faster increase in the bounding surface size.

Figure C.17 shows the stress path and average excess pore pressure during stress-controlled cyclic shearing. Across all V values, the stress paths exhibit a consistent leftward movement during cyclic loading, leading to the development of positive excess pore pressure. Notably, the magnitude of excess pore pressure decreases with reducing V values. Additionally, higher cyclic stress amplitudes are found to result in greater excess pore pressure development.

Figure C.18 demonstrates the accumulation of permanent deviatoric strain, $\varepsilon_{q,\text{per}}$, during cyclic shearing. Higher V values correlate with larger developments of $\varepsilon_{q,\text{per}}$. There is also a significant correlation between the increase in permanent deviatoric strain and the rise in stress amplitude. As observed previously in the sensitivity analysis of the parameter s_v, for all V values, $\varepsilon_{q,\text{per}}$ initially accumulates towards the extension side during the first 2 to 3 cycles, then shifts towards the compression side.

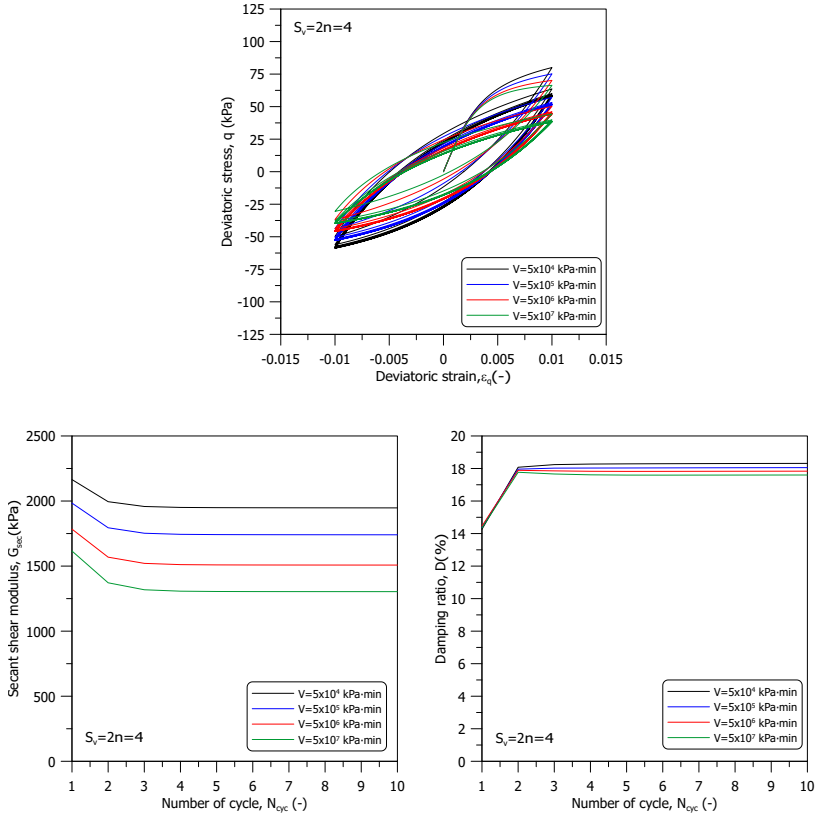

Figure C.15: Stress-strain curve, secant shear modulus, and damping ratio of strain-controlled cyclic shearing stage for different V value

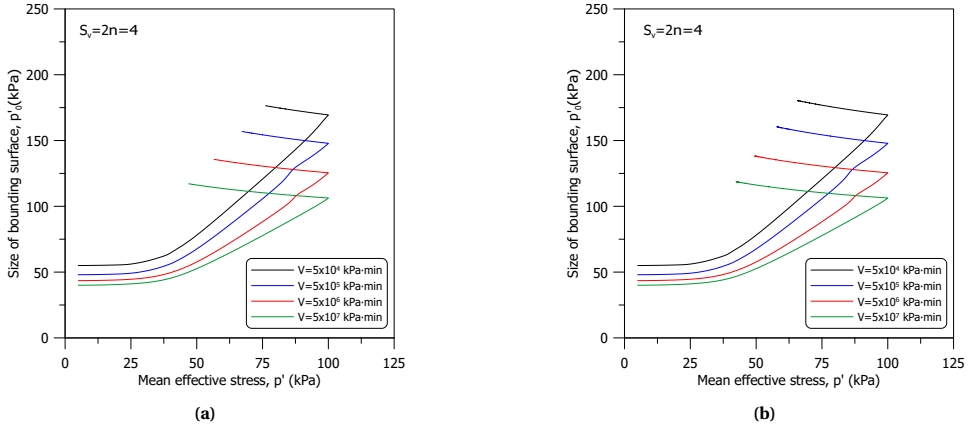

Figure C.16: Evolution of the size of bounding surface during consolidation and stress-controlled cyclic shearing stage for different V value : (a) $q_{\text{cyc}} = 0.15p'_i$ and (b) $q_{\text{cyc}} = 0.30p'_i$

C

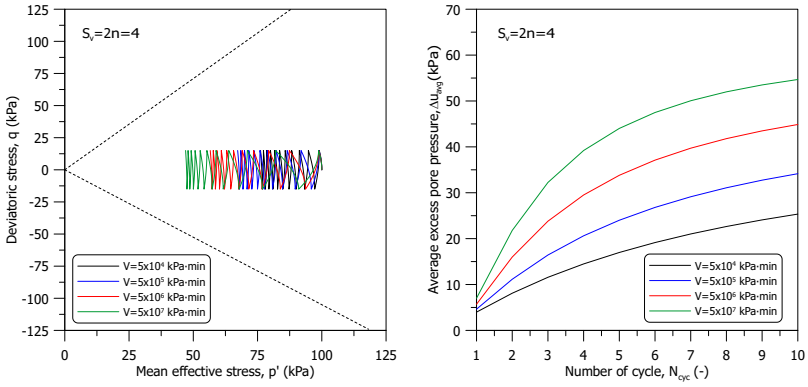

(a)

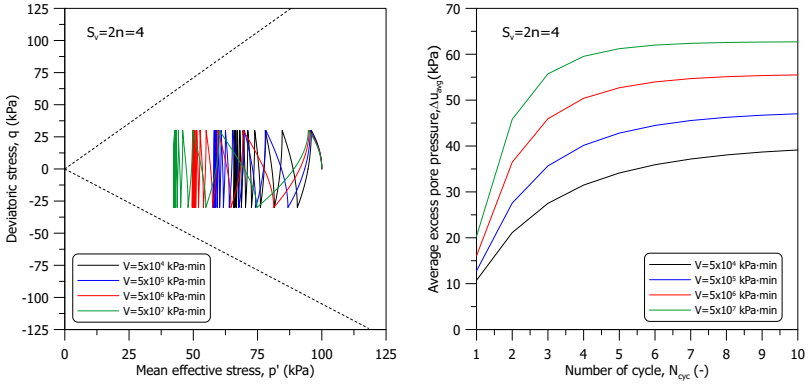

(b)

Figure C.17: Stress path and development of excess pore pressure of stress-controlled cyclic shearing stage for different V value : (a) $q_{\text{cyc}} = 0.15p'_i$ and (b) $q_{\text{cyc}} = 0.30p'_i$

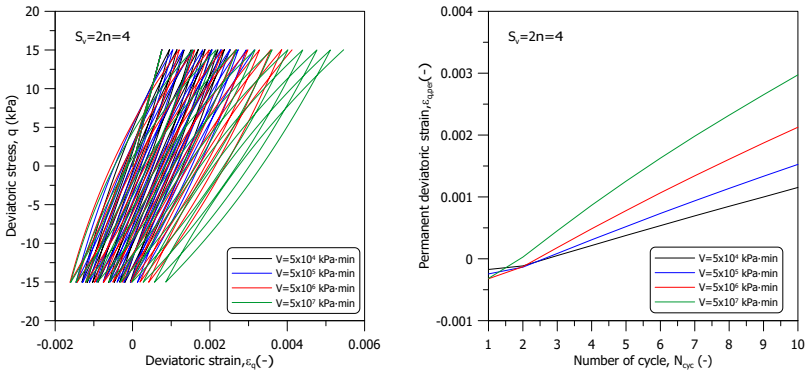

(a)

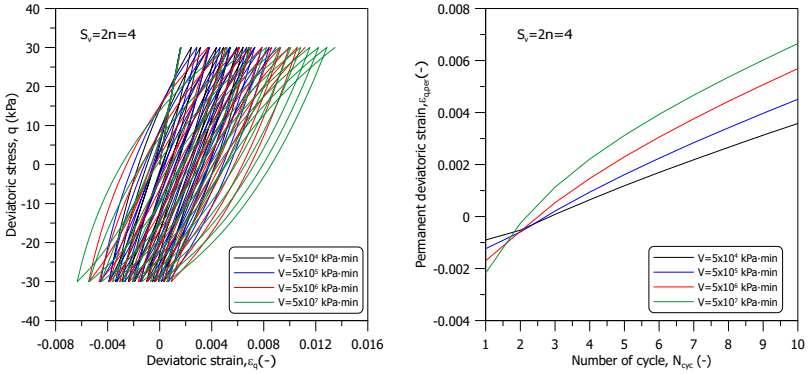

(b)

Figure C.18: Stress-strain curve and permanent deviatoric strain of stress-controlled cyclic shearing stage for different V value : (a) $q_{\text{cyc}} = 0.15p'_i$ and (b) $q_{\text{cyc}} = 0.30p'_i$

C.2.2. K_0 INITIAL STRESS STATE

The impact of the viscoplastic parameter V on cyclic behaviour, starting from a K_0 stress state, is investigated using strain-controlled cyclic shearing, with a cyclic strain amplitude ε_{cyc} set at 0.01. For this analysis, four distinct V values are considered. The additional model parameters not listed in Chapter 4 are detailed in Table C.2. The simulation process includes two stages: firstly, a K_0 consolidation stage, and secondly, a cyclic shearing stage. The consolidation stage lasts for 10,800 minutes, with the cyclic loading frequency and waveform details provided in Chapter 4.

C

Figure C.19 displays the evolution of bounding surface size during both the K_0 consolidation and strain-controlled cyclic shearing stages. Echoing results from simulations initiated from an isotropic stress state, lower V values lead to a more rapid change in the bounding surface size.

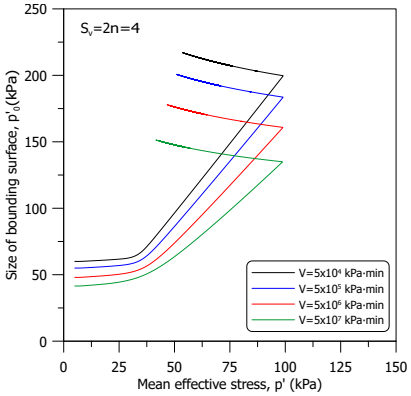

Figure C.19: Evolution of the size of bounding surface during consolidation and strain-controlled cyclic shearing stage for different V value

Figure C.20 presents the stress path and average excess pore pressure during cyclic shearing. In line with simulations from an isotropic stress state, lower V values are associated with higher peak deviatoric stresses during cyclic loading. Across all simulations, the average excess pore pressure initially increases in the first two to three cycles and then decreases. This pattern is tied to the image stress being on the dry side, as previously explained in the sensitivity analysis of parameter s_v. Moreover, the magnitude of excess pore pressure is greater with higher V values.

Figure C.21 illustrates the deviatoric stress-strain curve, along with the development of the secant shear modulus and damping ratio for various V values. Consistent with the results from the sensitivity analysis under isotropic stress state conditions, lower V values correlate with higher peak deviatoric stresses during cyclic shearing. Regarding the secant shear modulus, smaller V values lead to higher moduli, which exhibit a slight decrease as the number of loading cycles increases. The damping ratio generally increases as V values decrease, although the differences among the various V values are relatively minor. Additionally, a minor increase in damping ratio is observed with an increasing number of loading cycles.

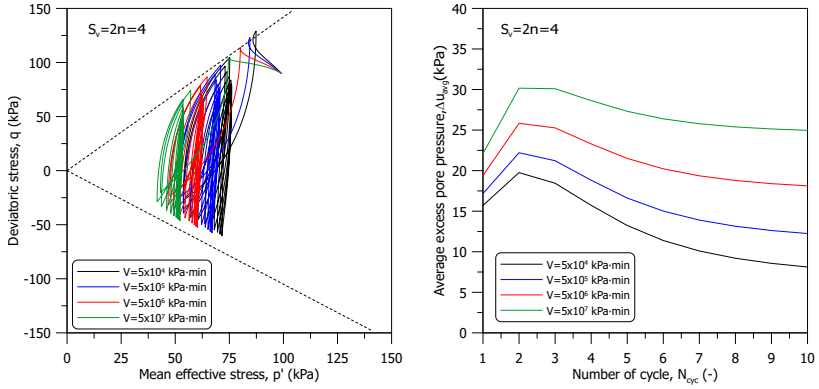

Figure C.20: Stress path and development of excess pore pressure of strain-controlled cyclic shearing stage for different V value

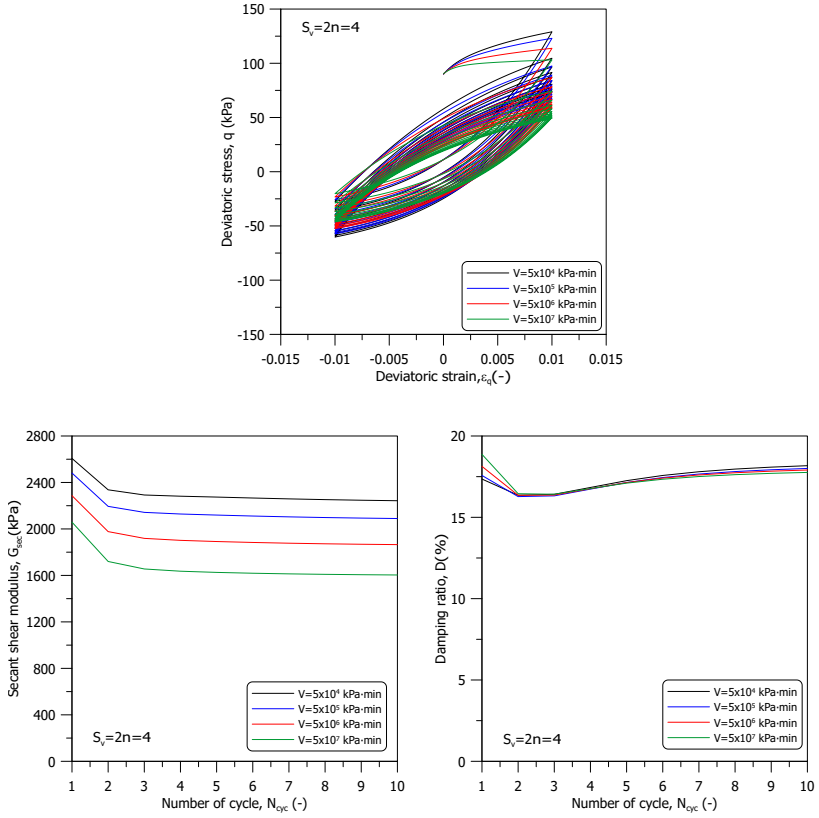

Figure C.21: Stress-strain curve, secant shear modulus, and damping ratio of strain-controlled cyclic shearing stage for different V value

C

The sensitivity analysis was extended to include stress-controlled cyclic shearing, employing two distinct cyclic stress amplitudes, q_{cyc} ($0.15p'_i$ and $0.30p'_i$, with $p'_i = 100$ kPa). Figure C.22 demonstrates the evolution of bounding surface size during both the K_0 consolidation and stress-controlled cyclic shearing stages.

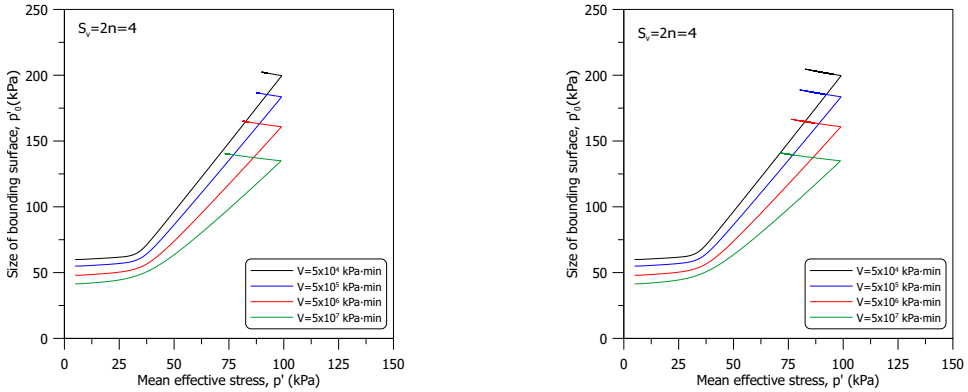

Figure C.22: Evolution of the size of bounding surface during consolidation and stress-controlled cyclic shearing stage for different V value : (a) $q_{cyc} = 0.15p'_i$ and (b) $q_{cyc} = 0.30p'_i$

Figure C.23 presents the stress path and average excess pore pressure observed during stress-controlled cyclic shearing. Across all V values, the stress paths show a consistent leftward movement during cyclic loading, leading to the development of positive excess pore pressure. Notably, lower V values tend to generate lower excess pore pressure during cyclic shearing. It is important to highlight that in simulations with higher cyclic stress amplitudes, a reduction in excess pore pressure is observed after the second cycle. This behaviour can be attributed to the adopted rotational hardening rule and the subsequent increase in bounding surface size during cyclic loading.

Figure C.24 illustrates the accumulation of permanent deviatoric strain, $\varepsilon_{q,per}$, during cyclic shearing. In alignment with results from simulations initiated from an isotropic stress state, higher V values correlate with larger accumulations of $\varepsilon_{q,per}$. A significant correlation exists between the increase in permanent deviatoric strain and higher stress amplitudes. Across all V values, $\varepsilon_{q,per}$ predominantly accumulates on the compression side. Notably, the magnitude of accumulated permanent deviatoric strain is considerably greater in these simulations compared to those originating from an isotropic stress state. It is important to note that in the simulation with $V = 5 \times 10^7$ kPa·min and $q_{cyc} = 0.30p'_i$, the target peak deviatoric stress was not achieved. Consequently, the permanent deviatoric strain in this particular simulation is less representative, due to the upper limit of cyclic strain imposed in the simulation.

Based on the discussion above, the impact of the V parameter on the predicted cyclic response is summarised. For the volumetric response, which includes the evolution of the stress path and the development of excess pore pressure, the size of the bounding surface at the end of the consolidation stage emerges as a key factor. This size significantly dictates the behaviour during cyclic shearing. In terms of deviatoric response,

lower λ^* values and larger bounding surface sizes contribute to increased secant shear modulus and reduced permanent deviatoric strain, $\varepsilon_{q,\text{per}}$, as V values decrease. However, the secant shear modulus reduction and damping ratio variations seem less dependent on V values. Besides the V parameter, other crucial factors influencing model predictions include the evolution of anisotropy (rotational hardening), updates to the projection centre, and the Lode angle dependency of the critical state stress ratio. Overall, while the influence of reducing V is akin to decreasing s_ν, the model prediction varies log linearly to changes in s_ν value.

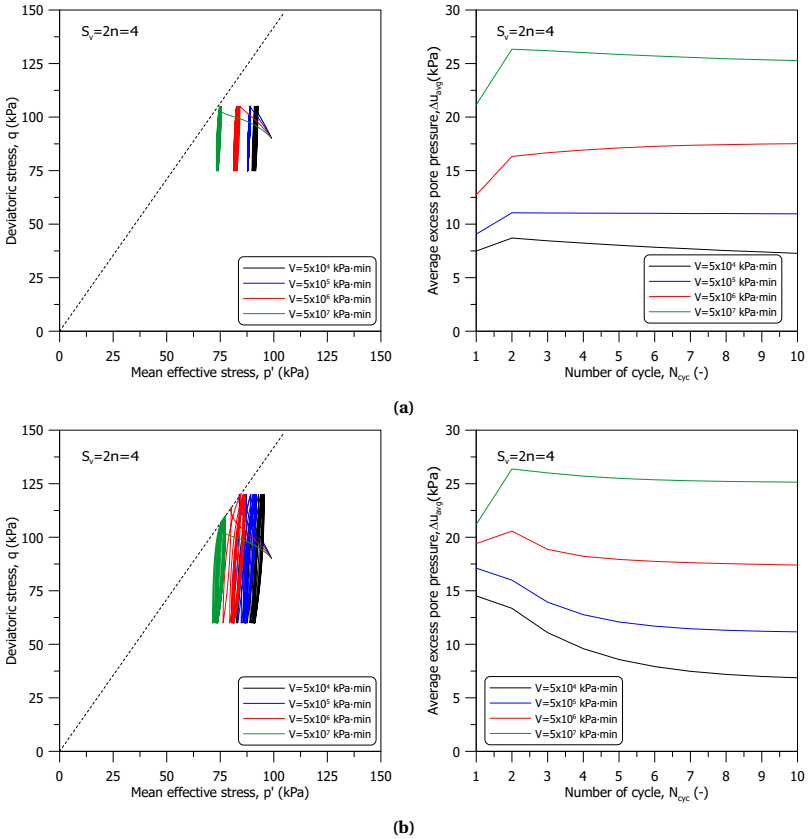

Figure C.23: Stress path and development of excess pore pressure of stress-controlled cyclic shearing stage for different V value : (a) $q_{\text{cyc}} = 0.15p'_i$ and (b) $q_{\text{cyc}} = 0.30p'_i$

C

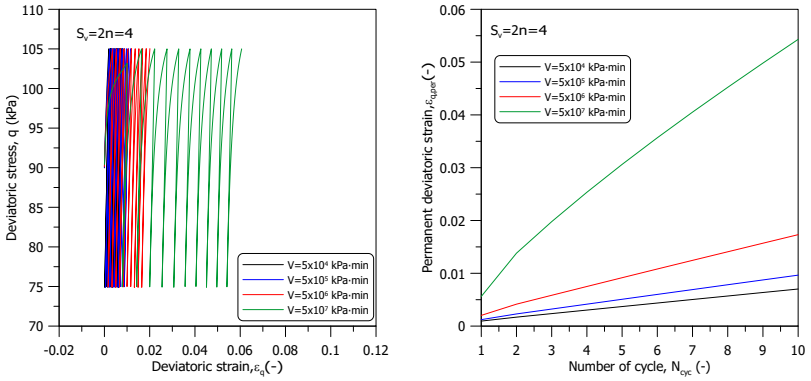

(a)

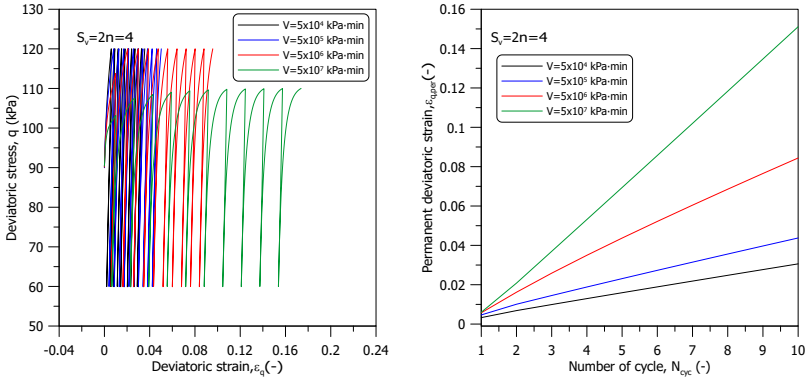

(b)

Figure C.24: Stress-strain curve and permanent deviatoric strain of stress-controlled cyclic shearing stage for different V value : (a) $q_{\text{cyc}} = 0.15p'_i$ and (b) $q_{\text{cyc}} = 0.30p'_i$

C.3. INFLUENCE OF PARAMETERS n ON THE CYCLIC RESPONSE

C.3.1. ISOTROPIC INITIAL STRESS STATE

In the following section, the sensitivity analysis of the viscoplastic parameter n is performed, starting with strain-controlled cyclic shearing. For this analysis, the cyclic strain amplitude is $\varepsilon_{cyc} = 0.01$, as used previously. As explored in Chapter 4, the impact of the parameter n is intricately linked to the 'normalized overstress', denoted as $\Delta\hat{\sigma}$. This relationship is recapped in equations C.1 and C.2:

$$\Phi = \frac{1}{V}\exp\left(\frac{q}{M_g p'}\right)(\Delta\hat{\sigma})^n \tag{C.1}$$

$$\begin{cases} \Delta\hat{\sigma} > 1, & b < \frac{s_v}{2(s_v-1)} \\ \Delta\hat{\sigma} = 1, & b = \frac{s_v}{2(s_v-1)} \\ \Delta\hat{\sigma} < 1, & b > \frac{s_v}{2(s_v-1)} \end{cases} \tag{C.2}$$

In this analysis, the impact of the parameter n in the context of three different s_v values is explored, given the relationship between the range of $\Delta\hat{\sigma}$ and the chosen s_v value. Four distinct n values are examined. Any model parameters not specified in Chapter 4 are available in Table C.3. The simulation comprises two stages: initially, a consolidation stage, followed by a cyclic shearing stage. The duration of the consolidation stage is set at 10,800 minutes. Comprehensive details on the cyclic loading frequency and waveform used in this analysis can be found in Chapter 4.

Table C.3: Model parameters adopted in sensitivity analysis

V	a_d	w
5×10^7 kPa·min	0	0

Figure C.25(a) to C.25(c) showcase the evolution of bounding surface size during both the consolidation and strain-controlled cyclic shearing stages. For a s_v value of 1.5, higher n values are observed to result in a more rapid change in the bounding surface size. In contrast, for s_v values of 2 and 2.5, higher n values lead to a lesser increase in the bounding surface size.

Figure C.26(a) to C.26(c) display the stress path and average excess pore pressure during cyclic shearing. For a s_v value of 1.5, higher n values are associated with increased peak deviatoric stresses during cyclic loading. Conversely, for s_v values of 2 and 2.5, higher n values result in lower peak deviatoric stresses. Across all investigated n and s_v values, the stress paths consistently move leftward during cyclic loading, indicating contractive behaviour and the development of positive excess pore pressure. The magnitude of excess pore pressure increases as n values rise for s_v values of 2 and 2.5, but decreases with increasing n values for an s_v of 1.5. The predicted response can be attributed to the variations in the 'normalized overstress', $\Delta\hat{\sigma}$, for different s_v values. Specifically, $\Delta\hat{\sigma}$ is greater than 1 when s_v equals 1.5. In contrast, for s_v values of 2 and 2.5, $\Delta\hat{\sigma}$ is less than 1, leading to a different influence from n value.

C

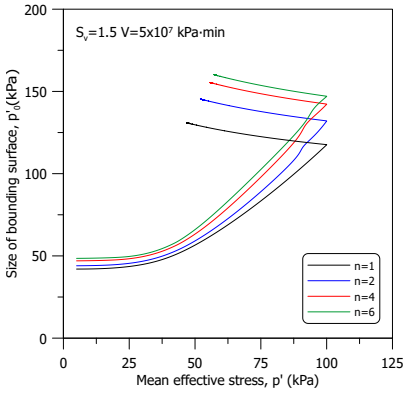

(a)

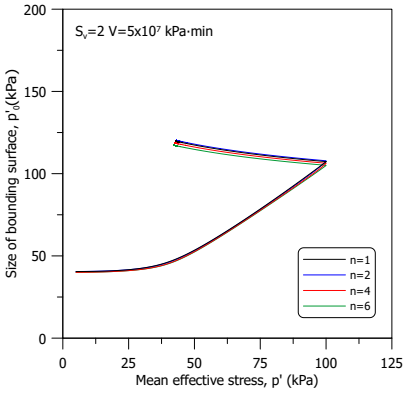

(b)

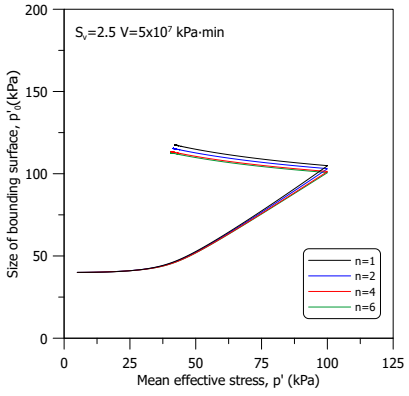

(c)

Figure C.25: Evolution of the size of bounding surface during consolidation and strain-controlled cyclic shearing stage for different n value : (a) $s_v = 1.5$ (b) $s_v = 2$ (c) $s_v = 2.5$

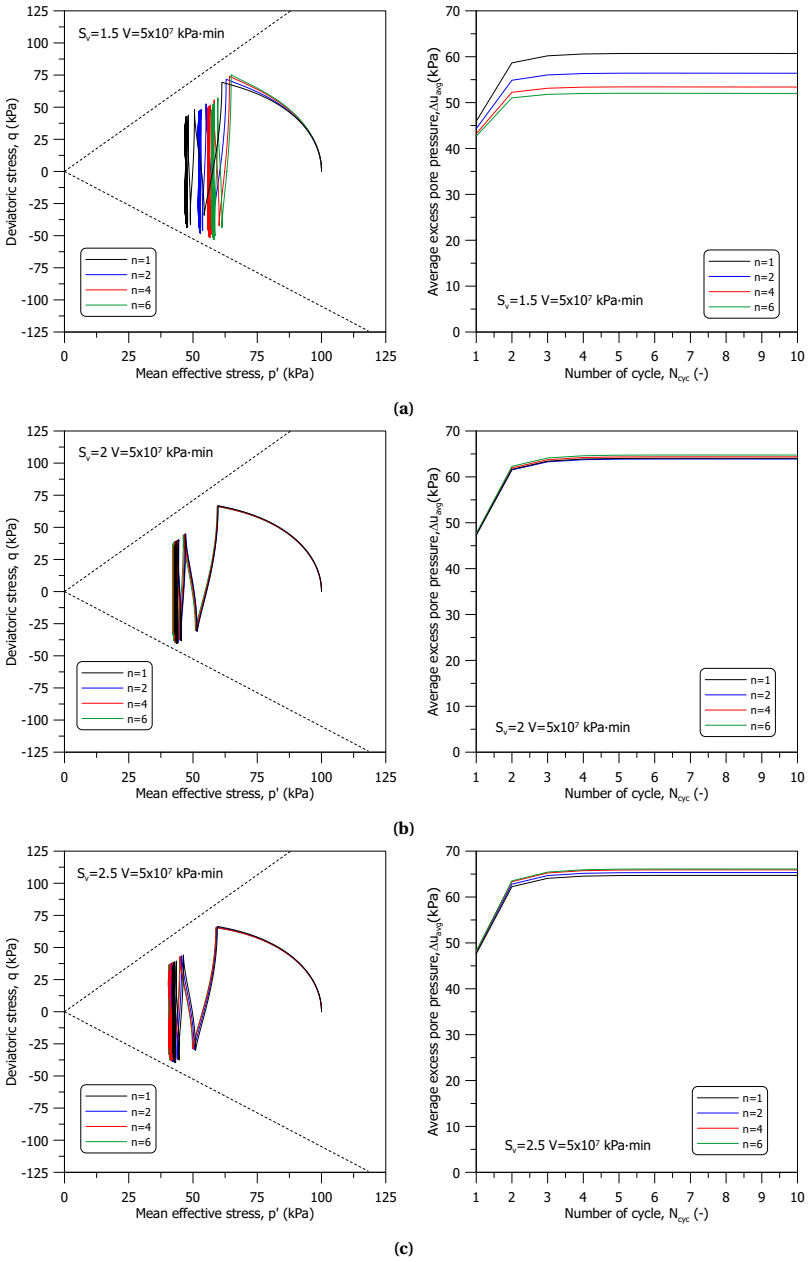

Figure C.26: Stress path and development of excess pore pressure of strain-controlled cyclic shearing stage for different n value : (a) $s_v = 1.5$ (b) $s_v = 2$ (c) $s_v = 2.5$

Figure C.27 to C.29 present the deviatoric stress-strain curve, as well as the variation of the secant shear modulus and damping ratio for a range of s_v and n values. Consistent with the stress path observations, lower n values correspond to higher peak deviatoric stresses during cyclic shearing for s_v values of 2 and 2.5. However, as the s_v value decreases to 1.5, larger n values are linked to smaller peak deviatoric stresses. Given that the cyclic strain amplitude is constant across all simulations, the n value has a same impact on the secant shear modulus. Additionally, the secant shear modulus tends to slightly decrease as the number of loading cycles increases. Regarding the damping ratio, the differences among various n values are minimal. Furthermore, no pronounced variation in the damping ratio is observed with an increase in loading cycles.

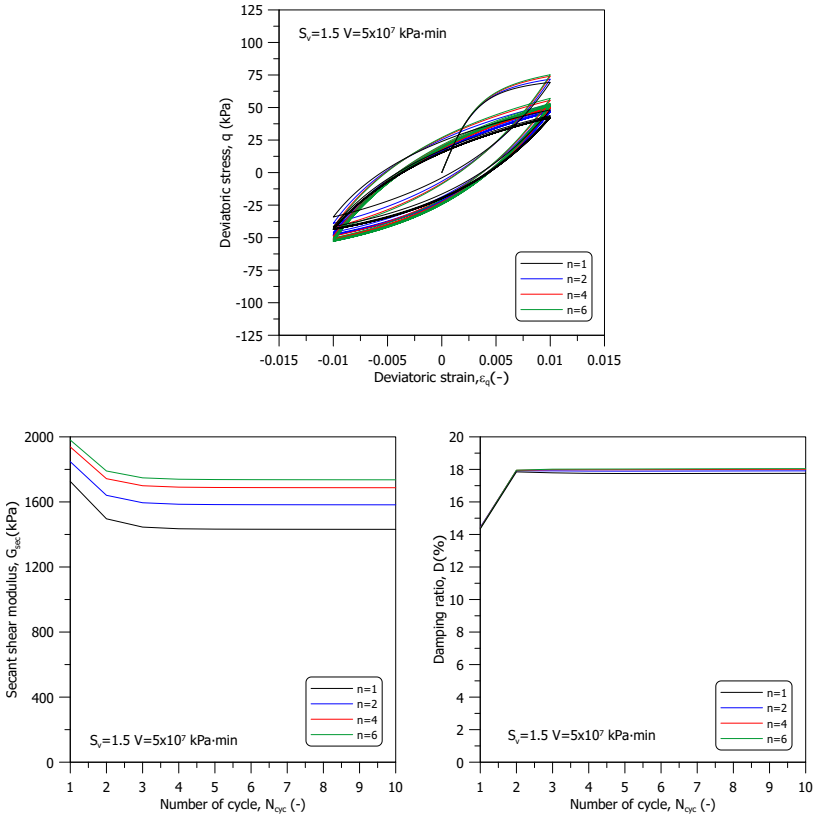

Figure C.27: Stress-strain curve, secant shear modulus, and damping ratio of strain-controlled cyclic shearing stage for different n value ($s_v = 1.5$)

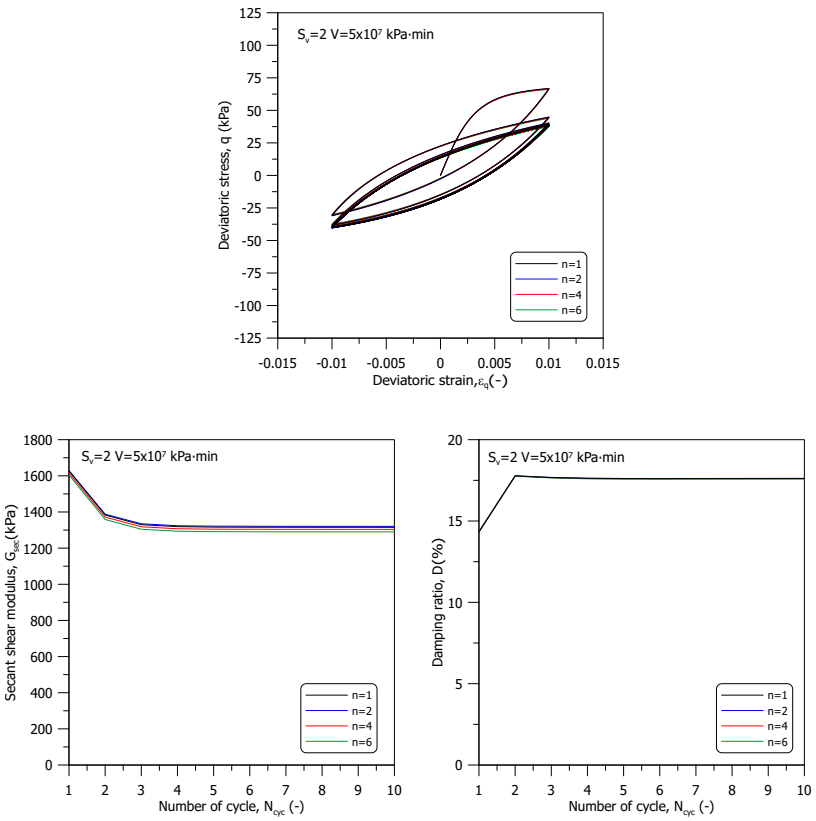

Figure C.28: Stress-strain curve, secant shear modulus, and damping ratio of strain-controlled cyclic shearing stage for different n value ($s_v = 2$)

C

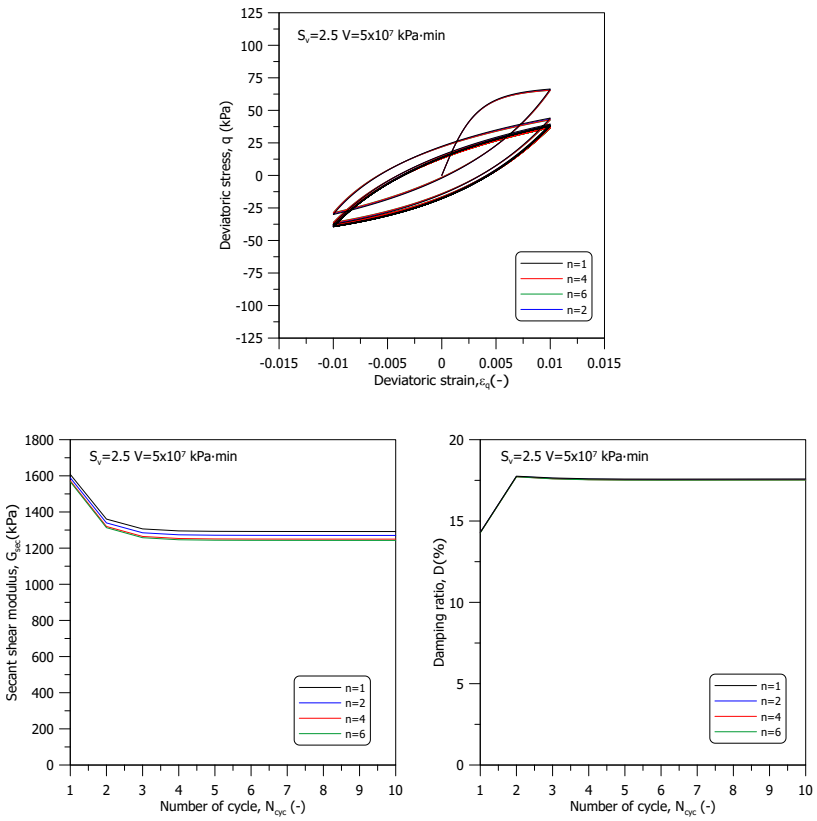

Figure C.29: Stress-strain curve, secant shear modulus, and damping ratio of strain-controlled cyclic shearing stage for different n value ($s_v = 2.5$)

The sensitivity analysis of the parameter n also encompasses stress-controlled cyclic shearing, using two distinct cyclic stress amplitudes, q_{cyc} ($0.15p'_i$ and $0.30p'_i$, with p'_i = 100 kPa), to assess the impact of loading magnitude. Figure C.30 to C.32 illustrate the evolution of bounding surface size during both the consolidation and stress-controlled cyclic shearing stages. In line with the strain-controlled simulation results, lower n values lead to a faster increase in bounding surface size for s_v values of 2 and 2.5. Conversely, for an s_v of 1.5, higher n values are linked to a quicker increase in bounding surface size.

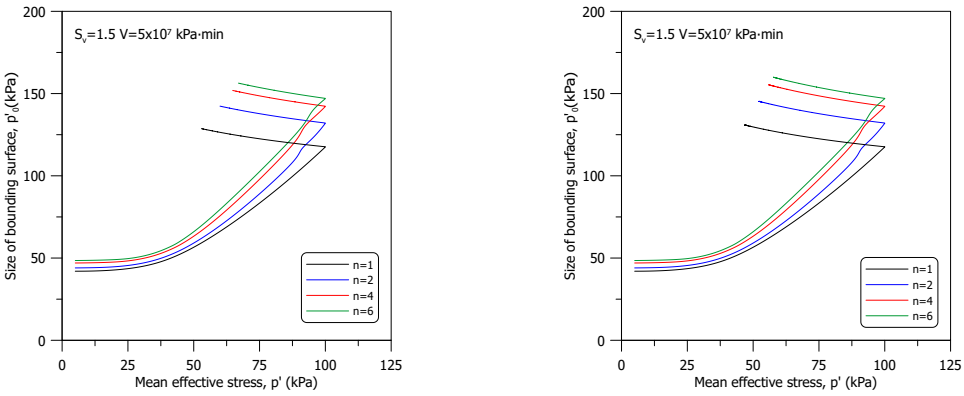

Figure C.30: Evolution of the size of bounding surface during consolidation and stress-controlled cyclic shearing stage for different n value (s_v = 1.5)

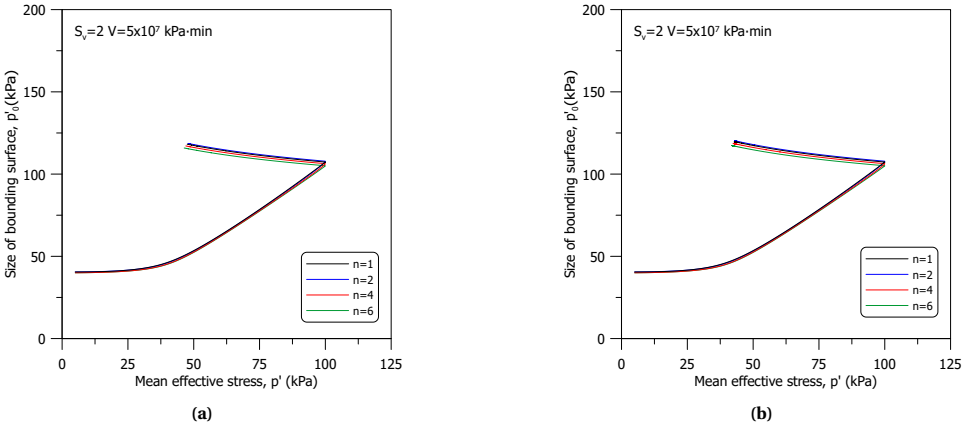

Figure C.31: Evolution of the size of bounding surface during consolidation and stress-controlled cyclic shearing stage for different n value (s_v = 2)

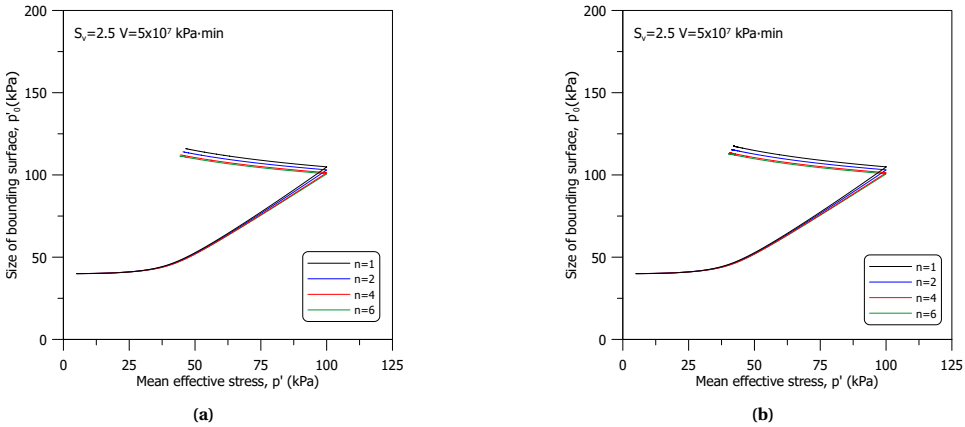

Figure C.32: Evolution of the size of bounding surface during consolidation and stress-controlled cyclic shearing stage for different n value ($s_v = 2.5$)

Figure C.33 to C.35 show the stress path and average excess pore pressure during stress-controlled cyclic shearing. Consistent across all s_v and n values, the stress paths move leftward during cyclic loading, leading to positive excess pore pressure development. For s_v values of 2 and 2.5, excess pore pressure decreases with reducing n values, while for an s_v of 1.5, it decreases with increasing n values. Higher cyclic stress amplitudes result in greater excess pore pressure development.

Figure C.36 to C.38 demonstrate the accumulation of permanent deviatoric strain, $\varepsilon_{q,\text{per}}$, during cyclic shearing. For s_v values of 2 and 2.5, higher n values correlate with larger accumulations of $\varepsilon_{q,\text{per}}$, whereas for an s_v of 1.5, smaller n values lead to larger accumulations. There is also a notable correlation between increased permanent deviatoric strain and higher stress amplitudes. Similar to previous observations in the sensitivity analysis of parameters s_v and V, $\varepsilon_{q,\text{per}}$ in all simulations initially accumulates towards the extension side in the first 2 to 3 cycles, then shifts towards the compression side.

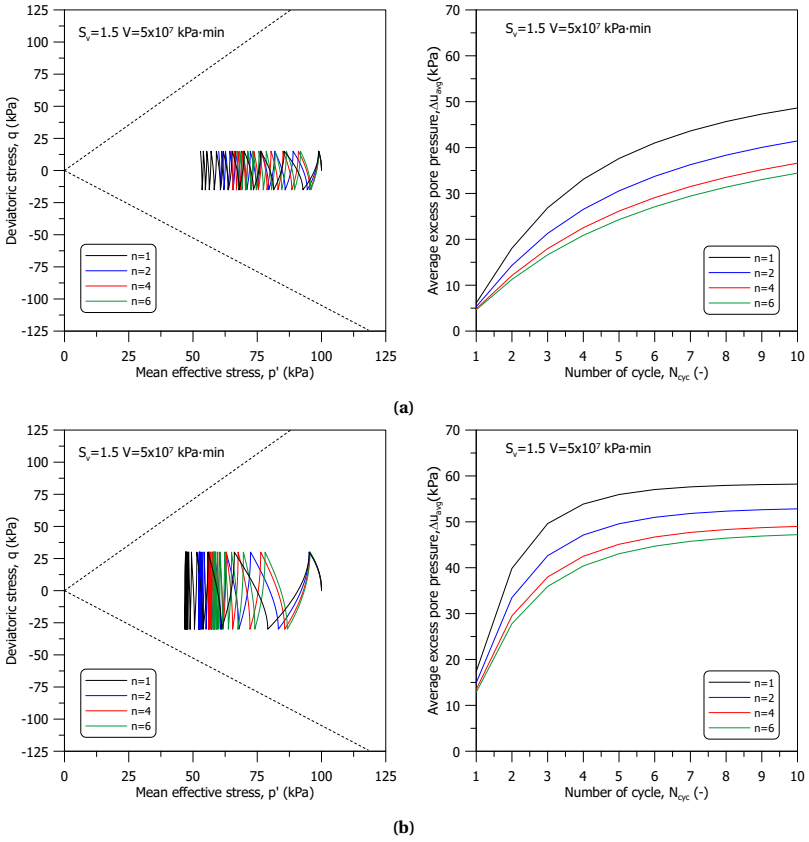

Figure C.33: Stress path and development of excess pore pressure of stress-controlled cyclic shearing stage for different n value ($s_v = 1.5$)

C

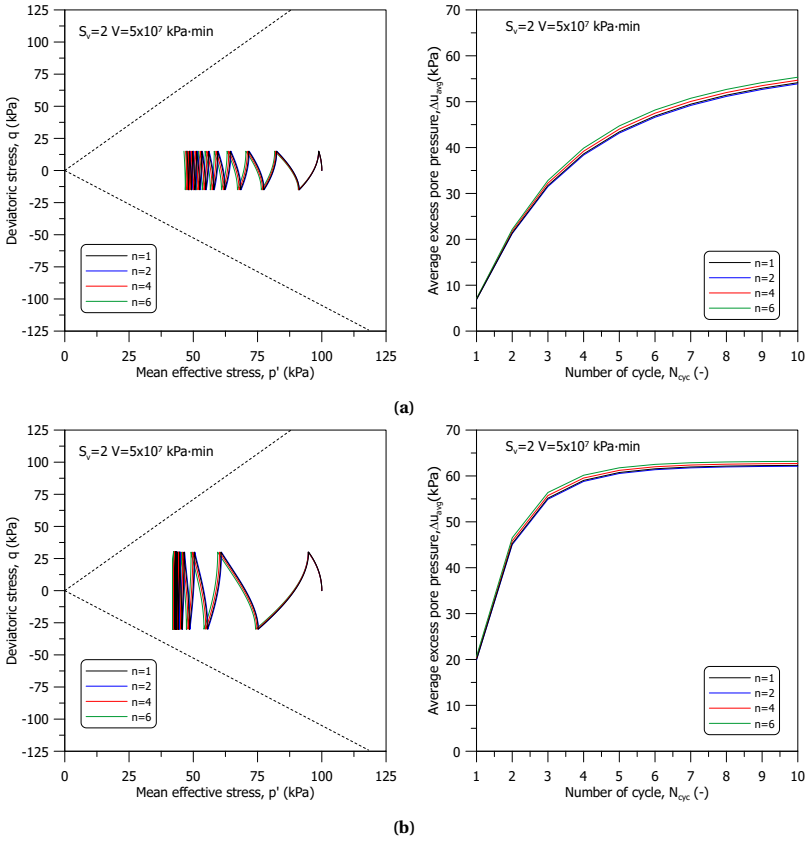

Figure C.34: Stress path and development of excess pore pressure of stress-controlled cyclic shearing stage for different n value ($s_v = 2$)

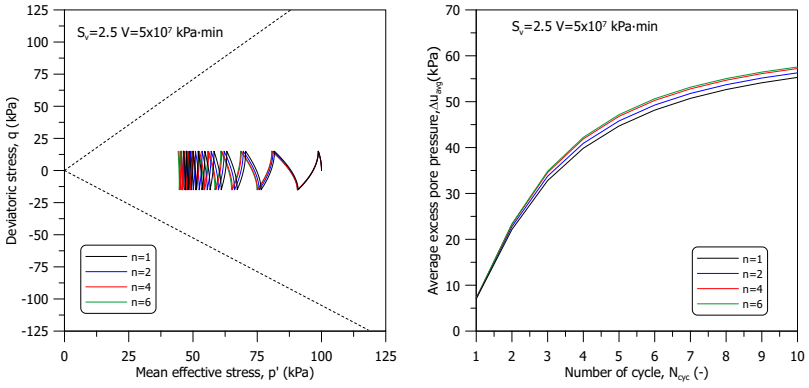

(a)

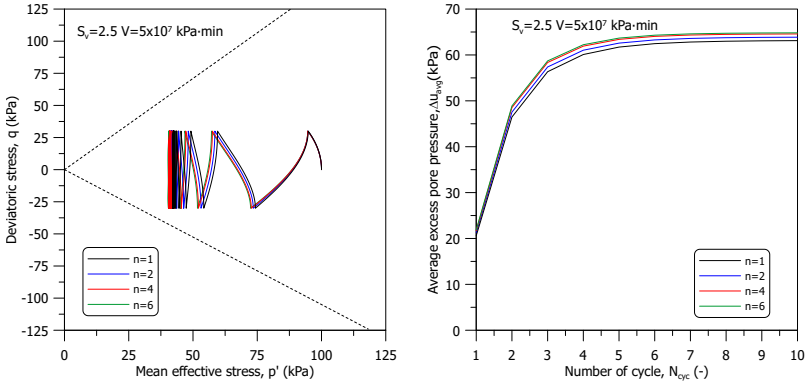

(b)

Figure C.35: Stress path and development of excess pore pressure of stress-controlled cyclic shearing stage for different n value ($s_v = 2.5$)

C

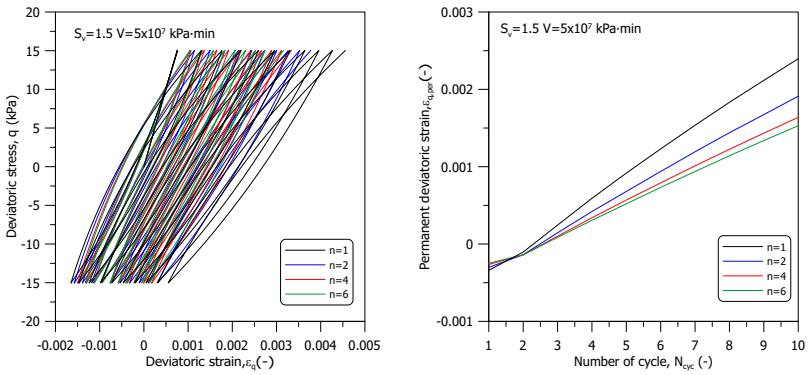

(a)

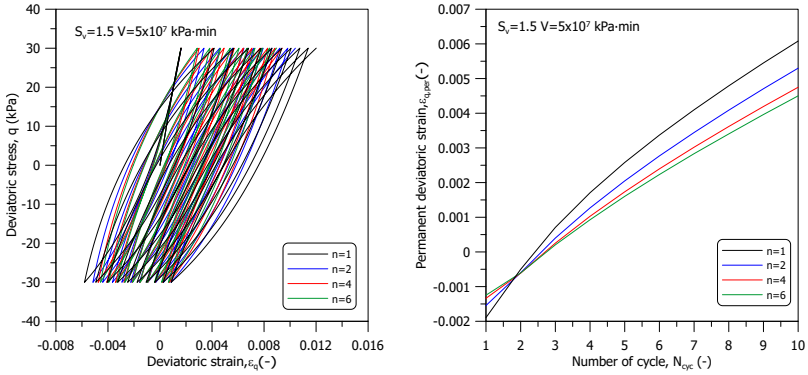

(b)

Figure C.36: Stress-strain curve and permanent deviatoric strain of stress-controlled cyclic shearing stage for different n value ($s_v = 1.5$)

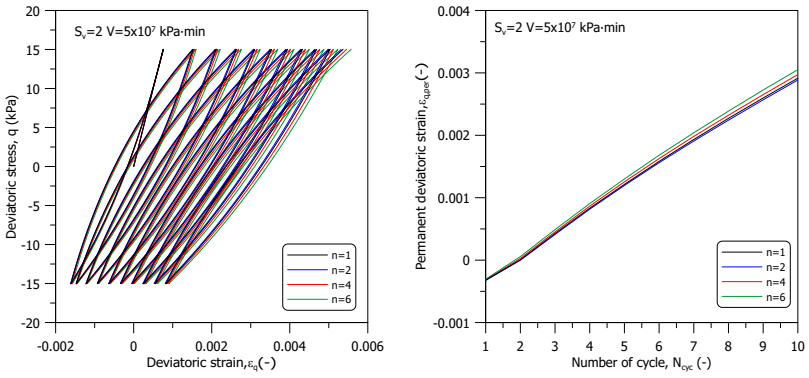

(a)

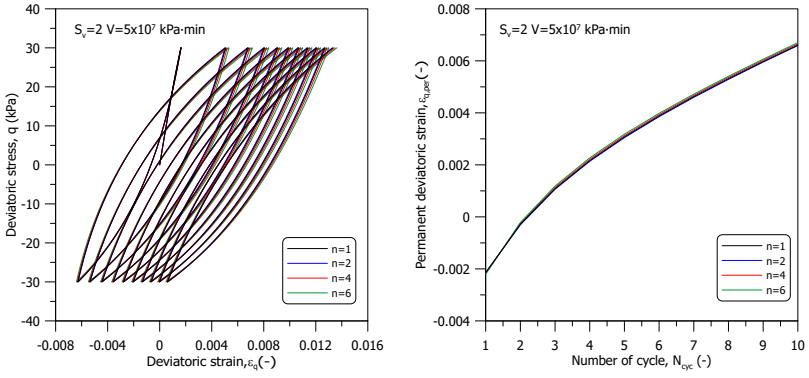

(b)

Figure C.37: Stress-strain curve and permanent deviatoric strain of stress-controlled cyclic shearing stage for different n value ($s_v = 2$)

C

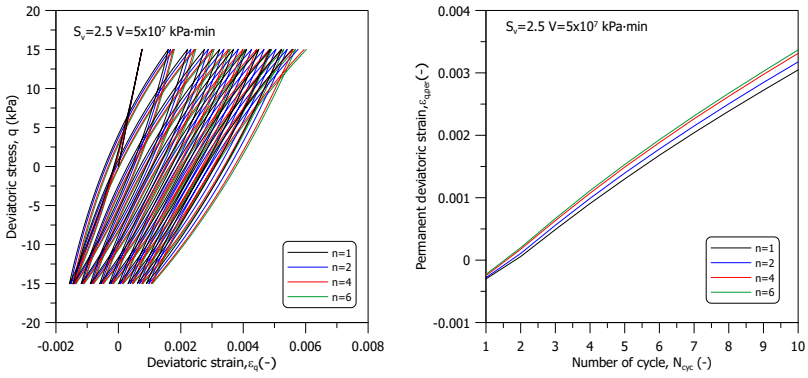

(a)

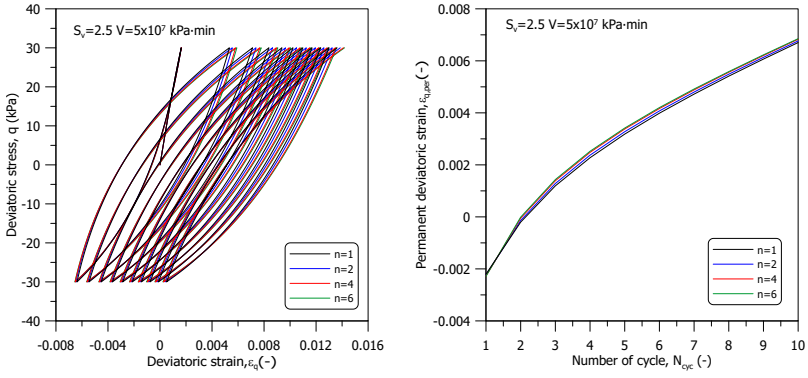

(b)

Figure C.38: Stress-strain curve and permanent deviatoric strain of stress-controlled cyclic shearing stage for different n value ($s_v = 2.5$)

C.3.2. K_0 INITIAL STRESS STATE

In the next section, a sensitivity analysis of the viscoplastic parameter n for initially K_0 consolidated stress state is conducted, starting with strain-controlled cyclic shearing. The same cyclic strain amplitude, $\varepsilon_{cyc} = 0.01$ is adopted. The combinations of s_v and n values examined remain consistent with those earlier. Additional model parameters not presented in Chapter 4 are detailed in Table C.3. The simulation process involves two stages: a K_0 consolidation stage followed by a cyclic shearing stage, with the consolidation lasting 10,800 minutes. The cyclic loading frequency and waveform details are as provided in Chapter 4.

Figure C.39(a) to C.39(c) illustrate the evolution of bounding surface size during both the K_0 consolidation and strain-controlled cyclic shearing stages. Across all combinations of s_v and n values, including $s_v = 1.5$, higher n values are associated with a lesser increase in bounding surface size. Notably, for $s_v = 1.5$ under isotropic consolidation, the 'normalized overstress', $\Delta\hat{\sigma}$, is greater than 1, but under K_0 consolidation, $\Delta\hat{\sigma}$ is less than 1, resulting in a different response to n values.

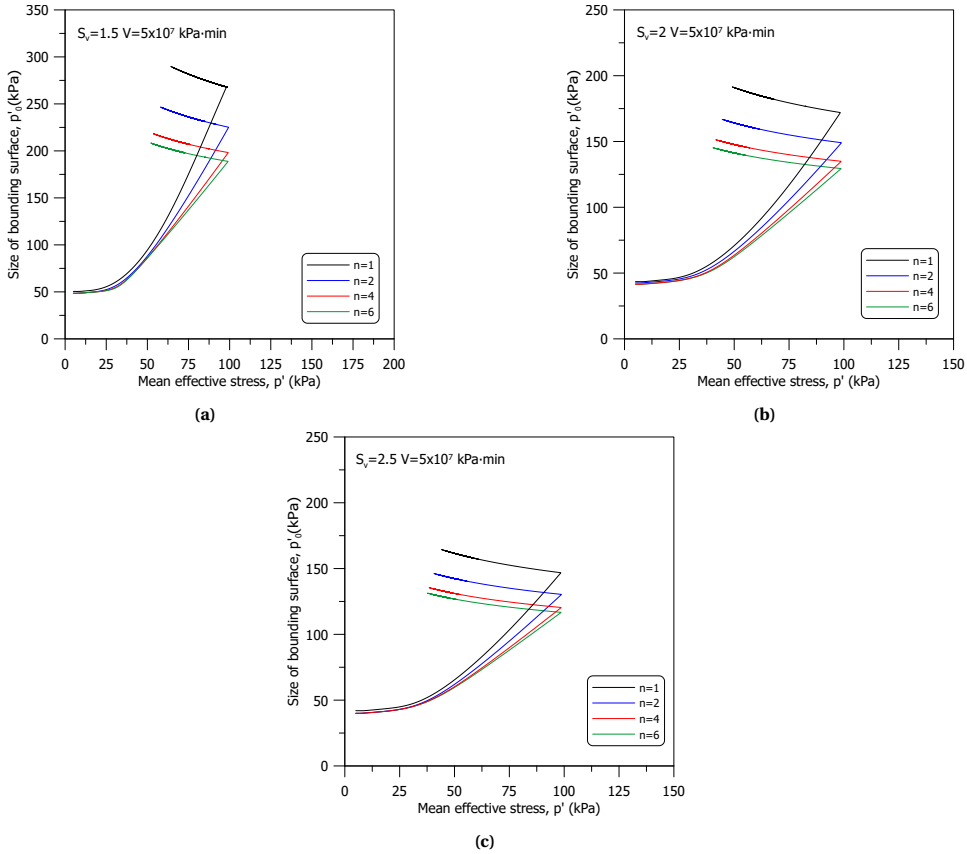

Figure C.39: Evolution of the size of bounding surface during consolidation and strain-controlled cyclic shearing stage for different n value : (a) $s_v = 1.5$ (b) $s_v = 2$ (c) $s_v = 2.5$

Figure C.40(a) to C.40(c) illustrate the stress path and average excess pore pressure during cyclic shearing. Across all simulations, lower n values are linked to increased peak deviatoric stresses during cyclic loading. Consistently, for all investigated n and s_v values, the stress paths exhibit a leftward movement during cyclic loading, suggesting contractive behaviour and the development of positive excess pore pressure. Notably, the magnitude of excess pore pressure rises with increasing n values for all s_v values. As previously mentioned and explained, the excess pore pressure begins to decrease between the 2nd and 3rd cycle.

Figure C.41 to C.43 present the deviatoric stress-strain curve, alongside the variation of the secant shear modulus and damping ratio for a range of n and s_v values. In alignment with the stress path observations, lower n values correlate with higher peak deviatoric stresses during cyclic shearing, indicating higher secant shear modulus for lower n values. Additionally, the secant shear modulus shows a slight decrease as the number of loading cycles increases. With respect to the damping ratio, differences among various n values are relatively minor. A small increase in damping ratio is also observed with an increasing number of loading cycles.

The sensitivity analysis of the parameter n under initially K_0 consolidated stress state also includes stress-controlled cyclic shearing. Two distinct cyclic stress amplitudes, q_{cyc} ($0.15p'_i$ and $0.30p'_i$, with $p'_i = 100\,\text{kPa}$), are used to evaluate the impact of loading magnitude. Figure C.44 to C.46 depict the evolution of bounding surface size during both the consolidation and stress-controlled cyclic shearing stages. Consistent with strain-controlled simulation results, lower n values result in a quicker increase in bounding surface size across all s_v values.

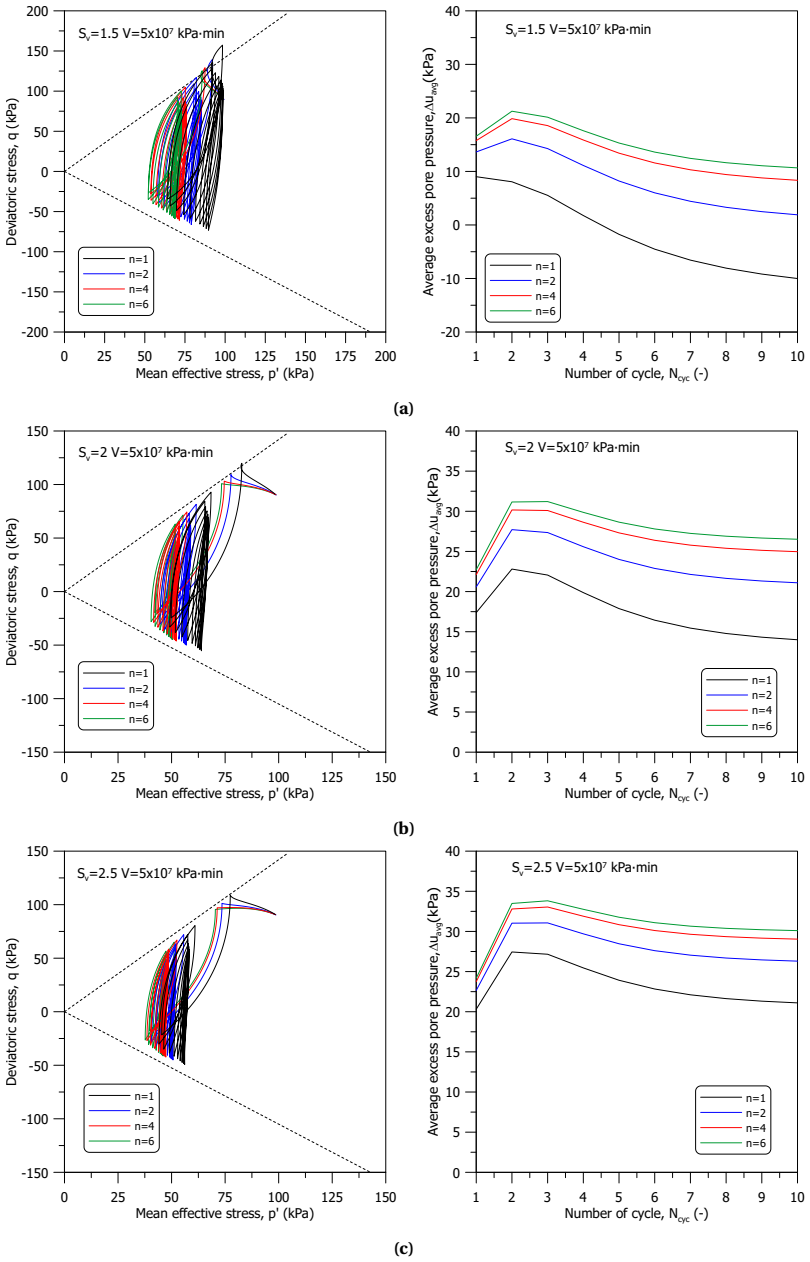

Figure C.40: Stress path and development of excess pore pressure of strain-controlled cyclic shearing stage for different n value : (a) $s_v = 1.5$ (b) $s_v = 2$ (c) $s_v = 2.5$

C

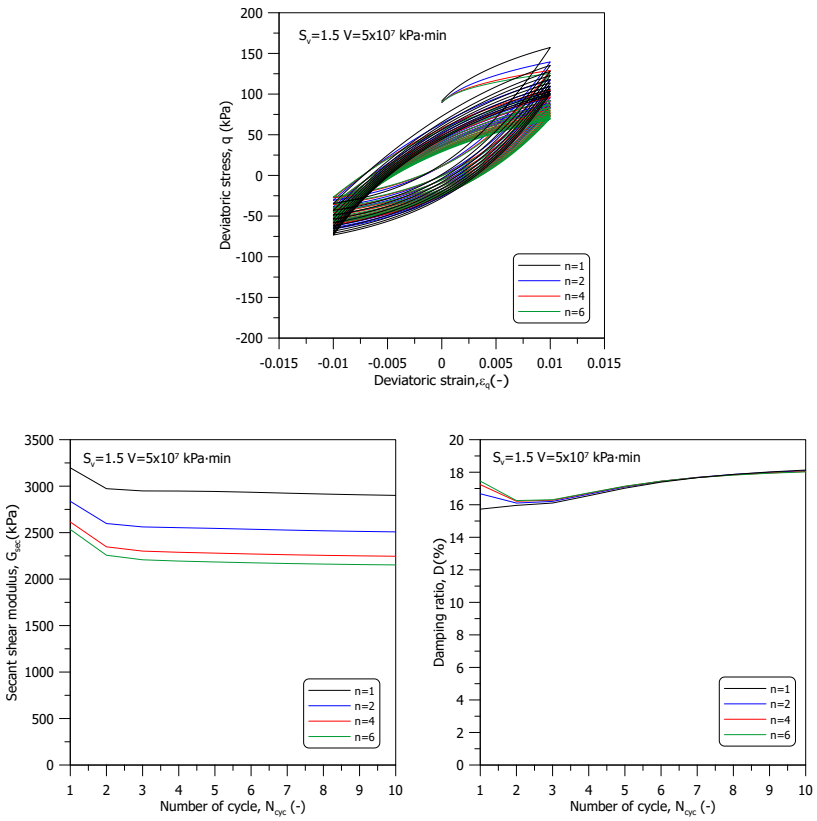

Figure C.41: Stress-strain curve, secant shear modulus, and damping ratio of strain-controlled cyclic shearing stage for different n value ($s_v = 1.5$)

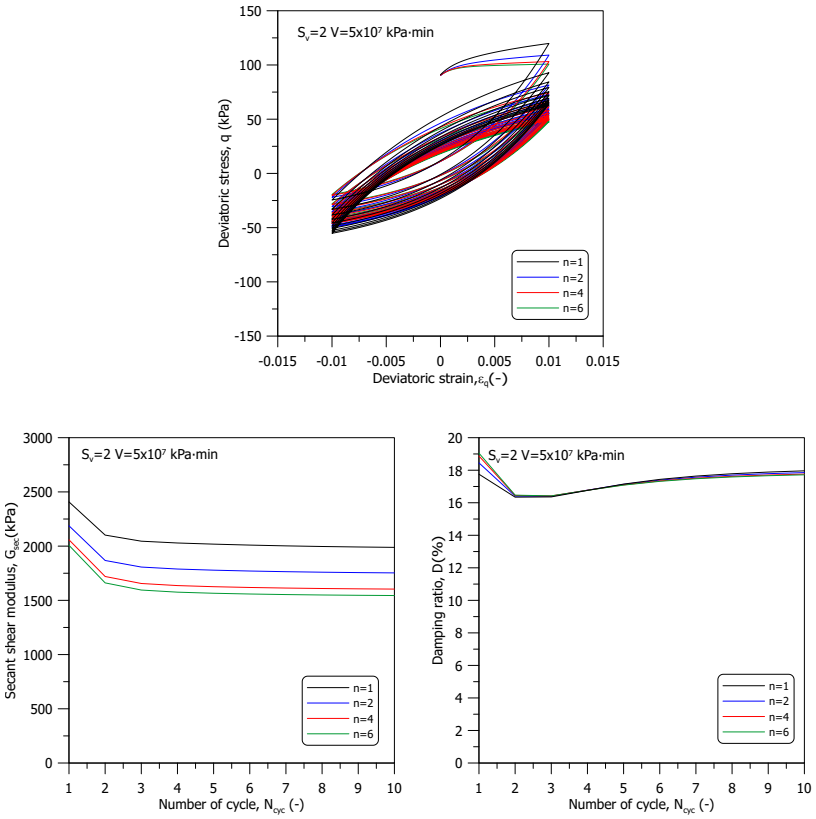

Figure C.42: Stress-strain curve, secant shear modulus, and damping ratio of strain-controlled cyclic shearing stage for different n value ($s_v = 2$)

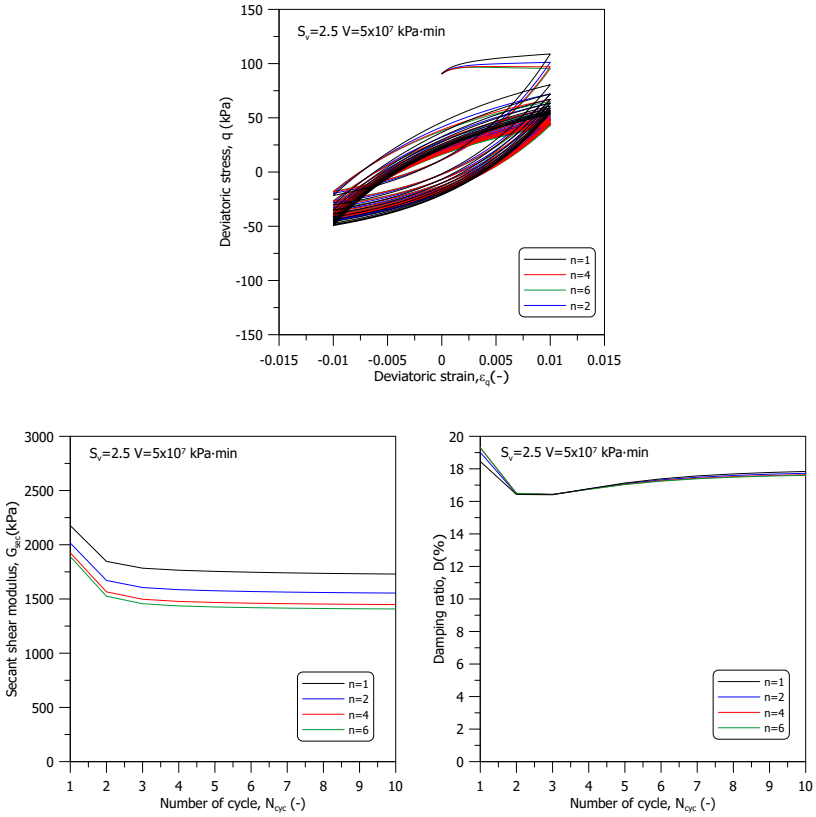

Figure C.43: Stress-strain curve, secant shear modulus, and damping ratio of strain-controlled cyclic shearing stage for different n value ($s_v = 2.5$)

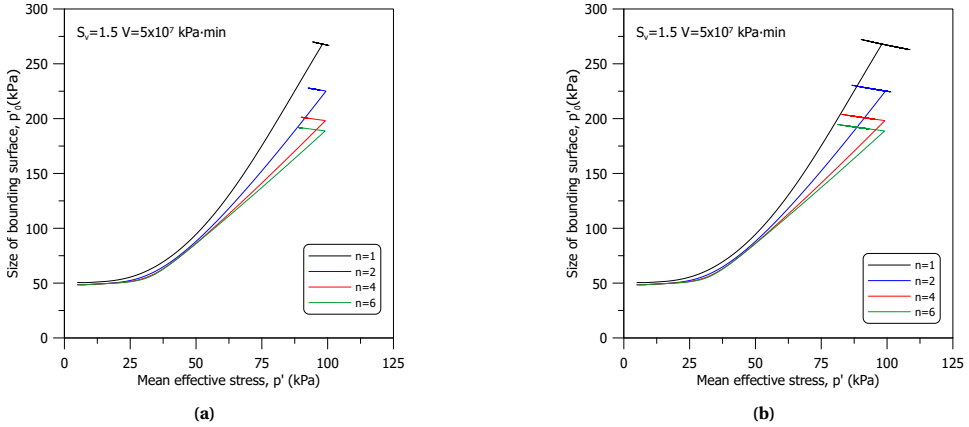

Figure C.44: Evolution of the size of bounding surface during consolidation and stress-controlled cyclic shearing stage for different n value ($s_v = 1.5$)

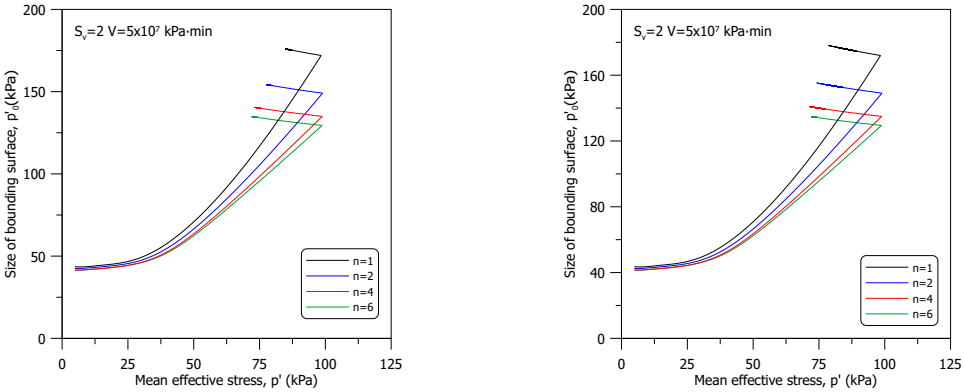

Figure C.45: Evolution of the size of bounding surface during consolidation and stress-controlled cyclic shearing stage for different n value ($s_v = 2$)

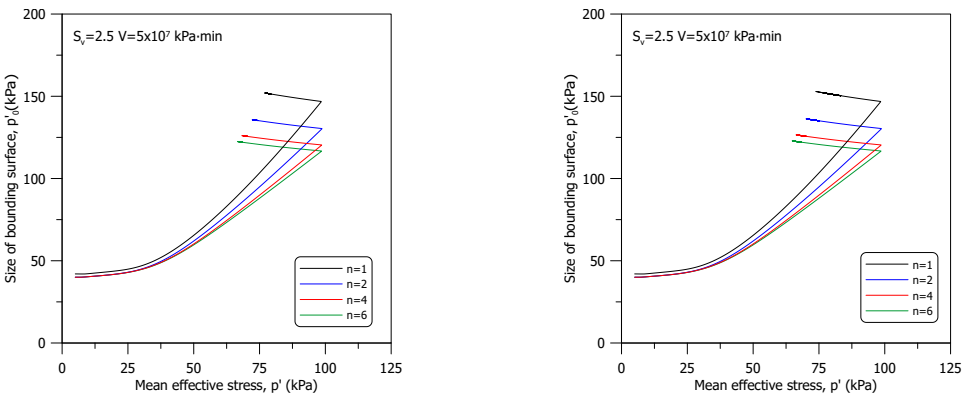

Figure C.46: Evolution of the size of bounding surface during consolidation and stress-controlled cyclic shearing stage for different n value ($s_v = 2.5$)

Figure C.47 to C.49 present the stress path and average excess pore pressure during stress-controlled cyclic shearing. Across all n values, the stress paths consistently move leftward during cyclic loading, resulting in the development of positive excess pore pressure. Lower n values tend to generate lesser excess pore pressure during cyclic shearing. In some simulations, a reduction in excess pore pressure is noted after the second cycle, a phenomenon previously explained. Additionally, higher cyclic stress amplitudes lead to greater excess pore pressure development.

Figure C.50 to C.52 illustrate the accumulation of permanent deviatoric strain, $\varepsilon_{q,\text{per}}$, during cyclic shearing. Higher n values are associated with larger accumulations of $\varepsilon_{q,\text{per}}$. There is a notable correlation between increased permanent deviatoric strain and higher stress amplitudes. Across all n values, $\varepsilon_{q,\text{per}}$ predominantly accumulates on the compression side. It is important to note that in a few simulations, the target peak deviatoric stress was not reached, making the permanent deviatoric strain less representative due to the upper limit of cyclic strain imposed in the simulation.

From the discussion above, the impact of the parameter n on the predicted cyclic response is distilled. For the volumetric response, encompassing the evolution of the stress path and the development of excess pore pressure, the size of the bounding surface at the end of the consolidation stage proves to be a crucial determinant. This size significantly influences the deviatoric response during cyclic shearing as well. Overall, the effect of the parameter n is primarily attributed to its role in the evolution of the bounding surface size. While the influence of n is somewhat similar to that of parameters s_v and V, its specific contribution is highly contingent on the chosen s_v value and the nature of the stress path during the consolidation stage. As discussed in Chapter 4, the parameter n functions as an exponent term of the 'normalized overstress', $\Delta\hat{\sigma}$. Its influence on the overstress function, Φ, can vary—being positive, neutral, or negative—when n is larger than 1. This characteristic affects the evolution rate of the overstress function and, consequently, the predicted response of the model. Considering the parameter n has similar influences to that of parameters s_v and V, unless specific experimental observations suggest otherwise, adopting a n value of 1 could simplify the model calibration process.

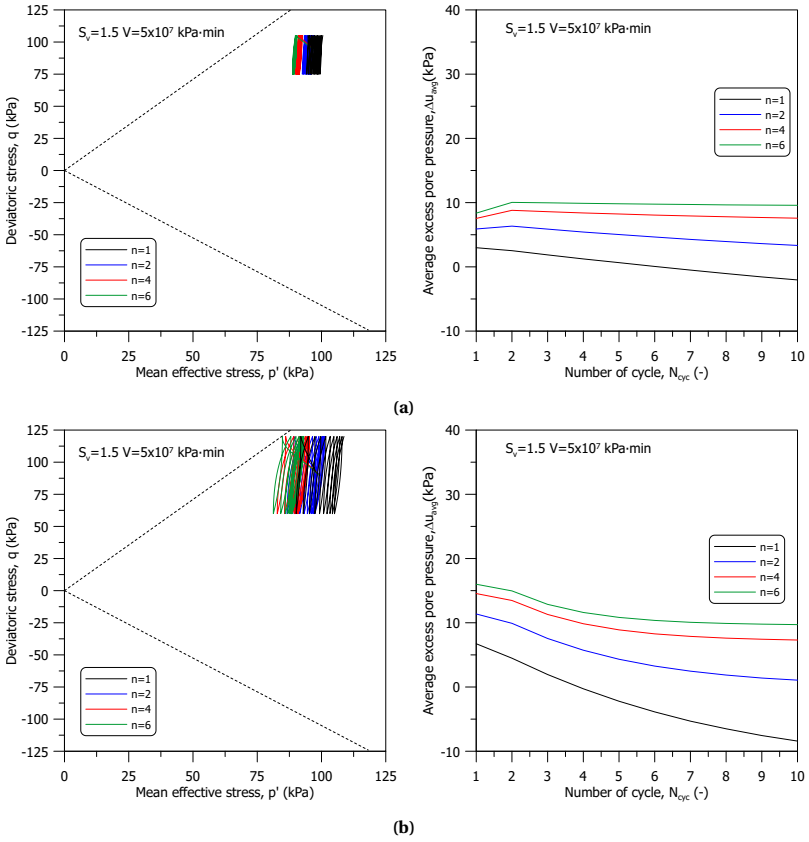

Figure C.47: Stress path and development of excess pore pressure of stress-controlled cyclic shearing stage for different n value ($s_v = 1.5$)

C

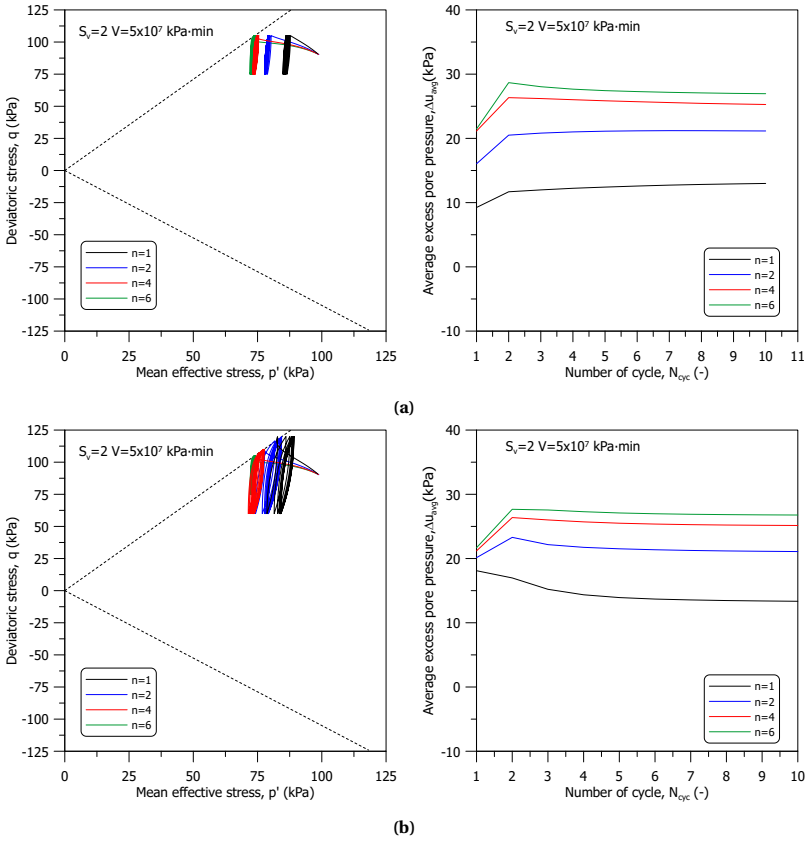

Figure C.48: Stress path and development of excess pore pressure of stress-controlled cyclic shearing stage for different n value ($s_v = 2$)

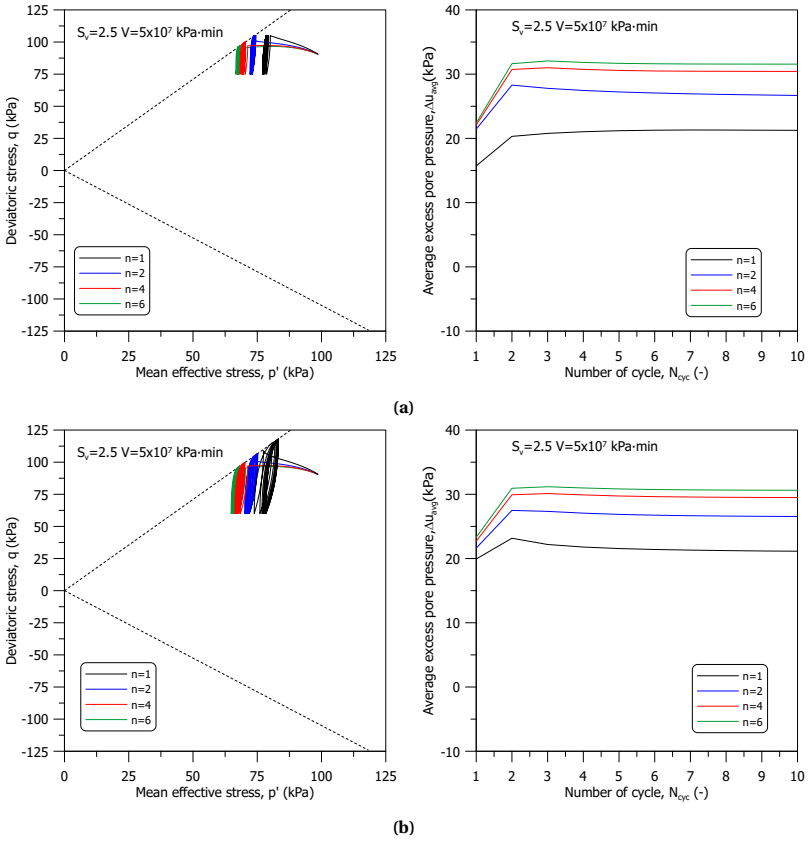

Figure C.49: Stress path and development of excess pore pressure of stress-controlled cyclic shearing stage for different n value ($s_v = 2.5$)

C

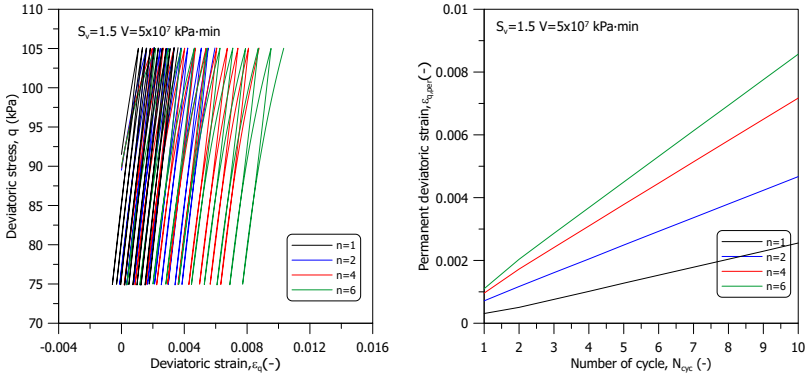

(a)

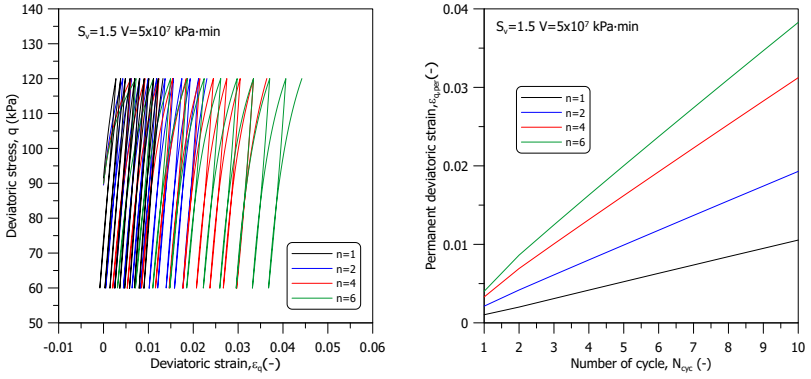

(b)

Figure C.50: Stress-strain curve and permanent deviatoric strain of stress-controlled cyclic shearing stage for different n value ($s_v = 1.5$)

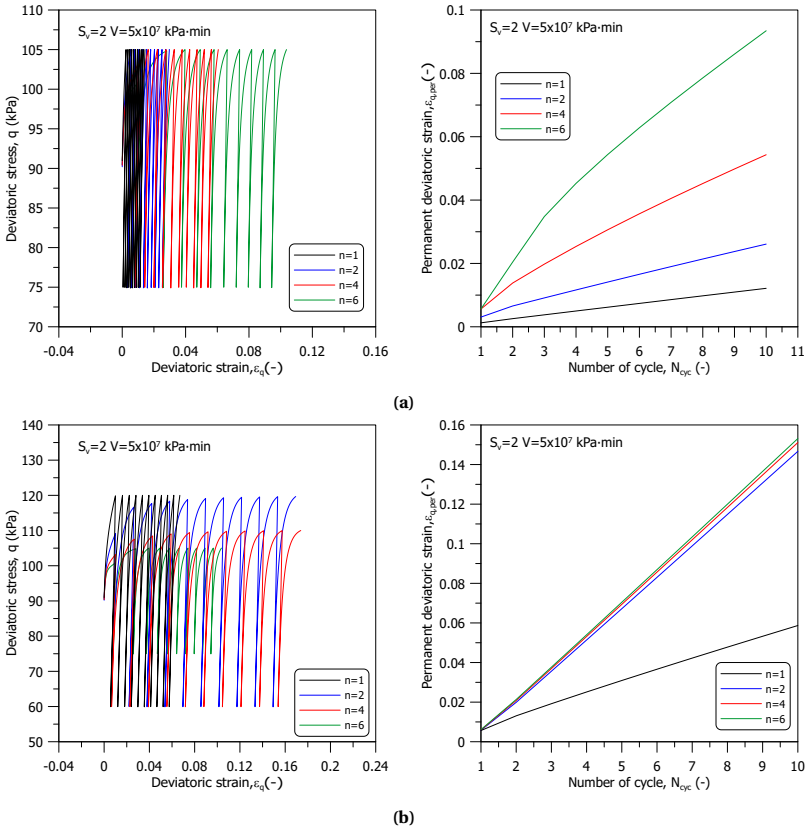

Figure C.51: Stress-strain curve and permanent deviatoric strain of stress-controlled cyclic shearing stage for different n value ($s_v = 2$)

C

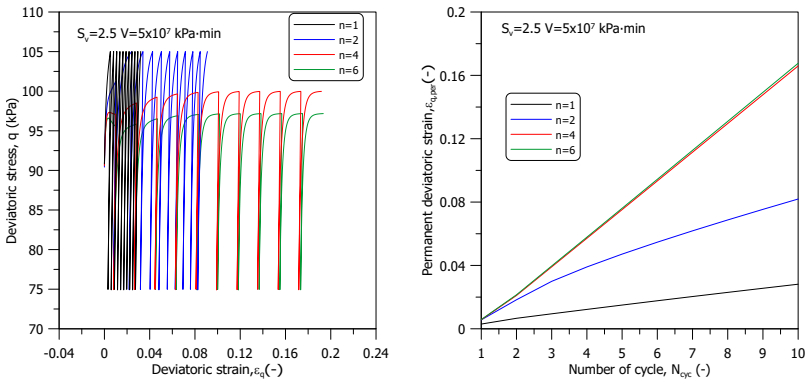

(a)

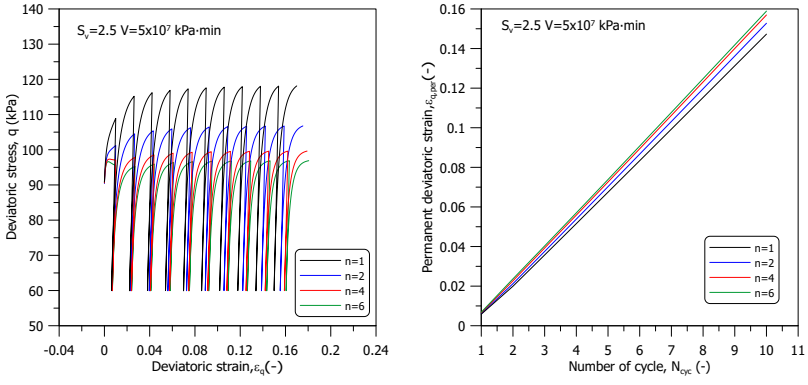

(b)

Figure C.52: Stress-strain curve and permanent deviatoric strain of stress-controlled cyclic shearing stage for different n value ($s_v = 2.5$)

C.4. INFLUENCE OF PARAMETERS a_d ON THE CYCLIC RESPONSE

C.4.1. ISOTROPIC INITIAL STRESS STATE, $a_d > 0$

In the previous sections, the sensitivity analysis was conducted for the viscoplastic related parameters s_v, V, and n. To the best of the author's knowledge, a thorough sensitivity analysis of the damage parameter a_d for viscoplastic bounding surface models has not yet been extensively explored. Therefore, the next section will be dedicated to the sensitivity analysis of the damage parameter a_d, aiming to elucidate its influence within the proposed model framework.

The impact of the positive damage parameter ($a_d > 0$) on cyclic response is initially explored using strain-controlled cyclic shearing, with the cyclic strain amplitude, ε_{cyc} set at 0.01. For this sensitivity analysis, five a_d values are considered. Model parameters that are not detailed in Chapter 4 can be found in Table C.4. The simulation process includes two stages: firstly, a consolidation stage, and secondly, a cyclic shearing stage. The consolidation stage spans 10,800 minutes. Details regarding the cyclic loading frequency and waveform used in this analysis are provided in Chapter 4.

Table C.4: Model parameters adopted in sensitivity analysis

s_v	V	n	w
1.75	5×10^7 kPa·min	4	0

Figure C.53 showcases the evolution of bounding surface size during both the consolidation and strain-controlled cyclic shearing stages. With the increase in the a_d value, which leads to a faster reduction in the plastic modulus, there is a faster increase in the bounding surface size.

Figure C.54 presents the stress path and average excess pore pressure during cyclic shearing. It is noted that for all a_d values, the simulations attain the same peak deviatoric stress in the first loading cycle. However, this peak deviatoric stress degrades more rapidly with increasing a_d values. In all simulations, the stress paths exhibit a consistent leftward movement during cyclic loading, suggesting contractive behaviour and the development of positive excess pore pressure. Furthermore, a minor reduction in excess pore pressure with an increase in loading cycles is observed for a_d values above 5.

Figure C.55 presents the deviatoric stress-strain curve, along with the development of the secant shear modulus and damping ratio for a range of a_d values. In alignment with the stress path observations, smaller a_d values are associated with a slower degradation of peak deviatoric stresses during cyclic shearing. When it comes to the secant shear modulus, lower a_d values lead to higher moduli and a more gradual reduction in modulus as the number of loading cycles increases. As for the damping ratio, it tends to decrease as a_d values increase, though the differences among various a_d values are relatively minor. Additionally, a decreasing trend in the variation of damping ratio with increasing loading cycles is observed for a_d values above 25.

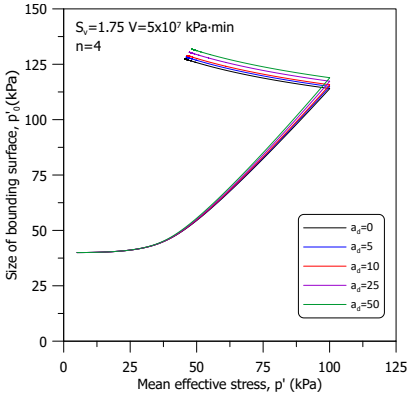

Figure C.53: Evolution of the size of bounding surface during consolidation and strain-controlled cyclic shearing stage for different a_d value

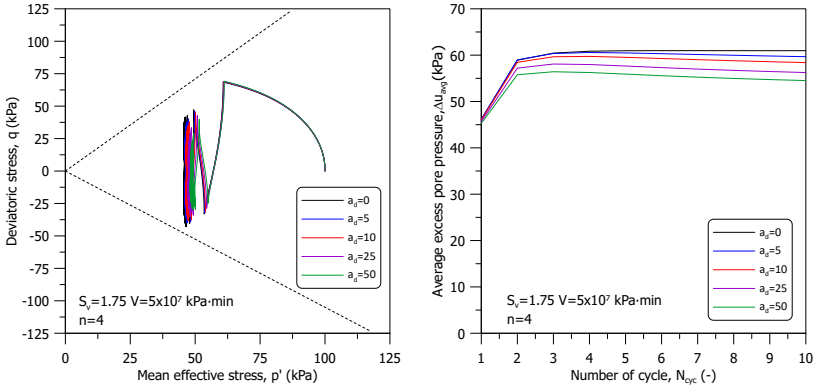

Figure C.54: Stress path and development of excess pore pressure of strain-controlled cyclic shearing stage for different a_d value

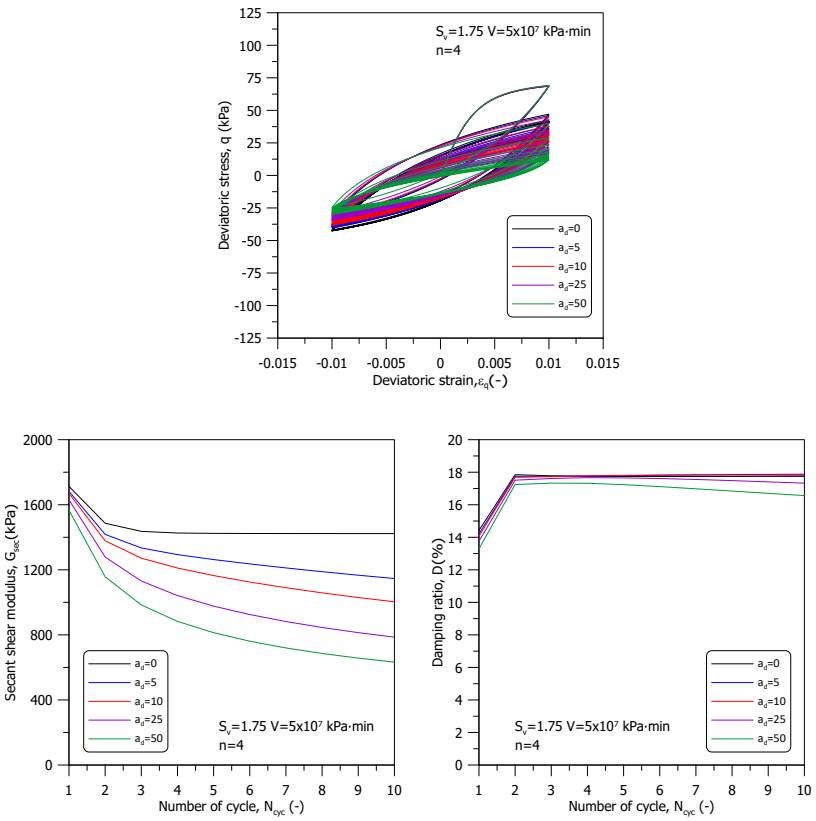

Figure C.55: Stress-strain curve, secant shear modulus, and damping ratio of strain-controlled cyclic shearing stage for different a_d value

C

To further investigate various aspects of the predicted cyclic response, a sensitivity analysis was also conducted using stress-controlled cyclic shearing. Two different cyclic stress amplitudes, q_{cyc} ($0.15p'_i$ and $0.30p'_i$, with $p'_i = 100$ kPa), were chosen to assess the impact of loading magnitude. Figure C.56 displays the evolution of the bounding surface size during both the consolidation and stress-controlled cyclic shearing stages. Similar to the strain-controlled simulations, a higher a_d value results in a larger bounding surface size.

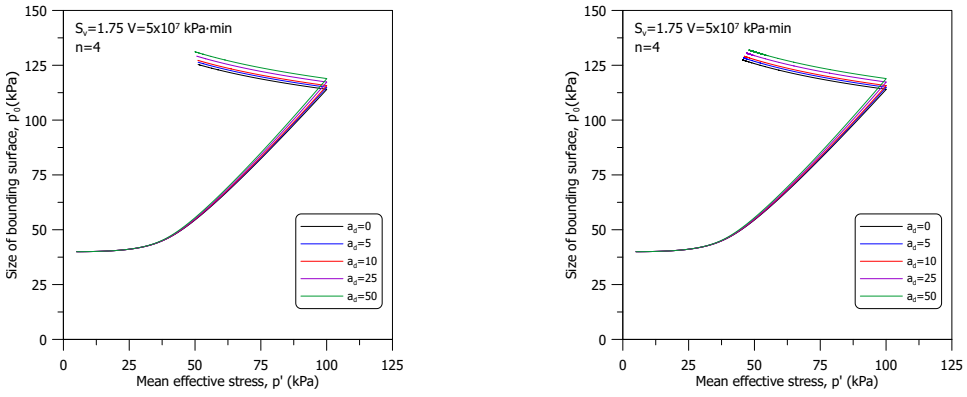

Figure C.56: Evolution of the size of bounding surface during consolidation and stress-controlled cyclic shearing stage for different a_d value : (a) $q_{\text{cyc}} = 0.15p'_i$ and (b) $q_{\text{cyc}} = 0.30p'_i$

Figure C.57 illustrates the stress path and average excess pore pressure during stress-controlled cyclic shearing. Consistently, for all a_d values, the stress paths exhibit a leftward movement during cyclic loading, indicative of contractive behaviour and the consequent development of positive excess pore pressure. Notably, there is a direct correlation between higher a_d values and increased excess pore pressure development. Furthermore, the simulations reveal that higher cyclic stress amplitudes lead to greater development of excess pore pressure. As indicated in Appendix B, for a_d values greater than 25, the stress paths exhibit a scimitar shape, and the excess pore pressure shows a decreasing trend.

Figure C.58 depicts the accumulation of permanent deviatoric strain, represented as $\varepsilon_{q,\text{per}}$, during cyclic shearing. Notably, despite similar levels of permanent deviatoric strain in the initial cycle across all simulations, higher a_d values are observed to result in larger accumulations of $\varepsilon_{q,\text{per}}$ as the shearing progresses. Additionally, a substantial correlation is evident between the increase in permanent deviatoric strain and higher stress amplitudes.

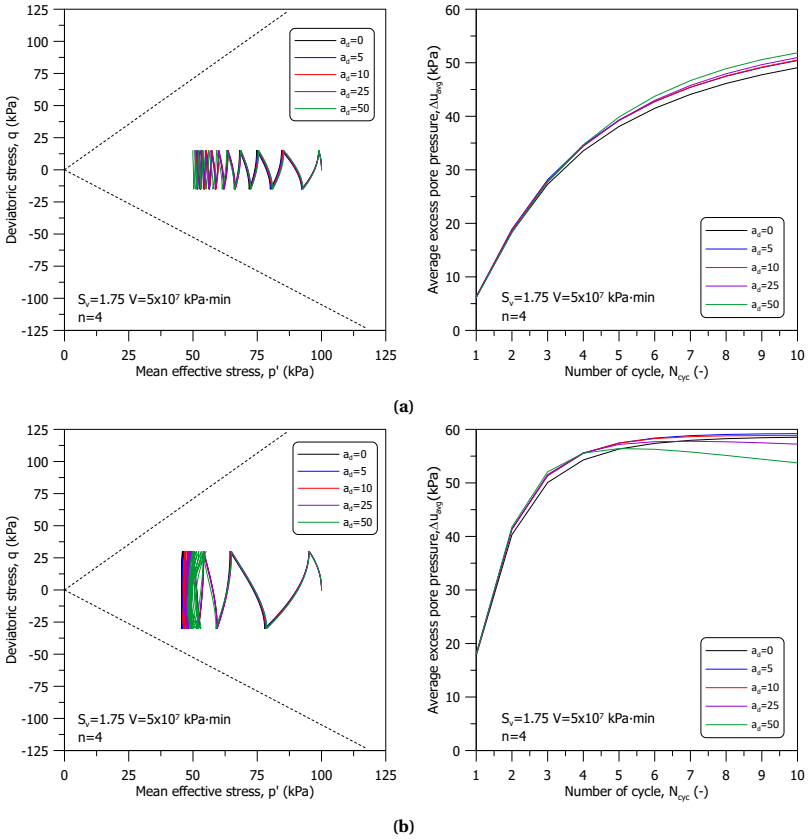

Figure C.57: Stress path and development of excess pore pressure of stress-controlled cyclic shearing stage for different a_d value : (a) $q_{\text{cyc}} = 0.15p'_i$ and (b) $q_{\text{cyc}} = 0.30p'_i$

C

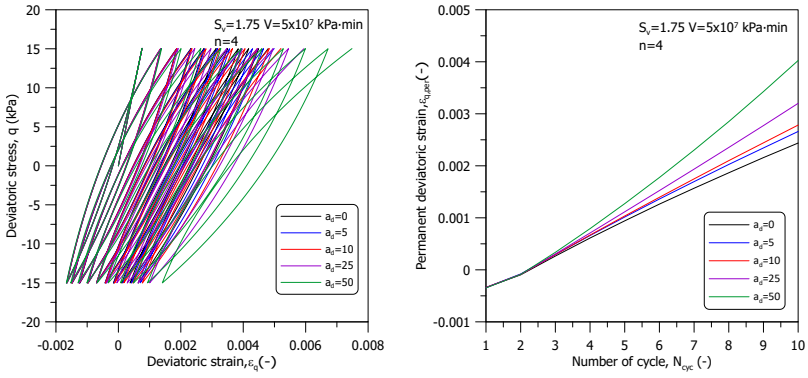

(a)

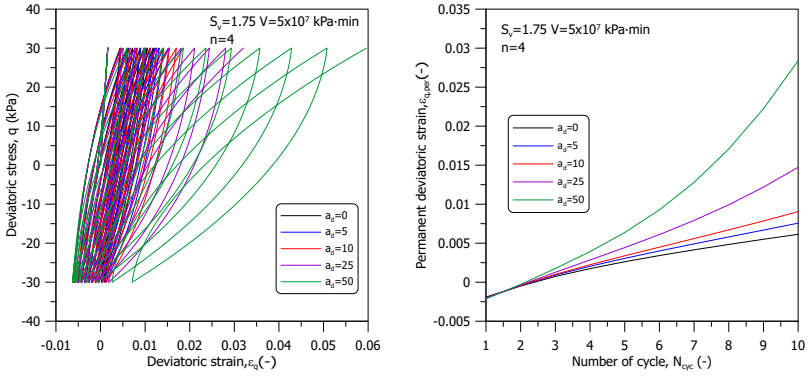

(b)

Figure C.58: Stress-strain curve and permanent deviatoric strain of stress-controlled cyclic shearing stage for different a_d value : (a) $q_{\text{cyc}} = 0.15p'_i$ and (b) $q_{\text{cyc}} = 0.30p'_i$

C.4.2. K_0 INITIAL STRESS STATE, $a_d > 0$

The impact of the positive damage parameter ($a_d > 0$) on cyclic response is also explored for initially K_0 consolidation stress state using strain-controlled cyclic shearing. The cyclic strain amplitude, ϵ_{cyc}, is set at 0.01. Model parameters that are not detailed in Chapter 4 can be found in Table C.4. The simulation process includes two stages: firstly, a K_0 consolidation stage, and secondly, a cyclic shearing stage. The consolidation stage spans 10,800 minutes.

Figure C.59 showcases the evolution of bounding surface size during both the K_0 consolidation and strain-controlled cyclic shearing stages. Similar to the simulation starting from the isotropic stress state, the increase in the a_d value leads to a faster increase in the bounding surface size.

Figure C.60 presents the stress path and average excess pore pressure during cyclic shearing. It is noted that for all a_d values, the simulations attain the same peak deviatoric stress in the first loading cycle. However, this peak deviatoric stress degrades more rapidly with increasing a_d values. In all simulations, the stress paths exhibit a consistent leftward movement during cyclic loading, suggesting contractive behaviour and the development of positive excess pore pressure. Furthermore, a reduction in excess pore pressure after the second loading cycle is also observed.

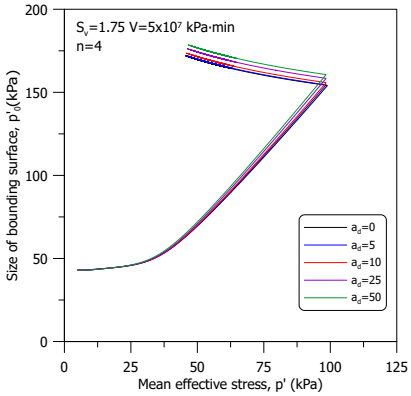

Figure C.59: Evolution of the size of bounding surface during consolidation and strain-controlled cyclic shearing stage for different a_d value

Figure C.61 presents the deviatoric stress-strain curve, along with the development of the secant shear modulus and damping ratio for a range of a_d values. In alignment with the simulation of initially isotropic consolidated, smaller a_d values are associated with a slower degradation of peak deviatoric stresses during cyclic shearing, a trend that is clearly evident in the deviatoric stress-strain evolution. When it comes to the secant shear modulus, lower a_d values lead to higher moduli and a more gradual reduction in modulus as the number of loading cycles increases. As for the damping ratio, it tends to decrease as a_d values increase, though the differences among various a_d values are relatively minor. Additionally, a decreasing trend in the variation of damping ratio with increasing loading cycles is observed for a_d values of 50.

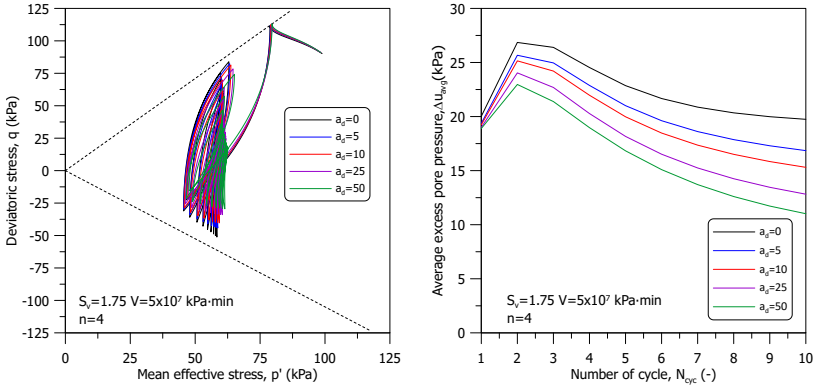

Figure C.60: Stress path and development of excess pore pressure of strain-controlled cyclic shearing stage for different a_d value

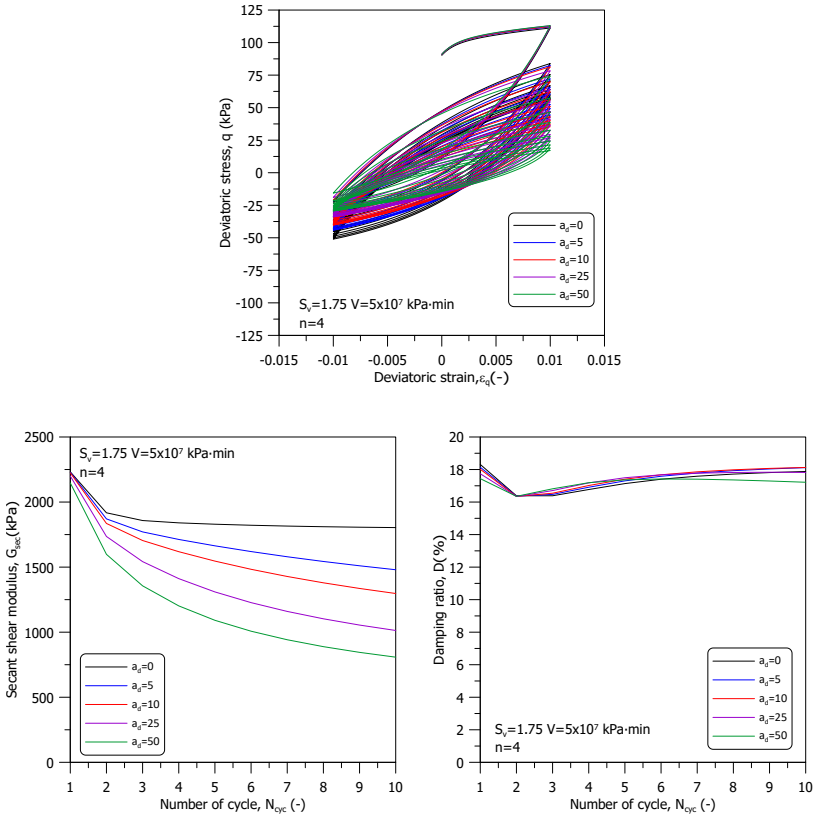

Figure C.61: Stress-strain curve, secant shear modulus, and damping ratio of strain-controlled cyclic shearing stage for different a_d value

To further investigate various aspects of the predicted cyclic response, a sensitivity analysis was also conducted using stress-controlled cyclic shearing. Two different cyclic stress amplitudes, q_{cyc} ($0.15p'_i$ and $0.30p'_i$, with $p'_i = 100$ kPa), were chosen to assess the impact of loading magnitude. Figure C.62 displays the evolution of the bounding surface size during both the consolidation and stress-controlled cyclic shearing stages. Same as the strain-controlled simulations, a higher a_d value results in a larger bounding surface size.

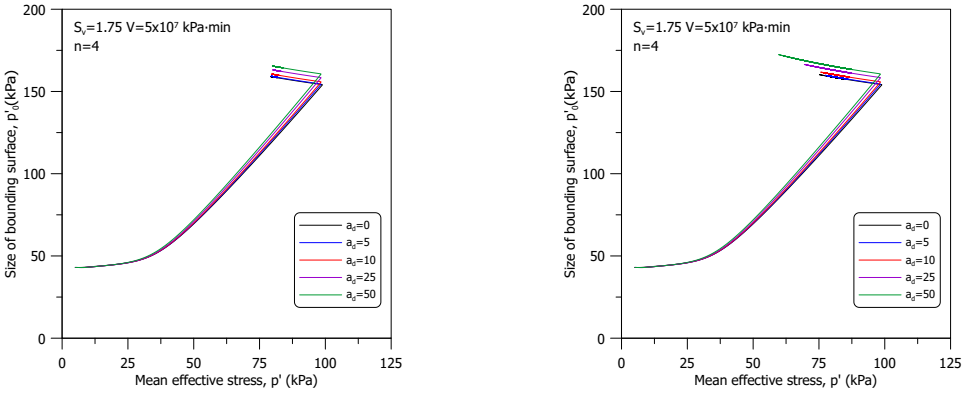

Figure C.62: Evolution of the size of bounding surface during consolidation and stress-controlled cyclic shearing stage for different a_d value : (a) $q_{\text{cyc}} = 0.15p'_i$ and (b) $q_{\text{cyc}} = 0.30p'_i$

Figure C.63 illustrates the stress path and average excess pore pressure during stress-controlled cyclic shearing. Consistently, for all a_d values, the stress paths exhibit a leftward movement during cyclic loading, indicative of contractive behaviour and the consequent development of positive excess pore pressure. The simulations reveal that higher cyclic stress amplitudes lead to slightly higher development of excess pore pressure. In simulations with a cyclic stress amplitude of $q_{\text{cyc}} = 0.30p'_i$ and a_d values less than 25, a distinct behaviour is observed where the stress paths stabilise, or 'freeze', upon reaching the critical stress state ratio. Correspondingly, the development of excess pore pressure in these cases reaches a plateau. However, in simulations with a_d values greater than 25, there is a noticeable increase in the slope of stress paths with each loading cycle, alongside an increasing trend in excess pore pressure. This contrasting behaviour is also attributed to the rapid reduction in plastic modulus during cyclic loading for higher damage parameters, leading to a faster change in the inclination of the bounding surface, as explained in the previous section.

Figure C.64 illustrates the accumulation of permanent deviatoric strain, denoted as $\varepsilon_{q,\text{per}}$, during cyclic shearing. While similar levels of $\varepsilon_{q,\text{per}}$ are observed in the initial cycle across all simulations, it is noted that higher a_d values lead to greater accumulations of $\varepsilon_{q,\text{per}}$ as the shearing continues. Compared to the results obtained under initially isotropic stress conditions, the accumulation of permanent deviatoric strain is significantly higher when the initial stress state is at K_0 condition. Furthermore, the permanent deviatoric strain increases with stress amplitude.

C

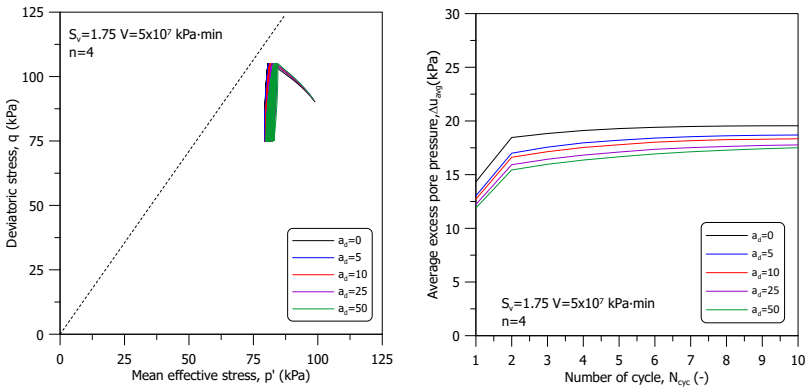

(a)

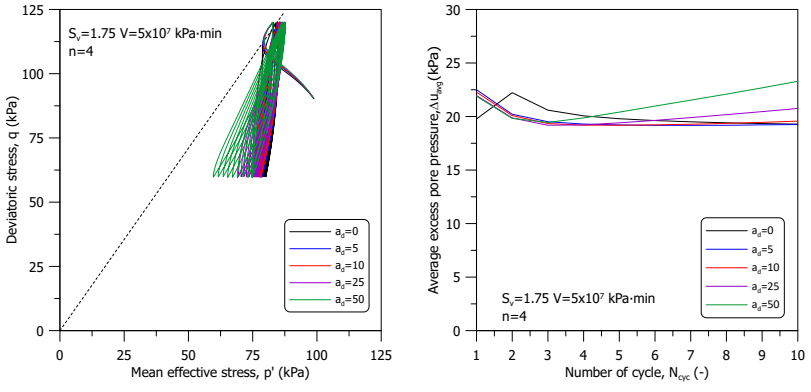

(b)

Figure C.63: Stress path and development of excess pore pressure of stress-controlled cyclic shearing stage for different a_d value : (a) $q_{\text{cyc}} = 0.15p'_i$ and (b) $q_{\text{cyc}} = 0.30p'_i$

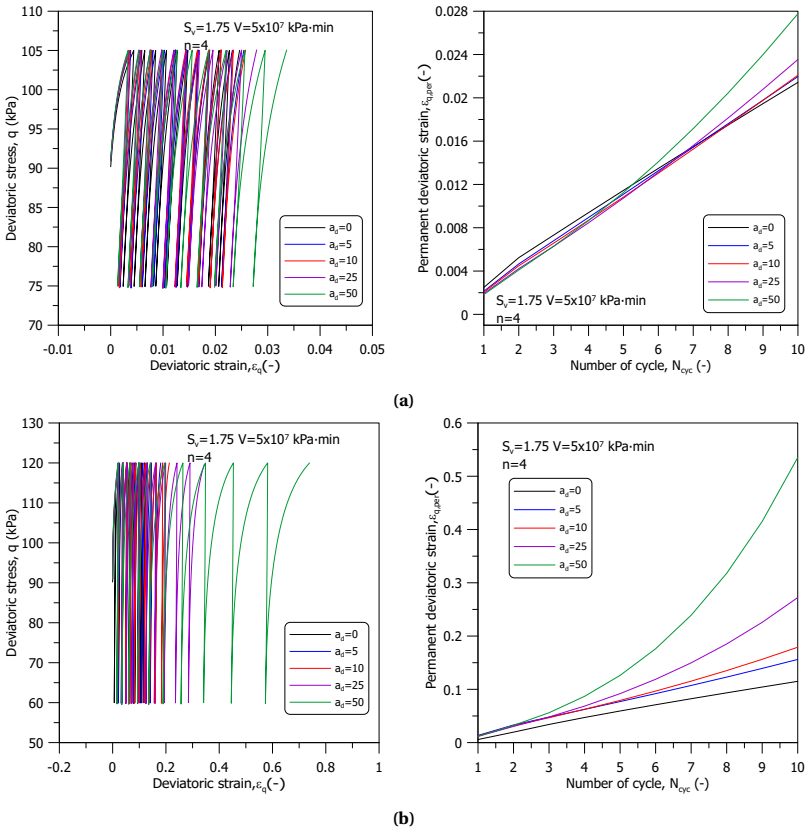

Figure C.64: Stress-strain curve and permanent deviatoric strain of stress-controlled cyclic shearing stage for different a_d value : (a) $q_{\text{cyc}} = 0.15p'_i$ and (b) $q_{\text{cyc}} = 0.30p'_i$

C.4.3. ISOTROPIC INITIAL STRESS STATE, $a_d < 0$

In the previous sections, the sensitivity analysis was conducted for the positive damage parameter ($a_d > 0$), the next section will be dedicated to the sensitivity analysis of the negative damage parameter a_d ($a_d < 0$), aiming to elucidate its influence within the proposed model framework. The impact of the negative damage parameter ($a_d < 0$) on cyclic response is initially explored using strain-controlled cyclic shearing, with the cyclic strain amplitude, ϵ_{cyc}, set at 0.01. For this sensitivity analysis, five a_d values are considered. Model parameters that are not detailed in Chapter 4 can be found in Table C.4. The simulation process includes two stages: firstly, a consolidation stage, and secondly, a cyclic shearing stage. The consolidation stage spans 10,800 minutes. Details regarding the cyclic loading frequency and waveform used in this analysis are provided in Chapter 4.

Figure C.65 showcases the evolution of bounding surface size during both the consolidation and strain-controlled cyclic shearing stages. With the decrease in the a_d value, which leads to a faster rise in the plastic modulus, there is a slower increase in the bounding surface size.

Figure C.66 presents the stress path and average excess pore pressure during cyclic shearing. It is noted that for all a_d values, the simulations attain the same peak deviatoric stress in the first loading cycle. In all simulations, the stress paths exhibit a consistent leftward movement during cyclic loading, suggesting contractive behaviour and the development of positive excess pore pressure. Furthermore, an increase in excess pore pressure with a higher a_d value is observed; this is attributed to the smaller bounding surface size at the end of the consolidation stage.

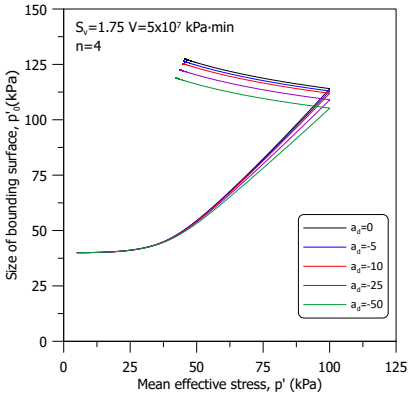

Figure C.65: Evolution of the size of bounding surface during consolidation and strain-controlled cyclic shearing stage for different a_d value

Figure C.67 presents the deviatoric stress-strain curve, along with the development of the secant shear modulus and damping ratio for a range of a_d values. In alignment with the stress path observations, when $a_d \geq -25$, smaller a_d values are associated with a faster rise of peak deviatoric stresses during cyclic shearing. When it comes to the secant shear modulus, except for $a_d = -50$, lower a_d values lead to higher moduli and a more gradual increase in modulus as the number of loading cycles increases. As for the

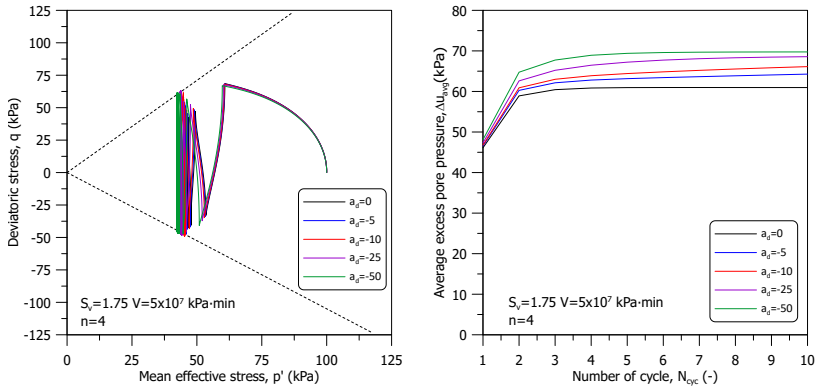

Figure C.66: Stress path and development of excess pore pressure of strain-controlled cyclic shearing stage for different a_d value

damping ratio, the differences for a_d values larger than -25 are relatively minor. Additionally, an increasing trend in the damping ratio with a rising number of loading cycles is noted for a_d values below -25. Also indicated in Appendix B, at an a_d value of -50, a rapid increase in plastic modulus occurs, leading to a viscoelastic response. This suggests that a reasonable range for the a_d value should be set above -50 to ensure a more accurate and realistic prediction of soil behaviour.

To further investigate various aspects of the predicted cyclic response, a sensitivity analysis was also conducted using stress-controlled cyclic shearing. Two different cyclic stress amplitudes, q_{cyc} ($0.15p'_i$ and $0.30p'_i$, with p'_i = 100 kPa), were chosen to assess the impact of loading magnitude. Figure C.68 displays the evolution of the bounding surface size during both the consolidation and stress-controlled cyclic shearing stages. Similar to the strain-controlled simulations, a lower a_d value results in a smaller bounding surface size.

Figure C.69 illustrates the stress path and average excess pore pressure during stress-controlled cyclic shearing. Consistently, for all a_d values, the stress paths exhibit a leftward movement during cyclic loading, indicative of contractive behaviour and the consequent development of positive excess pore pressure. Furthermore, the simulations reveal that higher cyclic stress amplitudes lead to greater development of excess pore pressure.

Figure C.70 depicts the accumulation of permanent deviatoric strain, represented as $\varepsilon_{q,\text{per}}$, during cyclic shearing. Despite similar levels of permanent deviatoric strain in the initial cycle across all simulations, lower a_d values are observed to result in smaller accumulations of $\varepsilon_{q,\text{per}}$ as the shearing progresses. Additionally, a substantial correlation is evident between the increase in permanent deviatoric strain and higher stress amplitudes.

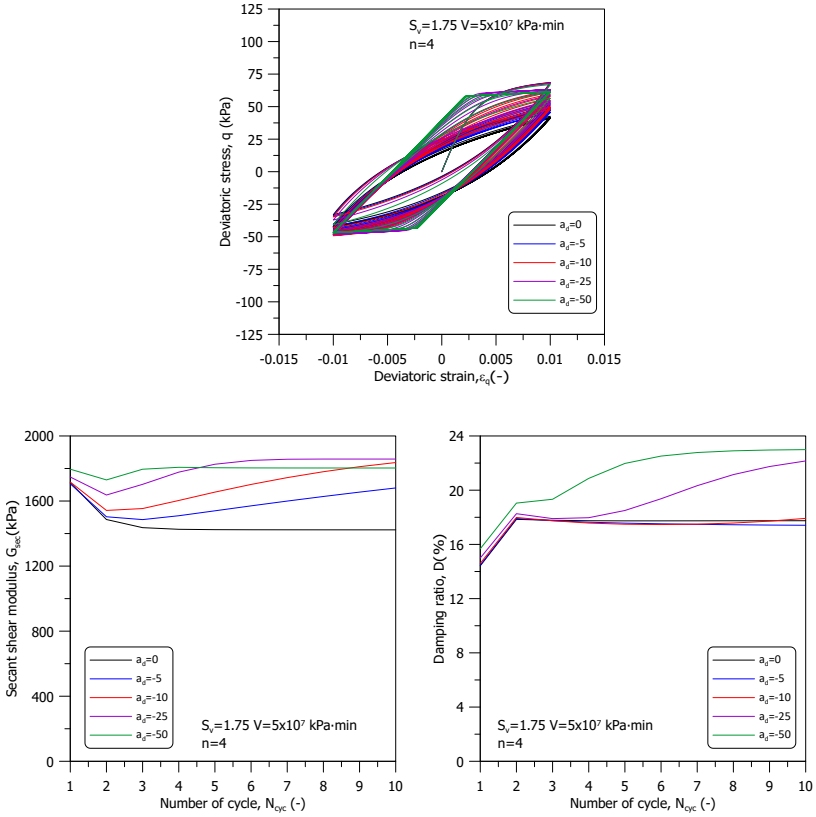

Figure C.67: Stress-strain curve, secant shear modulus, and damping ratio of strain-controlled cyclic shearing stage for different a_d value

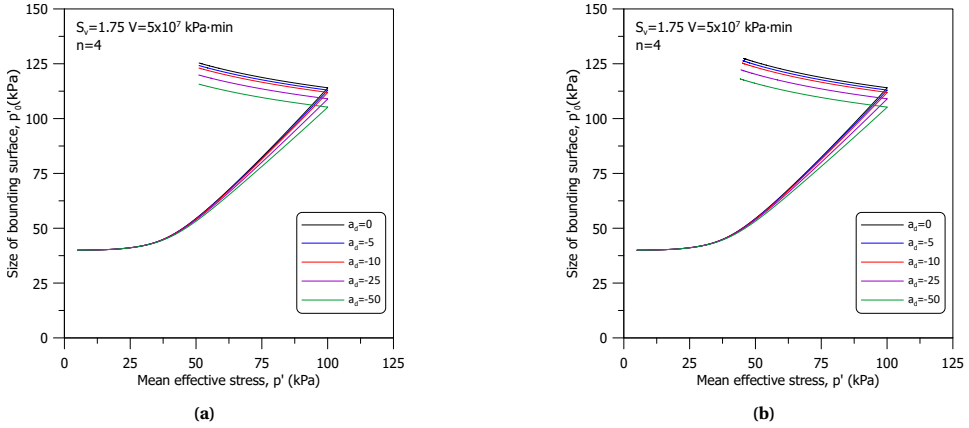

Figure C.68: Evolution of the size of bounding surface during consolidation and stress-controlled cyclic shearing stage for different a_d value : (a) $q_{\text{cyc}} = 0.15p'_i$ and (b) $q_{\text{cyc}} = 0.30p'_i$

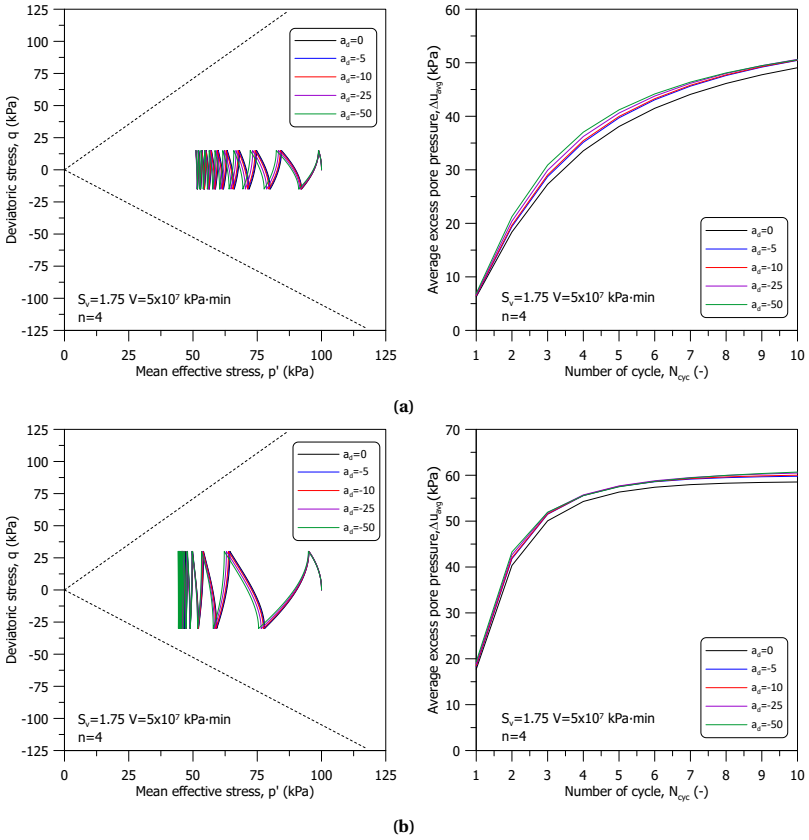

Figure C.69: Stress path and development of excess pore pressure of stress-controlled cyclic shearing stage for different a_d value : (a) $q_{\text{cyc}} = 0.15p'_i$ and (b) $q_{\text{cyc}} = 0.30p'_i$

C

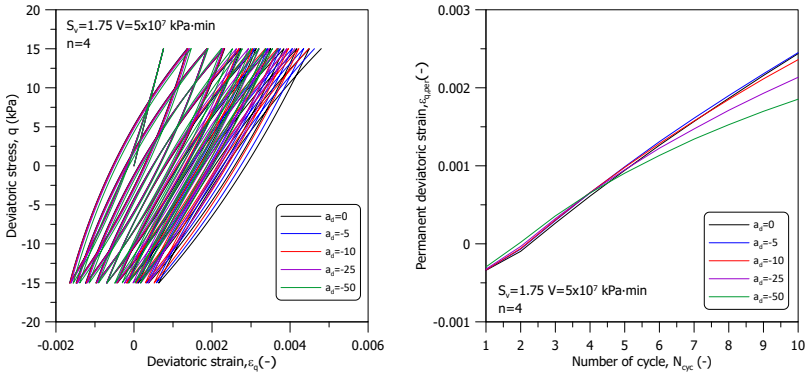

(a)

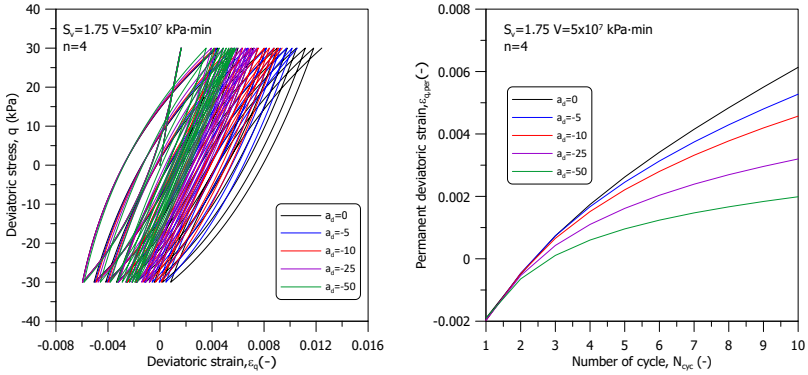

(b)

Figure C.70: Stress-strain curve and permanent deviatoric strain of stress-controlled cyclic shearing stage for different a_d value : (a) $q_{\text{cyc}} = 0.15p'_i$ and (b) $q_{\text{cyc}} = 0.30p'_i$

C.4.4. K_0 INITIAL STRESS STATE, $a_d < 0$

The impact of the negative damage parameter ($a_d < 0$) on cyclic response is also explored for initially K_0 consolidation stress state using strain-controlled cyclic shearing. The cyclic strain amplitude, ϵ_{cyc}, is set at 0.01. Model parameters that are not detailed in Chapter 4 can be found in Table C.4. The simulation process includes two stages: firstly, a K_0 consolidation stage, and secondly, a cyclic shearing stage. The consolidation stage spans 10,800 minutes.

Figure C.71 showcases the evolution of bounding surface size during both the K_0 consolidation and strain-controlled cyclic shearing stages. Similar to the simulation starting from the isotropic stress state, the reduction in the a_d value leads to a slower increase in the bounding surface size.

Figure C.72 presents the stress path and average excess pore pressure during cyclic shearing. It is noted that for all a_d values, the simulations attain the same peak deviatoric stress in the first loading cycle. However, this peak deviatoric stress rises more rapidly with reducing a_d values. In all simulations, the stress paths exhibit a consistent leftward movement during cyclic loading, suggesting contractive behaviour and the development of positive excess pore pressure. Furthermore, a reduction in excess pore pressure after the second loading cycle is also observed.

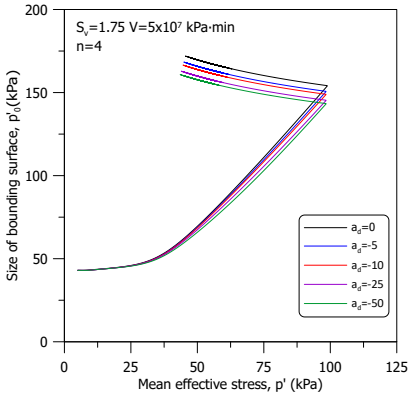

Figure C.71: Evolution of the size of bounding surface during consolidation and strain-controlled cyclic shearing stage for different a_d value

Figure C.73 presents the deviatoric stress-strain curve, along with the development of the secant shear modulus and damping ratio for a range of a_d values. In alignment with the simulation of initially isotropic consolidated, smaller a_d values are associated with a more rapid increase in modulus as the number of loading cycles increases. As for the damping ratio, it tends to decrease as a_d values increase when a_d is higher than -10, though the differences among various a_d values are relatively minor. Additionally, an increasing trend in the variation of damping ratio with increasing loading cycles is observed for a_d values of -25 and -50.

To further investigate various aspects of the predicted cyclic response, a sensitivity analysis was also conducted using stress-controlled cyclic shearing. Two different cyclic stress amplitudes, q_{cyc} ($0.15p'_i$ and $0.30p'_i$, with p'_i = 100 kPa), were chosen to assess the

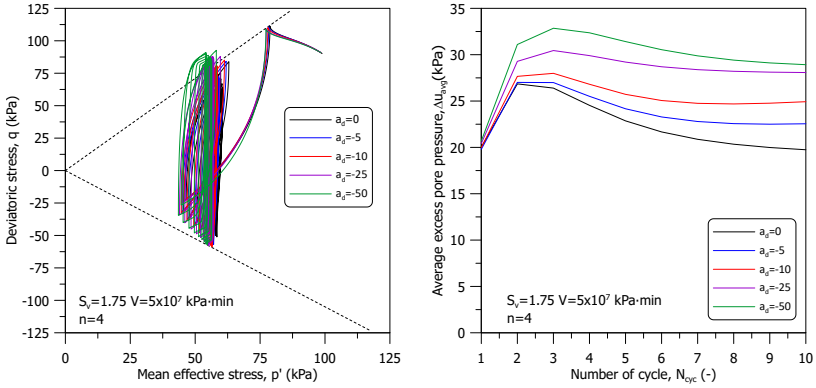

Figure C.72: Stress path and development of excess pore pressure of strain-controlled cyclic shearing stage for different a_d value

impact of loading magnitude. Figure C.74 displays the evolution of the bounding surface size during both the consolidation and stress-controlled cyclic shearing stages. Same as the strain-controlled simulations, a higher a_d value results in a larger bounding surface size.

Figure C.75 illustrates the stress path and average excess pore pressure during stress-controlled cyclic shearing. Consistently, for all a_d values, the stress paths exhibit a leftward movement during cyclic loading, indicative of contractive behaviour and the consequent development of positive excess pore pressure. There is a direct correlation between lower a_d values and increased excess pore pressure development. Furthermore, the simulations reveal that higher cyclic stress amplitudes lead to slightly higher development of excess pore pressure.

Figure C.76 illustrates the accumulation of permanent deviatoric strain, denoted as $\varepsilon_{q,\text{per}}$, during cyclic shearing. While similar levels of $\varepsilon_{q,\text{per}}$ are observed in the initial cycle across all simulations, it is noted that higher a_d values lead to greater accumulations of $\varepsilon_{q,\text{per}}$ as the shearing continues. Compared to the results obtained under initially isotropic stress conditions, the accumulation of permanent deviatoric strain is significantly higher when the initial stress state is at K_0 condition. Furthermore, there is a marked correlation between the increase in permanent deviatoric strain and higher stress amplitudes.

In summary, the impact of the parameter a_d under the elastoplastic-viscoplastic bounding surface framework is similar to the one under the elastoplastic bounding surface framework, as discussed and summarised in detail in Appendix B.

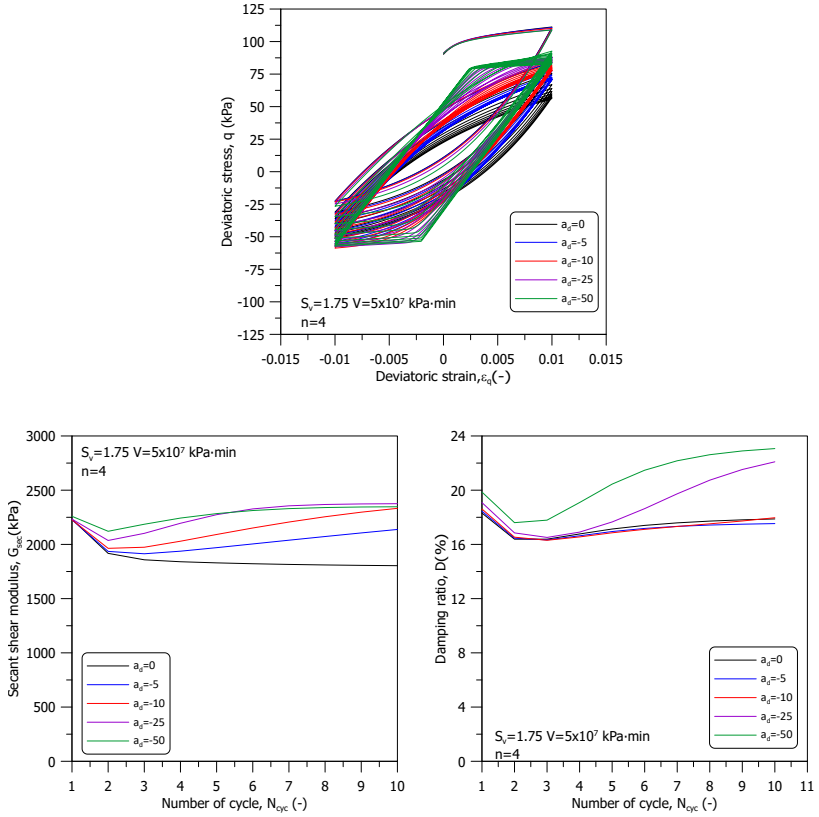

Figure C.73: Stress-strain curve, secant shear modulus, and damping ratio of strain-controlled cyclic shearing stage for different a_d value

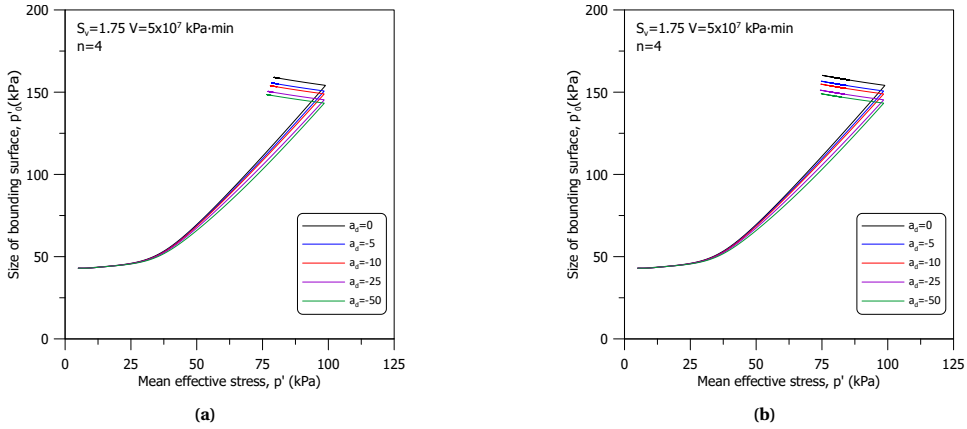

Figure C.74: Evolution of the size of bounding surface during consolidation and stress-controlled cyclic shearing stage for different a_d value : (a) $q_{\text{cyc}} = 0.15p'_i$ and (b) $q_{\text{cyc}} = 0.30p'_i$

C

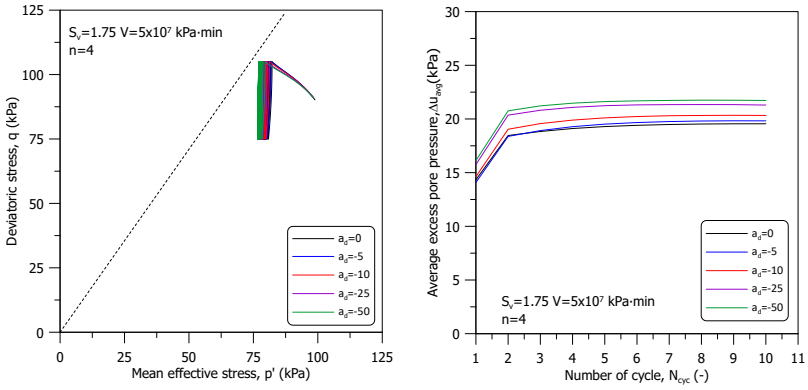

(a)

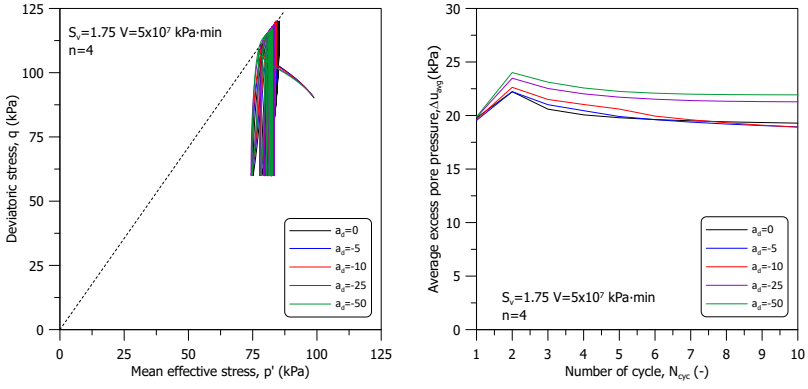

(b)

Figure C.75: Stress path and development of excess pore pressure of stress-controlled cyclic shearing stage for different a_d value : (a) $q_{\text{cyc}} = 0.15p'_i$ and (b) $q_{\text{cyc}} = 0.30p'_i$

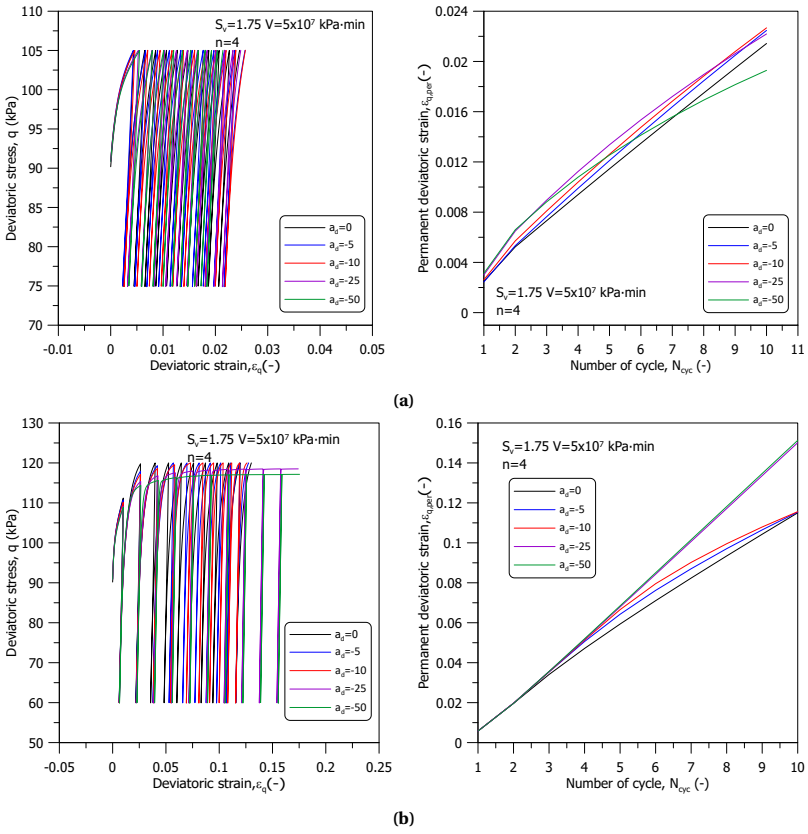

Figure C.76: Stress-strain curve and permanent deviatoric strain of stress-controlled cyclic shearing stage for different a_d value : (a) $q_{\text{cyc}} = 0.15p'_i$ and (b) $q_{\text{cyc}} = 0.30p'_i$

C.5. INFLUENCE OF PARAMETERS w ON THE CYCLIC RESPONSE

C.5.1. ISOTROPIC INITIAL STRESS STATE

In the subsequent section, a thorough sensitivity analysis of the hybrid flow rule parameter w is conducted. The upcoming analysis aims to investigate the influence of the hybrid flow rule parameter within the context of the viscoplastic bounding surface framework. This analysis is crucial to understanding the parameter's role in the model's predictive capability, particularly in representing complex soil behaviours under different loading conditions.

The impact of hybrid flow rule parameter w on cyclic response is explored using strain-controlled cyclic shearing, with the cyclic strain amplitude, ε_{cyc}, set at 0.01. For this sensitivity analysis, seven w values are considered. Model parameters that are not detailed in Chapter 4 can be found in Table C.5. The simulation process includes two stages: firstly, a consolidation stage, and secondly, a cyclic shearing stage. The consolidation stage spans 10,800 minutes.

Table C.5: Model parameters adopted in sensitivity analysis

s_v	V	n	a_d
1.75	5×10^7 kPa·min	4	0

Figure C.77 illustrates the evolution of bounding surface size during both the consolidation and strain-controlled cyclic shearing stages. The results indicate that the value of w does not affect the bounding surface size during the consolidation stage. However, during cyclic loading, an increase in the w value leads to an enlargement of the bounding surface.

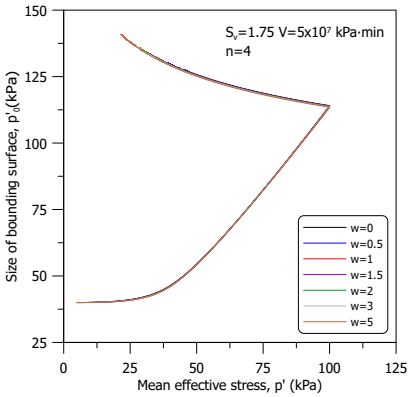

Figure C.77: Evolution of the size of bounding surface during consolidation and strain-controlled cyclic shearing stage for different w value

Figure C.78 depicts the stress path and average excess pore pressure observed during cyclic shearing. Notably, across all w values, the simulations consistently achieve similar peak deviatoric stress levels during cyclic loading. In each simulation, the stress paths consistently move leftward during cyclic loading, indicating contractive behaviour and

the consequent development of positive excess pore pressure. Furthermore, an increase in the w value leads to a more pronounced leftward shift of the stress path, signifying greater excess pore pressure development under cyclic loading. As expected, the simulation with a w value of zero shows stabilisation in both the stress path and pore pressure development.

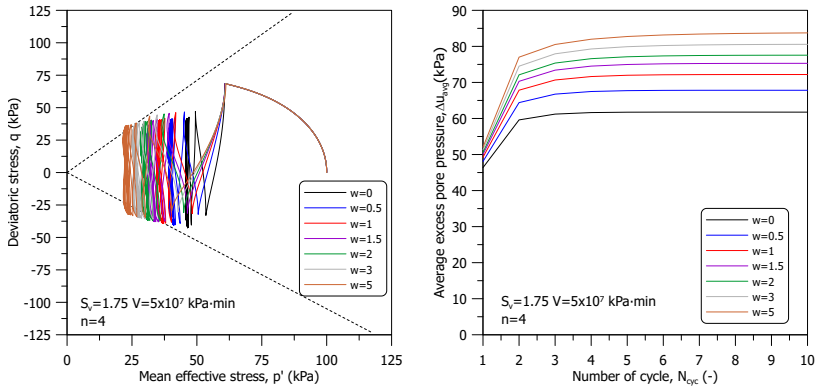

Figure C.78: Stress path and development of excess pore pressure of strain-controlled cyclic shearing stage for different w value

Figure C.79 illustrates the deviatoric stress-strain curve, along with the development of the secant shear modulus and damping ratio for a range of w values. More pronounced than in the stress path observations, a trend of reduction in peak deviatoric stress after the first loading cycle as the w value increases. In terms of the secant shear modulus, lower w values result in higher moduli and a lesser reduction in modulus with an increasing number of loading cycles. Regarding the damping ratio, it tends to decrease as w values increase, and the differences among various w values are more noticeable compared to other model parameters previously investigated. Additionally, for w values other than zero, there is a discernible decreasing trend in the variation of the damping ratio with increasing loading cycles.

The sensitivity analysis was extended to include stress-controlled cyclic shearing, utilising two distinct cyclic stress amplitudes, q_{cyc} ($0.15p'_i$ and $0.30p'_i$, with $p'_i = 100$ kPa), to determine the impact of loading magnitude. Figure C.80 illustrates the evolution of bounding surface size during both the consolidation and stress-controlled cyclic shearing stages. Echoing the strain-controlled simulation results, the value of w does not influence the bounding surface size during the consolidation stage. However, during cyclic loading, an increase in w leads to an enlargement of the bounding surface.

Figure C.81 illustrates the stress path and average excess pore pressure during stress-controlled cyclic shearing. Consistently, for all w values, the stress paths exhibit a leftward movement during cyclic loading, indicative of contractive behaviour and the consequent development of positive excess pore pressure. Notably, there is a direct correlation between higher w values and increased excess pore pressure development. Furthermore, the simulations reveal that higher cyclic stress amplitudes lead to greater development of excess pore pressure.

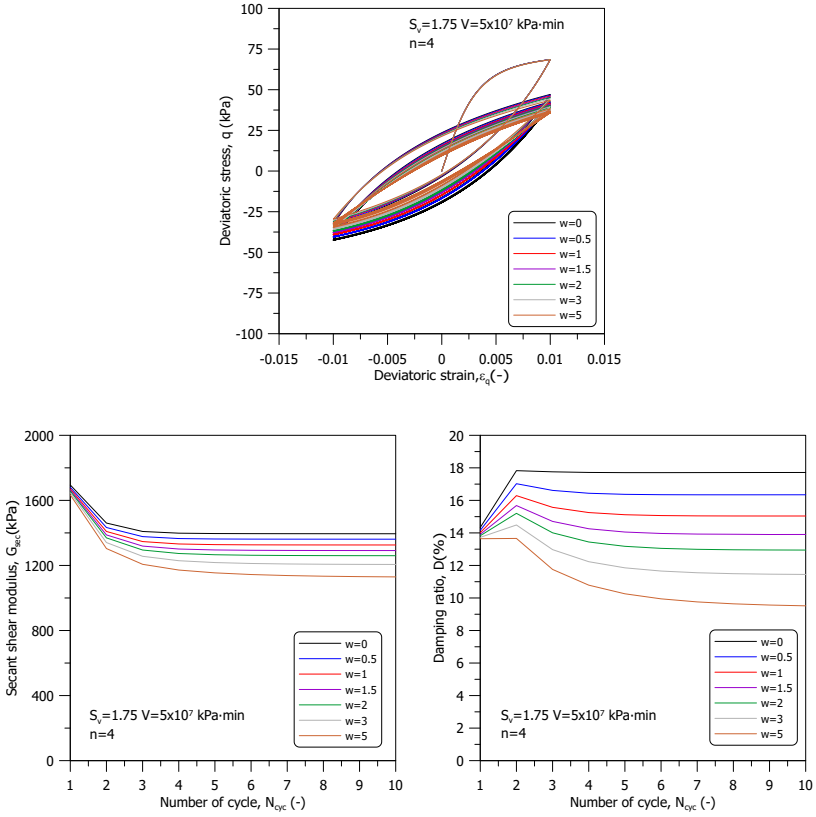

Figure C.79: Stress-strain curve, secant shear modulus, and damping ratio of strain-controlled cyclic shearing stage for different w value

Figure C.82 demonstrates the accumulation of permanent deviatoric strain, represented as $\varepsilon_{q,\text{per}}$, during cyclic shearing. In simulations with a cyclic stress amplitude of $q_{\text{cyc}} = 0.15p'_i$, higher w values lead to greater accumulations of $\varepsilon_{q,\text{per}}$ up to the 9^{th} loading cycle. Conversely, for $q_{\text{cyc}} = 0.30p'_i$, all w values result in similar accumulations of $\varepsilon_{q,\text{per}}$ up to the 3^{rd} loading cycle. Intriguingly, for w values above 2, $\varepsilon_{q,\text{per}}$ begins to decrease after the 3^{rd} loading cycle, while it continues to increase for w values below 2. This pattern is attributed to the variation in the deviatoric plastic strain increment, as explained in Appendix B. When w equals zero, the deviatoric plastic strain increment reaches its maximum as the image stress reaches and stabilises at the critical state stress ratio. However, with the adoption of the hybrid flow rule, the image stress can evolve towards the dry side of the critical state, leading to a reduction in the deviatoric plastic strain increment.

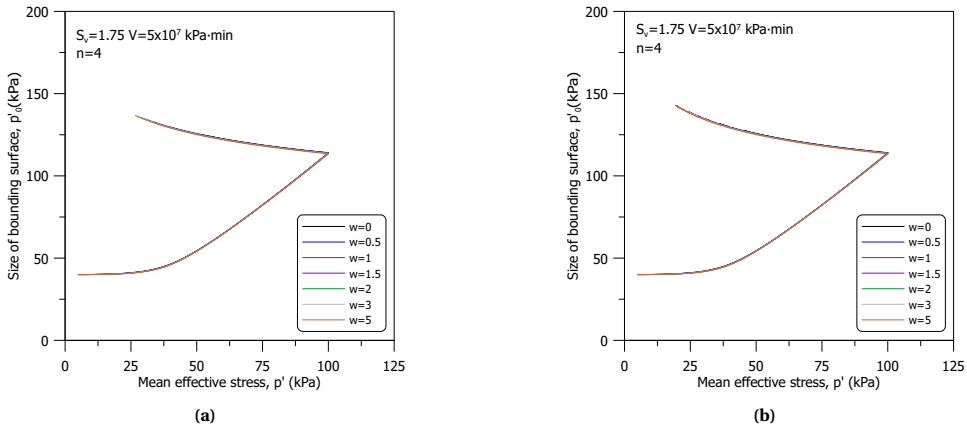

Figure C.80: Evolution of the size of bounding surface during consolidation and stress-controlled cyclic shearing stage for different w value : (a) $q_{\text{cyc}} = 0.15p'_i$ and (b) $q_{\text{cyc}} = 0.30p'_i$

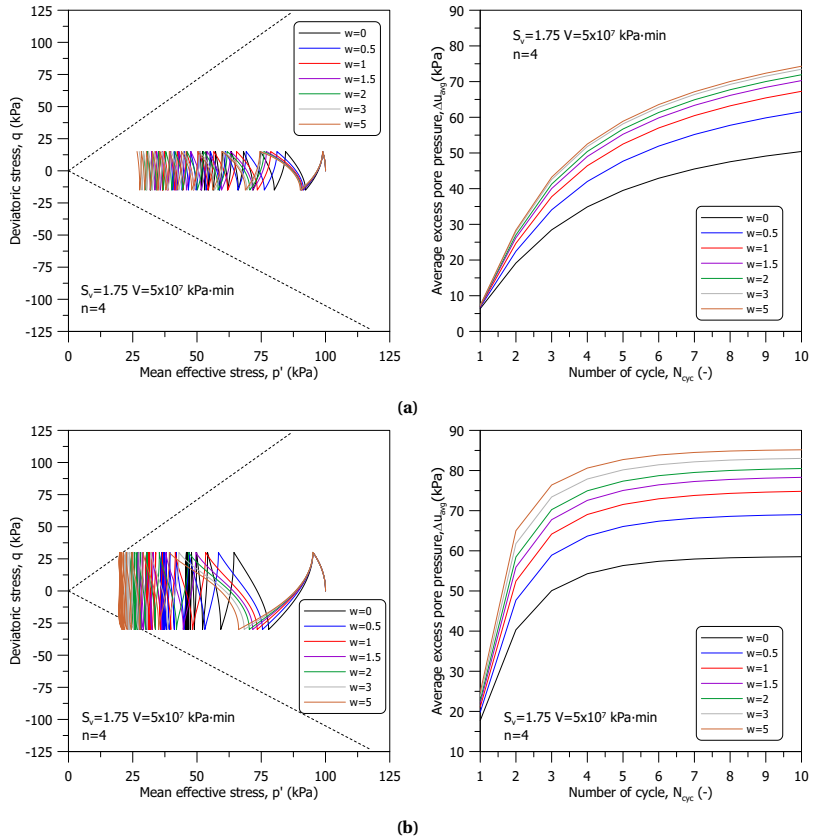

Figure C.81: Stress path and development of excess pore pressure of stress-controlled cyclic shearing stage for different w value : (a) $q_{\text{cyc}} = 0.15p'_i$ and (b) $q_{\text{cyc}} = 0.30p'_i$

C

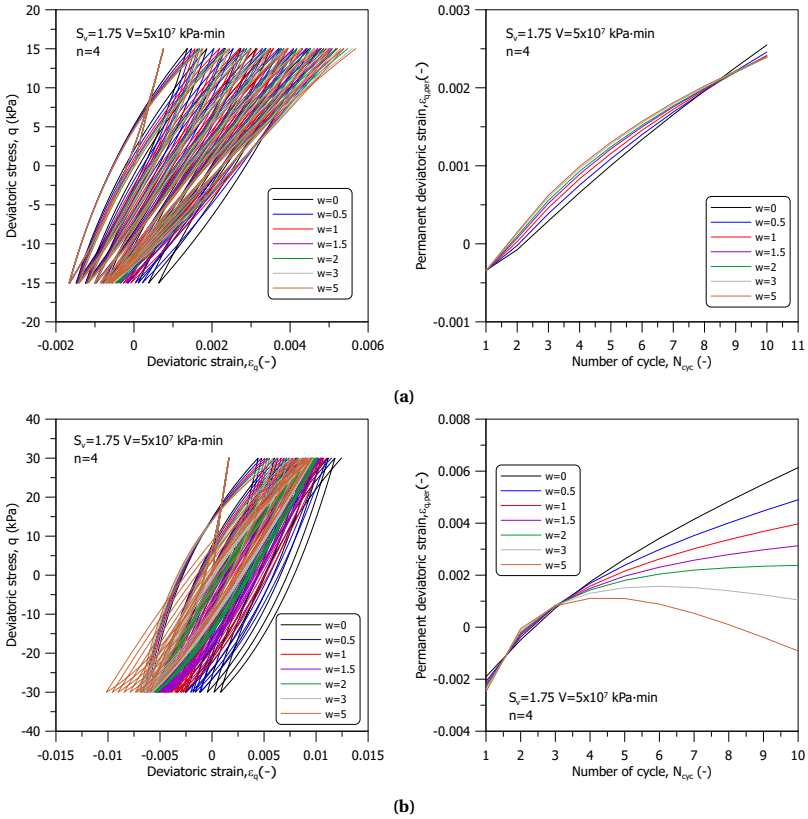

Figure C.82: Stress-strain curve and permanent deviatoric strain of stress-controlled cyclic shearing stage for different w value : (a) $q_{\text{cyc}} = 0.15p'_i$ and (b) $q_{\text{cyc}} = 0.30p'_i$

C.5.2. K_0 INITIAL STRESS STATE

The impact of hybrid flow rule parameter w on initially K_0 consolidated cyclic response is explored using strain-controlled cyclic shearing, with the cyclic strain amplitude, ε_{cyc}, set at 0.01. For this sensitivity analysis, seven w values are considered. Model parameters that are not detailed in Chapter 4 can be found in Table C.5. The simulation process includes two stages: firstly, a consolidation stage, and secondly, a cyclic shearing stage. The K_0 consolidation stage spans 10,800 minutes.

Figure C.83 illustrates the evolution of bounding surface size during both the K_0 consolidation and strain-controlled cyclic shearing stages. The results indicate that the value of w slightly affects the bounding surface size during the K_0 consolidation stage. However, during cyclic loading, an increase in the w value leads to an enlargement of the bounding surface.

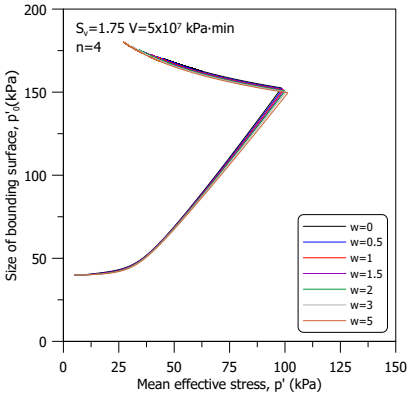

Figure C.83: Evolution of the size of bounding surface during consolidation and strain-controlled cyclic shearing stage for different w value

Figure C.84 depicts the stress path and average excess pore pressure observed during cyclic shearing. Notably, the influence of parameter w on peak deviatoric stress levels during cyclic loading is not obvious. In each simulation, the stress paths consistently move leftward during cyclic loading, indicating contractive behaviour and the consequent development of positive excess pore pressure. Furthermore, an increase in the w value leads to a more pronounced leftward shift of the stress path, signifying greater excess pore pressure development under cyclic loading.

Figure C.85 illustrates the deviatoric stress-strain curve, along with the development of the secant shear modulus and damping ratio for a range of w values. More pronounced than in the stress path observations, a trend of reduction in peak deviatoric stress after the first loading cycle as the w value increases. In terms of the secant shear modulus, lower w values result in higher moduli and a lesser reduction in modulus with an increasing number of loading cycles. Regarding the damping ratio, it tends to decrease as w values increase. Additionally, for w values larger than three, there is a decreasing trend in the variation of the damping ratio with increasing loading cycles.

The sensitivity analysis was extended to include stress-controlled cyclic shearing, utilising two distinct cyclic stress amplitudes, q_{cyc} ($0.15p'_i$ and $0.30p'_i$, with p'_i = 100

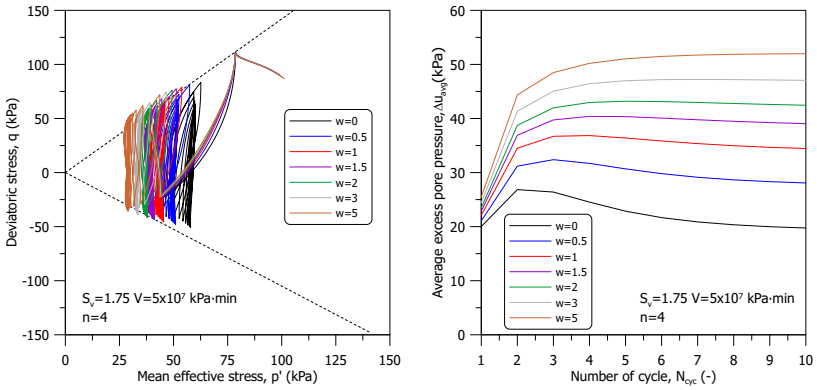

Figure C.84: Stress path and development of excess pore pressure of strain-controlled cyclic shearing stage for different w value

kPa), to determine the impact of loading magnitude. Figure C.86 illustrates the evolution of bounding surface size during both the consolidation and stress-controlled cyclic shearing stages. Similar to the strain-controlled simulation results, the value of w only has a minor impact on the bounding surface size during the consolidation stage. However, during cyclic loading, an increase in w leads to an enlargement of the bounding surface.

Figure C.87 illustrates the stress path and average excess pore pressure during stress-controlled cyclic shearing. Consistently, for all w values, the stress paths exhibit a leftward movement during cyclic loading, indicative of contractive behaviour and the consequent development of positive excess pore pressure. Notably, there is a direct correlation between higher w values and increased excess pore pressure development.

Figure C.88 demonstrates the accumulation of permanent deviatoric strain, represented as $\varepsilon_{q,\mathrm{per}}$, during cyclic shearing. In all simulations, higher w values and stress amplitude lead to greater accumulations of $\varepsilon_{q,\mathrm{per}}$.

In general, the influence of the hybrid flow rule parameter w under the elastoplastic-viscoplastic bounding surface framework is similar to the one under the elastoplastic bounding surface framework, as discussed and summarised in detail in Appendix B.

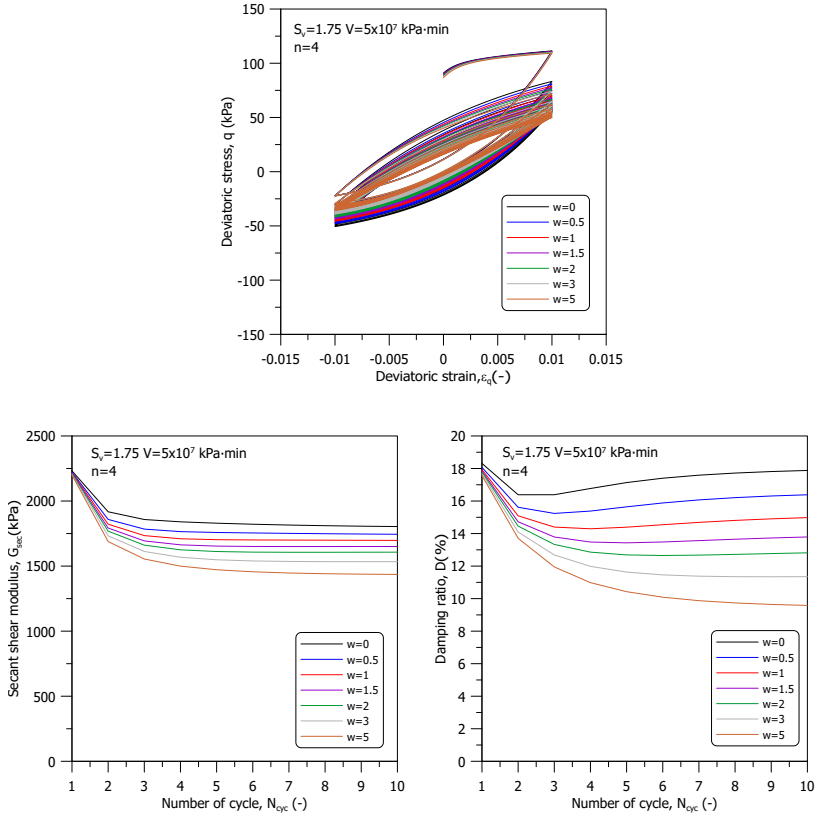

Figure C.85: Stress-strain curve, secant shear modulus, and damping ratio of strain-controlled cyclic shearing stage for different w value

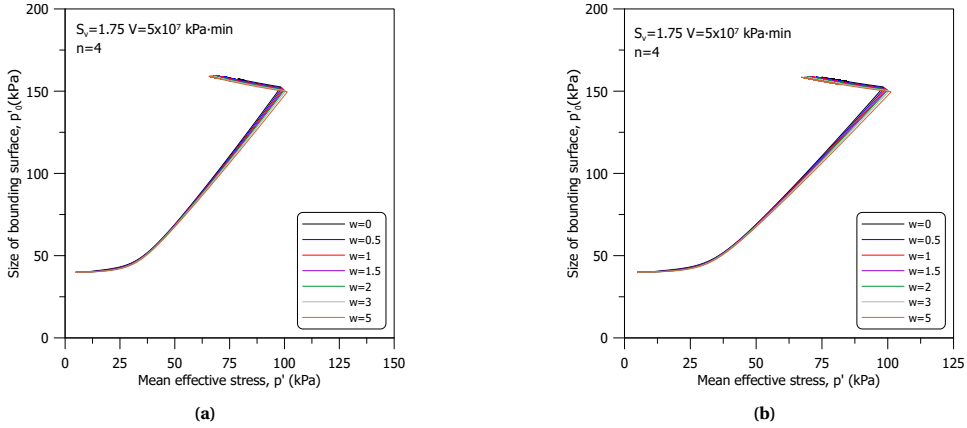

Figure C.86: Evolution of the size of bounding surface during consolidation and stress-controlled cyclic shearing stage for different w value : (a) $q_{\text{cyc}} = 0.15p'_i$ and (b) $q_{\text{cyc}} = 0.30p'_i$

C

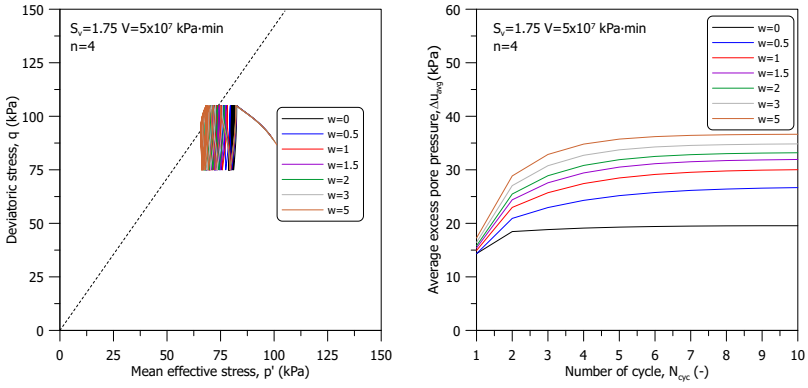

(a)

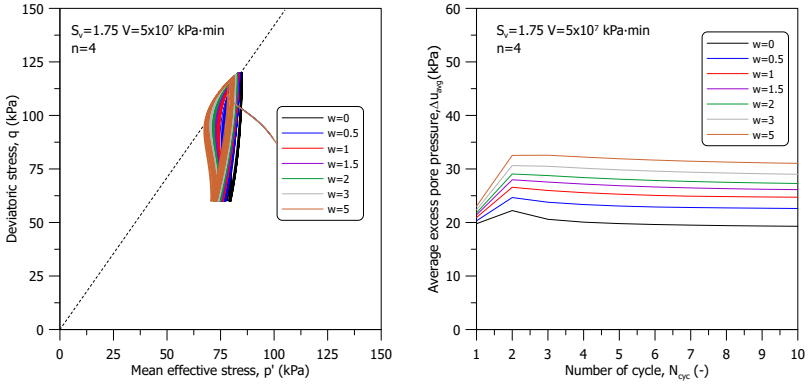

(b)

Figure C.87: Stress path and development of excess pore pressure of stress-controlled cyclic shearing stage for different w value : (a) $q_{\text{cyc}} = 0.15p'_i$ and (b) $q_{\text{cyc}} = 0.30p'_i$

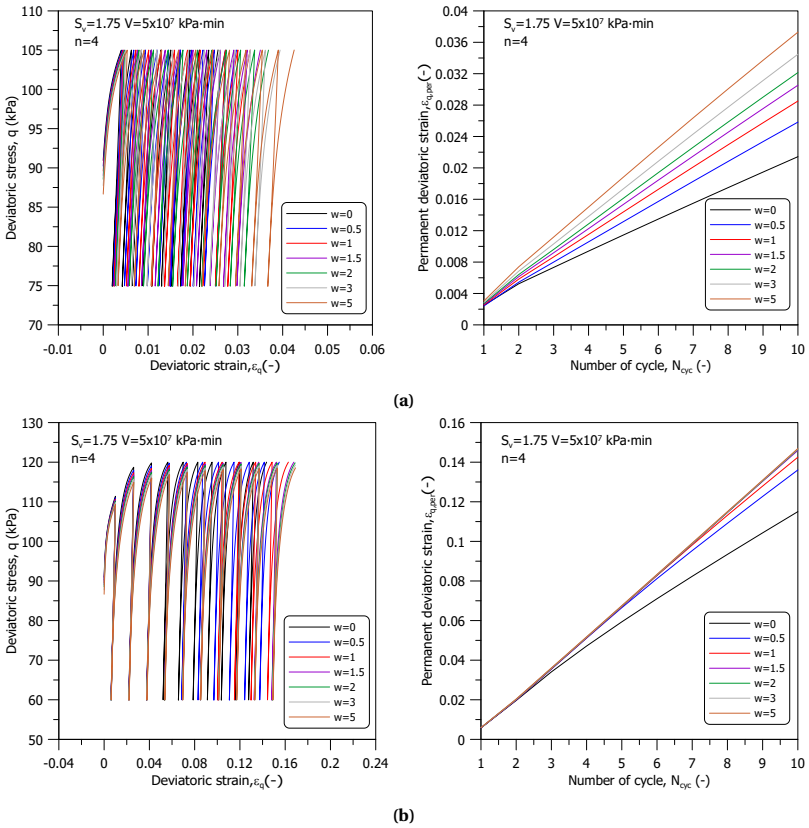

Figure C.88: Stress-strain curve and permanent deviatoric strain of stress-controlled cyclic shearing stage for different w value : (a) $q_{\text{cyc}} = 0.15p'_i$ and (b) $q_{\text{cyc}} = 0.30p'_i$

ACKNOWLEDGEMENTS

I would like to express my heartfelt gratitude to my supervisor, Prof. Cristina Jommi, for her unwavering support and guidance throughout my PhD. From her, I learned that a competent researcher in geotechnical engineering must not only focus on the scientific aspects but also consider the practical applications of their work.

I am also deeply grateful to my co-supervisor, Dr. Wout Broere, for his valuable insights and assistance in the development of new apparatus and sensors, as well as his help with the Dutch translations.

This research was financially supported by the Dutch Research Council (NWO) under the project 'SOFTTOP: Investigating Heterogeneous Soft Top Soils for Wave Propagation, Cyclic Degradation, and Liquefaction Potential', project number DEEP.NL.2018.006.

Special thanks go to Ing. Wim Verwaal and Ing. Kees van Beek for their invaluable assistance during the conceptualisation, design, and manufacturing phases of the new apparatus and sensors. I would also like to thank Ing. Michiel Slob, Jen van den Berg, Cristina Cavero Panez, and Marc Friebel for their help with the experimental work.

I am grateful to all my friends, colleagues, and staff members who have supported me throughout my PhD journey. In particular, I would like to thank Hilmi (for exploring Dutch life together during the early stages of the PhD), Inge (for the delicious homemade apple pie), Kostantinos (for sharing complaints), and Man (for the beers from various European cities).

To Stefano and Jinju: "선배는 길을 밝히는 등불이다." It has been an absolute pleasure having you both not only as friends but also as mentors in research and in life. My PhD journey would have been far more challenging without your companionship. During the COVID lockdowns, your presence was vital for our mental well-being. I am deeply grateful for all the time we have shared together. As the saying goes, "Chi trova un amico trova un tesoro" — finding a true friend is like discovering a treasure.

Luis: "La amistad es un contrato por el cual nos obligamos a hacer pequeños favores a los demás para que los demás nos los hagan grandes." This Spanish quote perfectly captures the beginning of our friendship. As experimentalists are becoming a minority in soil mechanics, it has been incredibly fortunate to have someone with whom I could share both small favours in the lab — lifting a triaxial cell or troubleshooting leaks — and meaningful discussions about science and life. Thank you for everything, Lucho!

To my family in Taiwan: Thank you for your constant support and encouragement throughout this PhD journey. 感謝家人們對我一路以來的支持和鼓勵！

To Makuro and Tea: Thank you for always lifting my spirits with your happy faces and enthusiastic welcomes, giving me the energy to tackle challenges during my PhD.

Finally, to Susu: "Shall we try living abroad?" — that was a question we asked ourselves during our trip to Melbourne in 2016. When I was working as a geotechnical engineer, I told you, "I want to learn new things and apply them to improve geotechnical engineering practices in Taiwan." You simply replied, "Why not do a PhD?" And now, here we are. This journey would have been impossible without your steadfast support and companionship. There are no words or sentences that can fully express my gratitude to you.

CURRICULUM VITÆ

Ching-Yu CHAO

29-01-1990	Born in Kaohsiung, Taiwan.

EDUCATION

2008–2013	Bachelor Degree in Civil Engineering National Cheng Kung University
2013–2015	Master Degree in Civil Engineering National Cheng Kung University
2019–2023	PhD candidate Delft University of Technology
Since 2023	Postdoctoral researcher Delft University of Technology

WORK EXPERIENCE

2016–2019	Geotechnical Engineer CECI Engineering Consultants, Taipei, Taiwan

AWARDS

2015	Honorary Membership of The Phi Tau Phi Scholastic Honour Society
2014	Scholarship of Civil Engineering Department, National Cheng Kung University
2012	Outstanding Student Award, National Cheng Kung University

LIST OF PUBLICATIONS

INTERNATIONAL REFEREED JOURNALS

5. **Chao, C.**, Muraro, S. and Jommi, C., *A new experimental data set supporting constitutive models for soft organic clays.*, International Journal for Numerical and Analytical Methods in Geomechanics, (under review).

4. **Chao, C.**, Parra-Gómez, L., Muraro, S., Broere, W. and Jommi, C., *A novel fibre-optic pore pressure sensor for soil element testing.*, Géotechnique Letters, (under review).

3. **Chao, C.**, Broere, W. and Jommi, C. *Development of an earthquake simulator for soft soils: Multidirectional Shear Testing Device.* Journal of Physics: Conference Series (Vol. 2647, No. 14, p. 142006) (2024).

2. Chang, W., Chou, S., Huang, H. and **Chao, C.**, *Development and verification of coupled hydro-mechanical analysis for rainfall-induced shallow landslides.*, Engineering Geology, 293, 106337 (2021).

1. Jommi, C., **Chao, C.**, Muraro, S. and Zhao, H., *Developing a constitutive approach for peats from laboratory data.*, Geomechanics for Energy and the Environment, 100220 (2020).

CONFERENCE PROCEEDINGS

6. Muraro, S., **Chao, C.**, Longge, S. and Jommi, C. *Back-analysis of a full-scale dyke stress test with advanced models for soft soils.* XVIII European Conference on Soil Mechanics and Geotechnical Engineering, Lisbon, Portugal (2024).

5. Muraro, S., Jommi, C. and **Chao, C.** *Interpreting repeated CPT in unsaturated soils.* 7^{th} International Conference on Geotechnical and Geophysical Site Characterization. ISC'7 2024 (pp. 566-573) (2024).

4. **Chao, C.**, Broere, W. and Jommi, C. *A new experimental setup to investigate the cyclic response of soft soils under induced earthquakes.* Symposium on Energy Geotechnics, Delft, The Netherlands (2023).

3. **Chao, C.**, Jommi, C., and Muraro, S., *Numerical investigation of the equipment set-up in triaxial testing of soft soils.* 10^{th} European Conference on Numerical Methods in Geotechnical Engineering, London, United Kingdom (2023).

2. **Chao, C.**, Muraro, S., Broere, W. and Jommi, C. *Experimental observation and constitutive modelling of the shear strength of a natural unsaturated soil.* 8^{th} International Conference on Unsaturated Soils, Milos, Greece (2023).

1. **Chao, C.**, Maarten, B. and Jommi, C. *Calibration of a simple 1D model for the hydraulic response of regional dykes in the Netherlands.* 4^{th} European Conference on Unsaturated Soils, Lisbon, Portugal (2020).

EPILOGUE

Science, like any form of exploration, is never complete. Each discovery leads to new questions, new challenges, and new opportunities for growth. As Albert Einstein wisely said, "The important thing is not to stop questioning. Curiosity has its own reason for existing." It is with this spirit of curiosity that I lay down the final words of this thesis—not as a conclusion, but as a trail. One that I hope others will follow, expand upon, and take further than I ever imagined.